

# **Direct utilization of methane: from mechanism understanding to process optimization**

Vorgelegt von  
Master-Ingenieurin  
Samira Parishan

von der Fakultät II – Mathematik und Naturwissenschaften  
der Technischen Universität Berlin  
zur Erlangung des akademischen Grades

Doktor der Ingenieurwissenschaften  
Dr.-Ing.

genehmigte Dissertation

Promotionsausschuss:

Vorsitzender: Prof. Dr. Michael Gradzielski, TU Berlin

Gutachter: Prof. Dr. Reinhard Schomäcker, TU Berlin

Gutachter: PD. Dr. Evgenii Kondratenko, Leibniz-Institut für Katalyse

Tag der wissenschaftlichen Aussprache: 14. Dezember 2018

Berlin 2019



## Acknowledgment

I like to use this chance and express my gratitude to all those who supported me in completing this thesis.

I wish to thank...

...First and foremost, my supervisor, Prof. Reinhard Schomäcker for trusting me and giving me the opportunity of doing my Ph.D. in his group. You taught me not only how to proceed with my research but also how to achieve my professional aims. It was great to know, whenever we need your support, your office door is open to us. Thanks for all you taught me, all your kindness and patience.

...Dr. Frank Rosowski and Prof. Arne Thomas for their support and the collaboration I could have with them during my work.

...PD Dr. Evgenii Kondratenko for accepting to be the examiner of my thesis.

...Prof. Dr. Michael Gradzielski for chairing my thesis examination.

...Dr. Ha Vu Le, Dr. Patrick Littelwood, Dr. Vinzenz Fleischer, Dr. Miriam Klapproth, Dr. Ewa Nowicka and Lukas Thum for the great collaboration and discussions which let me proceed faster and more successful in my work

...All my colleagues and friends from the group of Prof. Schomäcker for the beautiful time that I had with you. Special thanks to Dr. Yasemin Kasaka, Bachir Bibouche, and Dr. Daniel Peral for being on my side in the good and bad days of my staying in Berlin.

...Dr. Arash Rezaeian who strongly encouraged me to come to Germany to pursue my studies. I can hardly imagine to could reach where I am today without your support.

...My family who gave me their huge love and strong faith. My special thanks go to my older sister, Somayeh, who always supported me and pushed me to stand and fight problems rather than avoiding them.

## Abstract

Methane, which is a promising alternative to replace crude oil, is currently underutilized. Industrialization of either OCM or DMTM could realize utilization of methane to value-added chemicals. But, unfortunately, none of these reactions have still an industrially acceptable yield. In this thesis, it was searched for the solutions to overcome these yield barriers.

The focus in the OCM project was gaining a better understanding of the reaction mechanism. The  $\text{Mn}_x\text{O}_y\text{-Na}_2\text{WO}_4/\text{SiO}_2$  was chosen as the model catalyst here. It is found that under the studied conditions, the gas phase dehydrogenation of the ethane is the main reaction for the formation of ethene. The secondary oxidation of  $\text{C}_2$  components in the presence of the molecular gas phase oxygen is introduced as the main route to the formation of  $\text{CO}_x$ . The  $\text{Mn}_x\text{O}_y\text{-Na}_2\text{WO}_4$  catalyst was reported to have a low contribution to the conversion of  $\text{C}_2$  components. This behavior is assigned to the film diffusion limitations of the reaction. The so-called chemical looping reactor is proposed as an effective reactor concept for enhancing the performance of OCM toward  $\text{C}_{2+}$  products. Performing OCM in CLR resulted in the more efficient conversion of methane than the co-feeding reactor, especially at methane conversions lower than 30 %. However, the maximum yield of 30 %, required for industrializing the process, could not be achieved. This limitation is reported to be originated by the inherent nature of the  $\text{Mn}_x\text{O}_y\text{-Na}_2\text{WO}_4$  catalyst and the characteristics of the reaction mechanism. A modified two-stage process is proposed for controlling these problems. Finally, the effect of the catalyst composition on the redox behavior of the catalyst and consequently its conversion in the chemical looping reactor is investigated in more details.

In the DMTM project, the influence of the synthesis method on the performance of Cu/zeolite catalysts is investigated. The Cu/mordenite samples prepared via solid-state ion-exchanged were shown to have a much higher activity than the ones prepared by a conventional liquid-phase procedure. This behavior is assigned to the accelerated Cu exchange at the small pores of mordenite during the former procedure. The activation mechanism of methane over the Cu active sites are investigated. It is observed that different intermediates with various bonding strength are formed over the catalyst. Later, the effect of changing the support of the CuO catalyst from zeolite to SBA-15 on the production of methanol is demonstrated. A high selectivity (> 84%) via water-assisted extraction is measured for the CuO/SBA-15 sample. The cluster size of the CuO species on this sample is reported to be varied by changing the Cu-precursor applied for preparing the catalyst, leading to different catalytic performances.

## Zusammenfassung

Methan, welches ein vielversprechender Kandidat ist, Rohöl zu ersetzen, wird derzeit nur in geringem Maße eingesetzt. Die Industrialisierung von entweder OCM oder DMTM könnte die Nutzung von Methan zur Produktion werthaltiger Chemikalien ermöglichen. Ungünstigerweise erreicht allerdings keine der beiden Reaktionen eine industriell akzeptable Ausbeute. Im Rahmen dieser Arbeit wurden Lösungen gesucht, diese Limitierungen hinsichtlich der Ausbeute zu überwinden.

Der Fokus des OCM-Projektes war darauf gerichtet, ein besseres Verständnis des Reaktionsmechanismus zu entwickeln.  $Mn_xO_y-Na_2WO_4/SiO_2$  wurde hier als Modellkatalysator gewählt. Es wurde berichtet, dass unter den gewählten Reaktionsbedingungen die Gasphasendehydrierung von Ethan die Hauptreaktion zur Bildung von Ethylen darstellt. Die Sekundäroxidation von  $C_2$ -Komponenten in der Gegenwart von molekularem Gasphasensauerstoff wird als die Hauptroute zur Bildung von  $CO_x$  angeführt. Der  $Mn_xO_y-Na_2WO_4$  Katalysator liefert einen geringen Beitrag zum Umsatz der  $C_2$ -Komponenten. Dieses Verhalten wird der Filmdiffusionslimitierung unter den gewählten Reaktionsbedingungen zugeschrieben. Der sog. Chemical Looping Reaktor wurde als effektives Reaktorkonzept vorgeschlagen, um die Performance der OCM zu  $C_{2+}$ -Produkten zu verbessern. Die Reaktionsführung im CLR resultierte in einem effizienteren Umsatz von Methan verglichen mit Co-Feeding, insbesondere bei einem Methanumsatz kleiner 30%. Dennoch konnte die Ausbeute von 30%, welche für eine Industrialisierung des Prozesses nötig ist, nicht erreicht werden. Diese Limitierung wurde sowohl auf die inhärente Natur des Katalysators als auch die Charakteristika des Reaktionsmechanismus zurückgeführt. Ein modifizierter Zweistufenprozess wurde zur Minimierung der Probleme vorgeschlagen. Zuletzt wurde der Einfluss der Katalysatorzusammensetzung auf das Redoxverhalten des Katalysators und folglich den im Chemical Looping Reaktor erreichten Umsatz detaillierter untersucht.

Im DMTM-Projekt wurde der Einfluss der Synthesemethode auf die Performance von Cu/Zeolith-Katalysatoren bewertet. Cu/Mordenit-Proben, welche über Feststoffionenaustausch dargestellt wurden, zeigen eine viel höhere Aktivität als über das konventionelle Flüssigphasenverfahren präparierte Katalysatoren. Dies wurde zurückgeführt auf den im Feststoffionenaustausch beschleunigten Cu-Austausch in den kleinen Poren des Mordenit. Weiterhin wurde der Methanaktivierungsmechanismus an den aktiven Kupferzentren untersucht. Es wurde beobachtet, dass unterschiedliche Intermediate verschiedener Bindungsstärke auf der Katalysatoroberfläche gebildet werden. Darüber hinaus wurde der Effekt eines Wechsels des Trägers für den CuO-Katalysator von Zeolith zu SBA-15 im Hinblick auf die Bildung von Methanol aufgezeigt. Über wasserunterstützte Extraktion wurde für die CuO/SBA-15-Probe eine hohe Selektivität (> 84%) gemessen. Die Clustergröße der CuO-Spezies auf dieser Probe konnte durch Wechsel des Cu-Prekursors in der Katalysatorpräparation beeinflusst werden, was zu einer Änderung der katalytischen Aktivität führte.

## Erklärung zur Dissertation

Ich erkläre hiermit, dass ich bislang an keiner anderen Hochschule oder Fakultät meine Promotionsabsicht beantragt habe.

Die vorliegende Dissertation wurde bereits in Form von wissenschaftlichen Publikationen veröffentlicht. Es handelt sich hierbei um große Teile der folgenden Veröffentlichungen:

**Paper 1:** Investigation of the surface reaction network of the oxidative coupling of methane over  $\text{Na}_2\text{WO}_4/\text{Mn}/\text{SiO}_2$  catalyst by temperature programmed and dynamic experiments

Vinzenz Fleischer, Rolf Steuer, *Samira Parishan* and Reinhard Schomäcker

Journal of Catalysis, 2016, 341, 91-103, DOI: 10.1016/j.jcat.2016.06.014

Own contribution (Eigenanteil): I am the third author. This paper is investigating the surface-mediated reaction mechanism of OCM in the absence of gas phase oxygen. It explains the reducibility and oxygen desorption behavior of the  $\text{Mn}-\text{Na}_2\text{WO}_4/\text{SiO}_2$  catalyst. Moreover, the amount of oxygen availability of the catalyst is measured in a series of dynamic experiments. I conducted the TPSR experiments with ethane and ethylene and analyzed their results. Based on this data, I concluded that the conversion of ethane under our tested conditions is mainly conducted thermally in the gas phase rather than on the catalyst surface.

**Paper 2:** Chemical looping as a reactor concept for oxidative coupling of methane over a  $\text{Na}_2\text{WO}_4/\text{Mn}/\text{SiO}_2$  catalyst

Vinzenz Fleischer, Patrick Littlewood, *Samira Parishan*, and Reinhard Schomäcker

Chemical Engineering Journal, 2016, 306, 646-654, DOI: 10.1016/j.cej.2016.07.094

Own contribution (Eigenanteil): I am the third author. This paper explains the construction of the chemical looping reactor (CLR) in the lab scale to realize the separation of oxygen and methane feed in the OCM reactor. The OCM reaction performance was successfully enhanced in the CLR in comparison to the traditional co-feeding reactors. However, a maximum yield of 30 % which is needed for industrializing the process could not be achieved. I assisted in designing and building the reactor set up, calibrating the mass spectrometer, generating the measurement method, and analyzing the experimental results.

**Paper 3<sup>1</sup>:** Solid-state ion-exchanged Cu/mordenite catalyst for the direct conversion of methane to methanol

Ha V. Le, **Samira Parishan**, Anton Sagaltchik, Caren Göbel, Christopher Schlesiger, Wolfgang Malzer, Annette Trunschke, Reinhard Schomäcker, Arne Thomas

ACS Catalysis. 2017, 7, 1403–1412, DOI: 10.1021/acscatal.6b02372

Own contribution (Eigenanteil): I am the second author. This paper focuses on the synthesis and characterization of the typical Cu-Zeolite, which are known as the best performing heterogeneous catalysts, for the DMTM reaction. The copper species supported over mordenite were prepared through either solid or liquid phase ion exchange methods. First, the reaction performance of each of these samples is measured. Then, the behavior of the best performing catalyst is studied in more details using *in-situ* characterization techniques. I carried the performance test studies and did the calculations. I analyzed the TPR experimental results and based on the obtained results proposed the presence of at least two sorts of adsorbed methoxy species over the catalyst surface.

**Paper 4:** Chemical looping as a reactor concept for the oxidative coupling of methane over the  $Mn_xO_y-Na_2WO_4/SiO_2$  catalyst, benefits and limitations

**Samira Parishan**, Patrick Littlewood, Aleks Arinchtein, Vinzenz Fleischer, Reinhard Schomäcker

Catalysis Today, 2017, 311, 40-47, DOI: 10.1016/j.cattod.2017.08.019

Own contribution (Eigenanteil): I am the first author. This paper discusses the reasons for the yield limitation observed for OCM conducted in the chemical looping reactor (paper 2). I showed that both the inherent nature of the  $Mn_xO_y-Na_2WO_4$  catalyst and the characteristics of the reaction mechanism cause this limitation. Based on these results, I suggested a modified process concept for OCM in chemical looping reactor which may realize achieving the  $C_{2+}$  yield of higher than 30 %.

---

<sup>1</sup> Reproduced in part with permission from "ACS Catalysis. 2017, 7, 1403–1412, DOI: 10.1021/acscatal.6b02372" Copyright 2017, American Chemical Society

**Paper 5:** Investigation of the role of the  $\text{Na}_2\text{WO}_4/\text{Mn}/\text{SiO}_2$  catalyst composition in the oxidative coupling of methane by chemical looping experiments

***Samira Parishan*\***, ***Vinzenz Fleischer*\***, Ulla Simon, Maria Gracia Colmenares, Oliver Görke, Aleksander Gurlo, Wiebke Riedel, Lukas Thum, Johannes Schmidt, Thomas Risse, Klaus-Peter Dinse and Reinhard Schomäcker

Journal of Catalysis, 2018, 360, 102-117, DOI: 10.1016/j.jcat.2018.01.022

Own contribution (Eigenanteil): I am the first author together with Vinzenz Fleischer. This paper is studying the effect of the catalyst composition on the performance of OCM in CLR. The studies in paper 4 introduced the low conversion, rather than selectivity, as the main reason for the yield limitation of OCM in CLR. Therefore, to enhance the conversion level of the reaction, the redox capability of the catalyst was tuned by changing the concentration of the active metal species in it. The catalyst behavior was investigated in more details through implementing techniques such as EPR, XPS, and TEM. I assisted in planning the experiments and analyzing the data. I took responsibility for the catalyst characterization studies and prepared the samples for those analyses.

**Paper 6:** Investigation into consecutive reactions of ethane and ethene under the OCM reaction conditions over  $\text{Mn}_x\text{O}_y\text{-Na}_2\text{WO}_4/\text{SiO}_2$  catalyst

***Samira Parishan***, Ewa Nowicka, Vinzenz Fleischer, Christian Schulz, Maria G. Colmenares, Frank Rosowski, Reinhard Schomäcker

Catalysis Letters, 2018, 148, 1659-1675, DOI: 10.1007/s10562-018-2384-6

Own contribution (Eigenanteil): I am the first author. This paper is studying the consecutive reaction of  $\text{C}_2$  components under the OCM reaction conditions. The secondary oxidation of these components is already known as the main routes for producing  $\text{CO}_x$  in the OCM reactor. In this study, I could reveal the high contribution of molecular gas phase oxygen on the secondary oxidation of  $\text{C}_2$  components. I showed that under the OCM reaction conditions, the film diffusion limits the catalytical conversion of  $\text{C}_2$  components.

**Paper 7:** Stepwise methane-to-methanol conversion on  $\text{CuO}/\text{SBA-15}$

Ha V. Le, **Samira Parishan**, Anton Sagaltchik, Hamideh Ahi, Annette Trunschke, Reinhard Schomäcker, and Arne Thomas

Chem. Eur. J. 2018, 24, 12592 – 12599, DOI: 10.1002/chem.201801135

Own contribution (Eigenanteil) I am the second author. This paper surveys the possibility of changing the support of the Cu/Mordenite catalyst to SBA-15. Secondly, it investigates the mechanism of producing dimethyl ether besides methanol during the DMTM reaction. Moreover, it discusses the nature and location of the active sites of the CuO/SBA catalyst based on the results obtained in the *in-situ* characterization analysis. I did the data analysis and discussion of the water and methanol saturated washing experiments presented in this paper.

# Table of contents

<b>Introduction.....</b>	<b>1</b>
<b>1.1 Motivation.....</b>	<b>1</b>
<b>1.2 Theoretical background .....</b>	<b>2</b>
<b>1.3 Research scope and outline of this thesis .....</b>	<b>3</b>
<b>1.3.1 OCM.....</b>	<b>6</b>
<b>1.3.2 Mechanism.....</b>	<b>7</b>
<b>1.3.3 DMTM .....</b>	<b>10</b>
<b>Methods and materials .....</b>	<b>13</b>
<b>2.1 Catalyst preparation.....</b>	<b>13</b>
<b>2.1.1 OCM.....</b>	<b>13</b>
<b>2.1.2 MTM .....</b>	<b>13</b>
<b>2.2 Characterization of catalysts .....</b>	<b>14</b>
<b>2.2.1 Powder X-ray Diffraction (XRD) .....</b>	<b>14</b>
<b>2.2.2 N<sub>2</sub> sorption analysis.....</b>	<b>14</b>
<b>2.3 Feed Gases .....</b>	<b>14</b>
<b>2.4 Experimental setup .....</b>	<b>15</b>
<b>Results and discussion .....</b>	<b>17</b>
<b>3.1 OCM.....</b>	<b>17</b>
<b>3.1.1 TPSR investigations .....</b>	<b>15</b>
<b>3.1.2 TPSR investigation with methane .....</b>	<b>17</b>
<b>3.1.3 Details of the consecutive reaction of C<sub>2</sub> components.....</b>	<b>20</b>
<b>3.1.4 Chemical looping as a reactor concept for OCM.....</b>	<b>23</b>
<b>3.1.5 Role of the catalyst composition on the operation of Mn<sub>x</sub>O<sub>y</sub>-Na<sub>2</sub>WO<sub>4</sub>/COK-12 ...</b>	<b>30</b>
<b>3.1.6 Conclusions of OCM project.....</b>	<b>37</b>
<b>3.2 MTM .....</b>	<b>38</b>
<b>3.2.1 Solid-state ion-exchanged Cu/mordenite catalyst for the direct conversion of methane to methanol .....</b>	<b>38</b>
<b>3.2.2 Stepwise methane-to-methanol conversion on CuO/SBA-15.....</b>	<b>46</b>

<b>3.2.3</b>	<b>Conclusions of DMTM project .....</b>	<b>52</b>
	<b>Conclusions .....</b>	<b>53</b>
	<b>Reference .....</b>	<b>54</b>
	<b>Appendix .....</b>	<b>61</b>

## List of abbreviations

<b>Abbreviation</b>	<b>Description</b>
OCM	Oxidative coupling of methane
DMTM	Direct methane to methanol
DME	Dimethyl ether
HCN	Hydrogen cyanide
CLR	Chemical looping reactor
CLC	Chemical looping concept
TPSR	Temperature programmed surface reaction
TPR	Temperature program reduction
TDH	Thermal dehydrogenation
GC	Gas chromatography
MS	Mass spectrometer
XRD	X-ray powder diffraction
XPS	X-ray photoelectron spectroscopy
EPR	Electron paramagnetic resonance
TEM	Transition electron microscopy
EXAFS	Extended X-ray absorption fine structure
XANES	X-ray absorption near edge structure

# Introduction

## 1.1 Motivation

Crude oil remains the most important feedstock for producing the majority of the essential chemicals in the industry [1–4]. However, the concern of depletion of petroleum reserves, its volatile market, and growing environmental concerns, has increased the interest in shifting toward more reliable and cleaner sources of feedstocks [1,2,5]. One of the options considered to fulfill this aim is Biomass. However, there are strong concerns about the feasibility of the complete replacement of oil with this resource [1,2]. Firstly, the production of biomass is limited due to the restriction in accessing the cultivation areas. Secondly, the energy efficiency of biomass fuels is lower than oil-based fuels such as gasoline [1].

Methane, the main component of natural gas, is the other attractive alternative feedstock. This compound is cheaper and more abundant than crude oil [1,2,4–10]. Unfortunately, nowadays, almost 90 % of the global production of methane is just combusted to generate energy for different sectors [1,6,9]. The high transportation costs and stability of methane molecules are the most important reasons for its current underutilization [2,5,11]. Formation of HCN and syn-gas are almost the only industrial routes available for utilization of methane. Despite that the former process converts methane directly to a value-added product, the low market demand of HCN limits its application [5,7,11,12]. While the syn-gas is more demanded as it is processed to produce a wide range of essential chemicals like methanol, hydrogen, ammonia, and higher chain hydrocarbons [1,4–6,12–15]. One of the most important drawbacks of syn-gas production is the high energy intensity of its process. During this conversion, almost 25% of the natural gas feed is consumed to produce the heat of the reaction [16]. Therefore, it can be concluded that through realizing the direct conversion of methane to essential chemicals, the profitability of its utilization can be significantly enhanced. Oxidative coupling of methane (OCM) and the direct oxidation of methane to methanol (DMTM), respectively presented in Eq-1 to 3, might be the milestone to realize this goal [1,5,7]. Both these reactions convert methane directly to chemicals which are vastly used in the industry. Ethene, the product of OCM, is the building block for producing Polyethylene, polyvinyl chloride, polystyrene, ethylene glycol, etc. [17]. While methanol is used either as a fuel in the automotive industry or reactant to produce other important chemicals like formaldehyde, acetic acid, and dimethyl ether [2,18].



Nowadays, to produce ethene, steam-cracking of a range of petroleum-based feedstocks such as naphtha is conducting[19,20]. However, by realizing OCM, the reaction feedstock will be switched to methane. The current technologies applied for producing methanol are based on indirect utilization of methane [6,12,14,16,21]. Operating this process is not only expensive but also dangerous. On one side, the cost of syngas production should be covered, on the other side, the harsh operating conditions, such as high pressure and temperatures ( $p > 50$  bar,  $T > 800$  °C), required for converting the CO and H<sub>2</sub> to methanol should be managed [2]. However, through realizing the DMTM, methane can be converted to methanol at moderate reaction conditions (atmospheric pressure and  $T < 300$  °C).

## 1.2 Theoretical background

As presented in Eqs 1-3, both OCM and DMTM reactions are conducted in the presence of an oxidizing agent (normally oxygen). Oxidizers are the reactants for the latter reaction while they convert the former reaction from endothermic to exothermic [1,5,6,22–24]. However, the presence of oxidizing agents in the reactor brings the thermodynamically favored total and partial oxidation reactions, presented in Eqs 4 and 5, in competition with the selective ones, presented in Eqs 1-3 [2,24–26].



Noteworthy, C<sub>2</sub> components and methanol are more active than methane. Therefore, there is always the danger of their consecutive reaction to CO<sub>x</sub> [1,2,5,8]. The occurrence of burning reactions not only result in the loss of selectivity but also they generate a lot of heat which lead to the formation of hot-spots in the reactor [24,27]. So far, these obstacles have prevented the industrial application of both OCM and DMTM. The performance obtained in DMTM is still far below the industrially required values. While for OCM just one startup company, called Siluria Technology, has claimed to have succeeded in scaling up the process [28]. However, little information is released on their implemented process and its cost-effectivity. These are

indicating the necessity to find appropriate techniques which can help in enhancing the performance of both OCM and DMTM.

To achieve this goal, these reactions have been being investigated from different aspects within the cluster of excellence, unifying concepts in catalysis (Uni-Cat), in the last 10 years. These studies, which have been done so far more intensively on OCM than DMTM, cover the broad range of catalyst engineering [23,25,29–32], fundamental understanding of the reaction behavior [27,33–37], reactor design [38] and process scaling up [38–41]. This thesis is conducted in continuation to the former investigations conducted in Uni-Cat on the topic of methane activation over heterogeneous catalysis. It consists of the studies performed on both the OCM and DMTM reactions. The outline of the work and the most important findings of the research done on each of OCM and DMTM reactions are discussed in the following sections.

### **1.3 Research scope and outline of this thesis**

The research in this thesis covers both OCM and DMTM as two of the important reactions which make direct utilization of methane possible. The focus of the investigations performed on OCM was to gain a better and detailed understanding of the reaction behaviour. The  $Mn_xO_y-Na_2WO_4/SiO_2$ , which is known in the literature for its high stability and good performance for OCM, was chosen as the model catalyst in these studies [8,26,42–44]. The OCM reaction mechanism was surveyed with the aim of gaining a better understanding of the origin of the formation of the unselective reaction products, i.e., carbon oxides. Based on the mechanistic findings, a new reactor set up, known as chemical looping, was suggested for enhancing the performance of the OCM reaction toward  $C_{2+}$  products. The chemical looping reactor was built in our lab and its effect on suppressing the rate of unselective oxidation reactions was tested. Despite the improvement observed in the reaction performance, the minimum 30 % yield of  $C_2$  products could unfortunately not be overcome in the chemical looping reactor. As this yield limitation was not consistent with our understanding of the reaction mechanism, the reasons for this behavior were studied in the next step. Finally, the effect of the catalyst composition on the redox potential of the catalyst and consequently its activity was studied in the chemical looping reactor.

In the second project, the influence of the synthesis method on the performance of Cu/zeolite catalysts, which are known in the literature as the best performing heterogeneous catalysts for the DMTM reaction, were investigated. The behavior of the best performing sample was

surveyed in more details by implementing *in-situ* catalyst characterization and mechanism investigation techniques. Afterwards, certain reaction parameters were varied to find out more about their effect on the performance of the catalyst.

This thesis is built based on the results of these studies, which are published as 7 articles in peer-reviewed journals. In the following, you firstly find a brief explanation of the main points discussed in each of these articles then, the connection between them as presented Fig 1.1.

### **Oxidative Coupling of Methane (OCM):**

**Paper 1** is investigating the surface-mediated reaction mechanism of OCM in the absence of gas phase oxygen. The reducibility and oxygen desorption behavior of the Mn-Na<sub>2</sub>WO<sub>4</sub>/SiO<sub>2</sub> catalyst were investigated. The amount of oxygen availability of the catalyst was measured in a series of dynamic experiments.

**Paper 6** is studying the consecutive reaction of C<sub>2</sub> components, which are known as the main routes for producing CO<sub>x</sub> in the OCM reactor. These studies revealed the high contribution of molecular gas phase oxygen on the secondary oxidation of C<sub>2</sub> components. Based on these studies, implementing chemical looping reactor was suggested as the milestone to enhance the performance of OCM.

**Paper 2** explains the construction of the chemical looping reactor in the lab scale to realize the separation of oxygen and methane feed in the OCM reactor. The mechanistic studies presented in the sixth paper revealed the high contribution of molecular gas phase oxygen on secondary oxidation of C<sub>2</sub> components. Therefore, to suppress the rate of over oxidation reactions, the flow of oxygen and hydrocarbon were separated by implementing the chemical looping reactor. Under these circumstances, the reaction performance of OCM was successfully enhanced. However, a maximum yield of 30 % which is needed for industrialization of the process could not be achieved.

**Paper 4** discusses the reasons for the yield limitation observed for OCM conducted in the chemical looping reactor. The results of these studies lead to proposing a modified process concept which might be the milestone to industrializing the OCM using CLC.

**Paper 5** discusses the effect of the catalyst composition on the performance of OCM in CLR. Paper 4 introduced the methane conversion rather than the selectivity as the main parameter limiting the yield of OCM in the CLR. Therefore, by the aim of enhancing the reaction conversion, the redox capability of the catalyst was tuned through changing the concentration

of the active metal species in it. The behavior of the catalyst along the reaction was studied in more details in a series of EPR, XPS, and TEM analysis.

### Direct Methane to Methanol (DMTM)

**Paper 3** focuses on the synthesis and characterization of the typical Cu-zeolite catalysts known for the DMTM reaction. The catalysts are synthesized over several sorts of zeolites with either solid or liquid phase ion exchange methods. First, the reaction performance of each of these samples is measured. Then, the behavior of the best performing catalyst is studied by applying *in-situ* characterization techniques.

**Paper 7** firstly surveys the effect of changing the catalyst support from zeolite to SBA-15 on the performance of the DMTM reaction. Secondly, it investigates the possibility of producing more valuable dimethyl ether instead of methanol by modifying the reaction parameters.

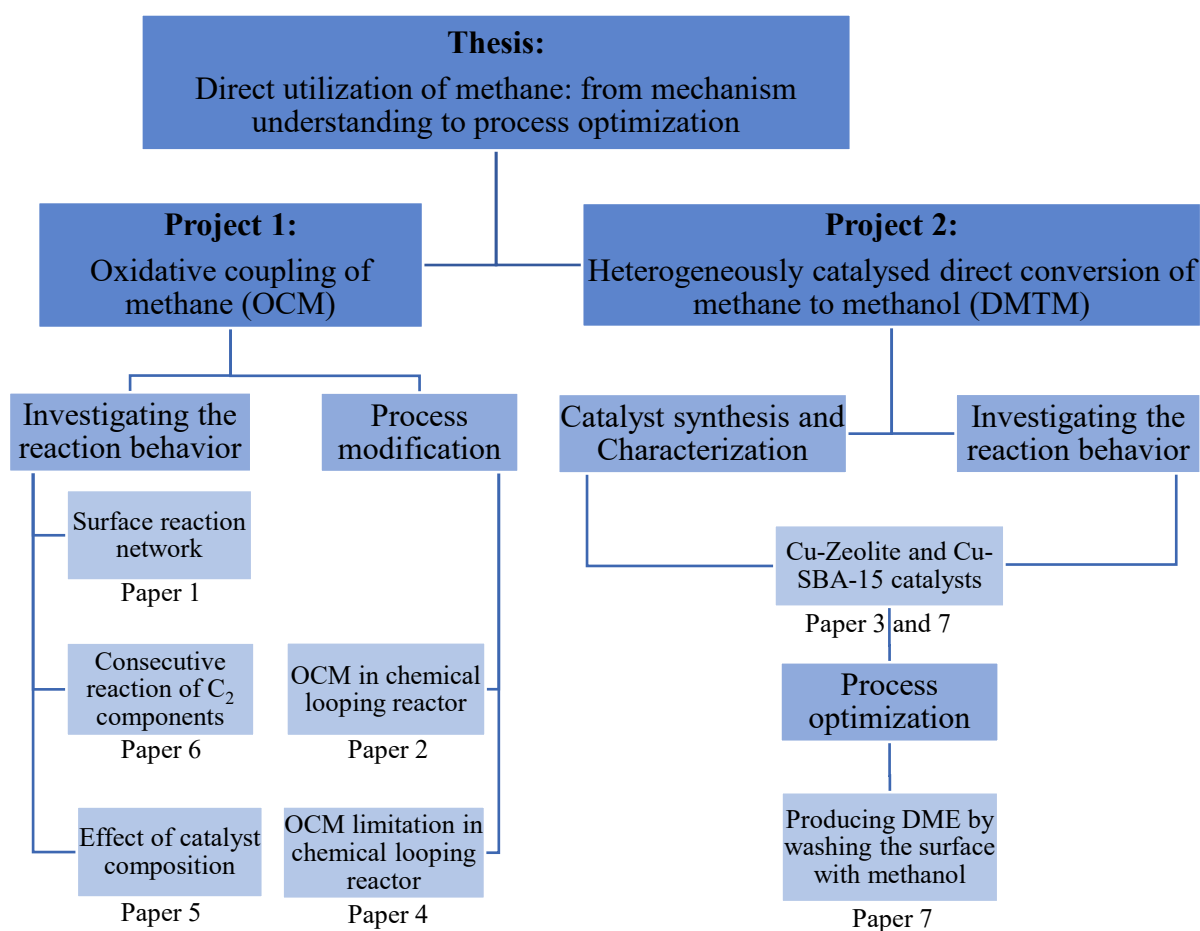


**Figure 1. 1** Schematic representation of the structure of the thesis

### 1.3.1 OCM

In this section, the literature findings on the OCM reaction which are important in discussing the results of this thesis are briefly reviewed.

#### 1.3.1.1 Catalyst material

Since the pioneering work of Keller and Bhasin, a large number of catalysts have been tested for OCM [45]. As mentioned earlier, unselective oxidation of methane is thermodynamically more favorable than the coupling reaction. Therefore, to decrease their reaction rate and controlling them kinetically, there is a vital need to use a catalyst [25,46]. In this regard, several different active metals, supports, catalyst promoters, and synthesis methods have been tested so far [25,47–49]. The latest statistical investigations, which analyzed 1868 data sets, reported the implementation of almost all possible combination of 69 different elements as the catalyst for OCM [50]. These large efforts on catalyst preparation were made to obtain a stable catalyst with a significant yield to C<sub>2</sub> products. However, almost all of these catalysts are still suffering from either long-term instability or low productivity [1,7,8,18,51].

To decrease the size of the practical efforts required for finding an appropriate catalyst, many theoretical and statistical studies have been made in parallel to experimental studies [49,50,52–54]. In one of those studies, the most active OCM catalysts were reported to be consisting of one host metal and two metal dopant oxides [50]. This idea is proved in a systematic experimental study [49]. In the other studies, the catalysts of OCM are proposed to be classifiable into 4 different groups. Those are (i) non-reducible metal oxides, (ii) reducible metal oxides, (iii) halogen-containing oxide materials, and (iv) solid electrolytes [51]. These classifications are done based on the characteristics and composition of the samples. For example, the non-reducible metal oxides are active in the co-feeding of oxygen and methane. But, the reducible metal oxides can store oxygen on their surface and provide the lattice oxygen when methane is present in the reactor. The samples in the third group, i.e., halogen-containing oxide materials, have a good performance. However, under the harsh reaction condition of OCM, the halogen leaves the surface and the catalyst loses its activity. The solid electrolytes are mainly implemented in the membrane reactors by the aim of separating oxygen and CH<sub>4</sub> flow from each other [51].

Nevertheless, despite this vast range of catalysts known for OCM, Li/MgO, La<sub>2</sub>O<sub>3</sub>, and Mn-Na<sub>2</sub>WO<sub>4</sub> could be named as the most frequently studied and best-performing candidates [22,25,51,55]. For several years, Li/ MgO was the model catalyst for many experimental and

theoretical studies[23,56–60]. However, it was finally concluded that this catalyst is an unsuitable candidate for industrialization of OCM as it loses its initial activity soon after starting the reaction [23,25]. However, both  $\text{La}_2\text{O}_3$  and  $\text{Mn-Na}_2\text{WO}_4/\text{SiO}_2$  are shown to have comparable stability and performance, which is several times better than  $\text{Li/MgO}$ . Therefore, their chance for industrialization is reported to be higher than  $\text{Li/MgO}$ . Surveying the literature shows that the interest in  $\text{Mn-Na}_2\text{WO}_4/\text{SiO}_2$  is exceeding that of  $\text{La}_2\text{O}_3$ . First, because of the significant increase recently observed in its performance by changing the support from silica gel to the ordered-mesopore SBA-15 [29]. Second, some features of the  $\text{Mn-Na}_2\text{WO}_4/\text{SiO}_2$  catalyst, such as the oxygen storage capability and higher resistance to attrition, make it industrially more attractive than  $\text{La}_2\text{O}_3$ . The  $\text{Mn-Na}_2\text{WO}_4/\text{SiO}_2$  is classified as a reducible metal oxide while  $\text{La}_2\text{O}_3$  is non-reducible [51]. This characteristic gives the former the possibility of storing oxygen which can be released in the presence of the reducing components. This feature allows implementing reactor techniques such as chemical looping in the presence of  $\text{Mn-Na}_2\text{WO}_4/\text{SiO}_2$  [37,38].

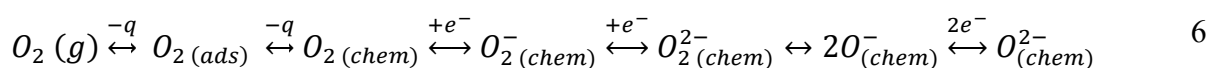
Moreover, as  $\text{Mn-Na}_2\text{WO}_4/\text{SiO}_2$  is a granular catalyst, it causes less pressure drop than the powder form  $\text{La}_2\text{O}_3$ . The simplicity and cheapness of the wetness impregnation method applied for synthesizing  $\text{Mn-Na}_2\text{WO}_4/\text{SiO}_2$  can be pointed out as one other advantage [61]. All these encouraged us to conduct our studies with  $\text{Mn-Na}_2\text{WO}_4/\text{SiO}_2$  instead of  $\text{La}_2\text{O}_3$ .

The effect of composition concentration and synthesis methods on the performance of this trimetallic catalyst, i.e.  $\text{Mn-Na}_2\text{WO}_4/\text{SiO}_2$ , is already investigated in the literature [8,62]. The highest  $\text{C}_{2+}$  yield was observed for the samples prepared through wetness impregnation and at the concentration ranges of 0.4%–2.3% Na, 2.2%–8.9% W and 0.5%–3% Mn [8,62,63]. Based on the powder X-Ray diffractograms (XRD) analysis, the  $\alpha$ -cristobalite silica,  $\text{Mn}_2\text{O}_3$ , and  $\text{Na}_2\text{WO}_4$  are introduced as the main phases over the catalyst surface [29,30,61,64]. These crystal phases seem to disappear at OCM reaction temperature (ca. 700 °C) [30,37,65–67]. This behavior is assigned to the transformation of the catalyst surface to a more flexible and quasi-liquid one under the reaction conditions [37,65–67].

### 1.3.2 Mechanism

OCM has a complicated reaction network consisting of both homogeneous and heterogeneous parts. The homogeneous part of the OCM mechanism is shown to be well presented by the Dooley gas phase micro-kinetic-model [68–70]. However, there are debates on the details of the heterogeneous part of the mechanism, which is also a function of the catalyst in use.

Nevertheless, there are still some surface reaction steps which are well accepted in the literature and are common between all types of catalysts. For example, it is proposed that during OCM, similar to several other selective oxidation reactions, oxygen is activated over the catalyst and forms different intermediate species as presented in Equation 6 [46]. Methane is reported to activate either homiletically or heterolytically in reaction with these oxygen species and form methyl radicals [2,24,51,71,72]. Next, methyl radicals participate in several parallel reactions, which their rate defines the final selectivity of OCM. While the consecutive reaction of methyl radicals with oxygen species is reported to result in the formation of CO<sub>x</sub>, the coupling of two of them is proposed to form ethane [24,51,72–76]. The nature of the surface oxygen species is the other parameter influencing the selectivity of OCM [33]. The O<sub>(chem)<sup>-</sup></sub> is proposed as the selective form while O<sub>2(ads)</sub> is reported to cause mostly over-oxidation reactions [37,46]. Noteworthy, ethen, the final product of OCM, is widely accepted to form by consecutive reaction of ethane rather direct conversion of methane [71].



Reaction network of OCM is certainly more complicated than that explained and it involves several other intermediates. Many efforts have been made to complete the picture of these changes as this information makes applying a systematical modification of the catalyst structure or process parameters easier.

Lunsford was one of the firsts who proposed a catalytic cycle to explain the OCM reaction over Li/MgO [24]. He introduced Li<sup>+</sup>O<sup>-</sup> as the active center of the catalyst [24]. However, this suggestion was in contrast to the later studies where no linear correlation was found between the loss of Li from the catalyst surface and the decrease in its activity [23]. Besides, the active sites over the pure MgO catalyst and the one doped with lithium were reported to be identical. These evidence left strong doubts on the accuracy of the reaction cycle suggested by Lunsford [23,52,54]. In recent literature, Li is mostly considered as the morphology and structure modifier for MgO. Li is reported to tun the steps and corners of the catalyst, which are proposed being the active centers of the catalyst [52,53].

The microkinetic model suggested by Sun fits the experimental results measured for Li/MgO better than the Lusfered model [77]. Lee *et al.* suggested a model similar to the Sun for the reaction of OCM over Mn<sub>2</sub>-Na<sub>2</sub>WO<sub>4</sub>/SiO<sub>2</sub> [74]. This model was completed by Beck *et al.*, who studied the surface reactions occurring over this catalyst through pump-probe experiments [33]. Beck proposed the formation of at least two different sorts of oxygen active species including

physisorbed and the strongly adsorbed chemisorbed ones over the surface of the Mn<sub>2</sub>-Na<sub>2</sub>WO<sub>4</sub>/SiO<sub>2</sub> catalyst. He reported that the former species cause unselective oxidation reactions while the latter mainly cause selective ones. Table 1.1 presents these three reaction models in comparison to each other.

**Table 1. 1** - Comparison of micro-kinetic surface reaction models from Lee *et al.*, Sun *et al.* and Beck *et al.* (x, y, z = stoichiometric factors). (**Paper 1**)

Sun <i>et al.</i> [77]	Lee <i>et al.</i> [74]	Beck <i>et al.</i> [33]
$O_2 + 2 * \rightleftharpoons 2 O *$	$O_2 + 2 * \rightleftharpoons 2 O *$	$O_2 + * \rightleftharpoons O_{2,ads}$ $O_{2,ads} \rightleftharpoons y O_x *$
$CH_4 + O * \rightleftharpoons CH_3 \cdot + OH *$	$CH_4 + O * \rightleftharpoons CH_3 \cdot + OH *$	$CH_4 + O * \rightleftharpoons CH_3 \cdot + OH *$
$C_2H_4 + O * \rightleftharpoons C_2H_3 \cdot + OH *$	$C_2H_4 + O * \rightleftharpoons C_2H_3 \cdot + OH *$	$C_2H_4 + O * \rightleftharpoons C_2H_3 \cdot + OH *$
$C_2H_6 + O * \rightleftharpoons C_2H_5 \cdot + OH *$	$C_2H_6 + O * \rightleftharpoons C_2H_5 \cdot + OH *$	$C_2H_6 + O * \rightleftharpoons C_2H_5 \cdot + OH *$
$2 OH * \rightleftharpoons H_2O * + O *$		$2 OH * \rightleftharpoons H_2O * + O *$
$CH_3 \cdot + O * \rightleftharpoons CH_3O \cdot *$	$CH_3 \cdot + 3 O * \rightleftharpoons HCO \cdot * + 2 OH *$	
$CH_3O \cdot * + O * \rightleftharpoons CH_2O * + OH *$		
$CH_2O * + O * \rightleftharpoons HCO \cdot * + OH *$		
$HCO \cdot * + O * \rightleftharpoons CO * + OH *$	$HCO \cdot * + O * \rightleftharpoons CO * + OH *$	
$CO * + O * \rightleftharpoons CO_2 * + *$	$CO * + O * \rightleftharpoons CO_2 * + *$	
$CO + * \rightleftharpoons CO *$		
$CO_2 + * \rightleftharpoons CO_2 *$		
$4 HO_2 \cdot \rightarrow 3 O_2 + 2 H_2$	$2 OH * \rightleftharpoons H_2O + O * + *$	
		$x O_{2,ads} + CH_4 \rightleftharpoons CO_y + z H_2O *$
		$x O_{2,ads} + C_2H_6 \rightleftharpoons 2 CO_y + z H_2O *$
		$x O_{2,ads} + C_2H_4 \rightleftharpoons 2 CO_y + z H_2O *$

In studying the surface mechanism, it is important to identify the role of each of the active metals on the reactions involved in the process. Investigating this parameter for our trimetallic model catalyst, Mn<sub>x</sub>O<sub>y</sub>-Na<sub>2</sub>WO<sub>4</sub>/SiO<sub>2</sub>, is quite difficult if not impossible. However, it is already known that the performance of this catalyst strongly depends on the concentration and dispersion of all the three metal active compounds present on the surface of the support [29,78,79]. It is observed that the cooperation between these metal oxides is vital to get an acceptable catalytic performance [8]. The most important role of Na is proposed to be facilitating the phase transition of the SiO<sub>2</sub> from amorphous to α-cristobalite [8]. The crystallization of the silica is shown to be a crucial step in catalyst performance as it turns the support from unselective to inert [8,43]. The phase transition of the support is also suggested to result in the stabilization of the surface tungsten species, probably WO<sub>4</sub> [37]. The tungsten oxides are reported to be the selective catalytic sites. They go through a redox mechanism involving W<sup>+6</sup>/W<sup>+5</sup> during the activation of methane [8,80]. The pure Mn<sub>x</sub>O<sub>y</sub>/SiO<sub>2</sub> is observed to have a low selectivity for methane activation [37]. This observation, which is in good agreement with the high reducibility of this metal oxide, is in contrast with its enhancing effect on the performance of OCM in combination with Na<sub>2</sub>WO<sub>4</sub> [37]. Some literature has explained

this behavior by suggesting  $Mn_xO_y$  as an oxygen spillover in cooperation with  $WO_4$  [8,81]. There is another idea which is less accepted and proposes  $Mn^{3+}$  as the oxygen activating center while the  $W_{6+}$  sites are considered to be participating in cleaving the C-H bond of  $CH_4$  [8].

### 1.3.3 DMTM

The DMTM reaction can be conducted in both catalytic and noncatalytic systems. The latter is performing through a homogeneous radical gas phase reaction which makes implementing high temperatures and pressure unavoidable [2,18,82,83]. However, to increase the reaction performance and making the operational conditions milder, the reaction is conducted catalytically [1,14,18,84]. Methanotrophic bacteria conduct the most selective DMTM reactions at room temperature [2,85–87]. They perform the reaction using so-called methane monooxygenases (MMO) enzymes. MMOs are classified into two groups of soluble MMO (sMMO) and particulate MMO (pMMO) [10]. The former oxidizes methane by a diiron cluster, which possesses a bis- $\mu$ -oxo diamond core structure [1,88]. But, the metal composition and location of the pMMO's active sites are not still truly known [88]. The activity of these enzymes is assigned to the presence of copper in the cluster structure [16,32,86,88]. In the last few decades, by inspiration of the MMOs, numerous novel catalysts have been synthesized and tested for the DMTM reaction [1,2,14,84,86,87]. The reaction performance of several homogeneous and heterogeneous catalytic systems have been investigated in the presence of a wide range of oxidizing agents such as  $N_2O$ ,  $O_2$ ,  $O_3$ ,  $CO_2$ ,  $H_2O_2$ ,  $H_2SO_4$ . A brief overview of the most important results of those studies is presented in section 1.3.3.1 [1,18,21,83,84].

#### 1.3.3.1 Homogeneous catalysts

Mercury(II) or platinum(II) based catalysts, known as Periana catalysts, are among the first well performing homogeneous catalysts tested for DMTM reaction using  $H_2SO_4$  as oxidant [1,83,84]. The performance of transition metal chloride solutions has been studied in the presence of  $H_2O_2$  and  $O_2$ . The productivity of methanol in these investigations especially in the presence of  $O_2$  was reported to be low [1]. The other widely studied group of homogeneous catalysts are those consisting of copper and Fe which mimics the structure of MMOs [84,86,89,90]. A recent review article surveyed the reaction performance of a wide range of homogeneous catalysts tested in the literature for DMTM. It has been reported that at least 14 of the studied samples show promising yield for the reaction, methane conversion higher than 10 % and methanol selectivity of above 50 %. However, because of the technical and economical limitations originated from the applied reaction conditions, none of these samples can be used on an industrial scale. The first drawback of these catalysts is their high price and

short lifetime. Under the applied reaction conditions, the expensive Nobel metals, such as Pt, Pd or Rh, implemented in these catalysts are reported to prefer to participate in the irreversible reduction reactions [1,2,84,91]. Some literature has even presented evidence regarding the leaching of the active metals in these catalysts [83]. Besides, in these studies, either H<sub>2</sub>O<sub>2</sub> or H<sub>2</sub>SO<sub>4</sub> has been used as the oxidizing agent which are not suitable options [84,91]. H<sub>2</sub>O<sub>2</sub> is more expensive than methanol; therefore, using it as the reactant is economically infeasible. On the other hand, sulfuric acid is highly corrosive and forms SO<sub>2</sub> [1,2,84,86,91]. The other challenge of homogeneous catalysts are the precision required for their preparation as they are mostly sensitive to air and moisture.

### 1.3.3.2 Heterogeneous catalysts

All the challenges discussed for the application of homogeneous catalyst complexes encourages the development of heterogeneously catalyzed systems [85,86]. The Pt (II) species stabilized on polymer-based framework might be considered as one of the pioneering heterogeneously catalyzed DMTM reactions [92]. Pt (II) species were successfully stabilized on a suitable polymer-based frame by inspiration of the Periana catalyst [92,93]. A turn over number (TON) of 246 was obtained for this catalyst which was comparable to a TON of 355 reported for its homogeneous counterpart, i.e., Periana catalyst [92,93]. However, the low stability of the catalyst and the difficulties in handling its oxidant, concentrated or fuming sulfuric acid, were serious drawbacks in its implementation [1,2,92,94]. The noble metals-based silica-supported Au nanoparticles and titania-supported AuPd are the other heterogeneous catalysts tested for this reaction [1,95,96]. Despite the good catalytic performance, the high expense of both the implemented noble metals and the reactive medium or/and oxidant makes the industrial application of these catalytic systems unlikely too [1].

Later on, the discovery of the ability of zeolite-based supports in stabilizing the binuclear iron and copper sites raised the hope for the success of heterogeneously catalyzed DMTM reaction [2,15,83,84,91,97,98]. Both Fe and Cu containing ZSM-5 are reported to be highly active in the batch reactors operating at elevated pressures and oxidizing with H<sub>2</sub>O<sub>2</sub> [90,99]. However, conducting the reaction neither at high pressure nor with H<sub>2</sub>O<sub>2</sub>, are desired for industrial applications. Fortunately, these catalysts are observed to be able to activate methane as they get oxidized with oxygen or N<sub>2</sub>O at moderate reaction conditions (P=1 bar and T ≤200 °C) [32,82–84,91,97–102]. Under these circumstances, the reaction should be performed in a stepwise mode to get an acceptable selectivity to methanol [18,83]. To do so, the catalyst is first activated at high temperatures, normally T > 450 °C. Then, the reactor is purged to remove

the gas phase oxygen. This is followed by sending methane to the reactor to form methoxy species stabilized over the catalyst surface at temperatures around 200 °C. Finally, methanol is obtained by washing the methoxy species over the surface through either mixing the catalyst with a defined volume of water or introducing it to a continuous flow of steam [18,32,83]. Noteworthy, online extraction of methanol with flowing steam is reported to be possible just with Cu/zeolites, not Fe/zeolites. This characteristic is essential for realizing a continuous process for the DMTM reaction. Because of that, the attention is attracted more to Cu than to Fe-zeolite catalysts [83,98,101,103].

In synthesizing most of the Cu loaded catalysts, Cu<sup>2+</sup> cations are loaded into zeolites *via* liquid-phase ion exchange. The recent studies showed that Cu/mordenite catalysts can also be formed through solid state ion exchange of H-mordenite and copper(I) chloride. But, the residual chlorine was observed to hinder the production of methanol after a few runs [32,104]. To solve this problem, the solid-state ion-exchanged Cu/mordenite catalysts were synthesized in our studies with chlorine-free copper precursors. The catalytic conversion of methane to methanol over several different catalyst samples were measured and compared to the literature data. Moreover, the behavior of these catalysts was studied in more details through implementing *in-situ* characterization techniques.

## Methods and materials

### 2.1 Catalyst preparation

#### 2.1.1 OCM

##### 2.1.1.1 Supported $Mn_xO_y-Na_2WO_4$ (Papers 1, 2, 4, 5, and 6)

$Mn_xO_y-Na_2WO_4$  supported over non-ordered mesoporous silica support ( $Mn_xO_y-Na_2WO_4/SiO_2$ ) was the model catalyst in OCM studies. In paper 5,  $Mn_xO_y-Na_2WO_4$  supported over ordered mesoporous silica COK-12 was investigated in comparison to  $Mn_xO_y-Na_2WO_4/SiO_2$ . All the samples were prepared through incipient wetness impregnation as described by Feng *et al.* [105]. COK-12 was prepared as explained in the literature [31], while non-ordered mesoporous  $SiO_2$  (Silica Gel, Davisil, Grade 636) was obtained from Sigma-Aldrich and sieved to the particle diameters of 200-350  $\mu m$ . The supports were impregnated in two steps using aqueous solutions of  $Mn(NO_3)_2 \cdot 4H_2O$  (p.a.,  $\geq 97\%$ , Sigma-Aldrich) and  $Na_2WO_4 \cdot 2H_2O$  (p.a.,  $\geq 99\%$ , Sigma-Aldrich) inadequate concentration. After each impregnation step, the samples were dried in a cabinet dryer at 100  $^{\circ}C$ , overnight. The samples were normally calcined under static air at 800  $^{\circ}C$  for 8 h. However, to get the samples at the different surface areas for studies in paper 5, the annealing temperature was varied between 750  $^{\circ}C$  and 850  $^{\circ}C$ . Noteworthy, the  $Mn_xO_y-Na_2WO_4/COK-12$  samples were taken as powder and were not pelletized. To determine the content of Na, Mn, and W of the samples, inductively coupled plasma optical emission spectroscopy (ICP-OES) was conducted.

#### 2.1.2 MTM

##### 2.1.2.1 Cu-containing zeolites (Paper 3)

Commercial mordenites including  $NH_4$ -mordenite ( $Si/Al = 10$ , denoted as  $NH_4$ -Mor-1) and Na-mordenite ( $Si/Al = 6.5$ , denoted as Na-Mor-2) were obtained from Alfa Aesar. Ammonium exchange of Na-Mor-2 was carried out according to the method described earlier in the literature [101]. A mixture of 2 g of Na-Mor-2 and 80 ml of 1 M  $NH_4NO_3$  solution was stirred vigorously for 2 h at 80  $^{\circ}C$ . The ion-exchange procedure was repeated 3 times. The sample was then filtered, washed with deionized water, and dried at 105  $^{\circ}C$  for 12 h. The prepared  $NH_4$ -mordenite is denoted as  $NH_4$ -Mor-2. A similar treatment with  $NH_4$ -Mor-1 in a 1 M solution of  $CH_3COONa$  was employed for the preparation of mordenite in the Na-form. Calcination was performed at 550  $^{\circ}C$  under static air for 3 h, yielding the Na-exchanged mordenite, which is denoted as Na-Mor-1.

After obtaining the supports, the  $\text{Cu}^{2+}$  cation exchange with  $\text{NH}_4$ -form zeolites was conducted under solid-state conditions using copper(II) acetylacetonate ( $\text{Cu}(\text{acac})_2$ ) [90]. The CuMor samples were prepared by intensively grinding a mixture of an adequate amount of  $\text{Cu}(\text{acac})_2$  and  $\text{NH}_4$ -Mor-1 in a mortar within 30 min. Ion exchange was performed in situ during the activation of the catalyst in the reactor. For comparison with the literature data, the conventional Cu/mordenites were also prepared by liquid phase ion exchange [101]. The solid-state ion exchange of  $\text{NH}_4$ -Mor-1 with copper(I) chloride was performed based on literature procedure [101]. The metal content of the samples was measured using an optical emission spectrometer (ICP).

### **2.1.2.2 Cu/SBA-15 (Paper 6)**

SBA-15 was prepared according to the procedure previously described [106,107]. A Cu-based precursor (Cu (II) acetylacetonate or Cu(II) acetate, 0.45 mmol) was added to a mixture of SBA-15 (0.975 g) and absolute ethanol (10 ml). After sonication for 10 min, evaporation of ethanol was conducted slowly at 40 °C under vigorous stirring until a sludge-like phase was obtained. The sample was dried at 80 °C for 12 h for complete removal of ethanol. The resulting powder was then pressed into pellets at 100 bars for 60 s, lightly grounded, and sieved to a 200-400  $\mu\text{m}$  diameter fraction. Calcination of the material was performed under static air at 550 °C for 4 h. The metal content was measured using an optical emission spectrometer (ICP).

## **2.2 Characterization of catalysts**

### **2.2.1 Powder X-ray Diffraction (XRD)**

Wide angle powder XRD was performed with a Bruker-AXS D8 advanced diffractometer with DAVINCI design using  $\text{CuK}\alpha$  radiation ( $\lambda = 1.5418 \text{ \AA}$ ) equipped with a Lynx Eye detector.

### **2.2.2 $\text{N}_2$ sorption analysis**

$\text{N}_2$  sorption analysis was performed at 77 K using a QUADRASORB SI, equipped with automated surface area analyzer. Before starting the analysis, the samples were degassed at 150 °C for 12 h. Specific surface areas (BET) were determined over a 0.05–0.30  $P/P_0$  range. The total pore volume was collected at  $P/P_0 = 0.99$ .

## **2.3 Feed Gases**

The reaction gases, Methane (99.95 %), Ethane (99.95 %), Ethene (99.90 %), Oxygen (99.998 %)  $\text{N}_2$  (99.95 %) and Helium (99.999 %), were purchased from Air Liquide. The pure labeled

methane ( $^{13}\text{CH}_4$  99 atom %  $^{13}\text{C}$ ) was obtained from Sigma Aldrich. All the gases were used in the experiments as received, without further purification.

## 2.4 Experimental setup

The experiments were conducted in two geometrically different fixed bed quartz reactors. One was a tubular fixed-bed reactor with 9 mm internal diameter i.d and 35 cm length. A quartz frit with the pore size of 120  $\mu\text{m}$ , was placed in the middle of this reactor to keep the catalyst in its position. The second reactor was a U-shaped fixed-bed reactor with 6 mm i.d and 25 cm length. During the experiments, these reactors were located in a temperature-controlled oven (T range 25-900  $^\circ\text{C}$ ). The temperature in the catalytic bed was measured using a type K thermocouple. Mass Flow Controllers (EL-FLOW, Bronkhorst) were used to regulate the flow of the gasses. To ensure a homogeneous reaction mixture, a mixing cylinder was built before the reactor inlet. The pre-catalytic pressure was monitored using a pressure indicator.

Depending on the experiment, the effluent was analyzed with either the mass spectrometer (MS), the gas chromatograph (GC) or the MS attached to a Hayesep Q column of Agilent GC. The MS was a quadrupole GAM 200, obtained from Inprocess Instruments and built in the experimental setup-1. The GC implemented to analyze the gas samples was an Agilent GC (7890 A) connected to the reactor setup-2. Both the Agilent GC and the MS were calibrated to distinguish alkanes and alkenes of  $\text{C}_{1-3}$ , methanol, dimethyl ether as well as  $\text{CO}$ ,  $\text{CO}_2$ ,  $\text{N}_2$ , and  $\text{O}_2$ . Since helium was used as the carrier gas of the Agilent GC, neither  $\text{H}_2$  nor He could be detected by it. However, this limitation did not apply to the measurements done with the MS. To detect methanol in the DMTM experiments, a Shimadzu GC 2010-Plus was implemented. The liquid samples obtained after washing the catalyst samples were transferred to a volumetric flask, mixed with a predetermined volume of acetonitrile as an internal standard and analyzed. More details on the operational differences, the construction of the reactor setup and calibration procedure followed in each of the studies are provided in the papers.

### 2.4.1 TPSR investigations

As mentioned earlier, the OCM reaction is performing both catalytically and in the gas phase [22,23,35]. Therefore, investigating its reaction mechanism is quite challenging. To decrease this complexity, in our studies, the surface and gas phase reactions were distinguished from each other by implementing the temperature programmed surface reaction (TPSR) technique [110]. This technique is quite informative in studying the reaction mechanism of the selective oxidation reactions, especially those which are taking place over a catalyst capable of either

storing oxygen, similar to  $Mn_xO_y-Na_2WO_4$  catalyst [36], or providing its bulk oxygen [110]. The first step in these experiments is oxidizing the catalyst surface at the reaction temperature. Next, the catalyst is cooled down under the flow of oxidizer to the room temperature. Afterward, the catalyst is heated, usually at a low heating ramp, to the reaction temperature while the reacting hydrocarbon is passing through it. Simultaneously, the changes in the composition of effluent are recorded and presented as a function of the catalyst bed temperature. This technique was implemented in **papers 1 and 6** for studying the reaction mechanism of three main hydrocarbons of OCM, methane, ethane, and ethene.

## Results and discussion

### 3.1 OCM

#### 3.1.1 TPSR investigation with methane

Fig-3.1 presents the results of TPSR experiments of methane at varying heating ramps ( $\beta$ ) discussed in **paper 1**. As it is presented in Fig-3.1, CO and ethane are the main reaction products measured in these experiments. In all cases, first ethane then CO, at a higher temperature, are detected in the reactor outlet. The peaks of the products have shifted to higher temperatures as the heating rate has been increased, see Fig-3.1 B and C. However, the temperature difference observed for the shift in the CO and ethane has been varying differently during these experiments. This behavior is assigned to the formation of ethane and CO through two different reaction routes. It should be noted that the first step in the formation of ethane is the cleavage of C–H bond in methane. Then, the formed methyl radicals will combine to form ethane or react with the surface oxygen species to CO. The time span observed in our experiments between detection of CO and ethane is significantly larger than the lifetime of methyl radical. Therefore, the formation of each of CO and ethane are assigned to the reaction of methane with two different oxygen species rather than the fast chain reaction of methane with a single oxygen active site. This suggestion is in good agreement with the results of Beck *et al.* who proposed the presence of at least two sorts of oxygen active species over the catalyst surface [33]. But, it is in contradiction with the reaction mechanism presented by Lee *et al.*, as he considered just one sort of surface species for all reactions of methane [74].

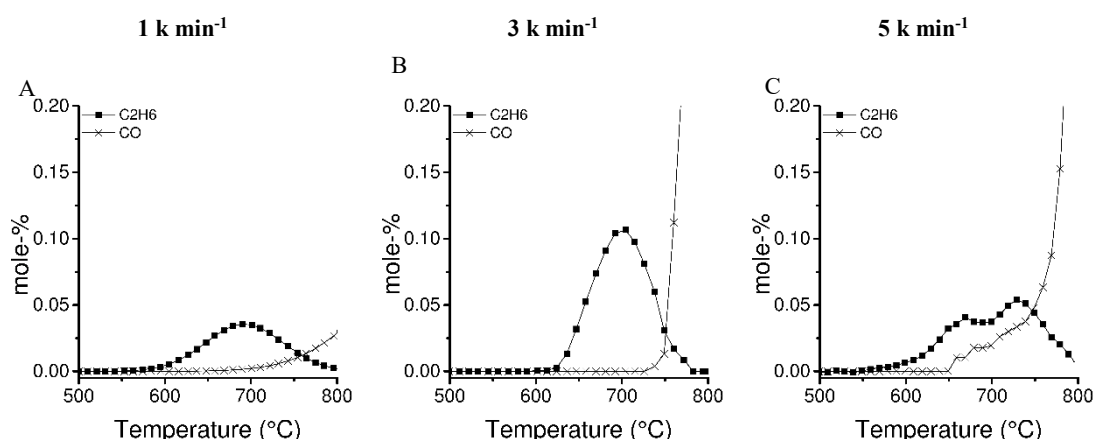


**Figure 3. 1** - TPSR product formation peaks of methane TPSR experiments at  $\beta$  equal to A) 1 K min<sup>-1</sup>, B) 3 K min<sup>-1</sup> and 5 K min<sup>-1</sup>. Catalyst amount= 1 g, total flow consisting of only CH<sub>4</sub> = 30 Nml min<sup>-1</sup>. (**Paper 1**)

Based on the results obtained from methane TPSR experiments, the surface apparent activation energy for converting methane to ethane could be calculated. For this purpose, the

mathematical method explained in detail in the literature is implemented [111]. There the  $\ln(\beta/T_A^2)$  is plotted versus the inverse of the peak amplitude temperature ( $T_A$ ) of the formed ethane, see Fig-3.2. The slope of this curve represents the  $-E_d/R$  which results in the activation energy of  $275 \pm 29$  kJ/mol for methane in our experiments. This value is significantly higher than the literature results where the activation energy of the same reaction has been reported to be between 133 kJ/mol up to 212 kJ/mol [112–114]. Noteworthy, our results are obtained during the TPSR experiments while the literature studies are performed in the steady-state modus. Therefore, this deviation in the results could be assigned to both the experimental mistakes and the changes in the reaction mechanism caused by changing the reaction condition from steady-state to TPSR. The mistakes in obtaining the accurate value of  $T_A$  or neglecting the effect of coking are two typical experimental mistakes which may have falsified our calculations. Unfortunately, small errors in considering the value of  $T_A$  can have a large effect on our calculations [111]. As it is presented in Fig-3 C of paper 1, the peak of ethane obtained for the experiment at heating rates of  $3 \text{ K min}^{-1}$  was quite noisy and weak. Therefore, the accuracy of the  $T_A$  considered for this experiment and consequently the activation energy obtained from our studies is strongly doubted.

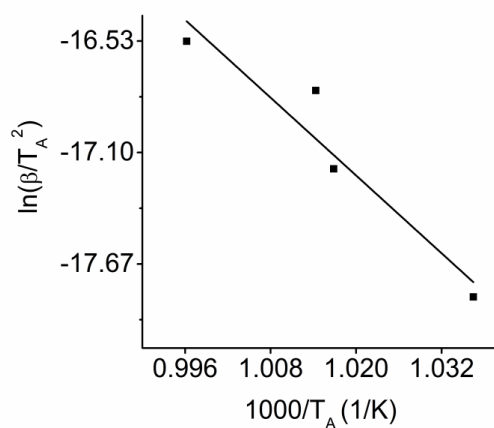


**Figure 3. 2** - Arrhenius type diagram of methane TPSR experiments using the ethane peak amplitudes, at a heating rate of  $1-4 \text{ K min}^{-1}$ . Catalyst amount=1, total flow consisting of only  $\text{CH}_4 = 30 \text{ Nml min}^{-1}$ . (**Paper 1**)

However, this deviation can also be explained by the assumption of the activation of methane over the surface by two different oxygen species as suggested by Beck [33]. It is assumed that in TPSR studies the strongly bounded oxygens, which are most probably the lattice oxygen ( $\text{O}_x^*$ ), are involved in the reaction mechanism. Formation of these species could have happened in an adsorption process ( $\text{O}_{2,\text{ads}}$ ), Eq-7, followed by a dissociation reaction as presented in Eq-8. This conversion may have also happened in a one-step reaction as shown by Eq-9.



To discuss the reaction behavior applied in our TPSR experiments, a possible energy profile is constructed for OCM based on the scenario suggested by Beck [33], see Fig-3.3. The difference between the two postulated oxygen species is in their interaction with the surface. The adsorbed, electrophilic oxygen species  $\text{O}_{2,\text{ads}}$  is suggested to be weakly bounded on the catalyst surface and mainly result in the formation of deep oxidation products. While the dissociation of this species causes a strong interaction with the surface and produces the nucleophilic  $\text{O}_x^*$ . Both oxygen species have different energy levels because of their binding situation. The activation of methane to deep oxidation products undergoes a transition state with  $\text{O}_{2,\text{ads}}$  (Fig-3.3,  $E_{A,1}$ ) in steady-state experiments. A similar activation energy in the range of 120–180 kJ/mol is expected for the activation of C-H bond in methane, ethane, and ethene if they all get activated via the same sort of oxygen species. The much higher activation energy of methane obtained from the TPSR experiments (Fig-3.3,  $E_{A,3}$ ), in comparison to the literature data reported for the steady state experiments, indicates the presence of the strongly bounded, presumably dissociated oxygen species, at a much lower energy level. Since these species are already formed during the pretreatment of the catalyst, a higher activation barrier must be overcome in TPSR experiments.

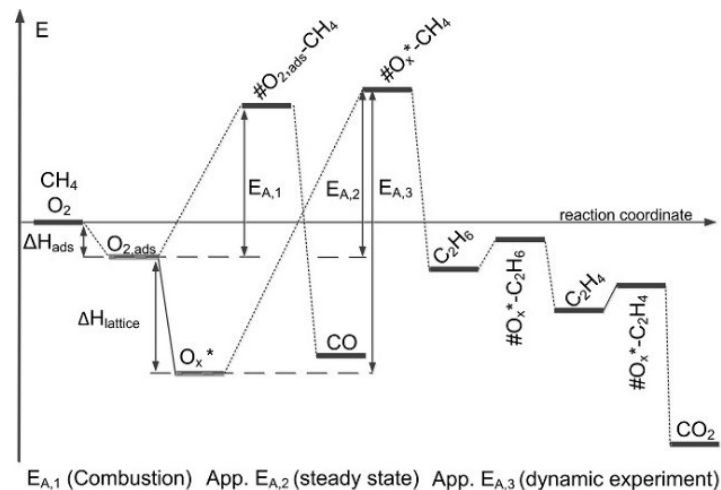


**Figure 3. 3** - Proposed energy profile for the OCM reaction at the  $\text{Mn}_x\text{O}_y\text{-Na}_2\text{WO}_4/\text{SiO}_2$  catalyst. (Paper 1)

### 3.1.2 Details of the consecutive reaction of C<sub>2</sub> components

The other important section of the reaction mechanism of OCM is the consecutive reaction of the main products of OCM, i.e. ethane and ethene. The secondary oxidation of C<sub>2</sub> components is reported to be the main pathway towards the production of carbon oxides in the OCM reactor [59]. To control the occurrence of these unselective reactions, their origin of formation should be known. Similar to methane, consecutive reactions of these hydrocarbons are proposed to be conducting both homogeneously and heterogeneously in the OCM reactor. Therefore, the heterogeneous mechanism was separately studied from the homogenous part by implementing the TPSR technique.

Two sets of experiments were conducted with either ethane or ethene as the reactant. The investigations were done in the presence of the catalyst, quartz sand, and silicon carbide, sequentially. The latter two materials were used as an inert surface to perform the blank experiments. All the details of the applied reaction conditions are presented in **paper 6**. The results of the catalytic studies with ethene and ethane as the reaction feed are presented as a function of the catalyst bed temperature in Fig-3.4 and Fig-3.5, respectively.

In the ethene TPSR experiments, a continuous increase in the carbon balance was observed with the reaction temperature (**Paper 6**, SI, Figure S8). This raise was simultaneous with the detection of hydrogen as the main product of the reaction (Fig-3.4 A). This observation was assigned to the high tendency of ethene to decompose under the applied reaction conditions [115–118]. As the rate of conversion of ethene in the blank TPSR experiment was observed not to be comparable to the catalytic one the decomposition of ethene is proposed to take place mostly over the catalyst surface (**Paper 6**, SI, Figure S9).

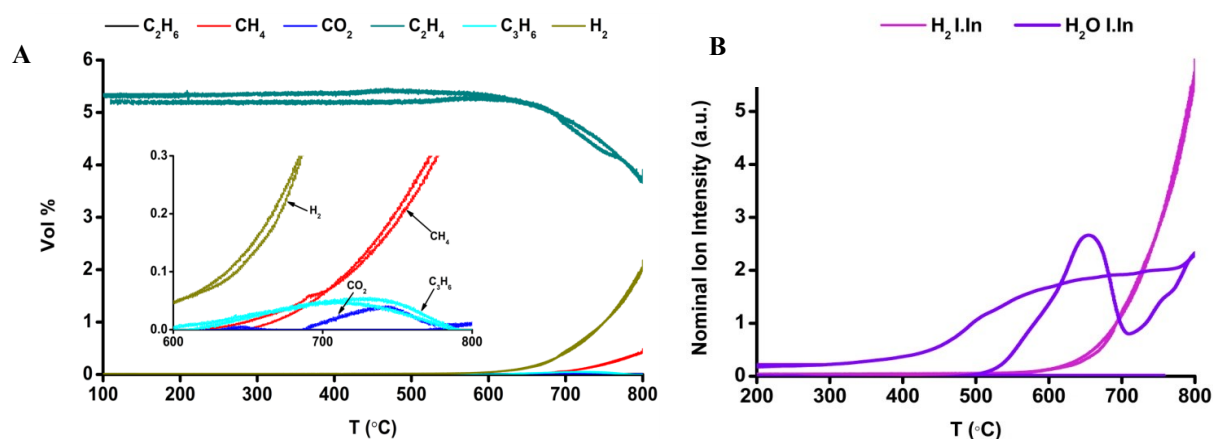


**Figure 3. 4** - Results of the TPSR experiment with ethene during the heating up and cooling down of the catalyst a) composition ratio of effluent b) nominal ion intensity of the water and H<sub>2</sub> in the reactor outlet vs. the temperature of the catalyst bed. Catalyst amount= 0.5 g, C<sub>2</sub>H<sub>4</sub>: He = 1:19 and total flow = 30 Nml min<sup>-1</sup>. (**Paper 6**)

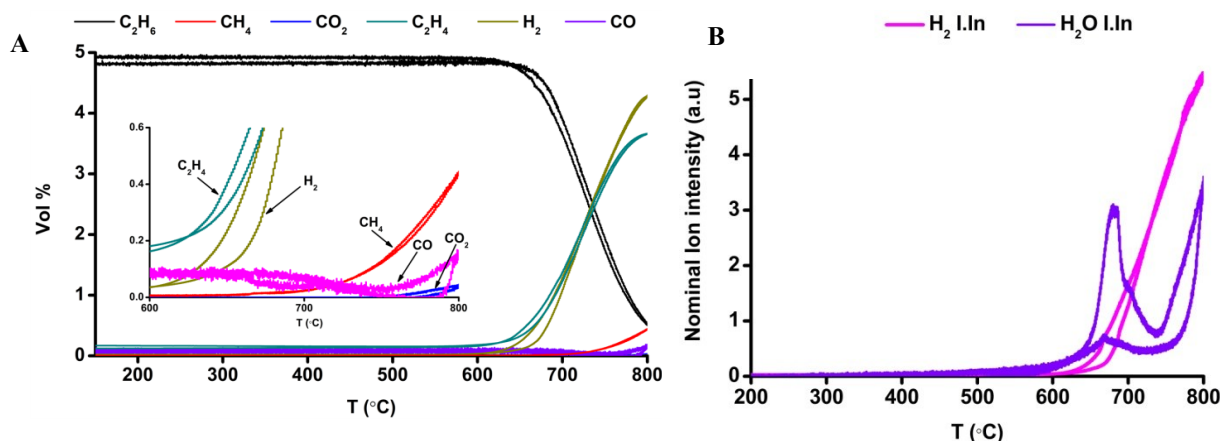


**Figure 3.5** - Results of the TPSR experiment with ethane during the heating up and cooling down of the catalyst a) composition ratio of effluent b) nominal ion intensity of the water and H<sub>2</sub> in the reactor outlet vs. the temperature of the catalytic bed. Catalyst amount=0.5 g, C<sub>2</sub>H<sub>6</sub>: He = 1:19 and total flow = 30 Nml min<sup>-1</sup>. (**Paper 6**)

The reaction in the ethane catalytic TPSR studies started at around 600 °C and produces ethene as expected, see Fig-3.5 A [71,75,119–121]. The general assumption is that this conversion occurs through dehydrogenation of ethane with the surface active oxygen species, known as oxidative dehydrogenation (ODH) presented in Eq-10 [44,71,74,77,114]. However, simultaneous detection of hydrogen and ethene at a molar ratio of one to one in our experiment (see Fig-3.5 A), proposed the thermal dehydrogenation (TDH), presented in Eq-11, as the main reason for this conversion. The other confirm to the occurrence of TDH of ethane to ethene could be the identical product pattern during the cooling as well as along the heating period as presented in Fig-3.5 A.



Noteworthy, the pattern of hydrogen and ethene formation during the ethane TPSR experiment presented in Fig-3.5 A remained identical until the temperature of the catalyst bed exceeded 750 °C. Afterward, the rate of decomposition of ethene increased and consequently, the concentration of hydrogen exceeded that of ethene.

Next, to find information about the catalytic or non-catalytic nature of ethane TDH reaction, the catalyst bed was substituted by either quartz sand or silicon carbide and the ethane TPSR experiment was repeated. The reaction performance in each of these experiments is calculated and presented in comparison to each other in Fig-3.6. As the level of conversion in the blank experiments (performed over the SiC and quartz) was equal to that of the catalytic test, the TDH of ethane was reported to be mostly non-catalytic.

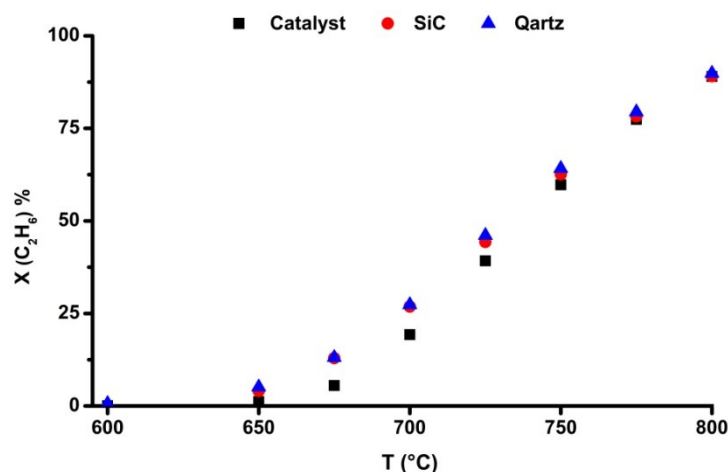


**Figure 3. 6** - The conversion of ethane as a function of the reactor temperature obtained in the TPSR experiments conducted over catalyst ■ silicon carbide ● quartz ▲  $C_2H_6$ : He ratio of 1:19 at a total flow of 30 Nml  $min^{-1}$ , heating rate 1 K  $min^{-1}$ . (**Paper 6**)

The other important observation made in the TPSR experiments was their lower rate of  $CO_X$  formation (see Fig-3.4 A and 3.5 A) in comparison to the co-feeding tests (see **paper 6 SI**, Figure S5, and S7). As the most important difference of the TPSR experiments to the co-feeding is the absence of the molecular gas phase oxygen in the former condition, this observation is assigned to the high contribution of gas phase oxygen on the rate of secondary oxidation of the  $C_2$  components. This idea was studied in more details and confirmed through experimental as well as simulation evidence, see **paper 6** for more information. Therefore, it is concluded that removing the oxygen from the homogeneous part of the reactor diminishes the formation of  $CO_X$ . Accordingly, chemical looping reactor, which realizes this condition, is proposed as a promising solution for enhancing the performance of the OCM reaction. The influence of this reactor set up on the performance of OCM is studied in **papers 2 and 4**.

In addition, the studies in **paper 6** revealed the film diffusion limitation as the main reason for the low influence of  $Mn_xO_y-Na_2WO_4$  on the conversion of ethane under the OCM reaction conditions.

Based on the results of the studies in **Paper 1 and 6** and the literature reports, the reaction network presented in Fig-3.7 is suggested for OCM performing over  $Mn_xO_y-Na_2WO_4/SiO_2$ .

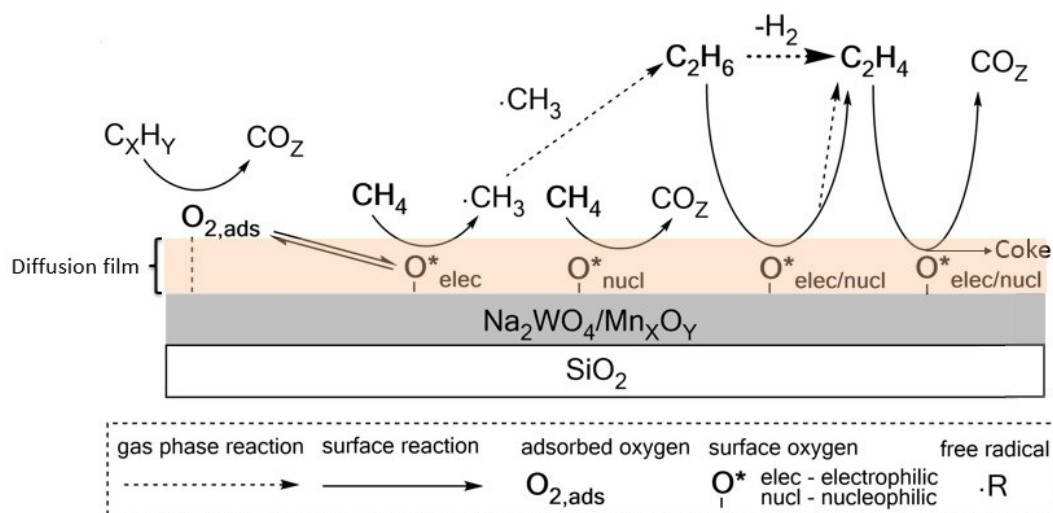


**Figure 3. 7** - Modified reaction mechanism proposed for OCM over Mn<sub>x</sub>O<sub>y</sub>- Na<sub>2</sub>WO<sub>4</sub>/SiO<sub>2</sub> under the usual experimental conditions. (**Paper 1 and 6**)

### 3.1.3 Chemical looping as a reactor concept for OCM

#### 3.1.3.1 From mechanism understanding to reactor design

The mechanistic studies have revealed two important facts regarding the formation of carbon oxides in the presence of Mn<sub>x</sub>O<sub>y</sub>-Na<sub>2</sub>WO<sub>4</sub>/SiO<sub>2</sub> [33,36]. First, the unselective oxygen species were reported to be weakly adsorbed on the catalyst surface [33]. Purging the reactor with an inert gas is observed to remove a part of these unselective species; however, it doesn't change the concentration of the selective sites [33,36]. Second, the total and partial oxidation of C<sub>2</sub> products, rather than that of methane, are introduced as the main routes to the formation of CO<sub>x</sub> in the OCM reactor [59,108,109]. Besides, the studies **in paper 6** revealed the high contribution of the molecular gas phase oxygen on speeding the occurrence of these reactions, i.e. secondary oxidation of C<sub>2</sub> components.

The discussed mechanistic features of OCM indicate the necessity for removing both the gas phase and the unselective ones weakly bounded to the surface, for enhancing the performance of OCM. Such a condition can be realized by implementing the chemical looping concept (CLC). This concept has existed for about a hundred years and is well-known for combustion processes. It not only separates the formed carbon dioxide from nitrogen but also avoids the formation of NO<sub>x</sub> [122–128]. It should be noted that to implement such a reactor concept for OCM there is a vital need to a catalyst material which has the ability to provide sufficient storage capacity for one of the reactants. The Mn<sub>x</sub>O<sub>y</sub>-Na<sub>2</sub>WO<sub>4</sub>/SiO<sub>2</sub> catalyst is already proven to have a good storage capacity (almost 20 μmol/g<sub>cat</sub>), **paper 1**, for oxygen. Therefore it could be used for performing OCM in the CLR.

A simulated chemical looping reactor was built in our laboratory by installing two pneumatic pulse valves at the inlet of a fixed bed reactor. Each of these valves was used for injecting one of the reactants in a step-wise manner to the reactor. All the details regarding the operation and construction of the set up are presented in **paper 2**.

### 3.1.3.1.1 Reaction performance in Chemical Looping Reactor

The performance of OCM at various reacting conditions was tested in the CLR. Fig-3.8 presents the selectivity toward  $C_{2+}$  products as a function of methane conversion obtained in these experiments. These results are presented in comparison to those reported in the literature for the same reaction done in the normal co-feeding reactors. As it is shown in Fig-3.8, at the same level of methane conversion, the selectivity toward  $C_{2+}$  components in the chemical looping reactor was higher than that measured in the co-feeding reactors. This effect is even more noticeable at the methane conversion levels lower than 20 %. Moreover, as in CLR the methane and oxygen feeds are sent separately to the reactor, the reaction is no longer limited by the explosion regime. Therefore, not only the operation safety is increased but also obtaining methane conversions higher than 50 % can be realized.

However, despite all these advantages, the minimum yield of 30% to  $C_{2+}$  components needed for industrializing the reaction, couldn't be achieved in chemical looping reactors, see Fig-3.8. Since, this observation didn't match our understanding of the reaction mechanism, the search for finding the reasons originating this limitation was continued and the results of these studies were presented in **paper 4**.

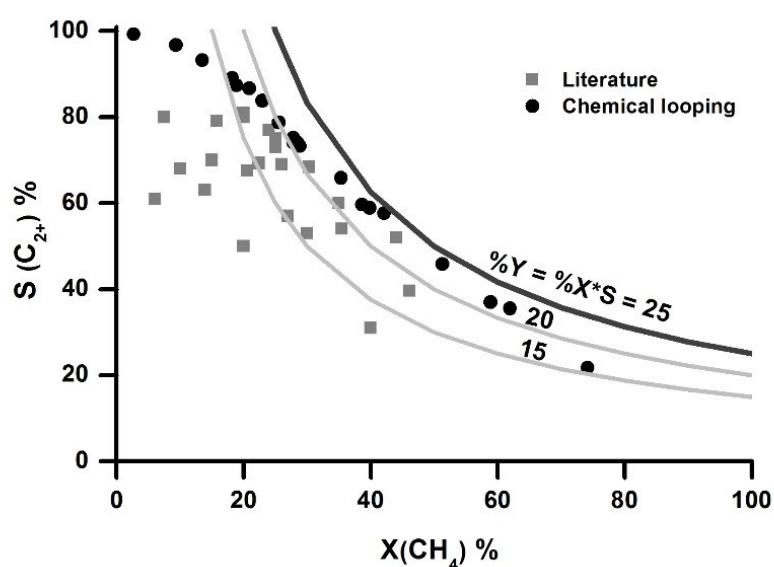


**Figure 3. 8** - Plot of  $X(CH_4)/S(C_{2+})$  over  $Mn_xO_y-Na_2WO_4/SiO_2$  reported in literature vs. chemical looping data. (**Paper 2**)

### 3.1.3.1.2 Limitation of OCM in Chemical Looping Reactor

The reasons for the observed yield limitation for OCM in CLR were searched by studying the influence of this reactor on the consecutive reaction of ethane and ethene. To do so, the reaction performance, conversion, and selectivity of ethane and ethene in CLR were measured. These results are presented in comparison to those obtained from the oxygen co-feeding reactions in Table 3.1 and 3.2.

As the data in Table 3.1 and 3.2 shows, the consecutive reactions of both ethane and ethene, i.e. OCM desired products, were successfully suppressed by implementing the chemical looping reactor. This observation clearly shows the efficiency of the CLC in suppressing the rate of unselective oxidation of OCM main products. Therefore, the idea that the yield barrier of OCM performed in the CLR originates from the promotion effect that this reactor concept has on the secondary oxidation of  $C_2$  products is rejected.

**Table 3.1** - Comparison of the reaction performance of ethane in CLR and co-feeding experiments. The reaction conditions in the CLR: Catalyst=1 g, T=750 °C, Volume of the ethane pulse=1 ml, Carrier gas flow=25 Nml min<sup>-1</sup>. The reaction conditions in the co-feeding reactor: TF=50 Nml min<sup>-1</sup> Catalyst=1 g, T=750 °C, C<sub>2</sub>H<sub>6</sub>/O<sub>2</sub>/He ratio=1/1/23. (**Paper 4**)

	X (C <sub>2</sub> H <sub>6</sub> )	S (C <sub>2</sub> H <sub>4</sub> and C <sub>3</sub> H <sub>x</sub> )	% S (CO <sub>x</sub> )	Y (C <sub>2</sub> H <sub>4</sub> and C <sub>3</sub> H <sub>x</sub> )	Y (CO <sub>x</sub> )
<b>CLR</b>	82	90	6	74	5
<b>Co-Feeding</b>	95	50	39	47	4

**Table 3.2** - comparison in the reaction performance of ethene in CLR and co-feeding experiments. The reaction conditions in the CLR: Catalyst=1 g, T=750 °C, Volume of the ethene pulse=1 ml, Carrier gas flow=25 Nml min<sup>-1</sup>. The reaction conditions in the co-feeding reactor: TF=50 Nml min<sup>-1</sup> Catalyst=1 g, T=750 °C, C<sub>2</sub>H<sub>4</sub>/O<sub>2</sub>/He ratio=1/1/23. (**Paper 4**)

	X (C <sub>2</sub> H <sub>4</sub> )	S (C <sub>2</sub> H <sub>6</sub> and C <sub>3</sub> H <sub>x</sub> )	% S (CO <sub>x</sub> )	Y (C <sub>2</sub> H <sub>4</sub> and C <sub>3</sub> H <sub>x</sub> )	Y (CO <sub>x</sub> )
<b>CLR</b>	15	26	67	4	10
<b>Co-Feeding</b>	48	8	81	4	4

However, the results of the multi-pulse experiment, done with ethane, introduced both the inherent nature of the Mn<sub>x</sub>O<sub>y</sub>-Na<sub>2</sub>WO<sub>4</sub> catalyst and the characteristics of the reaction mechanism as the reasons behind the yield limitation of OCM in CLR. In multi-pulse experiments, the catalyst surface was oxidized once and then presented to several pulses of ethane without repeating the oxidation step in between.

Figure 3.9 presents the changes in the effluent concentration vs. time on stream measured in the ethane multi-pulse experiment. For all the ethane pulses, almost the same conversion and

the same selectivity to  $C_{2+}$  products were obtained (**paper 4**, table S1). Although the product species, formed after each pulse, were observed to be identical, the distribution of some of them changed with the time (Figure 3.9). The most obvious difference was seen in the hydrogen concentration which shows a gradual increase throughout the whole period of the experiment. To give a better illustration of this phenomenon, the very first and the very last peak of effluent gas shown in Fig-3.9, are separately presented in Figure 3.10 A and B, respectively. As one may see, the concentration of hydrogen has been increasing continuously by time.

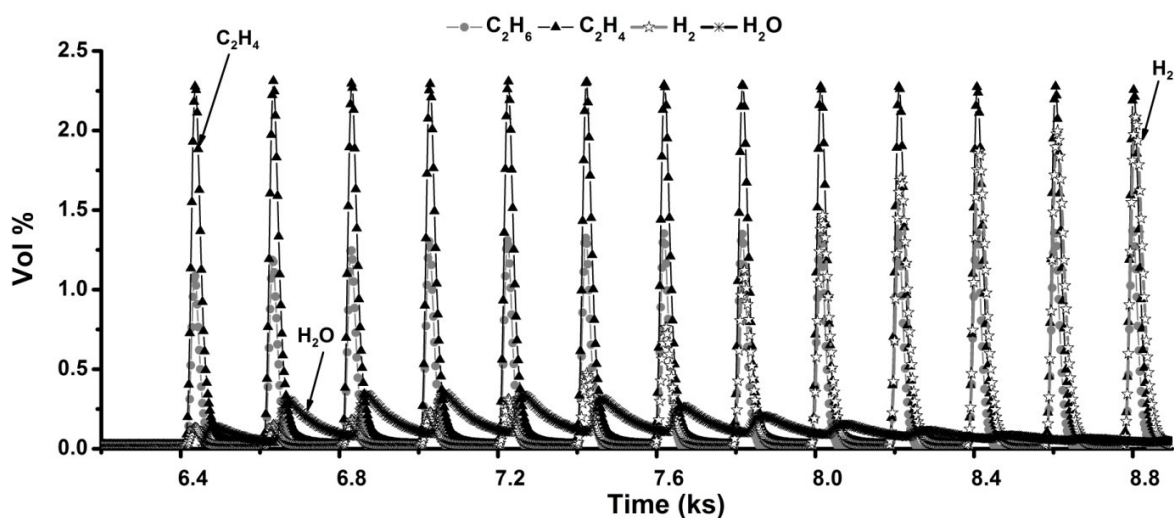


**Figure 3. 9** - The changes in the concentrations of the effluent gases during the ethane multi-pulse experiment vs. time. 1g catalyst, carrier gas flow:25 Nml min<sup>-1</sup> of He, 0.5 ml of the C<sub>2</sub>H<sub>6</sub> pulse, T= 750 °C. (**Paper 4**)

As it is shown in Fig-3.10 A, at the beginning of the experiment the concentration of H<sub>2</sub> was quite low. However, it has been gradually increased until it reached at the same concentration as ethene during the injection of the last pulse, see Fig-3.10 B. This observation was not in accordance to the mechanistic suggestions made for the reaction of ethane discussed in **paper 6**. As mentioned there, the formation of ethene in the OCM reactor is suggested to be mainly taking place through the non-catalytic thermal dehydrogenation (TDH) of ethane, see Eq-11. Therefore, it is expected that for all the pulses, hydrogen, which is the coupled product of TDH, would be formed and detected at the same molar ratio as ethene. However, this observation was made just for the last pulses of ethane, see Fig-3.9. This behavior might be caused by the occurrence of the Eq-12, i.e. oxidation of the formed hydrogen by surface oxygen species, during the injection of the first pulses of ethane.

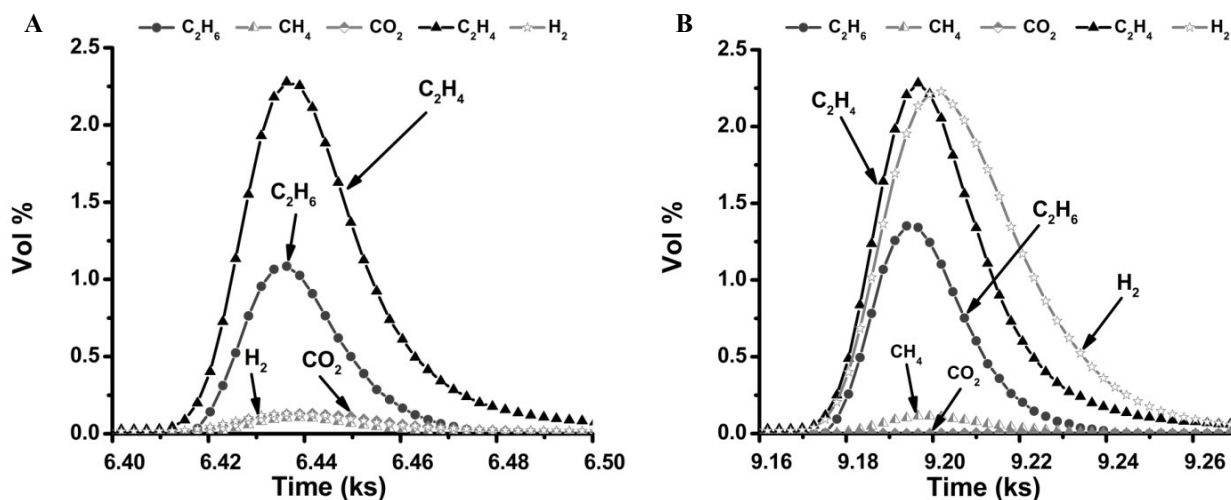


**Figure 3. 10-** The changes in the concentrations of the effluent gases in A) the very first and B) the very last peak measured during the ethane multi-pulse experiment. (Paper 4)

On the one hand, it is well known that at temperatures higher than 700 °C the active oxygen species on the  $Mn_xO_y-Na_2WO_4$  are capable of methane dehydrogenation [26,33,55,71,74,113,114,129,130]. On the other hand, methane and hydrogen have been reported to have the same bond dissociation energy (104 kcal mol<sup>-1</sup> [131]). Therefore, the activation of hydrogen molecules during the injection of the first pulses, where the surface is not fully reduced, is not avoidable. The detection of water in the reactor outlet, the intensity of which levels off from each pulse to the other, see Fig-3.9, is also an indication of the reaction of hydrogen with the surface oxygen species at the beginning of the experiment.



The occurrence of Eq-12 has been studied more precisely by testing the correlation between the concentrations of the surface adsorbed oxygen species and the hydrogen peak formed through the TDH of ethane, Eq-11. For this purpose, 1 g of the catalyst was treated under the normal chemical looping conditions. But, before introducing the ethane pulses to the reactor, the surface was reduced by sending either 1, 2 or 4 ml of hydrogen to the reactor. The changes in the molar fraction of the effluent gas obtained in each of these experiments were recorded via MS. The reaction performance calculated for each of the ethane pulses obtained in these experiments shows that the concentration of oxygen on the surface of the catalyst had a negligible influence on both the conversion and selectivity (to ethene and  $C_3H_x$  products) of

ethane reaction. However, the intensity of the hydrogen peak of the first ethane peak in each of these experiments continuously increased with a decrease in the concentration of surface oxygen species, see Fig-3.12. These observations strongly support the idea of the occurrence of the reaction 12 during OCM performing in the CLR.

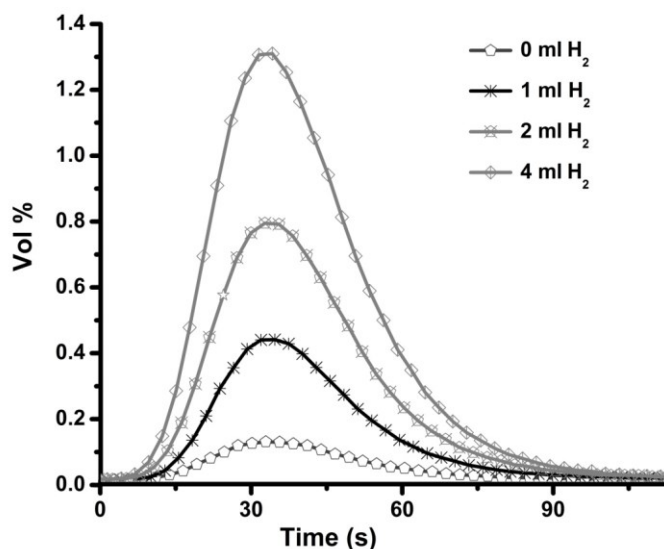


**Figure 3. 11** - Comparison of the hydrogen peak formed during the injection of the first pulse of the C<sub>2</sub>H<sub>6</sub> to the reactor when the catalyst surface is reduced with different amount of hydrogen. All the other reaction conditions are the same. 1g catalyst, carrier gas flow: 25 Nml/min of He, 0.5 ml of the C<sub>2</sub>H<sub>6</sub> pulse, T= 750 °C. (**Paper 4**)

### 3.1.3.1.3 Process modification

All these observations suggest that the limitation for OCM in CLR is more a conversion problem rather than selectivity. It is originated from the competition of H<sub>2</sub> with methane for reacting with the catalyst active sites. Therefore, it is concluded that to successfully apply OCM in CLR, it is vital to control the formation of hydrogen, or in other words TDH of ethane. Since TDH is an equilibrium reaction, its rate might be controlled by changing its operating conditions. For example, as the number of moles of the products in this reaction is higher than the reactants, increasing the pressure is expected to result in a decrease in the rate of production of hydrogen when it approaches its thermodynamic limit.

However, it should be noted that TDH of ethane is also the main route to the formation of the most valuable product of OCM, i.e. ethene. Regardless of the technique implemented for suppressing the rate of this reaction, which inhibits the formation of hydrogen and consequently saves the active site of the catalyst for methane activation, would unavoidably decrease the rate of formation of ethene. Therefore, the desired process modification would only be beneficial if a two steps process would be applied to run this reaction. In the first stage, a CLR is operated where methane coupling takes place at high selectivity. To make the CLR industrially more applicable, the purging step, needed for removing the weakly adsorbed and gas phase oxygen,

is tried to be avoided in this design. To do so, the catalyst oxidation and the methane coupling steps are designed to take place in two separate fluidized bed reactors. In the first reactor, the catalyst is oxidized by the flowing air. Then the purging and separation of the catalyst are done in the cyclone installed in the reactor upstream. The cyclone is still equipped with an inert gas line to make purging possible if needed. After that, the catalyst is sent to the second fluidized bed reactor where it reacts with methane before it would be recycled to the oxidation reactor. Under these conditions, continuous operation of the catalytic coupling section, which has a high priority for industrial application, can be realized.

In the methane coupling reactor, the further conversion of ethane to ethene and hydrogen either completely or partially should be suppressed. Next, the effluent of the coupling reactor is sent to another reactor where it can be converted thermally to ethene. In the final step, the produced  $C_{2+}$  products and unconverted methane are separated from the  $CO_x$  products. Details on the separation techniques applicable in the separation of  $CO_x$  from low chain hydrocarbons are already discussed in detail in the literature [132,133]. then, the flow of hydrocarbons goes through one more separation step to separate methane from  $C_{2+}$  products. The possible separation techniques needed here is widely discussed in the literature [132–134]. Next, the separated methane is recycled to the chemical looping reactor while value-added products are collected for further processing. A scheme of the discussed process concept is presented in Figure 3.12.

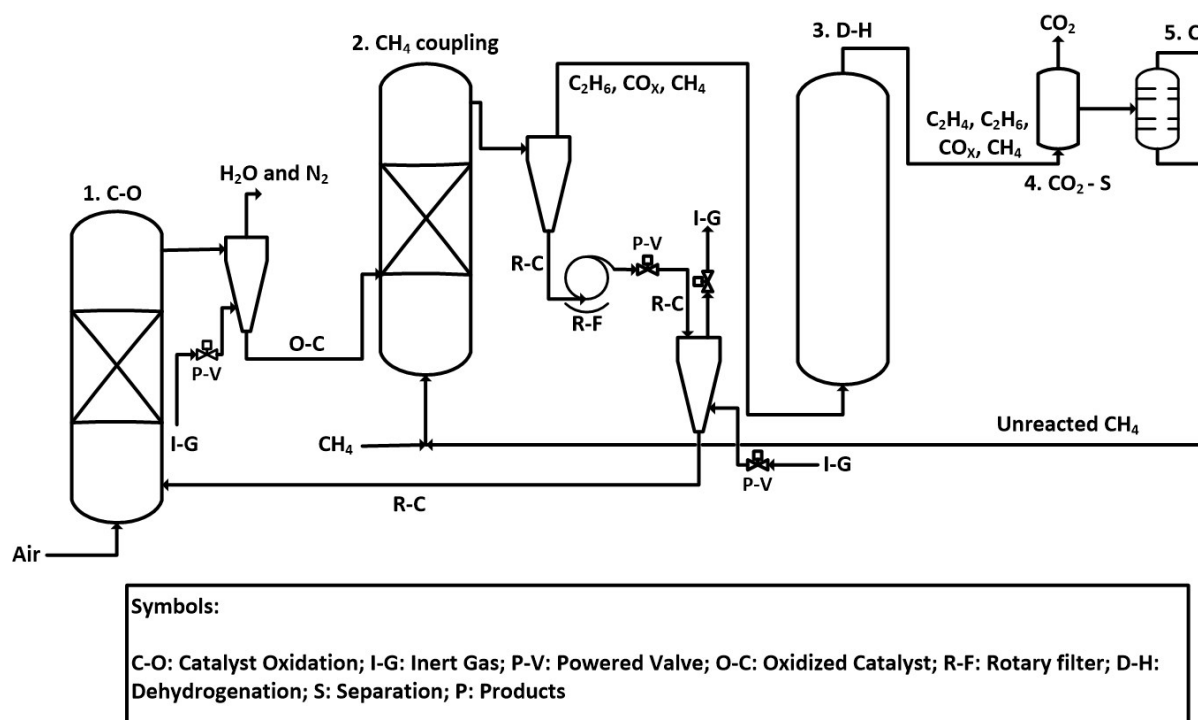


Figure 3. 12 - Schematic of the suggested process concept for doing OCM in two stages. (Paper 4)

### 3.1.4 Role of the catalyst composition on the operation of $Mn_xO_y-Na_2WO_4/COK-12$

An enhancement in the catalytic activity of  $Mn_xO_y-Na_2WO_4$  in the co-feeding reaction mode was observed by change of the catalyst support from Silica gel to ordered mesoporous SBA-15 [29]. Despite the better performance of this catalyst, the high price of the SBA-15 in comparison to silica gel is a serious drawback for its practical implementation. However, developing an inexpensive method for synthesizing and upscaling of another mesoporous silica, denoted as COK-12, with similar characteristics to SBA-15 [31,135], could solve this problem. The enhancement in the performance of the catalysts, loaded over ordered mesoporous silica is assigned to the better dispersion and interaction of the metal oxides over the support [29,31]. Noteworthy, the performance of methane oxidation over  $Mn_xO_y-Na_2WO_4$  is reported to depend on the degree of manganese oxide crystallinity [136]. The crystallinity is strongly dependent on manganese distribution on the catalyst surface. The more manganese oxide is deposited per surface unit area, the higher the degree of crystallinity [137]. The dispersion of the manganese oxide on the surface is reported to influence its oxidation state as well. [138]. At low manganese loadings,  $Mn_2O_3$  is predominant, while at higher loadings  $Mn_3O_4$  is formed [136]. These observations indicate the possibility of changing the catalyst properties through varying its structure. The redox potential of the catalyst, whose vital role on the conversion of methane in the CLR was discussed in detail **in paper 4**, is one of those parameters.

Based on this understanding, the possibility of enhancing the oxygen storage capacity of  $Mn-Na_2WO_4$  through tuning its composition and surface area was investigated in **paper 5**:  $Mn_xO_y-Na_2WO_4/COK-12$  was synthesised at 5 different Mn loadings and 4 different surface areas. The catalyst samples were tested in both single- and multi-pulse experiments. In each of the tests carried with surface area variation samples, 600 mg catalyst was used. The catalyst amount of the manganese and support material variation samples was 1 g.

The single pulse studies were done at a temperature range of 700-800 °C with total flows of 20 and 30 Nml min<sup>-1</sup>. The catalyst reduction and oxidation steps were carried by sending pulses of 1 ml oxygen and methane to the reactor. The catalyst stability and the trend of changes in their performance were the main parameters investigated in these studies.

The multi-pulse experiments were performed at 775 °C with a total flow of 30 Nml min<sup>-1</sup>. To conduct these experiments, first, the samples were oxidized, then applied to several pulses of

methane without repeating the oxidation step in between. The injection of methane was stopped as soon as no conversion was detected. The oxygen storage capacity of the catalyst was calculated in these studies based on the hypothesis that the formation of all the products is the result of oxidation of methane. In addition, it is assumed that during the reaction all the consumed oxygen is converted to either water or CO<sub>2</sub>. All the details on these calculations procedure are provided in the section 2.3.2 of the **paper 5**.

### **3.1.4.1 Varying the specific surface area**

#### **3.1.4.1.1 Single pulse studies**

The results of the catalyst testing in chemical looping experiments with the samples with different SSA are presented in Fig-3.13. It should be noted that all these samples have similar metal composition (2 wt-% Mn and 5 wt-% Na<sub>2</sub>WO<sub>4</sub>). An increase in the SSA leads to a linear increase of methane conversion, however, the sample with the largest SSA experienced a decrease in the methane conversion, see Fig-3.13 A. An inverse behavior is found for C<sub>2</sub> selectivity, which first decreases and then increases again, as presented in Fig-3.13 B. The same behavior was observed for the experiments done at different residence times and temperatures (See Fig-3.13). The calculation of the Weisz-Prater criteria revealed that mass transport limitation by pore diffusion can be excluded in these studies. Therefore, it was concluded that the mass transport effects are not responsible for these observations.

The increase in the reaction performance with increasing the SSA is in accordance with the literature reports [29]. This behavior is assigned to a better distribution of the active components on the catalyst surface. This results in an increase in the accessibility of the active sites per gram of the catalyst. However, the decline in the performance of the sample with the highest SSA was indicating the existence of an optimal surface area for these samples. The effect of this parameter in relation to the thickness of the active compounds covering the surface was investigated and clarified in these studies.

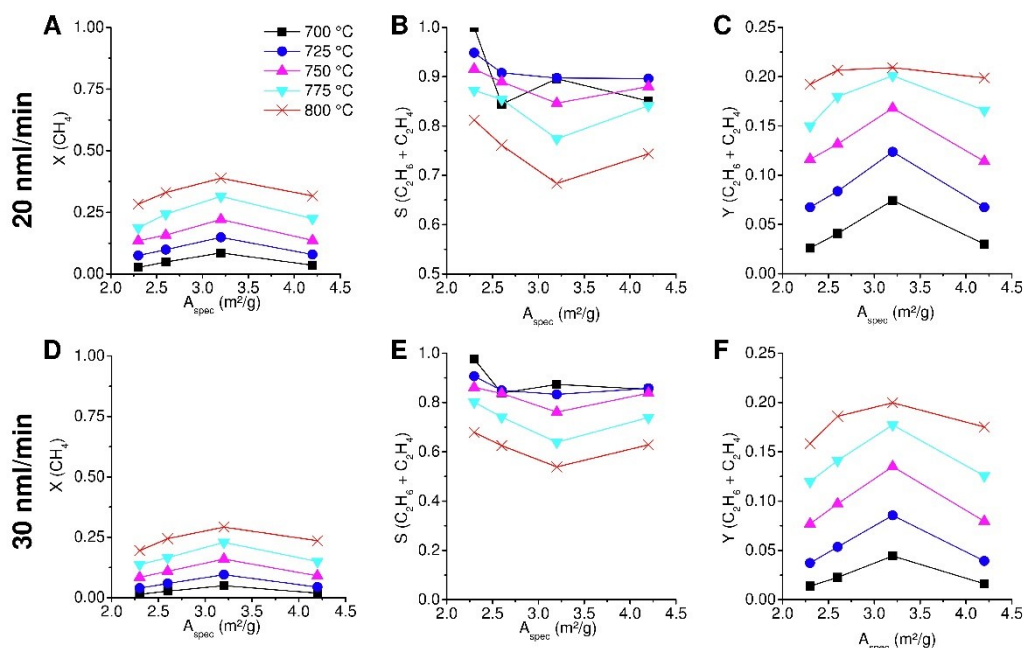


**Figure 3. 13** - Results of chemical looping experiments on  $\text{Na}_2\text{WO}_4$  (5 wt-%)/Mn (2 wt-%)/COK-12 catalysts with different specific surface areas at different temperatures, 0.6 g catalyst, 1 ml  $\text{CH}_4$  pulse in each experiment, A-C: methane conversion,  $\text{C}_2$  selectivity and  $\text{C}_2$  Yield at 20 nml/min, D-F: methane conversion,  $\text{C}_2$  selectivity and  $\text{C}_2$  Yield at 30 nml/min. **Paper 5**

To explain the observations made in Fig-3-13, it should be noted that the  $\text{Mn}_x\text{O}_y\text{-Na}_2\text{WO}_4$  is present as a film over the catalyst. This layer is suggested to go through a phase transfer and melts under the OCM reaction conditions [30,61,66,67,139]. This hypothesis was proven in our studies by doing a TEM analysis on one of the reduced samples which was quenched, as explained in section 3.2.1 of **paper 5**, to retard the recrystallization of the melted phases. As the TEM image in Fig-3.14 shows, rounded particles morphology with a spread over-layer and the loss of sharp edges is created over the used catalyst. This appearance of the particles is typical for a solidified material after melting. Therefore, we assumed that the deposited materials of the catalyst wet the surface of the support to form a homogeneous layer which behaves close to a melt or liquid phase under OCM conditions. This observation indicates the presence of a significant interaction between the active components ( $\text{Na}_2\text{WO}_4$  and Mn) and the support material under the reaction conditions. Decreasing the SSA, at a constant weight loading of the metal oxides, leads to a decrease in the thickness of the  $\text{Mn}_x\text{O}_y\text{-Na}_2\text{WO}_4$  layer over the surface of these catalysts. As the film of  $\text{Na}_2\text{WO}_4$  and Mn becomes thicker, their bounding to the support levels off.

A hypothetical thickness ( $d$ ) is calculated for the layer of the molten active catalyst materials  $\text{Na}_2\text{WO}_4$  and Mn covering the support. This calculation was conducted with a simple geometric model according to equations (15) – (17). It was assumed that the density of the catalyst compounds is similar to the ones of the bulk materials.

These calculations indicated that the samples with a low surface area result in a thicker film of  $\text{Na}_2\text{WO}_4$  and Mn. We suggest that the remaining pores after calcination and phase transition to  $\alpha$ -cristobalite of the mesoporous COK-12 are filled up with the active materials. Therefore, a closed film of  $\text{Na}_2\text{WO}_4$  and manganese oxide provides less surface area and less concentration of active metals over the surface. The theoretical number of active layers (# Layers) was derived according to equation (18). The bond length  $L(\text{W-O})$  and  $L(\text{Mn-O})$  was assumed in these calculations to be constant and equal to 0.1925 nm and 0.1984 nm, respectively [140]. Finally, a film consisting of 25 layers was suggested as the optimal thickness of the active compounds over the catalyst.

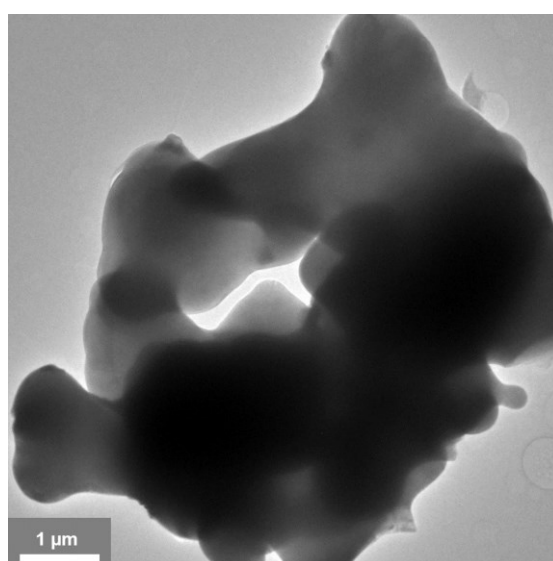


**Figure 3. 14-** TEM image of the catalyst sample after reduction with methane and quenching from 750°C to room temperature. Paper 5

$$d(\text{Na}_2\text{WO}_4) = \frac{w\%(\text{Na}_2\text{WO}_4)}{\rho(\text{Na}_2\text{WO}_4) \cdot A_{\text{spec,cat,P}}} \quad (15)$$

$$d(\text{Mn}_2\text{O}_3) = \frac{w\%(\text{Mn}_2\text{O}_3)}{\rho(\text{Mn}_2\text{O}_3) \cdot A_{\text{spec,cat,P}}} \quad (16)$$

$$d = d(\text{Na}_2\text{WO}_4) + d(\text{Mn}_2\text{O}_3) \quad (17)$$

$$\# \text{ Layer} = \frac{d(\text{Na}_2\text{WO}_4)}{L(\text{W-O})} + \frac{d(\text{Mn}_2\text{O}_3)}{L(\text{Mn-O})} \quad (18)$$

### 3.1.4.1.2 Multi-pulse studies

The results of the reaction activity for each of the pulses in the multi-pulse experiments with varying SSA is presented in Fig-3.15 A. After six consecutive methane pulses, the methane

conversion for all the samples reached the same level. The C<sub>2</sub> selectivity of these catalysts is also observed to be in the same range, varying between 0.8 - 0.9, but it decreased with each additional methane pulse (see Fig 4 of **paper 5**). The decrease of the C<sub>2</sub> yield in these experiments is primarily affected by the decrease of methane conversion. The results of the methane-based oxygen balances are presented in Fig-3.15 B. Variation of the specific surface area caused minor changes in the share of oxygen consumed for the formation of both ethane and ethene. However, the more methane is converted, the more CO<sub>2</sub> is formed.

Noteworthy, the most active catalyst material in the single pulse studies (SSA = 3.2 m<sup>2</sup>/g) also showed the highest amount of oxygen storage capacity and activity in the multi-pulse tests. This behaviour can be explained by our assumption about the thickness of the active compound layer discussed earlier. For a given loading, low SSA results in a high thickness of active layer [136]. A thick film of the active compounds would store most of the oxygen in its bulk phase, which is less accessible for the methane pulses. Under these circumstances, the ratio of O<sub>surface</sub>/O<sub>bulk</sub> is low. Therefore, oxygen availability and consequently the reactivity is expected to be lower for such a material. A decrease of the film thickness would mean that less oxygen is stored in the bulk and the ratio of O<sub>surface</sub>/O<sub>bulk</sub> increases. Thus, more oxygen is present on the catalyst surface and its availability for reaction increases. Further decrease of the film thickness may have a strong impact on the redox potential of metal oxides, probably Mn, due to a stronger binding to the support material.

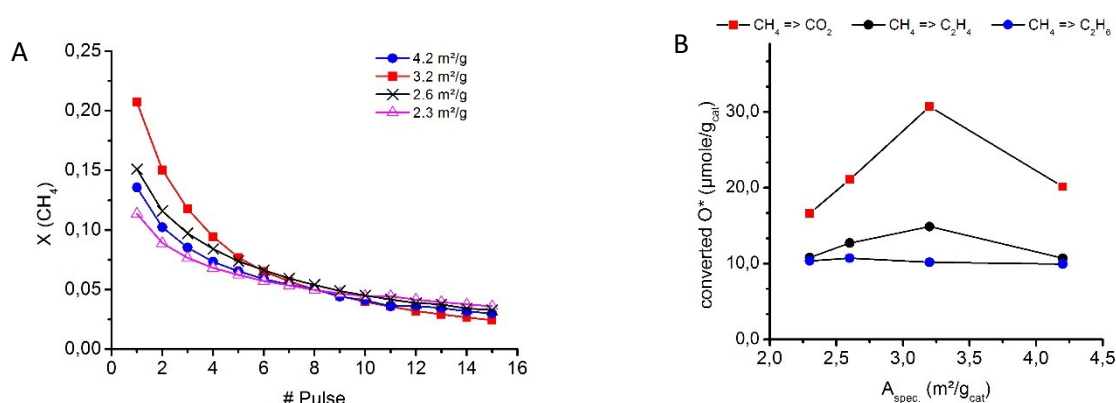


**Figure 3. 15-** Results of repetitive methane pulse experiments on Na<sub>2</sub>WO<sub>4</sub> (5 wt-%)/Mn (2 wt-%)/COK-12 at different specific surface areas, 30 nml/min, 775 °C, 0.6 g catalyst; A) methane conversion, B) Summation of the amounts of the converted oxygen for all methane pulses calculated for each of the catalysts. **Paper 5**

### 3.1.4.2 Influence of Mn variation on reaction performance

#### 3.1.4.2.1 Single pulse studies

In Fig.3.16 the results of testing the reaction over catalyst samples with various manganese loadings are presented. For both tested space velocities, a maximum methane conversion was

observed at around 2-wt % manganese loading. Increasing the manganese loading from 0 to 2-wt % results in a significant enhancement in the methane conversion. However, a further increase of the manganese loading is observed to decrease the catalyst activity again. The inverse trend was observed for the C<sub>2</sub> selectivity. A maximum C<sub>2</sub> yield of 0.25 was measured in these experiments. As mentioned in the last section, an increase of manganese loading affects the redox potential of the catalyst and results in a higher crystallinity. At manganese loadings higher than 2-wt %, manganese oxide species shift from Mn<sub>2</sub>O<sub>3</sub> to Mn<sub>3</sub>O<sub>4</sub>. Such an effect is observed at higher loadings (10-20 wt-% Mn) by XRD, and for loadings in the range of 3-10 wt-% by XANES and EXAFS for manganese oxides supported on silica. At loadings below 10 wt-% of Mn, XRD cannot detect Mn<sub>3</sub>O<sub>4</sub> formation [141]. Investigation of the catalyst material by in-situ XRD showed the formation of MnWO<sub>4</sub> under OCM reaction conditions [30]. Therefore, it would be possible to form MnO\*WO<sub>3</sub> instead of Mn<sub>3</sub>O<sub>4</sub>. For our catalyst with low manganese oxide loadings, the film on the surface of the support is thin but still densely covered with Mn/W oxides. An increase of the manganese loading also increases the film thickness. Therefore, the coupled effect of oxidation state and film thickness can explain the observations made in this series of experiments.

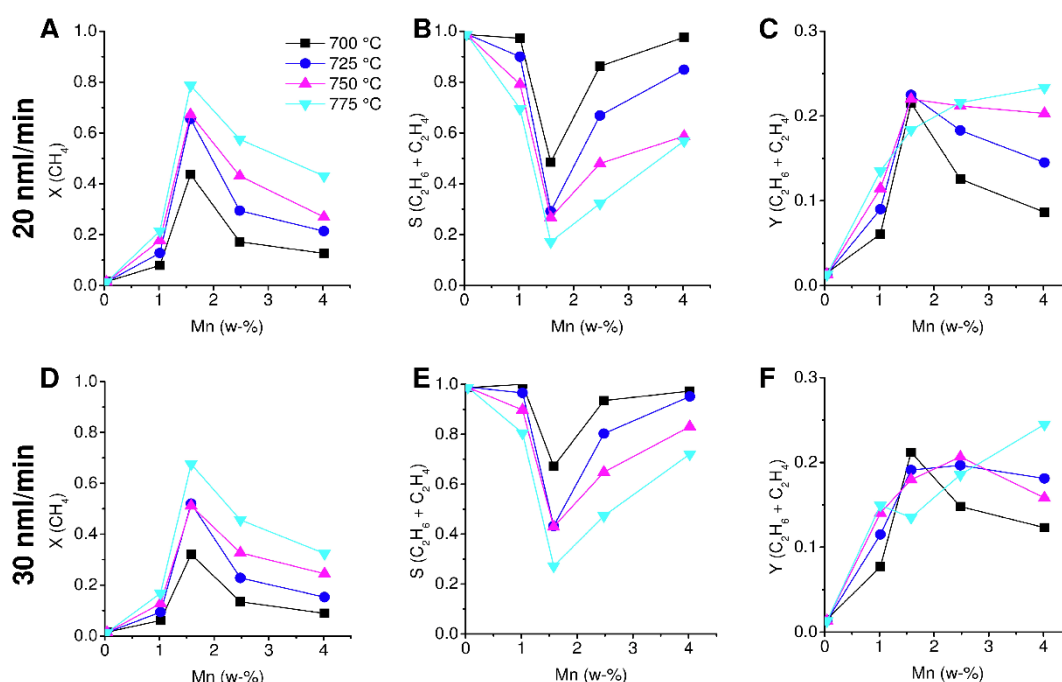


**Figure 3. 16** - Results of chemical looping experiments on Na<sub>2</sub>WO<sub>4</sub> (5 wt-%)/Mn (var. wt-%)/SiO<sub>2</sub> catalysts at different Mn loadings and temperatures, 1 g catalyst, 1 ml CH<sub>4</sub> pulse A-C: methane conversion, C<sub>2</sub> selectivity and C<sub>2</sub> Yield at 20 nml/min, D-F: methane conversion, C<sub>2</sub> selectivity and C<sub>2</sub> Yield at 30 nml/min, 1 ml CH<sub>4</sub> pulse. **Paper 5**

### 3.1.4.2.2 Multi-pulse studies

The results of our repetitive methane pulse experiments for different loadings of Mn are shown in Fig-3.17. No significant methane conversion was observed at 0.02 wt-% manganese loading.

However, it is known in literature that alkaline metal doped tungstate supported on silica shows substantial OCM activity in co-feed steady-state experiments [142,143]. Such a difference between literature and our results indicates that the oxygen storage functionality is related to manganese ions.

The more manganese is loaded with the catalyst, the higher is the oxygen storage capacity of the samples and more methane pulses are necessary to reduce the samples completely. The catalyst containing the highest amount of Mn, *i.e.* 4 wt-%, showed also the best C<sub>2</sub> yield for each of the methane pulses (see Fig 6 C in **paper 5**). This sample also endured the longest testing and was still active after dosing almost 25 pulses of methane. The total amount of converted oxygen for this catalyst is calculated to be at least 105 μmole/g<sub>cat</sub>.

To explain these observations a change in the oxidation state of at least one of the metal active components in these samples should be considered. Either W (between 6+ and 5+) [144] or Mn (between 3+ and 2+) are proposed to be able to switch their oxidation state in Mn<sub>x</sub>O<sub>y</sub>- Na<sub>2</sub>WO<sub>4</sub> catalyst. On one side, it needs to be considered that the concentration of the metal active compound which switches its oxidation state is strongly influencing the oxygen storage capacity of the catalyst. On the other side, the concentration of Mn is the only parameter which is changed in these studies. If the Na<sub>2</sub>WO<sub>4</sub> was responsible for the oxygen storage capacity in chemical looping experiments, we would expect that at least the amount of total oxygen converted in these studies had stayed constant. However, this was not the case. Therefore, Mn<sub>x</sub>O<sub>y</sub> is suggested to be the metal oxide which is switching its oxidation state in these studies. This idea was also proved by further XRD, EPR, and XPS analyses which are discussed in details in section 4.4 of **paper 5**.

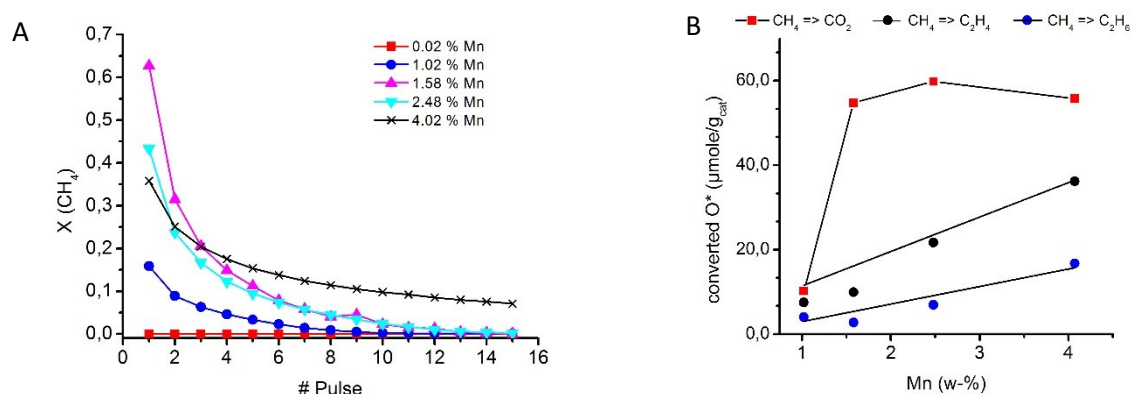


**Figure 3. 17-** Results of repetitive methane pulse experiments on Na<sub>2</sub>WO<sub>4</sub> (5 wt-%)/Mn (2 wt-%)/COK-12 at different Mn loading, 30 nml/min, 775 °C, 0.6 g catalyst; A) methane conversion, B) Summation of the amounts of the converted oxygen for all methane pulses calculated for each of the catalysts. **Paper 5**

### 3.1.5 Conclusions of OCM project

The reaction mechanism of OCM over  $Mn_xO_y-Na_2WO_4$  was investigated and its understanding was successfully enhanced.

The results of the TPSR investigations with methane are in accordance with the idea of the presence of more than one sort of oxygen species over the surface. During these studies, which were done in the absence of the gas phase oxygen, CO and  $C_2H_6$  were shown to be the main products of the reaction. The significant time delay observed between the formation of these products indicated the involvement of different oxygen species in the formation of each of these components. A considerable difference was observed between the apparent activation energy of methane calculated in our TPSR experiments (275 kJ/mol) and the literature data reported in steady state condition (133 kJ/mol). This was assigned to the absence of the weakly adsorbed oxygen in the former experiments. The chemisorbed species involved in the TPSR experiments have a lower level of energy. Consequently, their reaction results in a higher apparent activation energy than the physisorbed oxygens.

Ethane is shown to be the primary product of methane coupling reaction. This product is observed to consecutively dehydrogenate to form ethene. The conversion of ethane to ethene is proposed to perform thermally in the gas phase rather than oxidatively on the catalyst surface. The consecutive reaction of  $C_2$  components is introduced as the main pathway to the formation of unselective products, i.e.  $CO_x$ . It is observed that the secondary oxidation of these components, especially ethane is conducted mainly in the presence of the molecular gas phase oxygen. The theoretical and experimental evidence indicated the film diffusion limitation as the reason for the low contribution of the  $Mn_xO_y-Na_2WO_4$  catalyst on the conversion of  $C_2$  components under the applied reaction conditions.

These mechanistic findings suggested the possibility of enhancing the reaction performance by conducting the reaction in the absence of gas phase oxygen and those unselective surface species. This condition is realized by implementing the already known chemical looping concept for performing OCM. A simulated chemical looping reactor was built in our laboratory and implemented in testing OCM under various reacting conditions. This reactor resulted in a more efficient conversion of methane than the co-feeding experiments, especially at methane conversions lower than 30 %. Moreover, in the chemical looping reactor methane conversions higher than 50 % were achieved. This was not possible in the co-feeding reactors since the applied reaction conditions are limited by the explosive regime. However, despite all these

advantages, the maximum yield obtained in these experiments was also limited to 25 % which is still below the minimum value required for industrializing the process. It was observed that both the inherent nature of the  $\text{MnxOy-Na}_2\text{WO}_4$  catalyst and the characteristics of the reaction mechanism cause this limitation. It is shown that the conversion of methane in the CLR is performed with a high selectivity toward the coupling reaction. Since the mechanistic studies had revealed the TDH reaction as the main route for the conversion of ethane to ethene, therefore, it was expected that the rate of formation of hydrogen (the by-product of TDH) in the CLR consequently increases. Unlike the co-feeding reactors where the  $\text{H}_2$  converts in the presence of gas phase oxygen to water, in the CLR it competes with methane for consuming the oxygen of active centers on the catalyst surface. Under these conditions, the rate of activation of methane decreases, therefore despite the enhancement in the selectivity, the yield limitation could not be overcome. One of the possibilities for solving this limitation might be through implementing a two-stage process. There, the coupling of methane is occurring in the first stage while the dehydrogenation of ethane to ethene is postponed to a second reactor, where the formation of hydrogen does not limit methane conversion anymore. The other possibility for enhancing the methane conversion in the CLR is by enhancing its oxygen storage capacity. To tune this parameter a systematic variation in the catalyst composition and surface area was conducted. It was shown that at SSA lower than  $4 \text{ m}^2/\text{g}$  the conversion of methane and SSA correlate directly. Mn was introduced as the reason for the oxygen storage functionality of the  $\text{Na}_2\text{WO}_4/\text{Mn}/\text{SiO}_2$  catalyst. Unfortunately, none of the samples tested in these studies resulted in the  $\text{C}_2$  yield higher than 0.25.

A reversible reduction of Mn (III) was reported to be carrying on the  $\text{Na}_2\text{WO}_4/\text{Mn}/\text{SiO}_2$  catalyst since no indication for the presence of W (V) was found on the sample quenched after reduction. Besides, an optimal surface concentration of  $66 \text{ Mn}/\text{nm}^2$  and  $33 \text{ W}/\text{nm}^2$  was calculated for the catalyst in these studies. The highest catalytic performance for  $\text{Na}_2\text{WO}_4/\text{Mn}/\text{SiO}_2$  was reported to be obtained at about 25 catalyst layers.

## 3.2 MTM

### 3.2.1 Solid-state ion-exchanged Cu/mordenite catalyst for the direct conversion of methane to methanol

In recent years, many different bioinspired catalysts for the direct conversion of methane to methanol have been intensively studied with the aim of realizing this dream reaction over a heterogeneous catalyst under mild reaction conditions. Hammond *et al.* found that Fe-contain-

ing zeolites are active for the methane-to-methanol conversion in an aqueous solution of hydrogen peroxide [99]. Notably, the addition of Cu species to the catalyst structure was shown to significantly improve the reaction performance (10% methane conversion with 93% methanol selectivity) under appropriate reaction conditions [90]. However, as H<sub>2</sub>O<sub>2</sub> is more expensive than methanol, the direct use of O<sub>2</sub> as oxidant is inevitable for industrial applications [16]. Several research groups have demonstrated that iron-, cobalt-, and copper-loaded zeolites activated in O<sub>2</sub> or N<sub>2</sub>O can react with methane at low temperatures ( $\leq 200$  °C) and subsequently release methanol upon treatment with water or organic solvents (acetonitrile, ethanol, tetrahydrofuran) [83,91,98]. Among them, Cu/zeolites have currently been emerged as the best catalyst based on their experimental performances [83,91,97,101]. While, in most of these reports, Cu<sup>2+</sup> cations are typically loaded into zeolites *via* liquid-phase ion exchange, Bozbag *et al.* recently performed a solid-state ion exchange between H-mordenite with copper (I) chloride to achieve a Cu/mordenite catalyst. However, the residual chlorine was reported to hinder the production of methanol from methane in the first catalytic runs [104]. This problem was addressed **in paper 3**. In these studies, several Cu-mordenite catalysts were synthesized through the solid- and liquid-state ion exchange methods. Both the copper (II) acetylacetonate and copper(I) chloride were used as the copper precursors in these syntheses (see Table 1 of **paper 3**). The performance of the samples was compared with each other and solid-state ion-exchanged Cu/mordenite synthesized using copper (II) acetylacetonate was introduced as the best performing sample among all the tested ones. The behavior of this catalyst along the reaction was investigated in more details for the first time in this study by implementing several *in-situ* characterization methods.

### 3.2.1.1 Catalytic performance

Table 3 3 presents a list of all the catalyst samples tested in these studies. The advantage of the solid-state Cu exchange method vs. the traditional liquid state process was investigated through testing several different samples prepared through each of these preparation methods. To study the effect of the copper precursor on the catalyst performance, CuCl and Cu(acac)<sub>2</sub> were used for preparing Cu/mordenite samples. The Cu content within the mordenite was varied by changing the mordenite/Cu(acac)<sub>2</sub> ratio in the tested sample to investigate the effect of this parameter on the catalyst performance.

After loading Cu to the mordenites, only a negligible change in the BET surface area of the samples was observed (see Table S1 in **paper 3**). The XRD pattern of the Cu-loaded catalysts

was observed to be identical to the parent mordenites (see Figure S1 in **paper 3**), no additional peaks specific for elemental Cu or its oxides were detected in the patterns. This observation indicates that the Cu species in all the samples are well dispersed throughout the zeolite framework. However, it should be noted that despite their structural similarity, the activity of each of these samples was different than the others as discussed in more details in the following.

CuMorS-1, 2.58 wt.% Cu and CuMorL-1, 3.21 wt.% Cu (see table 3-3) were prepared as the reference solid-state and liquid-phase ion exchange samples, respectively. After activation at 550 °C, the former, CuMorS-1, was able to produce 55.3  $\mu\text{mol g}_{\text{cat}}^{-1}$  of methanol after treatment with methane at 200 °C for 60 min and off-line extraction with 5 ml of water while the latter, CuMorL-1, resulted in the formation of 28.2  $\mu\text{mol g}_{\text{cat}}^{-1}$  methanol under the same conditions. This observation indicates that the sample prepared through solid phase ion exchange shows a much better catalytic performance than the liquid phase ion exchange under the identical conditions even though the Cu content in the former is significantly lower.

The advantage of using  $\text{Cu}(\text{acac})_2$  rather than  $\text{CuCl}$  on the performance of the catalyst was proved by testing the performance of CuMorS-1 and CuClMorS. The copper loadings in both samples are similar. However, the yield to methanol in the former catalyst is observed to be significantly higher than the latter one. This behavior is assigned to the absence of  $\text{Cl}^-$  and lower concentration of  $\text{Cu}^+$  in the sample prepared with  $\text{Cu}(\text{acac})_2$ .

Based on these results, CuMorS, Cu/mordenite synthesized through solid phase ion exchange using  $\text{Cu}(\text{acac})_2$ , was identified as the best performing catalyst and chosen for the further investigations.

**Table 3 3** - Details of Cu/mordenite catalysts tested in this study

Entry	Catalyst	Preparation method <sup>(a)</sup>	Substrates <sup>(b)</sup>	Cu content (wt.%)	Produced Methanol ( $\mu\text{mol/g catalyst}$ ) <sup>(c)</sup>
1	CuMorS-1	SSIE	$\text{Cu}(\text{acac})_2$ and $\text{NH}_4\text{-Mor-1}$	2.58	55.3
2	CuMorS-2	SSIE	$\text{Cu}(\text{acac})_2$ and $\text{NH}_4\text{-Mor-1}$	1.01	35.7
3	CuMorS-3	SSIE	$\text{Cu}(\text{acac})_2$ and $\text{NH}_4\text{-Mor-1}$	1.84	51.8
4	CuMorS-4	SSIE	$\text{Cu}(\text{acac})_2$ and $\text{NH}_4\text{-Mor-1}$	3.74	44.2
5	CuMorS-5	SSIE	$\text{Cu}(\text{acac})_2$ and $\text{NH}_4\text{-Mor-2}$	2.66	59.4
6	CuClMorS	SSIE	$\text{CuCl}$ and $\text{NH}_4\text{-Mor-1}$	2.84	10.7
7	CuMorL-1	LIE	$\text{Cu}(\text{OAc})_2$ and $\text{Na-Mor-2}$	3.21	28.2

8	CuMorL-2	LIE	Cu(OAc) <sub>2</sub> and Na-Mor-1	3.10	32.3
9	CuMorL-3	LIE	Cu(OAc) <sub>2</sub> and NH <sub>4</sub> -Mor-1	2.07	16.7

<sup>(a)</sup> SSIE and LIE correspond to solid-state and liquid-phase ion exchange, respectively. Liquid-phase ion exchange was performed in 200 ml of water.

<sup>(b)</sup> Si/Al ratio = 10 in Mor-1 and 6.5 in Mor-2.

<sup>(c)</sup> These catalysts samples were tested in a stepwise manner, namely i) activation of the material at 550 °C under an O<sub>2</sub> flow for 8 h, ii) interaction of the material with methane at 200 °C, and iii) extraction of methanol using 5 ml of water at room temperature for 2 h.

First, the effect of the time of the interaction of the catalyst with methane on the formation of methanol was studied at 200 °C. In the first 30 min, a contentious increase of methanol production with increasing the catalyst time on stream was observed. However, after this reaction time, methane production reached a plateau, i.e. just a negligible yield improvement is seen within the next 30 min (see Figure 1 in **paper 3**).

Finally, the effect of the applied oxidation temperature on the reaction performance was studied. It was shown that the catalytic activity of CuMorS-1 was remarkably enhanced by raising the activation temperature up to 650 °C (see Figure 5 in **paper 3**). The reaction with methane at 200 °C yielded 37.3, 55.3, and 65.2  $\mu\text{mol g}_{\text{cat}}^{-1}$  of methanol using the CuMorS-1 catalyst activated at 450, 550, and 650 °C respectively. This behavior is assigned to the probable enhancement in the ion exchange, which is occurring *in-situ* in CuMorS-1, at higher activation temperatures. However, it should be noted that the activation of the catalyst at 750 °C results in a negligible further improvement in the reaction performance, yielding finally 65.8  $\mu\text{mol g}_{\text{cat}}^{-1}$  of methanol. To confirm the positive effect of higher activation temperatures, the same treatment was applied for a reference Cu/mordenite (CuMorL-1, 3.21 wt.% Cu) prepared by liquid-phase ion exchange between Na-mordenite and Cu(II) acetate. Also, in this case, a clear increase in the methanol production from 15.3  $\mu\text{mol g}_{\text{cat}}^{-1}$  to 28.2  $\mu\text{mol g}_{\text{cat}}^{-1}$  was observed when the activation step was raised from 450 °C to 550 °C. Therefore, it is concluded that a larger number of Cu species capable of reacting with methane can be achieved at elevated activation temperatures.

### 3.2.1.2 Mechanism investigations

#### 3.2.1.2.1 Catalyst surface intermediates

Next, the nature of the reaction intermediates resulted from activating methane on the catalyst surface was investigated in more details. To do so, two parallel experiments were conducted.

In both experiments, first, the oxidized CuMorS-1 was introduced at 200 °C to a flow of methane for 30 minutes then it cooled down to the room temperature under the same reaction flow. Afterward, both samples were heated to 550 °C at a rate of 1 K min<sup>-1</sup> one under the dry and the other under a wet flow of 50 Nml min<sup>-1</sup> of He. In these experiments, the effluent was contentiously analyzed with a quadrupole mass spectrometer (InProcess Instruments GAM 200). Figures 3.18 and 3.19 present the product spectrum and changes in the concentration of the measured components during the washing steps for dry and wet experiments respectively. Comparing the results of these two studies shed light on understanding the reaction procedure in more details as discussed in the following.

It should be noted that CO<sub>x</sub> are the only carbon-containing products detected in the reactor outlet of the dry washing experiment (see Figure 3.18). However, both methanol and dimethyl ether were detected at room temperature when the surface was washed with the wet flow of helium (see Figure 3.19). Based on this observation, it is concluded that the presence of water is essential for converting surface intermediate species to methanol.

Moreover, CO<sub>2</sub> is the first component detected during the dry experiment. The formation of this component is started at approx. 200 °C which is interestingly the temperature proposed in the literature for the formation of methoxy species bound to dicopper sites [145,146]. The corresponding formation of hydroxyl species between dicopper sites, generated by the remaining abstracted H atom from methane, is confirmed through detection of water starting at around 300 °C. Surprisingly, heating the methane-treated CuMorS-1 under dry inert gas resulted in the formation of more products namely hydrogen and CO. The formation of these species are also assigned to the decomposition of the surface adsorbed methoxy species. However, the higher formation temperature of these species than those of CO<sub>2</sub> indicates that their intermediates are adsorbed on the surface more strongly.

Noteworthy, from overall 84 μmol g<sub>cat</sub><sup>-1</sup> of carbon oxides detected during the dry experiments, 58 μmol g<sub>cat</sub><sup>-1</sup> was CO. This value is close to the methanol yield obtained during the catalytic test studies discussed in the previous section (see entry-1 of Table 3 3). Based on this observation it is concluded that methanol and dimethyl ether in the DMTM reaction besides H<sub>2</sub> and CO in the dry He flow experiment are formed from the same surface intermediate species. This idea is in accordance with the results of the wet He flow experiments as both methanol and dimethyl ether were detected there but no H<sub>2</sub> and CO (see Figure 3.19).

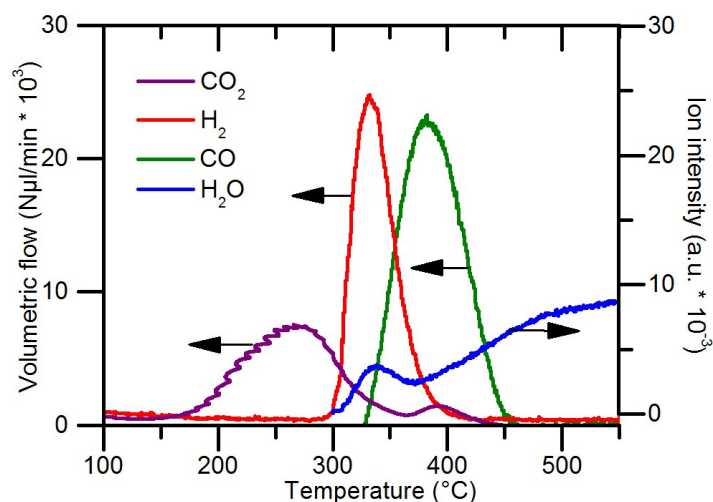


**Figure 3. 18** - Volumetric flows of CO<sub>2</sub>, H<sub>2</sub>, CO, and H<sub>2</sub>O calculated from the mass spectrometry data recorded during heating CuMorS-1 (after interaction with CH<sub>4</sub>) in a dry He flow. **Paper 3**

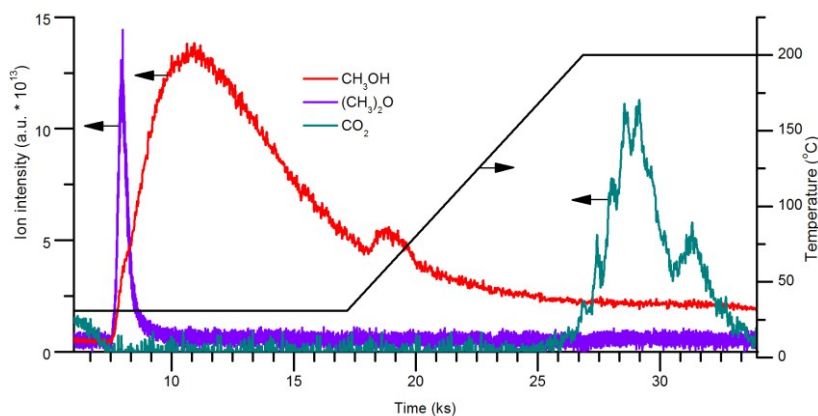


**Figure 3. 19** - Ion intensity-based signal of CH<sub>3</sub>OH ( $m/z = 31$ ), (CH<sub>3</sub>)<sub>2</sub>O ( $m/z = 46$ ), and CO<sub>2</sub> ( $m/z = 44$ ) detected by the MS during the treatment of CuMorS-1 in a wet He flow. **Paper 3**

### 3.2.1.2.2 Type of Cu active species

Later, the type and positions of Cu species located in the mordenite framework were investigated by subjecting the oxidized Cu/mordenites (both CuMorS-1 and CuMorL-1) to temperature-programmed reduction with H<sub>2</sub> (H<sub>2</sub>-TPR) to 900 °C.

The H<sub>2</sub>-TPR curves generally revealed three H<sub>2</sub> consumption features in the tested temperature range (see Figure 3-20 b). The first reduction peaks observed for both, CuMorS-1 and CuMorL-1 in the temperature range from 100 to 300 °C, were attributed to the most accessible Cu sites on the external zeolite surface and in the largest cage of mordenite, i.e. 12-MR channel (Figure 3-20 b) [147]. Compared to the H<sub>2</sub>-TPR profiles of bulk CuO and Cu<sub>2</sub>O (Figure 3-20 a), these reduction peaks of Cu/mordenites are present at lower temperatures probably due to the small size and the good dispersion of Cu clusters on mordenite [147,148]. The H<sub>2</sub> uptakes found at higher temperatures were assigned to the reduction of the less accessible Cu sites in the smaller channels (e.g. 8-MR pore, side pockets) [148]. Particularly, CuMorL-1 exhibits only a shoulder

peak for the second reduction step at approx. 370 °C while a separate feature at a much higher temperature (530 °C) was observed for CuMorS-1, indicating that a large number of Cu-based cations  $\text{Cu}^{2+}$  could be loaded into the ion-exchangeable positions of lower accessibility upon solid-state ion exchange. Furthermore, a broad reduction peak detected at the temperature above 750 °C for CuMorS-1 can be attributed to Cu cations highly stabilized in the zeolitic framework that can just be reduced at distinctly higher temperatures [148,149]. The  $\text{H}_2$  consumption at this temperature range was negligible for CuMorL-1, indicating that much more of these Cu sites exist in CuMorS-1. These results show the high efficiency of the solid-state ion exchange method for diffusion of Cu species to small pores of mordenite. The reason might be the large size of the copper complexes in the aqueous state used in the liquid phase ion exchange. There, the  $\text{Cu}^{2+}$  cations exist as  $[\text{Cu}(\text{H}_2\text{O})_6]^{2+}$  which are too large to easily access the small cages of the zeolite. However, the solid-state ion exchange works efficiently at these positions.

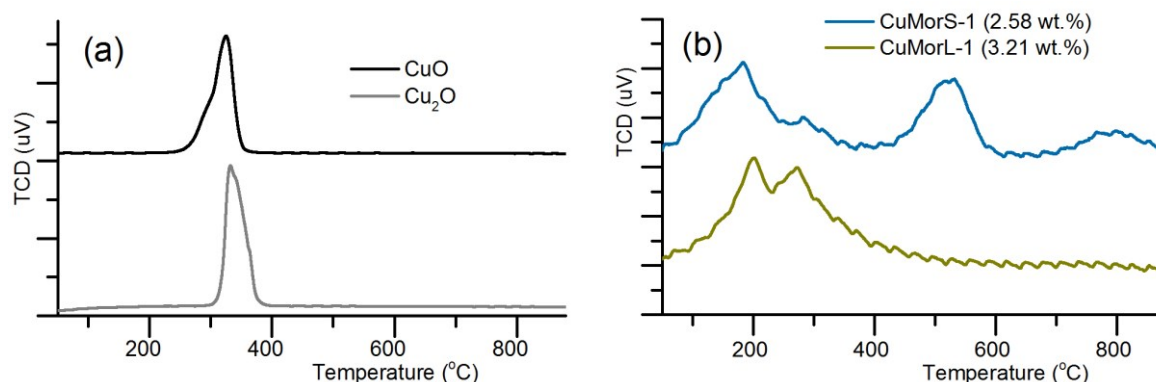


**Figure 3. 20** -  $\text{H}_2$ -TPR profiles of Cu-based materials, (a) reference copper oxides, (b)  $\text{O}_2$ -activated Cu/mordenites. **Paper 3**

Moreover, during the calibration of TPR for CuO, it was observed that  $\text{H}_2$  consumptions for the TPR experiments of CuMorS-1 (2.58 wt.%) and CuMorL-1 (3.21 wt.%) are close to the stoichiometric ratio required for the reduction of  $\text{Cu}^{2+}$  to  $\text{Cu}^0$  (namely, 1.08 and 1.10, respectively). Based on this observation it was concluded that the Cu species over the catalyst are mainly present as Cu(+II) species which is. This idea, which is in accordance with the literature studies [104,149,150], was also confirmed by the absence of indicating the  $\text{Cu}^+$  in the results of X-ray absorption near edge structure (XANES) analysis (Figure S3 of **paper 3**) for the oxidized Cu/mordenite. The measured spectra were completely consistent with those of Cu(II)-containing compounds.

Next, the in-situ UV-visible spectroscopy was carried out to detect and determine the active sites in Cu/zeolites and their structural changes more precisely. The UV-visible diffuse

reflectance spectra of CuMorS-1 and CuMorL-1 were recorded in situ while they were activated under a 50 Nml min<sup>-1</sup> O<sub>2</sub> flow. The materials were heated from room temperature to 550 °C, then cooled down to 200 °C. A band at about 33000 cm<sup>-1</sup>, assigned to the trinuclear copper-oxo clusters ([Cu<sub>3</sub>(μ-O)<sub>3</sub>]) [98,151], with increasing intensity was observed for both catalysts (Figure 3.21a and 3.22 a). It should be noted that even though the overall Cu content in CuMorS-1 (2.58 wt.%) is lower than the CuMorL-1 (3.21 wt.%) the intensity of the 33000 cm<sup>-1</sup> band for the former catalyst is significantly higher than the latter one. The 22200 cm<sup>-1</sup> band assigned to a mono-(μ-oxo) dicopper (II) core was not detected when the materials were heated to 550 °C and the temperature was held for 1 h. However, this band was observed for CuMorS-1 during the cooling period. The appearance of the band at 22200 cm<sup>-1</sup> became even more obvious as the temperature decreased to temperatures lower than 300 °C. This behavior was simultaneous with a decrease in intensity of the band centered at 33000 cm<sup>-1</sup>, suggesting that at low activation temperatures, a small fraction of the [Cu<sub>3</sub>(μ-O)<sub>3</sub>]<sup>2+</sup> clusters in CuMorS-1 was converted into the [Cu<sub>2</sub>(μ-O)]<sup>2+</sup> site (Figure 3.21b).

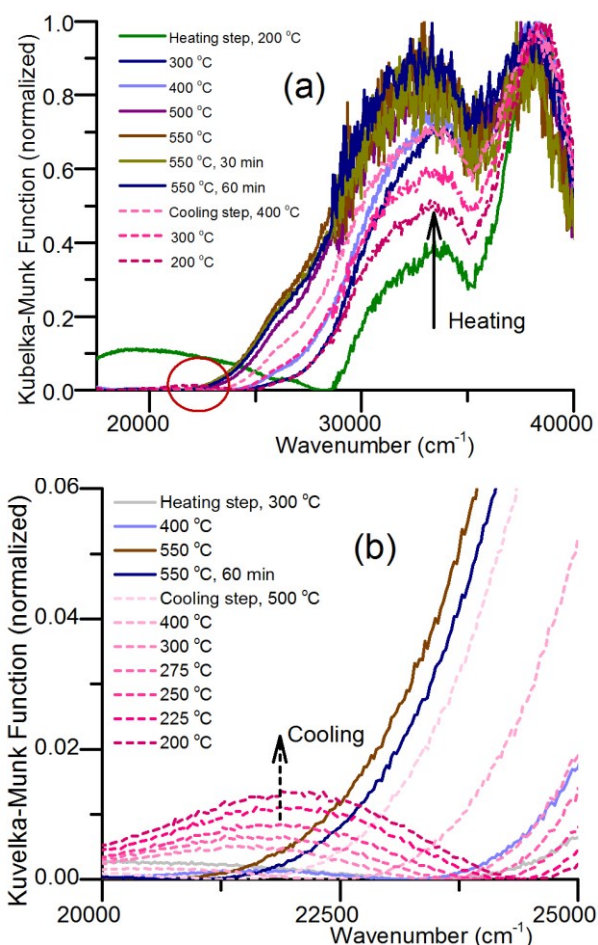


**Figure 3. 21** - In situ UV-vis spectra of CuMorS-1 activated under an O<sub>2</sub> flow in the band range of (a) 15000 – 40000 cm<sup>-1</sup>, (b) 20000 – 25000 cm<sup>-1</sup> (bands at 33000 cm<sup>-1</sup> and 22200 cm<sup>-1</sup> are indicated by the arrow). **Paper 3**

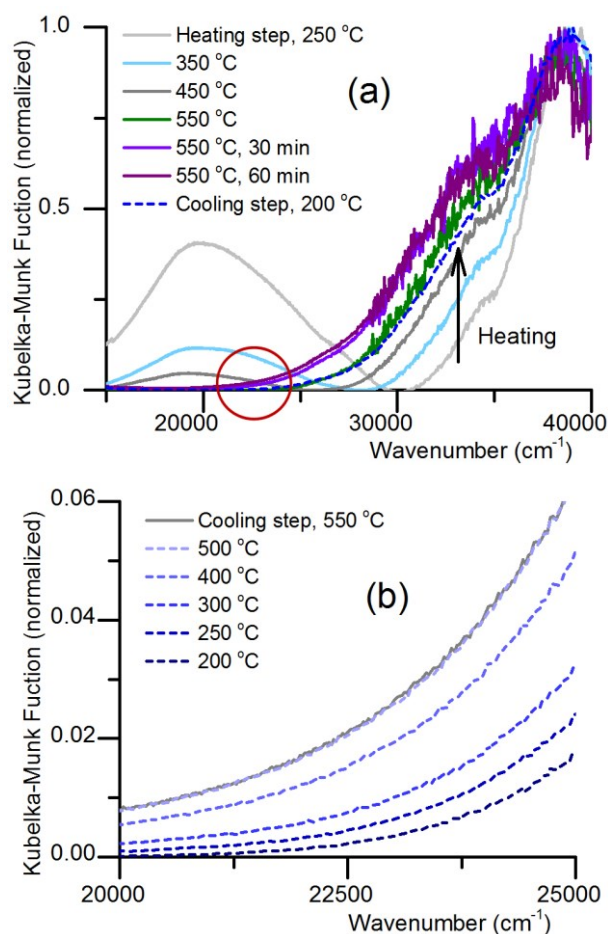


**Figure 3. 22** - In situ UV-vis spectra of CuMorL-1 activated under an O<sub>2</sub> flow in the band range of (a) 15000 – 40000 cm<sup>-1</sup>, (b) 20000 – 25000 cm<sup>-1</sup> (band at 33000 cm<sup>-1</sup> is indicated by the arrow). **Paper 3**

### 3.2.2 Stepwise methane-to-methanol conversion on CuO/SBA-15

As it was mentioned before, the formation of methanol in the heterogeneously catalyzed reactions is achieved through a stepwise reaction process similar to the chemical looping concept. Under these circumstances, the catalyst is first oxidized under the flow of O<sub>2</sub> or N<sub>2</sub>O at high temperatures (> 200 °C). Then, it reacts with methane at lower temperatures (≤ 200 °C) where surface adsorbed intermediates are formed. The subsequent transformation of intermediates to methanol is performed via a final treatment with water. So far Cu/zeolites are the most active and widely studied catalysts in the literature for this reaction. To expand this promising material class, we report here the first demonstration of direct methane-to-methanol conversion over an SBA-15-supported Cu catalyst. Unlike Cu-oxo complexes in zeolite matrix previously suggested as the active sites for the hydroxylation of methane, the small/ultrasmall CuO nanoclusters, that are highly dispersed throughout the framework, are reported as the active sites of SBA-15. Our results are expected to accelerate the development of novel Cu-based catalysts using other supports than zeolites for the “dream reaction” of DMTM.

### 3.2.2.1 Catalyst structure and performance

Two Cu containing catalyst supported over SBA-15 were synthesized by wet impregnation. The sample synthesized from Cu(II) acetylacetonate ( $\text{Cu}(\text{acac})_2$ ) was named Cu-AA/SBA while the one obtained using Cu(II) acetate ( $\text{Cu}(\text{OAc})_2$ ) was named Cu-OA/SBA. Similar Cu loadings ( $\sim 2.7$  wt.%) were obtained for both Cu-AA/SBA and Cu-OA/SBA. The textural properties, i.e. BET surface area, meso and micropore volume of both samples were reported to be similar (see Table 1 of **paper 7**). However, the results of the TEM and XRD analyses (see Figure-1 and 2 of **paper 7**) suggested that the Cu species in the Cu-AA/SBA catalyst are mainly located within the pores of SBA-15 while in the Cu-OA/SBA the larger CuO nanoparticles are also present on the outer surface of SBA-15.

The activity of both these samples was tested in the stepwise procedure. The catalyst was first activated in oxygen at  $550\text{ }^\circ\text{C}$ , then allowed to interact with methane at  $200\text{ }^\circ\text{C}$ . Then, the extraction of methanol was performed with either liquid water (off-line extraction) or steam (on-line extraction). For a catalytic comparison, CuMorS-1 with a Cu loading of  $\sim 2.6$  wt.% discussed in paper 3 was applied as a reference zeolite-based catalyst.

After treating the catalyst with water, methanol was detected in catalytic cycles over both CuO/SBA-15 catalysts. This observation indicates that methane was indeed activated by Cu sites in SBA-15 at low temperature ( $200\text{ }^\circ\text{C}$ ) and then converted to methanol upon treatment with water. A yield of  $30.2\text{ }\mu\text{mol g}_{\text{cat}}^{-1}$  of methanol (Table 3.4, Entry 1) was calculated for Cu-AA/SBA (Table 3.4, Entry 1 and 2) while a lower methanol amount of  $11.1\text{ }\mu\text{mol g}_{\text{cat}}^{-1}$  was produced over Cu-OA/SBA (Table 3.4, Entry 3). The higher production of methanol over Cu-AA/SBA is assigned to the better dispersion of Cu species in the SBA-15 framework in this catalyst. This observation indicates the high influence of the Cu source and the method of material preparation on both, the size of the formed Cu clusters and their catalytic performance.

**Table 3.4** - Catalytic performances of CuO/SBA-15 materials (obtained from paper 7)

Entry	Catalyst	Cu loading (wt.%)	Product yield ( $\mu\text{mol g}_{\text{cat}}^{-1}$ )			Oxidized $\text{CH}_4$ <sup>[c]</sup> ( $\mu\text{mol g}_{\text{cat}}^{-1}$ )	S (MeOH & DME) <sup>[d]</sup> %
			MeOH <sup>[a]</sup>	DME <sup>[b]</sup>	$\text{CO}_2$ <sup>[b]</sup>		
1	Cu-AA/SBA	2.71	30.2	0	3.4	33.6	89.9
2	Cu-AA/SBA <sup>c</sup>	2.71	31.7	0	5.8	37.5	84.5
3	Cu-OA/SBA	2.78	11.1	0	1.0	12.1	91.7

<sup>[a]</sup> Methanol was analyzed by GC after off-line extraction with liquid water.

<sup>[b]</sup> Gas-phase products were analyzed by MS during online extraction with steam.

<sup>[c]</sup> Amount of oxidized methane = moles (MeOH) + 2\*moles (DME) + moles ( $\text{CO}_2$ ).

<sup>[d]</sup> Selectivity to MeOH and DME = [moles (MeOH) + 2\*moles (DME)]/ moles (reacted  $\text{CH}_4$ )

<sup>[e]</sup> Reused catalyst for the second cycle.

Figure 3.23 presents the product spectrum and changes in the concentration of the measured components during the washing step for the Cu-AA/SBA sample. Similar to Cu/mordenite samples discussed in paper 3, methanol is formed here upon washing the surface at room temperature while  $\text{CO}_2$  is detected at temperatures higher than 100 °C (Figure 3.23). However, no dimethyl ether (DME) was produced using CuO/SBA-15 catalysts contrary to the zeolite-based Cu samples (Table 3.3). The formation of DME during the DMTM could be assigned to the consecutive reaction of in situ produced methanol over the acidic sites of the zeolite at elevated temperatures ( $\geq 135$  °C) as suggested in the literature [98,152]. However, in our studies, methanol and DME were detected simultaneously and at room temperature over Cu/mordenite. This observation indicates that upon treating the catalyst with steam methanol and dimethyl ether can be formed through parallel reactions. Besides, the possibility of forming DME through consecutive reaction of methanol was investigated through treating the CuO/SBA-15 and CuMorS-1 at room temperature instead of water with a methanol-saturated He flow. The yield of DME was raised in these experiments in comparison to the water-mediated extraction studies. The amount of extracted DME was raised from zero to  $27.6 \mu\text{mol g}_{\text{cat}}^{-1}$  and 1.6 to  $48.6 \mu\text{mol g}_{\text{cat}}^{-1}$  for Cu-AA/SBA and CuMorS-1, respectively. It should be noted that these yields of DME are close to the methanol amounts produced in the water extraction experiments. This observation suggests that the extra DME obtained during the methanol-saturated extraction experiments is mainly forming through the reaction of methanol molecules applied in the extraction protocol with the surface methoxy intermediate species. The rate of such a reaction could be significantly enhanced by acidic sites, which are abundantly available in zeolite catalysts.

Based on these studies and literature discussions the simplified reaction mechanism presented in Scheme 2 has been proposed for the DMTM reaction.

As it is presented in scheme 2, the consecutive reaction of *in situ*-produced methanol is one of the routes to form DME in water extraction experiments. Since formed methanol species will be retained for a longer time within the zeolite framework, mainly possessing micropores in comparison to the mesoporous in SBA-15 material, the amount of DME generated over SBA-15 material in the steam-assisted extraction step was significantly lower at room temperature.

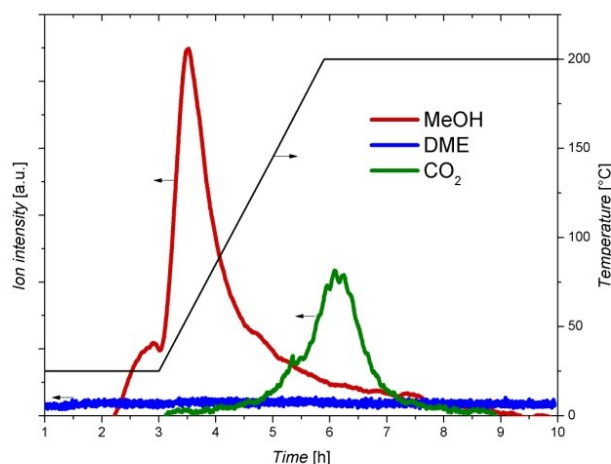


**Figure 3. 23** - Mass-spectral signals of products after interaction of Cu-AA/SBA with methane at 200 °C, followed by online extraction in an He flow saturated with water. **Paper 7**

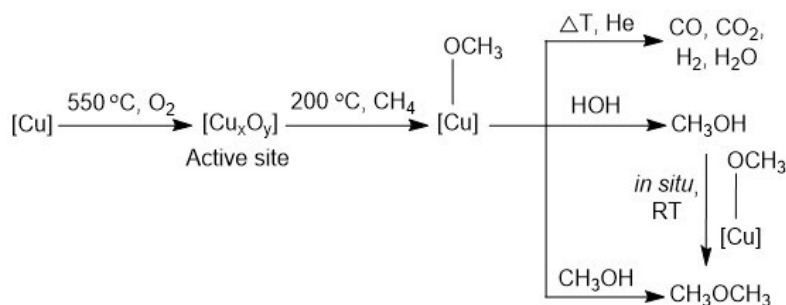


**Figure 3. 24** - Proposed reaction path for formation of products on the Cu-based catalyst based on the studies in paper 3, 7 and literature [83,153]. **Paper 7**

### 3.2.2.2 Identifying the position and nature of copper sites

Next, the location of the Cu sites in SBA-15 samples was investigated in the H<sub>2</sub>-TPR studies. The results of these experiments were compared to those of the bulk Cu oxide to identify the state of the Cu sites in SBA-15. The first reduction stage for CuO/SBA-15 samples is observed in the temperature range of 200 to 300 °C. This is attributed to the reduction of CuO nanoparticles which are located on the surface and at the facily accessible mesopores of SBA-15

(Figure 3.25). Most of Cu species in Cu-OA/SBA-15 were reduced in this temperature range. This behavior is consistent with the characterization results indicating that the Cu is mostly present on this sample as the large CuO nanoparticles. Besides, further H<sub>2</sub> reduction steps at 350 and 500 °C are found for the Cu-AA/SBA-15 sample, indicating that Cu species can be distributed at less accessible sites of SBA-15, namely micropores in the main-channel wall, by using Cu(acac)<sub>2</sub> for the preparation of the catalyst. The formation of smaller CuO clusters in Cu-AA/SBA is introduced as the main reason for the better catalytic performance of Cu-AA/SBA compared to the Cu-OA/SBA. Calculation of H<sub>2</sub> consumption in the TPR measurements further indicates that after activated in O<sub>2</sub>, the samples indeed contain Cu(II) species as found in Cu/zeolites.

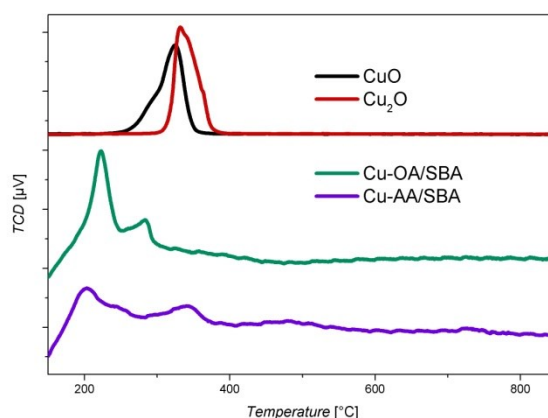


**Figure 3. 25** - H<sub>2</sub>-TPR profiles of Cu oxides, calcined Cu-OA/SBA and calcined Cu-AA/SBA. **Paper 7**

In addition, *in situ* UV-vis spectroscopy analysis is conducted to yield more information on the activated Cu sites. It should be noted that SBA-15 is known as a porous silica material without ion-exchangeable positions. Therefore, the formation of the isolated Cu-oxo species, which are defined as active sites for Cu/zeolites, in SBA-15 seems to be impossible. Indeed, no band in the region of 20 000–25 000 cm<sup>-1</sup> was found in the *in situ* UV-vis spectra demonstrating the absence of the mono- $\mu$ -oxo dicopper site in the Cu/SBA-15 samples activated in O<sub>2</sub> up to 550 °C (Figure 3.26 of **Paper 7**). However, similar to the results reported for Cu/mordenite (Figure 3.21), a considerable development of the broad band centered at  $\sim$  32 000 cm<sup>-1</sup> was observed for both Cu-AA/SBA and Cu-OA/SBA during the activation step (see Figures 6a and S7a of **Paper 7**). It should be noted that the  $\sim$  32 000 cm<sup>-1</sup> absorption commonly appears in UV-vis spectra of Cu-based materials due to a charge transfer of O<sup>2-</sup>  $\rightarrow$  Cu<sup>2+</sup> in CuO clusters [154]. This increasing feature observed in the UV-vis spectra of CuO/SBA-15 samples is therefore assigned to activated CuO species deposited on SBA-15. As can be expected, in the next step for

interaction with methane at 200 °C, the intensity of the 32 000 cm<sup>-1</sup> band started decreasing as methane was sent to the sample (Figures 3.26 b and Figure S7b of **Paper 7**), proving that the CuO species are reactive with methane. Analyzing the outlet stream with the MS during the contact of the samples with methane revealed that water which is typically generated upon the simple reduction of CuO in the presence of methane at higher temperatures (> 500 °C) [155], and methanol were not detected. Such a decrease in the 32 000 cm<sup>-1</sup> band intensity is therefore attributed to the activation of methane by CuO species at 200 °C, which yields the corresponding intermediate stabilized on the catalyst surface. However, the incomplete disappearance of the band after 2 h interaction with methane, which is more significantly observed for Cu-OA/SBA (Figure S7 of **paper 7**), showed that the CuO species in the samples consist of both active and inactive sites. Combining with the better production of methanol observed for Cu-AA/SBA, we therefore conclude that well-dispersed small CuO nanoparticles located within the SBA-15 framework are more active for the methane-to-methanol conversion.

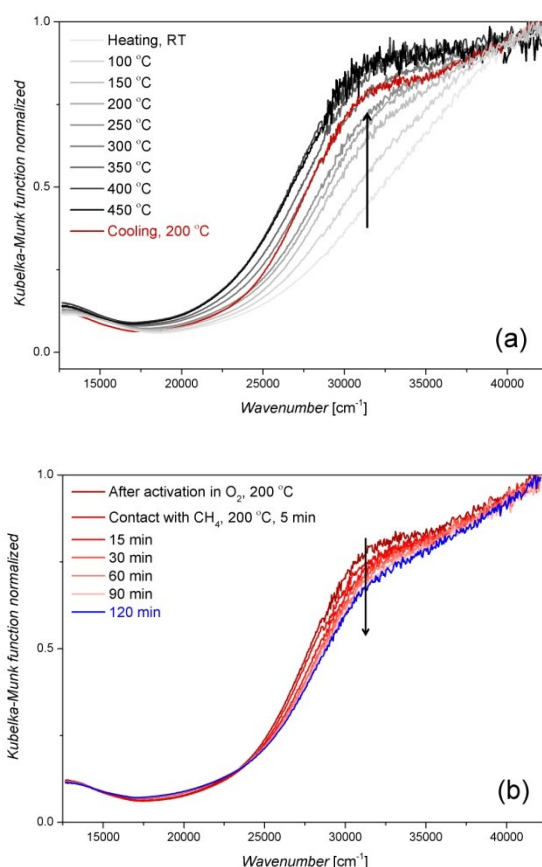


**Figure 3. 26** - In situ UV-vis spectra of Cu-AA/SBA (a) after activation in O<sub>2</sub> and (b) subsequent reaction with methane at 200 °C. **Paper 7**

### 3.2.3 Conclusions of the DMTM project

The solid-state ion-exchange method was reported to result in the formation of a better performing Cu/mordenites catalyst than the traditionally implemented liquid-phase ion-exchange synthesis method. The active Cu-oxo cores were reported to have a higher concentration in the catalysts made by the former than the latter method. This behavior is assigned to the acceleration of the exchange of the  $\text{Cu}^{2+}$  cations to the less accessible sites in small pores of the carrier due to the high temperatures generated during the solid-state treatment. This idea was proved by the results of the in-situ UV-vis analysis. It was observed in those studies that the spectroscopic features of activated Cu sites detected for the Cu/Mordenite catalysts synthesized through solid-state are much more intense than the liquid state. It was proposed that different active clusters including dicopper- and tricopper-oxo complexes could be formed in the Cu/mordenite catalysts. In addition, from the XRD and TPR analyses, it was learned that the Cu species are well dispersed as the nanoparticles at different positions in the mordenite framework.

The investigation of the performance of the Cu/supported catalyst for the MTM reaction was continued by focusing on CuO/SBA-15 catalysts. These studies showed that methanol is indeed produced on CuO/SBA-15. It is observed that CuO species are able to activate methane into methoxy species and stabilize them on the surface. During the reaction, depending on the solvent used in the subsequent extraction step, both Methanol and DME can be the main reaction product. The reactivity of CuO species on SBA-15 with methane was further demonstrated by the *in-situ* UV-vis spectroscopy measurements, in which intensity of the band centered at  $32\ 000\ \text{cm}^{-1}$  increased by an  $\text{O}_2$ -activation and considerably decreased after the contact with methane. This observation led to concluding CuO species as the active sites over CuO/SBA-15 samples. It was shown that the catalytic activity of CuO/SBA-15 be a function of the used Cu precursors. The catalyst prepared from  $\text{Cu}(\text{acac})_2$  had a better catalytic performance compared to the  $\text{Cu}(\text{OAc})_2$  based sample. This behavior is assigned to the better dispersion of small/ultra-small CuO species in the SBA-15 framework of the former sample in comparison to the latter one.

## Conclusions

The most important challenge of utilization of methane through both OCM and DMTM is running the reaction under the conditions which facilitate activation of highly stable methane molecules, while it suppresses the occurrence of the secondary oxidation reactions. Fulfilling these requirements simultaneously is unfortunately extremely challenging. Both these reactions are conducted catalytically in the presence of an oxidizing agent. Under these circumstances, milder reaction conditions are required for activating methane. Presence of an oxidizer is crucial for both DMTM and methane coupling since it is the reactant for the former reaction while it converts the latter one from endothermic to exothermic. However, it also brings the thermodynamically favored total and partial oxidations in competition with the selective reactions. In addition, C<sub>2</sub> components and methanol are more active than methane, therefore, there is always the danger of losing selectivity due to the consecutive reaction of these products to CO<sub>x</sub>.

First of all, the results of this thesis highlighted the high contribution of molecular gas phase oxygen on the rate of occurring burning reactions. In addition, It has been shown that different physi- and chemisorbed oxygen species are formed on the surface of the employed catalysts upon oxidation. The former has been reported to have a shorter lifetime and be unselective while the latter stays longer on the surface and results mostly in the selective oxidation reactions. Based on these mechanistic understandings the chemical looping concept was proposed as an effective technique for suppressing the rate of formation of CO<sub>x</sub> during both the DMTM and OCM reactions. Next, a simulated chemical looping reactor was built in our laboratory and implemented in testing these reactions under various reacting conditions. Running OCM under these reaction conditions resulted in a more efficient conversion of methane than the co-feeding reactor, however, the maximum yield of 30 %, required for industrializing the process, could not be achieved. By application of the stepwise reaction process, resembling the chemical looping concept, methanol could successfully be formed in the case of DMTM. Noteworthy, while performing OCM in CLR enhances just the reaction selectivity, DMTM can just be conducted in CLR and is not doable co-feeding modus.

To run the reaction in the CLR, a catalyst capable of storing oxygen needs to be implemented. In fact, this functionality defines the level of the reaction conversion. Since the studies in paper 4 indicated the conversion, rather than selectivity, as the main reason for the yield limitation of OCM in CLR, the redox behavior of the catalyst in this reactor was studied in paper 5 as a

function of the catalyst composition. It was shown that the oxygen storage capacity of the  $\text{Na}_2\text{WO}_4/\text{Mn}/\text{SiO}_2$  catalyst can be enhanced to some extent through increasing the surface area or Mn content. The studies done on DMTM showed that the activation level of the Cu-mordenite is a function of the oxidation temperature, methane time on stream, and the amount of water used in the washing step.

## Reference

- [1] E. V. Kondratenko, T. Peppel, D. Seeburg, V. Kondratenko, N. Kalevaru, A. Martin, S. Wohlrab, *Catal. Sci. Technol.* 7 (2017) 366–381.
- [2] C. Hammond, S. Conrad, I. Hermans, (2012) 1668–1686.
- [3] U.S. Energy Information Administration, *International Energy Outlook 2016*, 2016.
- [4] R. Diercks, J.-D. Arndt, S. Freyer, R. Geier, O. Machhammer, J. Schwartz, M. Volland, *Chem. Eng. Technol.* 31 (2008) 631–637.
- [5] P. Tang, Q. Zhu, Z. Wu, D. Ma, *Energy Environ. Sci.* 7 (2014) 2580–2591.
- [6] B. Vora, J.Q. Chen, A. Bozzano, B. Glover, P. Barger, *Catal. Today* 141 (2009) 77–83.
- [7] R. Horn, R. Schlögl, *Catal. Letters* 145 (2015) 23–39.
- [8] S. Arndt, T. Otremba, U. Simon, M. Yildiz, H. Schubert, R. Schomäcker, *Appl. Catal. A Gen.* 425–426 (2012) 53–61.
- [9] J.H. Lunsford, *Catal. Today* 63 (2000) 165–174.
- [10] N. Gunaseelan, *Biomass and Bioenergy* 13 (1997) 83–114.
- [11] H. Schwarz, *Angew. Chemie - Int. Ed.* 50 (2011) 10096–10115.
- [12] J. Rostrup-Nielsen, *Syngas for C1-Chemistry. Limits of the Steam Reforming Process*, 1988.
- [13] O.V. Krylov, *Catal. Today* 18 (1993) 209–302.
- [14] H.D. Gesser, N.R. Hunter, *Catal. Today* 42 (1998) 183–189.
- [15] V. L.Sushkevich, D. Palagin, M. Ranocchiari, J.A. van Bokhoven, *Science* (80-. ). 356 (2017) 523–527.
- [16] B. Han, Y. Yang, Y. Xu, U.J. Etim, K. Qiao, B. Xu, Z. Yan, *Cuihua Xuebao/Chinese J. Catal.* 37 (2016) 1206–1215.
- [17] *The Ethylene Technology Report 2016*, 2016.
- [18] C. Mesters, *Annu. Rev. Chem. Biomol. Eng.* 7 (2016) 223–238.
- [19] F. Cavani, F. Trifirò, *Catal. Today* 24 (1995) 307–313.
- [20] S. Seifzadeh Haghighi, M.R. Rahimpour, S. Raeissi, O. Dehghani, *Chem. Eng. J.* 228 (2013) 1158–1167.

- [21] A. Bansode, A. Urakawa, *J. Catal.* 309 (2014) 66–70.
- [22] C. Karakaya, R.J. Kee, *Prog. Energy Combust. Sci.* 55 (2016) 60–97.
- [23] S. Arndt, U. Simon, S. Heitz, a. Berthold, B. Beck, O. Görke, J.-D. Epping, T. Otremba, Y. Aksu, E. Irran, G. Laugel, M. Driess, H. Schubert, R. Schomäcker, *Top. Catal.* 54 (2011) 1266–1285.
- [24] J.H. Lunsford, *Angew. Chemie Int. Ed. English* 34 (1995) 970–980.
- [25] S. Arndt, G. Laugel, S. Levchenko, R. Horn, M. Baerns, M. Scheffler, R. Schlögl, R. Schomäcker, *Catal. Rev.* 53 (2011) 424–514.
- [26] S. Pak, P. Qiu, J.H. Lunsford, *J. Catal.* 179 (1998) 222–230.
- [27] H.R. Godini, V. Fleischer, O. Görke, S. Jaso, R. Schomäcker, G. Wozny, *Chemie Ing. Tech.* 86 (2014) 1906–1915.
- [28] [Http://siluria.com/Technology/Oxidative\\_Coupling\\_of\\_Methane](http://siluria.com/Technology/Oxidative_Coupling_of_Methane), (2018).
- [29] M. Yildiz, Y. Aksu, U. Simon, K. Kailasam, O. Goerke, R. Schomäcker, A. Thomas, S. Arndt, *Chem. Commun.* 50 (2014) 14440–14442.
- [30] M. Yildiz, Y. Aksu, U. Simon, T. Otremba, K. Kailasam, C. Göbel, F. Girgsdies, O. Görke, F. Rosowski, A. Thomas, R. Schomäcker, S. Arndt, *Appl. Catal. A Gen.* 525 (2016) 168–179.
- [31] M.G. Colmenares, U. Simon, M. Yildiz, S. Arndt, R. Schomaecker, A. Thomas, F. Rosowski, A. Gurlo, O. Goerke, *Catal. Commun.* 85 (2016) 75–78.
- [32] H. V. Le, S. Parishan, A. Sagaltchik, C. Goebel, C. Schlesiger, W. Malzer, A. Trunschke, R. Schomaecker, A. Thomas, *ACS Catal.* 7 (2017) 1403–1412.
- [33] B. Beck, V. Fleischer, S. Arndt, M.G. Hevia, A. Urakawa, P. Hugo, R. Schomäcker, *Catal. Today* 228 (2014) 212–218.
- [34] S. Sadjadi, S. Jašo, H.R. Godini, S. Arndt, M. Wollgarten, R. Blume, O. Görke, R. Schomäcker, G. Wozny, U. Simon, *Catal. Sci. Technol.* 5 (2015) 942–952.
- [35] S. Sadjadi, U. Simon, H.R. Godini, O. Görke, R. Schomäcker, G. Wozny, *Chem. Eng. J.* 281 (2015) 678–687.
- [36] V. Fleischer, R. Steuer, S. Parishan, R. Schomäcker, *J. Catal.* 341 (2016) 91–103.
- [37] V. Fleischer, U. Simon, S. Parishan, M. Gracia, O. Görke, A. Gurlo, W. Riedel, L. Thum, J. Schmidt, T. Risse, K. Dinse, R. Schomäcker, *J. Catal.* 360 (2018) 102–117.
- [38] V. Fleischer, P. Littlewood, S. Parishan, R. Schomäcker, *Chem. Eng. J.* 306 (2016) 646–654.
- [39] S. Parishan, P. Littlewood, A. Arinchtein, V. Fleischer, R. Schomäcker, *Catal. Today* 311 (2018) 40–47.
- [40] S. Jašo, S. Sadjadi, H.R. Godini, U. Simon, S. Arndt, O. Görke, a. Berthold, H. Arellano-Garcia, H. Schubert, R. Schomäcker, G. Wozny, *J. Nat. Gas Chem.* 21 (2012) 534–543.
- [41] H.R. Godini, A. Gili, O. Go, U. Simon, K. Hou, G. Wozny, O. Görke, U. Simon, K. Hou, G. Wozny, *Energy & Fuels* 28 (2014) 877–890.
- [42] S. Pak, J.H. Lunsford, *Appl. Catal. A Gen.* 168 (1998) 131–137.
- [43] A. Palermo, J. Pedro, H. Vazquez, A.F. Lee, M.S. Tikhov, R.M. Lambert, 266 (1998) 259–266.
- [44] D. Wang, M.P. Rosynek, J.H. Lunsford, *J. Catal.* 151 (1995) 155–167.

- [45] G.E. Keller, M.M. Bhasin, *J. Catal.* 73 (1982) 9–19.
- [46] J. Haber, *Handb. Heterog. Catal.* (2008) 3359–3384.
- [47] V.J. Ferreira, P. Tavares, J.L. Figueiredo, J.L. Faria, *Catal. Commun.* 42 (2013) 50–53.
- [48] D. Noon, A. Seubsai, S. Senkan, *ChemCatChem* 5 (2013) 146–149.
- [49] E. V. Kondratenko, M. Schlüter, M. Baerns, D. Linke, M. Holena, *Catal. Sci. Technol.* 5 (2015) 1668–1677.
- [50] U. Zavyalova, M. Holena, R. Schlögl, M. Baerns, *ChemCatChem* 3 (2011) 1935–1947.
- [51] E. V. Kondratenko, M. Baerns, in: *Hand B. Heterog. Catal.*, 2004, pp. 3010–3023.
- [52] P. Schwach, W. Frandsen, M.G. Willinger, R. Schlögl, A. Trunschke, *J. Catal.* 329 (2015) 560–573.
- [53] P. Schwach, N. Hamilton, M. Eichelbaum, L. Thum, T. Lunkenbein, R. Schlögl, A. Trunschke, *J. Catal.* 329 (2015) 574–587.
- [54] K. Kwapien, J. Paier, J. Sauer, M. Geske, U. Zavyalova, R. Horn, P. Schwach, A. Trunschke, R. Schlögl, *Angew. Chemie - Int. Ed.* 53 (2014) 8774–8778.
- [55] S. Arndt, T. Otremba, U. Simon, M. Yildiz, H. Schubert, R. Schomäcker, *Appl. Catal. A Gen.* 425–426 (2012) 53–61.
- [56] J. Galuszka, *Catal. Today* 21 (1994) 321–331.
- [57] N. Cant, E. Kennedy, P. Nelson, *J. Phys. Chem.* 97 (1993) 1445–1450.
- [58] C. a. Mims, R. Mauti, a. M. Dean, K.D. Rose, *J. Phys. Chem.* 98 (1994) 13357–13372.
- [59] C. Shi, M.P. Rosynek, J.H. Lunsford, *J. Phys. Chem.* 98 (1994) 8371–8376.
- [60] P.M. Couwenberg, Q. Chen, G.B. Marin, 5885 (1996) 3999–4011.
- [61] U. Simon, O. Görke, A. Berthold, S. Arndt, R. Schomäcker, H. Schubert, *Chem. Eng. J.* 168 (2011) 1352–1359.
- [62] S. Ji, T. Xiao, S. Li, C. Xu, R. Hou, K. S.Coleman, M. L.H Green, *Appl. Catal. A Gen.* 225 (2002) 271–284.
- [63] J. Wang, L. Chou, B. Zhang, H. Song, J. Zhao, J. Yang, S. Li, *J. Mol. Catal. A Chem.* 245 (2006) 272–277.
- [64] M.G. Colmenares, U. Simon, M. Yildiz, S. Arndt, R. Schomaecker, A. Thomas, F. Rosowski, A. Gurlo, O. Goerke, *Catal. Commun.* 85 (2016) 75–78.
- [65] G.D. Nipan, A.S. Loktev, K. V. Parkhomenko, S.D. Golikov, A.G. Dedov, I.I. Moiseev, *Dokl. Phys. Chem.* 448 (2013) 19–22.
- [66] G.D. Nipan, *Inorg. Mater.* 50 (2014) 1012–1017.
- [67] K. Takanae, A.M. Khan, Y. Tang, L. Nguyen, A. Ziani, B.W. Jacobs, A.M. Elbaz, S.M. Sarathy, F.F. Tao, *Angew. Chemie Int. Ed.* 56 (2017) 10403–10407.
- [68] S. Dooley, F.L. Dryer, B. Yang, J. Wang, T. a. Cool, T. Kasper, N. Hansen, *Combust. Flame* 158 (2011) 732–741.
- [69] S. Dooley, M.P. Burke, M. Chaos, Y. Stein, F.L. Dryer, V.P. Zhukov, O. Finch, J.M. Simmie, H.J.

- Curran, *Int. J. Chem. Kinet.* (2010) 528–549.
- [70] H. Schwarz, M. Geske, C. Franklin Goldsmith, R. Schlögl, R. Horn, *Combust. Flame* 161 (2014) 1688–1700.
- [71] K. Takanabe, E. Iglesia, *J. Phys. Chem. C* 113 (2009) 10131–10145.
- [72] M.Y. Sinev, Z.T. Fattakhova, V.I. Lomonosov, Y. a. Gordienko, *J. Nat. Gas Chem.* 18 (2009) 273–287.
- [73] S.-P. Lee, T. Yu, M.C. Lin, *Int. J. Chem. Kinet.* 22 (1990) 975–980.
- [74] M.R. Lee, M. Park, W. Jeon, J. Choi, Y. Suh, D. Jin, *Fuel Process. Technol.* 96 (2012) 175–182.
- [75] P.F. Nelson, C. a. Lukey, N.W. Cant, *J. Phys. Chem.* 92 (1988) 6176–6179.
- [76] K.D. Campbell, E. Morales, J.H. Lunsford, *J. Am. Chem. Soc.* 109 (1987) 7900–7901.
- [77] J. Sun, J. Thybaut, G. Marin, *Catal. Today* 137 (2008) 90–102.
- [78] R. Koirala, R. Büchel, S.E. Pratsinis, A. Baiker, *Appl. Catal. A Gen.* 484 (2014) 97–107.
- [79] G.D. Nipan, *Inorg. Mater.* 53 (2017) 553–559.
- [80] J. Wu, S.-B. Li, J. Niu, X. Fang, *Appl. Catal. A Gen.* 124 (1995) 9–18.
- [81] Z. Jiang, H. Gong, S. Li, *Stud. Surf. Sci. Catal.* 112 (1997) 481–490.
- [82] Z. Zakaria, S.K. Kamarudin, *Renew. Sustain. Energy Rev.* 65 (2016) 250–261.
- [83] P. Tomkins, M. Ranocchiari, J.A. Van Bokhoven, *Acc. Chem. Res.* 50 (2017) 418–425.
- [84] M. Ravi, M. Ranocchiari, J.A. van Bokhoven, *Angew. Chemie - Int. Ed.* 56 (2017) 16464–16483.
- [85] I. Siewert, C. Limberg, *Chem. - A Eur. J.* 15 (2009) 10316–10328.
- [86] V.C.C. Wang, S. Maji, P.P.Y. Chen, H.K. Lee, S.S.F. Yu, S.I. Chan, *Chem. Rev.* 117 (2017) 8574–8621.
- [87] I.Y. Hwang, S.H. Lee, Y.S. Choi, S.J. Park, J.G. Na, I.S. Chang, C. Kim, H.C. Kim, Y.H. Kim, J.W. Lee, E.Y. Lee, *J. Microbiol. Biotechnol.* 24 (2014) 1597–1605.
- [88] R. Banerjee, Y. Proshlyakov, J.D. Lipscomb, D.A. Proshlyakov, *Nature* 518 (2015) 431–434.
- [89] A.E. Shilov, G.B. Shul'pin, *Chem. Rev.* 97 (1997) 2879–2932.
- [90] C. Hammond, M.M. Forde, M.H. Ab Rahim, A. Thetford, Q. He, R.L. Jenkins, N. Dimitratos, J.A. Lopez-Sanchez, N.F. Dummer, D.M. Murphy, A.F. Carley, S.H. Taylor, D.J. Willock, E.E. Stangland, J. Kang, H. Hagen, C.J. Kiely, G.J. Hutchings, *Angew. Chemie - Int. Ed.* 51 (2012) 5129–5133.
- [91] P. Tomkins, A. Mansouri, S.E. Bozbag, F. Krumeich, M.B. Park, E.M.C. Alayon, M. Ranocchiari, J.A. Vanbokhoven, *Angew. Chemie - Int. Ed.* 55 (2016) 5467–5471.
- [92] R. Palkovits, M. Antonietti, P. Kuhn, A. Thomas, F. Schüth, *Angew. Chemie - Int. Ed.* 48 (2009) 6909–6912.
- [93] R.A. Periana, D.J. Taube, S. Gamble, H. Taube, T. Satoh, H. Fujii, *Science* 80. 280 (1998) 560–564.
- [94] M. Soorholtz, R.J. White, T. Zimmermann, M.-M. Titirici, M. Antonietti, R. Palkovits, F. Schüth, *Chem. Commun.* 49 (2013) 240–242.

- [95] M.H. Ab Rahim, M.M. Forde, R.L. Jenkins, C. Hammond, Q. He, N. Dimitratos, J.A. Lopez-Sanchez, A.F. Carley, S.H. Taylor, D.J. Willock, D.M. Murphy, C.J. Kiely, G.J. Hutchings, *Angew. Chemie - Int. Ed.* 52 (2013) 1280–1284.
- [96] T. Li, S.J. Wang, C.S. Yu, Y.C. Ma, K.L. Li, L.W. Lin, *Appl. Catal. A Gen.* 398 (2011) 150–154.
- [97] T. Ikuno, J. Zheng, A. Vjunov, M. Sanchez-Sanchez, M.A. Ortuño, D.R. Pahls, J.L. Fulton, D.M. Camaioni, Z. Li, D. Ray, B.L. Mehdi, N.D. Browning, O.K. Farha, J.T. Hupp, C.J. Cramer, L. Gagliardi, J.A. Lercher, *J. Am. Chem. Soc.* 139 (2017) 10294–10301.
- [98] S. Grundner, M.A.C. Markovits, G. Li, M. Tromp, E.A. Pidko, E.J.M. Hensen, A. Jentys, M. Sanchez-Sanchez, J.A. Lercher, *Nat. Commun.* 6 (2015) 7546.
- [99] C. Hammond, R.L. Jenkins, N. Dimitratos, J.A. Lopez-Sanchez, M.H. Ab Rahim, M.M. Forde, A. Thetford, D.M. Murphy, H. Hagen, E.E. Stangland, J.M. Moulijn, S.H. Taylor, D.J. Willock, G.J. Hutchings, *Chem. - A Eur. J.* 18 (2012) 15735–15745.
- [100] M.H. Mahyuddin, A. Staykov, Y. Shiota, K. Yoshizawa, *ACS Catal.* 6 (2016) 8321–8331.
- [101] M.J. Wulfers, S. Teketel, B. Ipek, R.F. Lobo, *Chem. Commun.* 51 (2015) 4447–4450.
- [102] V.L. Sushkevich, D. Palagin, M. Ranocchiari, J.A. Van Bokhoven, *Science.* 356 (2017) 523–527.
- [103] P. Vanelderen, R.G. Hadt, P.J. Smeets, E.I. Solomon, R.A. Schoonheydt, B.F. Sels, *J. Catal.* 284 (2011) 157–164.
- [104] S.E. Bozbag, E.M.C. Alayon, J. Pecháček, M. Nachtegaal, M. Ranocchiari, J.A. van Bokhoven, *Catal. Sci. Technol.* 6 (2016) 5011–5022.
- [105] X. Fang, S. Li, J. Gu, D. Yang, *J. Mol. Catal.* 6 (1992) 427–433.
- [106] D. Zhao, J. Feng, Q. Huo, N. Melosh, G.H. Fredrickson, B.F. Chmelka, G.D. Stucky, *Science* (80-). 279 (1998) 548–552.
- [107] J. Zhu, K. Kailasam, X. Xie, R. Schomaecker, A. Thomas, *Chem. Mater.* 23 (2011) 2062–2067.
- [108] A. Ekstrom, J. a. Lapszewicz, I. Campbell, *Appl. Catal.* 56 (1989) L29–L34.
- [109] P.F. Nelson, N.W. Cant, 32 (1990) 3756–3761.
- [110] a. M. Efstathiou, X.E. Verykios, *Appl. Catal. A Gen.* 151 (1997) 109–166.
- [111] J.L. Falconer, J. a. Schwarz, *Catal. Rev.* 25 (1983) 141–227.
- [112] M. Daneshpayeh, N. Mostoufi, A. Khodadadi, R. Sotudeh-gharebagh, *Energy & Fuels* 23 (2009) 3745–3752.
- [113] M. Daneshpayeh, A. Khodadadi, N. Mostoufi, Y. Mortazavi, R. Sotudeh-Gharebagh, A. Talebizadeh, *Fuel Process. Technol.* 90 (2009) 403–410.
- [114] S.M.K. Shahri, S.M. Alavi, *J. Nat. Gas Chem.* 18 (2009) 25–34.
- [115] L. Yu, W. Li, V. Ducarme, C. Mirodatos, G. a. Martin, *Appl. Catal. A Gen.* 175 (1998) 173–179.
- [116] A.M. Baró, H. Ibach, *J. Chem. Phys.* 74 (1981) 4194–4199.
- [117] J.A. Stroschio, S.R. Bare, W. Ho, *Surf. Sci.* 148 (1984) 499–525.
- [118] C. Park, M.A. Keane, *J. Catal.* 221 (2004) 386–399.
- [119] K. Asami, T. Shikada, K. Fujimoto, H. Tominaga, *Ind. Eng. Chem* 26 (1987) 2348–2353.

- [120] G.A. Martin, A. Bates, V. Ducarme, C. Mirodatos, *Appl. Catal.* 47 (1989) 287–297.
- [121] K. Takanabe, S. Shahid, *Aiche* 63 (2016) 3–194.
- [122] J. Adanez, A. Abad, F. Garcia-Labiano, P. Gayan, L.F. De Diego, *Prog. Energy Combust. Sci.* 38 (2012) 215–282.
- [123] S. Hurst, *Oil Soap* 16 (1939) 29–35.
- [124] S. Bhavsar, M. Najera, R. Solunke, G. Veser, *Catal. Today* 228 (2014) 96–105.
- [125] H. Fang, L. Haibin, Z. Zengli, *Int. J. Chem. Eng.* 2009 (2009) 16.
- [126] S. Bhavsar, G. Veser, *Ind. Eng. Chem. Res.* 52 (2013) 15342–15352.
- [127] M.M. Hossain, H.I. de Lasa, *Chem. Eng. Sci.* 63 (2008) 4433–4451.
- [128] M. Ishida, H. Jin, *Ind. Eng. Chem. Res.* 5885 (1996) 2469–2472.
- [129] K. Takanabe, E. Iglesia, *Angew. Chemie - Int. Ed.* 47 (2008) 7689–7693.
- [130] M. Daneshpayeh, A. Khodadadi, N. Mostoufi, Y. Mortazavi, R. Sotudeh-Gharebagh, A. Talebizadeh, *Fuel Process. Technol.* 90 (2009) 403–410.
- [131] S.J. Blanksby, G.B. Ellison, *Acc. Chem. Res.* 36 (2003) 255–263.
- [132] Y. Khojasteh Salkuyeh, T. a. Adams, *Energy Convers. Manag.* 92 (2015) 406–420.
- [133] M.S. Salehi, M. Askarishahi, H.R. Godini, O. Görke, G. Wozny, *Ind. Eng. Chem. Res.* 55 (2016) 3287–3299.
- [134] H.-R. Godini, S. Jaso, W. Martini, S. Stünkel, D. Salerno, S.N. Xuan, S. Song, S. Sadjadi, H. Trivedi, H. Arellano-Garcia, G. Wozny, *Tech. Trans.* 109 (2012) 63–74.
- [135] M.G. Colmenares, U. Simon, O. Cruz, A. Thomas, O. Goerke, A. Gurlo, *Microporous Mesoporous Mater.* 256 (2018) 102–110.
- [136] E.R. Stobbe, B.A. de Boer, J.W. Geus, *Catal. Today* 47 (1999) 161–167.
- [137] F. Arena, T. Torre, C. Raimondo, A. Parmaliana, *Phys. Chem. Chem. Phys.* 3 (2001) 1911–1917.
- [138] F. Buciuman, F. Patcas, R. Craciun, D.R.T. Zahn, *Phys. Chem. Chem. Phys.* 1 (1999) 185–190.
- [139] T.W. Elkins, H.E. Hagelin-Weaver, *Appl. Catal. A Gen.* 497 (2015) 96–106.
- [140] R.D. Shannon, *Acta Crystallogr. Sect. A* 32 (1976) 751–767.
- [141] C. Reed, Y.-K. Lee, S.T. Oyama, *J. Phys. Chem. B* 110 (2006) 4207–4216.
- [142] a. Erdohelyi, R. Németh, a. Hancz, a. Oszkó, *Appl. Catal. A Gen.* 211 (2001) 109–121.
- [143] a. Malekzadeh, a. K. Dalai, a. Khodadadi, Y. Mortazavi, *Catal. Commun.* 9 (2008) 960–965.
- [144] Z.-C. Jiang, L.-B. Feng, H. Gong, H.-L. Wang, *Methane and Alkane Conversion Chemistry*, Springer US, New York, 1995.
- [145] E.M. Alayon, M. Nachtegaal, J.A. Van Bokhoven, 48 (2012) 404–406.
- [146] E.M.C. Alayon, M. Nachtegaal, A. Bodi, J.A. Van Bokhoven, 4 (2014) 16–22.
- [147] A. Sainz-Vidal, J. Balmaseda, L. Lartundo-Rojas, E. Reguera, *Microporous Mesoporous Mater.* 185 (2014) 113–120.

- [148] L. Wang, W. Li, G. Qi, D. Weng, *J. Catal.* 289 (2012) 21–29.
- [149] P. Vanelderen, J. Vancauwenbergh, M.L. Tsai, R.G. Hadt, E.I. Solomon, R.A. Schoonheydt, B.F. Sels, *ChemPhysChem* 15 (2014) 91–99.
- [150] A.R. Kulkarni, Z.J. Zhao, S. Siahrostami, J.K. Nørskov, F. Studt, *ACS Catal.* 6 (2016) 6531–6536.
- [151] K. D.Vogiatzis, G. Li, E. J.M.Hensen, L. Gagliardi, E. A.Pidko, *J. Phys. Chem. C* 121 (2017) 22295–22302.
- [152] E. V. Starokon, M. V. Parfenov, L. V. Pirutko, S.I. Abornev, G.I. Panov, *J. Phys. Chem. C* 115 (2011) 2155–2161.
- [153] K. Narsimhan, K. Iyoki, K. Dinh, Y. Román-Leshkov, *ACS Cent. Sci.* 2 (2016) 424–429.
- [154] C.H. Liu, N.C. Lai, J.F. Lee, C.S. Chen, C.M. Yang, *J. Catal.* 316 (2014) 231–239.
- [155] T. Mattisson, M. Johansson, A. Lyngfelt, *Energy & Fuels* 18 (2004) 628–637.

# **Appendix**

## **Papers 1-7**

# Paper 1



# Investigation of the surface reaction network of the oxidative coupling of methane over $\text{Na}_2\text{WO}_4/\text{Mn}/\text{SiO}_2$ catalyst by temperature programmed and dynamic experiments



Vinzenz Fleischer, Rolf Steuer, Samira Parishan, Reinhard Schomäcker\*

Technische Universität Berlin, Institut für Chemie, Straße des 17. Juni 124, 10623 Berlin, Germany

## ARTICLE INFO

### Article history:

Received 1 December 2015

Revised 26 May 2016

Accepted 20 June 2016

Available online 16 July 2016

### Keywords:

Oxidative coupling of methane

$\text{Na}_2\text{WO}_4/\text{Mn}/\text{SiO}_2$

Temperature programmed experiments

Dynamic experiments

## ABSTRACT

In this work a series of temperature programmed experiments were carried out on a  $\text{Na}_2\text{WO}_4/\text{Mn}/\text{SiO}_2$  catalyst. In TPR experiments we tested the reducibility of this catalyst and  $\text{O}_2$  desorption behavior was investigated by TPD. TPSR experiments in a flow of methane, ethane or ethene gave information about the reaction network of OCM on the catalyst surface, without the presence of gas phase reactions, induced by gas phase oxygen. We found indications of involvement of two different active oxygen species on the catalyst surface. Furthermore an activation energy of 275 kJ/mole for selective methane activation was determined. Dynamic experiments were performed to determine the amount of available oxygen species for the OCM reaction. Variation of methane partial pressure and flow rate showed a linear correlation between methane partial pressure and surface oxygen conversion in dynamic experiments.

© 2016 Elsevier Inc. All rights reserved.

## 1. Introduction

A well-established process for ethylene production is the steam cracking process, which cracks naphtha to olefins and other hydrocarbons. Shortage of crude oil reserves has attracted attention toward alternative processes, which use more available feedstocks. The high availability of methane in natural gas makes it a suitable feedstock alternative for short-chain olefins [1,2]. The oxidative coupling of methane (OCM) is a promising reaction for ethylene production. One of the most stable catalysts described for OCM in the literature is  $\text{Na}_2\text{WO}_4/\text{Mn}/\text{SiO}_2$ , which has good performance and stability as shown in several publications [3–5].

One of the major challenges in experimental studies of OCM is the parallel reaction network of gas phase and surface reactions, which have a strong influence on each other. For gas phase reactions, Dooley and coworkers published an extended micro kinetic model [6]. This micro kinetic model considers a network of 1582 reactions and 269 species, which are mainly radical reactions. Unfortunately this complex reaction network allows only simulation of ideal reactors, because of the large set of reactions. However, the gas phase network is well described by the Dooley model, which was shown by Schwarz and Coworkers [7]. Formal kinetic models of OCM were published by several groups for

different catalysts [8–16]. All of these proposed mechanisms show similar pathways for reactants and products. All groups who carried out these experiments with extensive experimental efforts, were using similar reactors operated in the classical steady state mode.

The surface reaction network, which is not fully explored, is strongly influenced by gas phase reactions, and its kinetic parameters offer several constellations to fit experimental results. Such complexity is caused by the mentioned involvement of various radical species which are formed via gas phase reactions or during reactions on the catalyst surface [17–20]. In addition for several OCM catalysts different oxygen intermediates contribute to selective and unselective activation of methane on the catalyst surface. The presence of these different species is also influenced by gas phase oxygen [21–23].

A micro kinetic surface reaction model for the surface reactions was published by Lee and Coworkers for the  $\text{Na}_2\text{WO}_4/\text{Mn}/\text{SiO}_2$  catalyst [24]. Another one is the model published by Sun and Thybaut for a MgO catalyst [25]. Both models were developed for different catalysts but have similar elementary surface reaction steps which are shown in Table 1. Their models assume dissociative adsorption of oxygen on a free site of the catalyst (\*), which is in equilibrium with gas phase oxygen. Methane activation occurs by a surface reaction with dissociated oxygen ( $\text{O}^*$ ) and releases methyl radicals to the gas phase. The coupling reaction of the radicals happens in gas phase close to the catalyst surface where excess heat is released, which is not shown in Table 1. The same activation

\* Corresponding author.

E-mail addresses: [v.fleischer@mailbox.tu-berlin.de](mailto:v.fleischer@mailbox.tu-berlin.de) (V. Fleischer), [schomaecker@mailbox.tu-berlin.de](mailto:schomaecker@mailbox.tu-berlin.de) (R. Schomäcker).

**Table 1**  
Comparison of micro-kinetic surface reaction models from Lee et al. and Sun et al. ( $x, y, z$  = stoichiometric factors) [24–26].

Lee et al. [24]	Sun et al. [25]	Beck et al. [26]
$O_2 + 2^* \rightleftharpoons 2O^*$	$O_2 + 2^* \rightleftharpoons 2O^*$	$O_2 + * \rightleftharpoons O_{2,ads}$ $O_{2,ads} \rightleftharpoons yO_x^*$
$CH_4 + O^* \rightleftharpoons CH_3 + OH^*$	$CH_4 + O^* \rightleftharpoons CH_3 + OH^*$	$CH_4 + O^* \rightleftharpoons CH_3 + OH^*$
$C_2H_4 + O^* \rightleftharpoons C_2H_3 + OH^*$	$C_2H_4 + O^* \rightleftharpoons C_2H_3 + OH^*$	$C_2H_4 + O^* \rightleftharpoons C_2H_3 + OH^*$
$C_2H_6 + O^* \rightleftharpoons C_2H_5 + OH^*$	$C_2H_6 + O^* \rightleftharpoons C_2H_5 + OH^*$	$C_2H_6 + O^* \rightleftharpoons C_2H_5 + OH^*$
$CH_3 + 3O^* \rightleftharpoons HCO^* + 2OH^*$	$2OH^* \rightleftharpoons H_2O^* + O^*$ $CH_3 + O^* \rightleftharpoons CH_3O^*$ $CH_3O^* + O^* \rightleftharpoons CH_2O^* + OH^*$ $CH_2O^* + O^* \rightleftharpoons HCO^* + OH^*$	$2OH^* \rightleftharpoons H_2O^* + O^*$
$HCO^* + O^* \rightleftharpoons CO^* + OH^*$	$HCO^* + O^* \rightleftharpoons CO^* + OH^*$	
$CO^* + O^* \rightleftharpoons CO_2 + *$	$CO^* + O^* \rightleftharpoons CO_2 + *$ $CO^+ \rightleftharpoons CO^*$ $CO_2 + * \rightleftharpoons CO_2^*$ $4HO_2 \rightarrow 3O_2 + 2H_2$	$xO_{2,ads} + CH_4 \rightleftharpoons CO_y + zH_2O^*$ $xO_{2,ads} + C_2H_6 \rightleftharpoons 2CO_y + zH_2O^*$ $xO_{2,ads} + C_2H_4 \rightleftharpoons 2CO_y + zH_2O^*$
$2OH^* \rightleftharpoons H_2O + O^* + *$		

may also happen to the formed ethane and even ethene, which leads to the formation of  $C_2H_5$  or  $C_2H_3$  radicals. An interesting fact is that no ethene combustion on the catalyst surface is considered in both literature models. A typical formation route for deep oxidation products is the reaction of methyl radicals and surface bound oxygen which forms a  $HCO^*$  radical which is bound on the catalyst surface, which is further oxidized to  $CO^*$  and surface bound OH groups ( $OH^*$ ) in a parallel route to the coupling reaction. The origin of  $CO_2$  on the catalyst surface ( $CO_2^*$ ) is the oxidation of  $CO^*$  by  $O^*$ . A new aspect of the catalyst surface reaction network was published by Beck et al. for the  $Na_2WO_4/Mn/SiO_2$  as well as for  $MgO$ . In temporal analysis of products (TAP) experiments, they could show the presence of two different oxygen species, which exist in parallel on the catalyst surface. Furthermore they could show that both species have different reaction pathways [26]. One of them is weakly bound ( $O_{2,ads}$ ) and opens the route to deep oxidation products. The other, stronger bound oxygen species ( $O_x^*$ ) is responsible for the selective methane activation. Following these results a plausible surface reaction network is also presented in Table 1.

In addition, there is also a discussion about the formal kinetic mechanistic aspects of oxygen and methane activation described by an Eley-Rideal, Mars-van-Krevelen or dual site Langmuir Hinshelwood mechanism [12,27,28]. On the one hand, in the Eley-Rideal mechanism gas phase oxygen is required for selective activate methane in the OCM process. On the other hand, in a Mars-van-Krevelen type mechanism lattice oxygen is involved during C–H bond cleavage of methane to form a methyl radical. A possible interaction of lattice oxygen with methane offers the opportunity to avoid the presence of gas phase oxygen in temperature programmed experiments and dynamic experiments. During these unsteady state experiments the catalyst oxidation and the methane coupling reaction can be separated into two different steps. One of the first overviews about these techniques and experimental results from several groups was published by Falconer and Schwarz [29]. Another review about these techniques was presented by Niemantsverdriet [30].

One important factor in temperature programmed reduction experiments is the bond dissociation energy of the reactants. For methane (439 kJ/mole) and hydrogen (436 kJ/mole) these energies are similar, and for ethane (423 kJ/mole) it is lower than those of hydrogen and ethene (464 kJ/mole), which has the highest bond dissociation energy in this group of compounds [31]. Therefore it is possible to reduce the catalyst in the same manner as in a  $H_2$ -temperature programmed reduction (TPR) experiments using OCM reactants to study their pathways in the reaction network in absence of gas phase oxygen. These types of experiments were

introduced as temperature programmed surface reactions (TPSR) by McCarty and Wise some decades ago [32]. Heating rate variations in TPSR experiments allow the determination of the activation energy of desorption or surface reaction steps. This is known as the Redhead method [33]. In this work we want to study the OCM surface mediated reaction network in absence of gas phase oxygen, to understand the role of surface bound oxygen on the  $Na_2WO_4/Mn/SiO_2$  catalyst material. Temperature programmed reaction experiments utilizing methane, ethane and ethene as reactant give qualitative insights to their interaction with the surface bound oxygen species. In addition we performed a series of kinetic TPSR studies for the selective activation of methane. The focus of further dynamic experiments at constant temperature is to quantify the converted amount of strongly surface bound oxygen, the stability of the oxygen intermediates on the catalyst surface and the nature of active sites for that material.

## 2. Experimental

### 2.1. Catalyst preparation

The details of the preparation and the characterization of the catalyst are described elsewhere [34]. The final catalyst contains 5 wt.%  $Na_2WO_4$ , 2 wt.% Mn(II) ions and has a specific surface area of 1.86 m<sup>2</sup>/g. The catalyst material was analyzed by nitrogen adsorption and X-ray diffraction analysis after oxidation pretreatment and after dynamic experiments. The results are presented and discussed in the supporting information.

### 2.2. Experimental setup and mass spectrometer

All experiments were carried out in a fixed bed reactor made of quartz. The catalyst was placed on a quartz frit (200 μm pore size) in the isothermal zone. The isothermal zone is above the frit and has a length of 5 cm. A scheme of the reactor, a construction plan of the setup and analysis of temperature profile aspects are shown in the supporting information. The inner diameter is 9 mm. The type K thermocouple (NiCrNi) is covered by a quartz-made capillary ( $d_{in} = 4$  mm), which seals the reactor on top. The reactants come through the upper inlet. The bottom part of the reactor shrinks in diameter and is connected to a mass spectrometer or thermal conductivity detector. The feed composition was controlled by mass flow controllers (MFC) and switching valves were installed, enabling the ability to interrupt reactant flow immediately. Detection was carried out with a quadrupole mass spectrom-

**Table 2**  
Calibrated masses for compound detection in dynamic experiments.

Molecule	<i>m/e</i>
CO <sub>2</sub>	44
CO	28
He	4
H <sub>2</sub>	2
H <sub>2</sub> O	18; 17
CH <sub>4</sub>	16; 15
C <sub>2</sub> H <sub>6</sub>	30; 29; 28
C <sub>2</sub> H <sub>4</sub>	28; 27; 26
O <sub>2</sub>	32

eter (QMS, IPI GAM 200) with channeltron detector. The QMS was equipped with yttriated filaments. For O<sub>2</sub> detection in temperature programmed desorption experiments *m/e* = 32 was chosen and data points were recorded each 5 s. The *m/e* values for OCM compound calibration are listed in Table 2. Each compound was calibrated by utilization of a calibration gas bottle filled with 5 ± 0.005 vol.% of one compound and the rest was filled with Helium. The calibration of *m/e* = 28 for ethane and ethene was necessary to prevent false-signals for CO or other compounds. As indicator for ethane the *m/e* = 30 and for ethylene *m/e* = 27 were chosen, while the other listed masses were calibrated by their specific, relative intensities for these molecules. Therefore the feed compositions of these compounds were determined by three calibration factors for ethane and ethene to enhance detection accuracy.

The final mole fraction (*x<sub>i</sub>*) of each compound was calculated according to Eq. (1):

$$x_{\text{compound}}(x \dots z) = \frac{S_{\frac{m}{e}}(i \dots j)}{\gamma_i} \quad (1)$$

$S_{\frac{m}{e}}(i)$  – relative intensity matrix of compound *i*,  $\gamma(i)$  – calibration factor matrix for compound *i*.

The relative intensity was derived by

$$\begin{pmatrix} S_{\frac{m}{e},i} \\ \vdots \\ S_{\frac{m}{e},j} \end{pmatrix} = \begin{pmatrix} S_{\text{compound}_x}(S_{\frac{m}{e},i}) & \cdots & S_{\text{compound}_z}(S_{\frac{m}{e},j}) \\ \vdots & & \vdots \\ S_{\text{compound}_x}(S_{\frac{m}{e},i}) & \cdots & S_{\text{compound}_z}(S_{\frac{m}{e},j}) \end{pmatrix} \cdot \begin{pmatrix} x_{\text{compound}_x} \\ \vdots \\ x_{\text{compound}_z} \end{pmatrix} \quad (2)$$

$S_{m/e,i}$  – Sensitivity for a specific *m/e* ratio;

$S_{\text{compound}_x}(S_{\frac{m}{e},i})$  – Signal of compound *x* on *m/e*, *i*;

$x_{\text{compound}_x}$  – molefraction of compound *x*.

### 2.3. Temperature programmed reduction (TPR)

The fresh catalyst (60 mg) was placed in the reactor, which was heated up under synthetic air (N<sub>2</sub>:O<sub>2</sub> – 4:1, 99.9%, 30 sccm/min) with a temperature-ramp of 10 K/min to 1023 K, keeping this temperature for an hour and cooling down over night under constant air flow. To remove gas phase and adsorbed oxygen, a constant flow of nitrogen (30 sccm/min) purged through the reactor at room temperature for 30 min. The catalyst reduction was carried out by a feed stream of N<sub>2</sub>:H<sub>2</sub> (9:1, 60 sccm/min) with a heating rate of 2 K/min, heating up until 1093 K. The analysis of the effluent gas was done with a thermal conductivity detector (Messkonzept, FTD 200) monitoring the stream composition each 0.5 s.

### 2.4. Temperature programmed desorption (O<sub>2</sub>-TPD)

For temperature programmed desorption of oxygen, 1 g of fresh catalyst was used. The catalyst was heated up in a flow of He (99.999%, 20 sccm/min), with a temperature ramp of 5 K/min to

1093 K. In a second experiment 1 g of fresh catalyst was oxidized according to the method as mentioned in the TPR experiment. After the oxidation, the catalyst was treated as in the first O<sub>2</sub>-TPD experiment. The detection was carried by mass spectrometer, which was described before.

### 2.5. Temperature programmed surface reaction (TPSR)

Each TPSR experiment was carried out with 1 g Na<sub>2</sub>WO<sub>4</sub>/Mn/SiO<sub>2</sub> fresh catalyst. The catalyst oxidation in all experiments was the same procedure as described in the TPR experiment. To remove gas phase and adsorbed oxygen, the catalyst was purged for 30 min by a constant flow of He (99.999%, 30 sccm/min) at room temperature. For methane-TPSR, a flow of 30 sccm/min methane (99.99%) was chosen. Ethane and ethylene-TPSR were carried out in a flow of He:C<sub>2</sub>H<sub>x</sub> (95:5, 30 sccm/min, 99.98% C<sub>2</sub>H<sub>x</sub>). All TPSR experiments had an initial temperature of 298 K and the catalyst material was heated up under the reactant feed with a temperature ramp of 1 K/min with a final temperature of 1073 K. Each TPSR experiment was repeated by variation of the temperature with 3, 4 (only for methane) and 5 K/min. For product detection a QMS was used, as described above.

### 2.6. Dynamic experiments

The reactor, filled with 1 g fresh catalyst, was heated up to 1023 K under a constant flow of He:O<sub>2</sub> (9:1, 30 sccm/min). The final temperature was kept constant during the whole experiment. After 10 min at constant reaction temperature, the oxygen flow was stopped by deactivation of the mass flow controller (MFC) and closing the switching valve. A flow of Helium (20 sccm/min) was used as purging step to remove gas phase and weakly adsorbed oxygen for 5 min at constant temperature. Helium feed was immediately replaced by CH<sub>4</sub> (20 sccm/min) for the reaction mode, keeping the temperature constant. That was done by closing and opening of the switching valves, simultaneously. The methane flow reached the reactor after pressure fluctuation had already been compensated for in the feed tube. In the first series of dynamic experiments the purge time was varied from 10, 180 min to 300 min without using new catalyst material for each run. The methane step time was 10 min. After these experiments the catalyst material was not reoxidized and cooled down in a stream of He (30 sccm/min). The catalyst materials were analyzed by nitrogen adsorption (BET) and XRD. This was followed by a series of experiments reducing the purge time interval from 5 min down to 15 s, using fresh catalyst material again. During these set of experiments, the methane flow rate was 30 sccm/min and the methane time step was 10 min.

In addition, we also varied the methane partial pressure during the reaction sequence in another experimental series with fresh catalyst material. That was realized by a lower flow rate of purge gas down to 10 sccm/min or 15 sccm/min, while methane flow rate was set in parallel to 20 sccm/min or 15 sccm/min. In total a feed of 30 sccm/min reached the reactor. Here the reaction step for methane was set to 5 min.

### 2.7. Steady state experiment

The reactor was filled with 1 g fresh catalyst and heated up to 1023 K under He:O<sub>2</sub> (8:2, 30 sccm/min). The feed was changed to CH<sub>4</sub>:O<sub>2</sub> (95:5, 180 sccm/min) for 1 h, reaching the steady state conditions. The analyses of products were carried out with a QMS.

### 3. Results and discussion

#### 3.1. TPR

The result of the H<sub>2</sub>-TPR experiment is presented in Fig. 1. The oxidized catalyst showed one reduction pattern at 950 K. Furthermore the reduction curve shows early reduction by a slight decrease of the H<sub>2</sub> signal with respect to the baseline. This is also observed in the work of Shahri et al. [35]. They proposed that the early reduction is related to manganese oxide.

Peak integration was carried out and the amount of converted hydrogen was calculated according to Eq. (3). For the integration an adapted baseline was set to the corresponding hydrogen signals before and after the reduction pattern. The hydrogen consumption is equivalent to 17 O-atoms/nm<sup>2</sup>, which is an astonishing high value. Typically expected monolayer coverages of transition metal oxides on various support materials are between 0.1 and 10 atoms/nm<sup>2</sup> [36]. It was found that various manganese oxide species and supported manganese oxides on silica can be reduced to MnO under hydrogen atmosphere [37,38]. Furthermore it was shown in EPR experiments that only manganese ions are reduced at 1073 K in the Na<sub>2</sub>WO<sub>4</sub>/Mn/SiO<sub>2</sub> catalyst, while tungsten ions had a constant valency of +VI [39]. In addition, the active phase of this material has a very flexible structure [40]. Therefore it is possible that also sublayers are involved in the reduction reaction during TPR experiments, considering the small specific surface area of that catalyst.

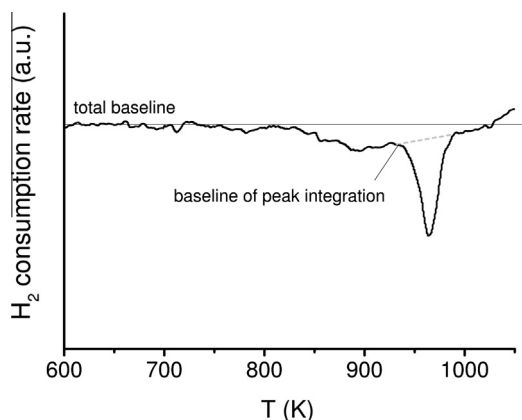


Fig. 1. H<sub>2</sub> TPR of oxidized Na<sub>2</sub>WO<sub>4</sub>/Mn/SiO<sub>2</sub> catalysts. 60 mg catalyst, N<sub>2</sub>:H<sub>2</sub> (9:1, 60 sccm/min), 2 K/min.

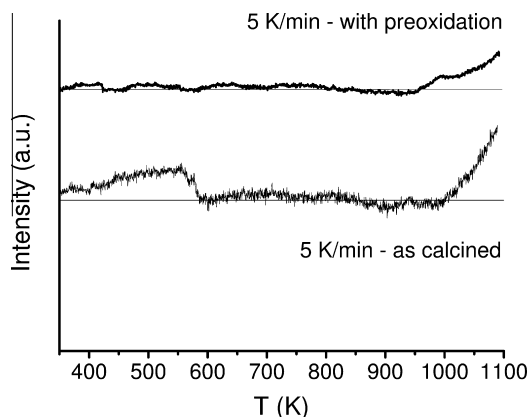


Fig. 2. O<sub>2</sub> TPD of different pretreated Na<sub>2</sub>WO<sub>4</sub>/Mn/SiO<sub>2</sub> catalysts. 1 g catalyst, He (99.999%, 20 sccm/min), 2 K/min.

$$n_{\text{H}_2} = \frac{A_{\text{H}_2, \text{peak}} [\% \text{ s}] \cdot \dot{V} \left[ \frac{\text{m}^3}{\text{s}} \right] \cdot p [\text{Pa}]}{R \left[ \frac{\text{J}}{\text{mol K}} \right] \cdot T [\text{K}]} \quad (3)$$

#### 3.2. O<sub>2</sub>-TPD

Experimental results of O<sub>2</sub>-TPD experiments are depicted in Fig. 2. The “as calcined” catalyst, without further oxidation treatment, shows an O<sub>2</sub> peak at 550 K. For the oxidized catalyst such peak is missing. Radhakrishnan et al. reported such early desorption patterns for different supported Mn<sub>x</sub>O<sub>y</sub> catalysts [41]. Furthermore this phenomenon is also observed for bulk manganese oxides [42]. This may explain also the early reduction of the catalyst, observed in TPR experiments. However, in both cases stronger O<sub>2</sub> desorption starts at 1000 K. TPD experiments for that catalyst material have already been published by different groups. In the review article by Arndt et al. it is mentioned, that O<sub>2</sub>-TPD experiments published by Fang et al. show no oxygen loss of the catalyst [43,44]. This is in clear contradiction to the report by Liu et al. [45]. They observed two oxygen signals at 1070 K and 1150 K, which were interpreted as surface layer oxygen and bulk oxygen. Especially the desorption peak at high temperatures in our experiments is in good agreement with their results.

#### 3.3. TPSR

The results of the TPSR experiments are shown in Fig. 3. Different symbols represent different compounds. Symbols do not represent data points, which are too many, to show due to the fast detection rate. They represent an interpolation of the recorded data. The results of methane feed TPSR experiments are shown in Fig. 3A–C, with increasing temperature ramps.

Only CO and ethane formation is observed in this set of experiments. In each case first ethane is formed and followed by detection of CO. Both peaks shift at higher heating rates to higher temperatures. The ethane formation shifts slightly and forms no clear peaks at heating rates above 4 K/min. Such spectra can be interpreted in different ways. The most important step for the formation of ethane is the selective activation of methane by C–H bond cleavage. These radicals combine and form an ethane molecule. Na<sub>2</sub>WO<sub>4</sub>/Mn/SiO<sub>2</sub> catalyst material was verified by Jiang et al. [46] According to the results of Lee et al. these radicals are also converted by surface bound oxygen into deep oxidation products [47]. On the other hand methane or ethane can be activated by another surface side, which leads also to the formation of deep oxidation products. We assume a short lifetime for the methyl radicals and therefore an immediate coupling or adsorption process on the catalyst surface. As mentioned before, in our TPSR experiments CO is formed much later and therefore the coupling process seems to be preferred. Furthermore the CO formation has to be observed parallel to ethane formation, when the oxidation of ethane is the origin of CO formation. Thus, the unselective activation of methane by another oxygen species on the catalyst surface is responsible for the formation of CO.

To analyze that situation in more detail, a series of simulations with the discussed reaction mechanisms in TPSR experiments were carried out and are presented in the supporting information. Our simulation results confirm that two active oxygen species on the catalyst surface in absence of gas phase oxygen contribute to OCM activity. Therefore not only gas phase and oxygen adsorption intermediates contribute to unselective methane activation. The nature of these species could be electrophilic and nucleophilic. On the one hand electrophilic oxygen is responsible for selective methane activation, which forms methyl radicals. On the other hand the nucleophilic species contributes to deep oxidation

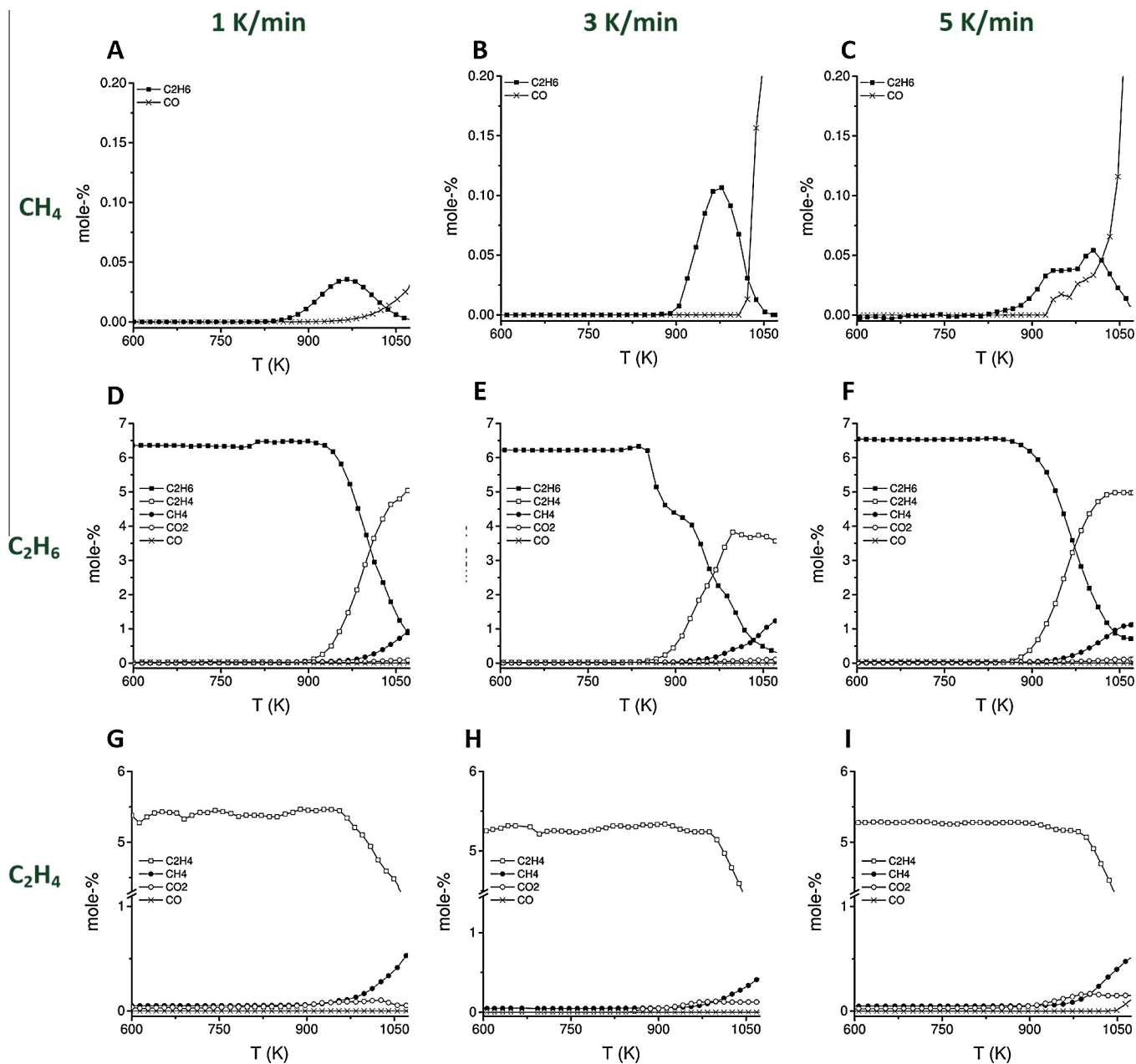


**Fig. 3.** TPSR product formation peaks of methane, ethane and ethene TPSR experiments at heating rates from 1 to 5 K/min, 1 g  $\text{Na}_2\text{WO}_4/\text{Mn}/\text{SiO}_2$ , A–C: methane TPSR, D–F: ethane TPSR (He: $\text{C}_2\text{H}_6$ , 95:5), G–I: ethene TPSR (He:  $\text{C}_2\text{H}_4$ , 95:5), 1 g  $\text{Na}_2\text{WO}_4/\text{Mn}/\text{SiO}_2$ , 30 sccm/min.

product formation. In the literature similar TPSR experiments were carried out with  $\text{Sr}_x\text{Ti}_y\text{MgO}$ , confirming our results [48]. The peak shift at different heating rates in TPSR experiments correlates with the slowest reaction in the reaction network. For OCM, this is assumed to be the methane activation reaction [49,50]. That effect is used in the next section to calculate the activation energy of selective methane activation.

It has to be noted that the variations in the peak areas in these experiments are caused in two different ways. On the one hand slow heating rates result in a longer reaction time for oxygen consumption for each temperature during the experiment. Therefore low amounts of methane can be converted already at lower temperatures. Thus, the peak amplitude is different for slow heating rates, because less oxygen is available on the catalyst surface at that time step. In addition, fast heating rates shift the methane activation by oxygen to higher temperatures and therefore the

reaction rate is much higher, because of higher temperature and more oxygen which was not converted so far. On the other hand, as shown in the last section, oxygen can desorb during the experiment. Therefore it is also possible that oxygen is released in gas phase, while methane adsorbs on the catalyst surface.

In the same manner as methane TPSR experiments, a series of TPSR experiments for ethane are shown in Fig. 3D–F. We observe ethane conversion to ethene starting at 890 K in all experiments. At 1050 K most of the ethane in the feed has been converted to ethene but conversion does not change further. The initial temperature of ethane consumption is higher than for methane activation in TPSR experiments. According to the different C–H bond strengths of methane and ethane, a lower activation temperature would be expected. However our TPSR experiments indicate a different activation mechanism for this molecule, which is not effected by C–H bond cleavage on the catalyst surface, which will

be discussed later. Furthermore, the formation of CO<sub>2</sub> and CH<sub>4</sub> can be observed at 950 K. These products indicate deep oxidation reaction steps as well as cracking reactions. Some carbon deposition as consecutive reaction product is also observed during reactor purging.

In TPSR experiments utilizing ethene as reactant only CO<sub>2</sub> and CH<sub>4</sub> formation at 920 K can be observed. That is in good agreement with our results of ethane TPSR experiments. CH<sub>4</sub> is a typical cracking product, which is formed from ethene during coke formation on the catalyst surface [51,52]. Carbon deposition was verified by oxidation of the catalyst subsequent to the TPSR experiment. Interestingly the formation of CO<sub>2</sub> and CH<sub>4</sub> starts in these experimental sets at the same temperature, which indicates a fast consecutive reaction from ethene to carbon deposition followed by CO<sub>2</sub> formation. Another possible explanation is a parallel reaction of ethene to cracking products and to carbon dioxide. The formation of deep oxidation and cracking products from ethene in absence of gas phase oxygen and the adsorption intermediate confirms our hypothesis that two active oxygen species seem to be responsible for ethene activation. On the one hand electrophilic oxygen can interact with the double bond of ethene, which could form ethylene oxygenates. These intermediates are further oxidized to deep oxidation products. On the other hand nucleophilic oxygen can activate ethene by C–H bond cleavage, which results into the formation of deep oxidation and cracking products. Such effect is well-known for ethylene oxide synthesis and for OCM on silver catalysts [53,54].

In Fig. 4A the product formation from ethane TPSR is presented in more detail for further discussion, than in Fig. 3. At 890 K small amounts of ethene can be observed, while water and hydrogen formation starts at the same temperature. At 950 K the amount of water decreases, while the amount of hydrogen still increases. As mentioned before, with increase of ethane conversion, CO<sub>2</sub> and methane signals can be observed. For monitoring the water formation in a consecutive reaction, the detailed product signals for ethane TPSR are shown in Fig. 4B. We observe at 920 K small amounts of water and CO<sub>2</sub> formation. At 1050 K the water amount decreases to the baseline level, while the CO<sub>2</sub> signal stays constant and methane formation can be observed. We observe also hydrogen formation at this temperature and much stronger ethene decomposition. Both product spectra show that the oxygen rich surface provides enough potential for oxidative dehydrogenation reaction steps, indicated by water formation. When that surface oxygen species is consumed, the reaction pathway changes to thermal decomposition reactions. For ethane TPSR experiments it is not

**Table 3**

Calculated free energy for oxidation and coking reactions from ethane and ethene at 1073 K.

No.	Reaction	ΔG (kJ/mole)
A	C <sub>2</sub> H <sub>6</sub> + ½ O <sub>2</sub> → C <sub>2</sub> H <sub>4</sub> + H <sub>2</sub> O	–187.4
B	C <sub>2</sub> H <sub>6</sub> → C <sub>2</sub> H <sub>4</sub> + H <sub>2</sub>	6.9
C	C <sub>2</sub> H <sub>6</sub> → 2 C + 3 H <sub>2</sub>	32.0
D	C <sub>2</sub> H <sub>6</sub> + H <sub>2</sub> → 2 CH <sub>4</sub>	–79.0
E	C <sub>2</sub> H <sub>4</sub> → 2 C + 2 H <sub>2</sub>	–107.4
F	C <sub>2</sub> H <sub>4</sub> → C + CH <sub>4</sub>	–118.9

clear whether thermal and oxidative dehydrogenation follows consecutive or parallel reaction routes.

To analyze this situation we calculated the free reaction energy for different coking and oxidation reactions at 1073 K by Eq. (4). The thermodynamic data for each compound was presented by McBride et al. [55]. The results are shown in Table 3.

$$\Delta G_R = \sum_i v_i \cdot \Delta H_{f,i} - T \cdot \sum_i v_i \cdot \Delta S_{f,i} \quad (4)$$

The oxidative dehydrogenation (ODH) is preferred compared to the thermal dehydrogenation (TDH) (Table 3, reaction A and B). Our ethane TPSR experiments in an empty reactor show thermal dehydrogenation in the same temperature range. According to that result we conclude that this phenomenon is a parallel route in the gas phase. The coupling process of two methyl radicals in gas phase at that temperature has a free energy of –328 kJ/mole. Thus, the energy must be transferred from the ethane intermediate for stabilization. Typically, that could be done by a collision with another molecule or the splitting of ethane into new molecules as ethene and hydrogen [6]. Decomposition of ethane to coke and hydrogen is not favored, but the backward reaction to methane by reduction may happen in the gas phase (Table 3, reaction C and D). The splitting reaction of ethane to methane hydrogen is necessary. As main hydrogen source the TDH of ethane may be responsible. Finally the ODH reaction of ethane is thermodynamically preferred but limited to the amount of stored oxygen on the catalyst surface. For TDH no adsorption of ethane on the catalyst surface is required.

The ethene decomposition to carbon and methane is slightly preferred, compared to the route of carbon and hydrogen formation only (Table 3, reaction E and F). The formation route of carbon dioxide cannot be resolved exactly, because the TPSR method is not sensitive enough for this reaction and the thermodynamic data for the Na<sub>2</sub>WO<sub>4</sub>/Mn/SiO<sub>2</sub> catalyst are unknown. Isotopic labeling

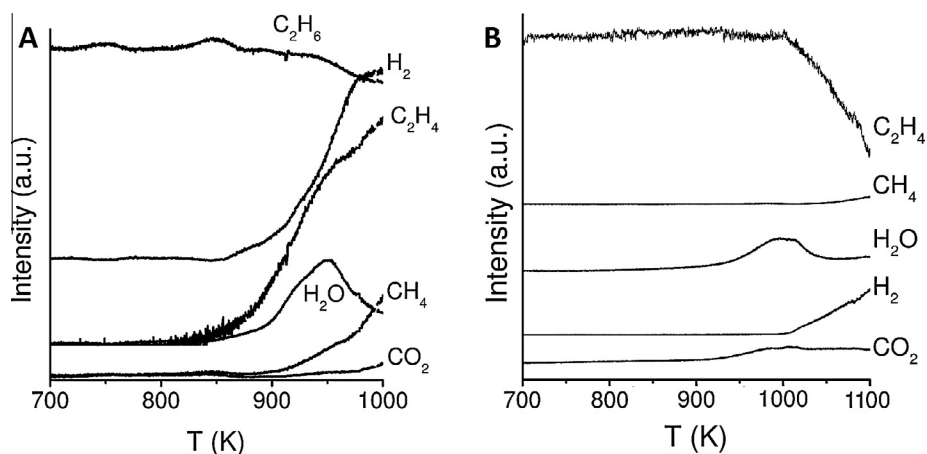


**Fig. 4.** Detailed ethane and ethene TPSR spectra, A: Ethane, B: Ethene, 3 K/min, 1 g Na<sub>2</sub>WO<sub>4</sub>/Mn/SiO<sub>2</sub>, 30 sccm/min flow (He:C<sub>2</sub>H<sub>x</sub>, 95:5).

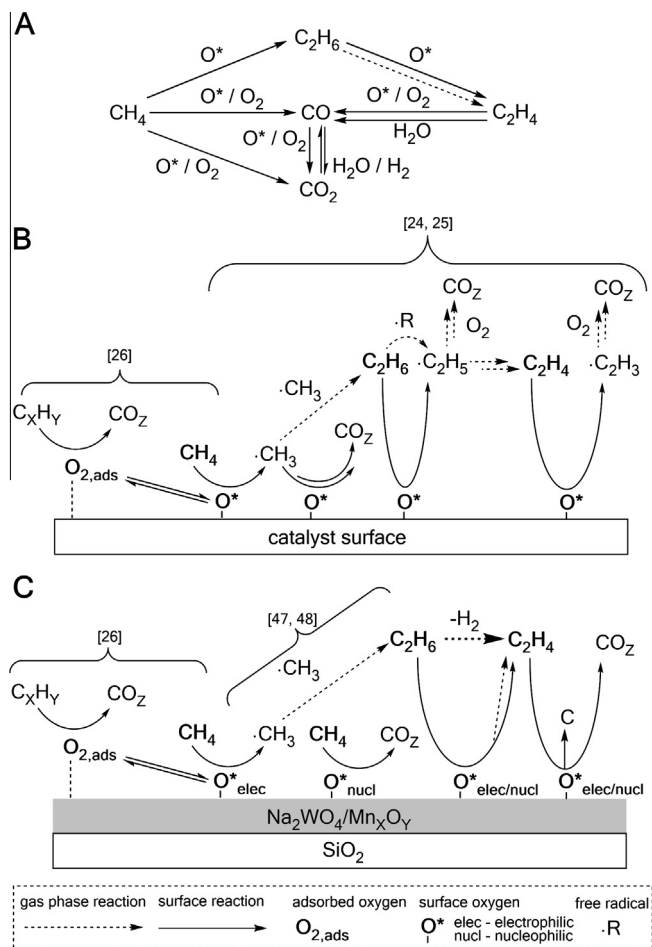


**Fig. 5.** A: Classical OCM reaction mechanism, including gas and surface reaction steps [8,9], B: OCM reaction network according to Table 1, C: Proposed reaction route for OCM surface reaction based on TPSR experiments for  $\text{Na}_2\text{WO}_4/\text{Mn}/\text{SiO}_2$  catalyst.

experiments with  $^{13}\text{C}$  in cofeed for that catalyst material are required to understand the origin of deep oxidation products.

To compare our findings, a well-established reaction network for the OCM is shown in Fig. 5A. It must be considered that the reaction network combines oxygen induced gas phase reactions, further gas phase activity by water and oxygen containing products, gas phase interactions of short lifetime intermediates as radicals and surface reactions in each step. Methane undergoes a parallel reaction to ethane or the deep oxidation product  $\text{CO}$ . The first route leads to ethene which can be converted to  $\text{CO}_2$ , which is in equilibrium with  $\text{CO}$  [56]. There are some modifications of this model, which were used for formal kinetic fitting procedures for the  $\text{Na}_2\text{WO}_4/\text{Mn}/\text{SiO}_2$  catalyst [8,9].

The micro kinetic model from the introduction part is presented in Fig. 5B for further comparison. Interpretation of the TPSR results leads to a similar reaction model which is presented in Fig. 5C. The methane activation on the catalyst surface is followed by coupling process or by methyl radical absorption and the formation of oxygenates. In contrast, our TPSR results indicate that methane activation is performed by two different surface oxygen species. Similar to the results of Sun et al. the ethane molecule is activated by oxygen on the catalyst surface or in gas phase by different radical species, which is common for the TDH reaction. The absence of gas phase oxygen leads to hydrogen production instead of water formation. Similar findings in these models show that the TDH is a serious parallel reaction route in the oxidative coupling of

methane. Such information is typically not obtainable in co-fed studies [57]. Furthermore this route reveals the complexity of different gas phase contributions to OCM, considering that the TDH is also a radical chain mechanism, as the selective methane activation on the catalyst surface is. Both reactions are initialized by methyl radical formation [50,58]. The mechanism of ethane activation on the catalyst surface by TPSR experiments cannot be revealed. In contradiction to the literature model, which requires gas phase oxygen for the formation of deep oxidation products by ethene oxidation, the TPSR results for the  $\text{Na}_2\text{WO}_4/\text{Mn}/\text{SiO}_2$  catalyst reveal that also lattice oxygen is able to form such kind of products. Therefore it is possible that a Mars-van-Krevelen type mechanism should be considered for ethylene oxidation. In addition, it must be considered that also the cracking mechanism of ethylene is based on radical reactions and coke formation is preferred at higher ethene partial pressures [59].

However, the proposed model is similar to the key steps of the reaction network for the  $\text{MgO}$  catalyst. It shows that the  $\text{MgO}$  catalyst and the  $\text{Na}_2\text{WO}_4/\text{Mn}/\text{SiO}_2$  catalyst have several similarities, despite their chemical difference.

### 3.4. Arrhenius parameter of methane TPSR

In the last section we pointed out, that the rate-determining step in TPSR experiments is strongly influenced by the heating rate. Redhead showed that desorption or the rate-determining reaction step follows an Arrhenius type function [33]. The rate constant of the surface reaction is proportional to the ratio of heating rate ( $\beta$ ) and peak amplitude temperature ( $T_A$ ) of the formed product, which is shown in Eq. (5). Following this method an Arrhenius plot can be constructed. Therefore we carried out methane TPSR experiments with heating rate variation from 1 to 4 K/min. Higher heating rates show no clear ethane peak as can be seen in the last section. For a more exact determination of the peak temperature from the observed ethane peaks, each peak was fitted to an empirical amplitude of the Gaussian function, which is shown in Eq. (6). All fits had an accuracy of 0.85 or better. The peak temperatures  $T_A$ , derived by this method are shown in Table 4.

$$k \sim \left( \frac{\beta}{T_A^2} \right) \quad (5)$$

$$x_i = x_{i0} + A \cdot \exp \left( -0.5 \cdot \left( \frac{T - T_A}{w} \right)^2 \right) \quad (6)$$

Fitting parameters:

- A – peak amplitude (ordinate).
- $T_A$  – temperature of peak (abscissa).
- $x_{i0}$  – offset of compound baseline.
- w – half width of peak signal.

The inverse temperatures of the ethane peaks were plotted to the Napierian logarithm of heating rate divided by the square of

**Table 4**

Ethane peak temperatures from methane TPSR experiments with heating rates from 1 to 4 K/min fitted by an empirical Gaussian function, 1 g  $\text{Na}_2\text{WO}_4/\text{Mn}/\text{SiO}_2$ , 30 sccm/min methane.

Heating rate $\beta$ (K/min)	Temperature of ethane peak amplitude $T_A$ (K)
1	964 ± 3
2	983 ± 1
3	985 ± 1
4	1003 ± 1



**Table 6**

Species based oxygen balance for the dynamic experiments of methane at purge process duration from 10 min to 300 min, 1023 K, 20 sccm/min CH<sub>4</sub> for 10 min, 1 g Na<sub>2</sub>WO<sub>4</sub>/Mn/SiO<sub>2</sub>.

Purge interval	10 min				180 min				300 min			
	CO <sub>2</sub>	CO	C <sub>2</sub> H <sub>6</sub>	C <sub>2</sub> H <sub>4</sub>	CO <sub>2</sub>	CO	C <sub>2</sub> H <sub>6</sub>	C <sub>2</sub> H <sub>4</sub>	CO <sub>2</sub>	CO	C <sub>2</sub> H <sub>6</sub>	C <sub>2</sub> H <sub>4</sub>
Aver. S	0.08	0.03	0.44	0.45	0.14	0.01	0.48	0.37	0.12	0.01	0.50	0.37
Aver. S	0.11		0.89		0.15		0.85		0.13		0.87	
#O/nm <sup>2</sup>	7.2	5.4	1.8	3.6	10.4	0.6	4.5	7.1	8.8	0.58	4.6	6.8
#O/nm <sup>2</sup>	18.00				21.66				20.66			

For the dynamic experiment, we assume that the activation of methane is the rate determining step. All reaction steps should have a reaction order of one, because of the activation by adsorption on the catalyst surface. We calculated the formation rates of all products during the first 20 s, using Eq. (11). It has to be noted that the methane partial pressure is not constant and still increasing in this time span. The experimental conditions and results for the dynamic experiment, with a purge time of 10 min, are shown in Table 6. A detailed discussion for the dynamic experiment follows in the next section.

$$r_{\text{CH}_4} = \sum_{\text{products},i} \left( \frac{n_{\text{CH}_4}(dt)}{m_{\text{cat}}} \cdot v_i \cdot \frac{dx_i}{dt} \right)_i \quad (11)$$

$n_{\text{CH}_4}$  – Moles of methane in 20 s.

$x_i$  – Mole fraction of detected compound.

$v_i$  – Stoichiometric factor.

In the steady state mode (242  $\mu\text{mol/g}_{\text{cat}} \text{min}^{-1}$ ), the rate is much higher compared to the dynamic mode (5.19  $\mu\text{mol/g}_{\text{cat}} \text{min}^{-1}$ ). The difference of almost two orders of magnitudes between both reaction rates indicates several effects.

On the one hand, in steady state mode the methane partial pressure is constant at 0.95 bar, while in the early period of the dynamic experiment methane partial pressure reaches only 0.1 bar. On the other hand, in steady state the major product is ethane, while in dynamic mode ethane and ethene have the same ratio. Therefore the formed ethane, which is even more reactive, competes in the dynamic experiment with the fed methane for the oxygen and therefore has also a substantial effect on the measured rate of methane consumption. We assume, that the low flow of 20 sccm/min in the dynamic experiment compared to 180 sccm/min in the steady state experiment allows more consecutive oxidative dehydrogenation of ethane. In addition the catalyst in steady state mode is continuously reoxidized by gas phase oxygen, which also enhances the reaction rate. Therefore not only the strongly bound oxygen intermediate is present on the catalyst surface. The weakly bound intermediate contributes also to the reaction rate. The reoxidation rate of the catalyst is fast compared to methane activation. Thus, the catalyst activity is not limited by the available amount of oxygen [47].

In contradiction, in dynamic experiments only small amounts of oxygen are stored on the catalyst surface, which are rapidly consumed. Further effects may limit the reaction rate by mass transport limitation. Possible is the formation of OH groups on Na<sub>2</sub>WO<sub>4</sub>/Mn/SiO<sub>2</sub>, which can even block sites for methane adsorption. An additional limiting effect is the formation of coke, which can also block or convert active sites. All these effects cannot be fully excluded.

However, the large difference in methane partial pressures in steady state and dynamic experiments and the big differences in availability of oxygen in both experimental modes seem to have

the strongest effects on the reaction rate. Thus, we assume to observe comparable initial activity of the active oxygen sites in both types of experiments.

### 3.5.2. Influence of purge time and flow rate in dynamic experiments

In the first series we carried out a variation of the purge time with Helium from 10 min to 5 h. The results for these experiments are shown in Fig. 8. At time 0 s, the methane flow reached the catalyst bed after purging with inert gas for different time intervals. In all experiments we obtained a C2 selectivity of 85% or better. The amplitudes of the product peaks are much higher compared to the TPSR experiments. In the TPSR experiments the time span between oxidation and reaction is dependent on the heating rate. Furthermore, in TPSR experiments the oxygen conversion starts at lower temperatures and the amount of stored oxygen decreases in a longer time span. Slow increase of temperature enhances this effect. Reaching high temperatures, most of the oxygen will be converted and the peak amplitude is low. In the TPD experiment we could observe an oxygen loss at these temperatures, which may also contribute.

During the first minute in all dynamic experiments we observe deep oxidation products, indicated by CO and CO<sub>2</sub> formation. In this time interval the partial pressure of methane is still increasing, because it replaces the He from the purging process. At high methane partial pressures and reaching the ethene peak amplitude, the CO signal vanishes. The same phenomenon is observed for the CO<sub>2</sub> signal, which has a longer time span than CO. The early decrease of the CO<sub>2</sub> signal indicates that the available amount of oxygen for OCM reaction decreases rapidly and only small amounts are consumed for ethane and ethene formation. The preferred route of deep oxidation product formation, from methane or ethene, during dynamic experiments cannot be revealed. Isotopic labeling experiments for the Na<sub>2</sub>WO<sub>4</sub>/Mn/SiO<sub>2</sub> catalyst reveal no kinetic isotope effect (KIE) of CH<sub>4</sub>/CD<sub>4</sub> for deep oxidation product formation [67]. It was concluded, that a different site on the catalyst surface is responsible for CO<sub>x</sub> formation, which was suggested to be MnO<sub>x</sub>.

To quantify our results an oxygen balance for each compound was calculated. To do so, the peak areas for each compound ( $A_{i,\text{peak}}$ ) were integrated with respect to the baseline level. The amount of each product was calculated as shown in Eq. (12) and the corresponding moles of consumed oxygen with respect to the stoichiometry were determined. We assume that surface bound oxygen (O\*) is an atomic species and quantitatively converted to water. The corresponding reactions are shown in Eqs. (13)–(16).

$$n_i = \frac{A_{i,\text{peak}}[\% \text{ s}] \cdot \dot{V} \left[ \frac{\text{m}^3}{\text{s}} \right] \cdot p[\text{Pa}]}{R \left[ \frac{\text{J}}{\text{mol K}} \right] \cdot T[\text{K}]} \quad (12)$$



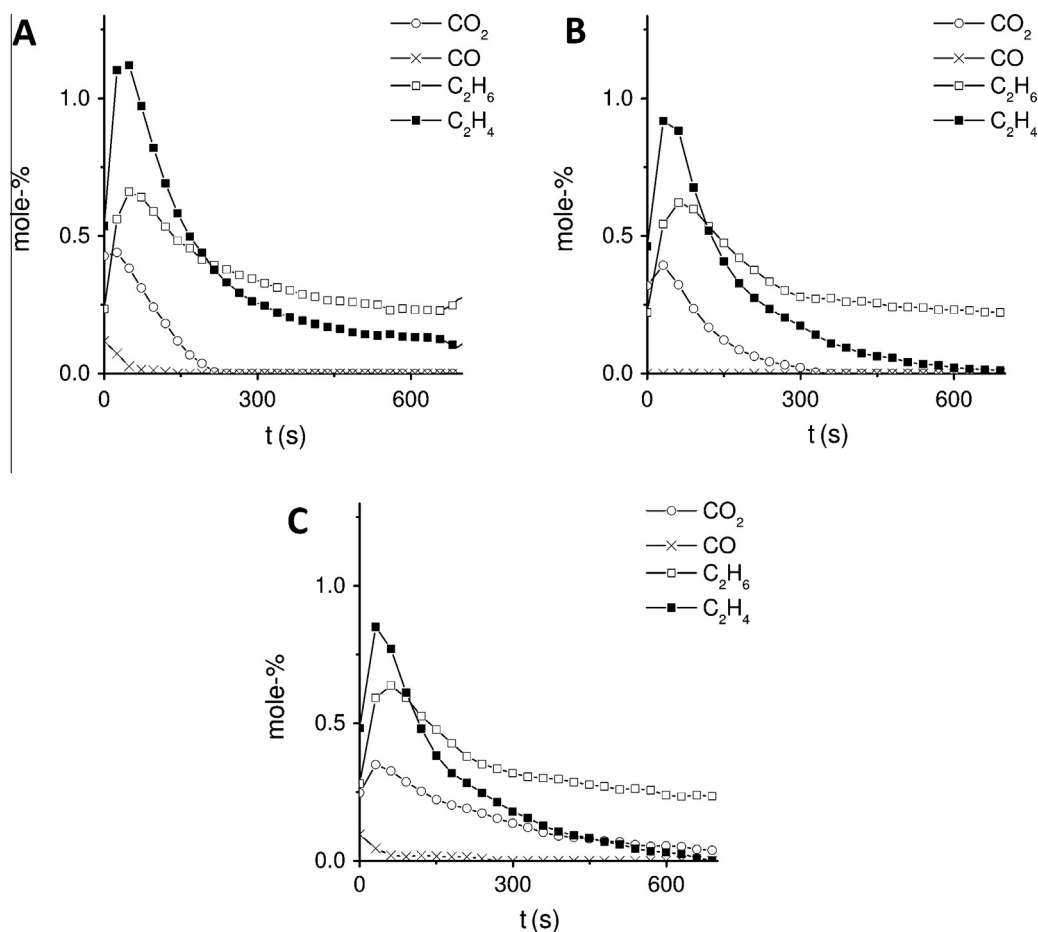


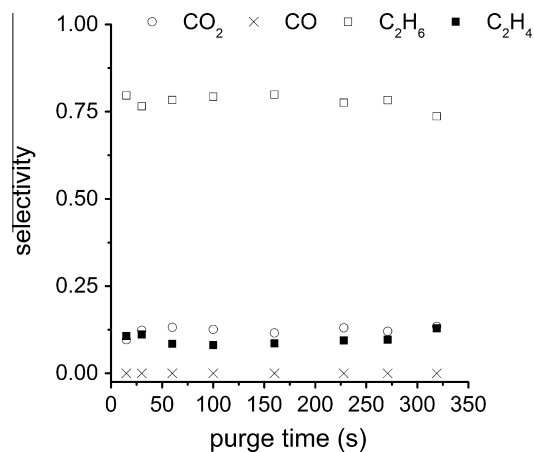
**Fig. 8.** OCM product signals from dynamic experiments with methane with increasing of purge duration at 1023 K, 20 sccm/min  $\text{CH}_4$  for 10 min, 1 g  $\text{Na}_2\text{WO}_4/\text{Mn}/\text{SiO}_2$ , A – 10 min He purge, B – 180 min He purge, C – 300 min He purge.



The results of these oxygen balances are listed in Table 6. The calculated oxygen amounts are similar to those from the  $\text{H}_2$ -TPR experiment. Increasing the purge time has no substantial influence on the available oxygen amount. As mentioned before, most oxygen was converted to form deep oxidation products. Only increasing of the purge time interval to 5 h decreases the peak amplitudes of all formed products slightly. Another effect is the decrease of the peak tailing of ethene, whereas the tailing of  $\text{CO}_2$  is increased. This implies that the catalyst structure could have changed. As demonstrated in our TPD experiment the catalyst material desorbs oxygen at high temperatures. That could lead to a change of the oxidation state of manganese oxide from  $\text{Mn}_2\text{O}_3$  to  $\text{Mn}_3\text{O}_4$ , for instance. Both species have different activity for unselective methane activation [38].

With this experiment, we can show that the provided oxygen is stored under harsh conditions even for hours. This implies that the active center on the  $\text{Na}_2\text{WO}_4/\text{Mn}/\text{SiO}_2$  for OCM is bound or integrated oxygen in the lattice structure, because simply adsorbed oxygen species should not survive such treatment without additional stabilization. From the mechanistic point of view these results support the theory of a Mars-van-Krevelen like mechanism for the OCM reaction on  $\text{Na}_2\text{WO}_4/\text{Mn}/\text{SiO}_2$ .

Similar step-change experiments in the OCM with this material were carried out by Salehoun and coworkers [68]. They could show an increase of the ethane peak by an increase of reaction

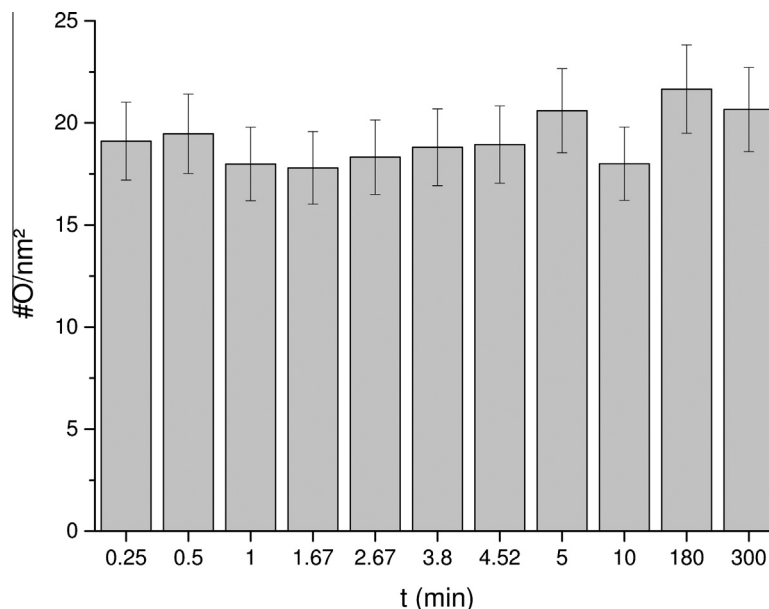
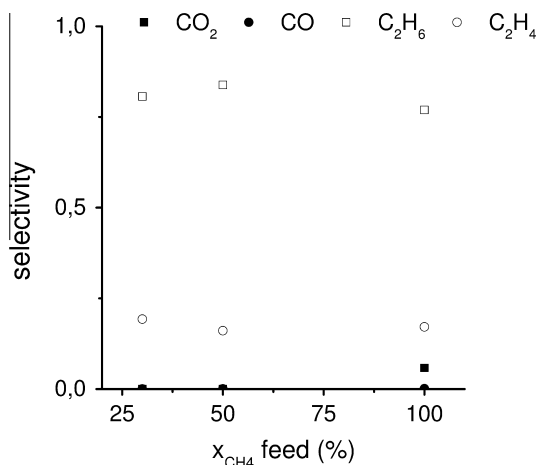


**Fig. 9.** Selectivity for purge time reduction of dynamic experiments from 5 min to 15 s, 1 g  $\text{Na}_2\text{WO}_4/\text{Mn}/\text{SiO}_2$ , 1023 K, 30 sccm/min  $\text{CH}_4$  for 10 min.

temperature, indicating larger amounts of available oxygen. An interesting difference is the observed ratio of ethane and ethene, because their results show strong ethane formation and less ethene formation, but overall C2 selectivity is close to our results. They also concluded that C2 products may come from lattice oxygen by selective methane activation, where CO is formed by unselective reaction of methane with gas phase oxygen. Both interpretations confirm our results. They mentioned also that the

**Table 7**Compound based oxygen balance for short He purge times in dynamic experiments from 300 s down to 15 s, 1 g Na<sub>2</sub>WO<sub>4</sub>/Mn/SiO<sub>2</sub>, 1023 K, 30 sccm/min CH<sub>4</sub> for 10 min.

Purge time (s)	CO <sub>2</sub> (#O/nm <sup>2</sup> )	CO (#O/nm <sup>2</sup> )	C <sub>2</sub> H <sub>6</sub> (#O/nm <sup>2</sup> )	C <sub>2</sub> H <sub>4</sub> (#O/nm <sup>2</sup> )	Σ (#O/nm <sup>2</sup> )
300	10.70	0	7.33	2.57	20.60
270	9.41	0	7.64	1.89	18.94
230	9.77	0	7.27	1.77	18.81
160	8.94	0	7.72	1.66	18.32
100	9.14	0	7.19	1.47	17.80
60	9.46	0	7.02	1.52	17.99
30	9.74	0	7.55	2.19	19.47
15	8.27	0	8.55	2.30	19.11

**Fig. 10.** Total number of oxygen atoms per nm<sup>2</sup> at different purge time durations in dynamic experiments, 1 g Na<sub>2</sub>WO<sub>4</sub>/Mn/SiO<sub>2</sub>, 1023 K, 20–30 sccm/min CH<sub>4</sub> for 10 min.**Fig. 11.** Selectivity of the varied methane feed concentration in dynamic experiments, 1 g Na<sub>2</sub>WO<sub>4</sub>/Mn/SiO<sub>2</sub>, 1023 K, 30 sccm/min CH<sub>4</sub> for 5 min.

reduced catalyst will be reoxidized by gas phase oxygen, while the catalyst reoxidation rate is much faster than its rate of reduction by bond cleavage of alkanes or alkenes.

The selectivities observed in short purge time experiments are shown in Fig. 9. A detailed oxygen balance for each compound can be found in Table 7. The C<sub>2</sub> selectivity changes substantially.

The major product is ethane, whereas ethene decreases and is in the range of the CO<sub>2</sub> signal, which is a minor product. During these experiments no CO was detected by decrease of residence time. On the one hand that could be interpreted, that no methane was activated in an unselective way and the CO<sub>2</sub> results from ethene activation, according to the discussed reaction network before. On the other hand it must be considered that CO could be also oxidized to CO<sub>2</sub> on the catalyst surface. Therefore it is not possible to distinguish between methane and ethene activation to form deep oxidation products.

The number of available oxygen atoms stays constant at 20 O/nm<sup>2</sup>. A more or less constant number of converted oxygen atoms from the catalyst surface indicate that no significant coke formation from ethene disproportionation blocks available surface oxygen for the OCM reaction, in both sets of experiments. These experiments imply that the feed contact time with the catalyst bed has a strong influence on the C<sub>2</sub> product ratio, but not on deep oxidation products. That supports our statement from the TPSR section that a different oxygen species must be responsible for deep oxidation product formation, which can interact with methane and ethene in a different, independent route. In our TPSR experiments we discussed that the parallel reactions ODH on the catalyst surface and TDH in gas phase are responsible for C<sub>2</sub>H<sub>4</sub> formation. It has to be noted that we cannot reveal how strong these routes are involved in product formation.

Another observed phenomenon is that there is still no influence of the purge interval on the OCM itself. Even for 15 s purge

**Table 8**  
Compound based oxygen balance for reduced methane partial pressure in the reactant feed of dynamic experiments, 1 g Na<sub>2</sub>WO<sub>4</sub>/Mn/SiO<sub>2</sub>, 1023 K, 30 sccm/min CH<sub>4</sub> for 5 min.

CH <sub>4</sub> feed ratio	CO <sub>2</sub> (#O/nm <sup>2</sup> )	CO (#O/nm <sup>2</sup> )	C <sub>2</sub> H <sub>6</sub> (#O/nm <sup>2</sup> )	C <sub>2</sub> H <sub>4</sub> (#O/nm <sup>2</sup> )	Σ (#O/nm <sup>2</sup> )
1.00	5.22	0.03	4.31	1.45	11.01
0.50	1.75	0.01	2.87	0.85	5.48
0.33	1.24	0.00	2.00	0.80	4.03

duration, there is no shift in the selectivities observed. This result is only plausible, when short purge processes are sufficient for removing all gas phase and adsorbed oxygen from the catalyst surface and the reoxidation rate of the catalyst is fast. A sum of the available oxygen on the Na<sub>2</sub>WO<sub>4</sub>/Mn/SiO<sub>2</sub> is shown in Fig. 10 that shows no significant change in the available oxygen amount on the catalyst surface for purge time variation.

### 3.5.3. Methane partial pressure variation in the reactant feed of dynamic experiments

The response of the selectivities to methane partial pressure variation in the reactant feed is shown in Fig. 11. The ethene selectivity increases slightly when reducing the methane partial pressure. CO<sub>2</sub> is only observed for pure methane feed and only small traces of CO appear. Therefore the C2 selectivity is around 0.9. A decrease of the methane partial pressure shifts the overall C2 selectivity for these experimental conditions to 0.96. By reducing the methane fraction in the feed, the converted oxygen amount from the catalyst surface decreases in the same ratio (Table 8). These numbers indicate that less oxygen is consumed, compared to the dynamic experiments before, which showed 20 O/nm<sup>2</sup>. In addition, reducing the reactant feed duration from 10 to 5 min leads to a decrease of the converted oxygen, in pure methane feed experiment, too.

This indicates again, that there is linear methane partial pressure dependence for the overall OCM process on Na<sub>2</sub>WO<sub>4</sub>/Mn/SiO<sub>2</sub> catalysts. Our results are in good agreement with isotopic labeling experiments of Burch et al., who found a similar correlation [67].

## 4. Conclusion

In our H<sub>2</sub>-TPR experiments we found reduction of Na<sub>2</sub>WO<sub>4</sub>/Mn/SiO<sub>2</sub> catalyst at 950 K. The O<sub>2</sub>-TPD shows weak early oxygen desorption at 540 K and a clear oxygen desorption peak at 1070 K. Both experiments show that the catalyst structure provides oxygen which interacts with different oxidation potentials.

In TPSR experiments we found that methane can be converted into CO or ethane. That is caused by two different oxygen species according to our simulation results. The formed ethane can be oxidized further to ethene in a parallel reaction, by oxidative or thermal dehydrogenation on the catalyst surface or in gas phase. This process is dependent on the available oxygen amount at the catalyst surface and a serious route in the OCM reaction. Ethene undergoes disproportion to coke and methane formation. We also observe CO<sub>2</sub> formation in a parallel pathway. All these pathways were only obtainable in non-cofeed experiments. Methane TPSR experiments at heating rates of 1–4 K/min result in an activation energy of 275 kJ/mole for methane activation and ethane formation by catalyst bound oxygen. This value is common by the assumption that lattice oxygen or a strongly adsorbed oxygen species is involved in the rate determining step of the OCM process on the Na<sub>2</sub>WO<sub>4</sub>/Mn/SiO<sub>2</sub> catalyst. The higher activation energy obtained from a TPSR experiment compared to methane activation energies from steady state experiments in the literature can be explained by an energy profile including such an activated oxygen species, which is shown in Fig. 7. We conclude that strongly

adsorbed or lattice oxygen is responsible for methane activation, which has a much lower energy level, compared to adsorbed molecular oxygen. In our dynamic experiments we found that around 20 O/nm<sup>2</sup> are available on the catalyst surface for the OCM process. This number is independent of purge times between 15 s and 300 min and even of the flow rate of methane, which has a strong effect on C2 selectivity but not on the total product amount. Such a high number of available oxygen atoms per surface area indicate involvement of lattice oxygen and may be from sublayers of the catalyst material, caused on its flexible structure properties. A linear decrease of the converted oxygen atoms on the catalyst surface is only observed when reducing the methane feed duration. Partial pressure variation of methane showed a linear dependence on the converted number of oxygen atoms, too.

Finally, the nature of oxygen adsorption and conversion by that catalyst material has strong similarities with other well-known partial oxidation reactions as the synthesis of formaldehyde or ethylene oxide from methanol or ethene on silver catalysts [53,54,69,70]. The function to store a selective oxygen species for chemical reactions under harsh conditions for different periods of time might be useful for dynamic reactor concepts, such as chemical looping. Such a concept has the advantage of excluding oxidation reactions in gas phase. Typical material properties for such a concept are fast storage of oxygen and fast oxygen release for chemical reactions [71]. In our work we could show that a reoxidation of the material is fast compared to the OCM reaction. A direct conversion of the strongly bound oxygen species on the catalyst surface by methane might be a proper manner for a modified chemical looping concept. Such a concept was already successfully tested for propane dehydrogenation and is reviewed in detail elsewhere [72,73].

## Acknowledgment

This work is part of the UNICAT excellence cluster, which is coordinated by the Technische Universität Berlin. The funding of this cluster by the German Research Foundation (DFG) is gratefully acknowledged.

## Appendix A. Supplementary material

Supplementary data associated with this article can be found, in the online version, at <http://dx.doi.org/10.1016/j.jcat.2016.06.014>.

## References

- [1] T. Ren, M.K. Patel, K. Blok, *Energy* 33 (2008) 817.
- [2] J.J.H. Lunsford, *Catal. Today* 63 (2000) 165.
- [3] H. Zhang, J. Wu, B. Xu, C. Hu, *Catal. Lett.* 106 (2006) 161.
- [4] A.V. Kruglow, M.C. Bjorklung, R.W. Carr, *Chem. Eng. Sci.* 51 (1996) 2945.
- [5] H.R. Godini, A. Gili, O. Görke, U. Simon, K. Hou, G. Wozny, *Energy Fuels* 28 (2014) 877.
- [6] S. Dooley, M.P. Burke, M. Chaos, Y. Stein, F.L. Dryer, V.P. Zhukov, O. Finch, J.M. Simmie, H.J. Curran, *Int. J. Chem. Kinet.* 42 (2010) 527.
- [7] H. Schwarz, M. Geske, C. Franklin Goldsmith, R. Schlögl, R. Horn, *Combust. Flame* 161 (2014) 1688.
- [8] T.P. Tiemersma, M.J. Tuinier, F. Gallucci, J.A.M. Kuipers, M.V.S. Annaland, *Appl. Catal. A Gen.* 433–434 (2012) 96.
- [9] K. Takane, E. Iglesia, *J. Phys. Chem. C* 113 (2009) 10131.

- [10] J.S. Ahari, R. Ahmadi, H. Mikami, K. Inazu, S. Zarrinpashne, S. Suzuki, K. Aika, *Catal. Today* 145 (2009) 45.
- [11] Y. Nakisa, G.M.H. Reza, *J. Nat. Gas Chem.* 18 (2009) 39.
- [12] N. Razmi Farooji, A. Vatani, S. Mokhtari, *J. Nat. Gas Chem.* 19 (2010) 385.
- [13] M. Ghiasi, A. Malekzadeh, S. Hoseini, Y. Mortazavi, A. Khodadadi, A. Talebizadeh, *J. Nat. Gas Chem.* 20 (2011) 428.
- [14] P.K. Kundu, A.K. Ray, A. Elkamel, *Can. J. Chem. Eng.* 90 (2012) 1502.
- [15] Z. Taheri, N. Seyed-Matin, A.A. Safekordi, K. Nazari, S.Z. Pashne, *Appl. Catal. A Gen.* 354 (2009) 143.
- [16] N. Yaghobi, M.R.H. Ghoreishy, V. Eslamimanesh, *Asia-Pac. J. Chem. Eng.* 3 (2008) 202.
- [17] H.R. Godini, V. Fleischer, O. Görke, S. Jaso, R. Schomäcker, G. Wozny, *Chemie Ing. Tech.* 86 (2014) 1906.
- [18] A. Ekstrom, R. Regtop, S. Bhargava, *Appl. Catal.* 62 (1990) 253.
- [19] G. Lane, E. Wolf, *J. Catal.* 113 (1988) 144.
- [20] C.J. Tjatjopoulos, I.A. Vasalos, *Appl. Catal. A Gen.* 88 (1992) 213.
- [21] M.S. Palmer, M. Neurock, M.M. Olken, *J. Am. Chem. Soc.* 124 (2002) 8452.
- [22] V.J.V.J. Ferreira, P. Tavares, J.L.J.L. Figueiredo, J.L. Faria, *Catal. Commun.* 42 (2013) 50.
- [23] Q.J. Yan, Y. Wang, Y.S. Jin, Y. Chen, *Catal. Lett.* 13 (1992) 221.
- [24] M.R. Lee, M.J. Park, W. Jeon, J.W. Choi, Y.W. Suh, D.J. Suh, *Fuel Process. Technol.* 96 (2012) 175.
- [25] J. Sun, J. Thybaut, G.B. Marin, *Catal. Today* 137 (2008) 90.
- [26] B. Beck, V. Fleischer, S. Arndt, M.G. Hevia, A. Urakawa, P. Hugo, R. Schomäcker, *Catal. Today* 228 (2014) 212.
- [27] L. Shu-Ben, *Chinese J. Chem.* 19 (2001) 16.
- [28] M. Sohrabi, B. Dabir, A. Eskandari, *J. Chem. Technol. Biotechnol.* 67 (1996) 15.
- [29] J.L. Falconer, J.A. Schwarz, *Catal. Rev. – Sci. Eng.* 25 (1983) 141.
- [30] J.W. Niemantsverdriet, in: *Spectrosc. Catal. An. Intro.*, 3rd ed., Wiley-VCH Verlag GmbH & Co. KGaA, Weinheim, 2007, pp. 11–31.
- [31] S.J. Blanksby, G.B. Ellison, *Acc. Chem. Res.* 36 (2003) 255.
- [32] J. Mccarty, H. Wise, *J. Catal.* 57 (1979) 406.
- [33] P.A. Redhead, *Vacuum* 12 (1962) 203.
- [34] U. Simon, O. Görke, A. Berthold, S. Arndt, R. Schomäcker, H. Schubert, *Chem. Eng. J.* 168 (2011) 1352.
- [35] S.M.K. Shahri, S.M. Alavi, *J. Nat. Gas Chem.* 18 (2009) 25.
- [36] I.E. Wachs, *Catal. Today* 27 (1996) 437.
- [37] N. Anacleto, O. Ostrovski, S. Ganguly, *ISIJ Int.* 44 (2004) 1615.
- [38] E.R. Stobbe, B.A. de Boer, J.W. Geus, *Catal. Today* 47 (1999) 161.
- [39] Z. Jiang, H. Gong, S. Li, *Stud. Surf. Sci. Catal.* 112 (1997) 481.
- [40] S. Sadjadi, S. Jašo, H.R. Godini, S. Arndt, M. Wollgarten, R. Blume, O. Görke, R. Schomäcker, G. Wozny, U. Simon, *Catal. Sci. Technol.* 5 (2015) 942.
- [41] R. Radhakrishnan, S.T. Oyama, J.G. Chen, K. Asakura, *J. Phys. Chem. B* 105 (2001) 4245.
- [42] H.C. Genuino, S. Dharmarathna, E.C. Njagi, M.C. Mei, S.L. Suib, *J. Phys. Chem. C* 116 (2012) 12066.
- [43] S. Arndt, T. Otremba, U. Simon, M. Yildiz, H. Schubert, R. Schomäcker, *Appl. Catal. A Gen.* 53 (2012) 425–426.
- [44] X. Fang, S. Li, J. Gu, D. Yang, *J. Mol. Catal.* (1992) 255.
- [45] Y. Liu, R. Hou, X. Liu, J. Xue, S. Li, *Stud. Surf. Sci. Catal.* 119 (1998) 307.
- [46] Z.-C. Jiang, L.-B. Feng, H. Gong, H.-L. Wang, *Methane and Alkane Conversion Chemistry*, Springer, US, New York, 1995.
- [47] M.R. Lee, M.-J. Park, W. Jeon, J.-W. Choi, Y.-W. Suh, D.J. Suh, *Fuel Process. Technol.* 96 (2012) 175.
- [48] K. Tomishige, X. Li, K. Fujimoto, *Phys. Chem. Chem. Phys.* 1 (1999) 3039.
- [49] G.E. Keller, M.M. Bhasin, *J. Catal.* 73 (1982) 9.
- [50] D.J. Driscoll, J.H. Lunsford, *J. Phys. Chem.* 89 (1985) 4415.
- [51] H. Zimmermann, R. Walzl, *Ullmann's Encycl. Ind. Chem.* 13 (2012) 547.
- [52] S.H. Khodamorad, D. Haghshenas Fatmehsari, H. Rezaie, A. Sadeghipour, *Eng. Fail. Anal.* 21 (2012) 1.
- [53] A.J. Nagy, G. Mestl, R. Schlögl, *J. Catal.* 188 (1999) 58.
- [54] R.B. Grant, R.M. Lambert, *J. Catal.* 92 (1985) 364.
- [55] B.J. McBride, S. Gordon, M.A. Reno, *NASA Rep. TM-4513*, 1993.
- [56] Z. Stansch, L. Mleczko, M. Baerns, *Ind. Eng. Chem. Res.* 36 (1997) 2568.
- [57] E. Morales, J. Lunsford, *J. Catal.* 5 (1989).
- [58] V.N. Snytnikov, T.I. Mishchenko, V.N. Snytnikov, S.E. Malykhin, V.I. Avdeev, V. N. Parmon, *Res. Chem. Intermed.* 38 (2012) 1133.
- [59] S. Wauters, G.B. Marin, *Ind. Eng. Chem. Res.* 41 (2002) 2379.
- [60] M. Daneshpayeh, A. Khodadadi, N. Mostoufi, Y. Mortazavi, R. Sotudeh-Gharebagh, A. Talebizadeh, *Fuel Process. Technol.* 90 (2009) 403.
- [61] M. Daneshpayeh, N. Mostoufi, A. Khodadadi, R. Sotudeh-gharebagh, *Energy Fuels* 23 (2009) 3745.
- [62] S. Pak, P. Qiu, J.H. Lunsford, *J. Catal.* 230 (1998) 222.
- [63] C.A. Jones, J.J. Leonard, J.A. Sofranko, *J. Catal.* 103 (1987) 311.
- [64] J.A. Sofranko, J.J. Leonard, C.A. Jones, *J. Catal.* 103 (1987) 302.
- [65] C.A. Jones, J.J. Leonard, J.A. Sofranko, *Energy Fuels* 1 (1987) 12.
- [66] M.Y. Sinev, *Russ. J. Phys. Chem. B* 1 (2007) 412.
- [67] R. Burch, S.C. Tsang, C. Mirodatos, J.G. Sanchez, *Catal. Lett.* 7 (1990) 423.
- [68] V. Salehoun, A. Khodadadi, Y. Mortazavi, A. Talebizadeh, *Chem. Eng. Sci.* 63 (2008) 4910.
- [69] A. Nagy, G. Mestl, T. Uhle, G. Weinberg, R. Schi, *J. Catal.* 179 (1998) 548.
- [70] P.A. Kilty, W.M.H. Sachtler, *Catal. Rev.* 10 (1974) 1.
- [71] E. Jerndal, T. Mattisson, A. Lyngfelt, *Chem. Eng. Res. Des.* 84 (2006) 795.
- [72] D. Creaser, B. Andersson, R.R. Hudgins, P.L. Silveston, *Chem. Eng. Sci.* 54 (1999) 4437.
- [73] A. Adesina, H. Budman, J. Brandner, G. Bunimovich, W. Epling, J. Hanika, K. Hashimoto, P. Haure, R. Hudgins, M. Kawase, C.-Y. Li, Y. Matros, G. Meira, M. Petkovska, M. Pritzker, A. Renken, A. Rodrigues, H. Sapoundjiev, J. Scharer, A. Seidel-Morgenstern, P. Silveston, *Periodic Operation of Reactors*, 2005.

# Investigation of the surface reaction network of the oxidative coupling of methane over $\text{Na}_2\text{WO}_4/\text{Mn}/\text{SiO}_2$ catalyst by temperature programmed and dynamic experiments - Supporting information

---

## 1. Experimental

### 1.1. Setup for TPSR and Dynamic experiments

The setup for dynamic experiments is illustrated in Figure 1. Different gases can be transported by mass flow controllers (MFC). In front of each MFC a switching valve (SV) was installed. The connection pipe between these valves and the reactor entrance has a length of 2 m to handle pressure fluctuation by switching the two way valves. All connections were tested by leakage spray to test for micro gas leakages. That was verified by mass spectroscopy to ensure that even no traces of gas phase oxygen by air leakage contribute to dynamic experiments. The methane MFC has two inlets, which can be selected by a three way valve. That allows the dose of ethane and ethylene. All MFC's were calibrated by an external flow meter (Gilian, Gilibrator-2 Calibrator) considering the different gases. A detailed analysis about the furnace temperature profile is reported in the next section. Finally the outlet of the reactor was connected to a quadrupole mass spectrometer (IPI QMS, GAM 200).

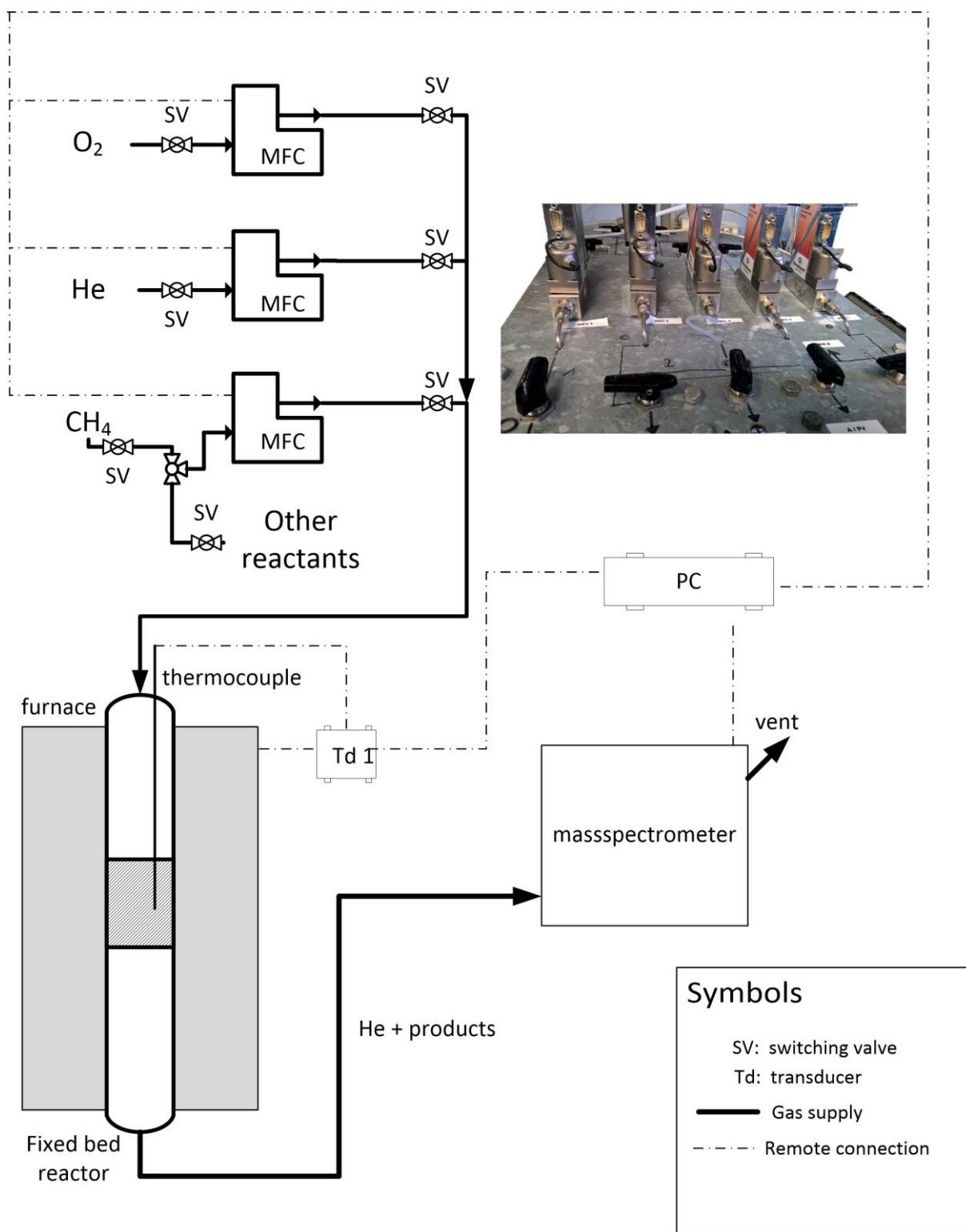


Figure 1 - Construction scheme of the dynamic setup

## 1.2.Reactor and Furnace

The quartz made reactor is presented in Figure 2. The type K thermocouple is placed in a quartz channel. The tip position of that channel is inside of the catalyst bed. That position was used for temperature control. The catalyst material is placed on a quartz frit, which is in the isothermal zone of the reactor.

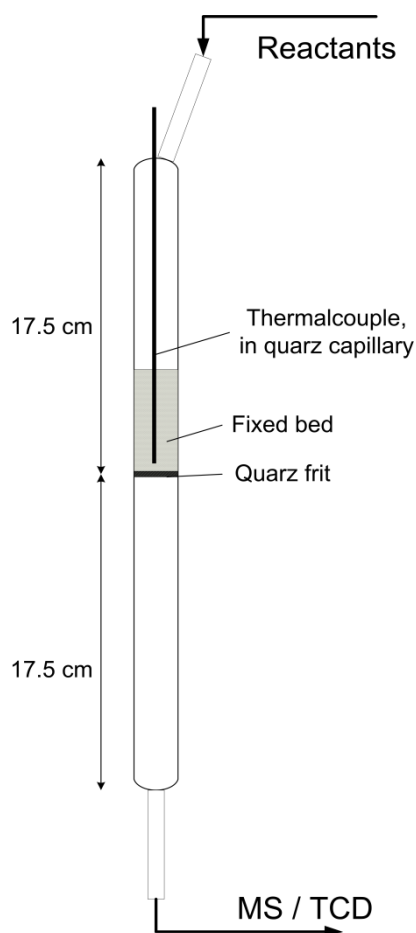


Figure 2- Detailed scheme of the fixed bed reactor ( $d_{in} = 9 \text{ mm}$ ,  $d_{capillary,thermocouple} = 4 \text{ mm}$ ).

A series of axial temperature profiles of the heated parts of the reactor were measured by an additional, movable type K thermocouple. The reactor was placed in the furnace and heated up to a fixed temperature. After reaching that temperature a movable thermocouple was introduced at the inlet or the outlet of the reactor to measure the local temperature on several positions. At this time, no gas was sent through the reactor. The results are presented in Figure 3. The position of the catalyst bed (2 g  $\text{Na}_2\text{WO}_4/\text{Mn}/\text{SiO}_2$ ) is also presented. It can be seen, that the catalyst bed is clearly in the axial isothermal zone of the reactor. The radial temperature profile was neglected because of symmetric geometry of the reactor and temperature control inside of the catalyst bed. During dynamic experiments no temperature increase was observed. Calculation of the adiabatic temperature increase results in 33 K, assuming the total oxidation of methane in gas phase according to equation (1). The concentration for oxygen was set to the presented value in the manuscript, considering the fictive free space of the catalyst material as reaction volume.



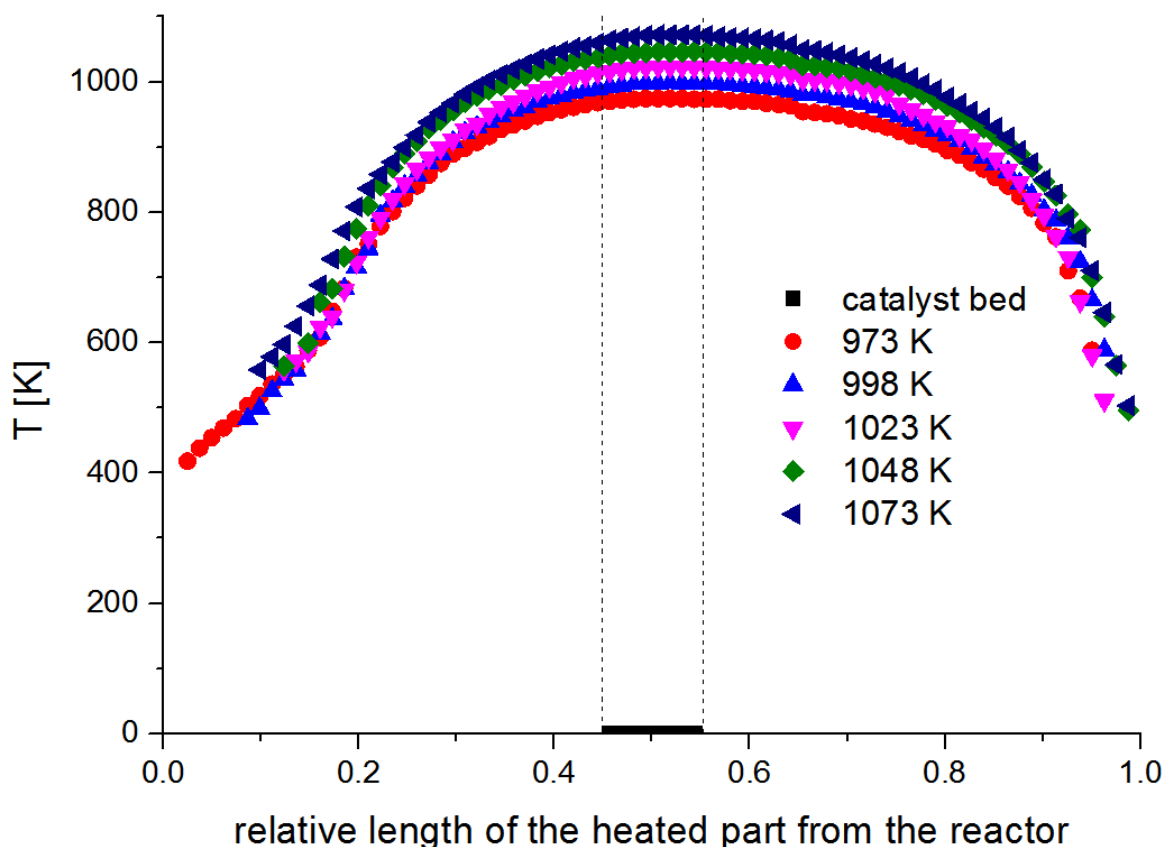


Figure 3 – Axial temperature profile of the heated reactor section at constant set temperature.

## 2. Catalyst characterization

### 2.1.BET

The nitrogen adsorption apparatus and sample preparation was described elsewhere. [1] Selected results are presented in Table 1. The enumeration of some experiments follows the experimental plan in Table 2. After the oxidation pretreatment procedure the catalyst material shows only small shrinkage of the specific surface area (SSA). After performing dynamic experiments only small deviation of the SSA is observed. That is a common effect for that material. [2,3]

Table 1 - Results of nitrogen adsorption experiment of pretreated and spend catalysts in dynamic experiments

Experiment	Initial specific surface area (m <sup>2</sup> /g)	After oxidation pretreatment of the catalyst material (m <sup>2</sup> /g)	After dynamic experiments (m <sup>2</sup> /g)
TPR 1	1.86	X	1.68
TPR 2	1.86	1.72	1.70
TPD 1	1.86	X	1.70
TPD 2	1.86	1.75	1.68
TPSR (CH <sub>4</sub> 3 K/min)	1.86	1.69	1.76
TPSR (C <sub>2</sub> H <sub>4</sub> 3K/min)	1.86	1.80	1.68
Dynamic experiment (purge time 10 min)	1.86	1.77	1.70
Dynamic experiment	1.86	1.72	1.70

(purge time 300 min)			
Dynamic experiment	1.86	1.74	1.69
(purge time 5 sec)			

## 2.2. X-ray diffraction analysis

The experimental details were described elsewhere. [1] The xray diffraction patterns of different treated  $\text{Na}_2\text{WO}_4/\text{Mn}/\text{SiO}_2$  catalysts are presented in Figure 4. The fresh catalyst shows diffraction patterns for Cristobalite, Tridymite,  $\text{Na}_2\text{WO}_4$  and  $\text{Mn}_2\text{O}_3$ . After the mentioned peroxidation method the XRD pattern reveal additional peaks for quartz and very weak signals for  $\text{MnWO}_4$ . No other phases were identified for the catalyst material after dynamic experiments. These results are in good agreement with other groups. [2–6]

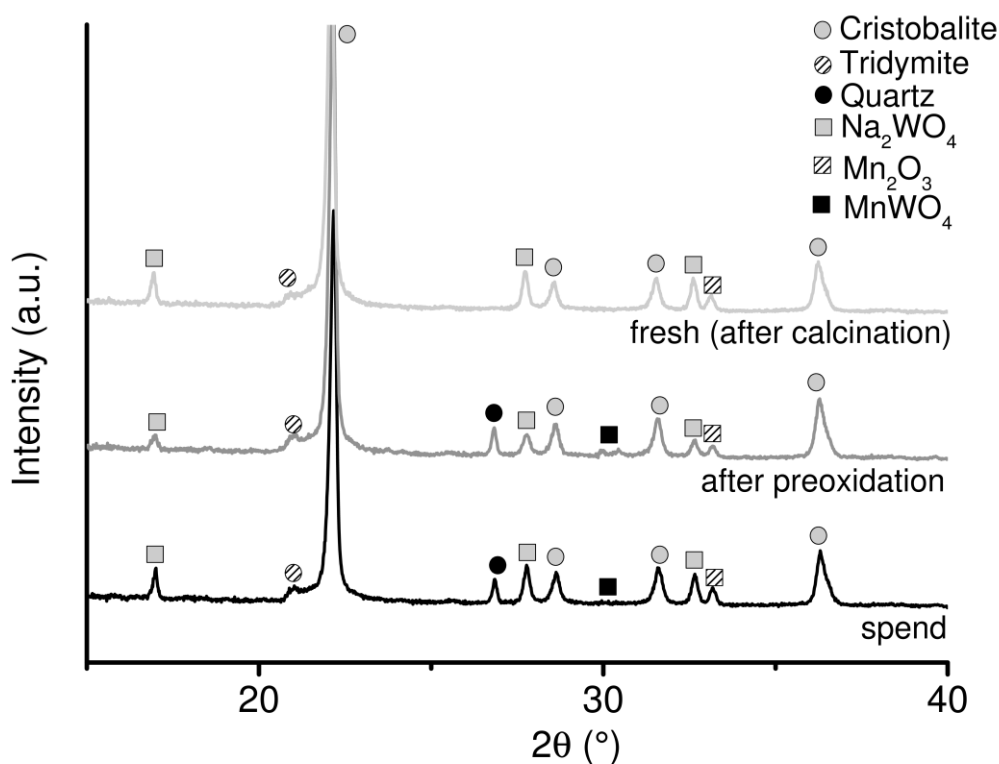


Figure 4 - XRD patterns of fresh, pretreated and spend  $\text{Na}_2\text{WO}_4/\text{Mn}/\text{SiO}_2$  catalysts

### 3. Experimental plan

An experimental plan of all experiments is listed in Table 2.

Table 2- Experimental plan of all temperature ramp and dynamic experiments

Experiment	Catalyst pretreatment	Catalyst Amount (g)	Temp. ramp (K/min)	Max. Temp. (K)	Reduction Feed composition	Total time of reduction Feed (min)
TPR 1	Purge He, no heating	0.06	2	1093	N <sub>2</sub> :H <sub>2</sub> (9:1, 60 sccm/min)	400
TPR 2	Oxidation 10 K/min – 1023 K for 1 h, Purge He	0.06	2	1093	N <sub>2</sub> :H <sub>2</sub> (9:1, 60 sccm/min)	400
O2 TPD	Purge He, no heating	1	5	1093	He (99.999 %, 20 sccm/min)	160
O2 TPD	Oxidation 10 K/min – 1023 K for 1 h, Purge He	1	5	1093	He (99.999 %, 20 sccm/min)	160
TPSR – CH4	Oxidation 10 K/min – 1023 K for 1 h, Purge He	1	1	1073	30 sccm/min methane (99.99 %)	800
TPSR – CH4	Oxidation 10 K/min – 1023 K for 1 h, Purge He	1	2	1073	30 sccm/min methane (99.99 %)	400
TPSR – CH4	Oxidation 10 K/min – 1023 K for 1 h, Purge He	1	3	1073	30 sccm/min methane (99.99 %)	265
TPSR – CH4	Oxidation 10 K/min – 1023 K for 1 h, Purge He	1	4	1073	30 sccm/min methane (99.99 %)	200
TPSR – CH4	Oxidation 10 K/min – 1023 K for 1 h, Purge He	1	5	1073	30 sccm/min methane (99.99 %)	160
TPSR – C2H6	Oxidation 10 K/min – 1023 K for 1 h, Purge He	1	1	1073	He:C <sub>2</sub> H <sub>6</sub> (95:5, 30 sccm/min, 99.98 % C <sub>2</sub> H <sub>6</sub> )	800
TPSR – C2H6	Oxidation 10 K/min – 1023 K for 1 h, Purge He	1	3	1073	He:C <sub>2</sub> H <sub>6</sub> (95:5, 30 sccm/min, 99.98 % C <sub>2</sub> H <sub>6</sub> )	265
TPSR – C2H6	Oxidation 10 K/min – 1023 K	1	5	1073	He:C <sub>2</sub> H <sub>6</sub> (95:5, 30 sccm/min, 99.98 %)	160

	for 1 h, Purge He				C <sub>2</sub> H <sub>6</sub> )	
<b>TPSR – C<sub>2</sub>H<sub>4</sub></b>	Oxidation 10 K/min – 1023 K for 1 h, Purge He	1	1	1073	He:C <sub>2</sub> H <sub>4</sub> (95:5, 30 sccm/min, 99.98 % C <sub>2</sub> H <sub>4</sub> )	800
<b>TPSR – C<sub>2</sub>H<sub>4</sub></b>	Oxidation 10 K/min – 1023 K for 1 h, Purge He	1	3	1073	He:C <sub>2</sub> H <sub>4</sub> (95:5, 30 sccm/min, 99.98 % C <sub>2</sub> H <sub>4</sub> )	265
<b>TPSR – C<sub>2</sub>H<sub>4</sub></b>	Oxidation 10 K/min – 1023 K for 1 h, Purge He	1	5	1073	He:C <sub>2</sub> H <sub>4</sub> (95:5, 30 sccm/min, 99.98 % C <sub>2</sub> H <sub>4</sub> )	160
<b>Dynamic Long purge time</b>	Oxidation 1023 K for 10 min, He purge 10 min	1	-	1023	20 sccm/min methane (99.99 %)	10
<b>Dynamic Long purge time</b>	Oxidation 1023 K for 10 min, He purge 180 min	1	-	1023	20 sccm/min methane (99.99 %)	10
<b>Dynamic Long purge time</b>	Oxidation 1023 K for 10 min, He purge 300 min	1	-	1023	20 sccm/min methane (99.99 %)	10
<b>Dynamic Short purge time</b>	Oxidation 1023 K for 10 min, He purge 300 s	1	-	1023	30 sccm/min methane (99.99 %)	10
<b>Dynamic Short purge time</b>	Oxidation 1023 K for 10 min, He purge 270 s	1	-	1023	30 sccm/min methane (99.99 %)	10
<b>Dynamic Short purge time</b>	Oxidation 1023 K for 10 min, He purge 230 s	1	-	1023	30 sccm/min methane (99.99 %)	10
<b>Dynamic Short purge time</b>	Oxidation 1023 K for 10 min, He purge 160 s	1	-	1023	30 sccm/min methane (99.99 %)	10
<b>Dynamic Short purge time</b>	Oxidation 1023 K for 10 min, He purge 100 s	1	-	1023	30 sccm/min methane (99.99 %)	10
<b>Dynamic Short purge time</b>	Oxidation 1023 K for 10 min, He purge 60 s	1	-	1023	30 sccm/min methane (99.99 %)	10
<b>Dynamic Short purge time</b>	Oxidation 1023 K for 10 min, He purge 30 s	1	-	1023	30 sccm/min methane (99.99 %)	10
<b>Dynamic Short purge time</b>	Oxidation 1023 K for 10 min, He purge 15 s	1	-	1023	30 sccm/min methane (99.99 %)	10
<b>Dynamic Partial pressure variation</b>	Oxidation 1023 K for 10 min, He purge 300 s	1	-	1023	30 sccm/min methane (99.99 %)	10
<b>Dynamic</b>	Oxidation 1023	1	-	1023	15 sccm/min methane	10

<b>Partial pressure variation</b>	K for 10 min, He purge 300 s				(99.99 %) + 15 sccm/min He (99.999 %)	
<b>Dynamic Partial pressure variation</b>	Oxidation 1023 K for 10 min, He purge 300 s	1	-	1023	10 sccm/min methane (99.99 %) + 20 sccm/min He (99.999 %)	10

## 4. Simulation of TPSR experiments

### 4.1. Modell and conditions

For TPSR experiments we assumed a large difference between methane feed concentration and the stored oxygen amount on the catalyst surface. That type of in-stationary process was modeled as batch-type reactor system. Furthermore the adsorption and desorption of educts and products do not contribute to the reaction progress, because the selective or unselective activation of methane is the rate limiting step. We considered different scenarios of one ( $O^*$ ) or two ( $O_\alpha^*$ ,  $O_\beta^*$ ) different oxygen species on the catalyst surface. The relative, initial concentration of methane was set to 0.999 and for  $O^*$  to 0.001 in the case of one oxygen species. In the case of two different oxygen species the relative methane concentration was set to 0.998, for  $O_\alpha^* = 0.001$  and  $O_\beta^* = 0.001$ . Furthermore it is possible that methane is converted by a parallel reaction to ethane and CO or due to a consecutive reaction, where ethane is an intermediate. The corresponding balances for each mechanism are presented in Table 3 as hypothetical scenario. Initial reactant A simulates methane, while B stands for ethane and C for CO. The rate constant for each reaction was derived by equation (2).

In all cases the pre exponential factor was set to  $10^9$  l/(mole·min). In literature it is assumed that methane activation is the rate limiting step and deep oxidation reactions are favored. That was considered by two different activation energy barriers ( $E_{A1} > E_{A2}$ ). Because of big differences for these parameters in several kinetic models we assumed  $E_{A1} = 150$  kJ/mole and  $E_{A2} = 100$  kJ/mole. [7–11] Please note, that such a model is only valid for fundamental demonstration aspects of heating rate variation experiments!

$$k_i = k_{oo,i} \cdot \exp\left(-\frac{E_{A,i}}{R \cdot (T_{ini} + \beta \cdot t)}\right) \quad (2)$$

$\beta$  = heating rate (K/min),  $t$  = simulation time (min),  $T_{ini} = 298$  K

Table 3 - Mass balances for different reaction mechanism in simulated temperature programmed experiments A – CH<sub>4</sub> B – C<sub>2</sub>H<sub>6</sub>, C - CO

<p><b>Parallel reaction – 1 oxygen species</b></p> <p>1. <math>A + O^* \rightarrow B + H_2O</math></p> <p>2. <math>A + O^* \rightarrow C + 2 H_2O</math></p>	<p><b>Consecutive reaction – 1 oxygen species</b></p> <p>1. <math>A + O^* \rightarrow B + H_2O</math></p> <p>2. <math>B + O^* \rightarrow C + H_2O</math></p>
$\frac{dc_A}{dt} = -k_1 \cdot c_A \cdot c_{O^*}^* - k_2 \cdot c_A \cdot c_{O^*}^*$ $\frac{dc_{O^*}}{dt} = -k_1 \cdot c_A \cdot c_{O^*}^* - k_2 \cdot c_A \cdot c_{O^*}^*$ $\frac{dc_B}{dt} = k_1 \cdot c_A \cdot c_{O^*}^*$ $\frac{dc_C}{dt} = k_2 \cdot c_A \cdot c_{O^*}^*$	$\frac{dc_A}{dt} = -k_1 \cdot c_A \cdot c_{O^*}^*$ $\frac{dc_{O^*}}{dt} = -k_1 \cdot c_A \cdot c_{O^*}^* - k_2 \cdot c_B \cdot c_{O^*}^*$ $\frac{dc_B}{dt} = k_1 \cdot c_A \cdot c_{O^*}^* - k_2 \cdot c_B \cdot c_{O^*}^*$ $\frac{dc_C}{dt} = k_2 \cdot c_B \cdot c_{O^*}^*$
<p><b>Parallel reaction – 2 oxygen species</b></p> <p>1. <math>A + O_{\alpha}^* \rightarrow B + H_2O</math></p> <p>2. <math>A + O_{\beta}^* \rightarrow C + 2 H_2O</math></p>	<p><b>Consecutive reaction – 2 oxygen species</b></p> <p>1. <math>A + O_{\alpha}^* \rightarrow B + H_2O</math></p> <p>2. <math>B + O_{\beta}^* \rightarrow C + H_2O</math></p>
$\frac{dc_A}{dt} = -k_1 \cdot c_A \cdot c_{O_{\alpha}}^* - k_2 \cdot c_A \cdot c_{O_{\beta}}^*$ $\frac{dc_{O_{\alpha}^*}}{dt} = -k_1 \cdot c_A \cdot c_{O_{\alpha}}^*$ $\frac{dc_{O_{\beta}^*}}{dt} = -k_2 \cdot c_A \cdot c_{O_{\beta}}^*$ $\frac{dc_B}{dt} = k_1 \cdot c_A \cdot c_{O_{\alpha}}^*$ $\frac{dc_C}{dt} = k_2 \cdot c_A \cdot c_{O_{\beta}}^*$	$\frac{dc_A}{dt} = -k_1 \cdot c_A \cdot c_{O_{\alpha}}^*$ $\frac{dc_{O_{\alpha}^*}}{dt} = -k_1 \cdot c_A \cdot c_{O_{\alpha}}^*$ $\frac{dc_{O_{\beta}^*}}{dt} = -k_2 \cdot c_B \cdot c_{O_{\beta}}^*$ $\frac{dc_B}{dt} = k_1 \cdot c_A \cdot c_{O_{\alpha}}^* - k_2 \cdot c_B \cdot c_{O_{\beta}}^*$ $\frac{dc_C}{dt} = k_2 \cdot c_B \cdot c_{O_{\beta}}^*$

## 4.2. Results and Discussion

The simulation results for different kinetic TPSR situation is presented in Figure 5. In all cases a higher temperature ramp shifts product formation signals to higher temperatures. In Figure 5-A a parallel reaction for selective (product B) and unselective (product C) methane activation on the same oxygen species O<sub>α</sub> is presented. Formation of product C is preferred at lower temperatures and followed by formation of product B. A hypothetical, consecutive reaction for selective methane activation and unselective ethane conversion is shown in Figure 5-B. Product B is converted immediately to product C, which leads consequently to no shift of peak amplitudes. Another situation (Figure 5-C) is found for a parallel reaction of reactant A, activated by two different oxygen species O<sub>α</sub> and O<sub>β</sub> on the catalyst surface. It can be seen that both reactions run independently from each other. Therefore peak formation and amplitude shift depend only on activation energy. Another possible situation for methane conversion is presented in Figure 5-D. Reactant A is converted to product B by O<sub>α</sub> which is followed by an unselective activation by O<sub>β</sub> forming product C. Therefore product B is formed and converted to product C at higher temperatures.

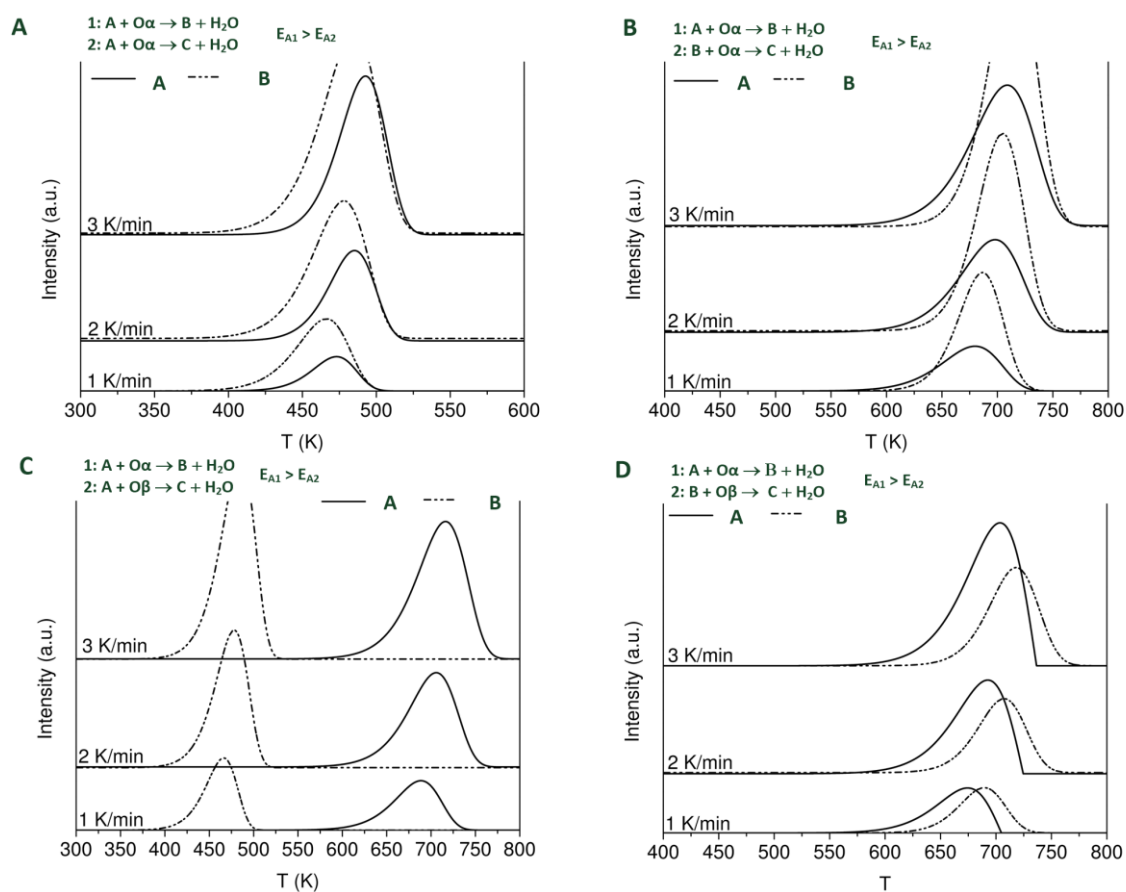


Figure 5 - Simulation results of TPSR experiments

## 5. References

- [1] M. Yildiz, U. Simon, T. Otremba, Y. Aksu, K. Kailasam, a. Thomas, R. Schomäcker, S. Arndt, *Catal. Today* 228 (2014) 5.
- [2] U. Simon, O. Görke, A. Berthold, S. Arndt, R. Schomäcker, H. Schubert, *Chem. Eng. J.* 168 (2011) 1352.
- [3] M. Yildiz, Y. Aksu, U. Simon, K. Kailasam, O. Goerke, F. Rosowski, R. Schomäcker, A. Thomas, S. Arndt, *Chem. Commun.* 50 (2014) 14440.
- [4] R. Koirala, R. Büchel, S.E. Pratsinis, A. Baiker, *Appl. Catal. A Gen.* 484 (2014) 97.
- [5] A. Malekzadeh, A.K. Dalai, A. Khodadadi, Y. Mortazavi, *Catal. Commun.* 9 (2008) 960.
- [6] S. Mahmoodi, M.R. Ehsani, S.M. Ghoreishi, *J. Ind. Eng. Chem.* 16 (2010) 923.
- [7] M.R. Lee, M.-J. Park, W. Jeon, J.-W. Choi, Y.-W. Suh, D.J. Suh, *Fuel Process. Technol.* 96 (2012) 175.
- [8] S.M.K. Shahri, S.M. Alavi, *J. Nat. Gas Chem.* 18 (2009) 25.
- [9] R. Ghose, H.T. Hwang, A. Varma, *Appl. Catal. A Gen.* 452 (2013) 147.
- [10] M. Daneshpayeh, N. Mostoufi, A. Khodadadi, R. Sotudeh-gharebagh, *Energy & Fuels* 23 (2009) 3745.

[11] N. Razmi Farooji, A. Vatani, S. Mokhtari, J. Nat. Gas Chem. 19 (2010) 385.

# Paper 2





# Chemical looping as reactor concept for the oxidative coupling of methane over a $\text{Na}_2\text{WO}_4/\text{Mn}/\text{SiO}_2$ catalyst



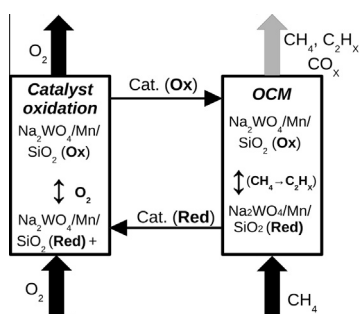
Vinzenz Fleischer, Patrick Littlewood, Samira Parishan, Reinhard Schomäcker\*

Technische Universität Berlin, Institut für Chemie, Straße des 17. Juni 124, 10623 Berlin, Germany

## HIGHLIGHTS

- Simulated chemical looping experiments were carried out on  $\text{Na}_2\text{WO}_4/\text{Mn}/\text{SiO}_2$  methane.
- The absence of gas phase oxygen results in high C2 selectivities (>80%) at moderate methane conversions (<30%).
- High methane conversion (80%) is also reachable, without the risk of explosive regime.

## GRAPHICAL ABSTRACT



## ARTICLE INFO

### Article history:

Received 2 May 2016

Received in revised form 25 July 2016

Accepted 26 July 2016

Available online 28 July 2016

### Keywords:

Oxidative coupling of methane  
 $\text{Na}_2\text{WO}_4/\text{Mn}/\text{SiO}_2$   
Chemical looping  
Simulated chemical looping

## ABSTRACT

In this work we present chemical looping and simulated chemical looping as a new reactor concept for the oxidative coupling of methane over  $\text{Na}_2\text{WO}_4/\text{Mn}/\text{SiO}_2$ . As a consequence of an alternating feed of oxygen and methane to the catalyst bed side reactions are avoided and the selectivity of the coupling reaction is greatly increased. By variation of methane pulse contact time and temperature a maximum yield of 0.25 is obtained. Although this does not exceed the often discussed yield limitation of OCM, it is achieved from a substantially lower amount of converted methane. A time on stream experiment were carried out at 775 and 800 °C for 150 min and showed stable performance and C2 yield.

© 2016 Elsevier B.V. All rights reserved.

## 1. Introduction

### 1.1. Oxidative coupling of methane

The oxidative coupling of methane (OCM) is an attractive alternative concept for ethylene production from methane based feedstocks, as natural gas or bio gas. Major issues for this reaction are high temperatures and therefore competing combustion reactions in the gas phase. Industrial application of OCM is currently not economically viable due to an apparent yield limitation of 0.25 achieved usually at around 0.6 conversion and 0.4 selectivity

[1–3]. Therefore a strong emphasis on reaction engineering is necessary to achieve higher selectivity and yields [4–6].

The basic principle of OCM is the activation of methane by a catalyst material which leads to methyl radical formation by C–H bond cleavage. The methyl radicals can couple to ethane in the gas phase, close to the catalyst surface [7]. A major problem of OCM is the parallel activation of methane and its coupling products in the gas phase. The mentioned components are oxidized to deep oxidation products, what causes a substantial reduction of the selectivity of the process. For improving the selectivity of this reaction a better control of the complex interaction of gas phase and surface reactions is necessary. An apparent yield limitation of 0.25 is an often observed phenomenon for several catalyst materials for OCM, which may be caused from these gas phase reactions.

\* Corresponding author.

E-mail address: [schomaecker@tu-berlin.de](mailto:schomaecker@tu-berlin.de) (R. Schomäcker).

The upper yield limit for C2 products in the absence of gas phase reactions is estimated to be 0.6 [8].

### 1.2. Chemical looping process and similar concepts

Chemical looping was applied as a reactor concept in the chemical industry for the first time around 100 years ago. This concept was a new route for the synthesis of hydrogen from methane and oxygen by iron particles (syngas chemical looping) [9]. The advantage of chemical looping is the separation of parallel reaction steps during steady state operation into consecutive reaction steps. Disadvantages of this process concept are high costs for capital investment, remote control and maintenance in comparison to

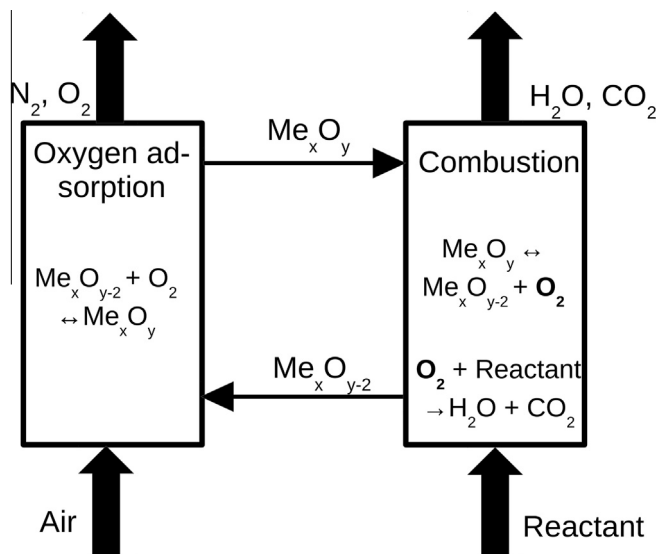


Fig. 1. Principal concept of a chemical-looping process for oxidation reactions.

classical steady state reactors. Today, some major research fields are devoted to the utilization of the concept, like chemical looping combustion (CLC) and syngas chemical looping (SLC) or chemical looping hydrogen system (CLH) [10].

A design layout for CLC is shown Fig. 1. Air flows over an oxygen-carrier material ( $\text{Me}_x\text{O}_{y-2}$ ), which contains less oxygen than  $\text{Me}_x\text{O}_y$ . On the outlet of the oxygen adsorption reactor, the air is (partially) depleted of oxygen. The carrier material, with high oxygen content, is transferred to the combustion reactor. The bound oxygen is released into the gas phase, which is achieved by temperature increase or pressure drop. A reactant can thus be oxidized by pure oxygen. The reduced oxygen-carrier is afterwards transferred back to the oxygen adsorption reactor. Such a process has the advantage that the stream of oxidation products contains no nitrogen from the air, which avoids a complex separation process or an air separation unit for the oxygen feed stream. Well-known materials for methane CLC and Chemical looping Reforming (CLR) are  $\text{CuO}$ ,  $\text{Mn}_2\text{O}_3$  or  $\text{Co}_3\text{O}_4$  [11–13]. These materials are often supported on silica to increase the specific surface area to optimize oxygen storage and release time. Both, CLC and CLR process operate in the temperature range of 800–1000 °C at ambient pressure.

### 1.3. Chemical looping concept for the oxidative coupling of methane

A basic concept for a simulated chemical looping process on the lab scale is presented in Fig. 2. It is based on the idea of dynamic experiments, where the feed is switched between different reactants. This is realized by two independently operated six-port pulse valves and a fixed bed reactor, which will be discussed below. The first step serves as the catalyst oxidation process, by dosing oxygen (Fig. 2 – 1), and the second step doses methane (Fig. 2 – 3) for the reduction of the catalyst and methane coupling reaction. The dosing of reactants is always followed by a purging process (Fig. 2 – 2 & 4), which is necessary to avoid mixing of oxygen and methane. A mixed pulse would directly lead to gas phase

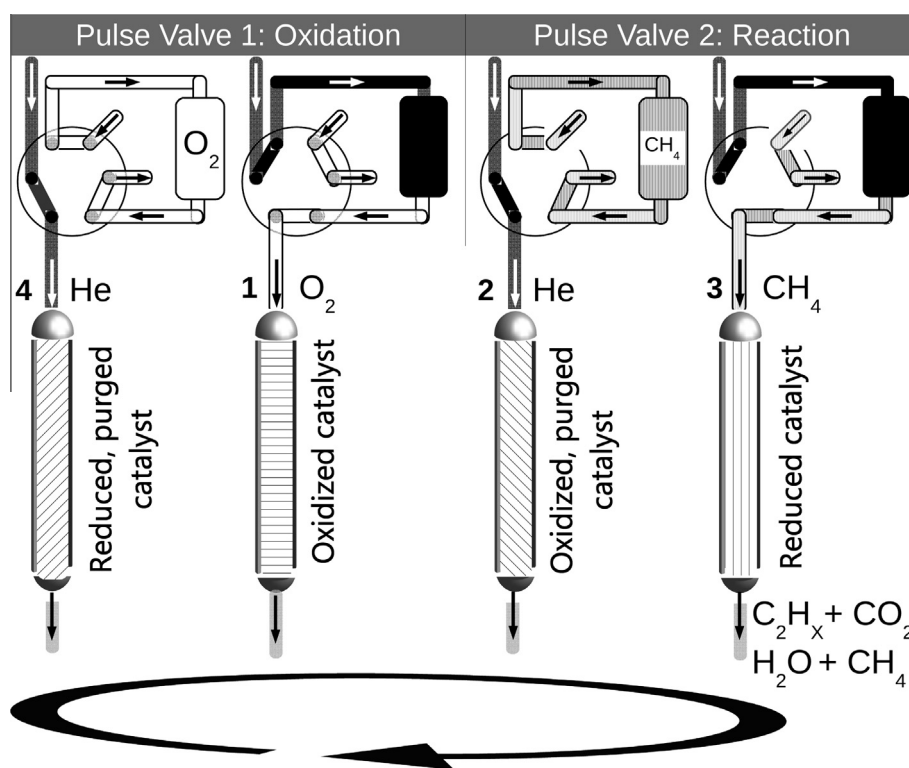


Fig. 2. Principal concept of chemical-looping in the oxidative coupling of methane by pulse valves.

combustion reactions. Beneficially, the purge gas is also the carrier gas for the reactant pulses, which allows dosing of well-defined amounts of oxygen and methane. A proper dosing strategy allows a continuous operation of this process.

The  $\text{Na}_2\text{WO}_4/\text{Mn}/\text{SiO}_2$  catalyst material was first introduced by Fang and coworkers and shows a stable catalytic activity for hundreds of hours [14]. Further it showed suitable stability and activity in dynamic experiments, similar to the chemical looping concept [15,16]. In this work we want to take the advantage to investigate the catalyst performance in yield boundary studies without any influences by gas phase combustion reactions. Furthermore this concept was tested in a repetitive continuous operation and compared to classical co-feed operation mode. This will support the investigation of the OCM surface reactions under process relevant conditions for the  $\text{Na}_2\text{WO}_4/\text{Mn}/\text{SiO}_2$  catalyst. It has to be noted, that the  $\text{Na}_2\text{WO}_4/\text{Mn}/\text{SiO}_2$  material fulfills two functionalities. On the one hand it serves as oxygen carrier material, according to the description before. Thus it will be oxidized to store oxygen, similar to the oxygen carrier materials in the CLC processes. On the other hand the material has also the role of a catalyst material. The stored oxygen is used in a dynamic operation to convert methane into C2 products by the OCM reaction. Other groups demonstrated that advanced reactor concepts for the OCM reaction showed improved C2 production performance. Kruglow and coworkers demonstrated the operation of a counter-current moving-bed chromatographic reactor. They separated the C2 products from unconverted reactants at low conversions and recycle those back [17]. They were able to reach 0.55 C2 yield. Godini and coworkers presented a membrane reactor with an optimized oxygen dosing strategy [18]. They fed oxygen by use of a membrane in small amounts to the catalyst fixed. Thus, gas phase reactions with gas phase oxygen were minimized.

## 2. Materials and methods

### 2.1. Setup design

The chemical looping concept was realized by two pneumatic six-port diaphragm valves (Vichi Valco DV22-2116). The concept of such a valve and its operation is shown in the [Supporting information](#).

A detailed flow chart of the complete setup is shown in [Fig. 3](#). The oxygen and methane supply for both pulse valves is realized by mass flow controllers (MFC, Bronkhorst), which are connected to the first inlet of the pulse valves (PV). It was chosen for purge gas, which is also controlled by a MFC. The pipe is split close to the pulse valves and connected to their second inlet, in order to supply both of them at the same time with carrier gas. Nitrogen supply (6 bar) for the pneumatic impulse is connected to a solenoid for each pulse valve. As mentioned before, the solenoids are connected to transducers (Td, Htronic 191030), which are connected to a PC for data acquisition. Pulse composition can be detected by a quadrupole mass-spectrometer (QMS, IPI GAM 200). Remote control software for the solenoids and the temperature control of the furnace was written in Visual Basic.

A scheme of the tubular fixed bed reactor is in the [Supporting information](#).

### 2.2. Catalyst preparation and catalytic tests

#### 2.2.1. Catalyst preparation and characterization

A detailed preparation and analysis of the  $\text{Na}_2\text{WO}_4/\text{Mn}/\text{SiO}_2$  catalyst is described elsewhere. The catalyst has a composition of 5 wt.%  $\text{Na}_2\text{WO}_4$  and 2 wt.% Mn(II) and a specific surface area of  $1.86 \text{ m}^2/\text{g}$  [19]. The catalyst particle size was 200–300  $\mu\text{m}$ .

#### 2.2.2. Simulated chemical looping experiments

All chemical looping experiments were performed between 700 and 800 °C and at ambient pressure. 2 g catalyst were placed into the isothermal zone of a fixed bed reactor, held by a quartz frit and heated up with 15 K/min under a flow of  $\text{He}:\text{O}_2$  (95:5, 30 nml/min). To start a series of experiments the reactor was first purged with He, since a constant signal was reached. The total feed flow rate was varied from 15 to 50 nml/min. Methane was dosed from a 1 ml storage loop. The residence time of the gas pulse in the catalyst bed depends strongly on the flow rate, which will be discussed later. After each methane pulse, the catalyst was re-oxidized for 5 min in a flow  $\text{He}:\text{O}_2$  (95:5, 30 nml/min) during yield study experiments, taking care for a complete reoxidation.

The pulses were detected by a quadrupole mass-spectrometer (QMS, IPI GAM 200). A small amount of the gas flow was sent through a capillary into the QMS high vacuum system, ionized by yttrium filaments and the signal was amplified and detected by a secondary electron multiplier (SEM). All compounds ( $Z = \text{CH}_4, \text{C}_2\text{H}_6, \text{C}_2\text{H}_4, \text{CO}, \text{CO}_2$  and  $\text{O}_2$ ) were calibrated with calibration gas bottles ( $Z: \text{He} = 5: 95 \pm 0.005\%$ , Deuste Steinger). The calibrated m/e ratios for all compounds are presented in the [Supplementary material](#). These one-point calibrations for each compound were repeated 15 times for a precise average value. The calibration was verified by utilization of calibration gas mixtures of ( $\text{CH}_4:\text{C}_2\text{H}_6:\text{C}_2\text{H}_4:\text{He}$ ) and ( $\text{CH}_4:\text{CO}:\text{CO}_2:\text{He}$ ) in the range from (5:5:5:85,  $\pm 0.005\%$ , Deuste Steinger) to (15:15:15:55,  $\pm 0.005\%$ , Deuste Steinger).

The measurement of  $\text{CH}_4, \text{C}_2\text{H}_6, \text{C}_2\text{H}_4, \text{CO}$  and  $\text{CO}_2$  by mass spectroscopy had an interval for each measurement of 5 s. Larger time scales for product detection allow a higher precision for the determination of individual compound concentrations, but has worse resolution for peak detection. Faster methods have a lower accuracy to distinguish ethane and ethene from each other. The number of detected data points for each pulse depends on the flow rate. Therefore the number of data points per detected peak differs from 8 to 34, which is an appropriate resolution for further analysis. The carbon balance for each pulse was between 0.88 (flow = 50 nml/min) and 0.95 (flow = 15 nml/min).

Repetitive continuous simulated chemical looping was carried out at 775 °C for 150 min (50  $\text{CH}_4$  pulses) and further on at 800 °C for another 150 min (50  $\text{CH}_4$  pulses) at 25 nml/min with 2 g catalyst. The experiment was started by an oxygen pulse followed by a time delayed methane pulse. The delay time between dosing of the individual reactants was chosen so that the overlap of methane and oxygen pulses was negligible (120 s). The volumes of the methane and oxygen pulses were set to 1 ml gas at 1 bar. That decision was made to reduce the oxidation time to the same length as the reaction time for the methane pulse.

#### 2.2.3. Steady state experiments

The steady state experiments were carried out in a fixed bed reactor. 250 mg of the catalyst material were placed in the isothermal zone of the reactor. A gas mixture of  $\text{CH}_4:\text{O}_2:\text{He}$  (3:1:4) was sent through the reactor at flow rates of 25 and 50 nml/min. This composition allows reduction of the gas phase activity and was chosen also on the mini plant scale in a fluidized bed reactor for a comparison of different reactor concepts [20]. The temperature was set to 800 °C. Detection was carried out by a QMS.

## 3. Results and discussion

### 3.1. Yield studies for simulated chemical looping

For a comparison of steady state and looping experiments performing OCM reactions, the characteristic contact time ( $t$ ) of

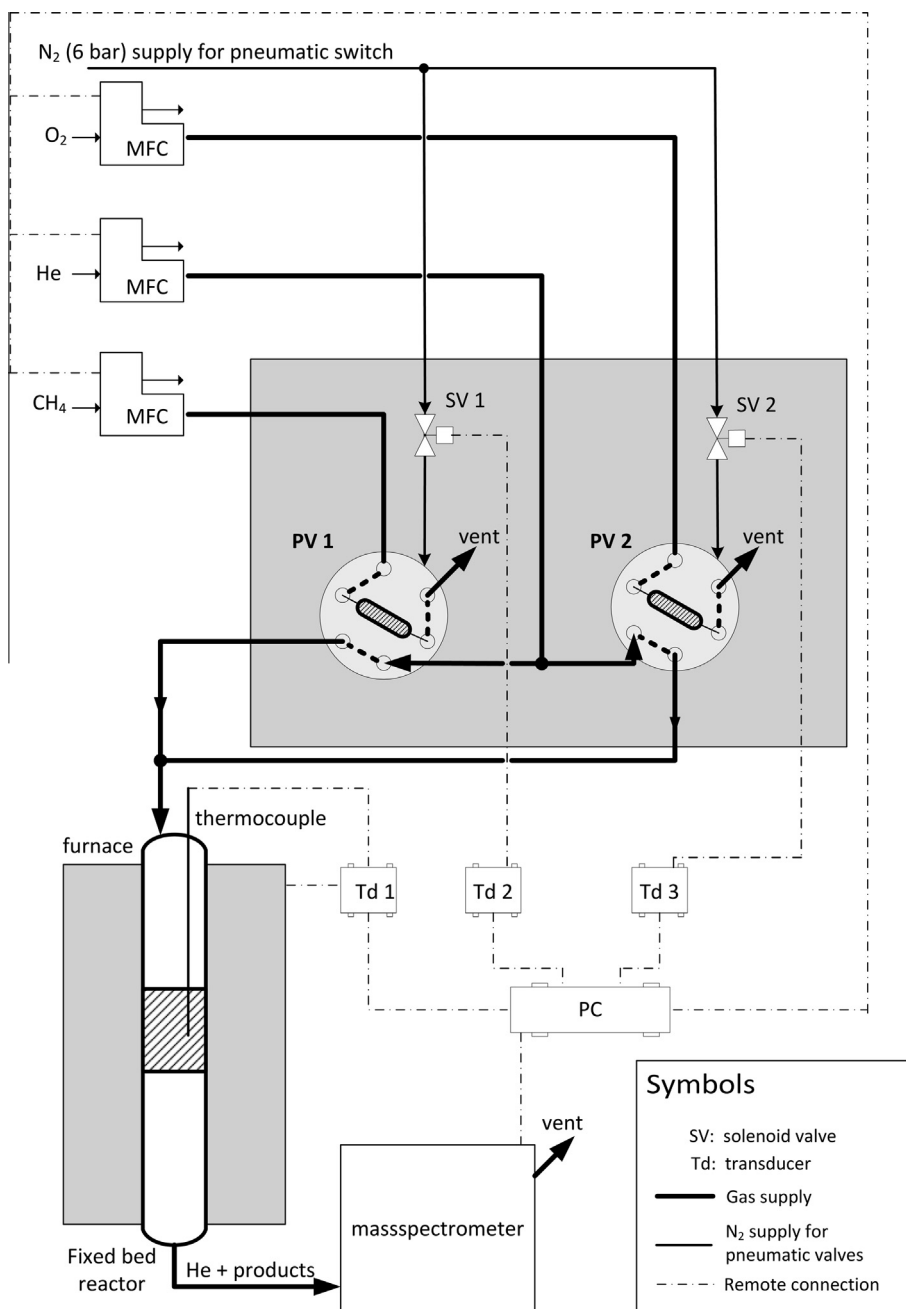


Fig. 3. Flow chart of the chemical looping setup.

each methane pulse was determined by Eq. (1). All pulses were integrated for a detailed carbon balance considering the mole number for each compound as calculated by Eq. (2).

$$t = m_{\text{cat}} \cdot \frac{A_{\text{spec}}}{V} \left[ g_{\text{cat}} \cdot \frac{\text{m}^2}{\text{g}} \cdot \frac{\text{s}}{\text{m}^3} = \frac{\text{s}}{\text{m}} \right]$$

$$m_{\text{cat}} = \text{amount of catalyst (g)}, \quad (1)$$

$A_{\text{spec}}$  = specific surface area of the catalyst ( $\text{m}^2/\text{g}$ ),  
 $\dot{V}$  = flow rate ( $\text{m}^3/\text{s}$ )

$$n_i = \frac{A_{i,\text{peak}}[\% \cdot \text{s}] \cdot \dot{V} \cdot p}{R \cdot T} \quad (2)$$

The carbon balance for each methane pulse was 0.88 in all experiments or better. During the oxidation treatment of the catalyst, after each methane pulse, no carbon oxides were detected.

This indicates that there is no carbon deposition on the catalyst surface. All values for conversion (Eq. (3)), selectivity (Eq. (4)) and yield (Eq. (5)) were calculated from the mole number of the detected compounds, derived from a carbon balance of the system.

$$X_{\text{CH}_4} = \frac{\text{CH}_{4,\text{in}} - \text{CH}_{4,\text{out}}}{\text{CH}_{4,\text{in}}} \quad (3)$$

$$S_{\text{C}_2} = \frac{2 \cdot \text{C}_2\text{H}_6 + 2 \cdot \text{C}_2\text{H}_4}{2 \cdot \text{C}_2\text{H}_6 + 2 \cdot \text{C}_2\text{H}_4 + \text{CO} + \text{CO}_2} \quad (4)$$

$$Y = X_{\text{CH}_4} \cdot S_{\text{C}_2} \quad (5)$$

The results of methane conversion, C2 selectivity and yield for flowrate and temperature variation are shown in Fig. 4A–C. The surfaces fitted to the data points are only supporting guidelines.

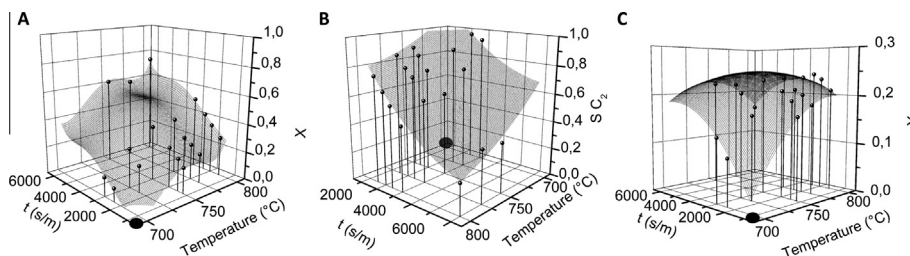


Fig. 4. Results of yield studies, 2 g catalyst, 15–50 nml/min, 700–800 °C, 1 ml CH<sub>4</sub>, A: conversion, B: C2 selectivity, C: C2 yield.

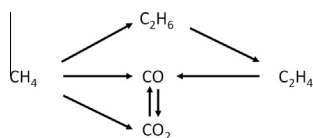


Fig. 5. Reaction scheme of the OCM [24–27].

Methane conversion varies from 0.15 to 0.8, while C2-selectivity is between 0.25 and 1. The highest observed yield was 0.25 at 0.6 C2 selectivity and 0.42 methane conversion. During the experiments CO is only observed at flow rates between 15 and 20 nml/min at temperatures between 775 and 800 °C. The predominant deep oxidation product is CO<sub>2</sub>.

A similar yield limitation was observed for this Na<sub>2</sub>WO<sub>4</sub>/Mn/SiO<sub>2</sub> catalyst in different other reactor systems, like fixed bed, micro-, fluidized-bed or membrane reactors [20–23]. The absence of gas phase oxygen during the methane pulse in chemical looping experiments allows exclusion of any gas phase deep oxidation reactions. We conclude that the still observed yield limitation is caused by the competition of consecutive surface reactions at this material. This can be explained by a recently proposed surface reaction network, which is shown in Fig. 5 [24–27]. We assume that the activation of methane is the rate determining step for the formation of ethane, while ethene formation and deep oxidation is much faster than this. In our yield studies we analyzed a wide range for the methane conversion and C2 selectivities. The results of this analysis showed a yield maximum of 0.25. The C2 selectivity is strongly controlled by ethene oxidation and methane direct oxidation as can be seen in the reaction network in Fig. 5. We assume that all reaction steps show first order behavior with respect to the hydrocarbon. Therefore all reaction rates are depending on the compound partial pressures and corresponding rate constants. Increasing the methane conversion increases the partial pressures of ethane and ethene, too. This has the consequence that the deep oxidation rate of ethene becomes much faster than the ethene formation rate. At lower methane conversions, the ethene partial pressure is still low. Therefore the formation of deep oxidation products is slow compared to the ethene formation rate.

As mentioned before, the direct oxidation of methane is also possible on the catalyst surface. Lunsford and coworkers found that the formation and coupling of methyl radicals leads to ethane formation [7]. According to their studies, the formation of deep oxidation products and methyl radicals involve two different oxygen species on the catalyst surface. On the one hand there is nucleophilic oxygen which forms carbon oxides. On the other hand there is electrophilic oxygen which leads to methyl radical formation. It has to be noted that these species also may interact with ethane and ethene. Especially the interactions with ethene may lead for both species to the formation of deep oxidation products [28]. These aspects imply that the oxygen species, which is stored on the catalyst surface, contribute to the yield limitation, because one selective route of methane activation competes with three unselective ones.

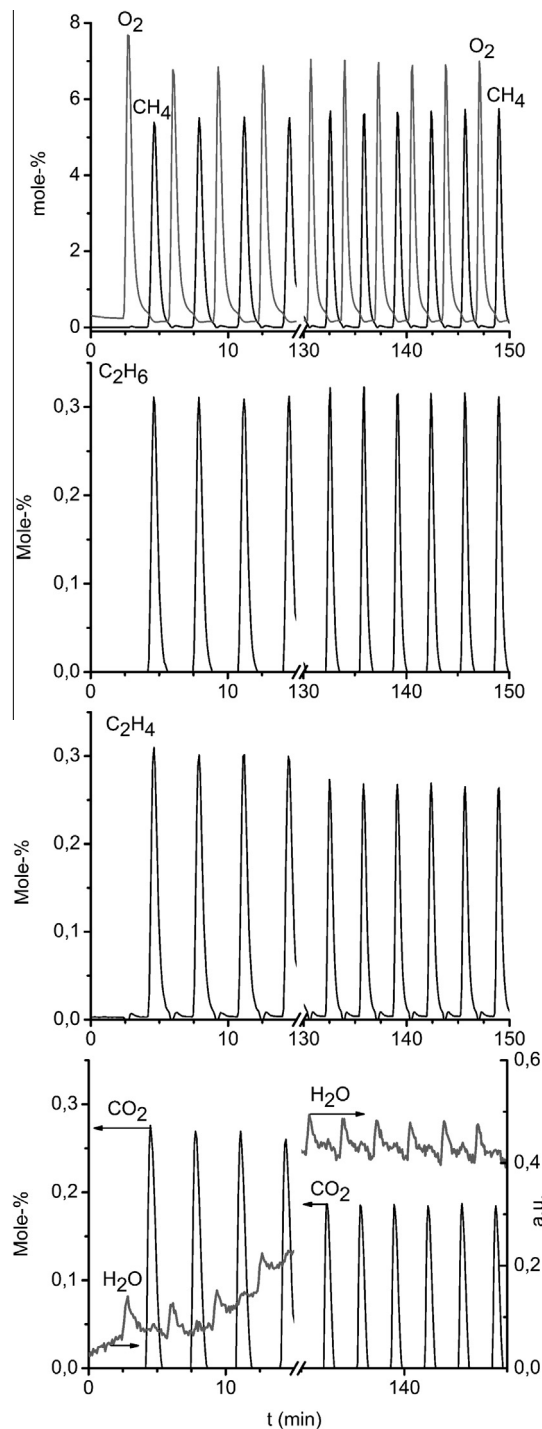


Fig. 6. Early and late reactant and product peaks during continuous simulated chemical looping, 775 °C, 25 nml/min, 2 g catalyst, pulse of 1 ml O<sub>2</sub> or 1 ml CH<sub>4</sub>.

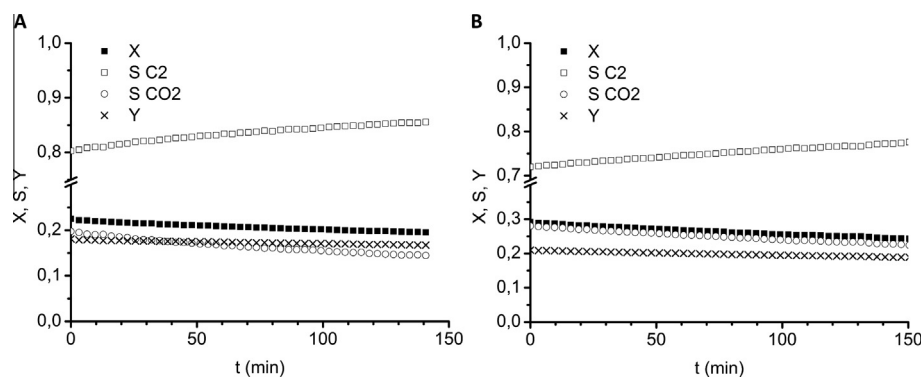


Fig. 7. Observed X, S C2 and Y of continuous simulated chemical looping, 2 g catalyst, 1 ml methane pulse, 25 nml/min, A – 775 °C, B – 800 °C.

### 3.2. Simulated chemical looping operation for 150 min

A detailed overview about reactant and product spectra at 775 °C is shown in Fig. 6 (25 nml/min,  $t = 2400$  s/m). We observed similar results at 800 °C. The first four peaks of all shown compounds represent the initial state of the experiment while the last four were observed after 150 min of operation. The formation of ethane, ethene and carbon dioxide is simultaneous to the methane pulse. Water is constantly removed by the oxygen pulse from the catalyst surface. The increase of the water signal with time is caused by accumulation of water in the detector of the mass spectrometer.

The amount of formed ethane stays constant, as the amount of ethene decreases slightly and carbon dioxide formation decreases clearly. The results for methane conversion, C2 selectivity and yield for both temperatures over the whole period of experiments are presented in Fig. 7. At 775 °C (Fig. 7A) the initial C2 selectivity is 0.8 and increases to 0.85 as CO<sub>2</sub> selectivity decreases. We observe a small decrease in the methane conversion, which is caused by a decrease of CO<sub>2</sub> formation. That is a common effect for that catalyst material in time on stream studies [29,30]. However, the C2 yield is constant at 0.19. The increase of the water signal is based on accumulation of that compound in the mass spectrometer. After this test the temperature was immediately increased to 800 °C and the experiment was continued for another 150 min. At 800 °C (Fig. 7B) the rates of carbon dioxide formation and methane conversion increase, while C2 selectivity decreases. However, the C2 yield increases to 0.21. The catalyst showed reasonable stability during the whole experiment. The space time yield (STY) in our experiments at 775 °C was 20 nmol(C<sub>2</sub>)/(s\*g<sub>cat</sub>) and 23 nmol(C<sub>2</sub>)/(s\*g<sub>cat</sub>) at 800 °C, respectively. To get an idea about the potential of this reactor concept for the OCM, a comparison with state of the art techniques is necessary.

### 3.3. Comparison of steady state and simulated chemical looping operation

The results of steady state experiments are shown in Table 1. The characteristic residence time was 300 s/m for 25 nml/min and 150 s/m for 50 nml/min. In all cases full oxygen conversion was obtained. The methane conversion was between 0.18 and 0.29 and a C2 yield of 0.18 was obtained. These results are in good agreement with the performance on a mini plant scale with a fluidized bed reactor with 50 g of catalyst [20]. Both experiments operate at similar methane conversions compared to the mentioned chemical looping process, which allows good comparison between both process concepts. Considering a much smaller characteristic residence time under steady state conditions than in chemical looping experiments, and full oxygen conversion, there

Table 1

Results from steady state experiments at different flow rates, 250 mg catalyst, 800 °C, CH<sub>4</sub>: O<sub>2</sub>: He (3:1:4).

Flowrate (nml/min)	X (CH <sub>4</sub> )	X (O <sub>2</sub> )	S C2	Y	STY nmol(C <sub>2</sub> )/(s*g <sub>cat</sub> )
25	0.29	1.00	0.63	0.18	147
50	0.18	1.00	0.81	0.15	269

Table 2

Comparison between steady state experiment (800 °C, 25 & 50 nml/min, 250 mg catalyst) and simulated chemical looping (2 g catalyst, 1 ml methane pulse).

Steady state		S C2	Y
X (CH <sub>4</sub> )	X (O <sub>2</sub> )		
0.29	1.00	0.63	0.18
0.18	1.00	0.81	0.15
Chemical looping – equal methane conversion		S C2	Y
X (CH <sub>4</sub> )	T (°C) Flowrate (nml/min)		
0.29	775 25	0.74	0.21
0.18	750 50	0.89	0.17
Chemical looping – equal C2 yield		S C2	Y
X (CH <sub>4</sub> )	T (°C) Flowrate (nml/min)		
0.21	775 30	0.87	0.18
0.19	725 25	0.87	0.16

is a much higher reaction rate in steady state experiments. This is also caused by much higher partial pressures of the reactants, compared to the pulses in simulated chemical looping experiments, where the carrier gas diluted the methane pulses. Consequently the STY is much higher compared to our chemical looping experiments as can be seen in the last column of Table 1. The space time yield is one of the most critical parameters for industrial application of a process. The large amount of carrier gas (50 ml per 1 ml of methane) is required for these experiments due to the dead volume of the reactor and the piping connecting it to the analytical equipment. In an industrial scale reactor such volumes are negligible in comparison to the catalyst bed and a carrier gas can be avoided. This should increase the STY of the chemical looping mode substantially. As demonstrated in our recent work, the catalyst reoxidation rate is much faster and therefore much shorter reoxidation times are needed compared to the OCM reaction [31]. We demonstrated also that no temperature swing for the oxidation step is required, as it can be seen from our continuous operation experiments.

For a direct comparison of steady state and chemical looping experiments, similar results for methane conversion should be considered as presented in Table 2. On the one hand, a comparison at the same methane conversion shows clearly that the simulated chemical looping achieves higher C2 selectivities and therefore higher yields.

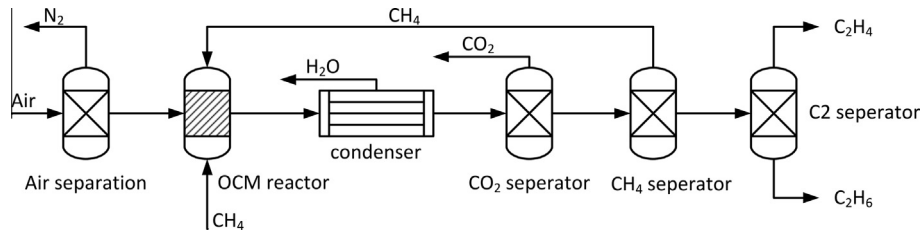


Fig. 8. Scheme of the classic OCM process [32].

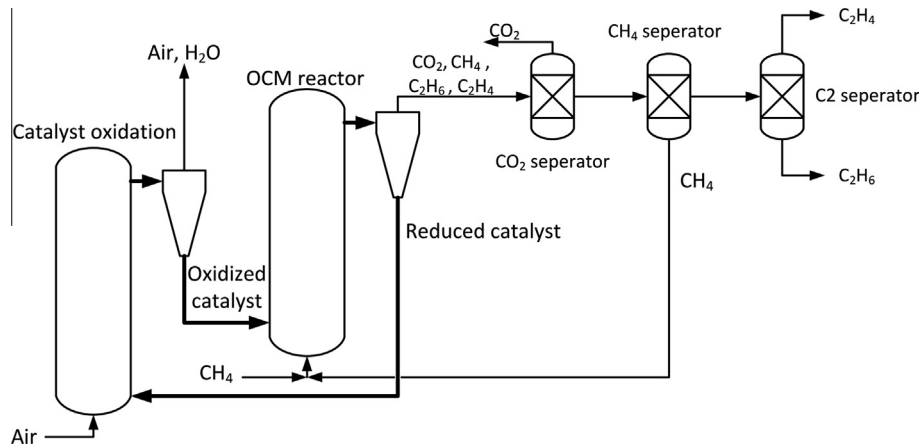


Fig. 9. Scheme of chemical looping of two fluidized bed reactors [32,35].

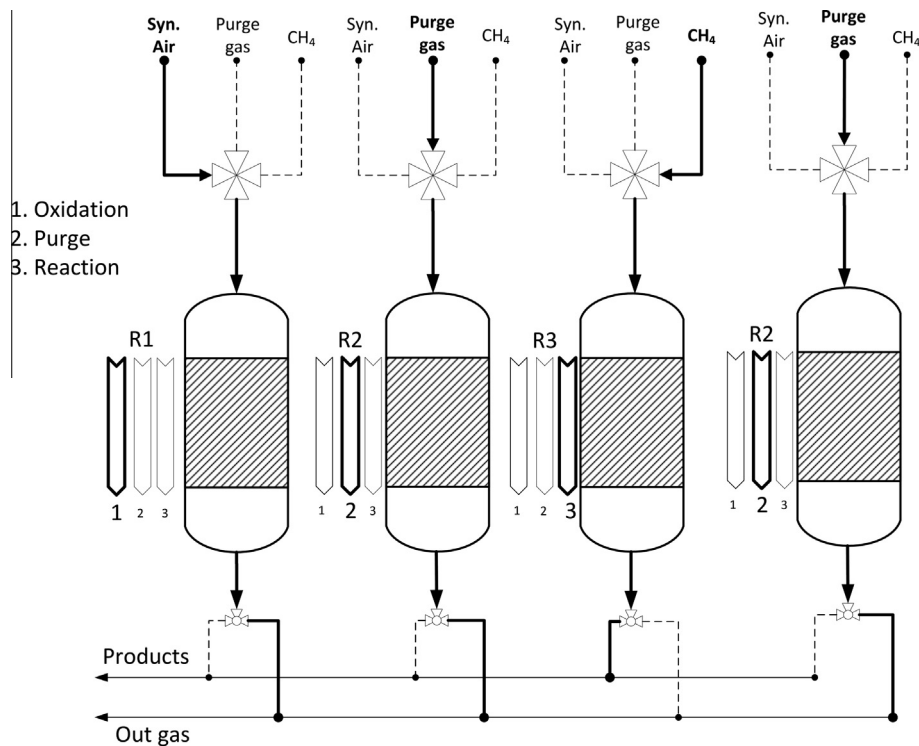
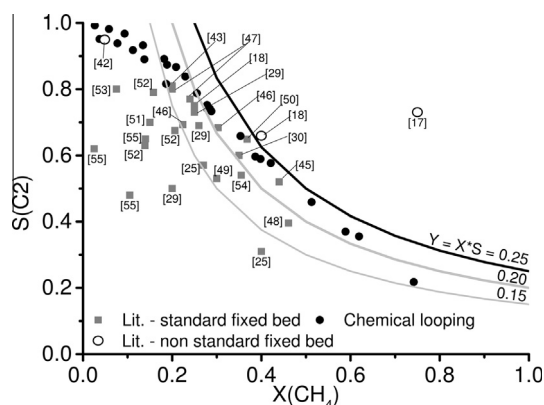


Fig. 10. Scheme of the chemical looping utilizing of fixed bed reactors.

The consequence of these results is that the chemical looping process clearly produces less  $\text{CO}_2$ . On the other hand, the chemical looping process can be operated at lower methane conversion for the same  $\text{C}_2$  yield due to the better selectivity. In both cases, the chemical looping has a better performance and is able to save raw material and energy for the product separation.

This becomes clear by a detailed discussion of the complete OCM process design, which is shown in Figs. 8 and 9. In a classic OCM process an air separation unit removes nitrogen, so that pure oxygen and methane are fed into the reactor. This is required for reducing the total equipment volume. Nitrogen in the feed would increase the total volume and therefore the volume and energy



**Fig. 11.** Conversion/selectivity plot of  $\text{Na}_2\text{WO}_4/\text{Mn}/\text{SiO}_2$  catalysts in standard steady state co-feed experiments (Literature, 775–850 °C, Feed:  $\text{CH}_4:\text{O}_2:\text{Inert}$ ), simulated countercurrent moving bed reactor ( $\text{Y}_1\text{Ba}_2\text{Zr}_3\text{O}_{9.5}$  catalyst) [17], cofeed experiments with addition of water [42], membrane fixed bed reactor [18] and simulated chemical looping experiments (700–800 °C) [25,29,30,18,43–55]

consumption of each separation unit would be much larger. Especially cryogenic distillation of methane and the C2 products are very cost intensive separation steps [32]. A proposal for an OCM process based on chemical looping is shown in Fig. 9. As mentioned in the introduction, the state of the art for a chemical looping process is a combination of two fluidized bed reactors. Successful operation of the  $\text{Na}_2\text{WO}_4/\text{Mn}/\text{SiO}_2$  catalyst in fluidized bed reactors was shown previously by several groups [32–34]. Therefore two fluidized bed reactors could be utilized for catalyst oxidation and OCM reaction. Based on the observed phenomena, air can be used directly for oxidation and in the same step to remove the water from the catalyst surface. The catalyst should be transported to the OCM reactor with methane atmosphere. Product separation is identical to the separation process shown in Fig. 8. Remembering the better performance of the simulated chemical looping, less  $\text{CO}_2$  has to be removed and much more methane can be recycled, saving costs of methane from fresh raw gas.

It has to be noted that the manganese oxide system of the  $\text{Na}_2\text{WO}_4/\text{Mn}/\text{SiO}_2$  system is very complex due to different oxidation states ( $\text{Mn}_2\text{O}_3$ ,  $\text{Mn}_3\text{O}_4$ ,  $\text{MnO}$ ). Supported manganese oxides on silica were studied by Stobbe and Coworkers [36]. They have discussed the kinetic and thermodynamic properties qualitatively and summarized that the oxidation rate of  $\text{MnO}$  to  $\text{Mn}_3\text{O}_4$  is faster than from  $\text{Mn}_3\text{O}_4$  to  $\text{Mn}_2\text{O}_3$  but the  $\text{Mn}_2\text{O}_3$  species is thermodynamically more favored. Furthermore that system provides the lowest oxygen capacity from all known oxygen storing systems [37].

A well-known problem of fluidized bed reactors is the comminution or abrasion of the catalyst particles [38–40]. An alternative chemical looping concept, utilizing fixed bed reactors, is presented in Fig. 10. Four fixed bed reactors can operated with alternating gas feed. Such a concept follows the idea which was presented in Fig. 2. Assuming that all procedures in chemical looping operate on similar time scale, continuous operation is possible. Such a concept was reviewed in detail by Kolios et al. [41]. The first reactor can be oxidized by air, while water from the catalyst surface is removed. In parallel, the second and fourth reactors are purged. All of these reactors can be connected to an outgas line. The third fixed bed reactor performs the OCM reaction and is connected to the product line. After this step all feed gases are changed to the next reactor in order to complete the chemical looping process. The outlets of each reactor must be switched to the according line. The separation process for the product line is similar to that discussed above.

## 4. Conclusion

In our work we tested the  $\text{Na}_2\text{WO}_4/\text{Mn}/\text{SiO}_2$  catalyst material in simulated chemical looping experiments. The advantage was that the contributions of gas phase oxygen were avoided, by split of the constant reactant gas feed into separated process steps. We demonstrated that the nature of the oxygen species, which are stored on the catalyst material, limits the C2 yield. We could demonstrate that the material is stable in a continuous simulated chemical looping experiment under OCM conditions. Finally we compared our dynamic experiment with a standard steady state one. We found that the chemical looping converts methane more efficiently at methane conversions lower than 0.3. Further we presented a hypothetical application of a chemical looping process and its advantages in comparison with the standard process. In addition, our results are compared in a plot of methane conversion and C2 selectivity with several published results for  $\text{Na}_2\text{WO}_4/\text{Mn}/\text{SiO}_2$  catalysts in Fig. 11. On the one hand, methane conversions higher than 0.5 were not possible to realize in standard fixed bed reactors because of the explosive regime of OCM reaction mixtures. On the other hand the chemical looping process concept provides higher C2 selectivities at methane conversions below 0.25. Furthermore non-standard reactor concepts have shown similar performance improvements which are also presented in Fig. 11. A simulated countercurrent moving bed reactor shows promising C2 yields by separation of C2 products and recycling of unconverted methane [17]. Another example for improved performance is a membrane fixed bed reactor with dosing of defined amounts of oxygen to the catalyst bed through a porous membrane [18]. Another option is the modification of the co feed stream by addition of water [42]. In conclusion, it can be seen that new reactor concepts enhance the overall performance of OCM processes.

## Acknowledgement

This work is part of the UNICAT excellence cluster, which is coordinated by the Technische Universität Berlin. The funding of this cluster by the German Research Foundation (DFG) is gratefully acknowledged.

## Appendix A. Supplementary data

Supplementary data associated with this article can be found, in the online version, at <http://dx.doi.org/10.1016/j.cej.2016.07.094>.

## References

- [1] U. Preub, M. Baerns, Chemical technology of natural gas – its present state and prospects, *Chem. Eng. J.* 10 (1987) 297–305.
- [2] M.J. Gradassi, N.W. Green, Economics of natural gas conversion processes, *Fuel Process. Technol.* 42 (1995) 65–83, [http://dx.doi.org/10.1016/0378-3820\(94\)00094-A](http://dx.doi.org/10.1016/0378-3820(94)00094-A).
- [3] T. Setoyama, The contribution of catalysis for the realization of GSC in the twenty-first century, *Catal. Surv. Asia* (2014) 183–192, <http://dx.doi.org/10.1007/s10563-014-9180-0>.
- [4] E.V. Kondratenko, M. Baerns, Oxidative coupling of methane, in: *Handb. Heterog. Catal.*, 2014, pp. 3010–3023.
- [5] Y.S. Su, J.Y. Ying, W.H. Green Jr., Upper bound on the yield for oxidative coupling of methane, *J. Catal.* 218 (2003) 321–333, [http://dx.doi.org/10.1016/S0021-9517\(03\)00043-5](http://dx.doi.org/10.1016/S0021-9517(03)00043-5).
- [6] Y.I. Pyatnitsky, N.I. Ilchenko, M.V. Pavlenko, Kinetic aspects of the methane oxidative coupling at elevated pressures, *Catal. Today* 42 (1998) 233–240, [http://dx.doi.org/10.1016/S0920-5861\(98\)00097-2](http://dx.doi.org/10.1016/S0920-5861(98)00097-2).
- [7] D.J. Driscoll, J.H. Lunsford, Gas-phase radical formation during the reactions of methane, ethane, ethylene, and propylene over selected oxide catalysts, *J. Phys. Chem.* 89 (1985) 4415–4418.
- [8] B. Beck, V. Fleischer, S. Arndt, M.G. Hevia, A. Urakawa, P. Hugo, R. Schomäcker, Oxidative coupling of methane—a complex surface/gas phase mechanism with strong impact on the reaction engineering, *Catal. Today* 228 (2014) 212–218.
- [9] S. Hurst, Production of hydrogen by the steam-iron method, *Oil Soap* 16 (1939) 29–35, <http://dx.doi.org/10.1007/BF02543209>.

- [10] J. Adanez, A. Abad, F. Garcia-Labiano, P. Gayan, L.F. de Diego, Progress in chemical-looping combustion and reforming technologies, *Prog. Energy Combust. Sci.* 38 (2012) 215–282, <http://dx.doi.org/10.1016/j.pecc.2011.09.001>.
- [11] T. Mattisson, A. Lyngfelt, H. Leion, Chemical-looping with oxygen uncoupling for combustion of solid fuels, *Int. J. Greenhouse Gas Control* 3 (2009) 11–19, <http://dx.doi.org/10.1016/j.ijggc.2008.06.002>.
- [12] Q. Zafar, T. Mattisson, B. Gevert, Integrated hydrogen and power production with CO<sub>2</sub> capture using chemical-looping reforming redox reactivity of particles of CuO, Mn<sub>2</sub>O<sub>3</sub>, NiO, and Fe<sub>2</sub>O<sub>3</sub> using SiO<sub>2</sub> as a support, *Ind. Eng. Chem. Res.* 2 (2005) 3485–3496, <http://dx.doi.org/10.1021/ie048978i>.
- [13] Q. Zafar, T. Mattisson, B. Gevert, Redox investigation of some oxides of transition-state metals Ni, Cu, Fe, and supported on SiO<sub>2</sub> and MgAl<sub>2</sub>O<sub>4</sub>, *Energy Fuels* 20 (2006) 34–44, <http://dx.doi.org/10.1021/ef0501389>.
- [14] X. Fang, S. Li, J. Gu, D. Yang, Preparation and characterization of W-Mn catalyst for oxidative coupling of methane, *J. Mol. Catal.* 255 (1992).
- [15] Y. Liu, R. Hou, X. Liu, J. Xue, S. Li, Performance of Na<sub>2</sub>WO<sub>4</sub>-Mn/SiO<sub>2</sub> catalyst for conversion of CH<sub>4</sub> with CO<sub>2</sub> into C<sub>2</sub> hydrocarbons and its mechanism, *Stud. Surf. Sci. Catal.* 119 (1998) 307–311, [http://dx.doi.org/10.1016/S0167-2991\(98\)80449-7](http://dx.doi.org/10.1016/S0167-2991(98)80449-7).
- [16] V. Salehoun, A. Khodadadi, Y. Mortazavi, A. Talebizadeh, Dynamics of catalyst in oxidative coupling of methane, *Chem. Eng. Sci.* 63 (2008) 4910–4916, <http://dx.doi.org/10.1016/j.ces.2007.08.013>.
- [17] A.V. Kruglov, M.C. Björklung, R.W. Carr, Optimization of the simulated countercurrent moving-bed chromatographic reactor for the oxidative coupling of methane, *Chem. Eng. Sci.* 51 (1996) 2945–2950.
- [18] H.R. Godini, A. Gili, O. Görke, U. Simon, K. Hou, G. Wozny, Performance analysis of a porous packed bed membrane reactor for oxidative coupling of methane: Structural and operational characteristics, *Energy Fuels* 28 (2014) 877–890, <http://dx.doi.org/10.1021/ef402041b>.
- [19] U. Simon, O. Görke, A. Berthold, S. Arndt, R. Schomäcker, H. Schubert, Fluidized bed processing of sodium tungsten manganese catalysts for the oxidative coupling of methane, *Chem. Eng. J.* 168 (2011) 1352–1359, <http://dx.doi.org/10.1016/j.cej.2011.02.013>.
- [20] S. Jaso, S. Sadjadi, H.R. Godini, U. Simon, S. Arndt, O. Görke, A. Berthold, H. Arellano-Garcia, H. Schubert, R. Schomäcker, G. Wozny, Experimental investigation of fluidized-bed reactor performance for oxidative coupling of methane, *J. Nat. Gas Chem.* 21 (2012) 534–543.
- [21] H. Bozorgzadeh, R. Ahmadi, M.M. Golkar, M.R. Khodagholi, Oxidative coupling of methane over different supported Mn/Na<sub>2</sub>WO<sub>4</sub> catalysts, *Pet. Coal* 53 (2011) 84–90. <[http://www.vurup.sk/sites/default/files/downloads/pc\\_2\\_2011\\_bozorgzadeh\\_109.pdf](http://www.vurup.sk/sites/default/files/downloads/pc_2_2011_bozorgzadeh_109.pdf)> (accessed July 1, 2013).
- [22] J.-L. Dubois, C.J. Cameron, Synergy between stable carbonates and Yttria in selective catalytic oxidation of methane, *Chem. Lett.* 1089–1092 (1991).
- [23] H.R. Godini, V. Fleischer, O. Görke, S. Jaso, R. Schomäcker, G. Wozny, Thermal reaction analysis of oxidative coupling of methane, *Chem. Ing. Tech.* 86 (2014) 1906–1915, <http://dx.doi.org/10.1002/cite.201400080>.
- [24] M.R. Lee, M.-J. Park, W. Jeon, J.-W. Choi, Y.-W. Suh, D.J. Suh, A kinetic model for the oxidative coupling of methane over Na<sub>2</sub>WO<sub>4</sub>/Mn/SiO<sub>2</sub>, *Fuel Process. Technol.* 96 (2012) 175–182, <http://dx.doi.org/10.1016/j.fuproc.2011.12.038>.
- [25] S.M.K. Shahri, S.M. Alavi, Kinetic studies of the oxidative coupling of methane over the Mn/Na<sub>2</sub>WO<sub>4</sub>/SiO<sub>2</sub> catalyst, *J. Nat. Gas Chem.* 18 (2009) 25–34, [http://dx.doi.org/10.1016/S1003-9953\(08\)60079-1](http://dx.doi.org/10.1016/S1003-9953(08)60079-1).
- [26] S. Lacombe, Z. Durjanova, L. Mleczko, C. Mirodatos, Kinetic modelling of the oxidative coupling of methane over lanthanum oxide in connection with mechanistic studies, *Chem. Eng. Technol.* 18 (1995) 216–223.
- [27] Z. Stansch, L. Mleczko, M. Baerns, Comprehensive kinetics of oxidative coupling of methane over the La<sub>2</sub>O<sub>3</sub>/CaO catalyst, *Ind. Eng. Chem. Res.* 36 (1997) 2568–2579.
- [28] R.B. Grant, R.M. Lambert, A single crystal study of the silver-catalysed selective oxidation and total oxidation of ethylene, *J. Catal.* 92 (1985) 364–375, [http://dx.doi.org/10.1016/0021-9517\(85\)90270-2](http://dx.doi.org/10.1016/0021-9517(85)90270-2).
- [29] R. Koirala, R. Büchel, S.E. Pratsinis, A. Baiker, Oxidative coupling of methane on flame-made Mn-Na<sub>2</sub>WO<sub>4</sub>/SiO<sub>2</sub>: influence of catalyst composition and reaction conditions, *Appl. Catal. A Gen.* 484 (2014) 97–107, <http://dx.doi.org/10.1016/j.apcata.2014.07.013>.
- [30] H. Liu, X. Wang, D. Yang, R. Gao, Z. Wang, J. Yang, Scale up and stability test for oxidative coupling of methane over Na<sub>2</sub>WO<sub>4</sub>-Mn/SiO<sub>2</sub> catalyst in a 200 ml fixed-bed reactor, *J. Nat. Gas Chem.* 17 (2008) 59–63, [http://dx.doi.org/10.1016/S1003-9953\(08\)60026-2](http://dx.doi.org/10.1016/S1003-9953(08)60026-2).
- [31] V. Fleischer, R. Steuer, S. Parishan, R. Schomäcker, Investigation of the surface reaction network of the oxidative coupling of methane over Na<sub>2</sub>WO<sub>4</sub>/Mn/SiO<sub>2</sub> catalyst by temperature programmed and dynamic experiments, *J. Catal.* (2016), accepted.
- [32] H.-R. Godini, S. Jaso, W. Martini, S. Stünkel, D. Salerno, S.N. Xuan, S. Song, S. Sadjadi, H. Trivedi, H. Arellano-Garcia, G. Wozny, Concurrent reactor engineering, separation enhancement and process intensification; comprehensive unicast approach for oxidative coupling of methane (OCM), *CzT* 109 (2012) 63–74.
- [33] A. Talebizadeh, Y. Mortazavi, A.A. Khodadadi, Comparative study of the two-zone fluidized-bed reactor and the fluidized-bed reactor for oxidative coupling of methane over Mn/Na<sub>2</sub>WO<sub>4</sub>/SiO<sub>2</sub> catalyst, *Fuel Process. Technol.* 90 (2009) 1319–1325, <http://dx.doi.org/10.1016/j.fuproc.2009.06.021>.
- [34] S. Jašo, S. Sadjadi, H.R. Godini, U. Simon, S. Arndt, O. Görke, A. Berthold, H. Arellano-Garcia, H. Schubert, R. Schomäcker, G. Wozny, Experimental investigation of fluidized-bed reactor performance for oxidative coupling of methane, *J. Nat. Gas Chem.* 21 (2012) 534–543, [http://dx.doi.org/10.1016/S1003-9953\(11\)60402-7](http://dx.doi.org/10.1016/S1003-9953(11)60402-7).
- [35] W. Xiang, S. Chen, Z. Xue, X. Sun, Investigation of coal gasification hydrogen and electricity co-production plant with three-reactors chemical looping process, *Int. J. Hydrogen Energy* 35 (2010) 8580–8591, <http://dx.doi.org/10.1016/j.ijhydene.2010.04.167>.
- [36] E.R. Stobbe, B.A. de Boer, J.W. Geus, The reduction and oxidation behaviour of manganese oxides, *Catal. Today* 47 (1999) 161–167, [http://dx.doi.org/10.1016/S0920-5861\(98\)00296-X](http://dx.doi.org/10.1016/S0920-5861(98)00296-X).
- [37] P. Gupta, F. Li, L. Velázquez-Vargas, D. Sridhar, M. Iyer, S. Ramkumar, L.-S. Fan, Chemical looping particles, in: *Chem. Looping Syst. Foss. Energy Conversions*, John Wiley & Sons, Hoboken, 2010, pp. 57–142. doi: 10.1002/9780470872888.ch2.
- [38] F. Scala, A. Cammarota, R. Chirone, P. Salatino, Comminution of limestone during batch fluidized-bed calcination and sulfation, *AIChE J.* 43 (1997) 363–373, <http://dx.doi.org/10.1002/aic.690430210>.
- [39] L. Chou, R. Wollast, Study of the weathering of albite at room temperature and pressure with a fluidized bed reactor, *Geochim. Cosmochim. Acta* 48 (1985) 2205–2217, [http://dx.doi.org/10.1016/0016-7037\(85\)90270-4](http://dx.doi.org/10.1016/0016-7037(85)90270-4).
- [40] X. Yao, H. Zhang, H. Yang, Q. Liu, J. Wang, G. Yue, An experimental study on the primary fragmentation and attrition of limestones in a fluidized bed, *Fuel Process. Technol.* 91 (2010) 1119–1124, <http://dx.doi.org/10.1016/j.fuproc.2010.03.025>.
- [41] G. Kolios, J. Frauhammer, G. Eigenberger, Autothermal fixed-bed reactor concepts, *Chem. Eng. Sci.* 55 (2000) 5945–5967, [http://dx.doi.org/10.1016/S0009-2509\(00\)00183-4](http://dx.doi.org/10.1016/S0009-2509(00)00183-4).
- [42] K. Takanabe, E. Iglesia, Rate and selectivity enhancements mediated by OH radicals in the oxidative coupling of methane catalyzed by Mn/Na<sub>2</sub>WO<sub>4</sub>/SiO<sub>2</sub>, *Angew. Chem. Int. Ed.* 47 (2008) 7689–7693, <http://dx.doi.org/10.1002/anie.200802608>.
- [43] D. Wang, M.P. Rosynek, J.H. Lunsford, Oxidative coupling of methane over oxide-supported sodium-manganese catalysts, *J. Catal.* 155 (1995) 390–402, <http://dx.doi.org/10.1006/jcat.1995.1221>.
- [44] A. Malekzadeh, A.K. Dalai, A. Khodadadi, Y. Mortazavi, Structural features of Na<sub>2</sub>WO<sub>4</sub>-MO<sub>x</sub>/SiO<sub>2</sub> catalysts in oxidative coupling of methane reaction, *Catal. Commun.* 9 (2008) 960–965, <http://dx.doi.org/10.1016/j.catcom.2007.09.026>.
- [45] A. Palermo, J.P.H. Vazquez, R.M. Lambert, New efficient catalysts for the oxidative coupling of methane, *Catal. Lett.* 68 (2000) 191–196.
- [46] J. Wang, L. Chou, B. Zhang, H. Song, J. Zhao, J. Yang, S. Li, Comparative study on oxidation of methane to ethane and ethylene over Na<sub>2</sub>WO<sub>4</sub>-Mn/SiO<sub>2</sub> catalysts prepared by different methods, *J. Mol. Catal. A Chem.* 245 (2006) 272–277, <http://dx.doi.org/10.1016/j.molcata.2005.09.038>.
- [47] A. Malekzadeh, M. Abedini, A.A. Khodadadi, M. Amini, H.K. Mishra, A.K. Dalai, Critical influence of Mn on low-temperature catalytic activity of Mn/Na<sub>2</sub>WO<sub>4</sub>/SiO<sub>2</sub> catalyst for oxidative coupling of methane, *Catal. Lett.* 84 (2002) 45–51. <<http://link.springer.com/article/10.1023/A:1021020516674>> (accessed July 1, 2013).
- [48] S. Mahmoodi, M.R. Ehsani, S.M. Ghoreishi, Effect of promoter in the oxidative coupling of methane over synthesized Mn/SiO<sub>2</sub> nanocatalysts via incipient wetness impregnation, *J. Ind. Eng. Chem.* 16 (2010) 923–928, <http://dx.doi.org/10.1016/j.jiec.2010.09.007>.
- [49] G.D. Nipan, Phase states of Na/W/Mn/SiO<sub>2</sub> composites at temperatures of catalytic oxidative coupling of methane, *Inorg. Mater.* 50 (2014) 1012–1017, <http://dx.doi.org/10.1134/S0020168514100112>.
- [50] Z. Jiang, H. Gong, S. Li, Methane activation over Mn<sub>2</sub>O<sub>3</sub>-Na<sub>2</sub>WO<sub>4</sub>/SiO<sub>2</sub> catalyst and oxygen spillover, *Stud. Surf. Sci. Catal.* 112 (1997) 481–490.
- [51] H. Zhang, J. Wu, B. Xu, C. Hu, Simultaneous production of syngas and ethylene from methane by combining its catalytic oxidative coupling over Mn/Na<sub>2</sub>WO<sub>4</sub>/SiO<sub>2</sub> with gas phase partial oxidation, *Catal. Lett.* 106 (2006) 161–165, <http://dx.doi.org/10.1007/s10562-005-9624-2>.
- [52] L. Chou, Y. Cai, B. Zhang, J. Niu, S. Ji, S. Li, Oxidative coupling of methane over Na-Mn-W/SiO<sub>2</sub> catalyst at higher pressure, *React. Kinet. Catal. Lett.* 76 (2002) 311–315, <http://dx.doi.org/10.1023/A:1016592129451>.
- [53] S. Pak, P. Qiu, J.H. Lunsford, Elementary reactions in the oxidative coupling of methane over Mn/Na<sub>2</sub>WO<sub>4</sub>/SiO<sub>2</sub> and Mn/Na<sub>2</sub>WO<sub>4</sub>/MgO catalysts, *J. Catal.* 230 (1998) 222–230. <<http://www.ingentaconnect.com/content/ap/ca/1998/00000179/00000001/art02228>> (accessed May 28, 2013).
- [54] S. Hou, Y. Cao, W. Xiong, H. Liu, Y. Kou, Site requirements for the oxidative coupling of methane on SiO<sub>2</sub>-supported Mn catalysts, *Ind. Eng. Chem. Res.* 45 (2006) 7077–7083, <http://dx.doi.org/10.1021/ie060269c>.
- [55] M. Yildiz, U. Simon, T. Otremba, Y. Aksu, K. Kailasam, A. Thomas, R. Schomäcker, S. Arndt, Support material variation for the Mn<sub>x</sub>O<sub>y</sub>-Na<sub>2</sub>WO<sub>4</sub>/SiO<sub>2</sub> catalyst, *Catal. Today* 228 (2014) 5–14, <http://dx.doi.org/10.1016/j.cattod.2013.12.024>.

# Chemical looping as reactor concept for the oxidative coupling of methane over a $\text{Na}_2\text{WO}_4/\text{Mn}/\text{SiO}_2$ catalyst – Supplementary material

---

## 1. Experimental – Mass spectrometer

The calibrated m/e ratios for all compounds in mass spectroscopy (QMS, IPI GAM 200) are presented in Table 1.

Table 1 - Calibrated m/e ratios for compound detection in chemical looping experiments

Molecule	m/e
$\text{CO}_2$	44
CO	28
He	4
$\text{H}_2$	2
$\text{H}_2\text{O}$	18; 17
$\text{CH}_4$	16; 15
$\text{C}_2\text{H}_6$	30; 29; 28
$\text{C}_2\text{H}_4$	28; 27; 26
$\text{O}_2$	32

## 2. Experimental – Pneumatic six-port diaphragm valves

A flowchart is presented in Figure 1. A reactant flows in by an inlet, passes through a sample loop and flows to the outlet. In parallel to this, a purge gas flows to the reactor from a second inlet (Figure 1 A). A pneumatic impulse from a solenoid valve switches the connectors to the second position (Figure 1 B). The reactant in the sample loop is conveyed by the purge gas to the reactor, while the reactant from the supply port goes directly to the outlet. The connectors switch back by pressure release. The pneumatic impulse can be controlled by a solenoid valve, which is connected to a 6 bar nitrogen supply line. There is a remote control connection from a computer followed by a transducer to the solenoid for precise realization of time controlled pulses. The sample loop (Vicci Valco CSL250, CSL500, CSL1K, CSL2K) can be varied in its volume from 250  $\mu\text{l}$  up to 2 ml for different amounts of pulsed reactants.

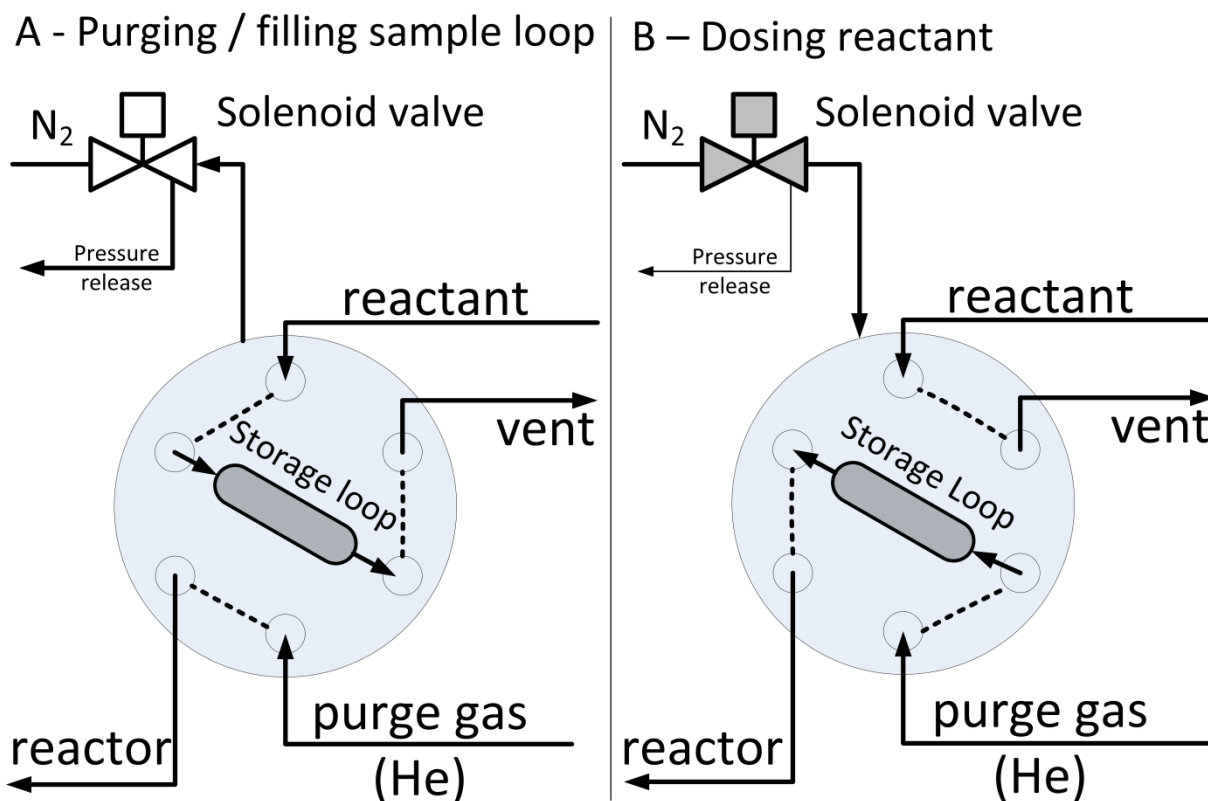


Figure 1 - Schematic function of a 6-port pulse valve, A: storage loop is filled by reactant, while purge gas goes to the reactor, B: purge gas transports the reactant to the reactor

### 3. Experimental – Fixed bed reactor

The catalyst bed is placed on a quartz frit (200  $\mu\text{m}$  pore size). The reactor inner diameter has a size of 9 mm. The type K thermocouple (NiCrNi) is covered by a quartz-made sheath (din = 4 mm), which also seals the reactor at the top. The fixed bed reactor for chemical looping experiments is presented in Figure 2. The reactants are fed through the upper entrance. The bottom part of the reactor is reduced in diameter and is connected to the analytical system. The isothermal zone is above the frit and has a height of around 5 cm.

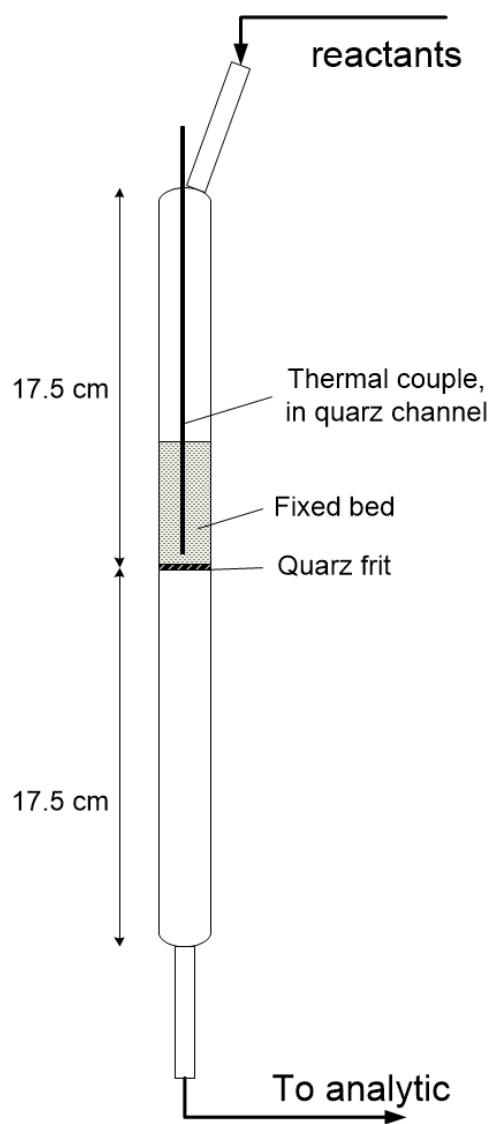


Figure 2 - Detailed scheme of the fixed bed reactor.

# Paper 3

# Solid-State Ion-Exchanged Cu/Mordenite Catalysts for the Direct Conversion of Methane to Methanol

Ha V. Le,<sup>†</sup> Samira Parishan,<sup>‡</sup> Anton Sagaltchik,<sup>§</sup> Caren Göbel,<sup>||</sup> Christopher Schlesiger,<sup>⊥</sup> Wolfgang Malzer,<sup>⊥</sup> Annette Trunschke,<sup>#</sup> Reinhard Schomäcker,<sup>‡</sup> and Arne Thomas<sup>\*,†,⊥</sup>

<sup>†</sup>Institute of Chemistry—Functional Materials, Technische Universität Berlin, BA2, Hardenbergstraße 40, 10623 Berlin, Germany

<sup>‡</sup>Institute of Chemistry—Technical Chemistry, Technische Universität Berlin, TC8, Straße des 17. Juni 124, 10623 Berlin, Germany

<sup>§</sup>BasCat—UniCat BASF Joint Lab, Technische Universität Berlin, EW K 01, Hardenbergstraße 36, 10623 Berlin, Germany

<sup>||</sup>Institute of Chemistry, Technische Universität Berlin, TK01, Straße des 17. Juni 135, 10623 Berlin, Germany

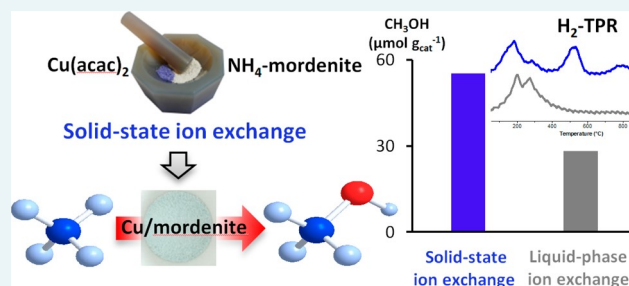
<sup>⊥</sup>Institute of Optics and Atomic Physics, Technische Universität Berlin, Hardenbergstraße 36, 10623 Berlin, Germany

<sup>#</sup>Department of Inorganic Chemistry, Fritz Haber Institute of the Max Planck Society, Faradayweg 4-6, 14195 Berlin, Germany

## Supporting Information

**ABSTRACT:** The selective oxidation of methane to methanol is a highly challenging target, which is of considerable interest to gain value-added chemicals directly from fuel gas. Copper-containing zeolites, such as Cu/mordenite, have been currently reported to be the most efficient catalysts for this reaction. In this work, it is shown that solid-state ion-exchanged Cu/mordenites exhibit a significantly higher activity for the partial oxidation of methane to methanol than comparable reference catalysts, i.e., Cu/mordenites prepared by the conventional liquid-phase ion exchange procedure. The efficiency of these Cu/mordenites remained unchanged over several successive cycles. From temperature-programmed reduction (TPR) measurements, it can be concluded that the solid-state protocol accelerates Cu exchange at the small pores of mordenite: those are positions where the most active Cu species are presumably located. *In situ* ultraviolet–visible (UV-vis) spectroscopy furthermore indicates that different active clusters including dicopper- and tricopper-oxo complexes are formed in the catalyst upon oxygen treatment. Notably after activation of methane, different methoxy intermediates seem to be generated at the Cu sites from which one is preferably transformed to methanol by reaction with water. It is furthermore described that the applied reaction conditions have considerable influence on the finally observed methanol production from methane.

**KEYWORDS:** zeolites, methane hydroxylation, selective oxidation, methane monooxygenase, microporous, mordenite



## 1. INTRODUCTION

The selective oxidation of methane to methanol is of considerable interest for obtaining valuable chemicals directly from abundant natural gas resources without the need of syngas production.<sup>1–4</sup> To reach this challenging target, harsh reaction conditions are required as activation of methane is hampered because of its strong C–H bonds. Moreover, the desired product, methanol, is more reactive than methane, which easily results in overoxidations into formic acid or carbon oxides.<sup>5–9</sup> Interestingly, methanotrophic bacteria in nature can selectively perform this “dream reaction” under ambient conditions, using methane monooxygenase enzymes, which contain di-iron or di-/tri-copper active clusters.<sup>10–13</sup> These enzymatic structures provide intriguing structural motifs for the development of biomimetic catalytic systems toward the activation of methane.<sup>12,14,15</sup>

To date, many different bioinspired catalysts for the direct methanol formation from methane have been synthesized and

intensively studied with the aim of improving the methanol yield under milder reaction conditions. Hammond et al. found that Fe-containing zeolites are active for the methane-to-methanol conversion in an aqueous solution of hydrogen peroxide.<sup>16</sup> Notably, the production of methanol could be significantly improved by the addition of Cu species and a 10% conversion of methane with 93% selectivity to methanol was achieved under appropriate reaction conditions. However, as H<sub>2</sub>O<sub>2</sub> is more expensive than methanol, the direct use of O<sub>2</sub> as an oxidant is inevitable for industrial applications.<sup>1</sup> Several research groups have demonstrated that iron-, cobalt-, and copper-loaded zeolites activated in O<sub>2</sub> or N<sub>2</sub>O can react with methane at low temperatures ( $\leq 200$  °C) and subsequently release methanol upon treatment with water or organic solvents

Received: August 18, 2016

Revised: December 22, 2016

Published: January 3, 2017

(acetonitrile, ethanol, tetrahydrofuran).<sup>6,17–23</sup> Among them, Cu/zeolites have currently been emerged as the best catalyst, based on their experimental performances.<sup>5,20,21,24</sup>

Cu<sup>2+</sup> cations are typically loaded into zeolites via liquid-phase ion exchange in most of these reports. Bozbag et al. have recently performed a solid-state ion exchange between H-mordenite with copper(I) chloride to achieve a Cu/mordenite catalyst. However, it was observed that residual chlorine hindered the production of methanol from methane in the first runs.<sup>25</sup> In this study, the activity of solid-state ion-exchanged Cu/mordenite prepared from NH<sub>4</sub>-mordenite and copper(II) acetylacetonate was investigated for the catalytic conversion of methane to methanol for the first time. The methanol yield was found to be considerably higher than the results achieved from Cu/mordenite conventionally prepared in the liquid phase.

## 2. EXPERIMENTAL SECTION

**2.1. Synthesis of Catalysts.** Commercial mordenites including NH<sub>4</sub>-mordenite (Si/Al = 10, denoted as NH<sub>4</sub>-Mor-1) and Na-mordenite (Si/Al = 6.5, denoted as Na-Mor-2) were obtained from Alfa Aesar.

**2.1.1. Conversion of Commercial Mordenites to the Na or NH<sub>4</sub> Form.** Ammonium exchange of Na-Mor-2 was carried out according to the method previously described.<sup>5</sup> A mixture of 2 g of Na-Mor-2 and 80 mL of 1 M NH<sub>4</sub>NO<sub>3</sub> solution was stirred vigorously for 2 h at 80 °C. The ion-exchange procedure was repeated three times. The sample was then filtered, washed with deionized water, and dried at 105 °C for 12 h. The as-prepared NH<sub>4</sub>-mordenite is denoted as NH<sub>4</sub>-Mor-2.

A similar treatment with NH<sub>4</sub>-Mor-1 in a 1 M solution of CH<sub>3</sub>COONa was employed for the preparation of mordenite in the Na-form. Calcination was performed at 550 °C under static air for 3 h, yielding the Na-exchanged mordenite, which is denoted as Na-Mor-1.

**2.1.2. Synthesis of Cu-Containing Zeolites.** Cu<sup>2+</sup> cation exchange with NH<sub>4</sub>-form zeolites was achieved under solid-state conditions using copper(II) acetylacetonate (Cu(acac)<sub>2</sub>).<sup>16</sup> In a typical procedure, CuMorS-1 (Table 1, entry 1) was prepared by intensively grinding a mixture of 0.120 g of Cu(acac)<sub>2</sub> and 0.975 g of NH<sub>4</sub>-Mor-1 in a mortar within 30 min. Ion exchange was performed *in situ* during the activation step of the catalytic testing. The Cu content in the materials was determined by inductively coupled plasma–optical emission spectrometry (ICP-OES).

A solid-state ion exchange of NH<sub>4</sub>-Mor-1 with copper(I) chloride producing the Cu/mordenite CuClMorS (Table 1, entry 6) was performed based on a modified procedure of Wulfers et al.<sup>5</sup> 0.043 g of CuCl was mixed with 0.975 g of NH<sub>4</sub>-Mor-1 as described above. Before the catalytic test, the mixture was heated at a rate of 2 °C min<sup>-1</sup> to 650 °C in a 50 NmL min<sup>-1</sup> flow of N<sub>2</sub>. The reactor was held at this temperature for 10 h, and then cooled to 550 °C under the same flow for the next activation step, as described in Section 2.2.

For comparison, conventional Cu/mordenites were prepared by liquid phase ion exchange.<sup>5</sup> For example, in order to obtain CuMorL-1 (Table 1, entry 7), 2 g of Na-Mor-2 were added to 200 mL of an aqueous solution containing 0.476 g of copper(II) acetate. This mixture was then stirred for 18 h at room temperature. The solid was collected by vacuum filtration, subsequently washed with deionized water, and dried at 105 °C for 12 h.

**Table 1. Details of Cu/Mordenites Used in the Study**

entry	catalyst	preparation method <sup>a</sup>	substrates <sup>b</sup>	Cu content (wt %)
1	CuMorS-1	SSIE	Cu(acac) <sub>2</sub> (0.120 g) and NH <sub>4</sub> -Mor-1 (0.975 g)	2.58
2	CuMorS-2	SSIE	Cu(acac) <sub>2</sub> (0.045 g) and NH <sub>4</sub> -Mor-1 (0.975 g)	1.01
3	CuMorS-3	SSIE	Cu(acac) <sub>2</sub> (0.084 g) and NH <sub>4</sub> -Mor-1 (0.975 g)	1.84
4	CuMorS-4	SSIE	Cu(acac) <sub>2</sub> (0.180 g) and NH <sub>4</sub> -Mor-1 (0.975 g)	3.74
5	CuMorS-5	SSIE	Cu(acac) <sub>2</sub> (0.120 g) and NH <sub>4</sub> -Mor-2 (0.975 g)	2.66
6	CuClMorS	SSIE	CuCl (0.043 g) and NH <sub>4</sub> -Mor-1 (0.975 g)	2.84
7	CuMorL-1	LIE	Cu(OAc) <sub>2</sub> (0.476 g) and Na-Mor-2 (2 g)	3.21
8	CuMorL-2	LIE	Cu(OAc) <sub>2</sub> (0.476 g) and Na-Mor-1 (2 g)	3.10
9	CuMorL-3	LIE	Cu(OAc) <sub>2</sub> (0.476 g) and NH <sub>4</sub> -Mor-1 (2 g)	2.07

<sup>a</sup>SSIE and LIE correspond to solid-state and liquid-phase ion exchange, respectively. Liquid-phase ion exchange was performed in 200 mL of water. <sup>b</sup>Si/Al ratio = 10 (in Mor-1) and 6.5 (in Mor-2).

**2.2. Catalytic Test.** Zeolite powder was pressed into pellets at a pressure of 100 bar for 60 s, lightly ground, and sieved to a 200–400 μm diameter fraction. 0.7 g of catalyst was loaded in a U-shaped quartz reactor (ID = 6 mm) and placed in an oven. In a typical catalytic experiment, the material was heated at a rate of 2 °C min<sup>-1</sup> to 550 °C in a 50 NmL min<sup>-1</sup> flow of O<sub>2</sub>, and this temperature was kept constant for another 8 h. After cooling to 60 °C, the excess gas phase O<sub>2</sub> was removed by a 50 NmL min<sup>-1</sup> flow of N<sub>2</sub> for 5 min. A mixture of 5 NmL min<sup>-1</sup> CH<sub>4</sub> and 30 NmL min<sup>-1</sup> N<sub>2</sub> was introduced into the reactor. The mixture was allowed to stand for 20 min before the catalyst was heated under the same flow to 200 °C with a rate of 5 °C min<sup>-1</sup>. After methane interaction for 60 min, the methane-containing flow was switched off, and the catalyst bed was cooled to room temperature. The resulting material was dispersed in 5 mL of water, under vigorous stirring, for 2 h to extract methanol. After centrifuging and filtration, the liquid phase was transferred to a volumetric flask, mixed with a predetermined volume of acetonitrile, as an internal standard, and analyzed via gas chromatography (GC).

Analysis of aqueous samples was performed using a Shimadzu Model GC 2010-Plus system that was equipped with a flame ionization detector (FID) and a SUPELCOWAX 10 column (length = 30 m, inner diameter = 0.53 mm, and film thickness = 1.00 μm). The oven was held at 60 °C for 8 min, and then heated at a rate of 30 °C min<sup>-1</sup> to 120 °C. The temperature of inlet and detector was set constant at 180 °C.

In an experiment using the online extraction method, the contact of catalyst with methane for 60 min at 200 °C was followed by the introduction of 50 NmL min<sup>-1</sup> of water-saturated N<sub>2</sub> flow to the reactor. The temperature of the used gas-washing bottle was set to 25 °C during the entire experiment. The reactor outlet was connected to a cold trap at –78 °C that was placed in an isopropanol/dry ice bath to condense the liquids. After 8 h, the cold trap was warmed to room temperature, diluted with water, mixed with acetonitrile, and then analyzed via GC, as described above.

Turnover numbers (TONs) were calculated based on the ratio of the methanol amount produced (mol) per Cu loading (mol).

**2.3. Characterization of Catalysts.** **2.3.1. Transmission Electron Microscopy (TEM).** Transmission electron microscopy (TEM) and energy-dispersive X-ray spectroscopy (EDX) measurements were recorded on a TECNAI Model G<sup>2</sup>20 S-TWIN electron microscope that was operated at 200 kV and equipped with an EDAX EDX system (Si(Li)) SUTW detector, with an energy resolution of 136 eV (for Mn K $\alpha$  radiation). For sample preparation, a drop of the material dispersed in ethanol was deposited onto a carbon-coated nickel grid via evaporation.

**2.3.2. N<sub>2</sub> Sorption Analysis.** N<sub>2</sub> sorption analysis was performed at 77 K using a QUADRASORB SI system, which was equipped with an automated surface area analyzer. Before analysis, samples were degassed at 150 °C for 12 h. Specific surface areas (BET) were determined over a 0.05–0.30  $P/P_0$  range. The total pore volume was collected at  $P/P_0 = 0.99$ .

**2.3.3. Powder X-ray Diffraction (XRD).** Wide-angle powder XRD was performed with a Bruker-AXS Model D8 Avance diffractometer with DAVINCI design, using Cu K $\alpha$  radiation ( $\lambda = 1.5418 \text{ \AA}$ ), that was equipped with a Lynx Eye detector.

**2.3.4. In Situ UV–Visible Spectroscopy.** UV–visible diffuse reflectance (UV-vis DRS) spectra were measured on a Cary Model 5000 spectrometer (Agilent) equipped with a Harrick Praying Mantis diffuse reflectance attachment (Model DRP-P72) and a reaction chamber (Model HVC-VUV). The *in situ* cell was connected to a gas delivery system for operation under flow conditions. Spectralon was used as a white standard. Spectra were taken in the 200–800 nm range with a step size of 1 nm every 3 min during the treatment of materials. Results were presented in the Kubelka–Munk function ( $F(R)$ ) calculated from recorded reflectance data.

The *in situ* cell was heated to 550 °C with a rate of 10 °C min<sup>-1</sup> in a 50 NmL min<sup>-1</sup> flow of O<sub>2</sub>. The sample was held at 550 °C for 60 min, and then cooled to 200 °C with a rate of 10 °C min<sup>-1</sup> under the same flow.

**2.3.5. Temperature-Programmed Reduction by Hydrogen (H<sub>2</sub>-TPR).** Temperature-programmed reduction by hydrogen (H<sub>2</sub>-TPR) experiments were conducted on a BELCAT II instrument (Version 0.4.5.13). Prior to measurements, Cu/mordenites were pretreated in a 50 NmL min<sup>-1</sup> flow of O<sub>2</sub> at 550 °C for 4 h, and then cooled to ~40 °C. This temperature was kept constant for a stabilization for 3 h under a 30 NmL min<sup>-1</sup> flow of 5% H<sub>2</sub>/N<sub>2</sub>. H<sub>2</sub>-TPR profiles of the samples were then recorded in the same flow at a heating rate of 3 °C min<sup>-1</sup> up to 900 °C.

**2.3.6. X-ray Absorption Spectroscopy.** X-ray absorption measurements were carried out with a novel self-developed wavelength dispersive spectrometer in von Hamos geometry. The spectrometer is equipped with a microfocus X-ray tube, a curved highly annealed pyrolytic graphite mosaic crystal and a charge-coupled device camera with a pixel size of 13.5  $\mu\text{m} \times 13.5 \mu\text{m}$ . The tube was operated with a high voltage of 13.5 kV and a current of 870  $\mu\text{A}$ . The samples were prepared as powders on cellophane tape and constantly moved during the measurements to minimize effects of local thickness inhomogeneity. The beam size on the samples is ~3 mm  $\times$  3 mm. The gathered spectral range covers the Cu K-absorption edge at 8980 eV.

### 3. RESULTS AND DISCUSSION

Solid-state Cu<sup>2+</sup> exchange of mordenite was carried out by treating a well-blended mixture of NH<sub>4</sub>-form mordenite and Cu(acac)<sub>2</sub> at high temperature under an O<sub>2</sub> flow (CuMorS). The copper content within the mordenite was varied by changing the mordenite/Cu(acac)<sub>2</sub> ratio. For comparison, CuCl also was used as a reactant (CuClMorS) and a conventional liquid-phase ion exchange method was also applied to prepare Cu/mordenites (CuMorL). Details on Cu/mordenites used in this study are summarized in Table 1. Only a small decrease in the BET surface area was observed after Cu was loaded into the mordenites by both methods (see Table S1 in the Supporting Information). Furthermore, XRD measurements show that the structure of Cu-loaded mordenites is in agreement with the parent mordenites (see Figure S1 in the Supporting Information). No additional peaks specific for elemental Cu or its oxides were detected in the patterns, confirming that the Cu species are highly dispersed throughout the zeolite framework and Cu-based nanoparticles, if any, are smaller than ~3 nm. The well-dispersed nanoparticles found in the TEM images of both catalysts are formed during the measurement due to irradiation within the high-energy electron beam (see Figure S2 in the Supporting Information).<sup>25,26</sup>

The catalytic procedure for the methane-to-methanol conversion over Cu/mordenites was performed as described previously in a stepwise manner, namely,

- (i) activation of the material at 550 °C under an O<sub>2</sub> flow for 8 h,
- (ii) interaction of the material with methane at 200 °C, and
- (iii) extraction of methanol using 5 mL of water at room temperature for 2 h.<sup>20,23,27</sup>

To investigate the activity of Cu/mordenite prepared via solid-state ion exchange using Cu(acac)<sub>2</sub> and to develop optimum reaction conditions, CuMorS-1 was tested initially. It was found that the CuMorS-1-catalyzed reaction yielded 39.3  $\mu\text{mol g}_{\text{cat}}^{-1}$  of methanol, while only 10.7  $\mu\text{mol g}_{\text{cat}}^{-1}$  was produced in a comparable experiment, using the mordenite ion-exchanged with CuCl (CuClMorS) with a similar copper loading. The catalytic performance of CuClMorS was consistent with the one reported in a recent study confirming the negative effect of chlorine in mordenite based on the ion exchange with CuCl on the methanol production.<sup>25</sup> Furthermore, XANES spectra obtained in this study showed the specific features of Cu<sup>+</sup> is still present in mordenite, even after activation in O<sub>2</sub>.<sup>25</sup> Such Cu<sup>+</sup> species has been described to be inactive for CH<sub>4</sub> activation. Besides the negative effect of chlorine, the appearance of stable Cu<sup>+</sup> sites also can be responsible for the poor performance of CuClMorS. Therefore, the use of Cu(acac)<sub>2</sub> as a precursor for Cu<sup>2+</sup> cation exchange under solid state is clearly preferable. Typically, both the H- and NH<sub>4</sub>-forms can be used for the preparation of metal-exchanged zeolites.<sup>28</sup> However, using the NH<sub>4</sub>-form zeolite offers a more simple and facile procedure for the preparation of Cu/zeolite. Indeed, to obtain the H-form, a further calcination step of the NH<sub>4</sub>-form zeolite is required, which can be performed well during solid-state ion exchange at high temperature between Cu(II) acetylacetonate and NH<sub>4</sub>-mordenite.<sup>29</sup> Furthermore, it has been shown that the degree of Cu-exchange using the NH<sub>4</sub>-zeolite is considerably higher than for using the H-zeolite at the same temperature.<sup>30</sup>

The interaction of the catalyst CuMorS-1 with methane at 200 °C was performed at different reaction times showing that

more methanol was generated on Cu/mordenite by prolonging the contact time. No methanol was extracted after the activated catalyst was purged with pure N<sub>2</sub>, indicating that methanol was indeed generated from methane. A methanol amount of 18.1  $\mu\text{mol g}_{\text{cat}}^{-1}$  was achieved within 5 min at 200 °C after the addition of methane (Figure 1). As can be expected, a steady

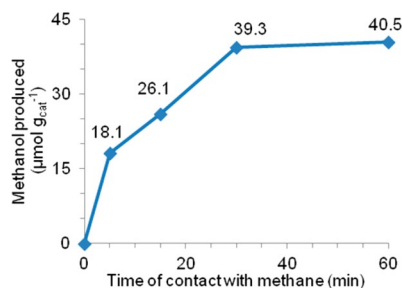


**Figure 1.** Effect of reaction time on methanol production using CuMorS-1 as a catalyst.

increase of methanol production with increasing reaction time was observed during the first 30 min. However, after this reaction time, methane production reached a plateau, i.e., just a negligible yield improvement is seen within the next 30 min. In total, a methanol amount of 40.5  $\mu\text{mol g}_{\text{cat}}^{-1}$  was obtained after 1 h. These results are consistent with previous studies, in which the activated catalysts had to be reacted for at least 20 min with methane to obtain significant methanol yields.<sup>5,20,21</sup> Note that the time required for completion of the reaction is dependent on Cu loading and methane concentration in the gas flow.

In earlier studies, greater amounts of methanol were obtained when ethanol or acetonitrile/water mixtures were used for extraction, compared to only dry acetonitrile or *n*-hexane. Therefore, the solvent was proposed to be acting not only as a methanol-desorption agent, but also as a proton source for hydrolysis of the intermediates, most likely methoxy species.<sup>26,27,31</sup> As mentioned previously, the solvent used in our studies was water. To investigate its role in the production of methanol, a high-temperature treatment of the catalyst in dry inert gas was performed, instead of dispersing the catalyst in liquid water. In particular, after interaction with CuMorS-1, the methane-containing flow was switched off and the reactor was cooled to room temperature. The material was then heated to 550 °C at the rate of 1 °C min<sup>-1</sup> in a 50 NmL min<sup>-1</sup> flow of helium. Products in the outlet stream were detected by a quadrupole mass spectrometer (InProcess Instruments, Model GAM 200) (Figure 2). Helium was considered as an internal standard to quantify the products. Neither methanol nor dimethyl ether was observed during heating under dry inert gas. This indicates the necessity of water for converting intermediate species, formed on the catalyst surface after reaction of Cu sites with methane, to methanol. Nevertheless, the presence of such intermediates on the catalyst surface is confirmed as CO<sub>2</sub> was detected starting from ~200 °C, in accordance to the proposed formation of methoxy species bound to dicopper sites from methane.<sup>27,31</sup> The corresponding formation of hydroxyl species between dicopper sites, generated by the remaining abstracted H atom from methane, is also indicated by detecting water, starting at ~300 °C. Surprisingly, other species than CO<sub>2</sub> and H<sub>2</sub>O were detected by heating the methane-treated CuMorS-1 under inert gas (namely, H<sub>2</sub> and CO). Formation of these species could also be the result of decomposition of methoxy species stabilized on

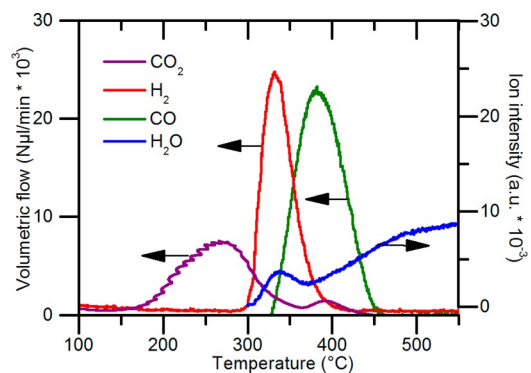


**Figure 2.** Volumetric flows of CO<sub>2</sub>, H<sub>2</sub>, CO, and H<sub>2</sub>O calculated from the mass spectrometry data recorded during heating CuMorS-1 (after interaction with CH<sub>4</sub>) in a dry helium flow.

the catalyst surface. However, observation of CO and H<sub>2</sub> at higher temperatures, compared to the case of CO<sub>2</sub>, indicates that the activation of methane by Cu/mordenite catalyst results in the formation of intermediates with different stabilities. The CO amount was 58  $\mu\text{mol g}_{\text{cat}}^{-1}$  from an overall carbon oxides amount of 84  $\mu\text{mol g}_{\text{cat}}^{-1}$ , which is close to the methanol yield obtained after the addition of liquid water (see below), suggesting that the intermediate, which is decomposed to H<sub>2</sub> and CO in the dry helium flow, is responsible for the methanol and dimethyl ether production by reaction with water. Indeed, when CuMorS-1 after methane activation was treated with a water-saturated He flow, methanol and dimethyl ether were detected already at room temperature, but no H<sub>2</sub> and CO were seen afterward when the catalytic bed was heated to higher temperatures, while CO<sub>2</sub> was formed again at 200 °C (Figure 3). Dimethyl ether was previously observed in the wet helium flow at 135 °C;<sup>21</sup> however, its early appearance at room temperature in the wet helium flow in the present study demonstrates that it should not be considered to be a product of dehydrated methanol and another single intermediate may be responsible for the production of dimethyl ether.

The last step in the catalytic cycle for methanol collection can be generally performed by using either liquid water or vapor stream. It was demonstrated that similar amounts of methanol could be collected with different extraction methods.<sup>20,25</sup> In the off-line extraction protocol, strong methanol adsorption on the zeolite surface can aggravate methanol extraction.<sup>32,33</sup> Indeed, increasing the water volume used for extraction from 5 mL to 10 mL per reaction batch (0.6 g of calcined catalyst) led to a notable further increase of extracted methanol (Figure 4). However, a further increase in the amount of water yielded no further improvement in the amount of methanol. In addition, an extraction protocol using a wet N<sub>2</sub> flow was performed for 8 h. It was observed that a very low amount of methanol (8  $\mu\text{mol g}_{\text{cat}}^{-1}$ ) was collected in the cold trap, compared to 55.3  $\mu\text{mol g}_{\text{cat}}^{-1}$  of methanol obtained from extraction in 10 mL of liquid water. After the online extraction, the water-saturated N<sub>2</sub> flow was switched off and the reactor was cooled to room temperature. A further extraction by liquid water was performed with the catalyst. Methanol was still found after the extraction, confirming that activated methane species are indeed strongly adsorbed at the catalyst surface. Therefore, the conditions of the extraction step should be chosen with care to obtain the maximum methanol amount that a catalytic cycle was able to produce.

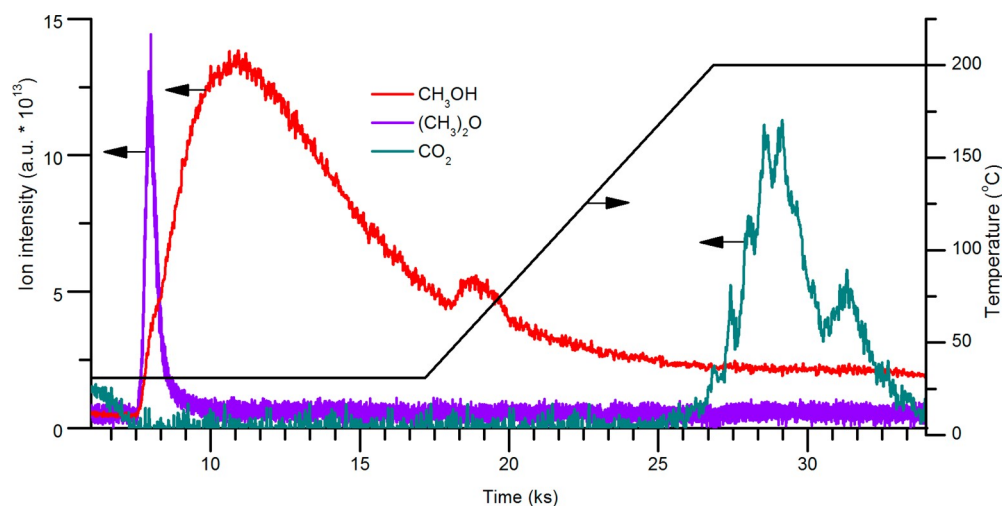


**Figure 3.** Ion intensity-based signal of  $\text{CH}_3\text{OH}$  ( $m/z = 31$ ),  $(\text{CH}_3)_2\text{O}$  ( $m/z = 46$ ), and  $\text{CO}_2$  ( $m/z = 44$ ) detected by the MS during the treatment of CuMorS-1 in a wet helium flow.

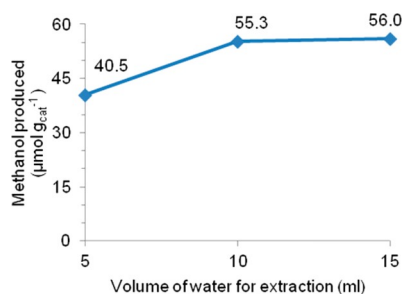


**Figure 4.** Effect of water amount for extraction on methanol production (water volumes used per reaction batch of 0.7 g of CuMorS-1).

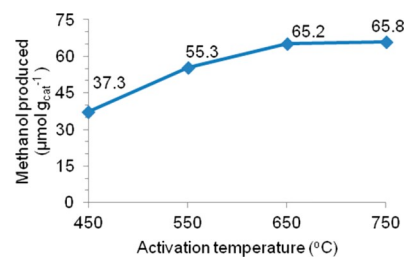


**Figure 5.** Effect of activation temperature on methanol production.

A typical MOR-type structure contains nonintersecting large 12-membered-ring (12-MR) channels ( $6.5 \text{ \AA} \times 7.0 \text{ \AA}$ ) with parallel small 8-MR channels ( $5.7 \text{ \AA} \times 2.6 \text{ \AA}$ ). The 12-MR and 8-MR pores are connected by small side pockets ( $3.4 \text{ \AA} \times 4.8 \text{ \AA}$ ).<sup>34–36</sup> Recent studies demonstrated that the Cu species located at 8 MR windows of the side pockets are able to produce oxygen-bridged dicopper/tricopper sites by high-temperature treatment in  $\text{O}_2$ , which were found to be reactive to methane.<sup>21,35,37,38</sup> However, it was reported that the activation step in oxygen has only minor influence on the methane-to-methanol performance.<sup>20</sup> In that work, high-temperature ( $450 \text{ }^\circ\text{C}$ ) activation of Cu/mordenite at 6 bar of oxygen even led to a decrease in methanol yield, compared to the result obtained at 1 bar of oxygen, while the effect of activation temperature was not further studied.<sup>20</sup> However, our results showed that the catalytic activity of CuMorS-1 was remarkably enhanced by raising the activation temperature up to  $650 \text{ }^\circ\text{C}$  (Figure 5). The reaction with methane at  $200 \text{ }^\circ\text{C}$  yielded  $37.3$ ,  $55.3$ , and  $65.2 \mu\text{mol g}_{\text{cat}}^{-1}$  of methanol using the catalyst CuMorS-1 activated at  $450$ ,  $550$ , and  $650 \text{ }^\circ\text{C}$ , respectively. Note that ion exchange in this study was carried out *in situ* during the activation of CuMorS-1 and the higher activation temperature might therefore also accelerate the  $\text{Cu}^{2+}$  exchange at the 8-MR side pockets, besides facilitating the formation of active Cu-oxo clusters. However, activation at  $750 \text{ }^\circ\text{C}$  results in no significant further improvement in the reaction performance, finally yielding  $65.8 \mu\text{mol g}_{\text{cat}}^{-1}$  of methanol.

To confirm the positive effect of higher activation temperatures, the same treatment was applied for a reference Cu/mordenite (CuMorL-1, 3.21 wt % Cu) prepared by liquid-phase ion exchange between Na-mordenite and copper(II) acetate. After activated at  $450 \text{ }^\circ\text{C}$ , CuMorL-1 was able to produce  $15.3 \mu\text{mol g}_{\text{cat}}^{-1}$  of methanol after treatment with methane at  $200 \text{ }^\circ\text{C}$  for 60 min and off-line extraction with 10 mL of water. This yield is in good agreement with the yields found in previous studies, in which the preparation of Cu/mordenite was performed in aqueous medium.<sup>20,23,27,39</sup> Also, in this case, a clear increase in methanol production to  $28.2 \mu\text{mol g}_{\text{cat}}^{-1}$  was observed when the activation step was carried out at  $550 \text{ }^\circ\text{C}$ . Therefore, it can be concluded that a larger number of Cu species that are sufficiently active to react with methane can be achieved at elevated activation temperatures. However, this comparison also shows that CuMorS-1 exhibits a much better catalytic performance for the partial oxidation of methane to methanol under the identical conditions than CuMorL-1, even though the Cu content in the former is significantly lower.

For a further comparison of the two ion exchange methods,  $\text{Cu}^{2+}$  cation exchange was carried out under liquid- and solid-phase conditions, using mordenites with different Si/Al ratios. At first, the similar activities of Cu/mordenites under identical conditions showed that the influence of the Si/Al ratio in zeolites on their catalytic performance seemed to be negligible (Figure 6). On the other hand, this study proves that solid-state ion exchange of  $\text{NH}_4\text{-Mor}$  with  $\text{Cu}(\text{acac})_2$  could produce more effective catalysts (CuMorS-1 and CuMorS-5) for the selective oxidation of methane to methanol. The solid-state reaction could promote the metal ion diffusion to all exchangeable charge-balancing sites in the porous zeolitic framework.<sup>40</sup>

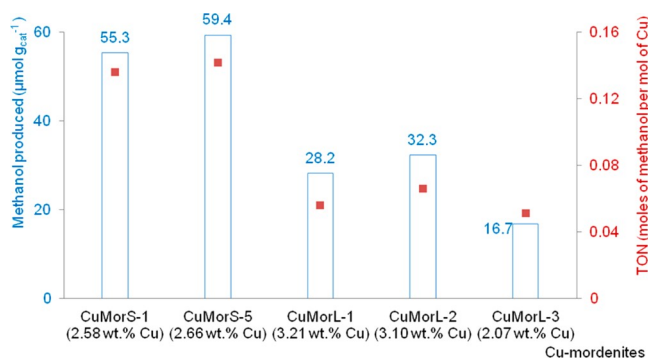


**Figure 6.** Catalytic performances of different mordenites-supported Cu catalysts.

Structural analysis of Cu/mordenites was carried out to elucidate the difference in catalytic performance. As XRD and TEM measurements show similar results for both CuMorS-1 and CuMorL-1, no conclusion for the different catalytic performances of these catalysts can be drawn from these analytic results.

Cu/mordenites after activation in O<sub>2</sub> were subjected to H<sub>2</sub>-TPR to 900 °C to determine the type and positions of Cu species located in the mordenite framework. Note that the temperature for the reduction of metal species is dependent on its stability and the accessibility of the species to H<sub>2</sub>.<sup>40–42</sup> The Cu species located at different cages in the zeolite structure have different correlative reducibility. The accessibility of the different Cu cores to H<sub>2</sub> and the activation energy for reduction change, depending on the pore size and the coordination of Cu into the framework, e.g., bulk CuO species on the surface and Cu sites the supercages are more easily reduced than Cu ions exchanged at smaller cages.<sup>40–48</sup>

The H<sub>2</sub>-TPR curves generally revealed three H<sub>2</sub> consumption features in the tested temperature range. The first reduction peaks observed for both CuMorS-1 and CuMorL-1, in the temperature range from 100 to 300 °C, were attributed to the most accessible Cu sites on the external zeolite surface and in the largest cage of mordenite, i.e., 12-MR channel (Figure 7b).<sup>40</sup> Compared to the H<sub>2</sub>-TPR profiles of bulk CuO and Cu<sub>2</sub>O (Figure 7a), these reduction peaks of Cu/mordenites are present at lower temperatures, probably due to the small size and the good dispersion of Cu clusters on mordenite.<sup>40,49,50</sup> The H<sub>2</sub> uptakes found at higher temperatures were assigned to the reduction of the less accessible Cu sites in the smaller channels (e.g., 8-MR pore, side pockets).<sup>40</sup> Particularly, CuMorL-1 exhibits only a shoulder peak for the second reduction step at ~370 °C, while a separate feature at much higher temperature (530 °C) was observed for CuMorS-1, indicating that a large number of Cu<sup>2+</sup> cations could be loaded into the ion-exchangeable positions of lower accessibility upon solid-state ion exchange. Furthermore, a broad reduction peak detected at the temperature above 750 °C for CuMorS-1 can be attributed to Cu cations highly stabilized in the zeolitic framework that can just be reduced at distinctly higher temperatures.<sup>47,49,51,52</sup> These cationic sites coordinate only with framework oxygen atoms at the small rings of zeolite (i.e., 5-MR, 6-MR) without any guest oxygen ligands.<sup>37,53–56</sup> The H<sub>2</sub> consumption at this temperature range was negligible for CuMorL-1, indicating that much more of these Cu sites exist in CuMorS-1. Although these Cu species have been described to be inactive for the activation of C–H bonding,<sup>37,57,58</sup> these

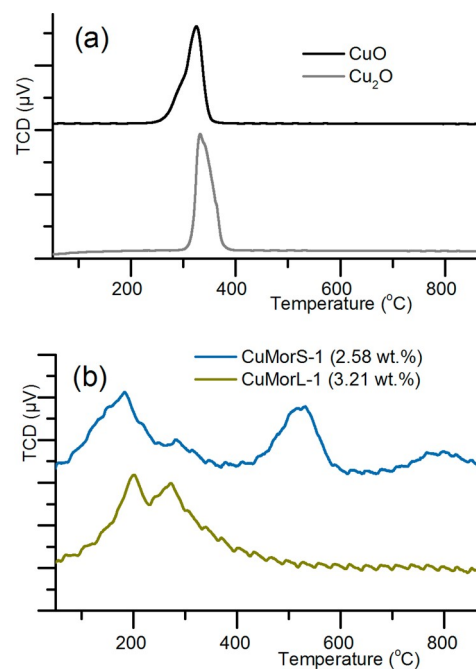


**Figure 7.** H<sub>2</sub>-TPR profiles of Cu-based materials: (a) reference copper oxides and (b) O<sub>2</sub>-activated Cu/mordenites.

results show the high efficiency of the solid-state ion exchange method for the diffusion of Cu species to small pores in mordenite. Indeed, in the dissolved aqueous state, the Cu<sup>2+</sup> cation exists as the [Cu(H<sub>2</sub>O)<sub>6</sub>]<sup>2+</sup> complex, which is too large to access the small cages of the zeolite. The efficient ion exchange at these positions as one of the most important advantages of the solid-state route was previously highlighted,<sup>28,59,60</sup> yielding a higher degree of ion exchange.<sup>29,61,62</sup> Furthermore, residual Na<sup>+</sup> cations that are always found in the Cu/zeolites prepared in an aqueous solution probably resulted in a negative impact on their catalytic performance.<sup>61,63</sup>

Further TPR measurements were carried out for CuMorS samples activated at different temperatures especially to gain further insight into the improvement of catalytic performance with increasing activation temperature (Figure 8). Increasing the activation temperature in the range from 450 °C to 650 °C led to an obvious shift of the second reduction peak to higher temperatures. This indicates an enhanced diffusion of Cu cations to the smaller pores in mordenite with increasing activation temperature. As a result, methanol production over the Cu/mordenites activated at elevated temperature was

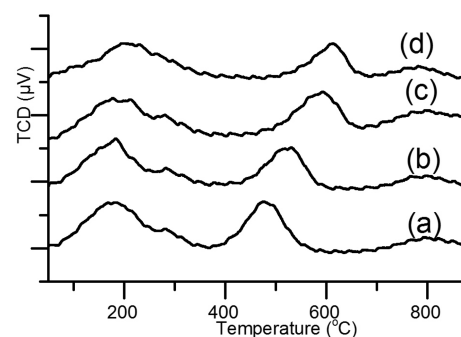


**Figure 8.** H<sub>2</sub>-TPR profiles of CuMorS-1 activated at (a) 450 °C, (b) 550 °C, (c) 650 °C, and (d) 750 °C.

significantly improved. Raising the activation temperature to 750 °C yields only a minor further increase in methanol production and indeed also just a small change in the temperature at which the second reduction occurred is observed for this material.

By using CuO TPR for calibration, it is seen that H<sub>2</sub> consumptions for the TPR experiments of CuMorS-1 (2.58 wt %) and CuMorL-1 (3.21 wt %) are close to the stoichiometric ratio for the reduction of Cu<sup>2+</sup> to Cu<sup>0</sup> (namely, 1.08 and 1.10, respectively). The small deviation, compared to the expected value (H<sub>2</sub>/Cu = 1), can be explained by the low Cu loadings in mordenite.<sup>64</sup> However, this result further verifies that the Cu species in the materials are Cu(II) species, consistent with earlier works, in which only Cu<sup>2+</sup> was found in zeolites after activation and responsible for the conversion of methane to methanol in the subsequent steps.<sup>25,31,51</sup> In addition, the oxidation state of Cu in the samples was also determined by X-ray absorption near-edge structure (XANES) analysis (see Figure S3 in the Supporting Information). No features of Cu<sup>+</sup> were observed for Cu/mordenite after activation in O<sub>2</sub>, and the spectra are completely consistent with those of Cu(II)-containing compounds.

*In situ* UV-vis spectroscopy is known as one of the most practical approaches to detect and determine the active sites in Cu/zeolites and their structural changes during the reaction. The spectroscopic region of 20000–30000 cm<sup>-1</sup> is typical for copper species that bind to extra-framework oxygen.<sup>5,65</sup> It was reported that high-temperature activation of Cu/ZSM-5 results in the appearance of a band at 22 700 cm<sup>-1</sup>, which was assigned to a mono-(μ-oxo)dicopper(II) complex ([Cu<sub>2</sub>(μ-O)]<sup>2+</sup>). The disappearance of the band after treatment with methane indeed suggests that a dinuclear Cu core is responsible for the activity of Cu/ZSM-5 toward the selective oxidation of methane to methanol.<sup>5,19,23,65–67</sup> An activated Cu/mordenite showed the same spectroscopic behavior with a band centered between 22 200 and 22 700 cm<sup>-1</sup>.<sup>27,35,40,51</sup> An additional absorption feature at 29 000 cm<sup>-1</sup> was observed on O<sub>2</sub>-activated Cu/ZSM-5 and assigned to a μ-(η<sup>2</sup>:η<sup>2</sup>)peroxy dicopper(II) site.<sup>60,65</sup> However, to date, the structure of active species formed and stabilized in Cu-exchanged zeolites has not been fully understood. Interestingly, in a study by Grundner et al., for Cu/mordenite activated in O<sub>2</sub> at 450 °C, a new broad band at about 31000 cm<sup>-1</sup> was observed while the band at ~22 700 cm<sup>-1</sup> disappeared. This observation is in accordance with the suggestion that the structure of the active clusters in the catalyst was different from those previously described.<sup>21</sup> The absence of the 22 700 cm<sup>-1</sup> band for Cu/mordenite activated at 200 °C was also reported by Tomkins et al., in which the active site was proposed to be dehydrated copper oxide clusters. This species was less active than the mono-(μ-oxo)dicopper(II) site and, therefore, only became reactive at a high methane pressure.<sup>20</sup>

UV-visible diffuse reflectance spectra of CuMorS-1 and CuMorL-1 were recorded *in situ* during activation under a 50 NmL min<sup>-1</sup> O<sub>2</sub> flow. The materials were heated from room temperature to 550 °C, then cooled to 200 °C. A band at ~33 000 cm<sup>-1</sup> with increasing intensity was observed for both catalysts (see Figure 9a and 10a). This UV-vis spectral feature is in good agreement with the finding previously reported.<sup>21</sup> Using *in situ* X-ray absorption spectroscopy (XAS) and density functional theory (DFT) calculation assisted by UV-vis analysis, it was proposed that the active sites in Cu/mordenite generated by activation in O<sub>2</sub> are trinuclear copper-oxo clusters, namely, [Cu<sub>3</sub>(μ-O)<sub>3</sub>]<sup>2+</sup>.<sup>21,68</sup> Note that even though the overall Cu

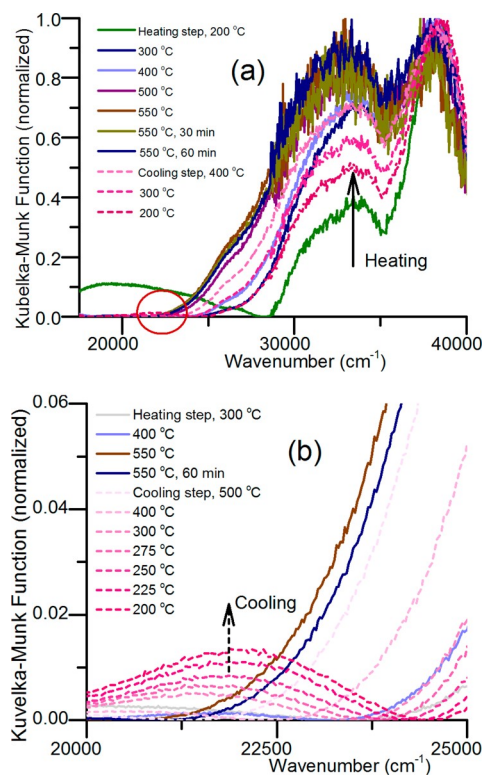


**Figure 9.** *In situ* UV-vis spectra of CuMorS-1 activated under an O<sub>2</sub> flow in the range of (a) 15 000–40 000 cm<sup>-1</sup>, (b) 20 000–25 000 cm<sup>-1</sup> (bands at 33 000 and 22 200 cm<sup>-1</sup> are indicated by the arrow).

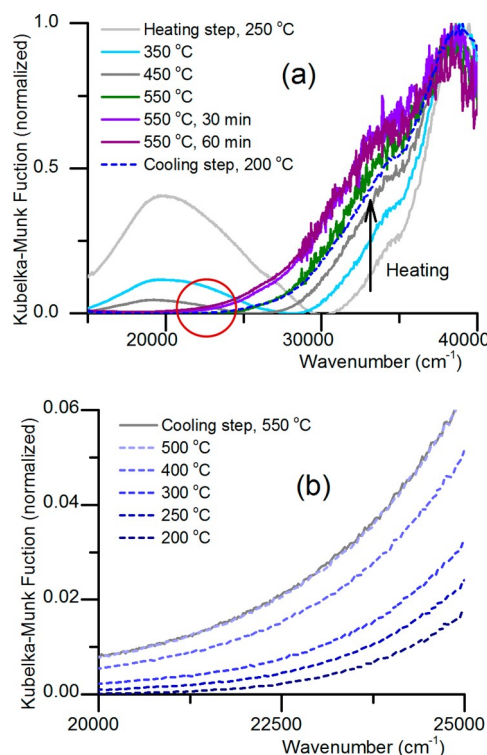


**Figure 10.** *In situ* UV-vis spectra of CuMorL-1 activated under an O<sub>2</sub> flow in the range of (a) 15 000–40 000 cm<sup>-1</sup>, (b) 20 000–25 000 cm<sup>-1</sup> (the band at 33 000 cm<sup>-1</sup> is indicated by the arrow).

content is lower in CuMorS-1, the intensity of the 33 000 cm<sup>-1</sup> band is significantly higher than that observed for CuMorL-1.

The 22 200  $\text{cm}^{-1}$  band assigned to a mono-( $\mu$ -oxo)dicopper(II) core was not detected when the materials were heated to 550  $^{\circ}\text{C}$  and the temperature was held for 1 h. However, this band was observed for CuMorS-1 when the material was cooled in an  $\text{O}_2$  atmosphere. The appearance of the band at 22 200  $\text{cm}^{-1}$  became even more obvious as the temperature decreased to  $<300$   $^{\circ}\text{C}$ . This was simultaneous with a decrease in intensity of the band centered at 33 000  $\text{cm}^{-1}$ , suggesting that a small fraction of the  $[\text{Cu}_3(\mu\text{-O})_3]^{2+}$  clusters was converted to the  $[\text{Cu}_2(\mu\text{-O})]^{2+}$  site in CuMorS-1 at low activation temperatures (Figure 9b). Vaneldegen et al. also observed the band at 22 200  $\text{cm}^{-1}$  at a low activation temperature (250  $^{\circ}\text{C}$ ) and a strong decrease in intensity by heating to  $>330$   $^{\circ}\text{C}$ .<sup>35</sup> However, the 22 200  $\text{cm}^{-1}$  feature was not found for CuMorL-1 during the cooling step (Figure 10b). Therefore, the *in situ* UV-vis results indicate that CuMorS-1 could produce a larger number of different active copper clusters than CuMorL-1, leading to a more efficient catalytic performance for the methane hydroxylation by  $\text{O}_2$ .

Furthermore, the study was extended to investigate the influence of the amount of Cu loaded in mordenite via solid-state ion exchange on the methanol production. No methanol was detected after interaction of methane with the fresh  $\text{NH}_4$  form, proving that the presence of Cu species is essential for production of methanol from methane. However, excellent performances were obtained even at low Cu loadings in mordenite. In particular, 35.7 and 51.8  $\mu\text{mol g}_{\text{cat}}^{-1}$  of methanol were produced over mordenite containing 1.01 and 1.84 wt % of Cu, respectively (Figure 11). Remarkably, the TON

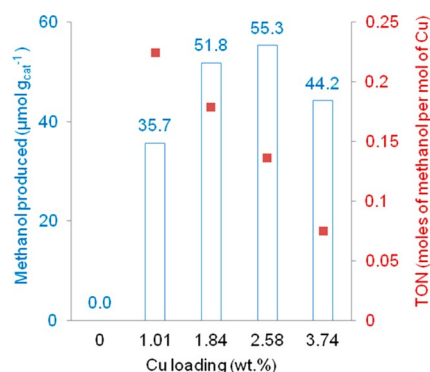


Figure 11. Effect of Cu loading on methanol production.

increased from 0.14 to 0.22 by reducing the Cu loading from 2.58 wt % to 1.01 wt %. It can be thus calculated that 44% of Cu sites in CuMorS-2 (1.01 wt % Cu) are active for activation of methane molecules based on the assumption that a mono( $\mu$ -oxo)dicopper species is responsible for the catalysis, and the proportion of active Cu sites should be 66% when a tricopper species is assumed.<sup>21,35,68</sup> However, increasing the Cu content further, from 2.58 wt % to 3.74 wt %, led to a large loss in the amount of methanol produced. We observed that, after calcination, this high-Cu-content catalyst turned gray instead of light blue as expected (see Figure S4 in the Supporting Information), indicating significant formation of larger CuO particles in mordenite.<sup>43</sup> The presence of bulk CuO is undesired in the direct hydroxylation of methane, because it is not only inactive but also could hinder the interaction of potential Cu sites with oxygen and, subsequently, methane. To explain the poor performance of 3.74 wt % CuMorS-4,  $\text{H}_2$ -TPR analysis on CuMorS catalysts with different Cu amounts were

performed. The comparative TPR profiles showed that the second reduction step occurred earlier as the Cu loading increased, indicating an impeded diffusion of Cu species to the smaller pores (see Figure S5 in the Supporting Information). Therefore, the efficiency of the catalyst based on the TON was enhanced as lower Cu loadings were applied for the preparation of Cu/mordenite via solid-state ion exchange at 550  $^{\circ}\text{C}$  in an  $\text{O}_2$  flow.

Recoverability and reusability of CuMorS-1 were studied over repeated catalytic cycles. After a multistep procedure including activation at 550  $^{\circ}\text{C}$  for 8 h in oxygen, reaction with methane at 200  $^{\circ}\text{C}$  for 1 h, and finally methanol extraction in water at room temperature, the catalyst was dried at 105  $^{\circ}\text{C}$  for 12 h and loaded in the reactor for the next cycle. No degradation in catalytic activity was observed with  $\sim 55$   $\mu\text{mol g}_{\text{cat}}^{-1}$  of methanol produced in the successive cycles (Figure 12). ICP-OES analysis showed that the Cu content in

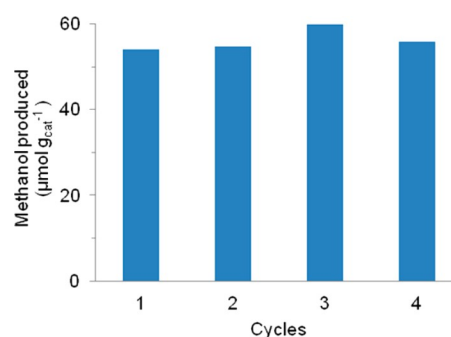


Figure 12. Recycling test.

mordenite almost remained unchanged after the fourth recycling step. XRD patterns of the reused catalyst are similar to those of the fresh mordenites and the catalyst activated in  $\text{O}_2$ .  $\text{N}_2$  adsorption measurements of the catalyst after several cycles showed an insignificant change in surface area (see Table S1 in the Supporting Information). These results indicate that the Cu sites loaded in mordenite by solid-state ion exchange are highly stable and can be reactivated for successive catalytic cycles.

#### 4. CONCLUSIONS

Cu-containing mordenite was prepared by a facile solid-state ion exchange of the  $\text{NH}_4$ -form of mordenite with  $\text{Cu}(\text{acac})_2$ . The Cu-exchanged mordenite was then used as a bioinspired solid catalyst for the partial oxidation of methane to methanol in a multistep procedure. The reaction of methane with the  $\text{O}_2$ -activated catalyst yielded high amounts of methanol upon off-line extraction in water. The improved catalytic activity of solid-state ion-exchanged Cu/mordenites, in comparison to Cu/mordenites, which have been traditionally prepared in this work via liquid ion exchange, was elucidated by *in situ* UV-vis analysis, as the spectroscopic features of activated Cu sites were detected with much higher intensity. We propose that different active clusters including dicopper- and tricopper-oxo complexes could be formed in the catalyst. In addition, TPR measurements indicated that the Cu species were located at different positions in mordenite and the  $\text{Cu}^{2+}$  cations could be exchanged to less-accessible sites in small pores of mordenite by high-temperature solid-state treatment, which probably resulted in the feasible formation of active Cu-oxo cores. The results of this study can guide synthetic approaches to further

enhance the activity of biomimetic Cu-based catalysts for the direct conversion of methane to methanol under mild conditions and provide Cu/zeolite material with great potential for obtaining more information about the Cu species on zeolite. Deeper investigation of this promising Cu/mordenite is currently carried out to clearly identify the active Cu sites formed and elucidate their changes during the catalytic cycle.

## ■ ASSOCIATED CONTENT

### Supporting Information

The Supporting Information is available free of charge on the ACS Publications website at DOI: 10.1021/acscatal.6b02372.

XRD, TEM, XANES measurements of Cu/mordenites; H<sub>2</sub>-TPR profiles of CuMorS with varied Cu loading; table summarizing porous characteristics of mordenites and Cu/mordenites (PDF)

## ■ AUTHOR INFORMATION

### Corresponding Author

\*E-mail: arne.thomas@tu-berlin.de.

### ORCID

Annette Trunschke: 0000-0003-2869-0181

Arne Thomas: 0000-0002-2130-4930

### Notes

The authors declare no competing financial interest.

## ■ ACKNOWLEDGMENTS

This work is funded by the Cluster of Excellence Unifying Concepts in Catalysis (UniCat) and was conducted in the framework of the BasCat collaboration between BASF SE, FHI, and TU Berlin. We acknowledge Christina Eichenauer for N<sub>2</sub> sorption measurements, Maria Unterweger for XRD measurements, Hamideh Ahi for help with *in situ* UV-vis experiments, and Gabriele Vetter for help with GC operation. H.V.L. would like to thank Deutscher Akademischer Austauschdienst (DAAD) for funding his Ph.D. fellowship, and Khoa D. Nguyen and Phuoc H. Ho for valuable discussions on H<sub>2</sub>-TPR.

## ■ REFERENCES

- (1) Olivos-Suarez, A. I.; Szécsényi, Á.; Hensen, E. J. M.; Ruiz-Martinez, J.; Pidko, E. A.; Gascon, J. *ACS Catal.* **2016**, *6*, 2965–2981.
- (2) Hammond, C.; Conrad, S.; Hermans, I. *ChemSusChem* **2012**, *5*, 1668–1686.
- (3) Holmen, A. *Catal. Today* **2009**, *142*, 2–8.
- (4) Palkovits, R.; von Malotki, C.; Baumgarten, M.; Müllen, K.; Baltes, C.; Antonietti, M.; Kuhn, P.; Weber, J.; Thomas, A.; Schüth, F. *ChemSusChem* **2010**, *3*, 277–282.
- (5) Wulfers, M. J.; Teketel, S.; Ipek, B.; Lobo, R. F. *Chem. Commun.* **2015**, *51*, 4447–4450.
- (6) Starokon, E. V.; Parfenov, M. V.; Arzumanov, S. S.; Pirutko, L. V.; Stepanov, A. G.; Panov, G. I. *J. Catal.* **2013**, *300*, 47–54.
- (7) Palkovits, R.; Antonietti, M.; Kuhn, P.; Thomas, A.; Schüth, F. *Angew. Chem., Int. Ed.* **2009**, *48*, 6909–6912.
- (8) Periana, R. A. *Science* **1998**, *280*, 560–564.
- (9) Guo, Z.; Liu, B.; Zhang, Q.; Deng, W.; Wang, Y.; Yang, Y. *Chem. Soc. Rev.* **2014**, *43*, 3480–3524.
- (10) Balasubramanian, R.; Smith, S. M.; Rawat, S.; Yatsunyk, L. A.; Stemmler, T. L.; Rosenzweig, A. C. *Nature* **2010**, *465*, 115–119.
- (11) Banerjee, R.; Proshlyakov, Y.; Lipscomb, J. D.; Proshlyakov, D. A. *Nature* **2015**, *518*, 431–434.
- (12) Bordeaux, M.; Galarneau, A.; Drone, J. *Angew. Chem., Int. Ed.* **2012**, *51*, 10712–10723.
- (13) Chan, S. I.; Lu, Y.-J.; Nagababu, P.; Maji, S.; Hung, M.-C.; Lee, M. M.; Hsu, I. J.; Minh, P. D.; Lai, J. C. H.; Ng, K. Y.; Ramalingam, S.; Yu, S. S. F.; Chan, M. K. *Angew. Chem., Int. Ed.* **2013**, *52*, 3731–3735.
- (14) Que, L.; Tolman, W. B. *Nature* **2008**, *455*, 333–340.
- (15) Haack, P.; Limberg, C. *Angew. Chem., Int. Ed.* **2014**, *53*, 4282–4293.
- (16) Hammond, C.; Forde, M. M.; Ab Rahim, M. H.; Thetford, A.; He, Q.; Jenkins, R. L.; Dimitratos, N.; Lopez-Sanchez, J. A.; Dummer, N. F.; Murphy, D. M.; Carley, A. F.; Taylor, S. H.; Willock, D. J.; Stangland, E. E.; Kang, J.; Hagen, H.; Kiely, C. J.; Hutchings, G. J. *Angew. Chem., Int. Ed.* **2012**, *51*, 5129–5133.
- (17) Beznis, N. V.; van Laak, A. N. C.; Weckhuysen, B. M.; Bitter, J. H. *Microporous Mesoporous Mater.* **2011**, *138*, 176–183.
- (18) Parfenov, M. V.; Starokon, E. V.; Pirutko, L. V.; Panov, G. I. *J. Catal.* **2014**, *318*, 14–21.
- (19) Sheppard, T.; Hamill, C. D.; Goguet, A.; Rooney, D. W.; Thompson, J. M. *Chem. Commun.* **2014**, *50*, 11053–11055.
- (20) Tomkins, P.; Mansouri, A.; Bozbag, S. E.; Krumeich, F.; Park, M. B.; Alayon, E. M. C.; Ranocchiaro, M.; van Bokhoven, J. A. *Angew. Chem., Int. Ed.* **2016**, *55*, 5467–5471.
- (21) Grundner, S.; Markovits, M. A. C.; Li, G.; Tromp, M.; Pidko, E. A.; Hensen, E. J. M.; Jentys, A.; Sanchez-Sanchez, M.; Lercher, J. A. *Nat. Commun.* **2015**, *6*, 7546.
- (22) Wood, B. J. *Catal.* **2004**, *225*, 300–306.
- (23) Groothaert, M. H.; Smeets, P. J.; Sels, B. F.; Jacobs, P. A.; Schoonheydt, R. A. *J. Am. Chem. Soc.* **2005**, *127*, 1394–1395.
- (24) Vanelderren, P.; Hadt, R. G.; Smeets, P. J.; Solomon, E. I.; Schoonheydt, R. A.; Sels, B. F. *J. Catal.* **2011**, *284*, 157–164.
- (25) Bozbag, S. E.; Alayon, E. M. C.; Pecháček, J.; Nachtegaal, M.; Ranocchiaro, M.; van Bokhoven, J. A. *Catal. Sci. Technol.* **2016**, *6*, 5011–5022.
- (26) Beznis, N. V.; Weckhuysen, B. M.; Bitter, J. H. *Catal. Lett.* **2010**, *138*, 14–22.
- (27) Alayon, E. M.; Nachtegaal, M.; Ranocchiaro, M.; van Bokhoven, J. A. *Chem. Commun.* **2012**, *48*, 404–406.
- (28) Abu-Zied, B. M.; Schwiager, W.; Unger, A. *Appl. Catal., B* **2008**, *84*, 277–288.
- (29) Lazar, K.; Pal-Borbely, G.; Beyer, H. K.; Karge, H. G. *J. Chem. Soc., Faraday Trans.* **1994**, *90*, 1329–1334.
- (30) Karge, H. G.; Wichterlova, B.; Beyer, H. K. *J. Chem. Soc., Faraday Trans.* **1992**, *88*, 1345–1351.
- (31) Alayon, E. M. C.; Nachtegaal, M.; Bodj, A.; van Bokhoven, J. A. *ACS Catal.* **2014**, *4*, 16–22.
- (32) Shah, R.; Gale, J. D.; Payne, M. C. *J. Phys. Chem.* **1996**, *100*, 11688–11697.
- (33) Mirth, G.; Lercher, J. A.; Anderson, M. W.; Klinowski, J. *J. Chem. Soc., Faraday Trans.* **1990**, *86*, 3039–3044.
- (34) Baerlocher, C.; McCusker, L. B.; Olson, D. H. In *Atlas of Zeolite Framework Types*, Sixth Edition; Elsevier Science B.V.: Amsterdam, 2007; pp 218–219.
- (35) Vanelderren, P.; Snyder, B. E. R.; Tsai, M.-L.; Hadt, R. G.; Vancauwenbergh, J.; Coussens, O.; Schoonheydt, R. A.; Sels, B. F.; Solomon, E. I. *J. Am. Chem. Soc.* **2015**, *137*, 6383–6392.
- (36) Liu, K.-L.; Kubarev, A. V.; Van Loon, J.; Uji-i, H.; De Vos, D. E.; Hofkens, J.; Roeffaers, M. B. J. *ACS Nano* **2014**, *8*, 12650–12659.
- (37) Kulkarni, A. R.; Zhao, Z.-J.; Siahrostami, S.; Nørskov, J. K.; Studt, F. *ACS Catal.* **2016**, *6*, 6531–6536.
- (38) Zhao, Z.-J.; Kulkarni, A.; Vilella, L.; Nørskov, J. K.; Studt, F. *ACS Catal.* **2016**, *6*, 3760–3766.
- (39) Narsimhan, K.; Michaelis, V. K.; Mathies, G.; Gunther, W. R.; Griffin, R. G.; Román-Leshkov, Y. *J. Am. Chem. Soc.* **2015**, *137*, 1825–1832.
- (40) Sainz-Vidal, A.; Balmaseda, J.; Lartundo-Rojas, L.; Reguera, E. *Microporous Mesoporous Mater.* **2014**, *185*, 113–120.
- (41) Ma, L.; Cheng, Y.; Cavataio, G.; McCabe, R. W.; Fu, L.; Li, J. *Chem. Eng. J.* **2013**, *225*, 323–330.
- (42) Sultana, A.; Nanba, T.; Sasaki, M.; Haneda, M.; Suzuki, K.; Hamada, H. *Catal. Today* **2011**, *164*, 495–499.

- (43) Pereda-Ayo, B.; De La Torre, U.; Illán-Gómez, M. J.; Bueno-López, A.; González-Velasco, J. R. *Appl. Catal., B* **2014**, *147*, 420–428.
- (44) Gentry, S. J.; Hurst, N. W.; Jones, A. J. *Chem. Soc., Faraday Trans. 1* **1979**, *75*, 1688–1699.
- (45) Liu, J.; Song, W.; Xu, C.; Liu, J.; Zhao, Z.; Wei, Y.; Duan, A.; Jiang, G. *RSC Adv.* **2015**, *5*, 104923–104931.
- (46) Qin, J.-X.; Wang, Z.-M.; Liu, X.-Q.; Li, Y.-X.; Sun, L.-B. *J. Mater. Chem. A* **2015**, *3*, 12247–12251.
- (47) Richter, M.; Fait, M.; Eckelt, R.; Schneider, M.; Radnik, J.; Heidemann, D.; Fricke, R. *J. Catal.* **2007**, *245*, 11–24.
- (48) Valverde, J.; Dorado, F.; Sánchez, P.; Asencio, I.; Romero, A. In *Interfacial Applications in Environmental Engineering*; Keane, M. A., Ed.; Marcel Dekker: New York, 2003.
- (49) Wang, L.; Li, W.; Qi, G.; Weng, D. *J. Catal.* **2012**, *289*, 21–29.
- (50) Luo, M.-F.; Fang, P.; He, M.; Xie, Y.-L. *J. Mol. Catal. A: Chem.* **2005**, *239*, 243–248.
- (51) Vanelderen, P.; Vancauwenbergh, J.; Tsai, M. L.; Hadt, R. G.; Solomon, E. I.; Schoonheydt, R. A.; Sels, B. F. *ChemPhysChem* **2014**, *15*, 91–99.
- (52) Bulánek, R.; Wichterlová, B.; Sobalík, Z.; Tichý, J. *Appl. Catal., B* **2001**, *31*, 13–25.
- (53) Sklenak, S.; Andrikopoulos, P. C.; Whittleton, S. R.; Jirglova, H.; Sazama, P.; Benco, L.; Bucko, T.; Hafner, J.; Sobalik, Z. *J. Phys. Chem. C* **2013**, *117*, 3958–3968.
- (54) Göttl, F.; Sautet, P.; Hermans, I. *Angew. Chem., Int. Ed.* **2015**, *54*, 7799–7804.
- (55) Liu, X. In *Zeolite Characterization and Catalysis*; Chester, A. W., Derouane, E. G., Eds.; Springer: Dordrecht, The Netherlands, 2009; pp 197–222.
- (56) Delabie, A.; Pierloot, K.; Groothaert, M. H.; Weckhuysen, B. M.; Schoonheydt, R. A. *Phys. Chem. Chem. Phys.* **2002**, *4*, 134–145.
- (57) Markovits, M. A. C.; Jentys, A.; Tromp, M.; Sanchez-Sanchez, M.; Lercher, J. A. *Top. Catal.* **2016**, *59*, 1554–1563.
- (58) Paolucci, C.; Parekh, A. A.; Khurana, I.; Di Iorio, J. R.; Li, H.; Albarracin Caballero, J. D.; Shih, A. J.; Anggara, T.; Delgass, W. N.; Miller, J. T.; Ribeiro, F. H.; Gounder, R.; Schneider, W. F. *J. Am. Chem. Soc.* **2016**, *138*, 6028–6048.
- (59) Townsend, R. P.; Coker, E. N. In *Studies in Surface Science and Catalysis*, Vol. 137; van Bekkum, H., Flanigen, E. M., Jacobs, P. A., Jansen, J. C., Eds.; Elsevier: Amsterdam, 2001; Ch. 11, pp 467–524.
- (60) Vanelderen, P.; Vancauwenbergh, J.; Sels, B. F.; Schoonheydt, R. A. *Coord. Chem. Rev.* **2013**, *257*, 483–494.
- (61) Karge, H. G.; Geidel, E. In *Characterization I*, Karge, H. G., Weitkamp, J., Eds.; Springer: Berlin, Heidelberg, 2004; pp 1–200.
- (62) Zhang, Y.; Drake, I. J.; Bell, A. T. *Chem. Mater.* **2006**, *18*, 2347–2356.
- (63) Grundner, S.; Luo, W.; Sanchez-Sanchez, M.; Lercher, J. A. *Chem. Commun.* **2016**, *52*, 2553–2556.
- (64) Tkachenko, O. P.; Klementiev, K. V.; van den Berg, M. W. E.; Koc, N.; Bandyopadhyay, M.; Birkner, A.; Wöll, C.; Gies, H.; Grünert, W. *J. Phys. Chem. B* **2005**, *109*, 20979–20988.
- (65) Smeets, P. J.; Hadt, R. G.; Woertink, J. S.; Vanelderen, P.; Schoonheydt, R. A.; Sels, B. F.; Solomon, E. I. *J. Am. Chem. Soc.* **2010**, *132*, 14736–14738.
- (66) Woertink, J. S.; Smeets, P. J.; Groothaert, M. H.; Vance, M. A.; Sels, B. F.; Schoonheydt, R. A.; Solomon, E. I. *Proc. Natl. Acad. Sci. U. S. A.* **2009**, *106*, 18908–18913.
- (67) Himes, R. A.; Karlin, K. D. *Proc. Natl. Acad. Sci. U. S. A.* **2009**, *106*, 18877–18878.
- (68) Li, G.; Vassilev, P.; Sanchez-Sanchez, M.; Lercher, J. A.; Hensen, E. J. M.; Pidko, E. A. *J. Catal.* **2016**, *338*, 305–312.

# Paper 4





# Chemical looping as a reactor concept for the oxidative coupling of methane over the $\text{Mn}_x\text{O}_y\text{-Na}_2\text{WO}_4/\text{SiO}_2$ catalyst, benefits and limitation

Samira Parishan<sup>a</sup>, Patrick Littlewood<sup>b</sup>, Aleks Arinchtein<sup>a</sup>, Vinzenz Fleischer<sup>a</sup>, Reinhard Schomäcker<sup>a,\*</sup>

<sup>a</sup> Technische Universität Berlin, Fakultät II, Institut für Chemie, Straße des 17. Juni 124, 10623 Berlin, Germany

<sup>b</sup> Northwestern University, Department of Chemistry, 2145 Sheridan Rd, Evanston, IL 60208, Chicago, USA

## ARTICLE INFO

### Keywords:

Oxidative coupling of methane  
 $\text{Mn}_x\text{O}_y\text{-Na}_2\text{WO}_4/\text{SiO}_2$   
 Chemical looping

## ABSTRACT

The chemical looping concept (CLC) has been implemented to suppress the formation of  $\text{CO}_x$  in an oxidative coupling of methane (OCM) reactor under a wide range of conditions. In comparison to the normal co-feeding strategy, this technique resulted in an enhanced  $\text{C}_2$  selectivity at the same methane conversions. Nevertheless, the obtained yield never exceeded 25% which is still lower than the minimum value needed for industrializing OCM. The CLC was applied in mechanistic studies to investigate the consecutive reaction of the main products of OCM, i.e. ethane and ethene. The performance of the reaction of  $\text{C}_2$  components at 750 °C in the chemical looping reactor was compared with that obtained in the co-feeding experiments. The effect of the surface adsorbed oxygen species on the reaction of both ethane and ethene was investigated. The results of these experiments reveal that some of the mechanistic assumptions about the OCM reaction are not compatible with the nature of  $\text{Mn}_x\text{O}_y\text{-Na}_2\text{WO}_4/\text{SiO}_2$ , one of the most stable and best performing catalysts known for this reaction. The yield limitation is shown to be inherent to the catalyst. However, this limitation should be solvable through the modified process concept aiming at the production of ethane in a separated first step.

## 1. Introduction

Ethene ( $\text{C}_2\text{H}_4$ ) is the building block for producing a vast range of chemicals from plastics to antifreeze and solvents. It is among the most produced organic compounds of the petrochemical industry. The market demand of ethene was more than 150 million tons in 2016 and its global growth rate is presumed to be around 3.5% over the next 5 years [1]. This chemical is usually produced in steam-cracking units from a range of petroleum-based feedstocks, such as naphtha, and therefore its production capacity and cost are strongly dependent on the availability and price of crude oil. The increasing demand for ethene [1] from the one side and the limitation in the oil reserves [2,3] from the other side make an alternative process for producing this essential compound highly desirable. Oxidative coupling of methane (OCM), which converts methane directly into  $\text{C}_2$  products and higher hydrocarbons (Eq. (1) and (2) [4,5]), may be the way to realize this aim. This reaction has received lots of attention during the last three decades, since the pioneering work of Bhasin and Keller [6]. In the OCM reaction, methane, which is a cheaper and more abundant resource than oil, is used as the feedstock for producing ethane and ethene ( $\text{C}_2$  hydrocarbons) [7].



The reaction is performed in the presence of an oxidizing agent (normally oxygen) to change the OCM process from endothermic to exothermic, which is thermodynamically preferable [4,7]. However, the presence of oxygen in the reactor also brings total and partial hydrocarbon oxidation reactions, which are thermodynamically even more favorable, in competition with the coupling reaction. In these conditions, not only methane, but also the main products of OCM, i.e.  $\text{C}_2+$  products, tend to react further and produce more of the  $\text{CO}_x$  components, see Fig. 1 [4,8–13]. Therefore, despite all the research done on OCM, the minimum yield of 30% towards  $\text{C}_2+$  products, which is required to make the reaction economically feasible, has still not been achieved.

To enhance the performance of this reaction toward  $\text{C}_2$  products, it is essential to have better control over the formation of carbon oxide components. To reach that point, the origin of the formation of  $\text{CO}_x$  should be known more precisely. There is already a consensus that carbon oxides are produced not only through the homogeneous gas

\* Corresponding author.

E-mail address: [schomaecker@tu-berlin.de](mailto:schomaecker@tu-berlin.de) (R. Schomäcker).

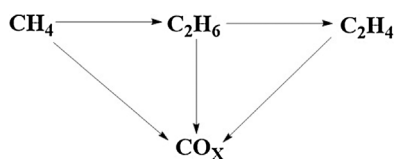


Fig. 1. Simplified reaction mechanism of OCM.

phase oxidation but also the heterogeneous catalytic oxidation of the OCM main hydrocarbons [14–21]. The occurrence of the surface reactions makes the mechanism of OCM a function of the particular catalyst in use. A vast range of metal oxide catalysts are known to activate this reaction [22,23]. The Mn<sub>x</sub>O<sub>y</sub>-Na<sub>2</sub>WO<sub>4</sub>/SiO<sub>2</sub> catalyst, which was first reported by Li [4], is known from a rich literature to be one of the most effective and stable catalysts for OCM [4,11,17,24–30]. So far, a C<sub>2</sub>+ yield of 25% has been achieved for OCM performed over this catalyst [4,31]. This promising performance has encouraged us to choose it as the model catalyst in this study.

Previous mechanistic studies have revealed two important facts regarding the formation of carbon oxides in the presence of Mn<sub>x</sub>O<sub>y</sub>-Na<sub>2</sub>WO<sub>4</sub>/SiO<sub>2</sub> catalyst [11,17]. Firstly, the results of the pump probe experiments have indicated that the oxygen is activated on the surface of the catalyst and forms either selective or unselective surface species [8]. The former species were reported to be strongly adsorbed on the surface while the latter were weakly bounded there. Therefore, purging the reactor with an inert gas was observed to remove a part of the unselective oxygen species from the surface of the catalyst while the concentration of the selective ones remained almost unchanged. Under these circumstances, an increase in the selectivity of the reaction toward the C<sub>2</sub> products was noticed [8,17]. Secondly, the total and partial oxidation of C<sub>2</sub> products rather than that of methane are revealed to be the main routes to the formation of CO<sub>x</sub> in the OCM reactor [17,32]. The secondary oxidation of C<sub>2</sub> components has been shown to mostly

occur in the presence of the gas phase oxygen [32].

The discussed mechanistic features of the reaction clearly indicate the necessity for removing both these oxygen species, those in the gas phase and the unselective weakly bounded surface species, for enhancing the performance of OCM. This can be realized by applying the chemical looping concept (CLC) to the reaction. This concept has existed for about a hundred years and is well-known for combustion processes in order to not only separate the formed carbon dioxide from nitrogen but also to avoid the formation of NO<sub>x</sub> [33–39]. To take advantage of such a reactor concept for OCM, the catalyst material needs to have the ability to provide a sufficient storage capacity for one of the reactants, in this case, oxygen. The Mn<sub>x</sub>O<sub>y</sub>-Na<sub>2</sub>WO<sub>4</sub>/SiO<sub>2</sub> catalyst is already proven to have a good oxygen storage capacity (almost 20 μmol/g<sub>cat</sub>) [40–42]. To realize this reactor concept on the laboratory scale two pneumatic pulse valves were installed at the inlet of a fixed bed reactor. All the details regarding the operation and construction of the reactor set up can be found in our recent publication [41].

The performance of oxidative coupling of methane over a wide range of reaction conditions was the first issue tested in this reactor set up [41]. Since a yield limitation of 25% was observed during these experiments, the reactor was applied for mechanistic studies to investigate the reasons causing this behaviour.

## 2. Experimental procedure

### 2.1. Catalyst preparation

All catalytic reactions were performed using Mn<sub>x</sub>O<sub>y</sub>-Na<sub>2</sub>WO<sub>4</sub>/SiO<sub>2</sub> catalyst. The preparation procedure and analytical information of the catalyst are described in detail elsewhere [32,43]. The final catalyst consists of 5 wt.% Na<sub>2</sub>WO<sub>4</sub>, 2 wt.% Mn(II) on SiO<sub>2</sub> and has a specific surface area of 3.2 m<sup>2</sup>/g and a particle size of 200–300 micrometer.

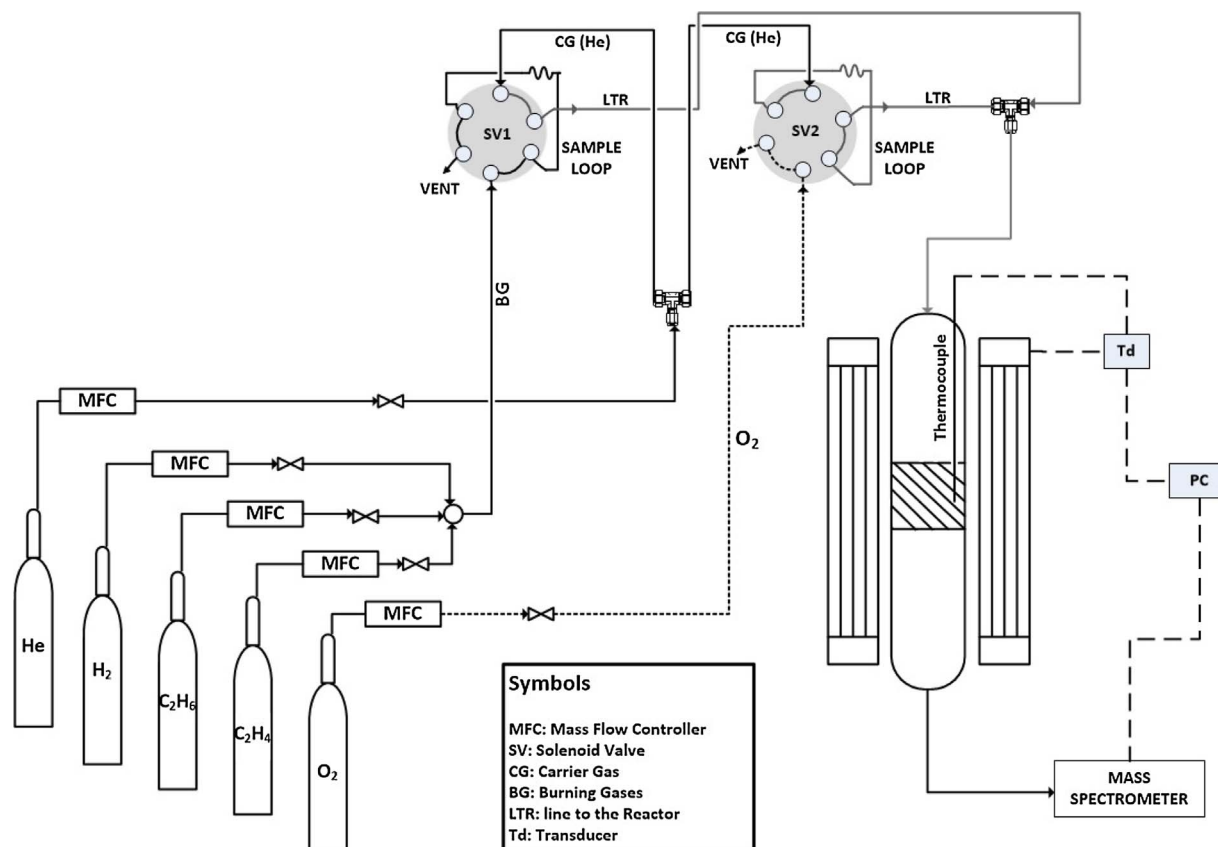


Fig. 2. Schematic of the experimental setup.

## 2.2. Feed stream

Methane (99.95%), Ethane (99.95%), Ethene (99.90%), Oxygen (99.998%) and Helium (99.999%) were purchased from Air Liquide and used in experiments as received, without further purification.

## 2.3. Simulated chemical looping experiments

The simplified schematic of the experimental setup is presented in Fig. 2. Since the reactor set up and its working procedure are explained in detail elsewhere, we have sufficed here to give only a brief description of it [41]. To simulate the chemical looping concept, two pneumatic valves, equipped with sampling loops, were installed in front of a fixed bed quartz reactor. Depending on the running experiment, sampling loops at volumes of 0.25, 0.5 or 1 ml were used to inject the gases into the reactor. One of the valves was always implemented for dosing either oxygen or hydrogen while the other one was used to inject hydrocarbons i.e. methane, ethane or ethene.

In all the experiments, a quadrupole mass spectrometer (MS) (GAM 200) was implemented to continuously measure the concentration of the effluent gas versus time in the reactor outlet.

The experiments were done using 1 g of the  $Mn_xO_y-Na_2WO_4/SiO_2$ . After placing the catalyst in the isothermal zone of the reactor (i.d. 9 mm, length 35 cm), it was heated under a fixed flow of helium to 750 °C with a rate of 10 K min<sup>-1</sup>. The flow of helium, which operated as the carrier gas and internal standard, was equally divided between the two pneumatic valves. The reason for doing the experiments with helium was to avoid any interference in its detection by MS with the other components of the reaction. Once the temperature reached 750 °C, the catalyst surface was always oxidized by injecting oxygen to the reactor. After each oxidation step, the reactor was purged with helium to remove both the remaining oxygen in the gas phase and those weakly adsorbed on the surface.

Depending on the investigated phenomenon, different experimental procedures were carried out after the first oxidation step.

To study the influence of the CLC on the reaction mechanism of C<sub>2</sub> components, the so-called chemical looping experiments were done. Under these conditions, each pulse of ethane or ethene was introduced to the reactor while the catalyst had been already fully oxidized by oxygen.

To investigate the effect of concentration of surface oxygen species on the consecutive reaction of C<sub>2</sub> components, the multi-pulse experiments were conducted. In those experiments, the oxidized catalyst was reduced by sending several pulses of reducing components (H<sub>2</sub>, ethane or ethene) without repeating the oxidation step in between.

In all the experiments, a quadrupole mass spectrometer (GAM 200) was implemented to continuously measure the concentration of the effluent gas versus time in the reactor outlet.

It should be noted that the selectivity of the reaction of C<sub>2</sub> components toward CH<sub>4</sub> is excluded from the data reported in this article. Therefore, the overall selectivity of the results reported in Tables 1 and 2, S1, S2, S3 and S4 slightly deviate from 100%.

## 3. Results and discussion

### 3.1. Effect of CLC on consecutive reactions of ethane and ethene (chemical looping tests)

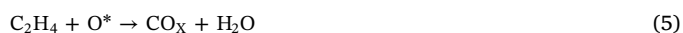
The performance of OCM at various reaction conditions over the  $Mn_xO_y-Na_2WO_4$  has already been tested in the chemical looping reactor (CLR) [41]. These results show that at the same level of methane conversion, the selectivity toward C<sub>2+</sub> products (ethane, ethene, propane, and propene) in the chemical looping reactor is higher than that measured in the co-feeding reactors. This effect is even more noticeable at lower methane conversion. However, this reactor concept didn't result in the desired yield of 30% toward the C<sub>2</sub> products which is needed for

commercializing the reaction. The origins of this limitation were investigated by studying the influence of CLC on the consecutive reaction of ethane and ethene. To do so, the catalyst bed was heated to 750 °C. Then the surface was oxidized and reduced again by sending pulses of oxygen and hydrocarbon to the reactor, respectively. The changes in the molar fraction of effluent gas obtained in these experiments using ethane and ethene as the hydrocarbon feed are presented in Figs. 3 and 4, respectively. The first pulse shown in Figs. 3 A and 4 A represents the oxygen peak recorded during the oxidation step, while the second one depicts the molar fraction of the components leaving the reactor during the reaction with the hydrocarbon. The latter peaks are enlarged and shown in Figs. 3 B and 4 B, respectively.

The reaction performance was calculated by comparing the integral of the curve of the mole fraction vs. time recorded for each component at room temperature (baseline measurement) with that during the reaction. The calculated data are presented in Tables 1 and 2 for the reaction of ethane and ethene, respectively. These results are presented in comparison to those obtained from the reaction of these components in the presence of gas phase oxygen done in a co-feeding reactor.

As the data in Tables 1 and 2 shows, the consecutive reactions of both ethane and ethene, i.e. OCM desired products, were successfully suppressed by implementing the chemical looping reactor. This effect was significantly higher for ethene where the conversion value decreased from 48% in the co-feeding reactor to 15% in the chemical looping one. Furthermore, the reaction selectivity of ethene towards CO<sub>x</sub> is lower under CLC conditions. Concerning the reaction of ethane in the chemical looping reactor, the selectivity was similarly significantly enhanced, with a selectivity of 90% toward ethene and C<sub>3</sub> products, while the selectivity of formation of carbon oxides decreased to 6%. Notably, the conversion for the reaction of ethane in both CL and Co-Feeding reactor are not that different. The reason for this behaviour is assigned to the high contribution of the non-catalytic thermal dehydrogenation of ethane to ethene and other products under the OCM reaction conditions [32,44,45].

It should be noted that the conversion of ethane to CO<sub>x</sub>, especially in the CLR, is already known to mainly occur through a sequential reaction pathway as presented in Eq. (3)–(5). Since ethene is the reaction intermediate in this conversion, the high selectivity of oxidation of C<sub>2</sub>H<sub>6</sub> in CLR in comparison to that of C<sub>2</sub>H<sub>4</sub> is assigned to the higher rate of reaction (3) and (4) in comparison to the reaction (5).



It is worth mentioning that in the ethene pulse experiment, the reverse reaction (3) and reaction (5) are the main pathways for converting ethene. However, the K<sub>eq</sub> calculated from Eq. (6) for the former reaction gave a value of 2.14 at 750 °C. This indicates that the reverse reaction (3), especially under the diluted conditions in the chemical looping reactor, is unlikely to take place. On the other side, the rate of deep oxidation reaction in the ethene pulse experiment is higher than in the ethane one. The first reason for this behaviour is the higher concentration of ethene in the reactor when it is pulsed as the reactant, in comparison to the ethane experiment, where ethene is gradually produced during the reaction. Besides, in the latter experiment, a part of the adsorbed oxygen species are consumed through the ODH reaction as presented in Eq. (4). Under these conditions, the concentration of the oxygen remaining on the surface would decrease which consequently results in a lower rate of reaction (5) in this experiment.

$$\Delta G = -RT \ln K_{eq} \quad (6)$$

These observations clearly confirm our interpretation of the mechanism of consecutive reactions of C<sub>2</sub> products [8,17,32] and show the efficiency of the CLC in suppressing the rate of unselective oxidation of

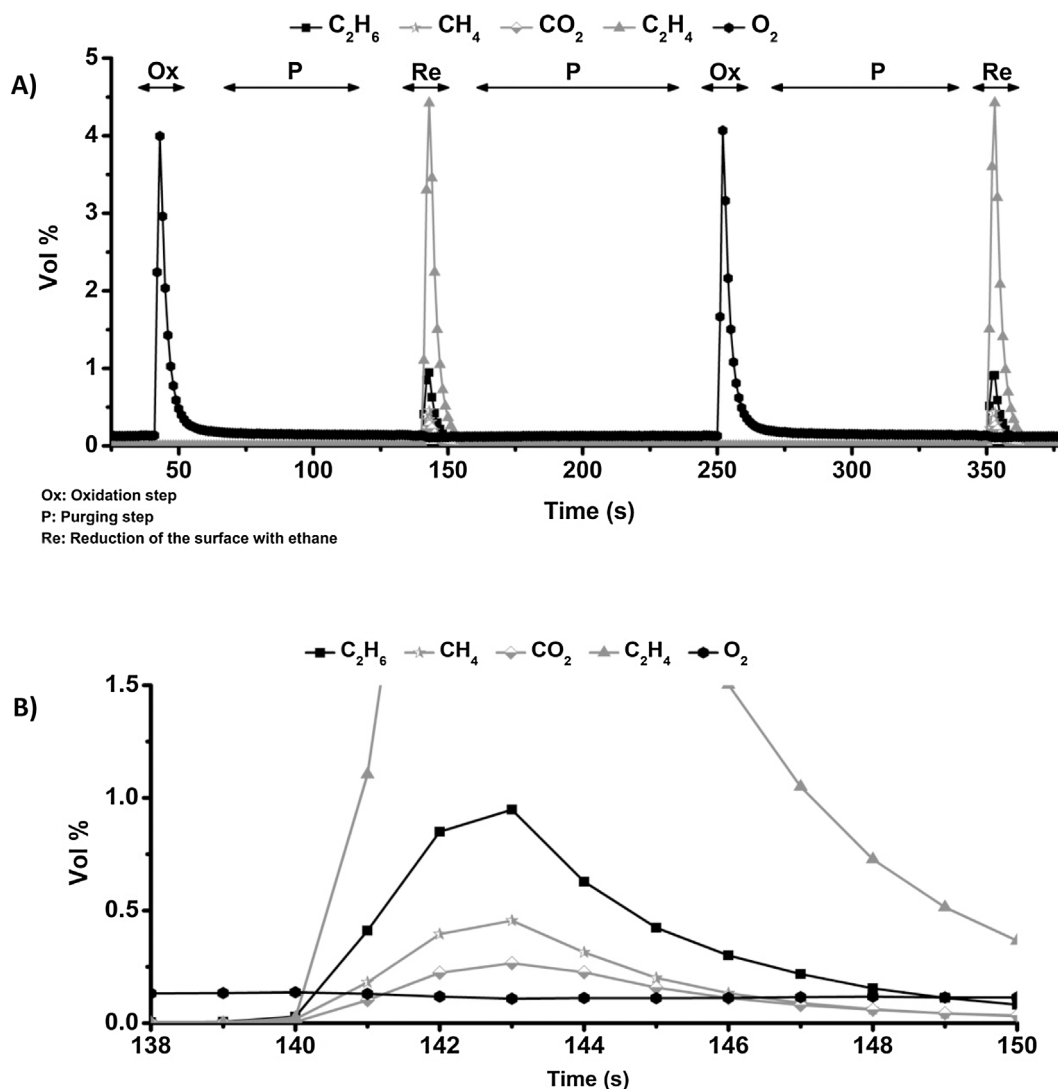


Fig. 3. Changes in the concentrations of effluent gases during the ethane pulse experiments. A) the detected peaks for the first two pulses of O<sub>2</sub> each followed with the effluent peak obtained after injection of ethane pulses to the reactor B) enlarged peak of the first reduction step. Catalyst=1 g, T=750 °C, Volume of the ethane pulse=1 ml, Carrier gas flow=25 Nml min<sup>-1</sup>.

these components. This rejects the idea that the yield barrier of OCM performed in the CLR originates from the incompatibility of this reactor concept with the reaction network of OCM and the promotion effect that it was assumed to have on the secondary oxidation of C<sub>2</sub> products.

### 3.2. Changes in the reaction performance during the multi pulse tests

The multi pulse experiments were carried out with 1 g of fresh catalyst. The reaction temperature was set to 750 °C and the catalyst was first oxidized by sending a pulse of oxygen to the reactor. Afterward, several pulses of hydrocarbons, i.e. ethane or ethene, were introduced to the surface one after the other. The oxidation step was not repeated in between the pulses.

Fig. 5 presents the changes in the concentration of the effluent gas as a function of time recorded during the ethane multi pulse experiment. For all the ethane pulses, almost the same conversion and also the same selectivity to C<sub>2+</sub> products was obtained (table S1). It is observed that, although the product species, formed after each pulse, were identical, the distribution of some of them changed with the time (Fig. 5). The most obvious difference was seen in the hydrogen concentration which shows a gradual increase throughout the whole period of the experiment. To give a better illustration of this phenomenon, the

very first and the very last peak of effluent gas shown in Fig. 5, are separately presented in Fig. 6A and B, respectively. The comparison between these two figures clearly shows that besides changes in hydrogen concentrations, the peaks of CO<sub>x</sub> also exhibit a change with time. The concentration of CO<sub>x</sub> at the end of the multipulse experiment (Fig. 6B) is lower in comparison to that after the first ethane pulse (Fig. 6A). This observation is assigned to the decrease in the concentration of the adsorbed oxygen on the catalyst surface after introducing several pulses of ethane. Under this conditions, the formation of CO<sub>x</sub> through partial and/or total oxidation reactions decrease over the time [17,32].

The increase in the hydrogen concentration is the most important observation made in this experiment, as previously mentioned. In the following paragraphs, the reasons causing this behaviour and its relation to the yield limitation of OCM reactions operated in the CLR are discussed.

As shown in Fig. 6A, the concentration of H<sub>2</sub> was quite low at the beginning of the experiment and gradually increased until it reached the same concentration as ethene during the injection of the last pulse, Fig. 6B. This behaviour does not match our mechanistic understanding of the reaction. As it was mentioned before, from our previous studies we already know that the formation of ethene in the OCM reactor is

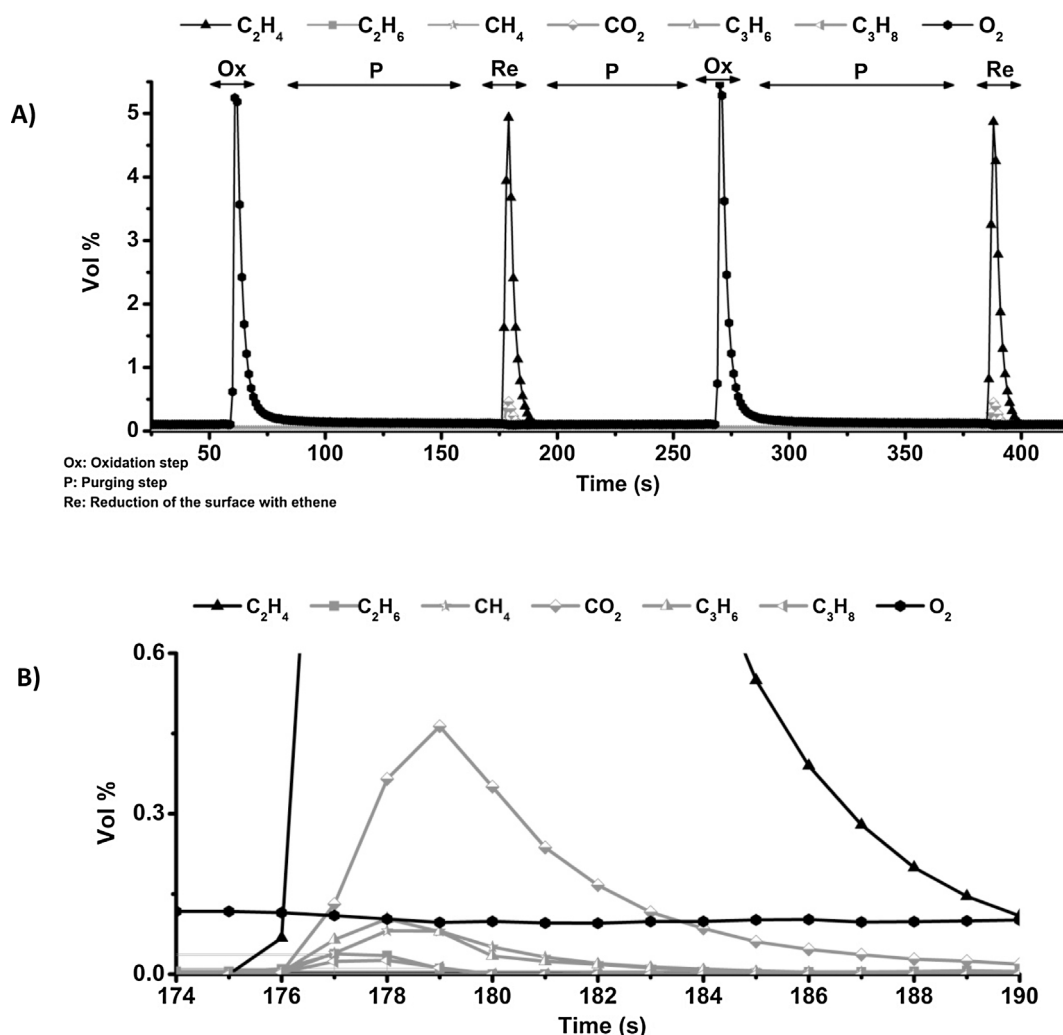


Fig. 4. Changes in the concentrations of effluent gases during the ethene pulse experiments. A) the detected peaks for the first two pulses of  $O_2$  each followed by the effluent peak obtained after injection of ethene pulses to the reactor B) enlarged peak of the first reduction step. Catalyst = 1 g,  $T = 750^\circ C$ , Volume of the ethene pulse = 1 ml, Carrier gas flow =  $25 \text{ Nml min}^{-1}$ .

mainly caused by the non-catalytic thermal dehydrogenation (TDH) of ethane, see Eq. (3) [14,26,36]. Therefore, it is expected that hydrogen, which is the coupled product of TDH, would be formed and detected at the same molar ratio as ethane for all the pulses. However, this observation was made just for the last pulses of ethane, see Fig. 5. This behaviour can be explained by the occurrence of the Eq. (7), i.e oxidation of the formed hydrogen by surface oxygen species, during the injection of the first pulses of ethane.

On the one hand, it is well known that at temperatures higher than  $700^\circ C$  the active oxygen species on the  $Mn_xO_y\text{-Na}_2WO_4$  are capable of methane dehydrogenation [4,8,13,29,46–50]. On the other hand, methane and hydrogen have been reported to have the same bond dissociation energy ( $104 \text{ kcal mol}^{-1}$  [51]). Therefore, the activation of hydrogen molecules during the injection of the first pulses, where the surface is not fully reduced, is not avoidable. The detection of water in the reactor outlet, the intensity of which levels off from each pulse to the other, is also an indication of the reaction of hydrogen with the surface oxygen species at the beginning of the experiment, see Fig. 5.

The occurrence of Eq. (7) has been studied more precisely by testing the correlation between the concentrations of the surface adsorbed oxygen species and the hydrogen peak formed through the TDH of ethane, Eq. (3). For this purpose, 1 g of the catalyst was treated exactly as explained earlier in this section. But, before introducing the ethane pulses to the reactor, the surface was reduced by sending either 1, 2 or

Table 1

comparison in the reaction performance of ethane in CLR and co-feeding experiments. The reaction conditions in the CLR: Catalyst = 1 g,  $T = 750^\circ C$ , Volume of the ethane pulse = 1 ml, Carrier gas flow =  $25 \text{ Nml min}^{-1}$ . The reaction conditions in the co-feeding reactor: TF =  $50 \text{ Nml min}^{-1}$  Catalyst = 1 g,  $T = 750^\circ C$ ,  $C_2H_6/O_2/He$  ratio = 1/1/23.

	X ( $C_2H_6$ ) %	S ( $C_2H_4$ and $C_3H_8$ ) %	S ( $CO_x$ ) %	Y ( $C_2H_4$ and $C_3H_8$ ) %	Y ( $CO_x$ ) %
CLR	82	90	6	74	5
Co-Feeding	95	50	39	47	37

Table 2

comparison in the reaction performance of ethane in CLR and co-feeding experiments. The reaction conditions in the CLR: Catalyst = 1 g,  $T = 750^\circ C$ , Volume of the ethane pulse = 1 ml, Carrier gas flow =  $25 \text{ Nml min}^{-1}$ . The reaction conditions in the co-feeding reactor: TF =  $50 \text{ Nml min}^{-1}$  Catalyst = 1 g,  $T = 750^\circ C$ ,  $C_2H_4/O_2/He$  ratio = 1/1/23.

	X ( $C_2H_4$ ) %	S ( $C_2H_6$ and $C_3H_8$ ) %	S ( $CO_x$ ) %	Y ( $C_2H_4$ and $C_3H_8$ ) %	Y ( $CO_x$ ) %
CLR	15	26	67	4	10
Co-Feeding	48	8	81	4	39

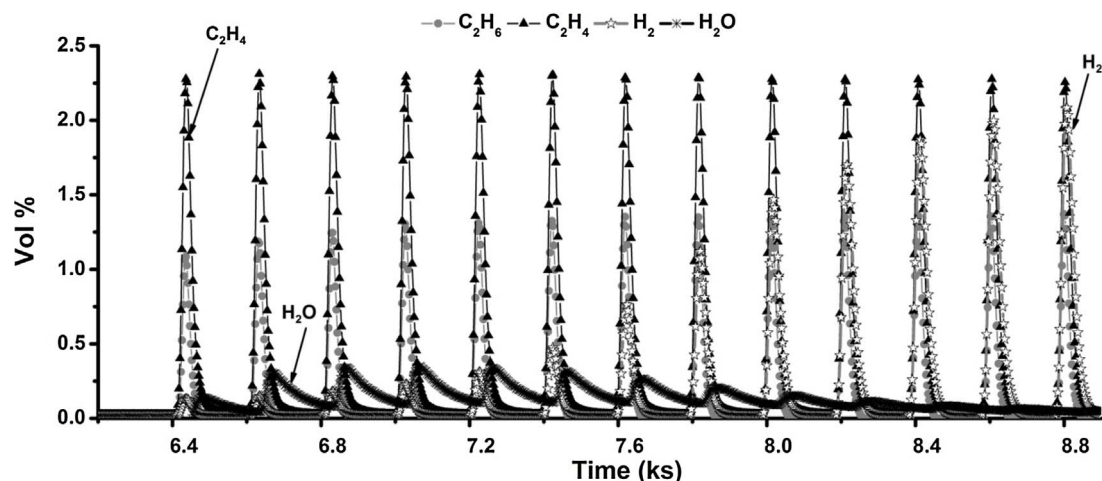
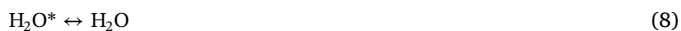


Fig. 5. The changes in the concentrations of the effluent gases during the ethane multi pulse experiment vs. time. 1 g catalyst, carrier gas flow: 25 Nml min<sup>-1</sup> of He, 0.5 ml of C<sub>2</sub>H<sub>6</sub> pulse, T = 750 °C.

4 ml of hydrogen to the reactor. The changes in the molar fraction of the effluent gas obtained in each of these experiments were recorded (Fig. S2 to S4). The reaction performance calculated for each of the ethane pulses obtained in these experiments show that the concentration of oxygen on the surface of the catalyst had negligible influence on both the conversion and selectivity (to ethene and C<sub>3</sub>H<sub>x</sub> products) of ethane reaction (Table S2 to S4). However, the intensity of the hydrogen peak of the first ethane peak in each of these experiments continuously increased with a decrease in the concentration of surface oxygen (Fig. S5). These observations strongly support the idea of the occurrence of the reaction 7 during OCM performing in the CLR.



It is important to note that this reaction is not taking place in the normal co-feeding reactors because gas phase oxygen is still present. Therefore, after the formation of H<sub>2</sub>, this quickly reacts in the gas phase through reaction 9 with a low chance of reaching over the catalyst surface. This leads to an important difference between OCM running in CLR and co-feeding reactors. In CLC reactors, hydrogen molecules compete through reaction 7 with methane molecules for reacting with the activated oxygen on the catalyst surface. Conversely, in the co-feeding reactors, the majority of the active sites are used for dehydrogenating the methane molecules. Therefore, it can be concluded that in the CLR the unreacted hydrogen has an inhibiting effect on the

conversion of methane. As a result, the yield barrier of the reaction cannot be overcome, despite the higher selectivity of OCM performed in the CLR.

All the previously discussed results suggest that, in order to successfully apply the CLR for OCM, it is vital to control the formation of hydrogen in the reactor. Fortunately, the mechanistic properties of the hydrogen formation, which will be discussed in the next section, still makes it possible to achieve this goal through applying some modifications in the reaction operating conditions.

### 3.3. Process modification

Formation of hydrogen in the OCM reactor is mainly caused by the occurrence of the TDH reaction presented in Eq. (3). The activation energy of this reaction has been calculated by running a temperature programmed experiment (TPSR) with ethane (explained in detail in our previous study) [32]. The values of ethane conversion at varying catalyst bed temperature obtained in this experiment are reported in Table S5. These data are presented in Fig. S6 and an activation energy equal to 149 KJ mol<sup>-1</sup> for the TDH reaction of ethane is calculated based on these results. This value is higher than the activation energy of methane activation on the Mn<sub>x</sub>O<sub>y</sub>-Na<sub>2</sub>WO<sub>4</sub> catalyst (with a value varying between 120 and 133 KJ mol<sup>-1</sup> [49,52]) reported in the literature. Accordingly, it can be concluded that running OCM at lower temperatures would be one of the possible approaches for enhancing the reaction performance. Because under the discussed kinetic conditions, decreasing the temperature results in an increase in the ratio of the rate of

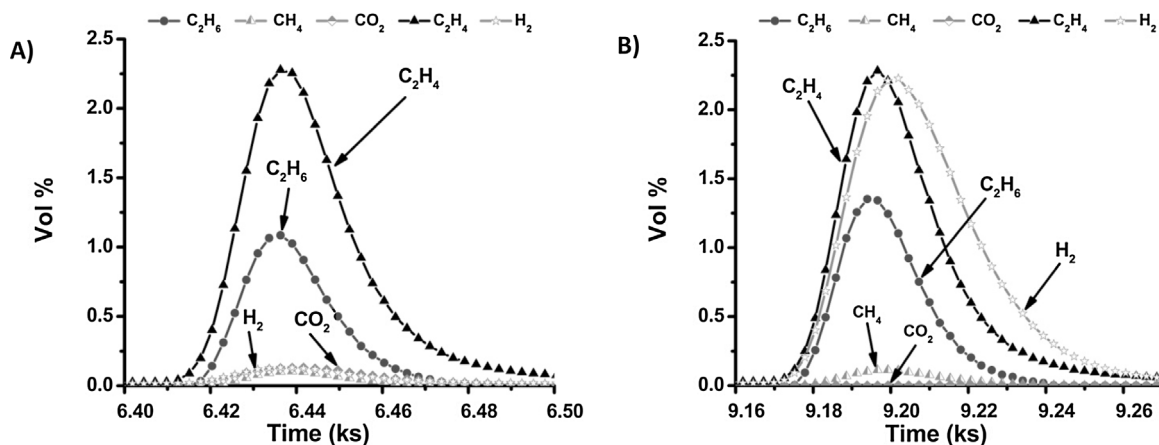


Fig. 6. The changes in the concentrations of the effluent gases in A) the very first and B) the very last peak measured during the ethane multi pulse experiment.

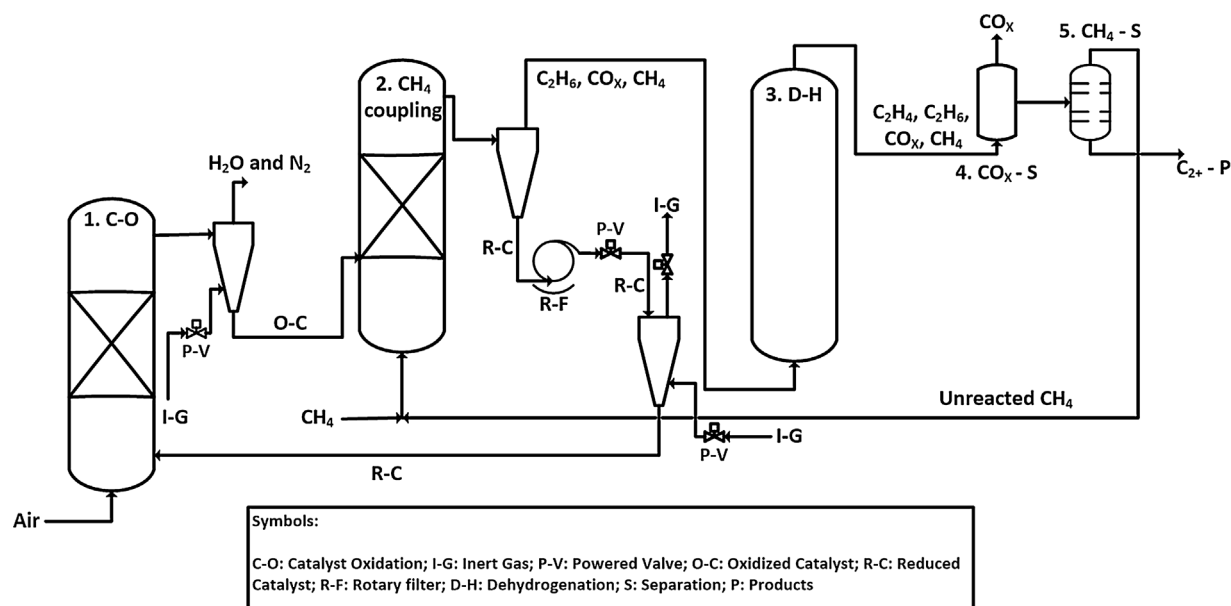


Fig. 7. schematic of the suggested process concept for doing OCM in two stages.

the coupling reaction to the TDH one. However, the major difficulty in realizing these conditions is finding a suitable catalyst. The catalyst candidate should be active enough to activate methane at lower temperature but not activate ethane, in a manner similar to the  $Mn_xO_y-Na_2WO_4$  catalyst. Fulfilling this requirement will certainly present a challenge, due to general trends in activation energies among small chain linear hydrocarbons over heterogeneous catalyst surfaces.

An alternative to kinetically controlling the rate of TDH reaction is to change the operating conditions. Since this reaction (TDH) is equilibrium controlled and the number of moles of its products is higher than the reactants, increasing the pressure causes less production of hydrogen when approaching the thermodynamic limit.

However, it should be noted that TDH of ethane is also the main route to the formation of the most valuable product of OCM, i.e. ethene. Regardless of the technique implemented, suppressing the rate of this reaction for inhibiting the formation of hydrogen and consequently saving the active site of the catalyst for methane activation would unavoidably decrease the rate of formation of ethene. Therefore, the desired process modification would only be beneficial if a two steps process would be applied to run this reaction. In the first stage, a CLR is operated where methane coupling takes place at a high selectivity. To make the CLR industrially more applicable, the purging step, needed for removing the weakly adsorbed and gas phase oxygen, is tried to be avoided in this design. To do so, the catalyst oxidation and the methane coupling steps are designed to take place in two separate fluidized bed reactors. In the first reactor, the catalyst is oxidized by the flowing air. Then the purging and separation of the catalyst are done in the cyclone installed in the reactor upstream. The cyclone is still equipped with an inert gas line to make purging possible if needed. Thereafter, the catalyst is sent to the second fluidized bed reactor where it reacts with methane before it would be recycled to the oxidation reactor. Under these conditions, continuous operation of the catalytic coupling section, which has a high priority for industrial application, can be realized.

In the methane coupling reactor, the further conversion of ethane to ethene and hydrogen either completely or partially should be suppressed. As discussed above, this aim is achievable by either running the process at elevated pressures or using a more active catalyst which allows lower reaction temperatures. Afterward, the effluent of the coupling reactor is sent to another reactor where it can be converted thermally to ethene. In the final step, the produced  $C_{2+}$  products and unconverted methane are separated from the  $CO_x$  products. Details on

the separation techniques applicable in the separation of  $CO_x$  from low chain hydrocarbons are already discussed in detail in the literature [53,54]. Afterward, the flow of hydrocarbons goes through one more separation step to separate methane from  $C_{2+}$  products. The possible separation techniques needed here is widely discussed in the literature [53–55]. Next, the separated methane is recycled to the chemical looping reactor while value added products are collected for further processing. A scheme of the discussed process concept is presented in Fig. 7.

#### 4. Conclusion

The chemical looping concept can successfully suppress the rate of unselective oxidation of OCM main hydrocarbons, i.e., methane, ethane, ethene. However, the maximum yield obtained by applying this concept to the reaction is still below the minimum value required for industrializing the process. It was observed that both the inherent nature of the  $Mn_xO_y-Na_2WO_4$  catalyst and the characteristics of the reaction mechanism cause this limitation. It is shown that the conversion of methane in the CLR is performed with a high selectivity toward the coupling reaction. This consequently results in a higher rate of formation of hydrogen in the reactor through the dehydrogenation reaction of ethane. Unlike the co-feeding reactors where the  $H_2$  converts in the presence of gas phase oxygen to water, in the CLR it competes with methane for consuming the oxygen of active centers on the catalyst surface. Under these conditions, the rate of activation of methane decreases, therefore despite the enhancement in the selectivity, the yield limitation could not be overcome.

Nevertheless, it is expected that operating the OCM reaction in the chemical looping reactor at a yield of more than 30% can still be successful. However, to reach that point it is necessary to modify the reaction conditions in a way that the rate of the coupling reaction would be enhanced while that of TDH is suppressed. To realize this goal, either the reaction should be operated at higher pressures or at temperatures lower than 750 °C. However, the decrease in the rate of TDH reaction would also result in a lower rate of formation of ethene, requiring an extra step in the process for converting ethane to ethene.

#### Acknowledgment

Financial support by the DFG (grant no. EXC 314) (UniCat Cluster of

Excellence) is gratefully acknowledged.

## Appendix A. Supplementary data

Supplementary data associated with this article can be found, in the online version, at <http://dx.doi.org/10.1016/j.cattod.2017.08.019>.

## References

- [1] The Ethylene Technology Report 2016, (2016).
- [2] N.A. Owen, O.R. Inderwildi, D.A. King, *Energy Policy* 38 (2010) 4743–4749.
- [3] U.S. Energy Information Administration, *International Energy Outlook 2016*, (2016).
- [4] S. Arndt, T. Otremba, U. Simon, M. Yildiz, H. Schubert, R. Schomäcker, *Appl. Catal. A Gen.* 425 (426) (2012) 53–61.
- [5] M.G. Colmenares, U. Simon, M. Yildiz, S. Arndt, R. Schomäcker, A. Thomas, F. Rosowski, A. Gurlo, O. Goerke, *Catal. Commun.* 85 (2016) 75–78.
- [6] G.E. Keller, M.M. Bhasin, *J. Catal.* 73 (1982) 9–19.
- [7] S. Arndt, G. Laugel, S. Levchenko, R. Horn, M. Baerns, M. Scheffler, R. Schlögl, R. Schomäcker, *Catal. Rev.* 53 (2011) 424–514.
- [8] B. Beck, V. Fleischer, S. Arndt, M.G. Hevia, A. Urakawa, P. Hugo, R. Schomäcker, *Catal. Today* 228 (2014) 212–218.
- [9] S. Sadjadi, S. Jašo, H.R. Godini, S. Arndt, M. Wollgarten, R. Blume, O. Görke, R. Schomäcker, G. Wozny, U. Simon, *Catal. Sci. Technol.* 5 (2015) 942–952.
- [10] S. Arndt, U. Simon, S. Heitz, A. Berthold, B. Beck, O. Görke, J.-D. Epping, T. Otremba, Y. Aksu, E. Irran, et al., *Top. Catal.* 54 (2011) 1266–1285.
- [11] B. Beck, V. Fleischer, S. Arndt, M.G. Hevia, A. Urakawa, P. Hugo, R. Schomäcker, *Catal. Today* 228 (2014) 212–218.
- [12] J.S. Lee, S.T. Oyama, *Catal. Rev.* 30 (1988) 249–280.
- [13] K. Takanae, E. Iglesia, *J. Phys. Chem. C* 113 (2009) 10131–10145.
- [14] J.H. Lunsford, *Angew. Chemie Int. Ed. English* 34 (1995) 970–980.
- [15] R.D. Golpasha, D. Karami, R. Ahmadi, E. Bagherzadeh, *Chem. Eng. Technol.* 16 (1993) 62–67.
- [16] Y. Feng, J. Niiranen, D. Cutman, *Phys. Chem.* 95 (1991) 6558–6563.
- [17] V. Fleischer, R. Steuer, S. Parishan, R. Schomäcker, *J. Catal.* 341 (2016) 91–103.
- [18] G.A. Martin, A. Bates, V. Ducarme, C. Mirodatos, *Appl. Catal.* 47 (1989) 287–297.
- [19] R. Burch, E.M. Crabb, G.D. Squire, S.C. Tsang, *Catal. Lett.* 2 (1989) 249–256.
- [20] M.Y. Sinev, *Catal. Today* 13 (1992) 561–564.
- [21] M.Y. Sinev, *Catal. Today* 24 (1995) 389–393.
- [22] U. Zavyalova, M. Holena, R. Schlögl, M. Baerns, *ChemCatChem* 3 (2011) 1935–1947.
- [23] E.V. Kondratenko, M. Baerns, *Hand B. Heterog. Catal.* (2004) 3010–3023.
- [24] M. Yildiz, U. Simon, T. Otremba, Y. Aksu, K. Kailasam, A. Thomas, R. Schomäcker, S. Arndt, *Catal. Today* 228 (2014) 5–14.
- [25] S. Pak, J.H. Lunsford, *Appl. Catal. A Gen.* 168 (1998) 131–137.
- [26] H. Liu, X. Wang, D. Yang, R. Gao, Z. Wang, *J. Nat. Gas Chem.* 17 (2008) 59–63.
- [27] T.P. Tiemersma, M.J. Tuinier, F. Gallucci, J. a. M. Kuipers, M.V.S. Annaland, *Appl. Catal. A Gen.* 433 (434) (2012) 96–108.
- [28] Z. Jiang, H. Gong, S. Li, *Stud. Surf. Sci. Catal.* 112 (1997) 481–490.
- [29] S. Pak, P. Qiu, J.H. Lunsford, *J. Catal.* 179 (1998) 222–230.
- [30] M. Yildiz, Y. Aksu, U. Simon, T. Otremba, K. Kailasam, C. Göbel, F. Girgsdies, O. Görke, F. Rosowski, A. Thomas, et al., *Appl. Catal. A Gen.* 525 (2016) 168–179.
- [31] H.R. Godini, A. Gili, O. Go, U. Simon, K. Hou, G. Wozny, O. Görke, U. Simon, K. Hou, G. Wozny, *Energy Fuels* 28 (2014) 877–890.
- [32] S. Parishan, E. Nowicka, V. Fleischer, M. Colmenares, R. Schomäcker, *Appl. Catal. A, Gen.* (2017) (submitted).
- [33] J. Adanez, A. Abad, F. Garcia-Labiano, P. Gayan, L.F. De Diego, *Prog. Energy Combust. Sci.* 38 (2012) 215–282.
- [34] S. Hurst, *Oil Soap* 16 (1939) 29–35.
- [35] S. Bhavsar, M. Najera, R. Solunke, G. Vesper, *Catal. Today* 228 (2014) 96–105.
- [36] H. Fang, L. Haibin, Z. Zengli, *Int. J. Chem. Eng.* 200 (2009) 9, <http://dx.doi.org/10.1155/2009/710515>.
- [37] S. Bhavsar, G. Vesper, *Ind. Eng. Chem. Res.* 52 (2013) 15342–15352.
- [38] M.M. Hossain, H.I. de Lasa, *Chem. Eng. Sci.* 63 (2008) 4433–4451.
- [39] M. Ishida, H. Jin, *Ind. Eng. Chem. Res.* 5885 (1996) 2469–2472.
- [40] E.R. Stobbe, B.A. de Boer, J.W. Geus, *Catal. Today* 47 (1999) 161–167.
- [41] V. Fleischer, P. Littlewood, S. Parishan, R. Schomäcker, *Chem. Eng. J.* 306 (2016) 646–654.
- [42] V. Fleischer, U. Simon, S. Parishan, M.G. Colmenares, O. Görke, A. Gurlo, W. Riedel, L. Thum, T. Risse, K.-P. Dinse, et al., *J. Catal.* (2017) (submitted).
- [43] U. Simon, O. Görke, A. Berthold, S. Arndt, R. Schomäcker, H. Schubert, *Chem. Eng. J.* 168 (2011) 1352–1359.
- [44] J. A. Labinger, K. C. Ottib, 1987, 2682–2684.
- [45] P.F. Nelson, C.A. Lukey, N.Q. Cant, *J. Phys. Chem.* 92 (1988) 6176–6179.
- [46] K. Takanae, E. Iglesia, *Angew. Chemie – Int. Ed.* 47 (2008) 7689–7693.
- [47] M.R. Lee, M.-J. Park, W. Jeon, J.-W. Choi, Y.-W. Suh, D.J. Suh, *Fuel Process. Technol.* 96 (2012) 175–182.
- [48] M. Daneshpayeh, A. Khodadadi, N. Mostoufi, Y. Mortazavi, R. Sotudeh-Gharebagh, A. Talebizadeh, *Fuel Process. Technol.* 90 (2009) 403–410.
- [49] S.M.K. Shahri, S.M. Alavi, *J. Nat. Gas Chem.* 18 (2009) 25–34.
- [50] M. Daneshpayeh, A. Khodadadi, N. Mostoufi, Y. Mortazavi, R. Sotudeh-Gharebagh, A. Talebizadeh, *Fuel Process. Technol.* 90 (2009) 1192.
- [51] S.J. Blanksby, G.B. Ellison, *Acc. Chem. Res.* 36 (2003) 255–263.
- [52] H.R. Godini, V. Fleischer, O. Görke, S. Jaso, R. Schomäcker, G. Wozny, *Chemie Ing Tech.* 86 (2014) 1906–1915.
- [53] Y. Khojasteh Salkuyeh, T.A. Adams, *Energy Convers. Manag.* 92 (2015) 406–420.
- [54] M.S. Salehi, M. Askarishahi, H.R. Godini, O. Görke, G. Wozny, *Ind. Eng. Chem. Res.* 55 (2016) 3287–3299.
- [55] H.-R. Godini, S. Jaso, W. Martini, S. Stünkel, D. Salerno, S.N. Xuan, S. Song, S. Sadjadi, H. Trivedi, H. Arellano-Garcia, et al., *Tech. Trans.* 109 (2012) 63–74.

**Supporting information chemical looping as a reactor concept for the oxidative coupling of methane over the  $\text{Mn}_x\text{O}_y\text{-Na}_2\text{WO}_4/\text{SiO}_2$  catalyst. benefits and limitation**

*Samira Parishan.<sup>a</sup> Patrick Littlewood.<sup>b</sup> Aleks Arinchtein<sup>a</sup>, Vinzenz Fleischer.<sup>a</sup> Reinhard Schomäcker<sup>a\*</sup>*

*<sup>a</sup> Technische Universität Berlin. Fakultät II. Institut für Chemie. Straße des 17. Juni 124. 10623 Berlin. Germany*

*<sup>b</sup> Northwestern University . Department of Chemistry. 2145 Sheridan Rd. Evanston. IL 60208. Chicago. USA*

*\* Correspondence to Prof. Reinhard Schomäcker. e-mail: [schomaecker@tu-berlin.de](mailto:schomaecker@tu-berlin.de)*

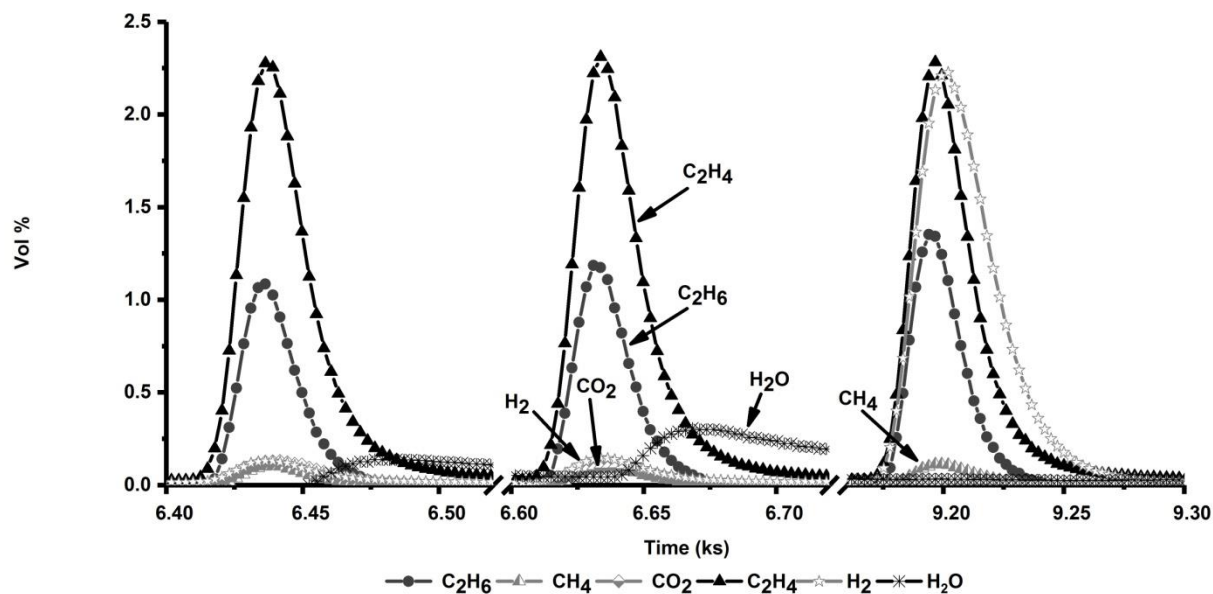


Fig. S1 The changes in the concentrations of the effluent gases in the very first, second and the very last peak measured during the ethane multi pulse experiment shown in Figure 5

Table S1 Reaction performance obtained from each pulse of ethane in multi pulse experiment (Fig. 5)

Pulse Nr	X (C <sub>2</sub> H <sub>6</sub> ) %	S (C <sub>2</sub> H <sub>4</sub> and C <sub>3</sub> H <sub>x</sub> ) %	S (CO <sub>x</sub> ) %
1	72	93	5
2	70	94	4
3	69	94	4
4	68	94	3
5	68	95	3
6	68	95	2
7	68	95	2
8	67	96	2
9	67	96	2
10	67	96	1
11	67	96	1
12	66	96	1

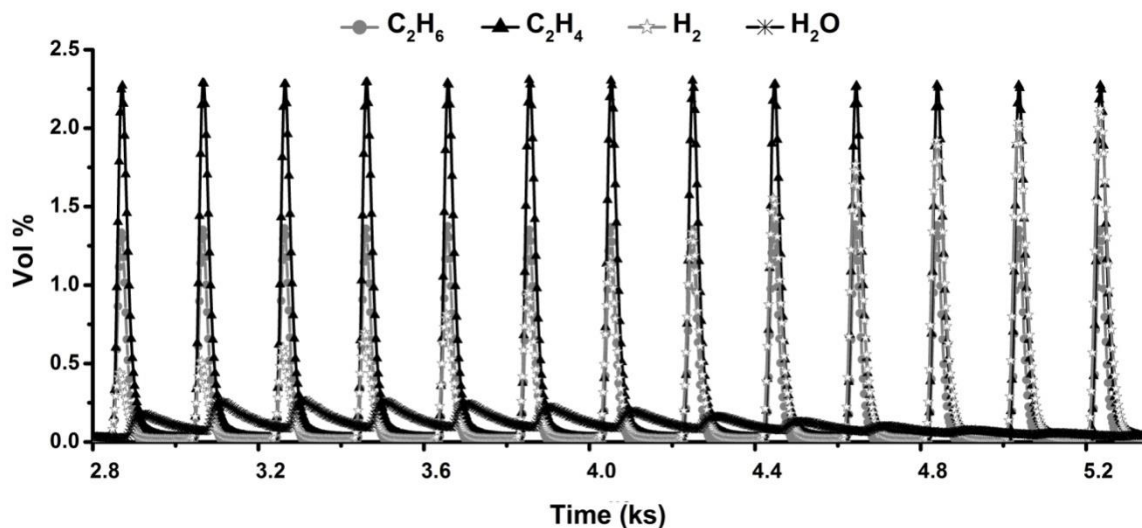


Fig. S2 The changes in the concentration of the effluent during the ethane multi pulse experiments after reducing the surface with 1 ml H<sub>2</sub> vs. time. 1g catalyst, carrier gas flow: 25 Nml/min of He, 0.5 ml of C<sub>2</sub>H<sub>6</sub> pulse, T= 750 °C

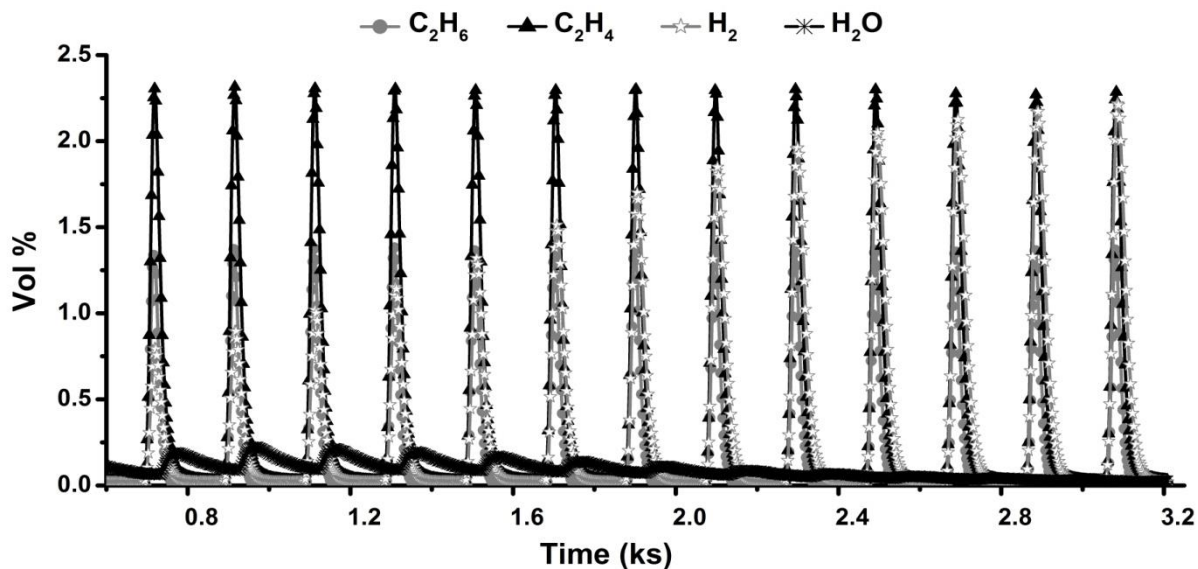
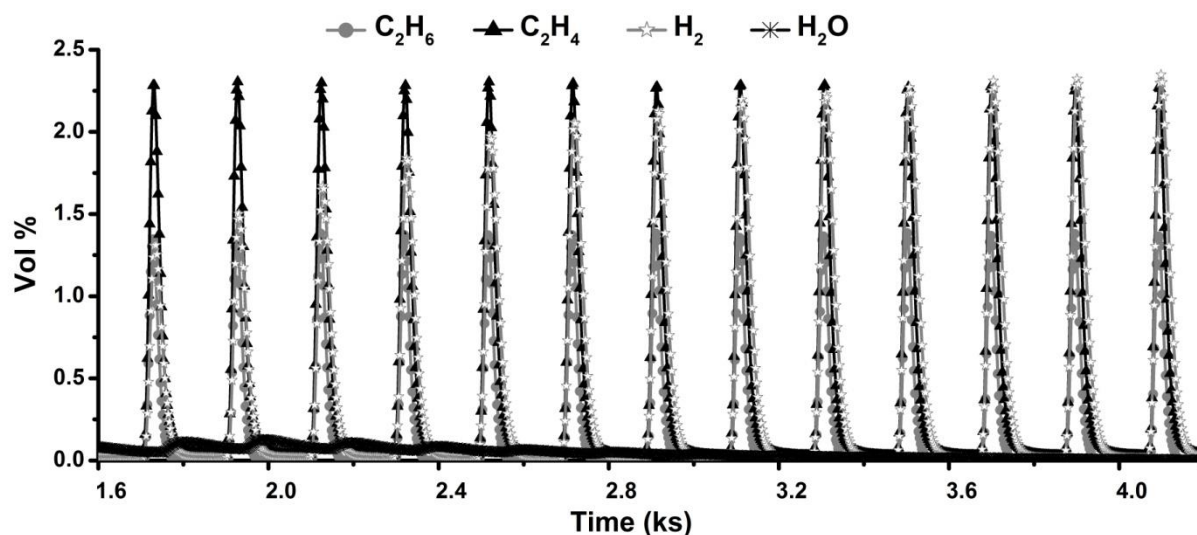


Fig. S3 The changes in the concentration of the effluent during the ethane multi pulse experiments after reducing the surface with 2 ml H<sub>2</sub> vs. time. 1g catalyst, carrier gas flow: 25 Nml/min of He, 0.5 ml of C<sub>2</sub>H<sub>6</sub> pulse, T= 750 °C



**Fig. S4** The changes in the concentration of the effluent during the ethane multi pulse experiments after reducing the surface with 4 ml H<sub>2</sub> vs. time. 1g catalyst, carrier gas flow: 25 Nml/min of He, 0.5 ml of C<sub>2</sub>H<sub>6</sub> pulse, T= 750 °C

**Table S2** Reaction performance obtained from each pulse of ethane in multi pulse experiment after reducing the surface with 1 ml H<sub>2</sub> (Fig. S2)

Pulse Nr	X (C <sub>2</sub> H <sub>6</sub> ) %	S (C <sub>2</sub> H <sub>4</sub> and C <sub>3</sub> H <sub>x</sub> ) %	S (CO <sub>x</sub> ) %
1	67	96	2
2	67	96	2
3	67	96	2
4	67	96	2
5	67	96	2
6	67	96	2
7	67	96	2
8	67	96	2
9	67	96	1
10	67	96	1
11	66	96	1
12	66	96	1
13	66	96	1

**Table S3** Reaction performance obtained from each pulse of ethane in multi pulse experiment after reducing the surface with 2 ml H<sub>2</sub> (Fig. S3)

<b>Pulse Nr</b>	<b>X (C<sub>2</sub>H<sub>6</sub>) %</b>	<b>S (C<sub>2</sub>H<sub>4</sub> and C<sub>3</sub>H<sub>x</sub>) %</b>	<b>S (CO<sub>x</sub>) %</b>
<b>1</b>	67	96	2
<b>2</b>	67	96	2
<b>3</b>	67	96	2
<b>4</b>	67	96	2
<b>5</b>	67	96	2
<b>6</b>	67	96	1
<b>7</b>	67	96	1
<b>8</b>	67	96	1
<b>9</b>	67	96	1
<b>10</b>	67	96	1
<b>11</b>	66	96	1
<b>12</b>	66	96	1
<b>13</b>	66	96	1

**Table S4** Reaction performance obtained from each pulse of ethane in multi pulse experiment after reducing the surface with 4 ml H<sub>2</sub> (Fig. S4)

<b>Pulse Nr</b>	<b>X (C<sub>2</sub>H<sub>6</sub>) %</b>	<b>S (C<sub>2</sub>H<sub>4</sub> and C<sub>3</sub>H<sub>x</sub>) %</b>	<b>S (CO<sub>x</sub>) %</b>
<b>1</b>	67	96	2
<b>2</b>	67	96	1
<b>3</b>	67	96	2
<b>4</b>	67	96	1
<b>5</b>	67	96	1
<b>6</b>	67	96	1
<b>7</b>	66	96	1
<b>8</b>	66	96	1
<b>9</b>	66	96	1
<b>10</b>	66	96	1
<b>11</b>	66	96	1
<b>12</b>	66	96	1
<b>13</b>	66	96	1

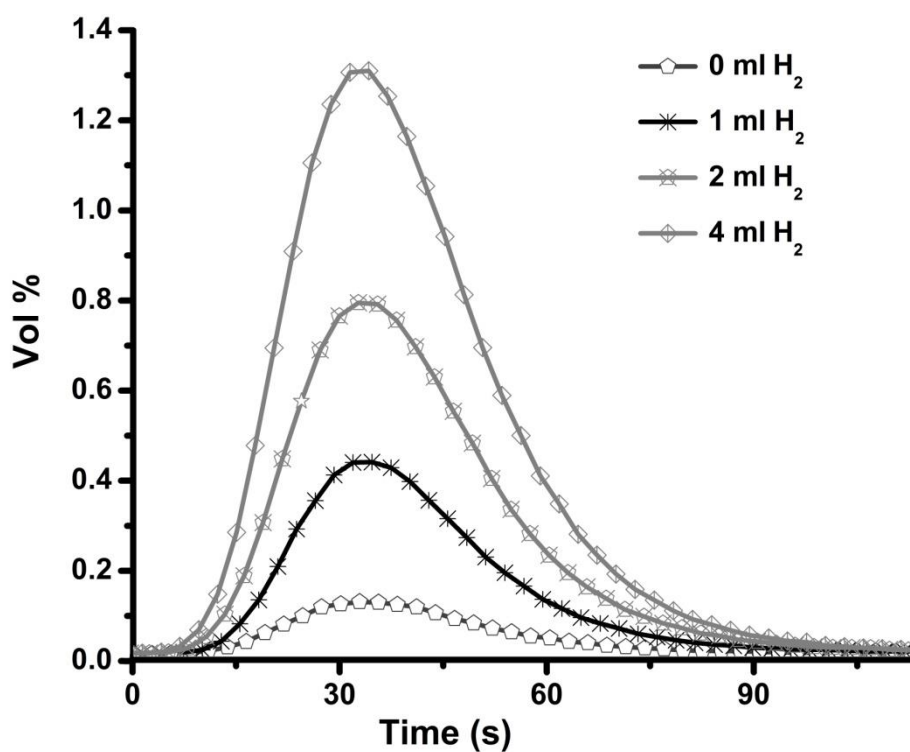


Fig. S5 Comparison of the hydrogen peak formed during the injection of the first pulse of the C<sub>2</sub>H<sub>6</sub> to the reactor when the catalyst surface is reduced with different amount of hydrogen. All the other reaction condition are the same. 1g catalyst, carrier gas flow: 25 Nml/min of He, 0.5 ml of C<sub>2</sub>H<sub>6</sub> pulse, T= 750 °C

Table S5 Conversion vs catalyst bed temperature obtained in TPSR experiment of ethane. Catalyst amount= 0.5 g, C<sub>2</sub>H<sub>6</sub>: He = 1:19 and total flow= 30 Nml min<sup>-1</sup>

T (°C)	X (C <sub>2</sub> H <sub>6</sub> %)
600	3.91
610	4.47
615	4.84
625	5.72
650	11.66

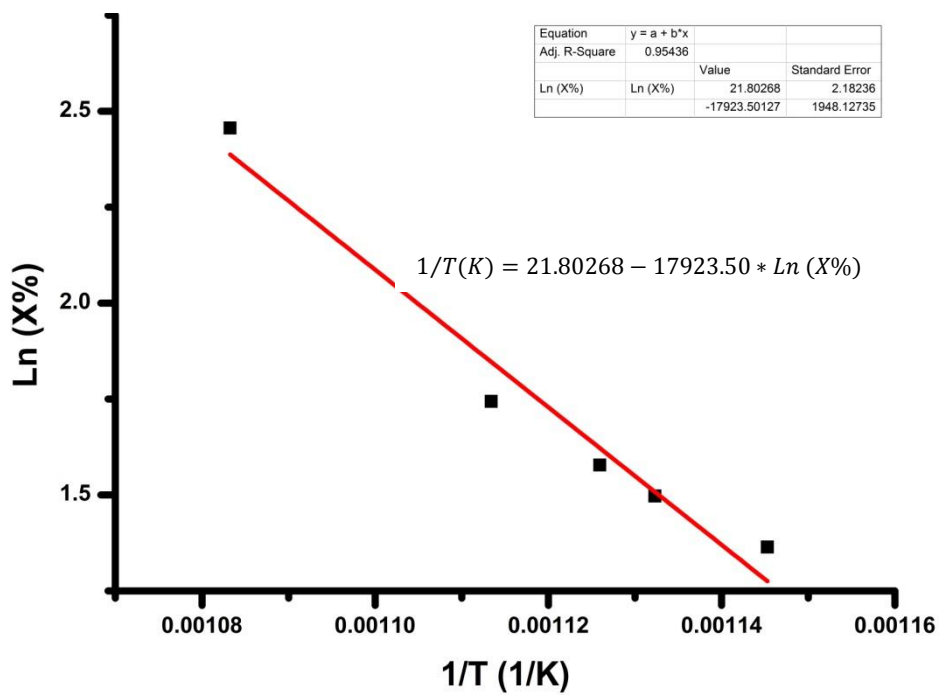


Fig. S 6 The curve of Ln (X%) vs T-1 of the data reported in Table S5

# Paper 5



# Investigation of the role of the $\text{Na}_2\text{WO}_4/\text{Mn}/\text{SiO}_2$ catalyst composition in the oxidative coupling of methane by chemical looping experiments

Vinzenz Fleischer<sup>a,1</sup>, Ulla Simon<sup>b</sup>, Samira Parishan<sup>a,1</sup>, Maria Gracia Colmenares<sup>b</sup>, Oliver Görke<sup>b</sup>, Aleksander Gurlo<sup>b</sup>, Wiebke Riedel<sup>c</sup>, Lukas Thum<sup>a</sup>, Johannes Schmidt<sup>d</sup>, Thomas Risse<sup>c</sup>, Klaus-Peter Dinse<sup>d</sup>, Reinhard Schomäcker<sup>a,\*</sup>

<sup>a</sup> Technische Universität Berlin, Institut für Chemie, Straße des 17. Juni 124, 10623 Berlin, Germany

<sup>b</sup> Fachgebiet Keramische Werkstoffe/Chair of Advanced Ceramic Materials, Institut für Werkstoffwissenschaften und -technologien, Technische Universität Berlin, Hardenbergstraße 40, 10623 Berlin, Germany

<sup>c</sup> Freie Universität Berlin, Institut für Chemie und Biochemie – Physikalische und Theoretische Chemie, Takustrasse 3, 14195 Berlin, Germany

<sup>d</sup> Technische Universität Berlin, Institut für Chemie, Fachgebiet Funktionsmaterialien Hardenbergstraße 40, 10623 Berlin, Germany

## ARTICLE INFO

### Article history:

Received 23 April 2017

Revised 18 January 2018

Accepted 19 January 2018

Available online 22 February 2018

### Keywords:

Oxidative coupling of methane

Chemical looping

Catalyst

Characterization

Oxygen storage capacity

EPR spectroscopy

XPS analysis

## ABSTRACT

A series of  $\text{Na}_2\text{WO}_4/\text{Mn}/\text{SiO}_2$  catalysts supported on mesoporous silica were prepared and tested for the oxidative coupling of methane in chemical looping experiments. The parameter variations were done for specific surface area, Mn-loading and support material. Chemical looping experiments reveal that highest catalytic activity is observed at 2 wt% Mn and 5 wt%  $\text{Na}_2\text{WO}_4$  on mesoporous silica. Repetitive methane pulse experiments allowed us to determine the oxygen uptake of the  $\text{Na}_2\text{WO}_4/\text{Mn}/\text{SiO}_2$  catalyst in chemical looping experiments. We found a correlation between oxygen storage capacity and manganese loading, which is in line with the reversible change of Mn(III) concentration observed in oxidation and reduction cycles of the material. Furthermore, we observed that ethylene formation is independent of the catalyst material in chemical looping conditions. No indication for the presence of W(V) was found.

© 2018 Elsevier Inc. All rights reserved.

## 1. Introduction

The steam cracking process, using naphtha as feedstock, is most widely utilized for ethylene production. In the last decade, the shale gas production came up as an alternative process to provide natural gas. Such gas contains different amounts of methane, ethane, and propane [1–3]. However, methane is still the major compound of shale gas, bio gas, and raw gas. Currently, methane is typically used for heat generation or energy production, but processes converting methane into more valuable chemicals are highly desirable [4–6]. The oxidative coupling of methane (OCM) is one such process to convert methane into ethane and ethylene and would hence allow utilizing the mentioned resources as additional feedstock for the formation of  $\text{C}_2$  compounds. A suitable catalyst material for this process is  $\text{Na}_2\text{WO}_4/\text{Mn}/\text{SiO}_2$ , which was introduced by Fang et al. [7]. This material shows stability and high-performance for several 100 h [8,9]. However, it was reported

that  $\text{C}_2$  yields of the OCM reaction in various reactor concepts never exceeded 0.25 [10–12]. To overcome this limitation, it is necessary to understand the mechanism of the OCM process and the functionality of this complex catalyst material.

For a better comprehension of this catalyst material, many groups carried out compound variations. Palermo et al. found that the phase transition of the support material from amorphous silica to  $\alpha$ -cristobalite is a key step for a high-performance catalyst, which can be induced by sodium ions [13]. The role of sodium in the catalytic activity was studied in more detail by exchange experiments with lithium, potassium, and cesium [14]. It was found that the  $\text{Na}_2\text{WO}_4/\text{Mn}$  film on the support material offers a high structural flexibility during the OCM process. This was due to the presence of the alkali metal ions, which offers the ability to adapt the structure to the key transition state of methyl radical formation by hydrogen abstraction [15–17]. A variation of tungsten oxide on “nano-catalysts” loading was studied by Mahmoodi et al. [18]. Exchanging tungsten by molybdenum, niobium, chromium or vanadium results in a different degree of crystallinity on the catalyst surface with decreasing ion radius of the transition metal ions. The formation of microcrystals on the catalyst surface

\* Corresponding author.

E-mail address: [schomaecker@mailbox.tu-berlin.de](mailto:schomaecker@mailbox.tu-berlin.de) (R. Schomäcker).

<sup>1</sup> Joined first authorship.

was found advantageous for C<sub>2</sub> selectivity rendering tungstate loaded catalyst the most selective one for C<sub>2</sub> production in this series. The crystallinity was directly related to the catalytic activity, which is in contrast to the findings of other groups. They reported that M–O–M and terminal M=O oxygen species from the lattice contribute to methane activation. However, the crystallization of the “nano-catalyst” is strongly affected by the presence of sodium ions [16].

The group of Mortazavi performed catalytic tests by exchanging the manganese ion by other transition metal ions in the catalysts [19]. They found that this compound is responsible for the redox reactivity potential of the catalyst material. Tuning of this potential has a tremendous influence on both C<sub>2</sub> selectivity and methane conversion. By varying the support material, Yildiz et al. showed the silica supported catalyst to have the best long-time stability as well as the highest performance in catalytic tests. Among different silica support materials, they observed the highest performance for a mesoporous structured silica catalyst [15]. The inexpensive analogue of SBA-15, COK-12, also showed good catalytic performance, which is important for industrial application [20–22]. Sadjadi et al. found that well dispersed active compounds will agglomerate under OCM conditions [23]. They also showed the presence of sodium ions to be responsible for the formation of an amorphous phase of the active compounds on the catalyst surface, which is in good agreement with the results of the Lambert group [13].

From the mechanistic point of view, the Wang group carried out detailed XPS and Raman spectroscopy studies focusing on tungsten oxide species to understand the role of the activation process [24]. EPR studies by Jiang et al. indicate that the manganese ion changes its oxidation state from + III to + II in non-steady-state experiments [25]. The latter are generated by methane reduction but can be reoxidized easily. Jiang et al. further concluded that manganese is reduced in an electron transfer from C–H bond cleavage induced by tungsten oxide. The reduction of manganese oxide was also reported to result in the formation of MnWO<sub>4</sub> [23,26]. The Na<sub>2</sub>WO<sub>4</sub>/Mn/SiO<sub>2</sub> catalyst exhibits two different oxygen species responsible for methane activation during steady-state conditions as deduced by Beck et al. from temporal analysis of products (TAP) experiments [27]. While the strongly bound oxygen species are responsible for selective methane activation, the weakly bound oxygen lead to deep oxidation products.

In our previous work, we investigated the catalyst material by temperature programmed and dynamic experiments [28]. Such experiments revealed that lattice oxygen seems to be involved in the OCM process on the Na<sub>2</sub>WO<sub>4</sub>/Mn/SiO<sub>2</sub> material, too. In addition, our results indicated that several oxygen species are stored on the catalyst material even in dynamic experiments. In another study, we could show that the involvement of lattice oxygen can be interpreted as oxygen storage function [29]. That functionality was successfully adapted for conducting OCM in a chemical looping process [29,30]. Such reactor concept allows separating parallel reaction steps in steady state operation into consecutive steps of catalyst reduction by methane conversion and subsequent catalyst reoxidation. This has the advantage that gas phase reactions induced by gas phase oxygen are excluded. In chemical looping processes, one of the most important parameters is the oxygen storage capacity [31]. The redox system of Mn(II)/Mn(III) is already known as an attractive oxygen storage system in chemical looping combustion [32].

In this work, we want to study the oxygen storage functionality and its mechanistic aspects for COK-12 supported Na<sub>2</sub>WO<sub>4</sub>/Mn/SiO<sub>2</sub> catalysts in chemical looping experiments. Furthermore, a non-ordered mesoporous silica supported catalyst will be compared. It has to be noted, that the Na<sub>2</sub>WO<sub>4</sub>/Mn/SiO<sub>2</sub> material acts as both an oxygen storage material and a catalyst, simultaneously.

An alternative mode in chemical looping experiments is the repetitive pulsing of a reactant. Such experiments will give new insights with respect to the involvement of lattice oxygen in the OCM surface reaction mechanism. For a better understanding of the pathways of stored oxygen, repetitive pulse experiments were modeled and simulated in Berkeley Madonna. Furthermore, gas phase simulations were carried out in Reaction Design Chemkin.

## 2. Experimental

### 2.1. Catalyst preparation

The catalyst support, COK-12, was synthesized in an up-scaled batch synthesis as previously described by Colmenares et al. [22]. The preparation of Na<sub>2</sub>WO<sub>4</sub>/Mn/SiO<sub>2</sub> catalysts supported on COK-12 follows the procedure described in [20] for powder catalysts. Solutions of appropriate amount of manganese (II) nitrate tetrahydrate (Merck) and sodium tungstate dihydrate (Sigma-Aldrich) were separately coated on the COK-12 support material via incipient wetness impregnation. After each impregnation step, the catalyst was dried overnight at 100 °C. Afterwards, the catalysts were annealed in air for 8 h at 800 °C with a 10 °C/min heating ramp in a muffle furnace. The Mn amount was varied from 0 to 4 wt%. In addition, catalysts with a variation in surface area were prepared by varying the annealing temperature between 750 °C and 850 °C. The COK-12 catalysts were taken as powders and were not pelletized. The reference catalyst supported on silica gel was prepared similar to the method described by Simon et al. [33]. The final 4 wt % Na<sub>2</sub>WO<sub>4</sub> and 2 wt% Mn reference catalyst had a specific surface area of 1.86 m<sup>2</sup>/g. The particle size of the SiO<sub>2</sub> support material (Davisil 636, Sigma Aldrich) was 150–350 μm.

### 2.2. Catalyst characterization

All samples were heated up to 150 °C for 24 h before nitrogen adsorption experiments were performed. The experiment was carried out in an Autosorb (Quantachrome, FL, USA) at –196.15 °C. The range of P/P<sub>0</sub> was varied from 0.05 to 0.25.

Inductively coupled plasma optical emission spectroscopy (ICP-OES) was carried out in a Horiba Scientific ICP Ultima2 (Horiba, Japan), to determine the content of Na, Mn, and W.

The X-ray powder diffraction was done with a Philips X-ray diffractometer utilizing a Bragg–Brentano geometry with a CuK<sub>α1</sub> radiation wavelength of 0.1541 nm (Philips, Germany) and a Bruker AXS D8 ADVANCE with a Bragg–Brentano geometry and a Lynx Eye 1D detector with a CuK<sub>α1</sub> radiation wavelength of 0.1541 nm (Bruker, Germany). Measurements were carried out in the range of 2θ values between 10° and 90° with a step time of 1 s and a step size of 0.02° at 40 kV and 30 mA and a step time of 370 s and a step size of 0.014° at 40 kV and 40 mA respectively. The patterns were analyzed using the Diffrac-Plus/EVA software from Bruker AXS.

XPS analysis was carried out by a Thermo Scientific K-Alpha spectrometer equipped with a monochromatic Al K<sub>α</sub> source (Thermo Scientific, Germany). The spectra were processed with Avantage software from Thermo Scientific.

EPR experiments were performed with a BRUKER ElexSys E680 spectrometer, operating in conventional continuous wave (cw) or in pulsed mode with a microwave (mw) frequency of approximately 9.5 GHz (X-band). Using cw mode detection with field modulation results in field-derivative spectra emphasizing structures with significant changes in EPR absorption, originating for instance from van Hove singularities in powder samples lacking orientational order. Such spectra were recorded for defining the total spectral range. For spectral analysis and curve fitting, we used pulse mode detection with a 2-pulse Hahn echo sequence

(Field Swept Echo detection (FSE-EPR)), by which the EPR absorption is directly displayed. The efficiency of FSE detection for the elucidation of paramagnetic species in powder samples of catalysts was recently demonstrated [34–36]. 34 GHz (Q-band) experiments were performed with a Bruker ElexSys E580 spectrometer. For Q-band experiments sample tubes of 2.9 mm o.d. were used, which were fitting in a home-built cavity (F. Lendtzian, TU Berlin). Sealed samples were prepared by cooling the catalyst after reaction to room temperature under high vacuum condition. More detailed catalyst characterizations as SEM and TEM of 4 wt% Na<sub>2</sub>WO<sub>4</sub> and 2 wt% Mn on COK 12 and silica gel are presented [20,33].

### 2.3. Catalytic performance test by chemical looping

#### 2.3.1. Single pulse experiments

A detailed description of the chemical looping setup was presented elsewhere [29]. All catalysts were tested at 700–800 °C. The absolute flow rate of the gases was 20 or 30 nml/min and the dosed amount of methane was 1 ml for each pulse. For the variation of the specific surface area, 600 mg catalyst was used for each test. The catalyst amount for the manganese and support material variation was 1 g.

The fresh catalyst was heated up at 10 °C/min under a flow rate of 30 nml/min O<sub>2</sub>: He (1:9). When reaching the reaction temperature, the reactor was purged by a flow of He (30 nml/min) until the oxygen partial pressure reached baseline level. The detection of the methane pulse was carried out by a quadrupole mass spectrometer (QMS, IPI GAM 200). The details of the calibration method were described in our previous work [28]. According to Eqs (1)–(4) methane conversion (X<sub>CH<sub>4</sub></sub>), C<sub>2</sub> selectivity (S<sub>C<sub>2</sub></sub>), and C<sub>2</sub> yield (Y<sub>C<sub>2</sub></sub>), for each methane pulse were calculated from the partial pressures of the components. The carbon balance had an accuracy of 89–99%.

$$n_i = \frac{A_{i,\text{peak}}[\% \cdot \text{s}] \cdot \dot{V} \cdot P}{R \cdot T} \quad (1)$$

$$X_{\text{CH}_4} = \frac{CH_{4,\text{in}} - CH_{4,\text{out}}}{CH_{4,\text{in}}} \quad (2)$$

$$S_{\text{C}_2} = \frac{2 \cdot C_2\text{H}_6 + 2 \cdot C_2\text{H}_4}{2 \cdot C_2\text{H}_6 + 2 \cdot C_2\text{H}_4 + \text{CO} + \text{CO}_2} \quad (3)$$

$$Y_{\text{C}_2} = X_{\text{CH}_4} \cdot S_{\text{C}_2} \quad (4)$$

This error is caused by the detection system of the mass spectrometer since the mass spectrum of methane, ethane, ethane, CO, and CO<sub>2</sub> show overlapping at several ion masses. The detection interval for the feed composition was 5 s, each. This value was a compromise between accuracy of compound detection and resolution of the pulse signal.

#### 2.3.2. Repetitive pulse experiments

Repetitive pulse experiments for each of the catalysts were carried out with 1 ml pulses of methane at 775 °C. The flow of He, the carrier gas for the pulse valve, was set at 30 nml/min. The delay between the methane pulses was chosen such that each methane pulse was fully separated from the following one. The experiment was stopped when no methane conversion was detected anymore, which was after sending about 15–25 pulses of methane to the reactor.

The methane conversion, C<sub>2</sub> selectivity and C<sub>2</sub> yield for each methane pulse were calculated as presented earlier for the single pulse experiments in Eqs. (1)–(4).

Oxygen balances for each methane pulse were calculated in two different ways. On the one hand, we calculated a methane-based oxygen balance. All detected products are based on methane

molecules, which were oxidized. We assume that all oxygen is finally converted to water or CO<sub>2</sub>. The molar amounts of products were calculated by Eq. (1) and the molar amounts of converted oxygen atoms (O\*) for each product was calculated by its oxygen stoichiometry as presented in Table 1. For instance, Eq. (5) calculates the related molar amount of converted oxygen, which is required to form the detected amounts of CO<sub>2</sub>. The total number of converted oxygen (O\*<sub>pulse</sub>, Eq. (6)) was calculated for each methane pulse. Finally, the total amounts of converted oxygen (O<sub>total</sub>) was obtained by summation of all O\*<sub>pulse</sub> as presented in Eq. (7).

$$\text{ConvertedO}^*(\text{CO}_2) = 4 \cdot n(\text{CO}_2) \quad (5)$$

$$\text{O}^*_{\text{pulse}} = 4 \cdot n(\text{CO}_2) + 1 \cdot n(\text{C}_2\text{H}_6) + 2 \cdot n(\text{C}_2\text{H}_4) + 3 \cdot n(\text{CO}) \quad (6)$$

$$\text{O}_{\text{total}} = \sum_i \text{O}^*_{\text{pulse},i} \quad (7)$$

In addition, we determined a molecule specific oxygen balance. The assumed surface reaction network for all catalysts in this study is presented in Fig. 1. This network is based on observations in our previous work [28]. In each reaction step, a certain number of oxygen atoms are being consumed to form a new molecule. Thus, the number of oxygen atoms was distinguished for each reaction step (O<sub>C<sub>2</sub>H<sub>6</sub></sub>, O<sub>C<sub>2</sub>H<sub>4</sub></sub>, O<sub>CO<sub>2</sub></sub>) and the consecutive routes were considered, too. For instance, for each ethene molecule, one O<sub>C<sub>2</sub>H<sub>6</sub></sub> and one O<sub>C<sub>2</sub>H<sub>4</sub></sub> were converted to water. For all reaction steps, we assume a second order behavior. Furthermore, we assumed that the activity of the oxygen species on the catalyst surface is not limited by mass transport effects. One limitation of this calculation is the ratio of k<sub>3</sub>/k<sub>4</sub>. Lunsford and coworkers carried out isotope labeling experiments with <sup>13</sup>C<sub>2</sub>H<sub>4</sub> [37,38]. They found that the ratio of k<sub>3</sub>/k<sub>4</sub> is between 2 and 7 at different reaction conditions. Therefore, both ratios were considered as limiting cases. The details of the mathematical calculations, modeling and simulation methods are presented in the supporting information.

The kinetic model was used to simulate 15 methane pulses. The decrease of stored oxygen (O\*<sub>pulse</sub>) was considered for each methane pulse as presented earlier. The final predicted concentrations for each pulse of the formed products (C<sub>2</sub>H<sub>6</sub>, C<sub>2</sub>H<sub>4</sub>, CO<sub>2</sub>) were used to calculate the molecule specific amounts of converted oxygen (O<sub>C<sub>2</sub>H<sub>6</sub></sub>, O<sub>C<sub>2</sub>H<sub>4</sub></sub>, O<sub>CO<sub>2</sub></sub>, C<sub>2</sub>H<sub>4</sub> and O<sub>CO<sub>2</sub>, CH<sub>4</sub></sub>), according to the finding of Lunsford and co-workers with k<sub>3</sub>/k<sub>4</sub> = 7 or 2 [37,38]. Finally, the amounts of converted oxygen for all 15 pulses were summed up (O<sub>total</sub>) and the ratio of O<sub>x</sub>/O<sub>total</sub> (x = O<sub>C<sub>2</sub>H<sub>6</sub></sub>, O<sub>C<sub>2</sub>H<sub>4</sub></sub>, O<sub>CO<sub>2</sub>, C<sub>2</sub>H<sub>4</sub></sub> or O<sub>CO<sub>2</sub>, CH<sub>4</sub></sub>) was derived, which is similar to an oxygen selectivity.

## 3. Results and discussion

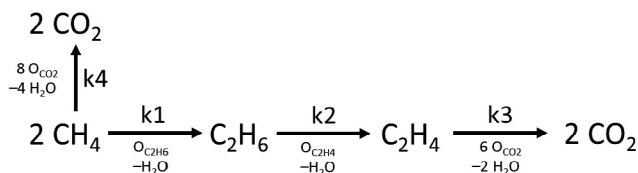
### 3.1. Results of catalyst characterization

The results of the catalysts characterization are presented in Table 2. ICP-OES results show clearly that manganese loading was successfully varied from 0 to 4 wt%, while the Na content remains approximately constant. At the lowest manganese loading, a higher specific surface area (SSA) can be observed. XRD patterns of the fresh catalyst materials prove similar crystalline phases. The main phases of the catalyst are α-cristobalite, Na<sub>2</sub>WO<sub>4</sub>, and Mn<sub>2</sub>O<sub>3</sub>, which might be also explained as braunite (MnMn<sub>6</sub>SiO<sub>12</sub>) phase, since patterns of Mn<sub>2</sub>O<sub>3</sub> and MnMn<sub>6</sub>SiO<sub>12</sub> are very similar and overlap. It should be noted that the catalyst with 0 and 0.04 w% Mn shows no reflections for manganese oxide in XRD. Some samples show also reflections of quartz.

The variation of the specific surface area (SSA) for the Na<sub>2</sub>WO<sub>4</sub>/Mn/SiO<sub>2</sub> catalyst show similar compound loadings in ICP-OES and

**Table 1**  
Chemical reactions for a methane-based oxygen balance.

No.	Reaction
1	$\text{CH}_4 + 4\text{O}^* \rightarrow \text{CO}_2 + 2\text{H}_2\text{O}$
2	$2\text{CH}_4 + \text{O}^* \rightarrow \text{C}_2\text{H}_6 + \text{H}_2\text{O}$
3	$2\text{CH}_4 + 2\text{O}^* \rightarrow \text{C}_2\text{H}_4 + 2\text{H}_2\text{O}$
4	$\text{CH}_4 + 3\text{O}^* \rightarrow \text{CO} + 2\text{H}_2\text{O}$

**Fig. 1.** Surface reaction network of the  $\text{Na}_2\text{WO}_4/\text{Mn}/\text{SiO}_2$  catalyst to determine a molecule specific oxygen balance.

crystalline phases in XRD. This is important for a comparison of this parameter and indicates that the effects observed during the catalytic tests are solely due to changes in the specific surface area. The shrinkage of the SSA is mainly caused by impregnation with  $\text{Na}_2\text{WO}_4$  and Mn and the calcination temperature, which induce a phase change of the support material. Upon  $\alpha$ -cristobalite formation, the ordered mesoporous structure of the COK-12 support material vanishes. Also, the main phase of the reference catalyst material is  $\alpha$ -cristobalite, which is important for a high-performance  $\text{Na}_2\text{WO}_4/\text{Mn}/\text{SiO}_2$  catalyst, as mentioned in the introduction.

### 3.2. Catalytic tests by chemical looping with different specific surface areas on $\text{Na}_2\text{WO}_4/\text{Mn}/\text{SiO}_2$ catalysts

#### 3.2.1. Single methane pulse experiments

It has to be noted, that an increase of the SSA, keeping the same weight loadings of the catalyst compounds, leads to a decrease in layer thickness covering the surface. The results of our chemical looping experiments with SSA variation at constant weight loadings are presented in Fig. 2. An increase of the SSA leads to a linear

increase of methane conversion, however, the sample with the highest SSA exhibits a decreased methane conversion. An inverse behavior is found for  $\text{C}_2$  selectivity, which first decreases and increases again as presented in Fig. 2B. The same results are observed at different residence times and different temperatures (see Fig. 2B and E).

The calculated BET surface area results indicate the absence of mesoporous structures. Calculation of the Weisz-Prater criteria revealed that mass transport limitation by pore diffusion can be excluded [39]. We concluded that no mass transport effects are responsible for our observations. In addition, ICP measurements showed that the composition of each material has just negligible deviation from the theoretical values.

It has to be noted, that the reaction rate in steady state experiments is much higher than the chemical looping tests. Because, in the former experiments the gas phase oxygen oxidizes the catalyst permanently, which is not the case in latter ones. Therefore, our comparison with results from steady-state experiments should be handled with care.

The rate of the reaction taking place over silica gel and COK-12 supported catalysts in the chemical looping reactor was calculated at 750 °C under a flow of 20 nml/min according to equation (8). The reaction rate for one methane pulse at the silica gel supported catalyst was  $2 \mu\text{mol}/\text{g}_{\text{cat}} \text{min}^{-1}$  and  $4 \mu\text{mol}/\text{g}_{\text{cat}} \text{min}^{-1}$  for COK-12 supported one. This observation is consistent with our earlier study where a reaction rate of  $5.2 \mu\text{mol}/\text{g}_{\text{cat}} \text{min}^{-1}$  was reported for the same reaction conducted at silica gel supported catalyst in dynamic mode but with a pure methane feed [28]. In comparison to recent steady-state experiments ( $242 \mu\text{mol}/\text{g}_{\text{cat}} \text{min}^{-1}$ ), these rates indicate limited amounts of stored oxygen in pulse experiments, which are available for the OCM reaction.

$$r_{\text{CH}_4} = \sum_{\text{products}, i} \left( \frac{n_{\text{CH}_4}(dt)}{m_{\text{cat}}} \cdot v_i \cdot \frac{dx_i}{dt} \right)_i \quad (8)$$

In steady state experiments, Yildiz et al. showed, that the increase of the SSA raises the methane conversion [40]. This is caused by more accessible active sites per gram of catalyst. Furthermore, a better distribution of the active components on the catalyst surface was reported. Such activity enhancement was also observed in our chemical looping experiments, but the decline of

**Table 2**  
Analytic results of  $\text{Na}_2\text{WO}_4/\text{Mn}/\text{SiO}_2$  catalysts, P: fresh, S: spend.

Parameters				Analysis				
Variation condition	Sample Nr	Mn (w%)	Annealing T (°C)	BET SSA (m <sup>2</sup> /g)	Crystalline phases	W (w%)	Mn (w%)	Na (w%)
Mn (COK-12)	1	0.02	800	P: 5.1 S: 3.7	Cristobalite, $\text{Na}_2\text{WO}_4$ , ( $\text{SiO}_2$ )	2.62	0.04	0.77
	2	1.00	800	P: 3.1 S: 2.6	Cristobalite, $\text{Na}_2\text{WO}_4$ , $\text{Mn}_2\text{O}_3$ /Braunite, Quartz	2.25	1.01	0.74
	3	1.90	800	P: 2.6 S: 2.6	Cristobalite, $\text{Na}_2\text{WO}_4$ ; $\text{Mn}_2\text{O}_3$ /Braunite, Quartz	2.16	1.58	0.72
	4	2.80	800	P: 2.8 S: 2.6	Cristobalite, $\text{Na}_2\text{WO}_4$ , $\text{Mn}_2\text{O}_3$ /Braunite, Quartz	2.54	2.37	0.70
	5	3.70	800	P: 3.1 S: 1.1	Cristobalite, $\text{Na}_2\text{WO}_4$ , $\text{Mn}_2\text{O}_3$ /Braunite, ( $\text{SiO}_2$ )	3.42	3.92	0.88
$A_{\text{spec}}$ (COK-12)	6	2.00	750	P: 4.2 S: 3.9	Cristobalite, $\text{Na}_2\text{WO}_4$ , $\text{Mn}_2\text{O}_3$ /Braunite	3.26	1.92	0.89
	7	2.00	775	P: 3.2 S: 3.0	Cristobalite, $\text{Na}_2\text{WO}_4$ , $\text{Mn}_2\text{O}_3$ /Braunite	3.26	1.91	0.89
	8	2.00	825	P: 2.6 S: 2.4	Cristobalite, $\text{Na}_2\text{WO}_4$ , $\text{Mn}_2\text{O}_3$ /Braunite	3.16	2.01	0.84
	9	2.00	850	P: 2.3 S: 2.1	Cristobalite, $\text{Na}_2\text{WO}_4$ , $\text{Mn}_2\text{O}_3$ /Braunite	3.02	1.96	0.83
Ref. (Silica Gel)	10	2.00	800	P: 1.9 S: 1.7	Cristobalite, $\text{Na}_2\text{WO}_4$ , $\text{Mn}_2\text{O}_3$ /Braunite	2.57	1.77	0.62

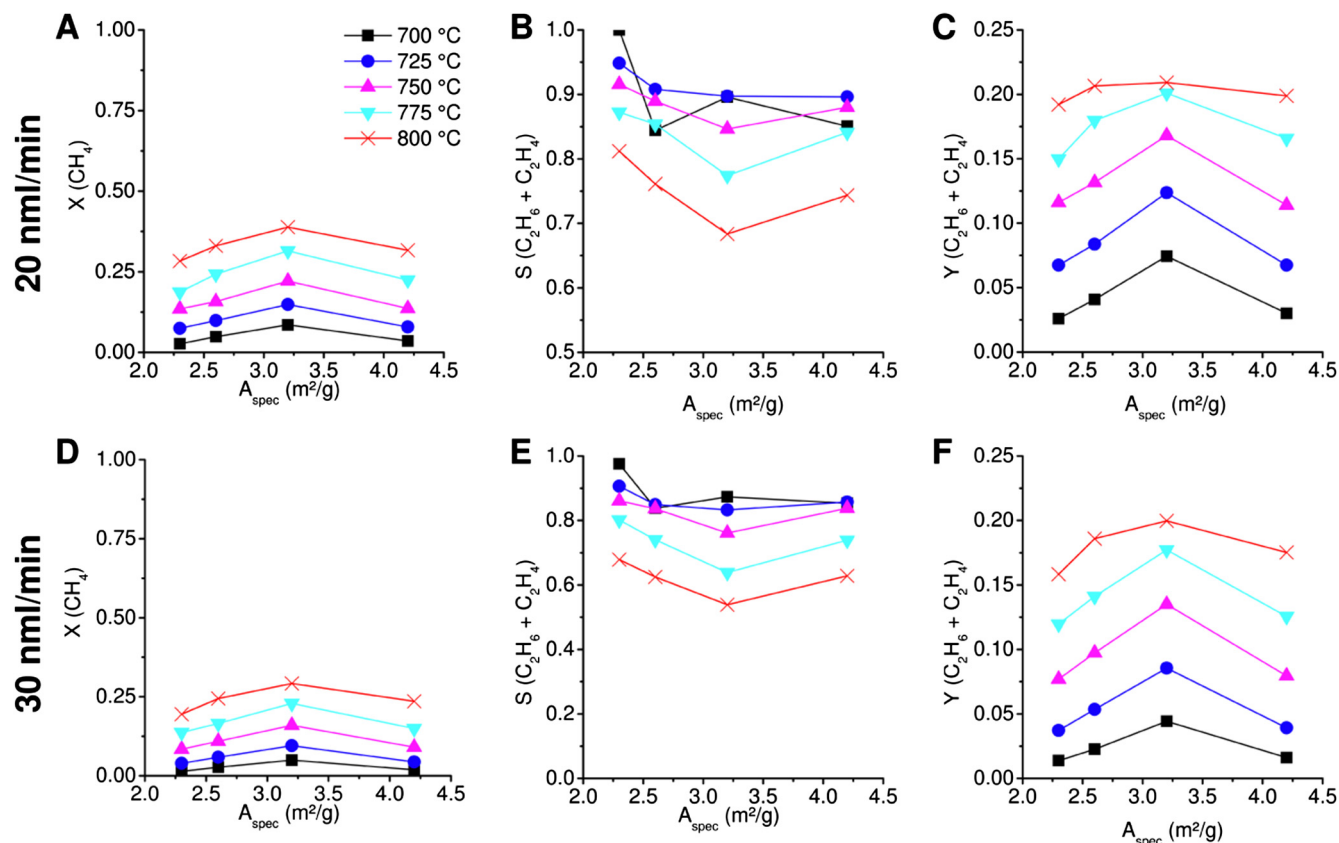


Fig. 2. Results of chemical looping experiments on  $\text{Na}_2\text{WO}_4$  (5 wt%)/Mn (2 wt%)/ $\text{SiO}_2$  catalysts with different specific surface areas at different temperatures, 0.6 g catalyst, 1 ml  $\text{CH}_4$  pulse in each experiment, A – C: methane conversion,  $\text{C}_2$  selectivity and  $\text{C}_2$  Yield at 20 nmol/min, D – F: methane conversion,  $\text{C}_2$  selectivity and  $\text{C}_2$  Yield at 30 nmol/min.

activity at our highest SSA indicates that this effect is limited and an optimal surface loading of the catalyst compounds was exceeded.

Stobbe et al. studied the reduction and oxidation behavior of supported manganese oxides on silica by temperature programmed experiments [41]. According to these results, the catalytic performance of methane oxidation depends on the degree of manganese oxide crystallinity. An additional dependence was reported for the oxidation state. The crystallinity is strongly dependent on manganese distribution on the catalyst surface. The more manganese oxide is deposited per surface area unit, the higher is the degree of crystallinity [42]. A similar relation between crystallinity and catalytic activity of such catalysts was reported in steady-state experiments, too [43]. The oxidation state of manganese oxide depends also on dispersion as shown by a Raman spectroscopy study by Buciuman et al. [44]. At low manganese loadings,  $\text{Mn}_2\text{O}_3$  is predominant, while at higher loadings  $\text{Mn}_3\text{O}_4$  is formed. At OCM reaction conditions both manganese oxide species were found to be present [41]. The transition temperature between these two species is 827 °C at 1 bar and under OCM feed gases. In temperature programmed experiments it was observed that manganese oxides are reduced quantitatively to MnO by methane, but  $\text{Mn}_2\text{O}_3$  is reduced at lower temperatures than  $\text{Mn}_3\text{O}_4$ . Therefore, both species should be active for oxygen storage on the  $\text{Na}_2\text{WO}_4$ /Mn/ $\text{SiO}_2$  catalyst for OCM reactivity. Such a change in oxidation state would also explain the results of temperature programmed desorption experiments of  $\text{O}_2$ , which indicate oxygen release at temperatures higher than 827 °C [9,28,45]. It was reported that  $\text{Na}_2\text{WO}_4$  without  $\text{Mn}_2\text{O}_3$  supported on silica also shows good performance in co-feed steady state OCM studies [13,19].

As mentioned in the introduction, the geometric structures of the deposited compounds ( $\text{Na}_2\text{WO}_4$  and Mn-oxides) observed at ambient temperatures, will significantly change under OCM conditions. Nippan, who constructed theoretical phase diagrams for the catalyst material, reported that the catalyst goes through a phase transfer under OCM reaction conditions [46]. This assumption was supported by the characterization results available in the literature [15,16,33,47]. To prove this assumption a TEM analysis was done on the reduced sample. The catalyst was quenched from 750 °C to room temperature after it was reduced with a flow of methane for more details see the SI. The reason for that was to retard the recrystallization of the melted phases as it is shown in Fig. 3, the TEM image shows a rounded particle morphology with a spread overlayer and the loss of sharp edges. The appearance of the particles is typical for a solidified material after melting. This image confirms the results of the earlier studies on the catalysts melting behavior by in-situ XRD [46] and thermal analysis [31]. Therefore, we assume that deposited material wets the surface of the support to form a homogeneous layer which behaves close to a melt or liquid phase under OCM conditions. This observation indicates a significant interaction between the active components ( $\text{Na}_2\text{WO}_4$  and Mn) and the support material. Therefore it can be concluded that the active compounds should be bound to the support stronger. The thicker the film of  $\text{Na}_2\text{WO}_4$  and Mn becomes, the larger amounts of both these components are not bound to the support material anymore.

A thickness ( $d$ ) of the layer of the molten active catalyst materials  $\text{Na}_2\text{WO}_4$  and Mn covering the support material was estimated with a simple geometric model according to Eqs. (9)–(11), where the density of the catalyst compounds was assumed to be similar to the ones of the bulk materials.

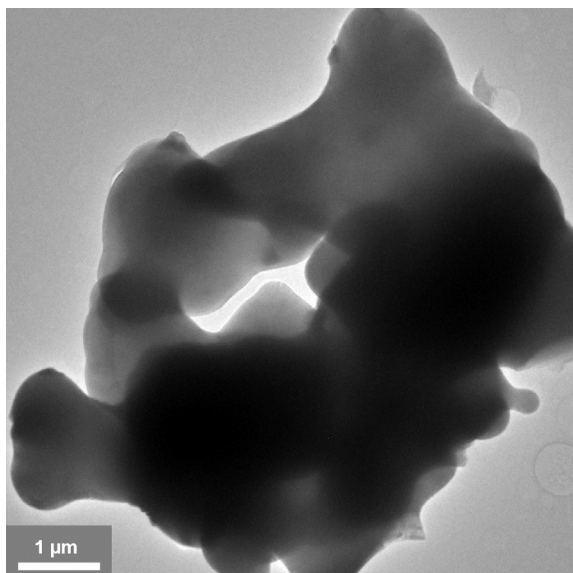


**Fig. 3.** TEM image of catalyst sample after reduction with methane and quenching from 750 °C to room temperature.

$$d(\text{Na}_2\text{WO}_4) = \frac{w\%(\text{Na}_2\text{WO}_4)}{\rho(\text{Na}_2\text{WO}_4) \cdot A_{\text{spec.cat.P}}} \quad (9)$$

$$d(\text{Mn}_2\text{O}_3) = \frac{w\%(\text{Mn}_2\text{O}_3)}{\rho(\text{Mn}_2\text{O}_3) \cdot A_{\text{spec.cat.P}}} \quad (10)$$

$$d = d(\text{Na}_2\text{WO}_4) + d(\text{Mn}_2\text{O}_3) \quad (11)$$

The results of the calculated film thickness and surface concentrations are presented in Table 3 for the fresh catalysts described in Table 2. Within a series of experiments the catalysts are ranked according to their specific surface area. The differences between the specific surface area varies by a factor of two. Especially thick films of  $\text{Na}_2\text{WO}_4$  and Mn have less surface area. We conclude that the remaining pores after calcination and phase transition to  $\alpha$ -cristobalite of the mesoporous COK-12 are filled up with the active materials by increase of the surface concentration. Therefore, a closed film of  $\text{Na}_2\text{WO}_4$  and manganese oxide provides less surface area. The theoretical number of layers (# Layers) was derived according to Eq. (12). We assumed a constant bond length  $L(\text{W-O})$  and  $L(\text{Mn-O})$  of 0.1925 nm and 0.1984 nm, respectively [48].

$$\#\text{Layer} = \frac{d(\text{Na}_2\text{WO}_4)}{L(\text{W-O})} + \frac{d(\text{Mn}_2\text{O}_3)}{L(\text{Mn-O})} \quad (12)$$

### 3.2.2. Repetitive methane pulse experiments

The results of our repetitive pulse experiments are shown in Fig. 4A–C. After six consecutive methane pulses, the methane conversion is more or less constant for each catalyst material. The  $\text{C}_2$  selectivities for each material were between 0.8 and 0.9 but it decreases with each additional methane pulse. The decrease of the  $\text{C}_2$  yield is primarily affected by the decrease of methane conversion. The results of the methane-based oxygen balances, summarized for all 15 methane pulses for each catalyst in total, are presented in Fig. 4D. Ethane and ethene formation show only minor changes for the variation of the specific surface area.  $\text{CO}_2$  formation correlates with our findings during chemical looping experiments. The more methane is converted, the more  $\text{CO}_2$  is formed. In Fig. 4E the results of the simulated repetitive experiment based on the kinetic model is presented for  $k_3/k_4 = 7$ , while Fig. 4F shows the results for  $k_3/k_4 = 2$ . The more oxygen is stored

and converted, the more oxygen is consumed by  $\text{CO}_2$  formation. This is reflected by an increase of  $\text{O}_{\text{CO}_2}$  and decrease of  $\text{O}_{\text{C}_2\text{H}_6}$ . Only a small change in all oxygen ratios can be observed when the value of  $k_3/k_4$  is changed to seven. This is caused by the high  $\text{C}_2$  selectivity of 0.8–0.9. Interestingly the fraction of  $\text{O}_{\text{C}_2\text{H}_4}$  is more or less constant in both cases.

The most active catalyst material in this set of experiments ( $\text{SSA} = 3.2 \text{ m}^2/\text{g}$ ) stores also the highest amount of oxygen. Such effect can be explained by our assumption about the thickness of the active compound layer. For a given loading low SSA results in high thickness of active layer [41]. Furthermore, the amount of stored oxygen must correlate with the amount of Mn or  $\text{Na}_2\text{WO}_4$ . A thick film of the active compounds would store most of the oxygen in its bulk phase, which is less accessible for the methane pulses. Under these circumstances, the ratio of  $\text{O}_{\text{surface}}/\text{O}_{\text{bulk}}$  is low. Therefore, oxygen availability and consequently the reactivity is expected to be lower for such a material. A decrease of the film thickness would mean that less oxygen is stored in the bulk and the ratio of  $\text{O}_{\text{surface}}/\text{O}_{\text{bulk}}$  increases. Thus, more oxygen is present on the catalyst surface and its availability for reaction increases. Further decrease of the film thickness may have a strong impact on the oxidation state of Mn, due to a stronger binding to the support material.

### 3.3. Catalytic tests by chemical looping with different manganese loadings on $\text{Na}_2\text{WO}_4/\text{Mn}/\text{SiO}_2$ catalysts

#### 3.3.1. Single methane pulse experiments

In Fig. 5 the results of testing the reaction over catalyst samples with various manganese loading are presented. For both applied residence times, a maximum methane conversion was observed at a certain manganese loading. First, by increasing the manganese loading, the methane conversion increases drastically. At 2-wt% the highest methane conversion is obtained. A further increase of the manganese loading is observed to decrease the catalyst activity again. The inverse trend was observed for the  $\text{C}_2$  selectivity. A maximum  $\text{C}_2$  yield of 0.25 was measured. As mentioned in the last section, the catalytic activity of the catalyst compounds depends on their crystallinity and oxidation state. An increase of manganese loading leads to higher crystallinity and different oxidation states, which results in higher methane conversion. Loadings higher than 2-wt% may shift manganese oxide species from  $\text{Mn}_2\text{O}_3$  to  $\text{Mn}_3\text{O}_4$ . Such effect is observed at higher loadings (10–20 wt% Mn) by XRD, and for loadings in the range of 3–10 wt% by XANES and EXAFS for manganese oxides supported on silica. At loadings below 10 wt% of Mn, XRD cannot detect  $\text{Mn}_3\text{O}_4$  formation [49]. Investigation of the catalyst material by in-situ XRD showed formation of  $\text{MnWO}_4$  under OCM reaction conditions [15]. Therefore, it would be possible to form  $\text{MnO}^*\text{WO}_3$  instead of  $\text{Mn}_3\text{O}_4$ . For our catalyst with low manganese oxide loadings, the film on the surface of the support is thin but still densely covered with Mn/W oxides. An increase of the manganese loading also increases the film thickness (Table 3). Therefore, the coupled effect of oxidation state and film thickness can explain the observations made in this series of experiments.

The findings of the catalytic activities in chemical looping experiments are in good agreement with the results in steady state experiments reported by the group of Mortazavi [14]. Koirala et al. found similar results for methane conversion and  $\text{C}_2$  selectivity at such manganese loadings in their co-feed steady state experiments for catalysts with low Mn loading. In contrast, they reported a constant methane conversion and  $\text{C}_2$  selectivity when the loading of Mn exceeded 2 wt% [50]. Ji et al. found similar correlations to ours between manganese loading methane conversion and  $\text{C}_2$  selectivity in steady state experiments [51].

**Table 3**Calculated theoretical film thickness  $d$  (Eq. (11)), number of compound layers (Eq. (12)).

	Sample Nr	$A_{\text{spec}}$ ( $\text{m}^2/\text{g}$ )	$d(\text{Na}_2\text{WO}_4)$ (nm)	$d(\text{Mn}_2\text{O}_3)$ (nm)	$d$ (nm)	# Layer
$A_{\text{spec}}$ (COK-12)	9	2.3	5.2	1.9	7.1	36.0
	8	2.6	4.6	1.7	6.3	31.8
	7	3.2	3.7	1.4	5.1	25.8
	6	4.2	2.8	1.1	3.9	19.7
Mn (COK-12)	1	5.1	2.4	0.0	2.4	12.1
	2	3.1	3.9	0.7	4.6	23.1
	3	2.6	4.6	1.6	6.2	31.4
	4	2.8	4.3	2.2	6.5	32.7
	5	3.1	3.9	2.7	6.5	32.8
Ref.	10	1.9	6.3	2.3	8.6	43.5

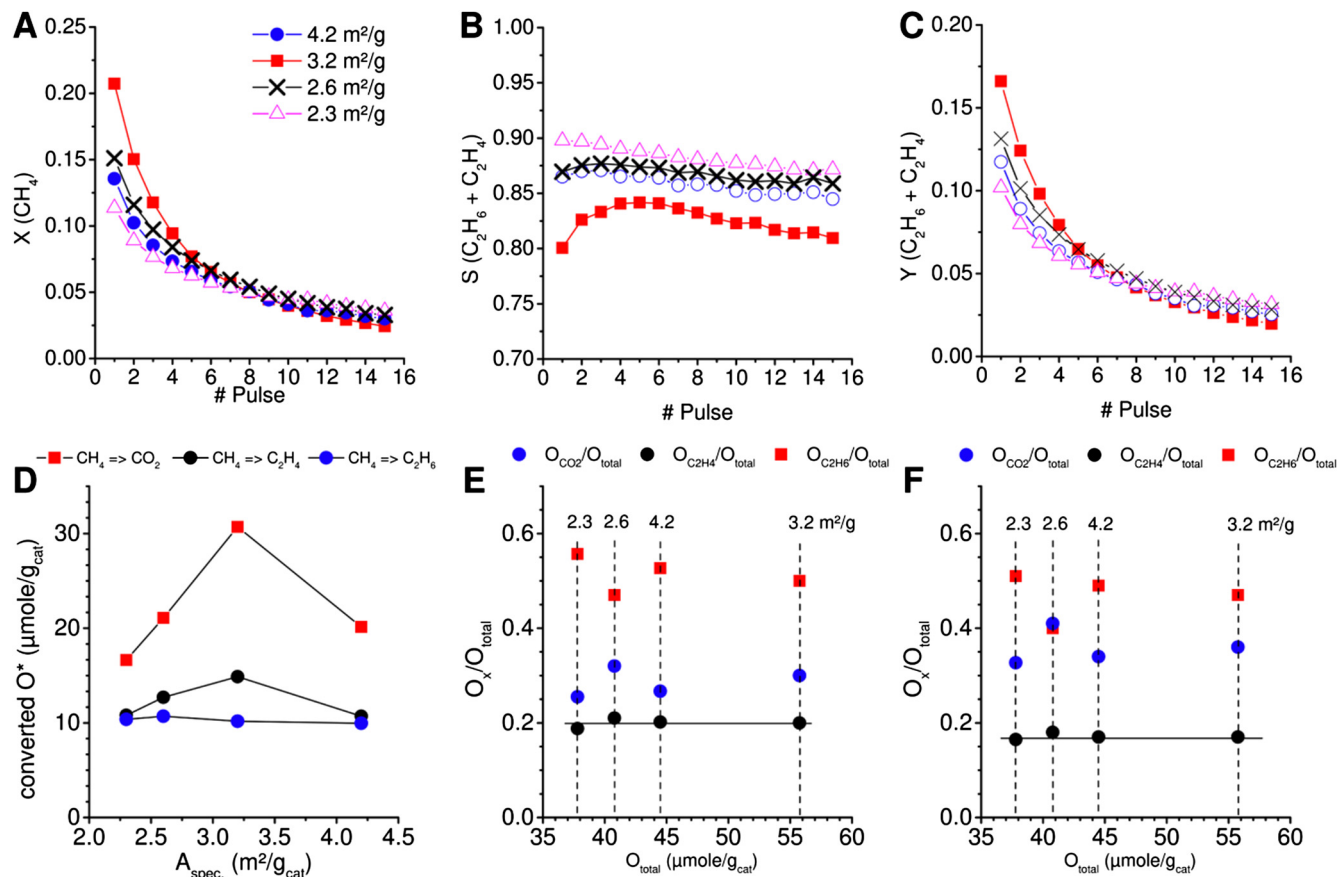


**Fig. 4.** Results of repetitive methane pulse experiments on  $\text{Na}_2\text{WO}_4$  (5 wt%)/Mn (2 wt%)/ $\text{SiO}_2$  with different specific surface areas, 30 nm/min, 775 °C, 0.6 g catalyst; A–C: methane conversion, selectivity and  $\text{C}_2$  yield for each methane pulse; D: Summation of the amounts of converted oxygen for all methane pulses per catalyst, based on Eq. (7), E: oxygen selectivity based on results of methane pulse simulation studies (molecule specific,  $k_3/k_4 = 7$ ) vs. amount of total converted oxygen (Eq. (7)), F: oxygen selectivity based on results of methane pulse simulation studies (molecule specific,  $k_3/k_4 = 2$ ) vs. amount of total converted oxygen (Eq. (7)).

### 3.3.2. Repetitive methane pulse experiments

The results of our repetitive methane pulse experiments for different loadings of Mn are shown in Fig. 6. At 0.02 wt% manganese loading, we cannot observe significant methane conversion. However, it was found that alkaline metal doped tungstate supported on silica shows substantial OCM activity in co-feed steady-state experiments [19,52]. Such a difference between their and our results indicates that the oxygen storage functionality is related to manganese ions.

The more manganese is loaded to the catalyst, the more methane pulses were necessary to reduce it completely and reach the inactive state of the material in the repetitive pulse experiments. The catalyst containing 4 wt% Mn shows a methane conversion of 0.1 and a  $\text{C}_2$  selectivity of 0.9 even after 15 methane pulses. This catalyst also

shows the highest  $\text{C}_2$  yield for each methane pulse. Calculation of the converted oxygen amounts showed that the highest  $\text{CO}_2$  formation was observed for a molar ratio of W:Mn (1:2), which is the classical high-performance composition (5 wt%  $\text{Na}_2\text{WO}_4$ , 2 wt% Mn) for this material. This is illustrated in Fig. 6D.

The results of our simulated kinetic model, presented in Fig. 6E and F, indicate similar results as presented in the last section. For  $\text{O}_{\text{C}_2\text{H}_4}$  we observe a constant ratio at different converted oxygen amounts, while  $\text{O}_{\text{C}_2\text{H}_6}$  is high at low oxygen conversion. An increase of the totally converted amount of oxygen shows a drastic increase of  $\text{O}_{\text{CO}_2}$ . The catalyst containing 4 wt% manganese loadings shows catalytic performance until 25 methane pulses were dosed, which is not presented. The total amount of converted oxygen was at least  $105 \mu\text{mole}/\text{g}_{\text{cat}}$ .

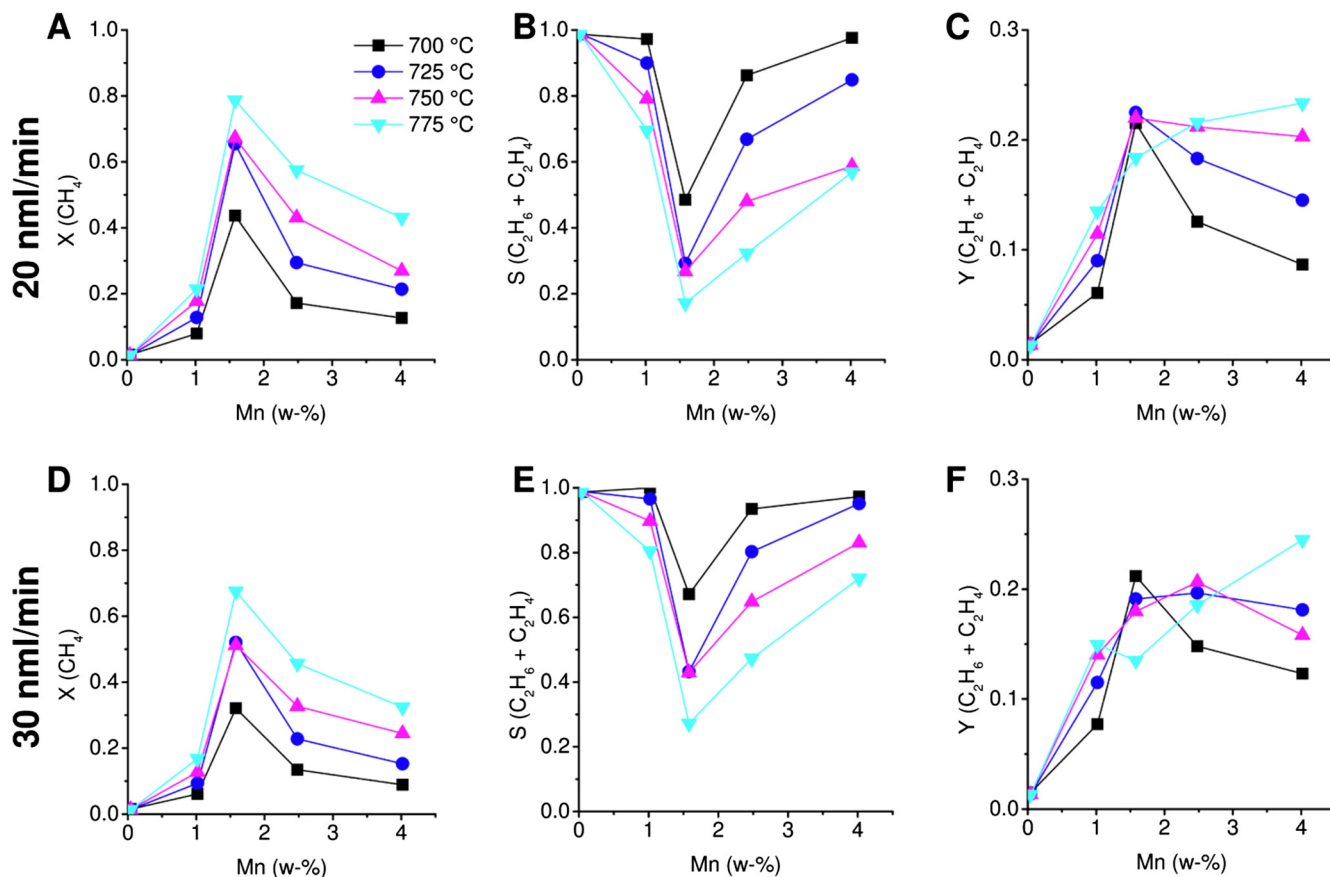


**Fig. 5.** Results of chemical looping experiments on  $\text{Na}_2\text{WO}_4$  (5 wt%)/Mn (var. wt%)/ $\text{SiO}_2$  catalysts at different Mn loadings and temperatures, 1 g catalyst, 1 ml  $\text{CH}_4$  pulse A – C: methane conversion,  $\text{C}_2$  selectivity and  $\text{C}_2$  Yield at 20 nml/min, D – F: methane conversion,  $\text{C}_2$  selectivity and  $\text{C}_2$  Yield at 30 nml/min, 1 ml  $\text{CH}_4$  pulse.

In order to explain our findings, a switch of the oxidation state of at least one of the metal active components is necessary. It has to be noted that  $\text{Na}_2\text{WO}_4$  may switch the oxidation state between  $\text{W}^{+6}$  to  $\text{W}^{+5}$ , according to the findings of Jiang et al. [53]. If  $\text{Na}_2\text{WO}_4$  would be responsible for the oxygen storage capacity in chemical looping experiments, we would expect that the amount of total converted oxygen would be constant here. However this was not the case, therefore,  $\text{Mn}_x\text{O}_y$  is suggested to be switching its oxidation state. To prove our hypothesis XRD, EPR and XPS experiments were carried out, which will be discussed later.

#### 3.4. Catalytic tests by chemical looping with different silica support materials on $\text{Na}_2\text{WO}_4$ /Mn/ $\text{SiO}_2$ catalysts

##### 3.4.1. Single methane pulse experiments

Fig. 7 summarizes the results of chemical looping experiments for  $\text{Na}_2\text{WO}_4$ /Mn/ $\text{SiO}_2$  catalysts with different support materials. The COK-12 supported catalyst with similar weight loadings of  $\text{Na}_2\text{WO}_4$  and Mn shows in all cases much higher catalytic activity compared to the silica gel supported catalyst (reference catalyst). Such an activity difference was also observed in the last subsection. The main difference in the support material variation is the SSA, the film thickness (Table 3) and also the dispersion of the catalyst compounds. Such findings support our hypothesis of an optimal loading of  $\text{Na}_2\text{WO}_4$  and Mn on the support material. Thick films of the active compounds decrease catalytic activity. Our results are in good agreement with the results of Yildiz et al., who studied the catalyst on different support materials in co-feed steady-state experiments [40].

##### 3.4.2. Repetitive methane pulse experiments

The results of our repetitive methane pulse experiments are shown in Fig. 8A–C. On the one hand, the COK-12 supported catalyst shows much higher activity, which finally ends after 14 methane pulses. On the other hand, the silica gel supported catalyst shows still catalytic activity after 15 methane pulses. That difference indicates the difference of the film thickness for these catalyst materials. In Fig. 8D–F the oxygen balances are presented from experimental and simulation studies. The COK-12 supported catalyst stores around three times more oxygen than the silica gel supported one, which can be activated for the OCM reaction in chemical looping experiments.

The COK-12 supported catalyst has a much higher SSA (Table 3) than the silica gel supported one. In addition, the dispersion of the active compounds is also higher. Therefore, more surface area is available for methane adsorption and conversion, which explains the higher activity. Due to the higher activity, the stored amount of oxygen is also faster depleted. The  $\text{C}_2$  selectivity for the COK-12 supported catalyst is at higher catalytic activity significantly lower, compared to those of the silica gel supported one. That is because of a competition between methane and  $\text{C}_2\text{H}_x$  activation. This is discussed in the next subsection in more detail.

In comparison, the silica gel supported catalyst has a much thicker film of the catalyst compounds. Therefore, less oxygen is stored on the catalyst surface at the top layers which becomes active for OCM reaction. Under these circumstances, more and more oxygen from deeper layers must be transported to the top layers to react over the active film. This behavior leads to the consumption of less oxygen from the catalyst surface by each methane

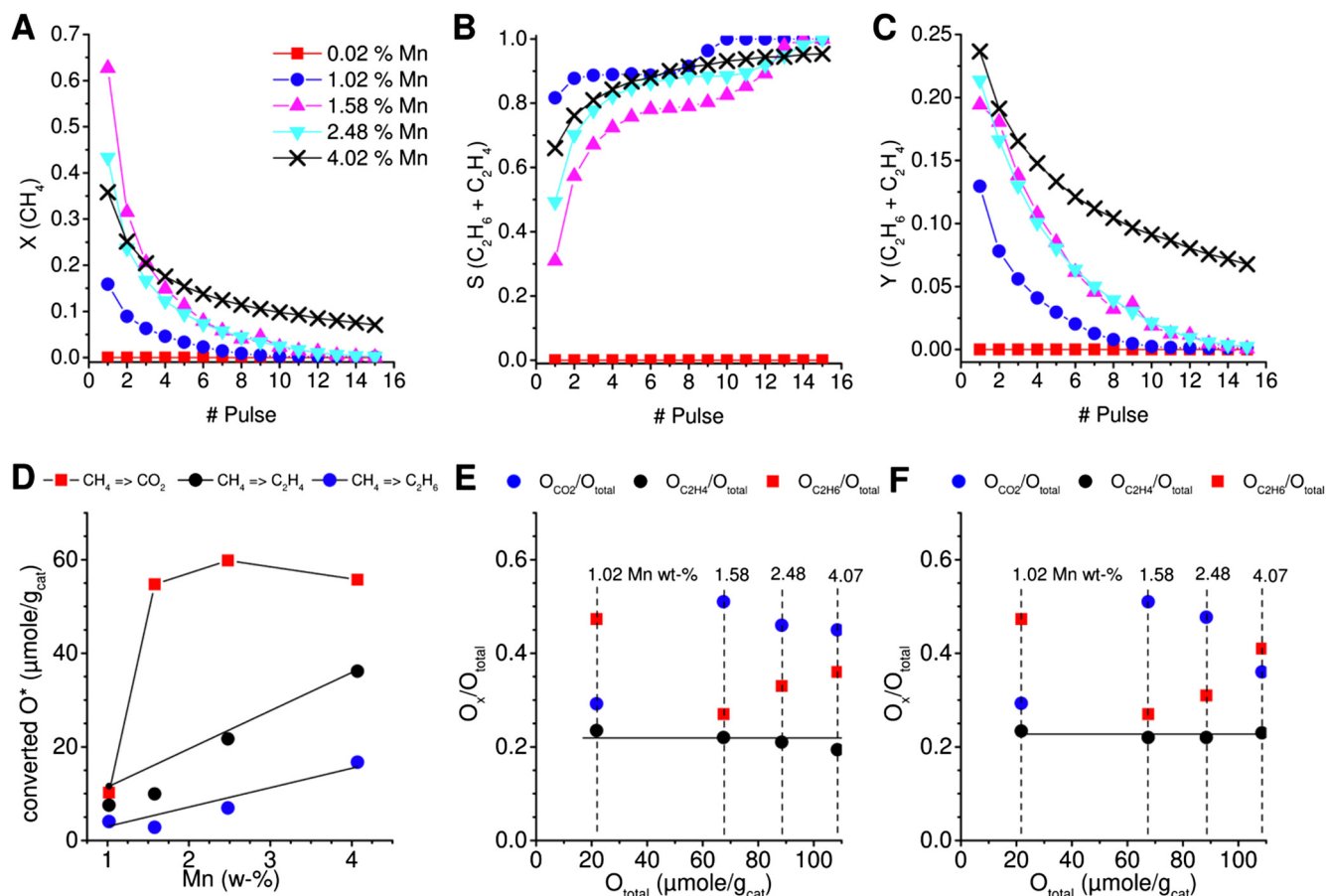


**Fig. 6.** Results of repetitive methane pulse experiments on  $\text{Na}_2\text{WO}_4$  (5 wt%)/Mn (2 wt%)/ $\text{SiO}_2$  at different Mn loadings, 30 nml/min, 775 °C, 0.6 g catalyst; A–C: methane conversion, selectivity, and  $\text{C}_2$  yield for each methane pulse; D: Summation of the amounts of converted oxygen for all methane pulses per catalyst based on Eq. (7). E: oxygen selectivity based on results of methane pulse simulation studies (molecule specific,  $k_3/k_4 = 7$ ) vs. amount of total converted oxygen (Eq. (7)), F: oxygen selectivity based on results of methane pulse simulation studies (molecule specific,  $k_3/k_4 = 2$ ) vs. amount of total converted oxygen (Eq. (7)).

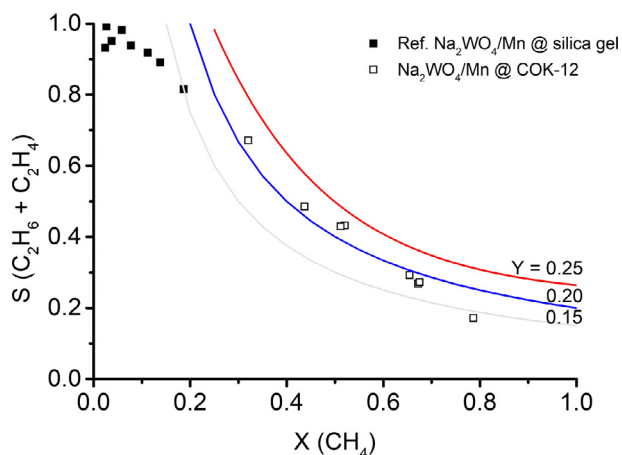


**Fig. 7.** Results of chemical looping experiments on  $\text{Na}_2\text{WO}_4$  (5 wt%)/Mn (2 wt%)/ $\text{SiO}_2$  catalysts at different support materials, 1 g catalyst, 700–775 °C, 20 & 30 nml/min, 1 ml  $\text{CH}_4$  pulse.

pulse, because the kinetic (diffusivity of oxygen within the film) or thermodynamic effects may limit the oxygen availability. As a consequence, more and more pulses were required until no further reactivity was observed for this catalyst. This effect can also be observed in the variation of the surface concentration of  $\text{Na}_2\text{WO}_4$  and Mn on COK-12 support in the first experiment set, discussed in the last subsection.

Such big differences in the oxygen storage capacity were also observed by different groups in different chemical looping experiments [54–56]. The most important factor in their findings is the effective oxidation state of the oxygen storage material, which is strongly influenced by the support material. As discussed earlier, there are additional aspects which also influence the oxidation state of the active compounds in our experiments, as compound dispersion and film thickness.

### 3.5. Investigation of reduced and re-oxidized $\text{Na}_2\text{WO}_4/\text{Mn}/\text{SiO}_2$ catalysts

As discussed earlier our findings indicate that the amount of manganese oxide correlates with the amount of available oxygen in chemical looping experiments. XRD, EPR and XPS investigations were performed to prove this hypothesis.

XRD diffractograms of the fresh  $\text{Na}_2\text{WO}_4$  (5 wt%)/Mn (2 wt%)/ $\text{SiO}_2$  catalyst supported on COK-12 are shown in Fig. 9 over the whole redox-cycle in OCM looping experiments. The fresh catalyst consists of the crystalline phases  $\alpha$ -cristobalite,  $\text{Na}_2\text{WO}_4$  and  $\text{Mn}_2\text{O}_3$  or braunite ( $\text{MnMn}_6\text{SiO}_{12}$ ), since the patterns of  $\text{Mn}_2\text{O}_3$  and  $\text{MnMn}_6\text{SiO}_{12}$  are highly similar. In addition, small amounts of a quartz phase are present. Oxidizing the catalyst has no significant impact on the XRD pattern. However, changes in the XRD pattern can be seen for the reduced catalyst. The reflections of the manganese oxide phase have vanished, while the intensities of the  $\text{Na}_2\text{WO}_4$  reflections have decreased. Additional small

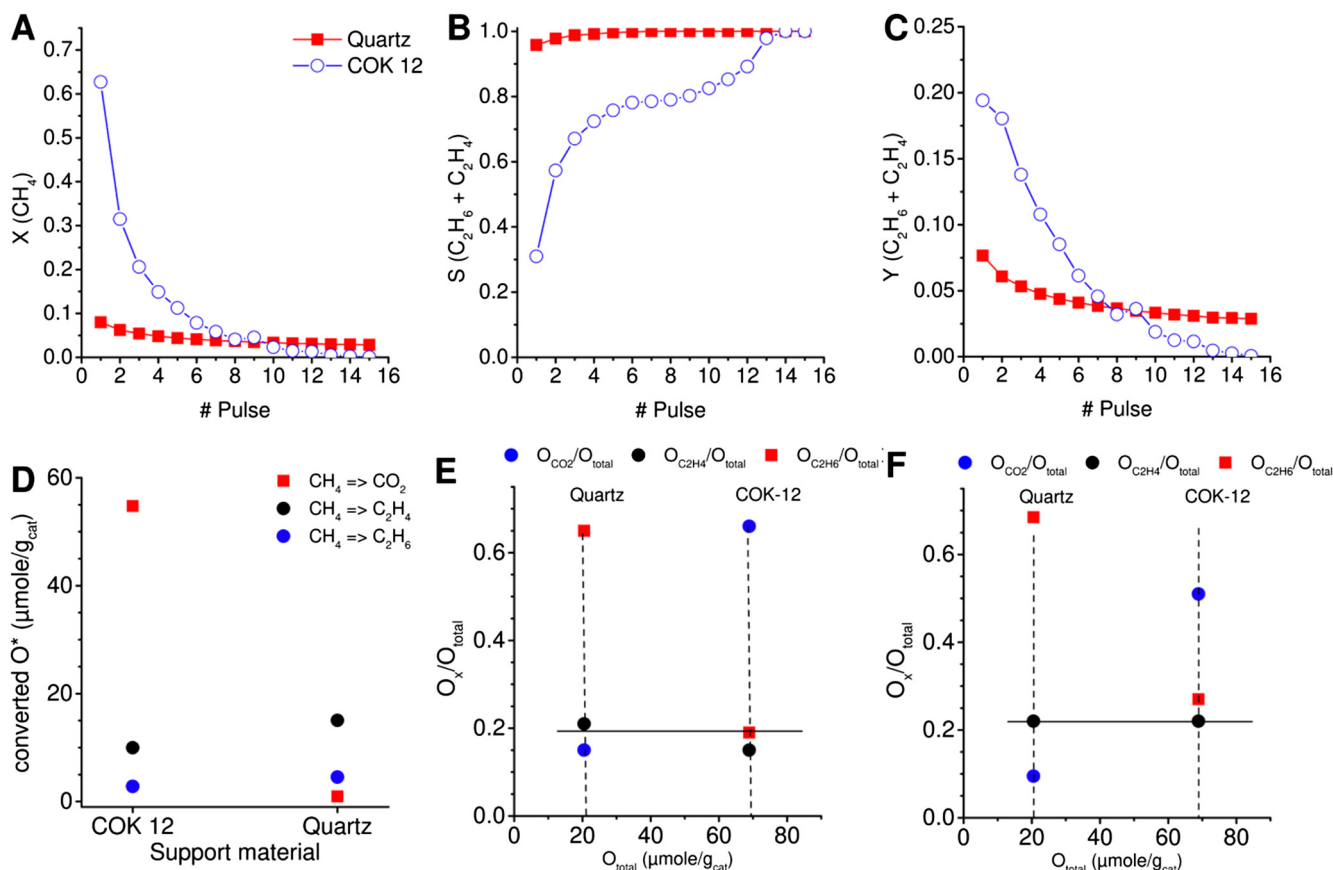


**Fig. 8.** Results of repetitive methane pulse experiments on  $\text{Na}_2\text{WO}_4$  (5 wt%)/ $\text{Mn}$  (2 wt%)/ $\text{SiO}_2$  with different silica support materials, 30 nml/min, 775 °C, 0.6 g catalyst; A–C: methane conversion, selectivity, and  $\text{C}_2$  yield for each methane pulse; D: Summation of the amounts of converted oxygen for all methane pulses per catalyst based on Eq. (7); E: oxygen selectivity based on results of methane pulse simulation studies (molecule specific,  $k_3/k_4 = 7$ ) vs. amount of total converted oxygen (Eq. (7)); F: oxygen selectivity based on results of methane pulse simulation studies (molecule specific,  $k_3/k_4 = 2$ ) vs. amount of total converted oxygen (Eq. (7)).

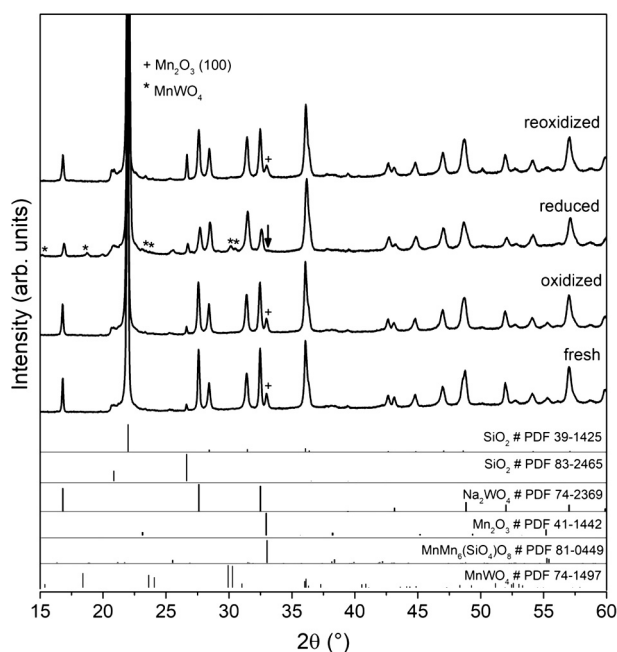


**Fig. 9.** XRD patterns of  $\text{Na}_2\text{WO}_4$  (5 wt%)/ $\text{Mn}$  (2 wt%)/ $\text{SiO}_2$  supported on COK-12 over the redox cycle. The diffraction intensities are normalized to  $\alpha$ -cristobalite (1 0 1) reflection.

reflections resemble the pattern of  $\text{MnWO}_4$ . After reoxidation, the intensities of the reflections of the manganese oxide and the  $\text{Na}_2\text{WO}_4$  phase have recovered. However, the reflections resembling the  $\text{MnWO}_4$  phase have vanished. The diffractogram is almost identical to that of the fresh catalyst, but, the intensities of the diffraction peaks, which were assigned to the quartz phase, have increased.

To further investigate the redox cycle of the catalyst, sealed samples of silica gel and COK-12 supported catalysts were studied by cw and pulsed EPR in order to identify the oxidation states of Mn and W ions. Using spin echo detection, we could observe a broad, nearly featureless absorption pattern at X-band (9.7 GHz) (Fig. S1, supporting information). The spectrum taken at 34 GHz (Q-band) (Fig. 10) was better resolved and could be fitted with a set of spin Hamilton parameters of a  $S = 2$  spin system, appropriate for Mn(III). This assignment was confirmed by using the same fit parameters for a simulation of the X-band pattern. Echo-detected spectra for the reduced and re-oxidized samples are shown in Fig. 11. For samples of both supported materials, we observed a significant reduction of echo detected spectral intensity when probing reduced samples.

Using conventional cw detection with field modulation, a strong signal with Lorentzian line shape ( $\Delta B_{pp} = 50$  mT,  $T = -123$  °C) was observed for the reduced samples (see Fig. 11). Although this line, with much reduced intensity, were also observed for the re-oxidized samples. The above described echo detected signal apparently does not noticeably contribute to the cw-detected

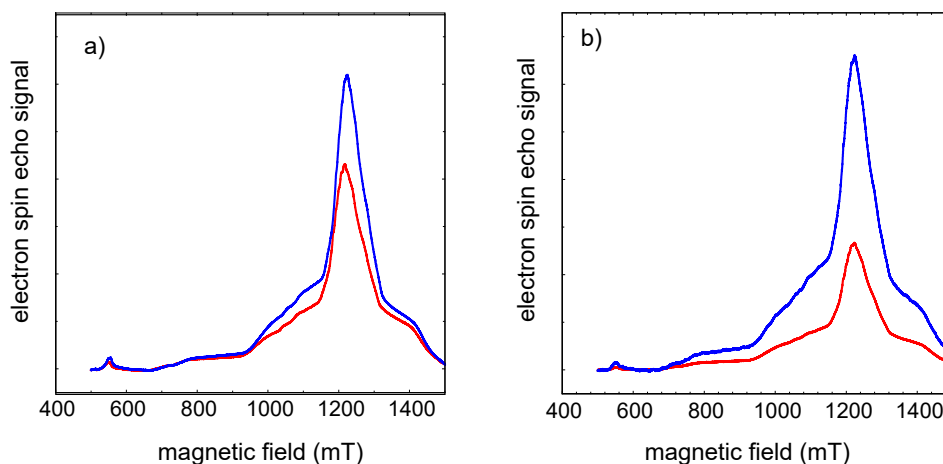


**Fig. 10.** 34 GHz FSE-EPR spectra of (a) silica gel- and (b) COK-12 supported  $\text{Na}_2\text{WO}_4/\text{Mn}/\text{SiO}_2$  catalysts, measured at 20 K. Spectra of reduced samples are shown as red traces, signals of re-oxidized samples are depicted in blue. Spectra were measured with a 2-pulse sequence with pulse separation of 150 ns.

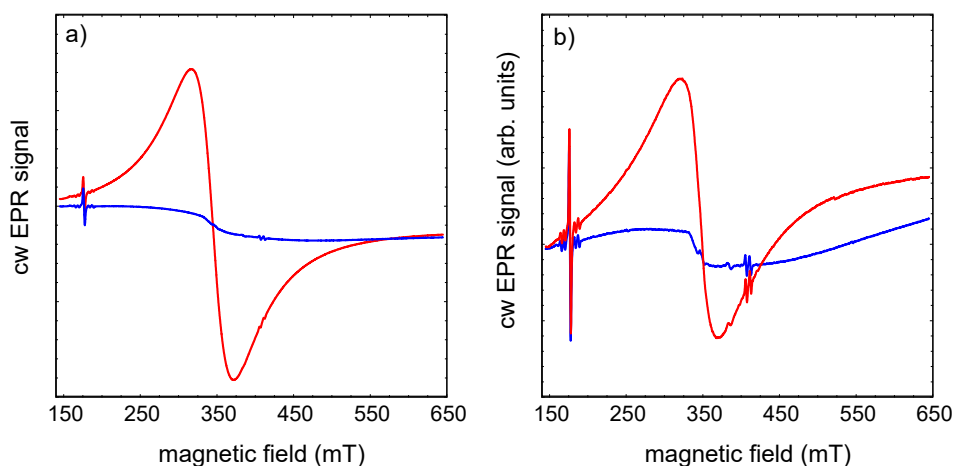


**Fig. 11.** X-band cw EPR spectra of (a) silica gel and (b) COK-12 supported  $\text{Mn}-\text{Na}_2\text{WO}_4$  catalysts, measured at  $-123^\circ\text{C}$ . Spectra of reduced samples are shown as red traces, signals from re-oxidized samples are given in blue. The narrow lines at 160 mT as well as the narrow doublet at 410 mT originate from paramagnetic centers in the EPR cavity and can be taken as intensity marker for comparing relative spin concentrations in different samples.

signal, because its much broader pattern extending over more than 300 mT is suppressed in this field-derivative detection mode.

No indication of this quite narrow (50 mT) Lorentzian signal is found in the echo detected spectra even when decreasing the pulse separation to 120 ns. This observation is indicating that this very strong signal originates from a spin system with very short relaxation time, probably less than 50 ns, thus preventing echo detection. We also found that the shape of this additional signal with a width of 50 mT is invariant when changing the microwave frequency from 9.7 to 34 GHz. This clearly shows that anisotropic  $g$  factor broadening can be excluded, leaving strong dipolar coupling as the most probable cause for the observed absorption pattern. A compilation of cw spectra taken at different spectrometer frequencies is shown in Fig. S2 (supporting information).

Despite the difficulty to quantify spin concentrations by pulsed EPR, a significant reduction of spectral intensity of the FSE spectra is evident when comparing reduced and re-oxidized samples, irrespective of the support material. This observation in combination with the cw-detected much narrower signal gives first evidence that this unstructured Lorentzian signal might originate from clustered Mn(II) sites, generated by partial reduction of Mn(III). This conclusion is further supported by various observations reported for Mn(II) in nano-structured samples [57,58]. In these studies,

the presence of a similar signal was reported, with line width depending on the nano cluster size. The reported increase in line width at lower temperatures and the deviation of the signal intensity from an ideal Curie dependence in the range below  $-173^\circ\text{C}$  was also seen in our samples. A full description of our EPR investigation will be published in a forthcoming paper.

The chemical composition and oxidation state of the surface of the  $\text{Na}_2\text{WO}_4$  (5 wt%)/Mn (2 wt%)/ $\text{SiO}_2$  catalyst supported on COK-12 are characterized using XPS over the whole redox-cycle during OCM looping experiments. Fig. 12 depicts high-resolution Mn 2p and W 4f XPS spectra for all samples. The Mn 2p spectrum of the fresh catalyst shows a doublet Mn  $2p_{3/2}$  – Mn  $2p_{1/2}$  with binding energy signals at 641.0 and 652.9 eV respectively with the spin-orbit splitting of 12.1 eV (see Fig. 12a). In addition, a small satellite feature at 146.2 eV and 5.4 eV from the main peak is observed, which indicates the existence of  $\text{Mn}^{2+}$  besides  $\text{Mn}^{3+}$  [59]. The fully oxidized catalyst shows a similar spectrum. However, by reducing the catalyst, the satellite structure at 146.2 eV gets more pronounced, which indicates an increase in  $\text{Mn}^{2+}$  amount. The spectra resemble those observed for  $\text{MnWO}_4$  [60], which supports the XRD results. By reoxidizing the catalyst, the height of the satellite structure decreases again. The spectra are similar to the ones of the original catalyst. Thus, Mn shows a reversible redox cycle during OCM.

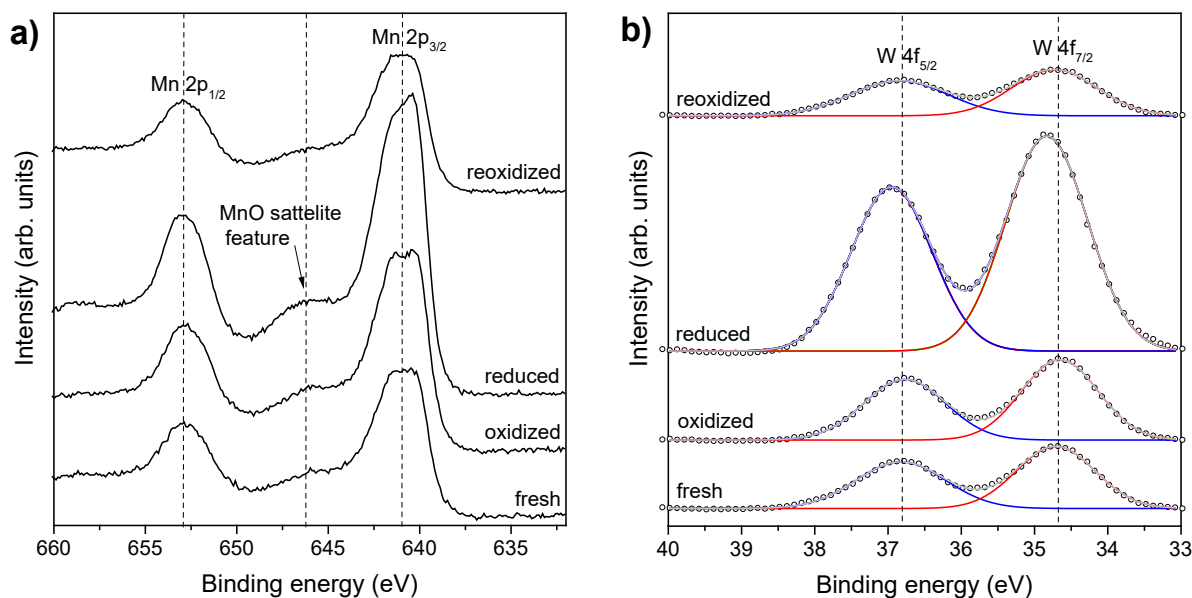


Fig. 12. XPS spectra of (a) Mn 2p and (b) W 4f level for  $\text{Na}_2\text{WO}_4$  (5 wt%)/Mn (2 wt%)/ $\text{SiO}_2$  supported on COK-12 over the redox-cycle.

For the W, 4f XPS spectra (Fig. 12b) of the fresh, the oxidized and the reoxidized catalyst, spin-orbit doublets at 34.7 and 36.8 eV ( $\Delta = 2.1$  eV) for  $\text{W } 4f_{7/2}$  and  $\text{W } 4f_{5/2}$  respectively, were assigned to oxidation state of  $\text{W}^{6+}$  [61]. By reducing the catalyst, the peaks are shifted to 34.8 and 37.0 eV respectively, probably due to the changed environment of W of  $\text{MnWO}_4$  compared to  $\text{Na}_2\text{WO}_4$ . The molar ratio of the chemical composition changes over the whole redox cycle. The fresh and the oxidized catalyst show a ratio of Mn to W of 85:15 showing an enriched surface loading with Mn in comparison to the bulk composition. By reducing the catalyst the Mn concentration in the surface decreases (ratio of Mn to W = 75:25). By reoxidizing the catalyst the ratio recovers to 85:15, as it was observed for the original fresh catalyst too. These results show the mobility of Mn on the catalyst surface.

### 3.6. Mechanistic aspects

A direct relation between catalyst compounds and oxygen storage capacity was only found for the manganese system, which is presented in Fig. 13 A. We plotted three theoretical trend lines, which show a projection of the amount of stored oxygen by different manganese oxide species. In all cases the amount of  $\text{Na}_2\text{WO}_4$  is constant. It has to be noted that MnO is probably present on the catalyst surface as  $\text{MnWO}_4$ , as discussed earlier. Therefore,  $\text{Mn}_3\text{O}_4$  can also be interpreted as  $\text{MnWO}_4 + \text{Mn}_2\text{O}_3$ . Our results indicate, that full manganese oxide reduction to Mn(II) was never reached, indicating that some amount may stay unconverted. A possible explanation is that the manganese oxide, which is stored close to the silica core is not affected by the redox mechanism as mentioned before. This is supported by our EPR results in Fig. 9. COK-12 and silica gel supported catalyst samples show significant electron spin echos of Mn(III) after reduction. The lack of any long-range magnetic ordering suggests a poor structural order in the reduced state, which is in agreement with the XRD results of the reduced catalyst. A more detailed account of these results will be presented in a forthcoming publication.

This is also consistent with our hypothesis about film thickness (Fig. 13B). A nearly linear dependency was found between oxygen storage capacity and Mn loading at constant loadings of  $\text{Na}_2\text{WO}_4$ , independent of the support material. If the number of layers of the active compounds falls below 25, the catalyst activity

decreases dramatically in all cases. Based on these findings, we assume an optimal film thickness of the  $\text{Na}_2\text{WO}_4$  and Mn. In thick films, high amounts of oxygen are stored inside and therefore only low catalytic activity in chemical looping experiments was observed. Because only top layer oxygen contributes to methane activation. A decrease of the film thickness improves the catalytic activity since more and more oxygen is exposed to the catalyst surface or in sublayers close to it. Further decrease of the film thickness may diminish the structural flexibility of the active film which is a key factor for a high-performance  $\text{Na}_2\text{WO}_4/\text{Mn}/\text{SiO}_2$  catalyst, as discussed before. Thus, an optimal film thickness of  $\text{Na}_2\text{WO}_4/\text{Mn}$  on  $\text{SiO}_2$  seems to be the key factor for a high-performance catalyst in chemical looping experiments. Our results from EPR investigations show that the reduced COK-12 sample has a larger difference of the electron spin echo intensity than silica gel supported catalyst. Therefore, it is concluded that in the thick film of the silica gel supported catalyst these species are less affected by the reduction.

EPR spectroscopy studies by Jiang et al. revealed a stable oxidation state of the tungsten oxide in dynamic experiments whereas the manganese oxide exhibits redox activity [25]. They predicted an electron transfer from C–H bond cleavage by tungsten oxide as the active center, while the electron is transferred to the manganese ion. Similar effects of supported manganese oxide catalysts in the OCM were also observed by Jones et al. [62]. They tested Mn/ $\text{SiO}_2$  catalysts with a variation of the manganese loading in dynamic experiments. The formation of Mn II+ was observed by Salehoun et al. They were able to observe the formation of  $\text{MnWO}_4$  after dynamic experiments by XRD [26].

A scheme of the catalyst functionality of the  $\text{Na}_2\text{WO}_4/\text{Mn}/\text{SiO}_2$  catalyst is presented in Fig. 14, which is based on the findings of other groups and ours.  $\text{Na}^+$  ions induce a phase change of the support material from  $\text{SiO}_2$  to  $\alpha$ -cristobalite during the calcination procedure [13]. Such transformation allows for the formation of an amorphous or glassy phase of  $\text{Na}_2\text{WO}_4$  and  $\text{Mn}_x\text{O}_y$ . The constitution of this phase depends on the amount of both compounds and their dispersion on the surface of the support material. Furthermore, this phase has a flexible structure under OCM conditions, which is responsible for selective methane activation [14,16,63]. When the formation of this phase is complete, no crystalline phases are detectable by XRD measurements for the

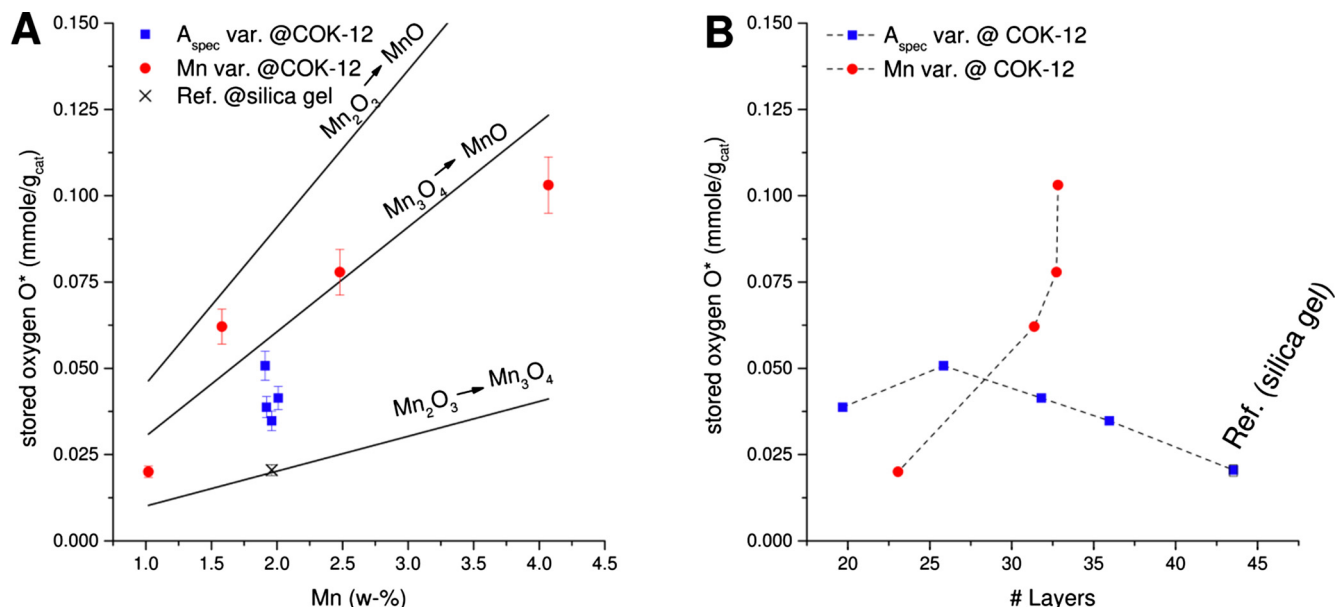


Fig. 13. Total stored amount of oxygen at different prepared  $\text{Na}_2\text{WO}_4/\text{Mn}/\text{SiO}_2$  catalyst materials, A – correlation between oxygen storage capacity and manganese oxide loading, B – correlation between oxygen storage capacity and film thickness of  $\text{Na}_2\text{WO}_4$  and  $\text{Mn}_2\text{O}_3$ .

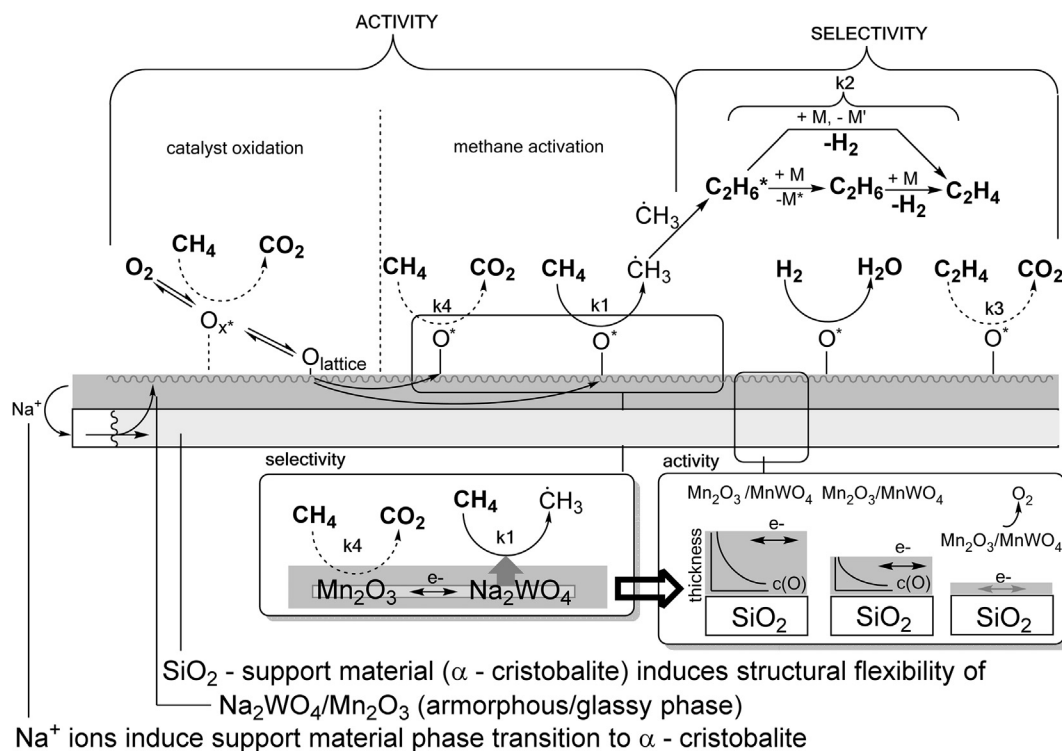


Fig. 14. Proposed OCM surface and gas phase reaction network for the  $\text{Na}_2\text{WO}_4/\text{Mn}/\text{SiO}_2$  catalyst in chemical looping experiments [13,14,18,19,23,27,28,30,40,67–69,71,72].

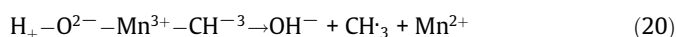
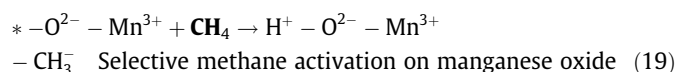
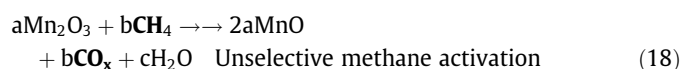
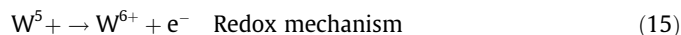
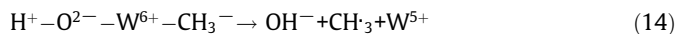
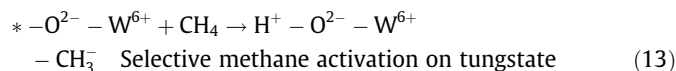
impregnated compounds [15]. This film can be oxidized by gas phase oxygen through adsorption ( $\text{O}_{x^*}$ ) and the conversion to top layer oxygen ( $\text{O}_{\text{lattice}}$ ), which may interact with sublayers, too [27].

Jiang et al. proposed the cooperative catalytic effect between  $\text{Na}_2\text{WO}_4$  and  $\text{Mn}_x\text{O}_y$  as oxygen-spillover effect [25,64]

They postulated a cooperating redox mechanism for selective methane activation according to Eqs. (13)–(17). It has to be noted, that Jones et al. found that  $\text{Mn}_x\text{O}_y/\text{SiO}_2$  is also active in OCM, but much less selective for  $\text{C}_2$  products [65]. Therefore, the proposed redox mechanism of Jiang et al. could be extended according to

Eqs. (18)–(20). Ji et al. demonstrated that even small amounts of sodium tungstate will increase methane conversion and  $\text{C}_2$  selectivity drastically [51]. According to their findings, the reaction rates of Eqs. (13) and (14) have to be much higher compared to the rate of reactions (19) and (20). Therefore, the manganese oxide seems to contribute to the selective activation of methane by a redox mechanism via tungstate, but unfortunately, it can also activate methane and may also other alkanes in an unselective reaction. A similar increase of catalytic activity in the OCM reaction by the addition of  $\text{Na}_2\text{O}$  to supported manganese oxide was also

reported by Wendt et al. [66]. However, it is not clear whether the oxygen spillover reaction effects sodium oxide itself or requires a tungstate matrix.



\*: free site on catalyst surface.

One important finding of our experiments was the influence of the film thickness of  $Na_2WO_4$  and  $Mn_xO_y$  on the catalytic activity. A thick film provides less oxygen in chemical looping experiments for methane conversion. Because most of the oxygen is stored inside the film, which is hard to access for gas phase reactants. Thin films may feel a less cooperated redox effect between  $Na_2WO_4$  and  $Mn_xO_y$ . Also, the oxygen seems to be less stable bound and an auto reduction reaction by oxygen desorption may occur. Both effects decrease the catalytic activity. Therefore, an optimal film thickness is required for enhancing the catalyst performance in chemical looping experiments.

The selective activation of methane results in the formation of methyl radicals which couple to ethane [67]. It is unclear whether this coupling process is occurring on the catalyst surface or in the gas phase. However, the combined radicals, which are energy-rich species, form an ethane molecule ( $C_2H_6^*$ ), which still contains the energy from these radicals. A collision partner (M) in the gas phase or a solid phase is necessary to emit this energy to form a stable ethane molecule. Another stabilization mechanism of  $C_2H_6^*$  would be luminescence, but we have to consider that the collision rate is high under OCM condition [68].

No changes in the ratio of  $O_{C_2H_4}$  was observed by using different catalyst materials, which provided different amounts of stored oxygen, see Figs. 4E, F and 6E, F. Such an effect is only plausible if ethylene formation is independent of the catalyst material and forms in the gas phase in chemical looping experiments. To test such a hypothesis we simulated a methane pulse with a model that combines gas phase and surface reactions in Chemkin. This is presented and discussed in the supporting information. Our findings indicate that the thermal dehydrogenation of  $C_2H_6$  to  $C_2H_4$  in gas phase is an important reaction route in chemical looping experiments. This reaction is initiated by a collision of ethane with other molecules [69]. Another possible route is the dehydrogenation of  $C_2H_6^*$ . During our chemical looping and repetitive pulse experiments, we only observed small traces of hydrogen. This observation is assigned to the reaction of hydrogen with stored oxygen on the catalyst surface to form water as discussed in the literature [30,25,70].

## 4. Conclusion

In this work, we studied a series of  $Na_2WO_4/Mn/SiO_2$  catalysts in chemical looping and repetitive methane pulse experiments. The variation of the specific surface area of this catalyst material at similar weight loadings indicates that a higher SSA increases the catalytic activity. This effect is limited to SSA's below  $4 \text{ m}^2/\text{g}$ . Catalysts with higher SSA showed lower catalytic activity in chemical looping experiments. The highest activity for varied manganese loadings was found at 5 wt%  $Na_2WO_4$  and 2 wt% Mn in chemical looping experiments. Unfortunately, no  $C_2$  yield higher than 0.25 was observed. COK-12 supported catalysts were much more active compared to silica gel supported one.

In the repetitive methane pulse experiments that ethylene formation consumes 25–30% of the total converted oxygen atoms. This indicates that ethylene formation is preferentially performed in the gas phase. This result was verified by simulations. The highest amount of converted oxygen was  $105 \mu\text{mol}(\text{O})/\text{g}_{\text{cat}}$  for 5 wt%  $Na_2WO_4$  and 2 wt% Mn on COK-12. We calculated an optimal surface concentration of  $66 \text{ Mn}/\text{nm}^2$  and  $33 \text{ W}/\text{nm}^2$ , which showed the highest oxygen storage capacity and highest catalytic activity, but also the lowest selectivity in our experiments. Our results obtained from the variation of the Mn loading indicate that this component is responsible for the oxygen storage functionality of the  $Na_2WO_4/Mn/SiO_2$  catalyst. In this context, it is worth noting that a reversible reduction of Mn(III) was observed while no indication for the presence of W(V) was found. A theoretical number of layers for the active phase ( $Na_2WO_4/Mn$ ) was calculated. The highest catalytic performance for  $Na_2WO_4/Mn/SiO_2$  catalysts was observed at about 25 layers and even small deviations from that number resulted in less performance in chemical looping experiments. The tungstate contributes to activity enhancement of selective methane activation. We assume that a multilayered redox reaction mechanism of this catalyst material is responsible for the OCM reaction in chemical looping experiments.

## Acknowledgement

This work is part of the UNICAT excellence cluster, which is coordinated by the Technische Universität Berlin. The financial support of this cluster is gratefully acknowledged. We thank Harald Link for ICP measurements, Jannes Mechler for his support in catalyst preparation and Christina Eichenauer for BET measurements.

## Appendix A. Supplementary material

Supplementary data associated with this article can be found, in the online version, at <https://doi.org/10.1016/j.jcat.2018.01.022>.

## References

- [1] A.M. Martini, J.M. Budai, L.M. Walter, M. Schoell, Microbial generation of economic accumulations of methane within a shallow organic-rich shale, *Lett. to Nat.* 383 (1996) 155–158, <https://doi.org/10.1038/383155a0>.
- [2] S. Depa, Review of Emerging Resources: U.S. Shale Gas and Shale Oil Plays, Washington D.C., 2011.
- [3] R. Diercks, J.-D. Arndt, S. Freyer, R. Geier, O. Machhammer, J. Schwartz, M. Volland, Raw material changes in the chemical industry, *Chem. Eng. Technol.* 31 (2008) 631–637, <https://doi.org/10.1002/ceat.200800061>.
- [4] P. Weiland, Biogas production: current state and perspectives, *Appl. Microbiol. Biotechnol.* 85 (2010) 849–860, <https://doi.org/10.1007/s00253-009-2246-7>.
- [5] L.R. Snowdon, Natural gas composition in a geological environment and the implications for the processes of generation and preservation, *Org. Geochem.* 32 (2001) 913–931, [https://doi.org/10.1016/S0146-6380\(01\)00051-1](https://doi.org/10.1016/S0146-6380(01)00051-1).
- [6] B. Vora, J.Q. Chen, A. Bozzano, B. Glover, P. Barger, Various routes to methane utilization-SAPO-34 catalysis offers the best option, *Catal. Today.* 141 (2009) 77–83, <https://doi.org/10.1016/j.cattod.2008.05.038>.
- [7] X. Fang, S. Li, J. Gu, D. Yang, Preparation and characterization of W-Mn catalyst for oxidative coupling of methane, *J. Mol. Catal.* 6 (1992) 427–433.

- [8] S. Li, Reaction chemistry of W-Mn/SiO<sub>2</sub> catalyst for the oxidative coupling of methane, *J. Nat. Gas Chem.* 12 (2003) 1–9.
- [9] J. Wang, L. Chou, B. Zhang, H. Song, J. Zhao, J. Yang, S. Li, Comparative study on oxidation of methane to ethane and ethylene over Na<sub>2</sub>WO<sub>4</sub>-Mn/SiO<sub>2</sub> catalysts prepared by different methods, *J. Mol. Catal. A Chem.* 245 (2006) 272–277, <https://doi.org/10.1016/j.molcata.2005.09.038>.
- [10] H.R. Godini, A. Gili, O. Go, U. Simon, K. Hou, G. Wozny, O. Görke, U. Simon, K. Hou, G. Wozny, Performance analysis of a porous packed bed membrane reactor for oxidative coupling of methane: structural and operational characteristics, *Energy Fuels* 28 (2014) 877–890, <https://doi.org/10.1021/ef402041b>.
- [11] M. Daneshpayeh, N. Mostoufi, A. Khodadadi, R. Sotudeh-gharebagh, Modeling of staged feeding in fluidized bed reactor of oxidative coupling of methane, *Energy Fuels* 23 (2009) 3745–3752.
- [12] G.W.S. Jaso, S. Sadjadi, H.R. Godini, U. Simon, S. Arndt, O. Görke, A. Berthold, H. Arellano-García, H. Schubert, R. Schomäcker, Experimental investigation of fluidized-bed reactor performance for oxidative coupling of methane S, *J. Nat. Gas Chem.* 21 (2012) 534–543.
- [13] A. Palermo, J. Pedro, H. Vazquez, A.F. Lee, M.S. Tikhov, R.M. Lambert, Critical Influence of the Amorphous Silica-to-Cristobalite Phase Transition on the Performance of Mn/Na<sub>2</sub> WO<sub>4</sub>/SiO<sub>2</sub> Catalysts for the Oxidative Coupling of Methane, 266 (1998) 259–266.
- [14] Z. Gholipour, A. Malekzadeh, M. Ghiasi, Y. Mortazavi, A. Khodadadi, Structural flexibility under oxidative coupling of methane; main chemical role of alkali ion in [ Mn + (Li, Na, K or Cs) + W ]/SiO<sub>2</sub> catalysts, *A2* (2012) 189–211.
- [15] M. Yildiz, Y. Aksu, U. Simon, T. Otremba, K. Kailasam, C. Göbel, F. Girgsdies, O. Görke, F. Rosowski, A. Thomas, R. Schomäcker, S. Arndt, Silica material variation for Mn<sub>x</sub>O<sub>y</sub>-Na<sub>2</sub>WO<sub>4</sub>/SiO<sub>2</sub>, *Appl. Catal. A Gen.* 525 (2016) 168–179, <https://doi.org/10.1016/j.apcata.2016.06.034>.
- [16] K. Takanabe, A.M. Khan, Y. Tang, L. Nguyen, A. Ziani, B.W. Jacobs, A.M. Elbaz, S. M. Sarathy, F.F. Tao, Integrated in situ characterization of molten salt catalyst surface: evidence of sodium peroxide and OH radical formation, *Angew. Chemie Int. Ed.* (2017), <https://doi.org/10.1002/anie.201704758>.
- [17] G.D. Nipan, Melt-assisted phase transformations of A/W/Mn/SiO<sub>2</sub> (A = Li, Na, K, Rb, Cs) composite catalysts, *Inorg. Mater.* 53 (2017) 553–559, <https://doi.org/10.1134/S0020168517060140>.
- [18] S. Mahmoodi, M.R. Ehsani, S.M. Ghoreishi, Effect of promoter in the oxidative coupling of methane over synthesized Mn/SiO<sub>2</sub> nanocatalysts via incipient wetness impregnation, *J. Ind. Eng. Chem.* 16 (2010) 923–928, <https://doi.org/10.1016/j.jiec.2010.09.007>.
- [19] A. Malekzadeh, A.K. Dalai, A. Khodadadi, Y. Mortazavi, Structural features of Na<sub>2</sub>WO<sub>4</sub>-MOx/SiO<sub>2</sub> catalysts in oxidative coupling of methane reaction, *Catal. Commun.* 9 (2008) 960–965, <https://doi.org/10.1016/j.catcom.2007.09.026>.
- [20] M.G. Colmenares, U. Simon, M. Yildiz, S. Arndt, R. Schomäcker, A. Thomas, F. Rosowski, A. Gurlo, O. Goerke, Oxidative coupling of methane on the Na<sub>2</sub>WO<sub>4</sub>-Mn<sub>x</sub>O<sub>y</sub> catalyst supported on ordered mesoporous silica: COK-12 as an inexpensive alternative to SBA-15, *Catal. Commun.* 85 (2016) 75–78, <https://doi.org/10.1016/j.catcom.2016.06.025>.
- [21] J. Jammaer, A. Aerts, J. D'Haen, J.W. Seo, J.A. Martens, Synthesis and characterization of cok-12 ordered mesoporous silica at room temperature under buffered quasi neutral pH, *Stud. Surf. Sci. Catal.* 175 (2010) 681–684.
- [22] M.G. Colmenares, U. Simon, O. Cruz, A. Thomas, O. Goerke, A. Gurlo, Batch and continuous synthesis upscaling of powder and monolithic ordered mesoporous silica COK-12, *Microporous Mesoporous Mater.* 256 (2018) 102–110.
- [23] S. Sadjadi, S. Jašo, H.R. Godini, S. Arndt, M. Wollgarten, R. Blume, O. Görke, R. Schomäcker, G. Wozny, U. Simon, Feasibility study of the Mn–Na<sub>2</sub>WO<sub>4</sub>/SiO<sub>2</sub> catalytic system for the oxidative coupling of methane in a fluidized-bed reactor, *Catal. Sci. Technol.* 5 (2015) 942–952, <https://doi.org/10.1039/C4CY00822G>.
- [24] Z.-C. Jiang, C.-J. Yu, X.-P. Fang, S.-B. Li, H.-L. Wand, Oxide/support interaction and surface reconstruction in the Na<sub>2</sub>WO<sub>4</sub>/SiO<sub>2</sub> system Zhi-Cheng, *J. Phys. Chem.* 97 (1993) 12870–12875.
- [25] Z. Jiang, H. Gong, S. Li, Methane activation over Mn<sub>2</sub>O<sub>3</sub>-Na<sub>2</sub>WO<sub>4</sub>/SiO<sub>2</sub> catalyst and oxygen spillover, *Stud. Surf. Sci. Catal.* 112 (1997) 481–490.
- [26] V. Salehoun, A. Khodadadi, Y. Mortazavi, A. Talebizadeh, Dynamics of catalyst in oxidative coupling of methane, *Chem. Eng. Sci.* 63 (2008) 4910–4916, <https://doi.org/10.1016/j.ces.2007.08.013>.
- [27] B. Beck, V. Fleischer, S. Arndt, M.G. Hevia, A. Urakawa, P. Hugo, R. Schomäcker, Oxidative coupling of methane—A complex surface/gas phase mechanism with strong impact on the reaction engineering, *Catal. Today.* 228 (2014) 212–218, <https://doi.org/10.1016/j.cattod.2013.11.059>.
- [28] V. Fleischer, R. Steuer, S. Parishan, R. Schomäcker, Investigation of the surface reaction network of the oxidative coupling of methane over Na<sub>2</sub>WO<sub>4</sub>/Mn/SiO<sub>2</sub> catalyst by temperature programmed and dynamic experiments, *J. Catal.* 341 (2016) 91–103, <https://doi.org/10.1016/j.jcat.2016.06.014>.
- [29] V. Fleischer, P. Littlewood, S. Parishan, R. Schomäcker, Chemical looping as reactor concept for the oxidative coupling of methane over a Na<sub>2</sub>WO<sub>4</sub>/Mn/SiO<sub>2</sub> catalyst, *Chem. Eng. J.* 306 (2016) 646–654, <https://doi.org/10.1016/j.cej.2016.07.094>.
- [30] S. Parishana, P. Littlewood, A. Arinchtin, V. Fleischer, R. Schomäcker, Chemical looping as a reactor concept for the oxidative coupling of methane over the Mn<sub>x</sub>O<sub>y</sub>-Na<sub>2</sub>WO<sub>4</sub>/SiO<sub>2</sub> catalyst, benefits and limitation, *Catal. Today.* (2017), <https://doi.org/10.1016/j.fuproc.2011.12.038>.
- [31] J. Adanez, A. Abad, F. Garcia-Labiano, P. Gayan, L.F. De Diego, Progress in chemical-looping combustion and reforming technologies, *Prog. Energy Combust. Sci.* 38 (2012) 215–282, <https://doi.org/10.1016/j.peccs.2011.09.001>.
- [32] T. Mattisson, A. Lyngfelt, H. Leion, Chemical-looping with oxygen uncoupling for combustion of solid fuels, *Int. J. Greenh. Gas Control.* 3 (2009) 11–19, <https://doi.org/10.1016/j.ijggc.2008.06.002>.
- [33] U. Simon, O. Görke, A. Berthold, S. Arndt, R. Schomäcker, H. Schubert, Fluidized bed processing of sodium tungsten manganese catalysts for the oxidative coupling of methane, *Chem. Eng. J.* 168 (2011) 1352–1359, <https://doi.org/10.1016/j.cej.2011.02.013>.
- [34] A. Dinse, A. Ozarowski, C. Hess, R. Schomäcker, K.-P. Dinse, Potential of high-frequency EPR for investigation of supported vanadium oxide catalysts, *J. Phys. Chem. C.* 112 (2008) 17664–17671, <https://doi.org/10.1021/jp807159f>.
- [35] A. Dinse, C. Carrero, A. Ozarowski, R. Schomäcker, R. Schlögl, K.-P. Dinse, Characterization and quantification of reduced sites on supported vanadium oxide catalysts by using high-frequency electron paramagnetic resonance, *ChemCatChem.* 4 (2012) 641–652, <https://doi.org/10.1002/cctc.201100412>.
- [36] A. Dinse, T. Wolfram, C. Carrero, R. Schlögl, R. Schomäcker, K.-P. Dinse, Exploring the structure of paramagnetic centers in SBA-15 supported vanadia catalysts with pulsed one- and two-dimensional electron paramagnetic resonance (EPR) and electron nuclear double resonance (ENDOR), *J. Phys. Chem. C.* 117 (2013) 16921–16932, <https://doi.org/10.1021/jp404234z>.
- [37] S. Pak, P. Qiu, J.H. Lunsford, Elementary reactions in the oxidative coupling of methane over Mn/Na<sub>2</sub>WO<sub>4</sub>/SiO<sub>2</sub> and Mn/Na<sub>2</sub>WO<sub>4</sub>/MgO catalysts, *J. Catal.* 179 (1998) 222–230.
- [38] C. Shi, M.P. Rosynek, J.H. Lunsford, Origin of carbon oxides during the oxidative coupling of methane, *J. Phys. Chem.* 98 (1994) 8371–8376, <https://doi.org/10.1021/j100085a017>.
- [39] P.B. Weisz, C.D. Prater, Measurements in experimental catalysis, in: *Adv. Catal. Relat. Subj.*, n.d.: pp. 143–195.
- [40] M. Yildiz, Y. Aksu, U. Simon, K. Kailasam, O. Goerke, F. Rosowski, R. Schomäcker, A. Thomas, S. Arndt, Enhanced catalytic performance of Mn<sub>x</sub>O<sub>y</sub>-Na<sub>2</sub>WO<sub>4</sub> SiO<sub>2</sub> for the oxidative coupling of methane using an ordered mesoporous silica support, *Chem. Commun.* 50 (2014) 14440–14442, <https://doi.org/10.1016/j.apcata.2012.02.046>.
- [41] E.R. Stobbe, B.A. de Boer, J.W. Geus, The reduction and oxidation behaviour of manganese oxides, *Catal. Today.* 47 (1999) 161–167, [https://doi.org/10.1016/S0920-5861\(98\)00296-X](https://doi.org/10.1016/S0920-5861(98)00296-X).
- [42] F. Arena, T. Torre, C. Raimondo, A. Parmaliana, Structure and redox properties of bulk and supported manganese oxide catalysts, *Phys. Chem. Phys.* 3 (2001) 1911–1917, <https://doi.org/10.1039/b100091h>.
- [43] Q.J. Yan, Y. Wang, Y.S. Jin, Y. Chen, Methane oxidative coupling over Na<sub>2</sub>WO<sub>4</sub>/SiO<sub>2</sub>, *Catal. Lett.* 13 (1992) 221–228.
- [44] F. Buciuman, F. Patcas, R. Craciun, D.R.T. Zahn, Vibrational spectroscopy of bulk and supported manganese oxides, *Phys. Chem. Chem. Phys.* 1 (1999) 185–190, <https://doi.org/10.1039/a807821a>.
- [45] Y. Liu, R. Hou, X. Liu, J. Xue, S. Li, Performance of Na<sub>2</sub>WO<sub>4</sub>-Mn/SiO<sub>2</sub> catalyst for conversion of CH<sub>4</sub> with CO<sub>2</sub> into C<sub>2</sub> hydrocarbons and its mechanism, *Stud. Surf. Sci. Catal.* 119 (1998) 307–311, [https://doi.org/10.1016/S0167-2991\(98\)80449-7](https://doi.org/10.1016/S0167-2991(98)80449-7).
- [46] G.D. Nipan, Phase states of Na/W/Mn/SiO<sub>2</sub> composites at temperatures of catalytic oxidative coupling of methane, *Inorg. Mater.* 50 (2014) 1012–1017, <https://doi.org/10.1134/S0020168514100112>.
- [47] T.W. Elkins, H.E. Hagelin-Weaver, Characterization of Mn–Na<sub>2</sub>WO<sub>4</sub>/SiO<sub>2</sub> and Mn–Na<sub>2</sub>WO<sub>4</sub>/MgO catalysts for the oxidative coupling of methane, *Appl. Catal. A Gen.* 497 (2015) 96–106, <https://doi.org/10.1016/j.apcata.2015.02.040>.
- [48] R.D. Shannon, Revised effective ionic radii and systematic studies of interatomic distances in halides and chalcogenides, *Acta Crystallogr. Sect. A.* 32 (1976) 751–767, <https://doi.org/10.1107/S0567739476001551>.
- [49] C. Reed, Y.-K. Lee, S.T. Oyama, Structure and oxidation state of silica-supported manganese oxide catalysts and reactivity for acetone oxidation using ozone, *J. Phys. Chem. B.* 110 (2006) 4207–4216.
- [50] R. Koirala, R. Büchel, S.E. Pratsinis, A. Baiker, Oxidative coupling of methane on flame-made Mn–Na<sub>2</sub>WO<sub>4</sub>/SiO<sub>2</sub>: influence of catalyst composition and reaction conditions, *Appl. Catal. A Gen.* 484 (2014) 97–107, <https://doi.org/10.1016/j.apcata.2014.07.013>.
- [51] S. Ji, T. Xiao, S. Li, C. Xu, R. Hou, K.S. Coleman, M.L. Green, The relationship between the structure and the performance of Na–W–Mn/SiO<sub>2</sub> catalysts for the oxidative coupling of methane, *Appl. Catal. A Gen.* 225 (2002) 271–284, [https://doi.org/10.1016/S0926-860X\(01\)00864-X](https://doi.org/10.1016/S0926-860X(01)00864-X).
- [52] A. Erdohelyi, R. Németh, A. Hancz, A. Oszkó, Partial oxidation of methane on potassium-promoted WO<sub>3</sub>/SiO<sub>2</sub> and on K<sub>2</sub>WO<sub>4</sub>/SiO<sub>2</sub> catalysts, *Appl. Catal. A Gen.* 211 (2001) 109–121, [https://doi.org/10.1016/S0926-860X\(00\)00859-0](https://doi.org/10.1016/S0926-860X(00)00859-0).
- [53] Z.-C. Jiang, L.-B. Feng, H. Gong, H.-L. Wang, Methane and Alkane Conversion Chemistry, Springer, US New York, 1995, 10.1007/s13398-014-0173-7.2.
- [54] M.M. Hossain, H.I. de Lasa, Chemical-looping combustion (CLC) for inherent CO<sub>2</sub> separations—a review, *Chem. Eng. Sci.* 63 (2008) 4433–4451, <https://doi.org/10.1016/j.ces.2008.05.028>.
- [55] T. Mattisson, A. Järnäs, A. Lyngfelt, Reactivity of some metal oxides supported on alumina with alternating methane and oxygen – application for chemical-

- looping combustion, *Energy and Fuels*. 17 (2003) 643–651, <https://doi.org/10.1021/ef020151i>.
- [56] Q. Zafar, T. Mattisson, B. Gevert, Integrated hydrogen and power production with CO<sub>2</sub> capture using chemical-looping reforming redox reactivity of particles of CuO, Mn<sub>2</sub>O<sub>3</sub>, NiO, and Fe<sub>2</sub>O<sub>3</sub> using SiO<sub>2</sub> as a support, *Ind. Eng. Chem. Res.* 2 (2005) 3485–3496, <https://doi.org/10.1021/ie048978i>.
- [57] I.V. Golosovsky, D. Arčon, Z. Jagličič, P. Cevc, V.P. Sakhnenko, D.A. Kurdyukov, Y. A. Kumzerov, ESR studies of MnO embedded into silica nanoporous matrices with different topology <GolosovskyPhysRevB2005.pdf>, *Phys. Rev. B*. 72 (2005) 144410–144416, <https://doi.org/10.1103/PhysRevB.72.144410>.
- [58] S. Sako, K. Ohshima, Antiferromagnetic transition temperature of MnO ultrafine particle, *J. Phys. Soc. Japan*. 64 (1995) 944–950.
- [59] V. Di Castro, G. Polzonetti, XPS study of MnO oxidation, *J. Electron Spectros. Relat. Phenomena*. 48 (1989) 117–123.
- [60] T.-D. Ngyuen, D. Mrabet, T.-D. Vu, C.-T. Dinh, T.-O. Do, Biomolecule-assisted route for shape-controlled synthesis of single-crystalline MnWO<sub>4</sub> nanoparticles and spontaneous assembly of polypeptide-stabilized mesocrystal microspheres, *CrystEngComm*. 13 (2011) 1450–1460.
- [61] F.Y. Xie, L. Gong, X. Liu, Y.T. Tao, W.H. Zhang, S.H. Chen, H. Meng, J. Chen, XPS studies on surface reduction of tungsten oxide nanowire film by Ar<sup>+</sup> bombardment, *J. Electron Spectros. Relat. Phenomena*. 185 (2012) 112–118.
- [62] C.A. Jones, J.J. Leonard, The oxidative conversion of methane to higherhydrocarbons, *J. Catal.* 103 (1987) 311–319.
- [63] G.D. Nipan, A.S. Loktev, K.V. Parkhomenko, S.D. Golikov, A.G. Dedov, I.I. Moiseev, Unexpected interaction between the components of a catalyst of methane oxidative coupling, *Dokl. Phys. Chem.* 448 (2013) 19–22, <https://doi.org/10.1134/S0012501613020012>.
- [64] L. Shu-Ben, Oxidative coupling of methane over W-Mn/SiO<sub>2</sub> catalyst, *Chinese J. Chem.* 19 (2001) 16–21.
- [65] C.A. Jones, J.J. Leonard, J.A. Sofranko, The oxidative conversion of methane to higher over alkali-promoted Mn/SiO<sub>2</sub> hydrocarbons, *J. Catal.* 103 (1987) 311–319.
- [66] G. Wendt, M. Sommer, D. Wolf, Phase formation in Na<sub>2</sub>O-MnOx catalysts for oxidative dimerization of methane, *React. Kinet. Catal. Lett.* 44 (1991) 457–462, <https://doi.org/10.1007/BF02073015>.
- [67] D.J. Driscoll, J.H. Lunsford, Gas-phase radical formation during the reactions of methane, ethane, ethylene, and propylene over selected oxide catalysts, *J. Phys. Chem.* 89 (1985) 4415–4418, <https://doi.org/10.1021/j100267a002>.
- [68] S. Storsæter, D. Chen, A. Holmen, Microkinetic modelling of the formation of C1 and C2 products in the Fischer-Tropsch synthesis over cobalt catalysts, *Surf. Sci.* 600 (2006) 2051–2063, <https://doi.org/10.1016/j.susc.2006.02.048>.
- [69] M. Frenklach, T. Bowman, G. Smith, GRI-Mech, Michael Frenklach, 2015, <<http://combustion.berkeley.edu/gri-mech/>>.
- [70] A. Malekzadeh, M. Abedini, A.A. Khodadadi, M. Amini, H.K. Mishra, A.K. Dalai, Critical influence of Mn of low-temperature catalytic activity of Mn/Na<sub>2</sub>WO<sub>4</sub>/SiO<sub>2</sub> catalyst for oxidative coupling of methane, *Catal. Lett.* 84 (2002) 45–51, <https://doi.org/10.1023/A:1021020516674>.
- [71] J.S. Ahari, R. Ahmadi, H. Mikami, K. Inazu, S. Zarrinpashne, S. Suzuki, K. Aika, Application of a simple kinetic model for the oxidative coupling of methane to the design of effective catalysts, *Catal. Today*. 145 (2009) 45–54, <https://doi.org/10.1016/j.cattod.2008.07.036>.
- [72] M. Yildiz, U. Simon, T. Otremba, Y. Aksu, K. Kailasam, A. Thomas, R. Schomäcker, S. Arndt, Support material variation for the Mn<sub>x</sub>O<sub>y</sub>-Na<sub>2</sub>WO<sub>4</sub>/SiO<sub>2</sub> catalyst, *Catal. Today*. 228 (2014) 5–14, <https://doi.org/10.1016/j.cattod.2013.12.024>.

# Investigation of the role of the $\text{Na}_2\text{WO}_4/\text{Mn}/\text{SiO}_2$ catalyst compounds in the oxidative coupling of methane by chemical looping experiments – supporting information

---

## 1 EPR spectroscopy

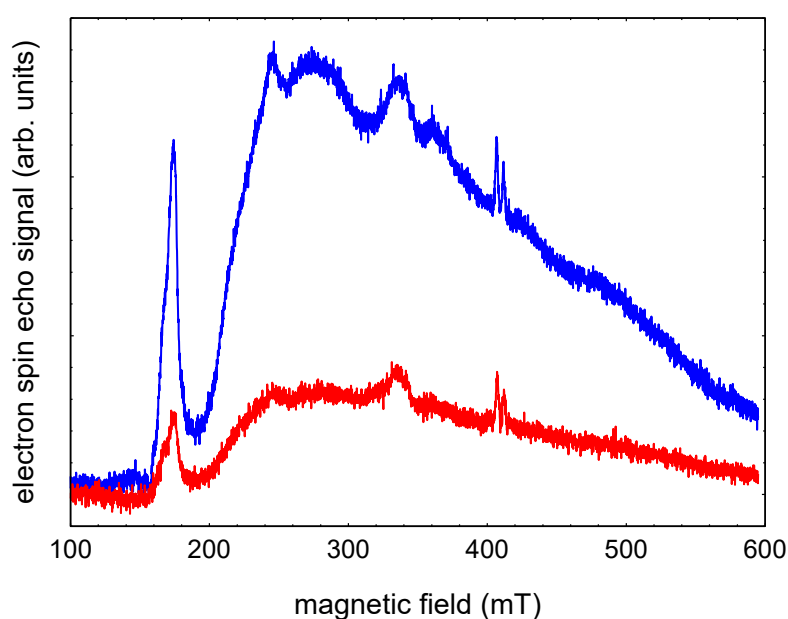


**Figure S1** - 9.7 GHz FSE-EPR spectra of quartz supported reduced (red) and re-oxidized (blue)  $\text{Mn-Na}_2\text{WO}_4$  catalysts. Spectra were recorded at 20 K with a 2-pulse echo sequence ( $\tau = 300$  ns). Narrow signals at 410 mT are caused by impurities in the BRUKER cavity.

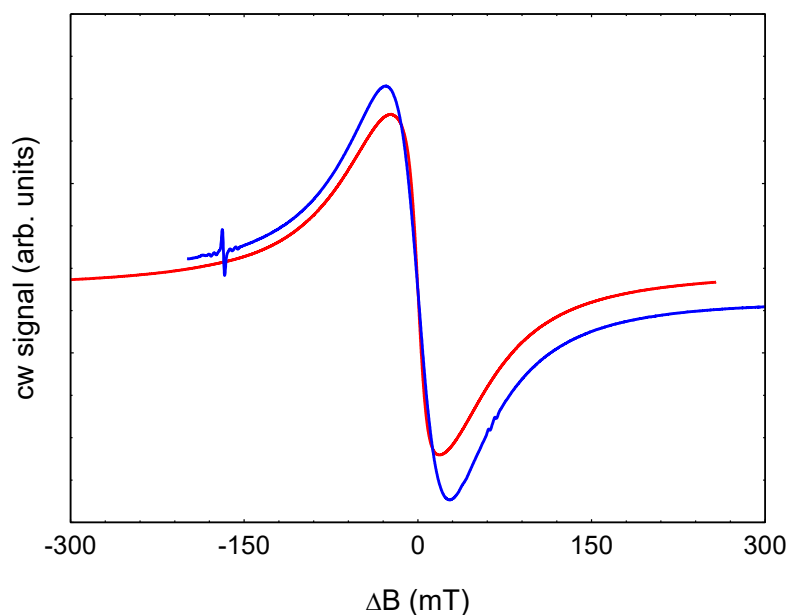


**Figure S2** - Cw EPR spectra of quartz supported reduced Mn-Na<sub>2</sub>WO<sub>4</sub> catalysts measured at 9.7 GHz (150 K, blue) and 33.9 GHz (300 K, red). Spectra were shifted to a common zero crossing to allow comparison of their line shapes.

## 2 Experimental -

### 2.1 Residence time analyses

The residence time of gas pulses was analyzed by pulse marking experiments. The sample loop (1 ml) was filled with N<sub>2</sub> or Ar, which was used as inert tracer gas. First the pulse was injected to the tube system of the setup, without reactor. After that the reactor was filled with 0.5 or 1 g catalyst material and heated up under He (30 nml/min). Reaching 775 °C, the tracer gas was injected to the setup with installed reactor. The detection of the tracer pulse was carried out by a thermal conductivity detector (Messkonzept 200) which was located directly at the reactor outlet. The detection of the signal was each 0.5 s.

### 2.2 Sample Quenching

To retard the recrystallization of the melted phases, a catalyst sample was quenched after the reduction. To do so, 200 g of the catalyst sieved in the range of 200-300 μm located in the isotherm zone of a U-shaped reactor explained in detail elsewhere (Le et al., 2017). The catalyst was heated to 750 °C with a ramp of 10 K min<sup>-1</sup> under a flow of 25/10/35 Nml min<sup>-1</sup> of CH<sub>4</sub>/O<sub>2</sub>/N<sub>2</sub>. First, the sample was reduced at isothermal temperature for 4 hours. Afterwards, the catalyst was rapidly cooled down under the same reaction flow by bringing the whole reactor out of the heating oven. In less than 15 minutes, when the sample temperature arrived the room temperature, the MFCs were stopped. At the end, the reactor was separated from the experimental set up while the catalyst sample was isolated from air contact by closing the plug valves in the inlet and outlet of the reactor. To do the TEM analyses the isolated sample was transferred to the sample holder in a (N<sub>2</sub>) glove box.

### 3 Modelling and simulation

#### 3.1 Residence time analyses

The residence time distribution function  $E(t)$  for each experiment was derived according to equations (1) and (2). The amount of tracer ( $n_{\text{tracer}}$ ) was calculated according to the ideal gas law for 1 ml gas at 298 K and 101300 Pa.

$$E(t) = \dot{V} \cdot \frac{c(t)}{n_{\text{tracer}}} \quad (1)$$

$$\int E(t) dt = 1 \quad (2)$$

All residence time experiments were modelled and fitted by Berkley Madonna. The experimental without dispersion effects of the reactor were fitted by an empirical square-pulse function. The function generates a rectangular signal and the fitting parameters were the delay time  $t_{\text{delay}}$ , the time of square-pulse duration  $t_{\text{dose}}$  and the amplitude of the square pulse. The delay time represents the time, were no tracer signal was detected and the gas pulse remains in the piping system. The time of square-pulse duration represents the time since the complete tracer gas enters and passed the reactor. The amplitude of the square-pulse was set as the area of the signal is one, according to equation (2).

The heated reactor was modelled by the dispersion model (equation (3)), which has as fitting parameters the velocity of the flow ( $u$ ) and an axial dispersion coefficient ( $D_{\text{ax}}$ ). The axial coordinate is expressed as  $z$ . That coefficient is correlated to the Bodenstein number according to equation (4), where  $L$  is the length of the reactor.

$$\frac{dc}{dt} = -u \frac{dc}{dz} + D_{\text{ax}} \frac{d^2c}{dz^2} \quad (3)$$

$$D_{\text{ax}} = \frac{u \cdot L}{\text{Bo}} \quad (4)$$

The model was fitted by implementation of high number (200) of spatial segments  $M$ . This is shown in equation (5). The length of each segment is defined according to equation (6). The boundary condition for the  $M = 0$  was the implementation of the squarepulse function (equation (7)).

$$\frac{dc[1..M]}{dt} = -u \frac{(c[i+1] - c[i-1]))}{2 \cdot L_i} + D_{\text{ax}} \frac{c[i+1] - c[i] + c[i-1]}{(2 \cdot L_i)^2} \quad (5)$$

$$L_i = \frac{L}{M} \quad (6)$$

$$\frac{dc[0]}{dt} = -u \cdot \frac{(-\text{squarepulse}(t_{\text{dose}}, t_{\text{delay}}) \cdot \text{amplitude} + c[i+1])}{L_i} + D_{\text{ax}} \frac{c[i+1] - c[i]}{(L_i)^2} \quad (7)$$

#### 3.2 Kinetic modelling of repetitive pulse experiments

To understand the reaction routes and the consumption of stored oxygen according to Figure 1 in more detail the repetitive pulse experiments were fitted and simulated in Berkley Madonna. We assumed that each pulse is similar to batch process, where the initial concentration for methane is constant for each methane pulse, while the oxygen concentration decreases with each pulse.

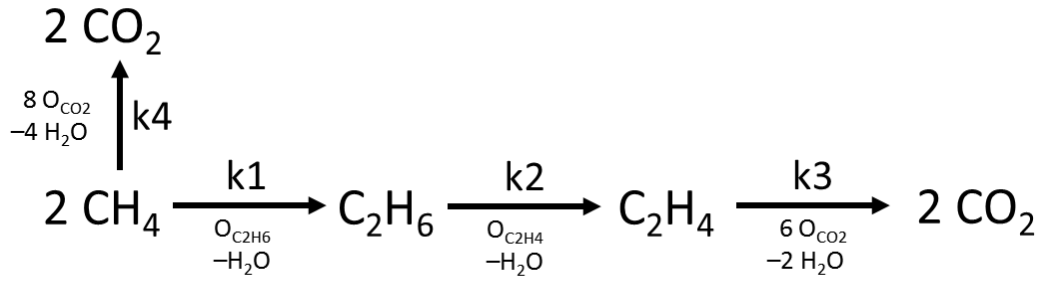


Figure 1 - Surface reaction network of the  $\text{Na}_2\text{WO}_4/\text{Mn}/\text{SiO}_2$  catalyst to determine a molecule specific oxygen balance

The reactions were expressed according to equations (8)-(11), where N is the total number of methane pulses, which were 15.

$$R1[1..N] = k1 * \text{CH}_4 * \text{O}[i] \quad (8)$$

$$R2[1..N] = k2 * \text{C}_2\text{H}_6[i] * \text{O}[i] \quad (9)$$

$$R3[1..N] = k3 * \text{C}_2\text{H}_4[i] * \text{O}[i] \quad (10)$$

$$R4[1..N] = k4 * \text{CH}_4 * \text{O}[i] \quad (11)$$

The fitting parameters were the rate constants  $k1 - k4$ . The ratio of  $k3/k4$  was set in the first run to 7 and in a second simulation to 2. For each repetitive pulse experiment the first four methane pulses were fitted to the presented parameters, getting a higher model precision. The initial concentration of oxygen was set according to the calculated ones by methane based oxygen balance, which is presented in the manuscript (Table 1). If N is 1 the total amount of stored oxygen was set as initial parameters. That was subtracted for the next pulse by the amount of converted oxygen (equation (12)).

$$\text{O}[i + 1] = \text{O}_{\text{total}} - \sum_i \text{O}_{\text{converted}}[i] \quad (12)$$

The amount of methane was derived according to the ideal gas law. We assume 1 ml gas, 298 K and 101,300 Pa. The initial concentrations were set according to equation (13).  $V_{\text{space}}$  stands for the free gas space in the catalyst bed.

$$c_X = \frac{n_X}{V_{\text{space}}} \quad (13)$$

The free space was estimated according to equation (14), where the volume of the catalyst bed (ca. 6  $\text{cm}^3 = 1 \text{ g catalyst}$ ) were multiplied by the void fraction  $\epsilon$  which was assumed to be 0.45. That value is common for several fixed beds. [1]

$$V_{\text{space}} = V_{\text{catalyst bed}} \cdot \epsilon \quad (14)$$

The material balances were derived according to equations (15)-(20).

$$\frac{d(\text{CH}_4[1..N])}{dt} = -2 \cdot R1[i] - R4[i] \quad (15)$$

$$\frac{d(C_2H_6[1..N])}{dt} = \frac{1}{2} \cdot R1[i] - R2[i] \quad (16)$$

$$\frac{d(C_2H_4[1..N])}{dt} = R2[i] - \frac{1}{2} \cdot R3[i] \quad (17)$$

$$\frac{d(CO_2; C_2H_4[1..N])}{dt} = 2 \cdot R3[i] \quad (18)$$

$$\frac{d(CO_2; CH_4[1..N])}{dt} = R4[i] \quad (19)$$

$$\frac{d(CO_2[1..N])}{dt} = CO_{2;C_2H_4}[i] + CO_{2;CH_4}[i] \quad (20)$$

The residence time was set according to our findings of the residence time analyses experiments, which are discussed in the next section.

### 3.3 Simulation in Chemkin

To simulate a pulse experiment in Reaction Design Chemkin we choose a 0-D Batch reactor model, because of the fact that both reactor concepts are non-continuous. All model parameters are listed in Table 1. The corresponding reactor volume was defined as the free gas space in the fixed bed. The residence time was derived from the methane pulse width and the initial mole fraction of methane as mean amplitude of the methane pulse. The specific surface area corresponds to 0.6 g catalyst with a specific surface area of 5 m<sup>2</sup>/g.

**Table 1 - Model parameter of Chemkin simulation**

Parameter	Value for simulation
Reactor volume (cm <sup>3</sup> )	3
Residence time (s)	55
Spezific surface area (m <sup>2</sup> /g)	3
Temperature (°C)	775
Pressure (bar)	1
Initial molefraction CH <sub>4</sub> , rest is N <sub>2</sub>	0.05

One well-known model for the gas phase reaction network involved in OCM is the Dooley mechanism. [36] It considers 1582 reactions, 269 species and showed adequate simulation results for profile fixed bed reactor. [37] It must be considered that such a micro kinetic network for gas phase reactions is strongly influenced by a micro kinetic surface reaction model. Therefore, only well-tested micro kinetic models for the surface reaction can lead to adequate simulation results. There is no such model available for the Na<sub>2</sub>WO<sub>4</sub>/Mn/SiO<sub>2</sub> catalyst, hence, we approximate it by a formal kinetic model. One of the latest models was published by Daneshpayeh and Coworkers, which showed adequate agreement with their experimental results. [11,38] One of the major issues of their network is the poor prediction of methane conversions higher than 0.1. Furthermore, their network contains gas phase and surface reactions in a homogenous model. Therefore we choose only parameters for methane activation in a selective and unselective route, similar to our recent work. [39] Lunsford and Coworkers found that the methane activation and ethane formation is dependent on methyl radical formation and coupling. [40] Furthermore it is widely accepted in micro kinetic models that the unselective reaction route for methane on the catalyst surface proceeds via a CH<sub>3</sub>O-species. [41–45] Therefore both reactions were implemented as surface reactions. The pre-exponential factor k<sub>oo</sub> of Daneshpayeh et al. was adapted with respect to catalyst amount and specific surface area. As thermodynamic data for all species on the catalyst surface dummy values of

0 were set, which is an adequate method if thermodynamic data for such species are not available. The final surface reaction model is presented in Table 2. The number of active sites for this material was set to 1/nm<sup>2</sup>. This results from the fact that transition metal oxides, which are supported on silica, have monolayer coverage between 0.1 – 1 atom per square nanometer. [46]

**Table 2 - Micro kinetic reaction routes on the catalyst surface and their parameters [11,38]**

Reaction	$k_{oo}$ (1/s)	$E_a$ (kJ/mol)
$CH_4 + O^*_{\text{electrophile}} \Rightarrow CH_3\cdot + OH^*$	44.100	212.60
$CH_4 + O_2^*_{\text{nucleophile}} \Rightarrow CH_3O\cdot + OH^*$	0.614	98.54

## 4 Results

### 4.1 Residence time analyses

The experimental results of tracer pulses of the piping system are presented in Figure 2 A. The final fitting parameters are presented in Table 3. These parameters were used to fit the experimental results of the residence time analyses with reactor at OCM conditions. This is presented in Figure 2 B for 1 g catalyst. The final value of the Bodenstein numbers were 26.5 (0.5 g cat) and 26.8 (1 g catalyst), which indicates strong dispersion effects. The pulse width was set as residence time ( $\tau$ ) of the kinetic model, which was 50 s.

**Table 3 - Fitting results of residence time experiments**

Parameter	Final value
$t_{\text{delay}}$	16.98 [s]
$t_{\text{dose}}$	20.35 [s]
amplitude	0.049

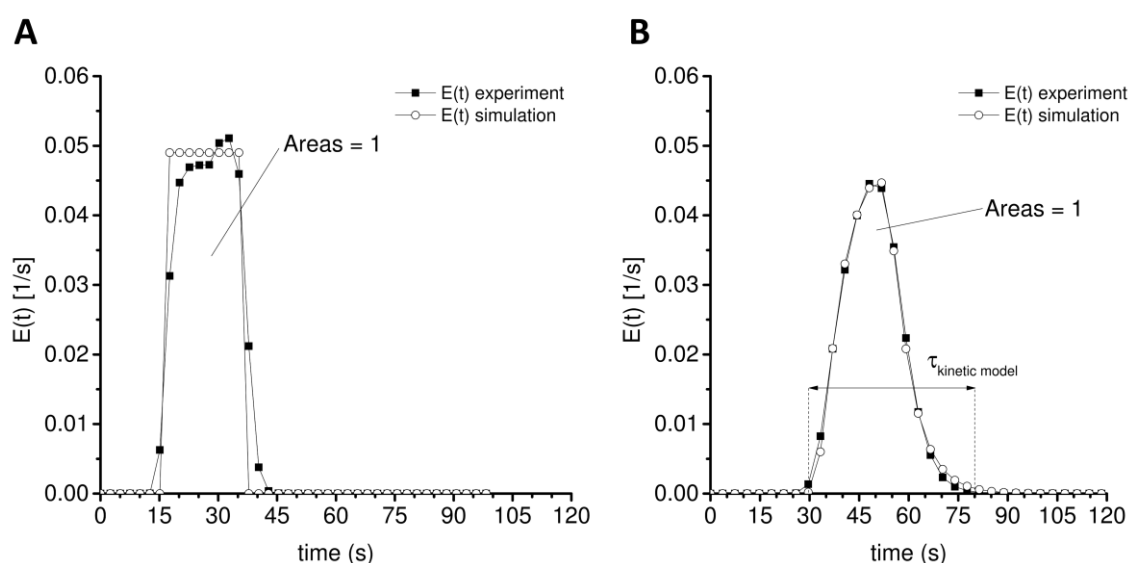


**Figure 2 - Results of experimental and simulated residence time distribution functions of 1 ml tracer and 30 nml/min. A – tracer pulse through tube system without reactor, B – tracer pulse through tube system and reactor at 775 °C, 1 g catalyst**

## **4.2 Modelling of repetitive pulse experiments**

The results of the repetitive pulse fitting procedure are listed in Table 4. Variation of the specific surface area of the  $\text{Na}_2\text{WO}_4/\text{Mn}/\text{SiO}_2$  catalyst has a smaller influence on the rate constants as the variation of the manganese oxide loading.

Table 4 - Fitted rate constants of repetitive methane pulse experiments

Variation		k3/k4 = 7 [ml/(mole·s)]				k3/k4 = 2 [ml/(mole·s)]			
		k1	k2	k3	k4	k1	k2	k3	k4
<b>Mn (COK-12)</b>	1.00 w-%	3109	2283	12	84	3109	2283	42	84
	1.90 w-%	1183	2997	21	150	1183	2997	75	150
	2.80 w-%	1709	1651	8	54	1675	1616	83, 5	167
	3.70 w-%	1246	654	4	30	1278	589	49	98
<b>Aspec (COK-12)</b>	2.3 m <sup>2</sup> /g	976	516	4	30	957	501	31	62
	2.6 m <sup>2</sup> /g	1375	713	6	40	1349	691	46, 5	93
	3.2 m <sup>2</sup> /g	1513	814	7	47	1476	787	60	120
	4.2 m <sup>2</sup> /g	1335	709	7	47	1358	694	50	100
<b>Reference catalyst</b>		1990	1713	3	21	1939	1647	23	46

### 4.3 Simulation of repetitive pulse experiments

The calculated amounts of C<sub>2</sub>H<sub>6</sub>, C<sub>2</sub>H<sub>4</sub> and CO<sub>2</sub> of the first four methane pulses from experiments and simulations are presented in Figure 3 as parity plot. The kinetic model shows adequate reliability to calculate to amounts of each reactant. Based on these models, the amounts of oxygen for each reaction were calculated.

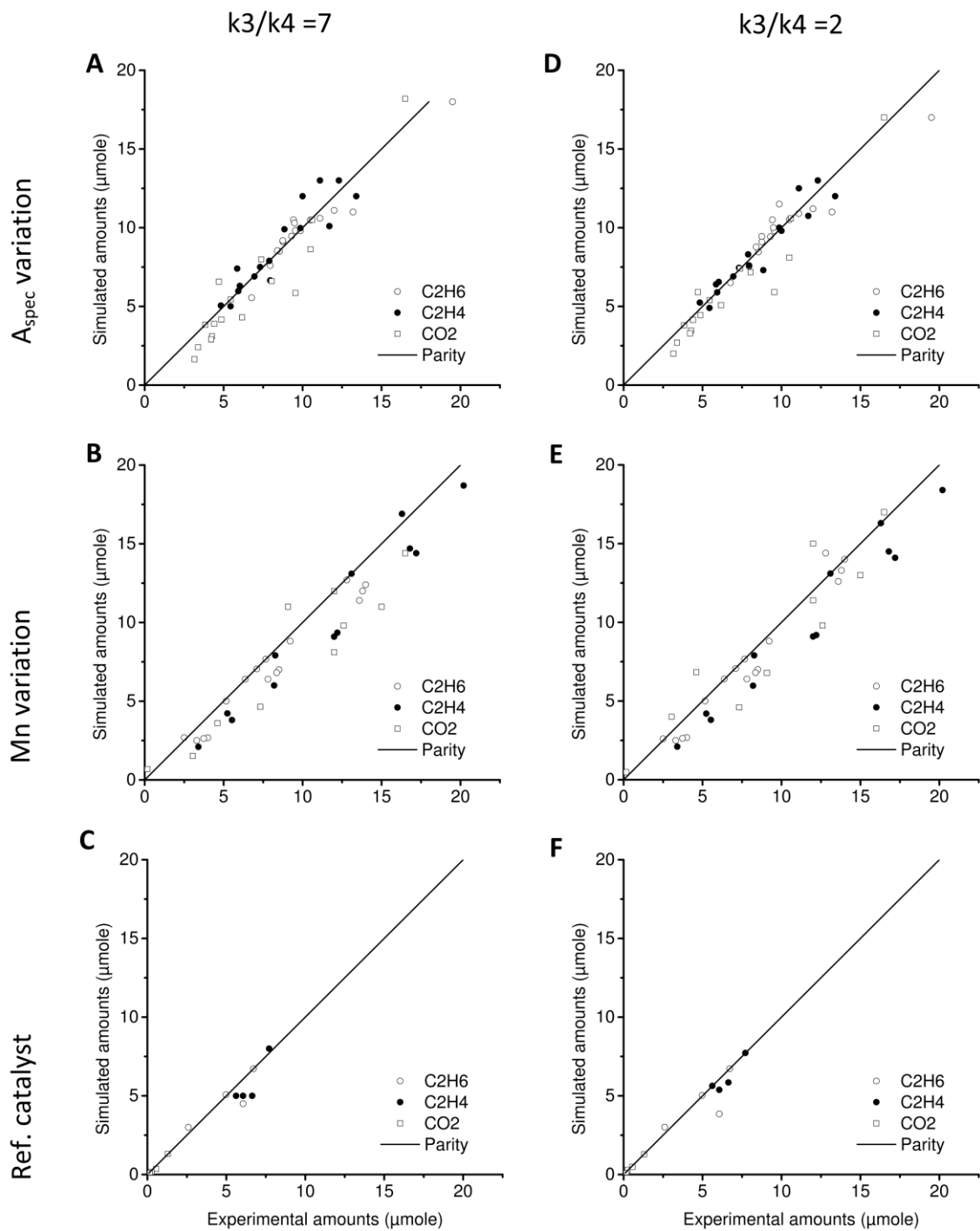


Figure 3 - Parity plot of the initial four 1 ml CH<sub>4</sub> pulses for all catalyst materials in repetitive pulse experiments vs. simulation results at different ratios of  $k_3/k_4$ . A- C  $k_3/k_4 = 7$ ; D-F  $k_3/k_4 = 2$

#### 4.4 Simulation results of single pulse experiments in Chemkin to analyze ethene formation route

The number of active sites was set to  $1/\text{nm}^2$  in our simulations. This was estimated from the fact that such a number is the monolayer coverage for a supported transient metal oxide on silica. We discussed that a film of several multilayers of the active compounds is present on the catalyst surface. Therefore, we assume that around one O atom per squared nanometer is directly available on the top layer of the catalyst surface, while the rest is stored in subsurface layers.

The result of a simulation of a methane pulse to the catalyst bed in Chemkin is shown in Figure 4. As can be seen in Figure 4 – A the original parameters of Daneshpayeh et al. show only poor methane conversion. [11,38] This is in straight contradiction to our results in the last section.  $\text{CH}_2\text{O}$  is formed as an intermediate species which is formed from  $\text{CH}_3\text{O}$  decomposition. Further decomposition of  $\text{CH}_2\text{O}$  forms CO and  $\text{H}_2$ . It can be seen that ethane and ethene are formed and the  $\text{C}_2$  selectivity is in good agreement with our results of the single methane pulse experiments in the variation of the specific surface areas. For a sufficient comparison at same methane conversion both surface reaction rates were increased by factor 300. The results of this simulation are shown in Figure 4 – B. The methane conversion is in the range of our observations in chemical looping experiments, now. CO is dominating the overall selectivity, while ethene [72] is the major product among the  $\text{C}_2$  compounds. Ethane shows a typical trend of an intermediate species in a consecutive reaction pathway. This indicates that thermal dehydrogenation is a serious reaction pathway to convert ethane to ethene in oxygen free gas phase. Such a simulation supports our observation of a constant ratio of converted  $\text{O}_{\text{C}_2\text{H}_4}$  as mentioned in the last section.

At this point it has to be noted that the simulation is only a rough estimation for testing our hypothesis. The increase of the surface reaction rates, the lack of an experimental investigation of the number of active sites and a well explored surface reaction network for this material indicate that a lot of important parameters are still missing for an adequate micro kinetic surface reaction model. Due to the fact, that only small amounts of hydrogen were observed in our experiments, we assume that the  $\text{H}_2$  reduces also the catalyst material, similar to the results, which were found in temperature programmed reduction experiments. [16,60]

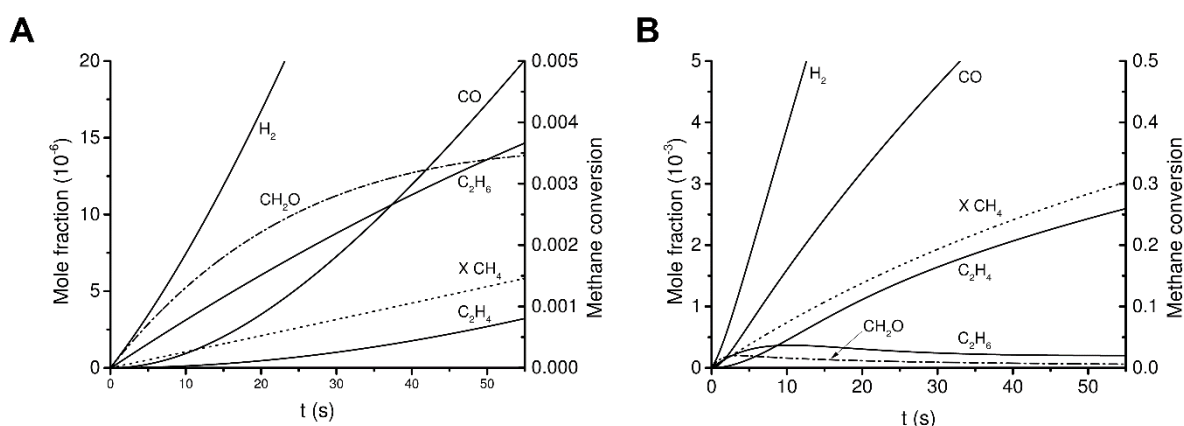


Figure 4 - Results of a methane pulse simulation in chemkin, A: original reaction parameters by Daneshpan et al. [11,38], B: Surface reaction rates increased by factor 300

## 5 References

- [1] M. Kraume, Einphasig durchströmte Feststoffschüttungen, in: Transportvorgänge in der Verfahrenstechnik, 2012: pp. 247–273.

# Paper 6





# Investigation into Consecutive Reactions of Ethane and Ethene Under the OCM Reaction Conditions over $Mn_xO_y-Na_2WO_4/SiO_2$ Catalyst

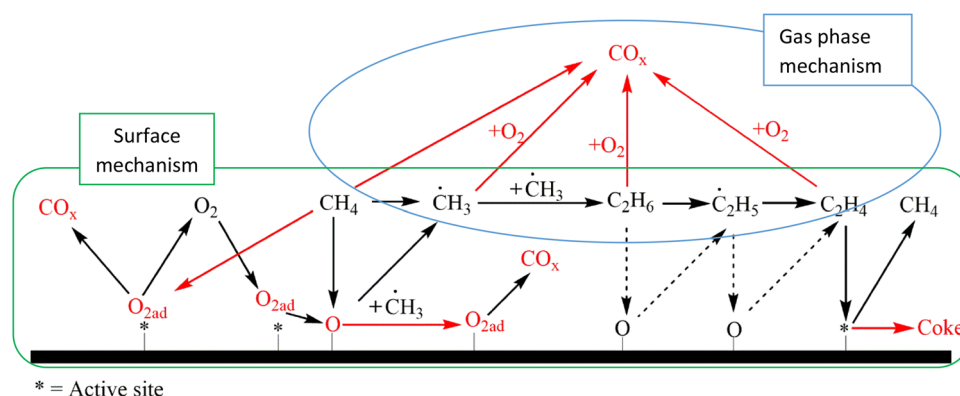
Samira Parishan<sup>1</sup> · Ewa Nowicka<sup>1</sup> · Vinzenz Fleischer<sup>1</sup> · Christian Schulz<sup>2</sup> · Maria G. Colmenares<sup>3</sup> · Frank Rosowski<sup>2</sup> · Reinhard Schomäcker<sup>1</sup>

Received: 8 February 2018 / Accepted: 4 April 2018 / Published online: 18 April 2018  
© Springer Science+Business Media, LLC, part of Springer Nature 2018

## Abstract

The reaction mechanism of ethane and ethene oxidation was studied under the OCM reaction conditions over  $Mn_xO_y-Na_2WO_4/SiO_2$ . The consecutive reaction of  $C_2$  components is observed to be the main route to the formation of  $CO_x$  under the applied reaction conditions here. The homogeneous or heterogeneous nature of these unselective reactions was investigated in more details. For this purpose, the temperature programmed surface reaction (TPSR) technique was applied. The results of these experiments indicate that the consecutive reaction of ethane is mainly occurring in the gas phase of the reactor. This point was confirmed when the activation energy of ethane both, in the presence of the catalyst and silicon carbide, as the inert surface, was shown to be at the same level. The concentration profile of the effluent obtained by simulating the reaction of  $C_2$  components using the Dooley mechanism in ChemkinPro was also in good agreement with this proposal. The reason for the low influence of the catalyst on conversion of ethane was ascribed to the film diffusion limitation that is occurring under the OCM reaction conditions applied in these studies. Finally, a set of experiments were performed with  $^{13}CH_4$  to study the effect of methane on the consecutive reaction of ethane in the OCM reactor.

## Graphical Abstract



**Keywords** Oxidative coupling of methane ·  $Mn_xO_y-Na_2WO_4/SiO_2$  · Thermal dehydrogenation of ethane · Oxidative coupling of labelled methane · Stationary co-feeding experiments

**Electronic supplementary material** The online version of this article (<https://doi.org/10.1007/s10562-018-2384-6>) contains supplementary material, which is available to authorized users.

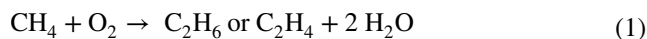
✉ Reinhard Schomäcker  
schomaecker@tu-berlin.de

Extended author information available on the last page of the article

## 1 Introduction

The large known resources of natural gas [1–4] as well as the volatile petroleum market and growing environmental concerns, attract an increasing attention to the processing of natural gas into value-added products (VAP) [5–9]. The

conversion of methane to C<sub>2</sub> products and higher hydrocarbons, known as oxidative coupling of methane (OCM) (Eq. 1), could be a possible direct method for fulfilling this aim [3, 8, 10–12].



One of the advantages of this direct method for utilization of methane is that it is exothermic and therefore is not thermodynamically limited [3]. In addition, it represents the highest possible carbon efficiency of the converted methane compared to that of the other direct methods for conversion of methane to VAP [5]. However, despite all the research done on this process, it has not yet been commercialized, as the minimum yield of 30% towards C<sub>2</sub> products required to make this process economically viable, was not achieved.

The major reason for this limitation is the occurrence of side reactions which are thermodynamically more favorable and mainly lead to the production of carbon oxides. To improve the C<sub>2</sub> selectivity and yield of the process, it is essential to have a better control over the formation of unselective products. To reach that point, a good knowledge of the reaction mechanism and the origin of the formation of CO<sub>x</sub> are essential. There is already a consensus that OCM follows a complex reaction network and carbon oxides are produced through both homogeneous and heterogeneous oxidation of its main hydrocarbons, i.e., methane, ethane, and ethene, see Fig. 1 [3, 6, 8, 11, 13–20]. Nevertheless, the total and partial oxidation of the C<sub>2</sub> components are reported based on isotope-labelled experiments to be the main routes for the production of CO<sub>x</sub> [11, 21, 22]. Therefore, to enhance the reaction performance, the main focus should be on suppressing the oxidation of the ethane and ethene. The milestone to this aim is a detailed understanding of the mechanism of consecutive reactions of both these components. Investigating issues such as the contribution

of the catalyst on their selective and unselective conversion should reveal more details.

In the literature, the mechanistic studies are carried out mostly by tracing the reaction of methane. Under these circumstances, the conversion of C<sub>2</sub> components take place both in sequence and parallel to the direct conversion of methane. In Fig. 1 the status of the discussion of the OCM mechanism is summarized [3–23]. Therefore, the results of the methane coupling reaction do not provide sufficient information about the mechanism of ethane and ethene consecutive reactions.

To solve this problem, we investigated the reaction of ethane and ethene separately from methane, but under the conditions close to OCM. First, the temperature programmed surface reaction (TPSR), co-feeding and isotope-labelled experiments were conducted to study the reaction network of C<sub>2</sub> components. Then, the experimental observations were verified by simulating the reaction of ethane and ethene in Chemkin Pro. Finally, in <sup>13</sup>C methane isotope labelled experiments the influence of methane on the consecutive reaction of C<sub>2</sub> components was compared with the conditions applied in our tests without methane. The Mn<sub>x</sub>O<sub>y</sub>-Na<sub>2</sub>WO<sub>4</sub>/SiO<sub>2</sub>, which is already known as one of the most stable and best-performing catalysts for OCM, [1, 3, 8, 23, 24] was chosen as the model catalyst in these studies.

## 2 Experimental Section

### 2.1 Catalyst Preparation

All catalytic reactions were performed using a Mn<sub>x</sub>O<sub>y</sub>-Na<sub>2</sub>WO<sub>4</sub>/SiO<sub>2</sub> catalyst. This material was chosen as the model catalyst based on the previous reports documenting it as one of the most efficient and stable catalysts

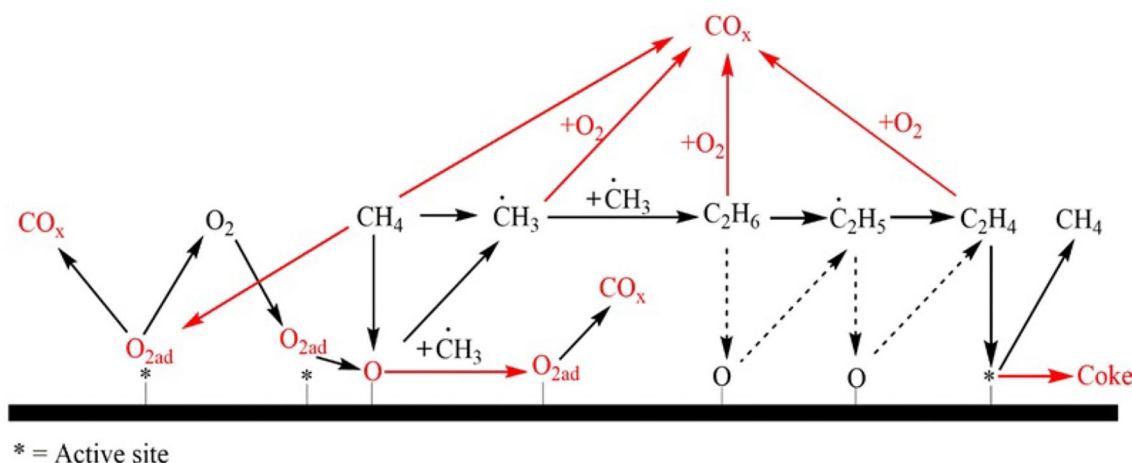


Fig. 1 Simplified reaction network of OCM

for OCM [3, 20, 25–27]. The material was prepared by incipient wetness impregnation as described by Fang et al. [28]. First, amorphous  $\text{SiO}_2$  (Silica Gel, Davisil, Grade 636, Sigma-Aldrich) was sieved to the particles diameter of 200–350  $\mu\text{m}$ , and impregnated in two steps using aqueous solutions of  $\text{Mn}(\text{NO}_3)_2 \cdot 4\text{H}_2\text{O}$  (p.a.,  $\geq 97\%$ , Sigma-Aldrich) and  $\text{Na}_2\text{WO}_4 \cdot 2\text{H}_2\text{O}$  (p.a.,  $\geq 99\%$ , Sigma-Aldrich) in adequate concentration. After each impregnation step, the sample was dried in a cabinet dryer at 100  $^\circ\text{C}$ , overnight. The obtained solid was then calcined at 800  $^\circ\text{C}$  for 8 h under static air. An annealing procedure was performed using a heating rate of 1 K/min. The final catalyst was none porous and had a specific surface area of 3.2  $\text{m}^2/\text{g}$ . It consists of 5 wt%  $\text{Na}_2\text{WO}_4$  and 2 wt% Mn(II) on  $\text{SiO}_2$ .

## 2.2 Feed Gases

Methane (99.95%), ethane (99.95%), ethene (99.90%), oxygen (99.998%) and helium (99.999%) were purchased from Air Liquide. The pure labelled methane ( $^{13}\text{CH}_4$  99 atom %  $^{13}\text{C}$ ) was provided by Sigma Aldrich. All the gases were used in the experiments as received, without further purification.

## 2.3 Reactor Setup

A simplified scheme of the experimental setup is presented in Fig. 2. The dashed line shows the path of the effluent in the isotope-labelled experiments. In all the other experiments the gas stream goes directly to the analytical instrument as presented by the solid line.

Unless noted, all the catalytic and blank tests are performed using 1 g of the solid material sieved in the range of 200–300  $\mu\text{m}$ . Two reactors which were different in geometry, but both made of quartz were used in our studies. These reactors were located in a temperature controlled oven (T range 25–900  $^\circ\text{C}$ ). The temperature in the catalytic bed was measured using a type K thermocouple. To regulate the flow of the gasses, Mass Flow Controllers (EL-FLOW, Bronkhorst) were used. To ensure a homogeneous reaction mixture a mixing cylinder was built before the reactor inlet. The pre-catalytic pressure was monitored using the P-I-1, the pressure indicator 1. Depending on the experiment, either the mass spectrometer (MS), the gas chromatograph (GC) or the MS attached to a GC column were employed to analyse the composition

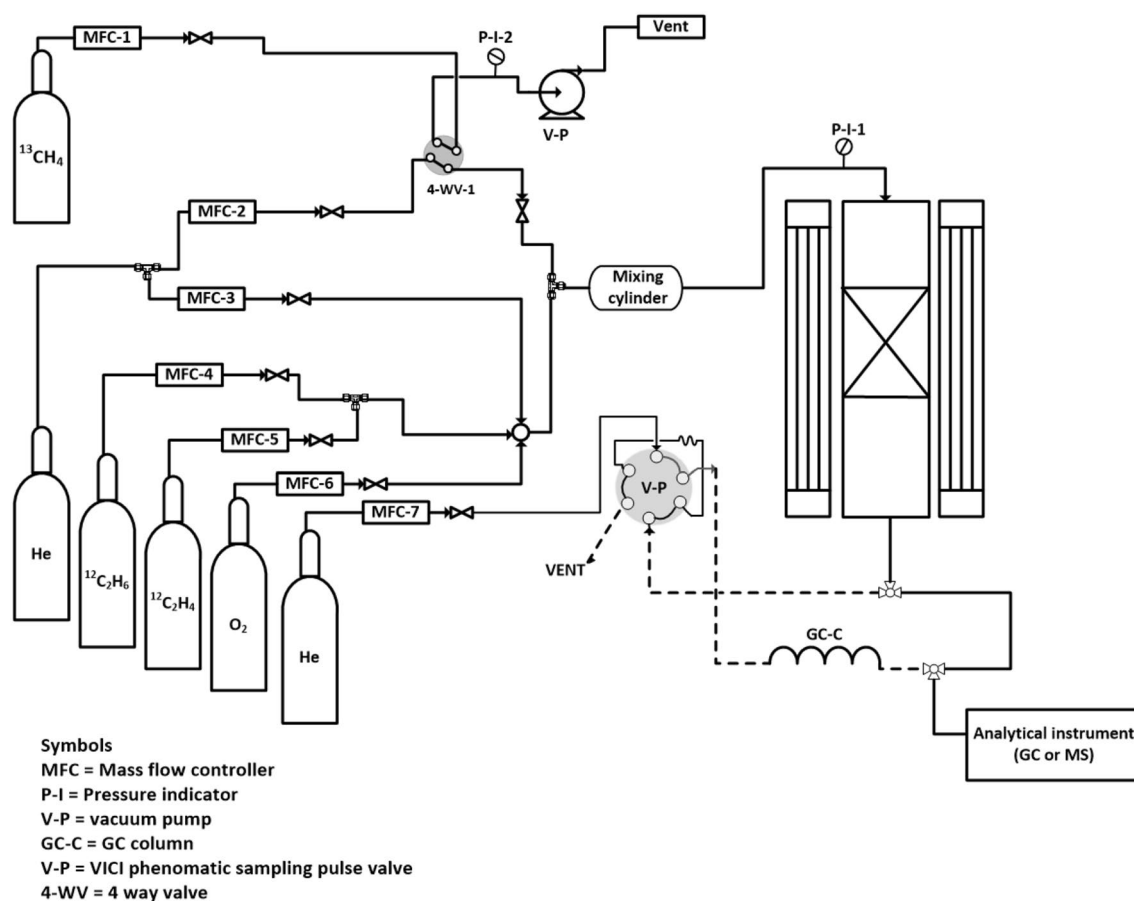


Fig. 2 Schematic of the experimental setup

of the effluent. Nevertheless, both the GC and MS were calibrated to distinguish alkanes and alkenes of  $C_{1-3}$  as well as  $CO$ ,  $CO_2$ ,  $N_2$ , and  $O_2$ . Since helium was used as the carrier gas of the GC, neither  $H_2$  nor He could be detected by GC, however, this limitation does not apply to the measurements done with the MS.

Unless otherwise mentioned, all the tests were performed in a tubular fixed-bed reactor with 9 mm internal diameter i.d and 35 cm length. A quartz frit with the pore size of 120  $\mu m$ , was placed in the middle of this reactor to keep the catalyst in its position. This set up was equipped with a quadrupole mass spectrometer (Inprocess Instruments GAM 200) [29].

Kinetic investigations were conducted in a U-shaped fixed-bed reactor with 6 mm i.d and 25 cm length. The total flow and the volumetric flow of hydrocarbon in the reaction mixture were kept constant in these experiments. However, the concentration of oxygen was varied by substituting it with the same flow of the inert gas. The reaction performance was calculated in a temperature range of 570–630  $^{\circ}C$ . To measure the composition of effluent with a high accuracy, an Agilent GC (7890 A) was used for gas analyses. The GC was equipped with a flame ionization detector (FID) and a thermal conductivity detector (TCD). The separation of effluent was done in a HP-PLOT/Q and a HP Molsieve column. As mentioned earlier, the GC carrier gas was He (Air Liquide, purity 99.999%) therefore the detection of  $H_2$  and He was not possible in these experiments [30].

For the isotope-labelled experiments, the post and pre catalyst sections of the tubular reactor were modified. The experiments were performed using a mixture of  $^{13}CH_4$  and  $^{12}C_2H_6$  hydrocarbons. The total flow of the reaction mixture was fixed at 70 Nml/min. The volumetric flow of methane was changed from 0 to 5 Nml/min by substituting its flow by the inert gas. A vacuum pump was installed on the set up to purge all the lines connected to the bottle of the labeled gas. The effluent was consisting of a range of products with overlapping ionic masses such as  $CO$ ,  $C_2H_4$ ,  $C_2H_6$  and their isotopes. Therefore, for reliable analytical results, the gas components were separated, before entering the MS. For this purpose a Hayesep Q column of Agilent was installed at the inlet of the mass spectrometer. The effluent was sent to a VICI pneumatic sampling pulse valve with helium as the carrier gas, see Fig. 2. To ensure that the investigations are carried out under steady-state conditions, the effluent was injected to the analytical instrument at least 5 min after the reaction started. More details regarding the construction of the set up, in addition to the calibration and measurement methods applied in these experiments are provided elsewhere [31–33].

## 3 Methods and Experiments

### 3.1 Temperature Programmed Surface Reaction (TPSR)

To distinguish between the catalytic and non-catalytic consecutive reactions of  $C_2$  components from each other, the temperature programmed surface reaction (TPSR) technique was implemented. These experiments were conducted either by using 0.5 g of the catalyst or equal volume of an inert bed (quartz sand or silicon carbide). The first step in each of these experiments consisted of surface oxidation at 820  $^{\circ}C$  under a flow of 40 Nml/min of He and  $O_2$  at a ratio of 1 to 1. Then, the temperature was decreased to room temperature under the same reaction flow. At the end, the bed was heated with a ramp of 1 K/min to 800  $^{\circ}C$ ; while, a flow of 30 Nml/min of 5% ethane or ethene diluted with He was passing through the reactor. The catalyst was kept at 800  $^{\circ}C$  for 10 min before it was cooled down under the same reaction flow to room temperature with a ramp of 1 K/min. The changes in the composition of effluent were continuously recorded by the mass spectrometer and the results were presented as a function of the catalyst bed temperature.

### 3.2 Mechanistic Studies in Stationary Co-feeding Mode

A total flow of 70 Nml/min of either  $C_2H_6/O_2/He$  or  $C_2H_4/O_2/He$  (volume ratio 1/1/33) was used as the feed. The reason for working with highly diluted gas mixture was to mimic the concentration ratio of  $C_2$  components formed during OCM. To distinguish the surface reactions from those occurring in the gas phase one catalytic and two blank co-feeding experiments were performed. The first blank experiment was conducted in the empty reactor and the second was carried out in the presence of SiC (particle size 200–300  $\mu m$ ) as the inert surface. The amount of SiC in the later condition was set in a way that it provides the same volume as 1 g catalyst. However, the total flow in the former study was raised to 175 Nml/min to compensate the changes in the residence time caused by the removal of fixed bed. All the other reaction conditions applied in the catalytic and blank experiments were kept identical in these experiments. The oven was heated with a rate of 1 K/min to a maximum temperature of 750  $^{\circ}C$ . To ensure a constant flow during the heating of catalyst bed, the reaction mixture was introduced to the reactor at least 2 h prior to turning the oven on.

### 3.3 Kinetic Studies in Stationary Co-feeding Mode

These studies were performed to measure the activation energy and the reaction order of oxygen for the consecutive reaction of ethane. The first investigations were done in the presence of 1 g of the catalyst while the blank experiments were conducted using SiC. The amount of SiC was set in a way that its volume would be equal to the volume of 1 g of the catalyst. These experiments were performed in the U-shaped reactor connected to the GC. The total flow was set at 90 Nml/min throughout the whole experiment. The reaction mixture was consisting of a fixed amount of C<sub>2</sub>H<sub>6</sub> (25 Nml/min) while the volumetric flow of oxygen varied between 0, 3, 4, 5, 6, 7 Nml/min. The reaction performance was measured for each of the described reaction mixtures at the temperature range of 585, 600, 615 and 630 °C, in the catalytic experiment, and at 585, 600, 615, 630 and 645 °C, in the blank tests.

### 3.4 Experiments with <sup>13</sup>C Labelled Methane

For this experiment, 1 g of the catalyst was placed in the isothermal zone of the fixed bed reactor. To keep the residence time constant the total flow, 70 Nml/min, was kept constant for the extent of the experiment. First, the catalyst was heated under the flow of He to 700 °C with a temperature ramp of 10 K/min. As soon as the target temperature was established the gas composition was switched from He to a mixture of 3/3/64 Nml/min of C<sub>2</sub>H<sub>6</sub>/O<sub>2</sub>/He. The helium flow was divided between two different flow controllers, MFC-2 and MFC-3, which were set at 5 and 59 Nml/min respectively. The reason for this was to ensure continuous flow in the line connecting the 4-WV-1 (4 way valve-1, Fig. 1) to the reactor when the flow of methane was switched off. Otherwise, either back mixing or dead volume could have been created in these lines and falsify the experimental results.

In the next step, labeled methane was added to the earlier reaction mixture by switching the flow from 5 Nml/min of helium to <sup>13</sup>CH<sub>4</sub>. The MFC-1 (used for dosing methane) was set at 5 Nml/min before the direction of the valve was changed. The gas composition of 3/3/59/5 Nml/min of C<sub>2</sub>H<sub>6</sub>/O<sub>2</sub>/He/<sup>13</sup>CH<sub>4</sub> was sent to the reactor. All the other reaction conditions were kept constant. The changes in the composition ratio of effluent were continuously recorded by the MS.

To improve the accuracy of the analyses, the post-reactor section of the set up was modified to operate as a GC-MS. The effluent was sent to the sampling loop of a VICI pneumatic

pulse valve which used 10 Nml/min of helium as the carrier gas. A GC Hayesep Q column was installed between the pulse valve and the MS. The carrier gas was passing through the column creating the baseline in the MS. For measurements, the valve was switched toward the sampling loop, where the carrier gas could take the reaction sample to the analyzer. The gas species in the reaction mixture were first separated by the GC column, before entering the MS. Since, the CO, O<sub>2</sub> and CH<sub>4</sub> could not adsorb on the Hayesep Q column, they were detected at the same time shortly after the injection. This was followed by the detection of the well-separated peaks of CO<sub>2</sub>, C<sub>2</sub>H<sub>4</sub>, and C<sub>2</sub>H<sub>6</sub> one after the other. To calculate the concentration of the isotopes of each of the components, the changes in the ion intensity of a specific ionic mass at the corresponding residence time of the component was put into consideration, see Table 1. The first measurements were conducted at least 30 min after each of the reaction conditions were established. A 15 min time interval was applied between every two measurements, conducted under the same reaction conditions.

### 3.5 Design of the Experiments

The consecutive reaction of ethane and ethene in the OCM reactor is assumed to be taking place on both the catalyst surface and in the gas phase [22, 23, 34]. Under these circumstances, investigating the reaction mechanism of these components is quite difficult. First, to decrease the complexity of these studies, the latter reactions were distinguished from that of the former one by applying the TPSR technique [34]. This technique is quite informative in studying the reaction mechanism of the selective oxidation reactions, especially those which are taking place over a catalyst capable of either storing oxygen, similar to our catalyst [23, 35], or providing its bulk oxygen.

In the next step, the conversion of ethane and ethene in the presence of gas phase oxygen, i.e., in the co-feeding mode, was analyzed. The purpose of these experiments was to study the phenomena observed in the TPSR experiments more in detail. Furthermore, the influence of the gas phase mechanism on the reaction network of C<sub>2</sub> components was surveyed. The condition of the catalyst pore and film diffusion limitation in these experiments were determined by calculating the Weisz-Prater and Mears criterion parameters.

Further, the kinetic parameters for the reaction of ethane were measured to examine the accuracy of the mechanistic studies. The conversion of C<sub>2</sub> components, under the experimental conditions applied in the co-feeding experiments was

**Table 1** The ionic masses considered to quantify the isotopes at the residence time specified for each of the components

Component	<sup>12</sup> CO	<sup>13</sup> CO	<sup>12</sup> CO <sub>2</sub>	<sup>13</sup> CO <sub>2</sub>	<sup>12</sup> C <sub>2</sub> H <sub>4</sub>	<sup>13</sup> CH <sub>2</sub> CH <sub>2</sub>	<sup>13</sup> C <sub>2</sub> H <sub>4</sub>	<sup>12</sup> C <sub>2</sub> H <sub>6</sub>	<sup>13</sup> CH <sub>3</sub> CH <sub>3</sub>	<sup>13</sup> C <sub>2</sub> H <sub>6</sub>
Ionic mass	28	29	44	45	25	29	30	25	31	32

verified by simulating these reactions in Chemkin-Pro. To conduct the simulation, Dooley's mechanism [36, 37], which was shown to be the best available microkinetic model, presenting the gas phase reactions of the OCM process [38], was implemented.

Finally, the influence of methane on the reactions of  $C_2$  components was studied by adding labelled methane to the reaction mixture.

## 4 Results and Discussion

### 4.1 Origin of the Secondary Oxidation of $C_2$ Components

As the literature studies show, the consecutive reaction of  $C_2$  components is the main pathway towards the formation of carbon oxides in the OCM reactor [11, 21, 22]. The same conclusion was made from a series of co-feeding experiments conducted in this study. A flow of 70 Nml/min of  $CH_4/O_2/He$ ,  $C_2H_6/O_2/He$  or  $C_2H_4/O_2/He$  with the ratios of 4/1/5, 1/1/33 and 1/1/33, respectively, were fed to the reactor loaded with the catalyst. The former reaction mixture ( $CH_4/O_2/He$  at the ratio of 4/1/5) was the standard gas composition ratio used to investigate the OCM reaction, while the latter two were set to mimic the real concentration of  $C_2$  components formed during OCM. The performance of the reaction of each of these gas mixtures was calculated at 750 °C and considered as the base of our analysis. As the results in Table 2 show, conversion of both ethane and ethene, despite their high dilution has resulted in a significantly higher yield of carbon oxides in comparison to the experiment performed with the OCM standard gas composition. As shown in Table 2, CO is the main unselective reaction product in oxidation of ethane and ethene. This is very different from methane which resulted in formation of  $CO_2$  as main unselective products. This difference in product distribution can be related to the initial concentration of molecular oxygen in  $C_2$  co-feeding experiment ( $O_2:C_2H_x:He$  ratio of 1:1:33) that is lower than in the normal OCM reaction mixture ( $O_2:CH_4:He$  ratio of 1:4:4). As shown in Fig S5  $CO_2$  is the main carbon oxide product in the reaction using

ethene. This trend is sustained as long as the concentration of oxygen remains relatively high. Once almost all oxygen is consumed (temperature around 700 °C) the concentration of CO continuously increases with reaction temperature while that of  $CO_2$  decreases. The outcome of this experiments as well as results obtained in the TPSR experiments suggest CO as the primary product of the unselective oxidation of ethene. If enough oxygen would be available in the reactor (e.g. like in the standard OCM reaction), then CO will be further oxidized to  $CO_2$ . The difference in the nature of the main carbon oxide product observed in our studies (CO) and in the literature reports ( $CO_2$ ) is then further explained by the reaction mechanism. This observation is in good agreement with the literature studies where the  $C_2$  components are reported to have a higher reaction rate for total oxidation reactions than methane [22, 39–41]. Based on these results, it is concluded that the secondary oxidation of ethane and ethene is the main route towards the production of undesired products in the presence of  $Mn_xO_y-Na_2WO_4/SiO_2$  catalyst, as well.

When the consecutive reaction of  $C_2$  components was identified as the main pathway towards the production of carbon oxides in the OCM reactor, the mechanism of formation of these unselective products became a matter of investigation. As it was mentioned earlier, the reaction of OCM is accepted to take place both homo- and heterogeneously [3, 5, 13, 42]. First, the heterogeneous mechanism was studied separately from the homogenous part by implementing the TPSR technique [43].

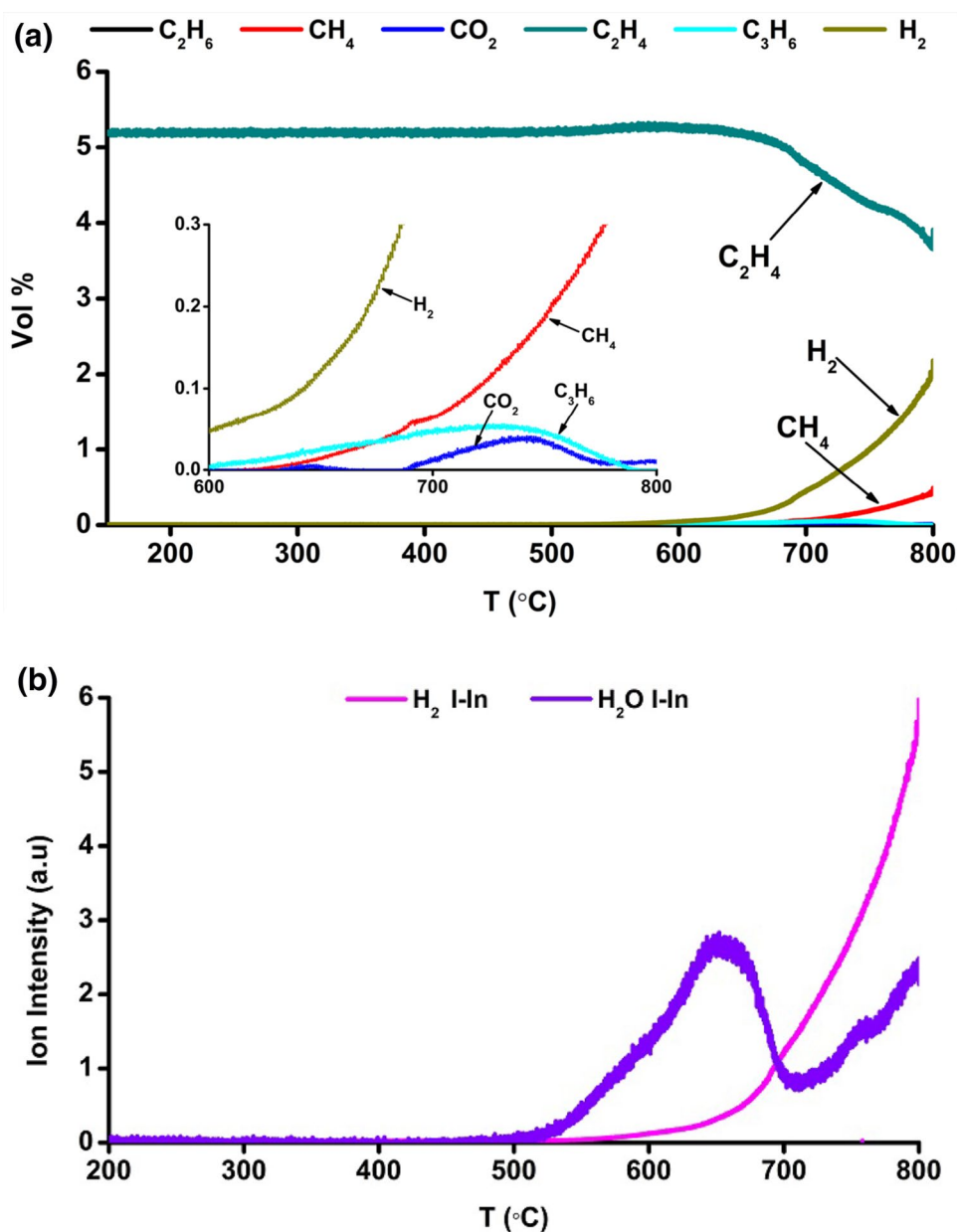
Two sets of experiments were conducted with either ethane or ethene as the reactant. The investigations were done in the presence of the catalyst, quartz sand, and silicon carbide, sequentially. The latter two materials were used as an inert surface to perform the blank experiments. In each of the experiments, the surface was firstly oxidized under a flow of  $O_2$  at 820 °C for 30 min. Then, the reactor was cooled down to room temperature under the same reaction flow. Finally, the surface was heated slowly (1 K/min) to 800 °C under a flow of either ethane or ethene, which were diluted with He. The changes in the composition of effluent were continuously recorded with the mass spectrometer. The results of the catalytic experiments are presented as a

**Table 2** The performance of the reaction using  $CH_4 : O_2 : He = 4:1:5$ ,  $C_2H_6 : O_2 : He = 1:1:33$ , and  $C_2H_4 : O_2 : He = 1:1:33$  at 750 °C, total flow 70 Nml/min (using 1 g  $Mn_xO_y-Na_2WO_4/SiO_2$  catalyst)

	$X(C_xH_y)$	$S(C_2H_6)$	$S(C_2H_4)$	$S(CO_2)$	$S(CO)$	$Y(C_{2+})^a$	$Y(CO_x)$
$CH_4 : O_2 : He$	19.45	25.47	34.48	34.89	0.7	12.72	6.92
$C_2H_6 : O_2 : He$	94.57	–	50.34	2.9	35.8	50.22	36.58
$C_2H_4 : O_2 : He$	47.96	2.9	–	6.91	74.15	3.65	38.88

<sup>a</sup> $(C_{2+})$  in the experiment carried out using ethane is defined to be the sum of  $C_2H_4$ ,  $C_3H_8$ , and  $C_3H_6$ , while that in the experiments with ethene includes the latter two hydrocarbons plus formed  $C_2H_6$

**Fig. 3** Results of the TPSR experiment with ethene, **a** composition ratio of effluent, **b** nominal ion intensity of the water and H<sub>2</sub> in the reactor outlet vs. the temperature of the catalytic bed. Catalyst amount = 0.5 g, C<sub>2</sub>H<sub>4</sub>:He = 1:19 and total flow = 30 Nml/min



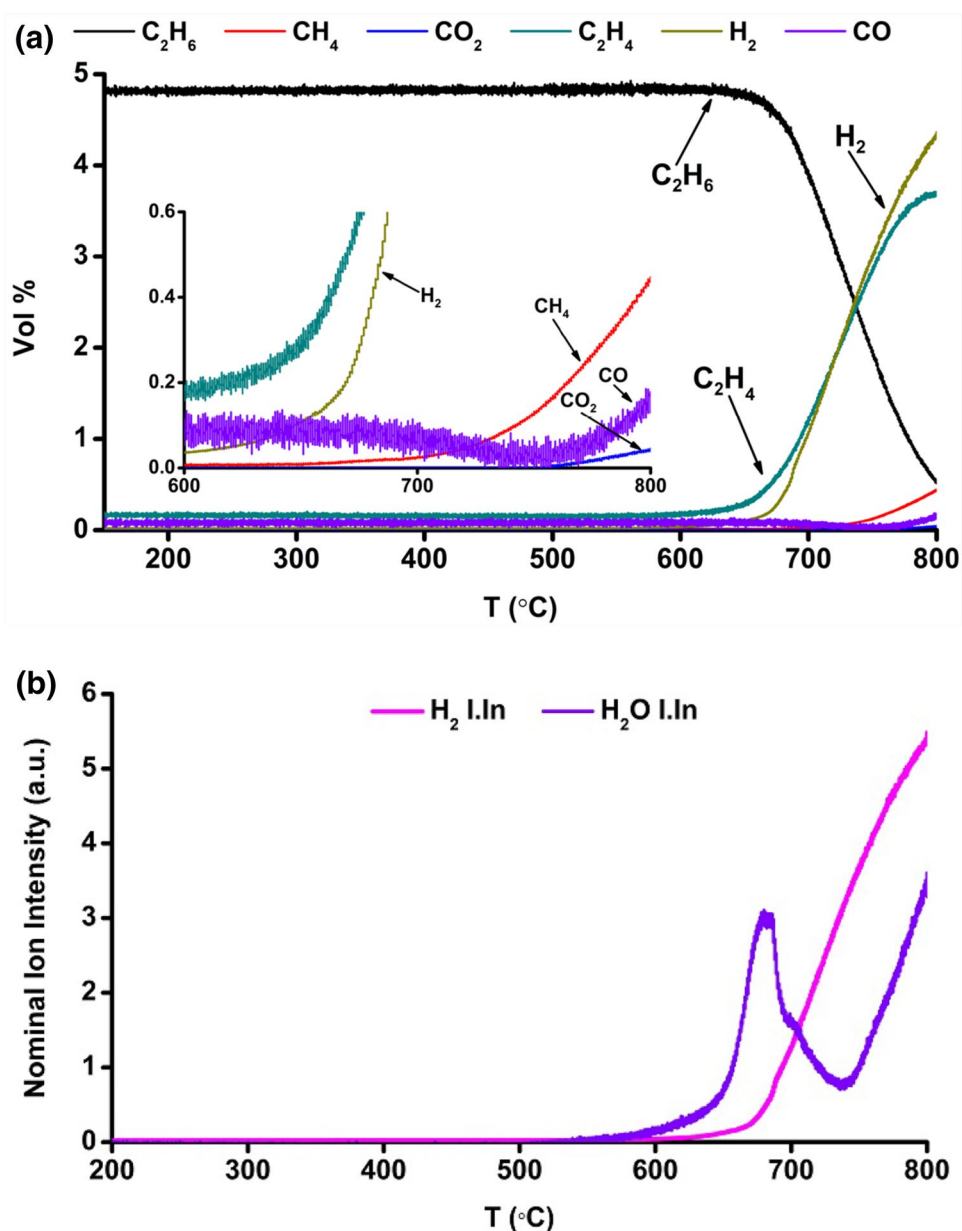
function of the temperature in Figs. 3 and 4. The reaction behavior in these experiments was compared with the stationary co-feeding ones (SI, Figure S5 and S7). With these experiments, not only some characteristics of the reaction mechanism of C<sub>2</sub> components were revealed, but also the origin of their secondary oxidation was clarified as discussed in the following paragraph.

In the ethene TPSR experiments, a continuous increase in the carbon balance was observed with the reaction temperature (SI, Figure S8). The raise was simultaneous with the detection of hydrogen as the main product of the reaction (Fig. 3a). This observation was assigned to the high tendency of ethene to decompose (reaction 2) under the applied reaction conditions [40, 44–46]. The decomposition of ethene

is proposed to take place mostly over the catalyst surface since the rate of conversion in the blank TPSR experiment (SI, Figure S9) was not comparable to the catalytic one. In contrast to the TPSR experiments, where coke was the main reaction product, in the co-feeding experiment mostly carbon monoxide was formed (see SI, Figure S5). The level of conversion in the TPSR experiments was several times lower than in the co-feeding one. Therefore, the formation of CO<sub>x</sub> in the latter experiment is assigned to both the oxidation of coke (the product of ethene decomposition reaction) and the direct oxidation of ethene.

It is worth emphasizing that the chance of selective reaction of ethene and oxygen to form VAP is higher over the catalyst surface than in the gas phase [47]. But even on the

**Fig. 4** Results of the TPSR experiment with ethane, **a** composition ratio of effluent, **b** nominal ion intensity of the water and H<sub>2</sub> in the reactor outlet vs. the temperature of the catalytic bed. Catalyst amount = 0.5 g, C<sub>2</sub>H<sub>6</sub>:He = 1:19 and total flow = 30 NmL/min



surface, oxygen forms either electrophilic or nucleophilic species [48]. At the high temperature of OCM, both these oxygen species convert ethene unselectively to CO<sub>x</sub> products. The nucleophilic species cleave the C-H bond in ethene and form unstable and highly active radicals. These radicals are then over-oxidized in the presence of gas phase oxygen either directly or after forming higher chain hydrocarbons. Moreover, there is a high chance for the collision of radical intermediates to any available surface which results in the formation of coke. On the other side, the electrophilic oxygen would attack the C-C double bond in ethene and forms the epoxies which quickly convert to deep oxidation products at OCM temperature. Therefore, as observed in these studies and reported in the literature [11, 39, 49], the

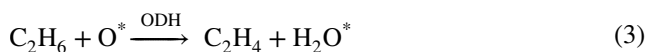
possibility of selective conversion of this component under the harsh reaction conditions of OCM, is always low.

In a second TPSR experiment, ethane was employed as a substrate (Fig. 4). As it is shown in Fig. 4a, ethane starts to react at around 600 °C and produces ethene as expected [13, 49–52]. However, the general assumption is that this conversion occurs by dehydrogenation of ethane with the active oxygen species at the catalyst surface. This reaction is known as oxidative dehydrogenation (ODH) and is presented by Eq. (3) [13, 17, 27, 42, 53]. However, simultaneous detection of hydrogen and ethene at a molar ratio of one to one in our experiment (see Fig. 4a), proposed the thermal dehydrogenation (TDH), presented in Eq. (4), as the main route for this conversion. The pattern of hydrogen and ethene formation

remained identical until the temperature of the catalyst bed exceeded 750 °C. When the concentration of formed ethene and the reaction temperature increased the rate of the ethene decomposition reaction also increases. Therefore, the concentration of hydrogen exceeds that of ethene during this period of the reaction. The proposed TDH reaction was confirmed by observing an identical product pattern during the cooling as well as along the heating period (SI, Figure S10 and S11).

In the next step, the catalytic or non-catalytic nature of TDH reaction of ethane was surveyed. To do so, the catalyst bed was substituted by either quartz sand or silicon carbide and the ethane TPSR experiment was repeated. The reaction performance was calculated for each of these experiments and the results were presented in comparison with each other in Fig. 5. The level of conversion in the blank experiments (performed over the SiC and quartz) was equal to that in the catalytic test. Therefore, it was concluded that the TDH of ethane is not a catalytic reaction.

It was also shown that the occurrence of the TDH reaction in the gas phase has no thermodynamic constraints under the OCM reaction conditions. This is because, a negative free enthalpy was calculated for this reaction at temperatures higher than 400 °C using the thermodynamic data reported by Deutschmann [54].



$$\Delta G = -RT \ln K_x \quad (5)$$

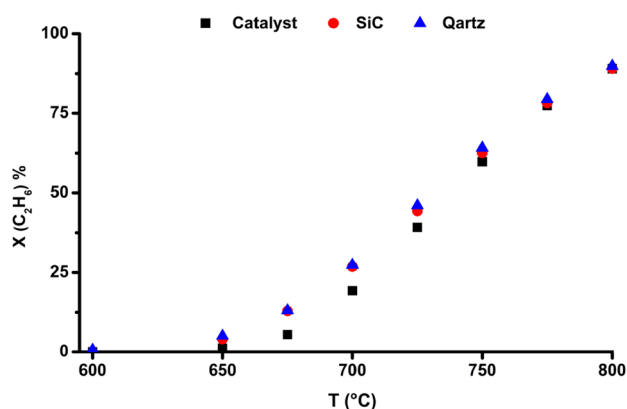


**Fig. 5** The conversion of ethane as a function of the reactor temperature obtained in the TPSR experiments conducted over catalyst (filled square), silicon carbide (red colored circle), quartz (filled triangle),  $\text{C}_2\text{H}_6$ :He ratio of 1:19 at a total flow of 30 Nml/min, heating rate 1 K/min

The possibility of TDH reaction as the main route for converting ethane under the studied experimental conditions was confirmed by comparison of the theoretical and experimental conversion. An equilibrium constant ( $K_x$ ) of 2.14 was calculated for the TDH of ethane under the applied reaction conditions at 750 °C. For this purpose, Eq. (5) was used. This value of  $K_x$  corresponds to a theoretical conversion of around 67% which correlates well with the experimentally measured value of 77%. The 10% difference between the experimental and theoretical conversions reported here is assigned to the occurrence of less dominating reactions such as oxidative dehydrogenation (ODH), unselective oxidation or coke formation reactions.

Based on all these evidence, the TDH of ethane was assumed as the main reaction for producing ethene under the applied reaction conditions here. This reaction is also shown to be mostly taking place in the gas phase of the reactor as reported in the earlier studies, too [52, 55]. Besides, these mechanistic interpretations are in accordance with the literature observations, where the rate of formation of ethene is shown to be independent of the concentration of surface active oxygen ([56]) and the type of catalyst [57].

Another important observation made in the TPSR experiments was related to the lower rate of  $\text{CO}_x$  formation (see Figs. 3a, 4a) in comparison to the co-feeding tests (SI, Figure S5 and S7). It is worth mentioning that the most important difference between the former and the latter experiments was the absence of the molecular gas phase oxygen in the reactor. Therefore, this behavior is assigned to the high contribution of gas phase reactions to the rate of secondary oxidation of the  $\text{C}_2$  components. Accepting this point would have a drastic influence on the choice of the reaction techniques leading to an improvement in the performance of OCM. Therefore, this idea was studied in more details experimentally as well as by conducting simulations.

The experimental studies were conducted by studying the reaction of ethane and ethene in two different blank co-feeding experiments. The details regarding the reaction conditions applied in each of these experiments (in empty reactor and using SiC) are explained in detail in the experimental section. The results of the reaction performance obtained in these experiments are presented in comparison to the catalytic test in Fig. 6. As shown, the reaction performance obtained in these three studies were almost identical. It should be noted that the experiment conducted in the presence of the SiC was performed with a time delay of about 1 year from the other two studies. Therefore, the differences observed in its performance from the latter two tests are suggested to be mostly related to the variations occurring in the set points of the set up such as calibration factors of both the mass flow controllers and the mass spectrometer. However, the small differences observed in the conversion and selectivity of the catalytic reaction with the one

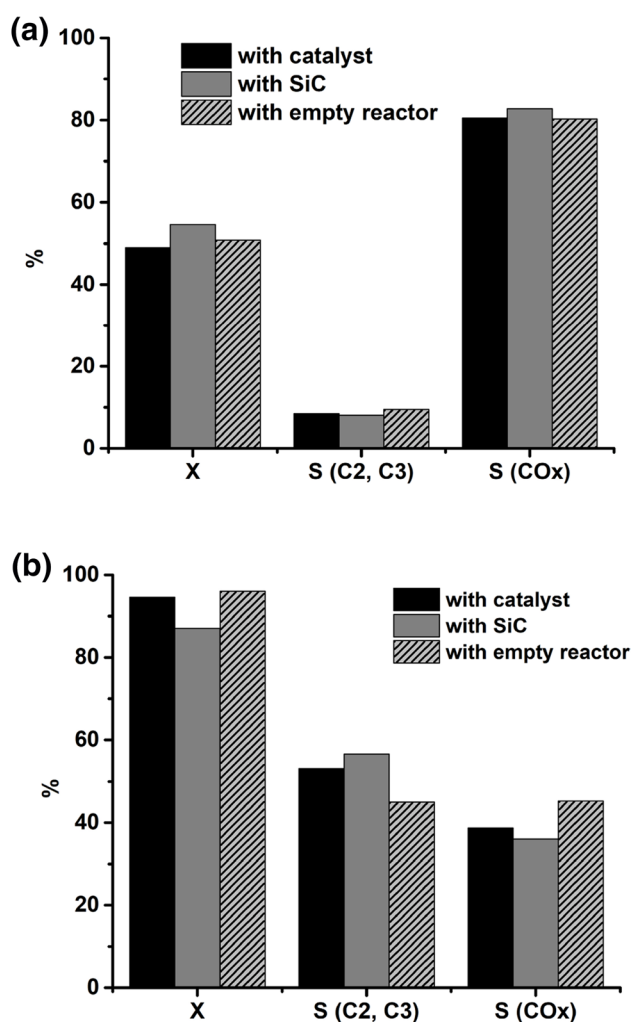


**Fig. 6** Comparison of the reaction performance of **a** C<sub>2</sub>H<sub>4</sub>, **b** C<sub>2</sub>H<sub>6</sub> in the presence of Mn–Na<sub>2</sub>WO<sub>4</sub> catalyst, inert SiC material or empty reactor

conducted in the empty reactor could be explained by taking the gas phase reactions into consideration.

It should be noted that the gas phase reactions are mainly occurring as radical chain reactions. First, the radicals are formed in the rate-limiting step (initiation). Then, they react with the stable components and form new radicals (propagation step). Finally, the radicals would be converted to stable species in the termination step [58]. The interaction of these reactions establishes a steady state situation with a constant concentration of radicals in a radical pool. Therefore, it is expected that the concentration of the radicals would have a strong effect on the level of the conversion of the gas phase reactions. In the presence of the catalyst, a part of the radicals is quenched on the catalyst surface. Under these circumstances, less reactant can be activated during the reaction and this consequently results in a lower level of conversion, as observed in our studies.

The higher selectivity of the reaction observed in the presence of the catalyst is also consistent with our interpretations of the reaction mechanism of C<sub>2</sub> components. In the catalytic tests, a part of the oxygen was adsorbed on the surface of the catalyst. This resulted in a decrease in the concentration of the gas phase oxygen in the reactor. If the secondary oxidation of C<sub>2</sub> components is considered as reactions which mainly take place in the presence of the molecular O<sub>2</sub>, then the lower rate of formation of CO<sub>x</sub> would be an expected consequence.

This observation which was also reported earlier [40, 55], clearly shows the high influence of the gas phase reactions on the consecutive reaction of C<sub>2</sub> components. A difference between the nature of the gas phase conversion of ethane and ethene was also noticed when the results of these experiments were considered alongside the TPSR studies. The contribution of the homogeneous and heterogeneous reactions to the conversion of ethene is observed to change with the presence of oxygen in the reactor. However, ethane is shown to react mainly through the non-catalytic dehydrogenation reaction and the oxygen doesn't have a strong influence on the rate of this conversion. However, it can shift the equilibrium forward by reacting with hydrogen, the product of TDH of ethane.

The last experimental approach to verify the gas phase nature of the consecutive reaction of ethane was made by measuring its kinetic parameters in the presence and absence of the catalyst. A formal kinetic model was used for these studies. For this, activation energy and the reaction order of oxygen were calculated.

The activation energy was measured by calculating the conversion of ethane at different temperatures while a constant reaction mixture was sent to the reactor. The reaction was studied at temperatures of 585, 600, 615 and 630 °C, in the presence of the catalyst and at 585, 600, 615, 630 and 645 °C in the presence of silicon carbide (blank experiment). The logarithmic rate of consumption of ethane was plotted vs. the inverse of the reaction temperature (see SI, Figure S12). The slope of these curves is a function of the activation energy of the reaction as presented in Eq. (6). These results indicate that activation energy of ethane in the presence of catalyst is lower (256 KJ/mol) than in the presence of inert material, Si C (285 KJ/mol), showing an important role of the catalyst in the overall reaction.

$$\text{Slope} = -E_a/R \quad (6)$$

The reaction order of oxygen was calculated in the presence of both the catalyst and silicon carbide at temperatures of 585, 600, 615 and 630 °C. To do so, the rate of conversion of ethane was studied at each temperature while the initial concentration of oxygen was changing. The oxygen flow varied between 0, 3, 4, 5, 6, 7 Nml/min by substituting the flow of helium with oxygen. Both the total flow and

ethane flow were kept constant in the whole period of the studies. The rate of conversion of ethane at each of the tested temperatures was calculated. The results were depicted as a function of the oxygen concentration in a double logarithmic plot (see SI, Figures S13 and 14). The reaction order of oxygen in both conditions, in the presence of the catalyst or silicon carbide, was measured to be between 0.2 and 0.3 which is lower than the 0.5 reported in the literature [13, 51]. This observation indicates the low dependency of the reaction rate of ethane to the oxygen concentration at low conversions.

The similarity of the activation energy of ethane in addition to the low reaction order of oxygen in the blank and catalytic studies are in good agreement with the idea that the  $\text{Mn}_x\text{O}_y\text{-Na}_2\text{WO}_4/\text{SiO}_2$  has a negligible effect on the conversion of ethane under the applied reaction conditions.

Finally, the conversion of  $\text{C}_2$  components under the co-feeding reaction conditions was simulated with Chemkin-Pro. The simulation was done using the Dooley mechanism. The reaction conditions applied to conduct the simulation were the same as those used in the co-feeding studies. The reaction was defined to occur in a plug flow reactor with the same dimensions as the experimental reactor. It was assumed that the reactor works in an isothermal situation. The temperature profile along the reactor, when the oven temperature was set at 750 °C, was measured and the obtained profile was exported to Chemkin to simulate the reaction behavior. The reaction mixture was defined as the mixture of 70 Nml/min of  $\text{O}_2/\text{C}_2\text{H}_6/\text{He}$  at a ratio of 1/1/33. The concentration profile of the components along the whole length of the reactor was calculated by the model. The concentration of the main products of the reaction, i.e.  $\text{C}_2\text{H}_x$ ,  $\text{CO}_x$ , and  $\text{H}_2$  at the reactor output were compared with the same values obtained during the experiment, see Fig. 7. As expected, the Dooley gas phase microkinetic model could

predict the reaction behaviour of ethane and ethene well. The most noticeable deviation between the experimental and simulation results is related to the concentration of  $\text{H}_2$  (not shown in Fig. 7). The reason for this observation is assigned to the fact that the Dooley mechanism doesn't consider the decomposition reaction. This leads to an overestimation of ethene and simultaneously the underestimation of  $\text{H}_2$  concentration predicted by the model.

## 4.2 Isotope-Labelled Experiments

So far, the reaction mechanism of  $\text{C}_2$  components was investigated in the absence of the most abundant hydrocarbon in the OCM reactor, i.e. methane. Under these circumstances, the concentration of methyl radicals in the reactor is low. Therefore, it can be argued that the reaction mechanism of  $\text{C}_2$  components obtained from our studies does not indicate the behavior of these compounds during OCM. The effect of partial pressure of methane on the consecutive reaction of  $\text{C}_2$  components is already studied briefly [39, 40, 59, 60]. Unfortunately, the investigations over  $\text{Mn}_x\text{O}_y\text{-Na}_2\text{WO}_4/\text{SiO}_2$  were performed without isotope labelled hydrocarbons [39], that could lead to inaccurate interpretation due to the applied experimental procedure. In those studies, only the partial pressure of  $\text{CH}_4$  was changed in a mixture of  $\text{C}_2$ ,  $\text{O}_2$ , and  $\text{N}_2$ . The conversion of each of the hydrocarbons was calculated by comparing their concentration in the feed stream with that measured after the reaction. A decrease in the conversion of ethane and ethene was reported when the partial pressure of methane was increasing [39]. However, the occurrence of methane coupling reaction is not considered in that analysis. By increasing the concentration of methane in the reactor, the rate of conversion of methane to  $\text{C}_2$  products has been enhanced. This automatically results in a higher concentration of  $\text{C}_2$  components measured in the reactor

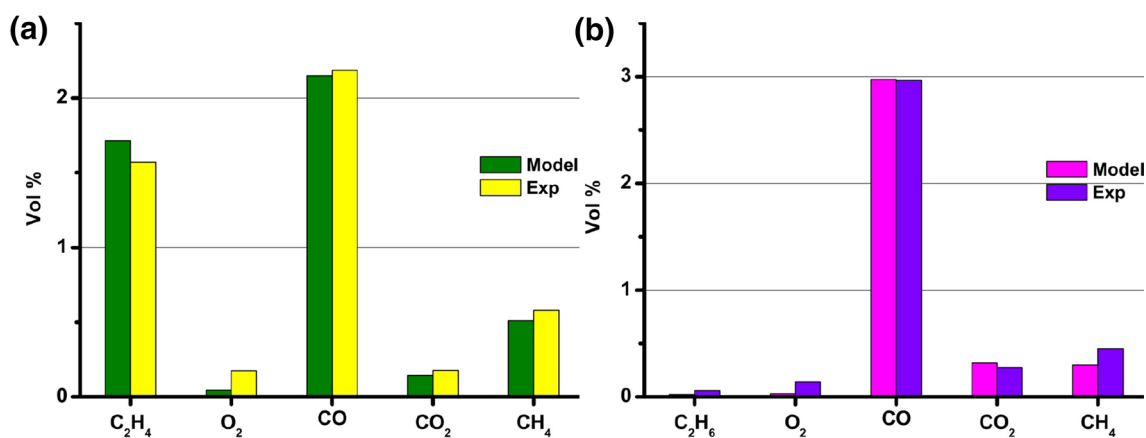


**Fig. 7** Comparison of the concentration of the reaction products obtained experimentally with that calculated by Chemkin for the conversion of **a** ethane, **b** ethene

outlet. Since in the reaction mixture neither methane nor ethane were labelled, the authors could not distinguish the ethane formed from methane coupling reaction and the one introduced with the reaction mixture. To avoid the discussed misinterpretation, the same experiments were repeated in these studies using  $^{13}\text{C}$  labelled methane.

The reaction of ethane in the co-feeding mode was investigated at a temperature of 700 °C. All the reaction conditions were constant except the partial pressure of the labelled methane in the feed. First, the reaction of ethane was tested by sending a flow of 3, 3 and 64 Nml/min of  $\text{C}_2\text{H}_6$ ,  $\text{O}_2$  and He to the reactor. Then, a flow of 5 Nml/min of labelled methane ( $^{13}\text{C}$ ) was added to the reaction mixture. To keep the residence time constant, methane was substituted by the same flow of inert gas. The effluent was continuously analyzed by a semi GC–MS.

The changes in the I.In of  $\text{CO}_x$ ,  $\text{C}_2\text{H}_4$ ,  $\text{C}_2\text{H}_6$  in the effluent was the determining parameter in these studies. Each of these components was detected by mass spectrometer at different time intervals. The labelled and non-labelled forms of the species were distinguished from each other by measuring their individual ionic masses as reported in Table 1. The results obtained from these measurements are presented in Fig. 8.

As it is shown in Fig. 8a, negligible changes were observed in the concentration of  $\text{C}_2\text{H}_6$  in the presence and absence of the labelled methane ( $^{13}\text{CH}_4$ ). This observation is consistent with the proposed gas phase nature for the conversion of ethane in the OCM reactor. However, the intensity of the ionic mass 25, assigned to the  $\text{C}_2\text{H}_4$ , was observed to increase slightly in the experiment performed in the presence of labelled methane, see Fig. 8a. It should be noted that the conversion of  $^{13}\text{CH}_4$  results in the formation of both, labelled ethane (see Fig. 8e) and ethene (either  $^{13}\text{CH}_2\text{CH}_2$  or  $^{13}\text{C}_2\text{H}_4$ , see Fig. 8f). The former product creates a peak at the ion mass of 25 similar to the normal ethene ( $^{12}\text{C}_2\text{H}_4$ ). This suggests that the mentioned increase in the I.In of mass 25 observed in Fig. 8a is probably caused by measurement errors. Therefore, contrary to ethane, to draw a conclusion about the effect of methane on the behavior of ethene, more evidences are needed. This information is gained by comparing the rate of  $\text{CO}_x$  formation (presented in Fig. 8b–d). When the labelled methane was added to the reaction mixture, the rate of production of  $^{12}\text{CO}_x$  decreased while the  $^{13}\text{CO}_x$  was detected in the effluent. This observation indicates the consumption of a part of the surface oxygen by  $\text{CH}_4$  as soon as it is introduced to the reactor (Fig. 8b, c). As discussed in the previous section, the heterogeneous reactions have a higher contribution to consecutive conversion of ethene than ethane. In addition, the conversion of ethene on the catalyst was shown to result in the formation of unselective products, either coke (from decomposition) or carbon oxidizes (if reacted with oxygen). In the presence of

methane, the rate of oxidation of ethene is suppressed since there would be a competition between these two hydrocarbons to react with the surface oxygen species. These observations which are consistent with the literature reports, confirm the validity of the mechanistic modification suggested for consecutive reaction of  $\text{C}_2$  components as discussed in the earlier section. The reasons for the influence of methane on the rate of secondary oxidation of these components reported in the earlier studies [39, 40, 59, 60] could also be explained by the competition for the surfaced bound oxygen.

Despite all these evidences confirming the gas phase nature of the consecutive reaction of ethane in the OCM reactor, it may be questioned how the  $\text{Mn}_x\text{O}_y\text{--Na}_2\text{WO}_4$  catalyst which can activate the more stable methane and ethene molecules has negligible influence on the conversion of ethane. This point is addressed in the last section of this study where the external mass transfer limitation is shown to be causing this behaviour.

### 4.3 Mass Transfer Condition in the Co-feeding Experiments

The concentration ratio of  $\text{C}_2$  components and  $\text{O}_2$  in the reaction mixture of the co-feeding experiments was chosen to simulate the real condition in the OCM reactor to a certain extent. Therefore, via calculating the Weisz–Prater ( $\Psi$ ) and Mears ( $C_m$ ) criterion [61, 62], valuable information regarding the mass transfer situation of methane, ethane, and ethene under OCM reaction conditions was obtained.

The Weisz–Prater criterion was calculated at 750 °C for each of the three co-feeding experiments (for the details of calculation see the supporting information). The value of Weisz–Prater in all the experiments was far smaller than one, see Table 3. Therefore, it is concluded that the rate of reaction of these components is not limited by any internal mass transfer limitation.

In the next step, the Mears criterion was calculated to study the external mass transfer situation in the performed experiments. Details of the calculation procedure are provided in the supporting information. For the reaction of methane, the parameter was much lower than 0.15, whereby in the reactions of ethane and ethene it exceeded this limit, i.e. 0.15, see Table 4. This observation indicated the influence of the external mass transfer on the reaction of  $\text{C}_2$  components, especially ethane. This phenomenon was investigated for the reaction of ethane in more detail in a series of experiments. Conversion of ethane was tested in the co-feeding modus by keeping the feed composition constant (1/1/33  $\text{C}_2\text{H}_6/\text{O}_2/\text{He}$ ) while the total flow was increased from 70 to 140, 200, and 250 Nml/min. The conversion of ethane in each of these experiments was calculated and the results are presented in Fig. 9 as a function of the catalyst bed temperature. In the absence of mass transfer limitation, the rate

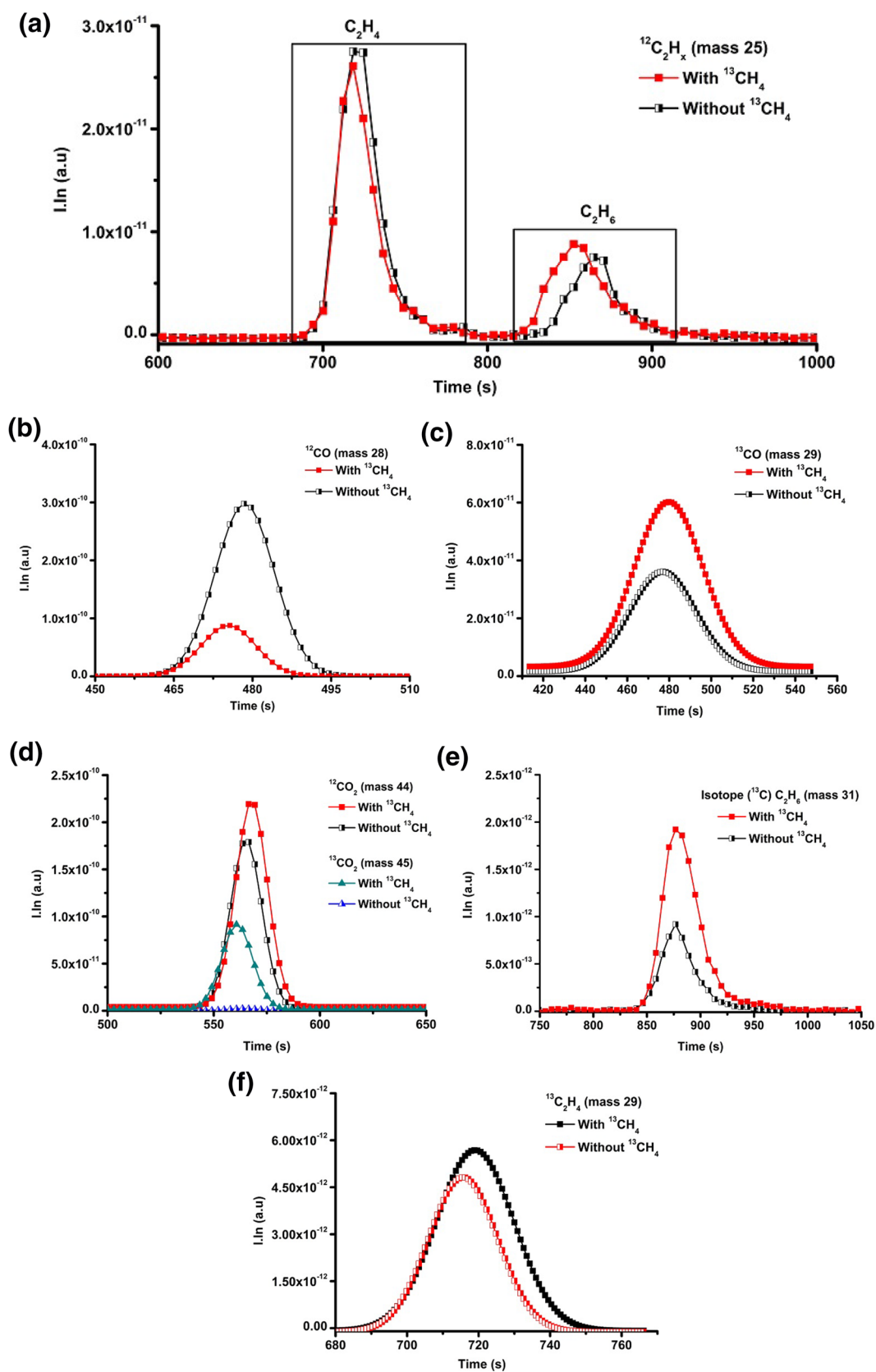


**Fig. 8** Changes in the Ionic masses corresponding to the reaction products in the experiments done with (solid symbols), and without (the half-filled symbols), mixing  $\text{CH}_4$  in the reaction mixture

**Table 3** The calculated Weisz–Prater Criterion and the characteristic values implemented in calculating this criterion for each of CH<sub>4</sub>, C<sub>2</sub>H<sub>6</sub>, and C<sub>2</sub>H<sub>4</sub>

	CH <sub>4</sub>	C <sub>2</sub> H <sub>6</sub>	C <sub>2</sub> H <sub>4</sub>
Mean free path of the molecule, $\Lambda$ (m)	1.5E–07	4.1E–08	7.7E–08
Diffusion coefficient in the free gas space, $D_g$ (cm <sup>2</sup> /s)	0.86	0.17	0.34
Initial concentration of the reactant, $C_{i,0}$ (mol/l)	1.6E–05	1.2E–06	1.2E–06
Reaction order, $n$	1	1	1
Effective diffusion coefficient, $D_{i,e}$ (cm <sup>2</sup> /s)	0.09	0.02	0.03
Effective reaction rate at 775 °C, $r_1$ (mol/(g·s))	3.7E–6	2.0E–05	3.3E–05
Weisz–Prater Criterion	1.2E–07	5.6E–05	1.7E–06

**Table 4** The calculated Mears Criterion and the characteristic values implemented in calculating this criterion for each of CH<sub>4</sub>, C<sub>2</sub>H<sub>6</sub>, and C<sub>2</sub>H<sub>4</sub>

	CH <sub>4</sub> :O <sub>2</sub> :He	C <sub>2</sub> H <sub>6</sub> :O <sub>2</sub> :He	C <sub>2</sub> H <sub>4</sub> :O <sub>2</sub> :He
Gas mixture ratio	4:1:5	1:1:33	1:1:33
$v_{\text{mix}}$ (m <sup>2</sup> /s)	5.9E–05	9.99E–05	9.99E–05
Reynold Nr	0.25	0.15	0.15
Schmidt Nr	8.3	69.6	35.6
Sherwood Nr	2.6	2.9	2.8
$k_c$ (m/s)	0.06	0.01	0.02
$C_m$	8.8E–04	0.59	0.15

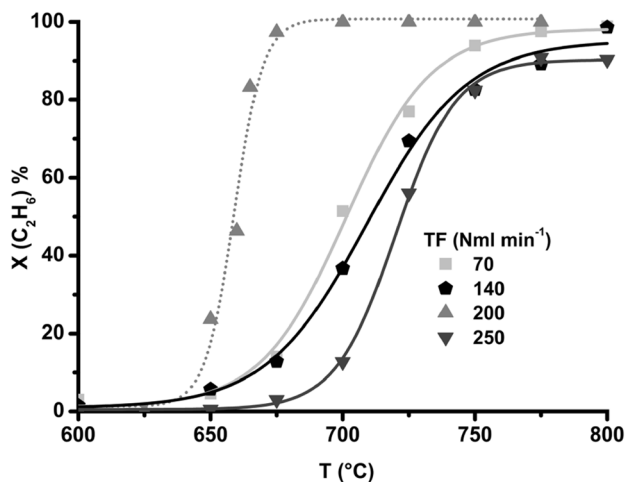


**Fig. 9** Changes in the conversion of ethane in the co-feeding experiments performed at 70, 140, 200, 250 Nml/min total flow vs. temperature, reactant ratio: C<sub>2</sub>H<sub>6</sub>/O<sub>2</sub>/He of 1/1/33, catalyst amount: 1 g

of conversion is expected to decrease at lower residence times. However, in our experiments, no direct correlation was seen between these two parameters, see Fig. 9.

First, the conversion of ethane decreased when the flow was raised from 70 to 140 Nml/min. This observation indicates that in this experiment, the residence time is the only parameter that controls the reaction performance. But, as the flow was further raised to 200 Nml/min an increase

in the conversion was observed. This behavior is assigned to the destruction of the diffusion layer surrounding the catalyst particles which allows ethane to reach the surface more easily. The increase made in the reaction rate under these circumstances has been so high that it has compensated the negative effect of the residence time. Therefore, a higher conversion was recorded for the reaction at the end. After this point, the most important parameter, influencing the reaction rate, should be the residence time again. This was also observed when a lower conversion of ethane was obtained by further increasing the flow rate to 250 Nml/min, see Fig. 9.

Based on the theoretical suggestion made by the Mears criteriums which were also proven experimentally (as discussed earlier), it was concluded that the consecutive reaction of ethane and ethene can be limited by the film diffusion under the OCM reaction conditions. Film diffusion limit also explains the results of our mechanistic studies, where it was shown that the conversion of ethane and ethene would mainly take place in the gas phase.

It worth mentioning that the selectivity of the reaction in the experiment done without the film diffusion limitation (TF 200 Nml/min) was observed to be substantially lower compared to the one with film diffusion limitation. (TF 70 Nml/min) (SI, Figure S15). This behavior is consistent with the high tendency of C<sub>2</sub> components to react through unselective oxidation or decomposition reactions over the catalyst surface as discussed earlier. This behavior indicates the possibility of controlling the reaction performance by adjusting the formation of diffusion layer as discussed in the following paragraph.

As it was mentioned earlier, when no layer is surrounding the catalyst, the rate of secondary conversion of C<sub>2</sub> components increased. This behavior shows that the presence of the film enhances the selectivity of the reaction. Thankfully, the mechanistic features of OCM enable to take advantage of the film diffusion limit to also enhance the performance of the reaction.

There is a conscience that the formation of ethane during OCM occurs by the coupling of methyl radicals in the gas phase of the reactor [3, 6, 17, 52, 63–65]. When the catalyst is covered with a film of an optimal thickness, methane can

diffuse through the film and form methyl radicals. The latter diffuse out of the film as easy as methane. Methyl radicals go through the coupling reaction to form ethane which can react further to form ethene. The cross-section area of C<sub>2</sub> components are almost twice as big as both methane and methyl radicals. Therefore, their transportation is limited along the diffusion layer. Under this circumstance the diffusion film would inhibit ethane and ethene from the consecutive reaction over the catalyst surface. It is therefore emphasized that the diffusion layer should not be too thick, otherwise it would prevent the diffusion of methane and methyl radicals. Accordingly, it is concluded that an optimized particle size, which gives the best influence of the diffusion film, can improve the performance of OCM.

## 5 Conclusions

The results of these studies indicated that the Mn<sub>x</sub>O<sub>y</sub>-Na<sub>2</sub>WO<sub>4</sub>/SiO<sub>2</sub> catalyst has a negligible effect on the consecutive dehydrogenation of ethane to ethene. The reason for this behavior is the external mass transfer limitation caused by the film surrounding the catalyst particles. The mass transfer limitation has shown to have a positive effect on the selectivity of the reaction to C<sub>2</sub> products. Under these conditions, the contact between the catalyst and both, ethene and ethane is reduced. Therefore, the rate of over-oxidation and decomposition of these components on the surface decreases.

The mechanistic investigations have shown that under the OCM reaction conditions the TDH rather than ODH reaction is the main route for converting ethane to ethene. Despite the complex mechanism of the OCM, the formation of CO<sub>x</sub> is observed to be the result of over-oxidation of all the three main hydrocarbons of OCM, i.e. methane, ethane, and ethene. The secondary oxidation of C<sub>2</sub> components is observed to take place in the presence of gas phase oxygen. Therefore, it is concluded that regardless of the applied catalyst, suppression of oxygen from the homogeneous part of the reactor diminishes the formation of CO<sub>x</sub>. Accordingly, implementing reactor concepts like chemical looping or membrane reactor, which fulfills this requirement, can be a promising solution for enhancing the performance of the OCM reaction.

**Acknowledgements** Financial support by the DFG (Grant No. EXC 314) (UniCat Cluster of Excellence) is gratefully acknowledged.

## References

1. Lunsford JH (2000) Catalytic conversion of methane to more useful chemicals and fuels: a challenge for the 21st century. *Catal*

- Today 63:165–174. [https://doi.org/10.1016/S0920-5861\(00\)00456-9](https://doi.org/10.1016/S0920-5861(00)00456-9)
2. Malekzadeh A, Abedini M, Khodadadi A (2002) Critical influence of Mn on low-temperature catalytic activity of Mn/Na<sub>2</sub>WO<sub>4</sub>/SiO<sub>2</sub> catalyst for oxidative coupling of methane. *Catal Lett* 84:45–51
3. Arndt S, Otremba T, Simon U, Yildiz M, Schubert H, Schomäcker R (2012) Mn–Na<sub>2</sub>WO<sub>4</sub>/SiO<sub>2</sub> as catalyst for the oxidative coupling of methane. What is really known? *Appl Catal A*. <https://doi.org/10.1016/j.apcata.2012.02.046>
4. Lunsford JH (1990) Catalytic conversion of methane to higher hydrocarbons. *Catal Today* 6:235–259. [https://doi.org/10.1016/0920-5861\(90\)85004-8](https://doi.org/10.1016/0920-5861(90)85004-8)
5. Sinev MY, Fattakhova ZT, Lomonosov VI, Gordienko YA (2009) Kinetics of oxidative coupling of methane: bridging the gap between comprehension and description. *J Nat Gas Chem* 18:273–287. [https://doi.org/10.1016/S1003-9953\(08\)60128-0](https://doi.org/10.1016/S1003-9953(08)60128-0)
6. Kondratenko EV, Peppel T, Seeburg D, Kondratenko V, Kalevaru N, Martin A, Wohlrab S (2017) Methane conversion into different hydrocarbons or oxygenates: current status and future perspectives in catalyst development and reactor operation. *Catal Sci Technol* 7:366–381. <https://doi.org/10.1039/C6CY01879C>
7. Schwarz H (2011) Chemistry with methane: concepts rather than recipes. *Angew Chemie* 50:10096–10115. <https://doi.org/10.1002/anie.201006424>
8. Lunsford JH (1995) The catalytic oxidative coupling of methane. *Angew Chemie* 34:970–980. <https://doi.org/10.1002/anie.199509701>
9. Gesser HD, Hunter NR (1998) A review of C–I conversion chemistry. *Catal Today* 42:183–189. [https://doi.org/10.1016/S0920-5861\(98\)00090-X](https://doi.org/10.1016/S0920-5861(98)00090-X)
10. Yildiz M, Aksu Y, Simon U, Kailasam K, Goerke O, Schomäcker R, Thomas A, Arndt S (2014) Enhanced catalytic performance of Mn<sub>x</sub>O<sub>y</sub>-Na<sub>2</sub>WO<sub>4</sub>/SiO<sub>2</sub> for the oxidative coupling. *Chem Commun* 50:14440–14442. <https://doi.org/10.1016/j.apcata.2012.02.046>
11. Shi C, Rosynek MP, Lunsford JH (1994) Origin of carbon oxides during the oxidative coupling of methane. *J Phys Chem* 98:8371–8376. <https://doi.org/10.1021/j100085a017>
12. Keller GE, Bhasin MM (1982) Synthesis of ethylene via oxidative coupling of methane I. Determination of active catalysts. *J Catal* 73:9–19. [https://doi.org/10.1016/0021-9517\(82\)90075-6](https://doi.org/10.1016/0021-9517(82)90075-6)
13. Takanabe K, Iglesia E (2009) Mechanistic aspects and reaction pathways for oxidative coupling of methane on Mn/Na<sub>2</sub>WO<sub>4</sub>/SiO<sub>2</sub> catalysts. *J Phys Chem C* 113:10131–10145. <https://doi.org/10.1021/jp9001302>
14. Takanabe K, Iglesia E (2008) Rate and selectivity enhancements mediated by OH radicals in the oxidative coupling of methane catalyzed by Mn/Na<sub>2</sub>WO<sub>4</sub>/SiO<sub>2</sub>. *Angew Chemie* 47:7689–7693. <https://doi.org/10.1002/anie.200802608>
15. Thybaut JW, Sun J, Olivier L, Van Veen AC, Mirodatos C, Marin GB (2011) Catalyst design based on microkinetic models: oxidative coupling of methane. *Catal Today* 159:29–36. <https://doi.org/10.1016/j.cattod.2010.09.002>
16. Yildiz M, Aksu Y, Simon U, Otremba T, Kailasam K, Göbel C, Girgsdies F, Görke O, Rosowski F, Thomas A, Schomäcker R, Arndt S (2016) Silica material variation for Mn<sub>x</sub>O<sub>y</sub>-Na<sub>2</sub>WO<sub>4</sub>/SiO<sub>2</sub>. *Appl Catal A* 525:168–179. <https://doi.org/10.1016/j.apcata.2016.06.034>
17. Lee MR, Park M, Jeon W, Choi J, Suh Y, Jin D (2012) A kinetic model for the oxidative coupling of methane over Na<sub>2</sub>WO<sub>4</sub>/Mn/SiO<sub>2</sub>. *Fuel Process Technol* 96:175–182. <https://doi.org/10.1016/j.fuproc.2011.12.038>
18. Beck B, Fleischer V, Arndt S, Hevia MG, Urakawa A, Hugo P, Schomäcker R (2014) Oxidative coupling of methane—A complex surface/gas phase mechanism with strong impact on the reaction engineering. *Catal Today* 228:212–218. <https://doi.org/10.1016/j.cattod.2013.11.059>

19. Sinev MY (1992) Elementary steps of radical-surface interactions in oxidative coupling of methane. *Catal Today* 13:561–564. [https://doi.org/10.1016/0920-5861\(92\)80081-W](https://doi.org/10.1016/0920-5861(92)80081-W)
20. Pak S, Qiu P, Lunsford JH (1998) Elementary reactions in the oxidative coupling of methane over Mn/Na<sub>2</sub>WO<sub>4</sub>/SiO<sub>2</sub> and Mn/Na<sub>2</sub>WO<sub>4</sub>/MgO Catalysts. *J Catal* 179:222–230
21. Ekstrom A, Lapszewicz Ja, Campbell I (1989) Origin of the low limits in the higher hydrocarbon yields in the oxidative coupling reaction of methane. *Appl Catal* 56:L29–L34. [https://doi.org/10.1016/S0166-9834\(00\)80153-0](https://doi.org/10.1016/S0166-9834(00)80153-0)
22. Nelson PF, Cant NW (1990) Oxidation of C2 hydrocarbon products during the oxidative coupling of methane over Li MgO. *J Phys Chem* 94:3756–3761
23. Parishana S, Littlewood P, Arinchtein A, Fleischer V, Schomäcker R (2017) Chemical looping as a reactor concept for the oxidative coupling of methane over the Mn<sub>x</sub>O<sub>y</sub>-Na<sub>2</sub>WO<sub>4</sub>/SiO<sub>2</sub> catalyst, benefits and limitation. *Catal Today*. <https://doi.org/10.1016/j.fuproc.2011.12.038>
24. Zavyalova U, Holena M, Schlögl R, Baerns M (2011) Statistical analysis of past catalytic data on oxidative methane coupling for new insights into the composition of high-performance catalysts. *ChemCatChem* 3:1935–1947 <https://doi.org/10.1002/cctc.20110186>
25. Pak S, Lunsford JH (1998) Thermal effects during the oxidative coupling of methane over Mn/Na<sub>2</sub>WO<sub>4</sub>/SiO<sub>2</sub> and Mn/Na<sub>2</sub>WO<sub>4</sub>/MgO catalysts. *Appl Catal A* 168:131–137
26. Palermo A, Pedro J, Vazquez H, Lee AF, Tikhov MS, Lambert RM (1998) Critical influence of the amorphous silica-to-cristobalite phase transition on the performance of Mn/Na<sub>2</sub>WO<sub>4</sub>/SiO<sub>2</sub> catalysts for the oxidative coupling of methane. *J Catal* 177:259–266
27. Wang D, Rosynek MP, Lunsford JH (1995) The effect of chloride ions on a Li + MgO catalyst for the oxidative dehydrogenation of ethane.pdf. *J Catal* 151:155–167
28. Fang X, Li S, Gu J, Yang D (1992) Preparation and characterization of W-Mn catalyst for oxidative coupling of methane. *J Mol Catal* 6:427–433
29. V. Fleischer, R. Steuer, S. Parishan, R. Schomäcker (2016) Investigation of the surface reaction network of the oxidative coupling of methane over Na <inf> 2</inf> WO <inf> 4</inf>/Mn/SiO <inf> 2</inf> catalyst by temperature programmed and dynamic experiments. *J Catal*. <https://doi.org/10.1016/j.jcat.2016.06.014>.
30. Yildiz M, Simon U, Otremba T, Aksu Y, Kailasam K, Thomas A, Schomäcker R, Arndt S (2014) Support material variation for the Mn<sub>x</sub>O<sub>y</sub>-Na<sub>2</sub>WO<sub>4</sub>/SiO<sub>2</sub> catalyst. *Catal Today* 228:5–14. <https://doi.org/10.1016/j.cattod.2013.12.024>
31. Fleischer V, Steuer R, Parishan S, Schomäcker R (2016) Investigation of the surface reaction network of the oxidative coupling of methane over Na<sub>2</sub>WO<sub>4</sub>/Mn/SiO<sub>2</sub> catalyst by temperature programmed and dynamic experiments. *J Catal* 341:91–103. <https://doi.org/10.1016/j.jcat.2016.06.014>
32. Le HV, Parishan S, Sagaltchik A, Goebel C, Schlesiger C, Malzer W, Trunschke A, Schomaecker R, Thomas A (2017) Solid-state ion-exchanged Cu/mordenite catalysts for the direct conversion of methane to methanol. *ACS Catal*. <https://doi.org/10.1021/acscatal.6b02372>
33. Arndt S, Simon U, Heitz S, Berthold a, Beck B, Görke O, Epping J-D, Otremba T, Aksu Y, Irran E, Laugel G, Driess M, Schubert H, Schomäcker R (2011) Li-doped MgO from different preparative routes for the oxidative coupling of methane. *Top Catal* 54:1266–1285. <https://doi.org/10.1007/s11244-011-9749-z>
34. Efstathiou aM, Verykios XE (1997) Transient methods in heterogeneous catalysis: experimental features and application to study mechanistic aspects of the CH<sub>4</sub>/O<sub>2</sub> (OCM), NH<sub>3</sub>/O<sub>2</sub> and NO/He reactions. *Appl Catal A* 151:109–166. [https://doi.org/10.1016/S0926-860X\(96\)00262-1](https://doi.org/10.1016/S0926-860X(96)00262-1)
35. Fleischer V, Littlewood P, Parishan S, Schomäcker R (2016) Chemical looping as reactor concept for the oxidative coupling of methane over a Na<sub>2</sub>WO<sub>4</sub>/Mn/SiO<sub>2</sub> catalyst. *Chem Eng J* 306:646–654. <https://doi.org/10.1016/j.cej.2016.07.094>
36. Dooley S, Dryer FL, Yang B, Wang J, Cool Ta, Kasper T, Hansen N (2011) An experimental and kinetic modeling study of methyl formate low-pressure flames. *Combust Flame* 158:732–741. <https://doi.org/10.1016/j.combustflame.2010.11.003>
37. Dooley S, Burke MP, Chaos M, Stein Y, Dryer FL, Zhukov VP, Finch O, Simmie JM, Curran HJ (2010) Methyl formate oxidation: speciation data, laminar burning velocities, ignition delay times, and a validated chemical kinetic model, *Int J Chem Kinet*. <https://doi.org/10.1002/kin>
38. Schwarz H, Geske M, Franklin Goldsmith C, Schlögl R, Horn R (2014) Fuel-rich methane oxidation in a high-pressure flow reactor studied by optical-fiber laser-induced fluorescence, multi-species sampling profile measurements and detailed kinetic simulations. *Combust Flame* 161:1688–1700. <https://doi.org/10.1016/j.combustflame.2014.01.007>
39. Lomonosov V, Usmanov T, Sinev M, Bychkov V (2014) Ethylene oxidation under conditions of the oxidative coupling of methane. *Kinet Catal* 55:474–480. <https://doi.org/10.1134/S0023158414030070>
40. Yu L, Li W, Ducarme V, Mirodatos C, Martin Ga (1998) Inhibition of gas-phase oxidation of ethylene in the oxidative conversion of methane and ethane over CaO, La<sub>2</sub>O<sub>3</sub>/CaO and SrO–La<sub>2</sub>O<sub>3</sub>/CaO catalysts. *Appl Catal A Gen* 175:173–179. [https://doi.org/10.1016/S0926-860X\(98\)00208-7](https://doi.org/10.1016/S0926-860X(98)00208-7)
41. Roos JA, Korf SJ, Veehof RHJ, Van ommen JG, Ross JRH (1989) Reaction-path of the oxidative coupling of methane over a lithium-doped magnesium-oxide catalyst—factors affecting the rate of total oxidation of ethane and ethylene. *Appl Catal* 52:147–156. [https://doi.org/10.1016/s0166-9834\(00\)83378-3](https://doi.org/10.1016/s0166-9834(00)83378-3)
42. Sun J, Thybaut J, Marin G (2008) Microkinetics of methane oxidative coupling. *Catal Today* 137:90–102. <https://doi.org/10.1016/j.cattod.2008.02.026>
43. Falconer JL, Schwarz Ja (1983) Temperature-programmed desorption and reaction: applications to supported catalysts. *Catal Rev* 25:141–227. <https://doi.org/10.1080/01614948308079666>
44. Baró AM, Ibach H (1981) Thermal evolution and decomposition of ethylene on Pt(111). *J Chem Phys* 74:4194–4199. <https://doi.org/10.1063/1.441549>
45. Stroschio JA, Bare SR, Ho W (1984) The chemisorption and decomposition of ethylene and acetylene on Ni(110). *Surf Sci* 148:499–525. [https://doi.org/10.1016/0039-6028\(84\)90596-X](https://doi.org/10.1016/0039-6028(84)90596-X)
46. Park C, Keane MA (2004) Catalyst support effects in the growth of structured carbon from the decomposition of ethylene over nickel. *J Catal* 221:386–399. <https://doi.org/10.1016/j.jcat.2003.08.014>
47. Haber J (2008) Fundamentals of hydrocarbon oxidation, *Handb Heterog Catal*. <https://doi.org/10.1002/9783527610044.hetcat0170>
48. Linic S, Barteau MA (2005) Heterogeneous catalysis of alkene epoxidation. *Handb Heterog Catal*. <https://doi.org/10.1002/9783527610044.hetcat0175>
49. Martin GA, Bates A, Ducarme V, Mirodatos C (1989) Oxidative conversion of methane and C2 hydrocarbons on oxides: homogeneous versus heterogeneous processes. *Appl Catal* 47:287–297. [https://doi.org/10.1016/S0166-9834\(00\)83234-0](https://doi.org/10.1016/S0166-9834(00)83234-0)
50. Asami K, Shikada T, Fujimoto K, Tominaga H (1987) Oxidative coupling of methane over lead oxide catalyst: kinetic study and reaction mechanism. *Ind Eng Chem Res* 26:2348–2353
51. Takanabe K, Shahid S (2016) Dehydrogenation of ethane to ethylene via radical pathways enhanced by alkali metal based catalyst in oxysteam condition. *Aiche* 63:3–194. <https://doi.org/10.1002/aic.15447>

52. Nelson PF, Lukey Ca, Cant NW (1988) Isotopic evidence for direct methyl coupling and ethane to ethylene conversion during partial oxidation of methane over lithium/magnesium oxide. *J Phys Chem* 92:6176–6179. <https://doi.org/10.1021/j100333a003>
53. Shahri SMK, Alavi SM (2009) Kinetic studies of the oxidative coupling of methane over the Mn/Na<sub>2</sub>WO<sub>4</sub>/SiO<sub>2</sub> catalyst. *J Nat Gas Chem* 18:25–34. [https://doi.org/10.1016/S1003-9953\(08\)60079-1](https://doi.org/10.1016/S1003-9953(08)60079-1)
54. Quiceno JWR, Deutschmann O (2005) Gas phase reactions: total and partial oxidation of C1-4 alkanes in the high and medium temperature range. *Eur Combust Meet* 64:1–41
55. Mims Ca, Mauti R, Dean aM, Rose KD (1994) Radical chemistry in methane oxidative coupling: tracing of ethylene secondary reactions with computer models and isotopes. *J Phys Chem* 98:13357–13372. <https://doi.org/10.1021/j100101a041>
56. Fleischer V, Simon U, Parishan S, Colmenares MG, Görke O, Gurlo A, Riedel W, Thum L, Schmidt J, Risse T, Dinse K-P, Schomäcker R (2018) Investigation of the role of the Na<sub>2</sub>WO<sub>4</sub>/Mn/SiO<sub>2</sub> catalyst composition in the oxidative coupling of methane by chemical looping experiments. *J Catal* 360:102–117
57. Kennedy EM, Cant NW (1991) Comparison of the oxidative dehydrogenation of ethane and oxidative coupling of methane over rare earth oxides. *Appl Catal* 75:321–330. [https://doi.org/10.1016/S0166-9834\(00\)83141-3](https://doi.org/10.1016/S0166-9834(00)83141-3)
58. Côme G-M (2001) Gas-phase thermal reactions: chemical engineering kinetics. Springer, Dordrecht. <https://doi.org/10.1007/978-94-015-9805-7>
59. Mackie JC, Smith JG, Nelson PF, Tyler RJ (1990) Inhibition of C2 oxidation by methane under oxidative coupling conditions. *Energy Fuels* 4:277–285. <https://doi.org/10.1021/ef00021a011>
60. Pogosyan NM, Pogosyan MD, Strekova LN, Tavadyan LA, Arutyunov VS (2015) Effect of the concentrations of methane and ethylene on the composition of the products of their cooxidation. *Russ J Phys Chem B* 9:218–222. <https://doi.org/10.1134/S1990793115020104>
61. Dittmeyer R, Emig G (2006) Simultaneous heat and mass transfer and chemical reaction. In: Ertl G, Knözinger H, Schüth F, Weitkamp J (eds) *Handbook of heterogeneous catalysis*. Wiley, Hoboken, pp 1727–1784. <https://doi.org/10.1002/9783527610044.hetcat0094>
62. Mohagheghi M, Bakeri G, Saeedizad M (2007) Study of the effects of external and internal diffusion on the propane dehydrogenation reaction over Pt-Sn/Al<sub>2</sub>O<sub>3</sub> catalyst. *Chem Eng Technol* 30:1721–1725. <https://doi.org/10.1002/ceat.200700157>
63. Campbell KD, Morales E, Lunsford JH (1987) Gas-phase coupling of methyl radicals during the catalytic partial oxidation of methane. *J Am Chem Soc* 109:7900–7901. <https://doi.org/10.1021/ja00259a059>
64. Driscoll DJ, Martir W, Wang JX, Lunsford JH (1985) Formation of gas-phase methyl radicals over MgO. *J Am Chem Soc* 107:58–63. <https://doi.org/10.1021/ja00287a011>
65. Lee JS, Oyama ST (1988) Oxidative coupling of methane to higher hydrocarbons. *Catal Rev* 30:249–280. <https://doi.org/10.1080/01614948808078620>

## Affiliations

Samira Parishan<sup>1</sup> · Ewa Nowicka<sup>1</sup> · Vinzenz Fleischer<sup>1</sup> · Christian Schulz<sup>2</sup> · Maria G. Colmenares<sup>3</sup> · Frank Rosowski<sup>2</sup> · Reinhard Schomäcker<sup>1</sup>

<sup>1</sup> Fachgebiet Technische Chemie, Institut für Chemie, Technische Universität Berlin, Straße des 17. Juni 124, 10623 Berlin, Germany

<sup>2</sup> BasCat - UniCat BASF Joint Lab, Technische Universität Berlin, Hardenbergstr. 36, 10623 Berlin, Germany

<sup>3</sup> Fachgebiet Keramische Werkstoffe/Chair of Advanced Ceramic Materials, Institut für Werkstoffwissenschaften und Technologien, Technische Universität Berlin, Hardenbergstraße 40, 10623 Berlin, Germany

**The origin of carbon oxides during Oxidative Coupling of Methane in the presence of  $Mn_xO_y$ - $Na_2WO_4/SiO_2$  catalyst**

*Samira Parishan,<sup>a</sup> Ewa Nowicka,<sup>a</sup> Vinzenz Fleischer,<sup>a</sup> Christian Schulz,<sup>b</sup> Maria G. Colmenares,<sup>c</sup> Frank Rosowski,<sup>b</sup> Reinhard Schomäcker<sup>a\*</sup>*

<sup>a</sup> *Fachgebiet Technische Chemie, Institut für Chemie, Technische Universität Berlin, Straße des 17. Juni 124, 10623 Berlin, Germany*

<sup>b</sup> *BasCat - UniCat BASF Joint Lab, Technische Universität Berlin, Hardenbergstr. 36, 10623 Berlin, Germany*

<sup>c</sup> *Fachgebiet Keramische Werkstoffe / Chair of Advanced Ceramic Materials, Institut für Werkstoffwissenschaften und technologien, Technische Universität Berlin, Hardenbergstraße 40, 10623 Berlin, Germany*

## Weisz Prater Criterion

The conversion for the reaction of CH<sub>4</sub>, C<sub>2</sub>H<sub>6</sub>, and C<sub>2</sub>H<sub>4</sub> in the co-feeding experiments presented in Figure S1 to S3 are observed to be high. Therefore, the Weisz-Prater criterion is calculated for each of these reactions at 775 °C to ensure that the rate of these reactions are not influenced by the internal mass transfer limitation. The Equation-S1 is applied to calculate the Weisz-Prater criterion. The parameters used in this equation are introduced in the following.

$$\Psi = L_C^2 \frac{n+1}{2} * \frac{r \cdot \rho_K}{D_{i,e} \cdot C_{i,0}} \quad \text{Eq-S1}$$

$\Psi$ : Weisz-Prater Criterion,

$L_C$ : Characteristic length of the catalyst (cm),

$n$ : Reaction order,

$r$ : Effective reaction rate (mol/(g.s)),

$\rho_k$ : Density of the catalyst (g/cm<sup>3</sup>),

$D_{i,e}$ : Effective diffusion coefficient (cm<sup>2</sup>/s),

$C_{i,0}$ : Initial concentration of the reactant (mol/l)

The characteristic length of the catalyst is defined as the length of the pores available on the catalyst surface. However, the BET analysis has shown that the Mn<sub>x</sub>O<sub>y</sub>-Na<sub>2</sub>WO<sub>4</sub>/SiO<sub>2</sub> is not a porous catalyst. Therefore, the average radius of the particles (125 μm), which is the largest imaginable length for the hypothetical pores on the surface, is considered as the characteristic length to do these calculations. Each of CH<sub>4</sub>, C<sub>2</sub>H<sub>6</sub>, and C<sub>2</sub>H<sub>4</sub> are assumed to have a reaction order of one under our studied condition. The rate of their conversion at the temperature of 775 °C is reported in Table-S1. The density of the catalyst is estimated to be equal to the support density (α-cristobalite) because the metal loading is almost negligible. The initial molar flow of ethene is calculated using the ideal gas law and converted to the concentration by taking the total flow (70 Nml/min) in consideration. To calculate the effective diffusion coefficients, the gas diffusion coefficient of the component is calculated using Equation-S2.  $\Lambda$  stands for the mean free path of the molecules and  $w$  for the mean velocity of the molecules under the reaction conditions. These values are calculated using Equation-S3 and S4. Noteworthy,  $k_B$  is the Boltzmann constant,  $\sigma$  for the collision cross section,  $m$  the mass of the molecule,  $T$  reaction temperature and  $P$  the pressure of the reactor.

$$D_g = \frac{1}{2} \Lambda w \quad \text{Eq-S2}$$

$$\Lambda = \frac{k_B T}{\sqrt{2} \pi \sigma^2 P} \quad \text{Eq-S3}$$

$$w = \sqrt{\frac{8 k_B T}{\pi m}} \quad \text{Eq-S4}$$

After calculating the gas diffusion coefficients ( $D_g$ ), the effective diffusion coefficients ( $D_{i,e}$ ) can be calculated. To do so, first the type of the diffusion which is applied to the investigated catalyst should be specified. The decision on the most compatible diffusion model to the studied system is made based on the difference between the mean free path of the molecule and the average diameter of the catalyst pores. The former values are presented in table-S1, whereas, for the non-porous  $Mn_xO_y-Na_2WO_4/SiO_2$ , the diameter of the pores is indefinable. Therefore the porosity of the catalyst bed, which has been calculated through a series of simplification assumptions (see Figure S1), has been the basis for the decision here. Since the pore diameter of the catalyst bed (36  $\mu\text{m}$ ) is far lower than the mean free path of the molecules (Table S-1) the Equation-S5 which describes the normal diffusion is used in calculating the  $D_{i,e}$ .

$$D_{i,e} = D_{i,g} \frac{\varepsilon}{\tau} \quad \text{Eq-S5}$$

As a rule of thumb, the values of 0.5 and 5 are considered for the porosity of the catalyst bed ( $\varepsilon$ ) and Tortuosity ( $\tau$ ).

At this stage, the Weisz-Prater Criterion can be calculated by substituting all the discussed parameters in Equation-S1. Since, the obtained value of this parameter for the reaction of each of  $CH_4$ ,  $C_2H_6$ , and  $C_2H_4$  are at least two orders of magnitude lower than 1, it can be concluded that none of these components were reacting under the mass transfer limitation [1].

### Mears Criterion

Deciding whether or not a chemical reaction is faced with external mass transfer limitation is made by calculating the Mears Criterion for it [2–4]. If this criterion would be less than 0.15, the external mass transfer diffusion can be neglected [2,4]. Equation-S6 is used to calculate this parameter. The  $d_p$  in this equation is representing the catalyst particle diameter which is equal to 250 m) and  $k_c$  is the mass transfer coefficient (m/s). The rest of the parameter are defined along with their respective values in the previous section.

$$C_m = \frac{r \rho_c (1 - \varepsilon) d_p n}{2 k_c C_{i,0}} < 0.15 \quad \text{Eq-S6}$$

The Mears Criterion is calculated for the reaction of each of methane, ethane, and ethene in the co-feeding experiments at 775 °C. First, the value of mass transfer coefficient ( $k_c$ ) should be calculated. The Equation-S7 is used for this purpose. Sh, Re, and Sc symbols in this equation represent dimensionless parameters of Sherwood, Reynold, and Schmidt. The gas velocity needed for calculating the Reynold number is calculated to be equal to 2.75 (m/min) from the 70 Nml/min total flow and 9 mm internal diameter of the reactor. The values for the kinematic viscosity of each of the gas components are taken from the airlíquide encyclopedia.

Then the values of kinematic viscosity of each of the gas mixtures are calculated from Eq-S10.

$$Sh = \frac{k_c d_p}{D_{Ab}} = 2 + 0.6 Re^{1/2} Sc^{1/3} \quad \text{Eq-S7}$$

$$Re = \frac{d_p U}{\nu_{mix}} \quad \text{Eq-S8}$$

$$Sc = \frac{\nu_{mix}}{D_{i,e}} \quad \text{Eq-S9}$$

$$\nu_{mix} = x_i \nu_i \quad \text{Eq-S10}$$

## Figures

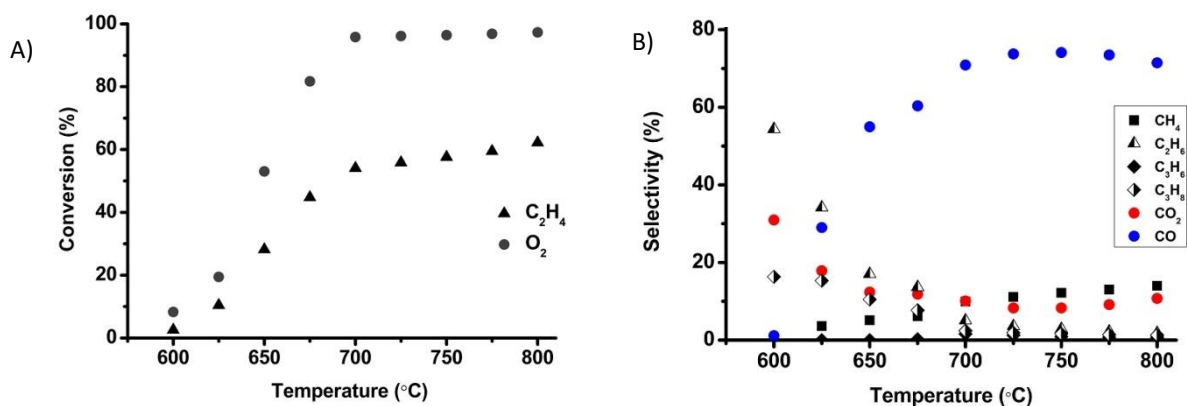


Figure S1 - Changes in the a) conversion and b) selectivity of the reaction vs. temperature in the co-feeding experiment of ethene, total flow 70 Nml/min, reactants ratio:  $C_2H_4/O_2/He$  of 1/1/33, catalyst amount:1 g.

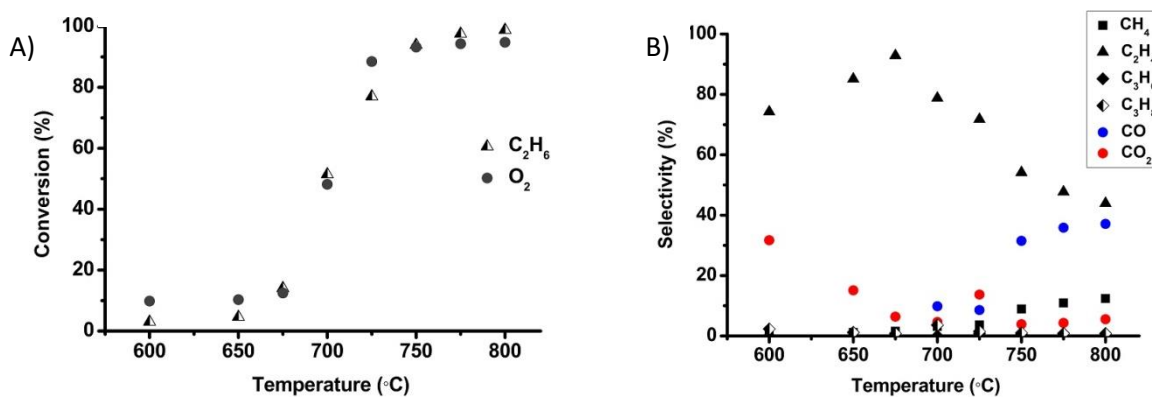


Figure S2 - Changes in the a) conversion and b) selectivity of the reaction vs. temperature in the co-feeding experiment of ethane, total flow 70 Nml/min, reactants ratio:  $C_2H_6/O_2/He$  of 1/1/33, catalyst amount:1 g.

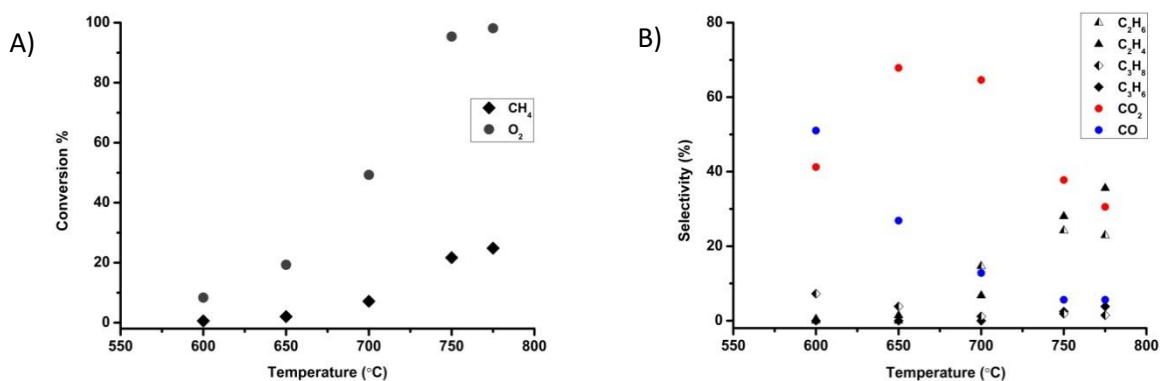


Figure S3 - Changes in the a) conversion and b) selectivity of the reaction vs. temperature in the co-feeding experiment of ethane, total flow 70 Nml/min, reactants ratio:  $C_2H_6/O_2/He$  of 1/1/33, catalyst amount:1 g.

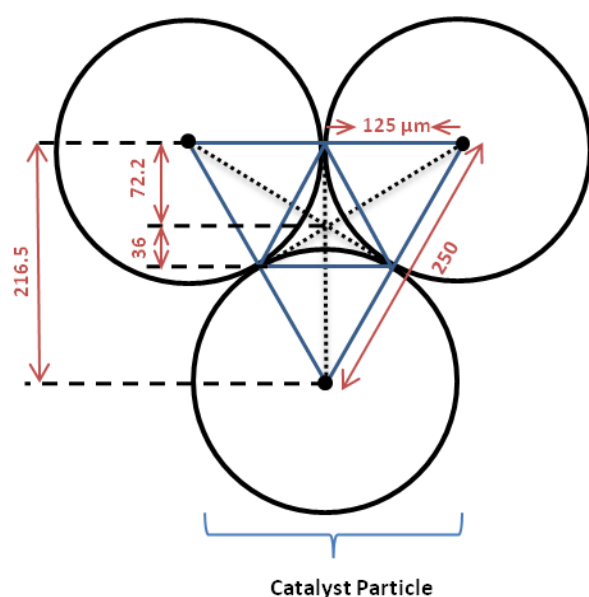


Figure S4 - Pore diameter calculated for the catalyst bed, all the numbers have the unit of micrometer

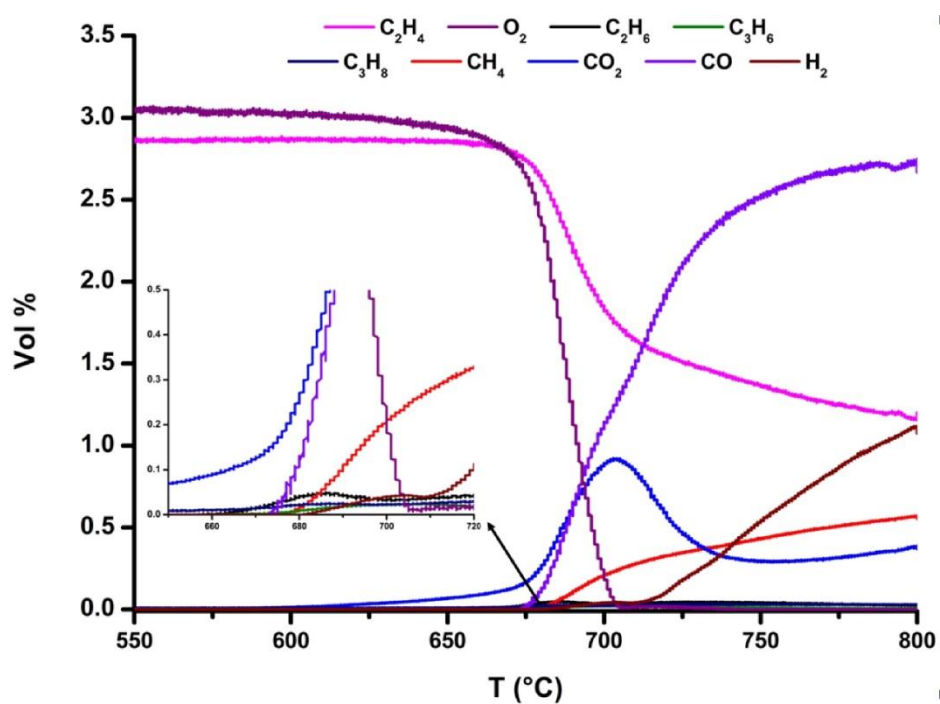


Figure S5 - Changes in the composition fraction of gas stream vs. temperature of catalytic bed, total flow 70 Nml/min, reactant ratio: C<sub>2</sub>H<sub>4</sub>/O<sub>2</sub>/He of 1/1/33, catalyst amount:1 g

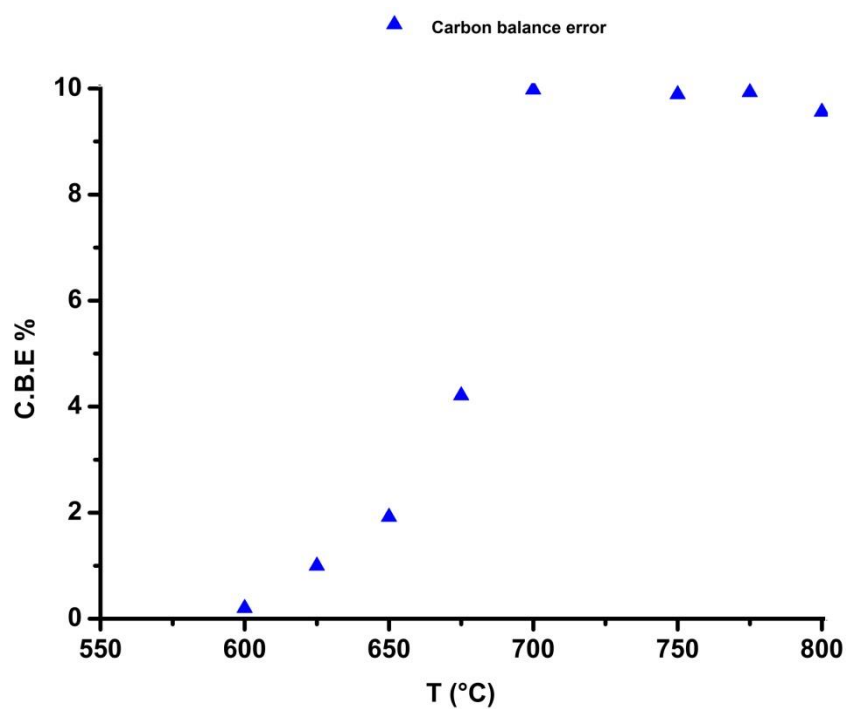


Figure S6 - Changes in the carbon balance error vs. temperature of catalytic bed, total flow 70 Nml/min, reactant ratio:  $C_2H_4/O_2/He$  of 1/1/33, catalyst amount:1 g

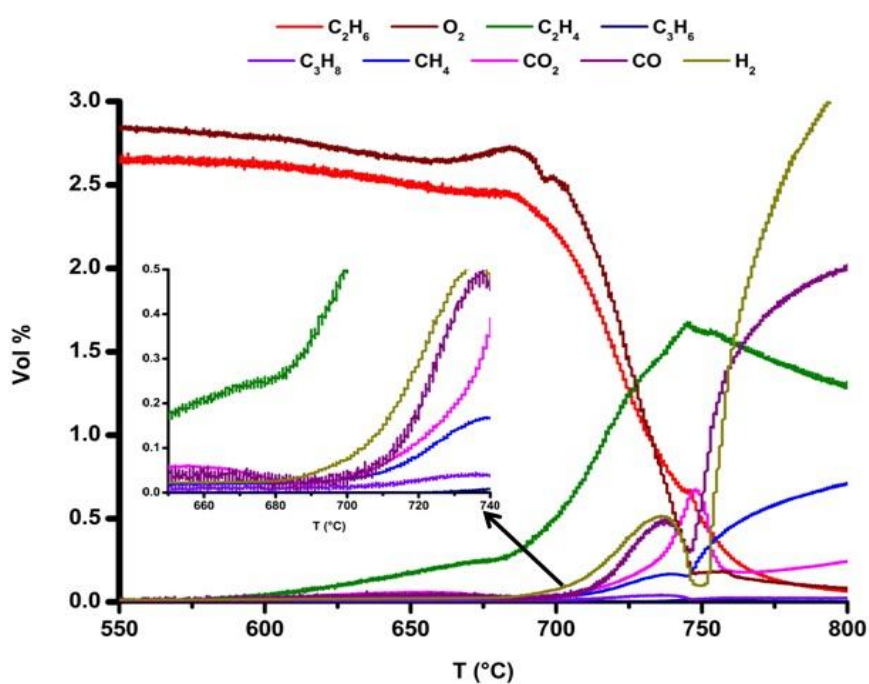


Figure S7 - Changes in the composition fraction of gas stream vs. temperature of catalytic bed, total flow 70 Nml/min, reactants ratio:  $C_2H_6/O_2/He$  of 1/1/33, catalyst amount:1 g

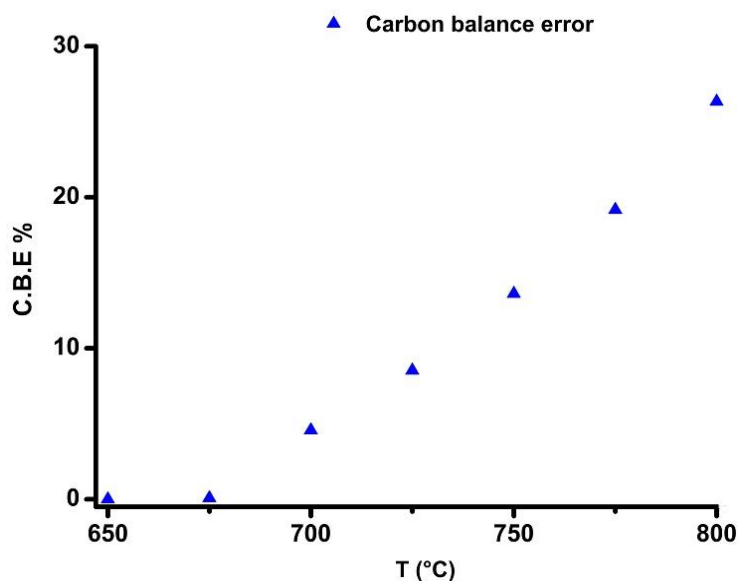


Figure S8 – Deviation from carbon balance vs. temperature of catalytic bed in the TPSR experiment with ethene. Catalyst amount= 0.5 g, C<sub>2</sub>H<sub>4</sub>: He = 1:19 and total flow= 30 Nml min<sup>-1</sup>

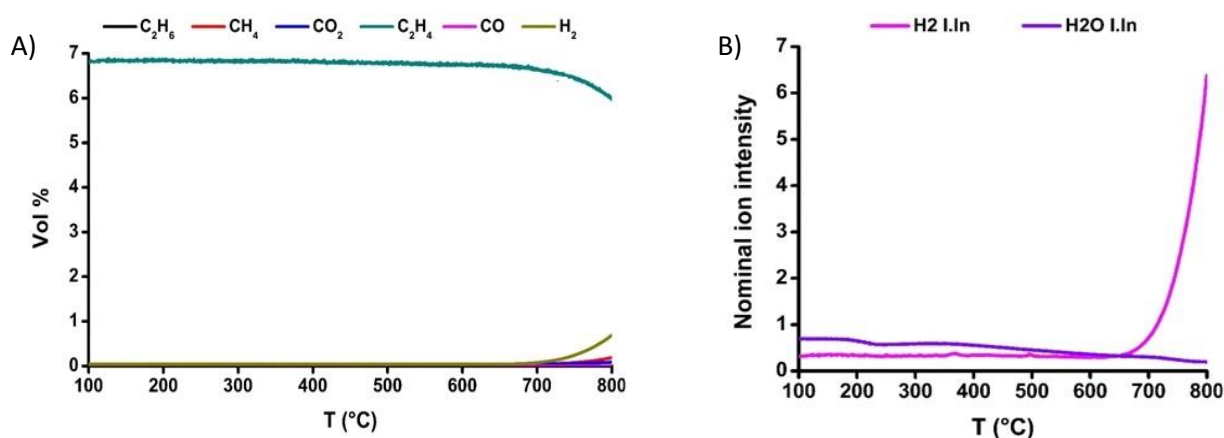


Figure S9 - The results of the TPSR experiment with ethene a) composition fraction of effluent b) nominal ion intensity of the water and H<sub>2</sub> in the reactor outlet vs. the temperature of inert bed, Inert material (Quartz)= 0.5 g, C<sub>2</sub>H<sub>4</sub>: He = 1:19 and total flow= 30 Nml min<sup>-1</sup>

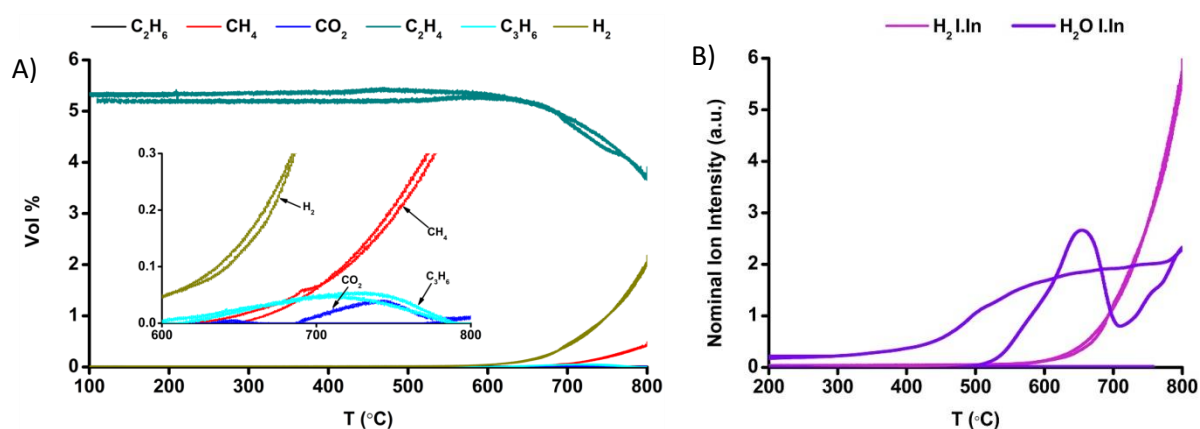


Figure S10 - Results of the TPSR experiment with ethene during the heating up and cooling down of the catalyst a) composition ratio of effluent b) nominal ion intensity of the water and H<sub>2</sub> in the reactor outlet vs. the temperature of catalyst bed. Catalyst amount= 0.5 g, C<sub>2</sub>H<sub>4</sub>: He = 1:19 and total flow= 30 Nml min<sup>-1</sup>

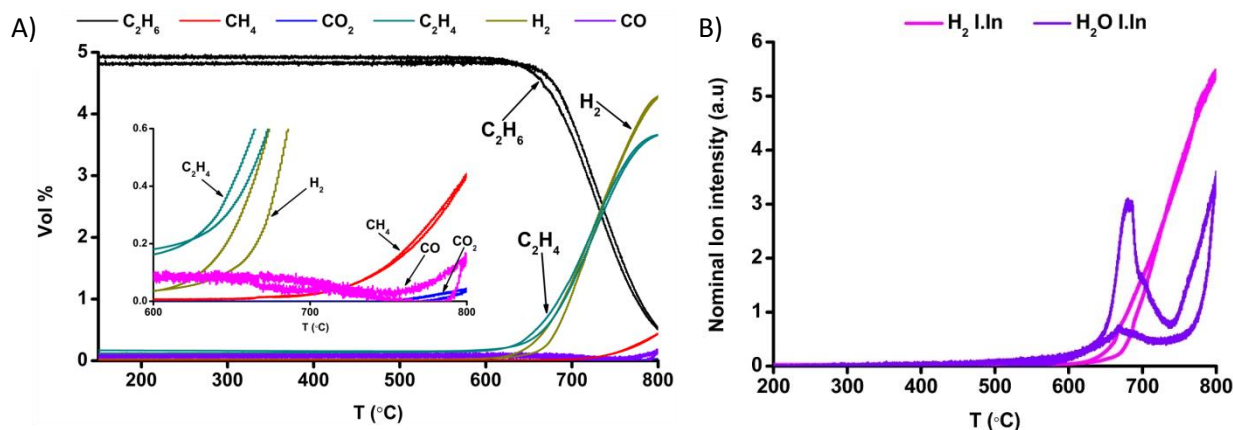


Figure S11 - Results of the TPSR experiment with ethane during the heating up and cooling down of the catalyst a) composition ratio of effluent b) nominal ion intensity of the water and H<sub>2</sub> in the reactor outlet vs. the temperature of the catalytic bed. Catalyst amount= 0.5 g, C<sub>2</sub>H<sub>6</sub>: He = 1:19 and total flow= 30 Nml min<sup>-1</sup>

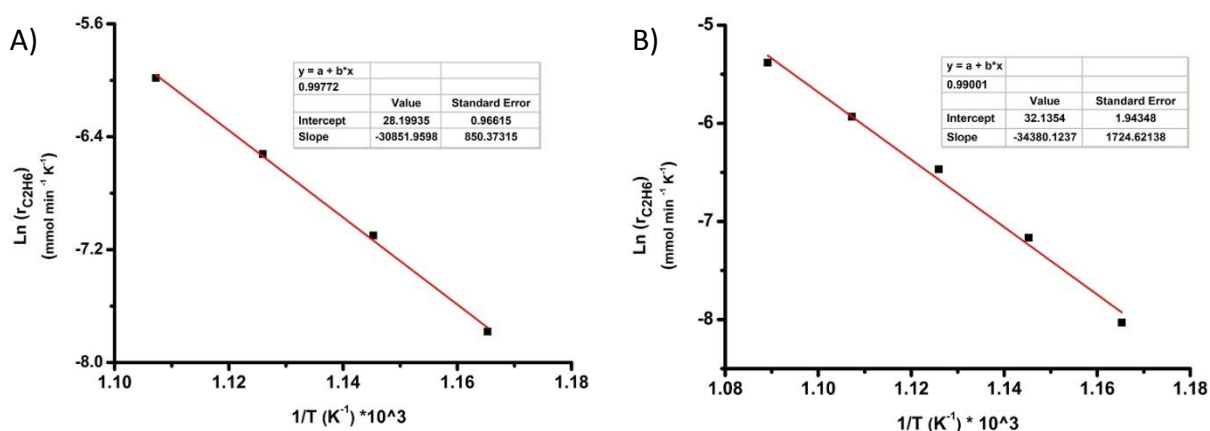
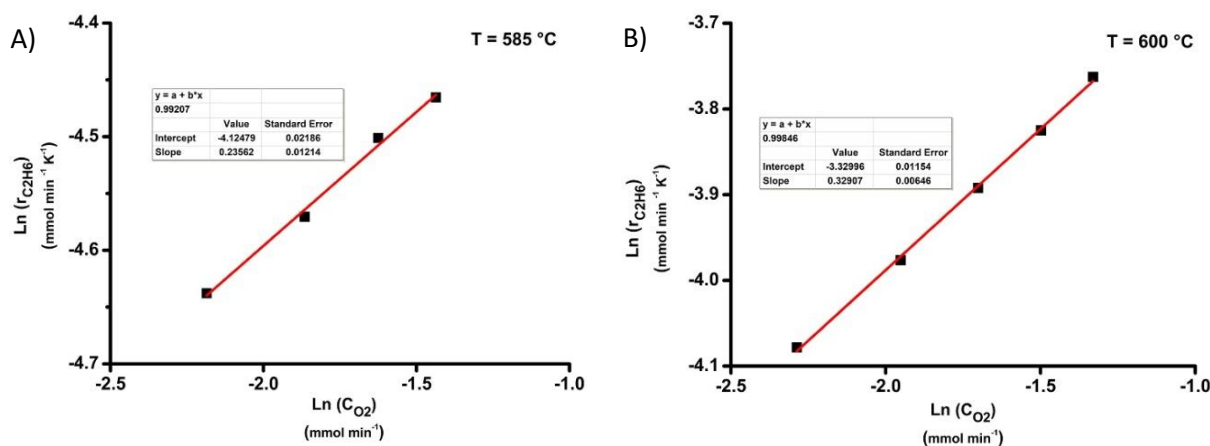


Figure S12 – Logarithmic changes in the rate of conversion of ethane vs. inverse of temperature A) in the presence of catalyst B) in the presence of the silicon carbide. Reaction flow consisting of 25 Nml min<sup>-1</sup> of C<sub>2</sub>H<sub>6</sub> mixed with 65 Nml min<sup>-1</sup> of Helium



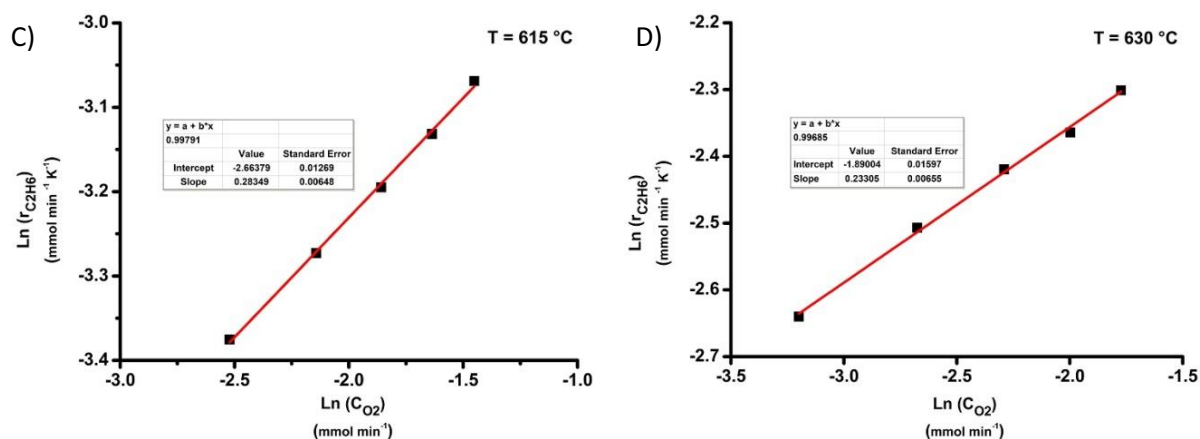


Figure S13 - The logarithmic rate of conversion of ethane vs. the logarithm of the concentration of  $O_2$  in the reactor outlet at temperatures of A) 585, B) 600, C) 615 and D) 630 °C obtained in the catalytic test. Total flow was set at 90 Nml  $\text{min}^{-1}$  and it was consisting of 25 Nml  $\text{min}^{-1}$  of  $C_2H_6$ . The initial concentration of oxygen was changed between 3, 4, 5, 6 and 7 Nml  $\text{min}^{-1}$

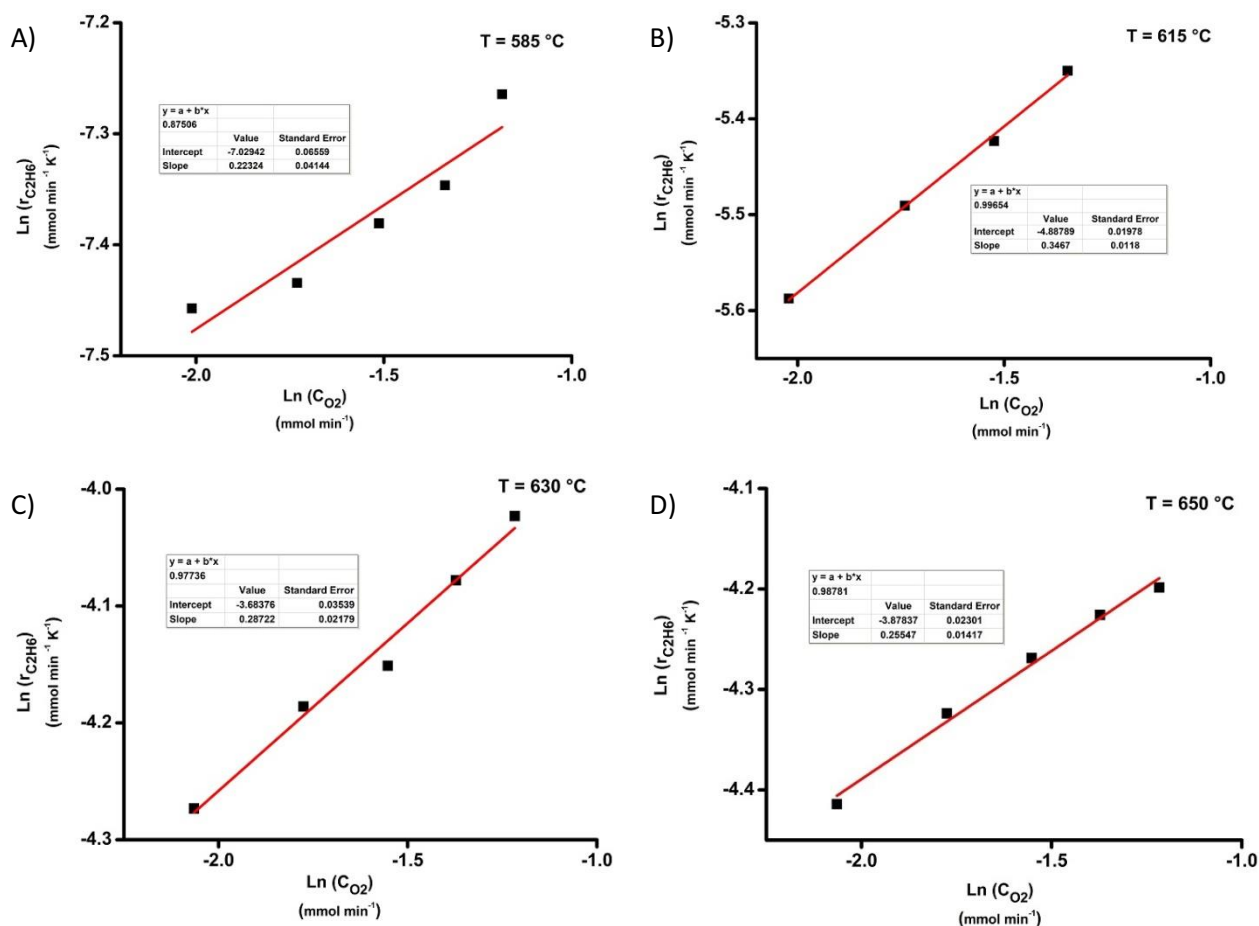


Figure S14 - The logarithmic rate of conversion of ethane vs. the logarithm of the concentration of  $O_2$  in the reactor outlet at temperatures of A) 585, B) 615, C) 630 and D) 650 °C obtained in the presence of silicon carbide. Total flow was set at 90 Nml  $\text{min}^{-1}$  and it was consisting of 25 Nml  $\text{min}^{-1}$  of  $C_2H_6$ . The initial concentration of oxygen was changed between 3, 4, 5, 6 and 7 Nml  $\text{min}^{-1}$

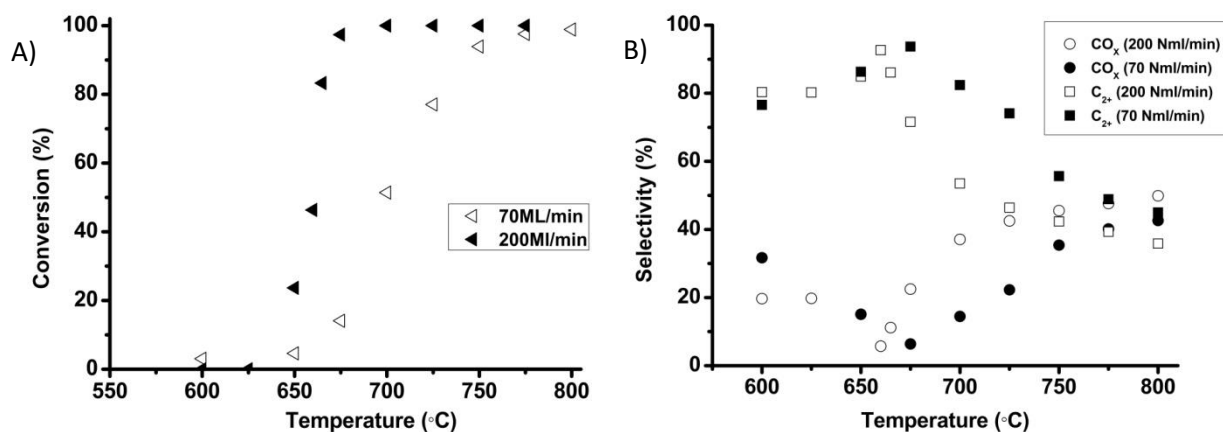


Figure S15 - Comparison between A) conversion and B) selectivity of the reaction of ethane in the co-feeding experiments performed at 200 and 70 Nml/min of total flow vs. temperature, reactant ratio: C<sub>2</sub>H<sub>6</sub>/O<sub>2</sub>/He of 1/1/33, catalyst amount: 1g

## References

- [1] Hugo.p, Seidel-Morgenstern.A, Steinbach.J, Schomäcker.R, Grundzüge der Technische Chemie I, in: Technical University of Berlin, 2004: pp. 40–41.
- [2] F. Scott, External Diffusion Effects on Heterogeneous Reactions, in: Elem. Chem. React. Eng., 5th ed., 2008: pp. 757–811.
- [3] R. Dittmeyer, G. Emig, Simultaneous Heat and Mass Transfer and Chemical Reaction, in: Hand B. Heterog. Catal., 2006: pp. 1727–1784.  
doi:10.1002/9783527610044.hetcat0094.
- [4] M. Mohagheghi, G. Bakeri, M. Saeezad, Study of the effects of external and internal diffusion on the propane dehydrogenation reaction over Pt-Sn/Al<sub>2</sub>O<sub>3</sub> catalyst, Chem. Eng. Technol. 30 (2007) 1721–1725. doi:10.1002/ceat.200700157.

# Paper 7



## Supported Catalysts | Hot Paper |

## Stepwise Methane-to-Methanol Conversion on CuO/SBA-15

Ha V. Le,<sup>[a]</sup> Samira Parishan,<sup>[b]</sup> Anton Sagaltchik,<sup>[c]</sup> Hamideh Ahi,<sup>[c, d]</sup> Annette Trunschke,<sup>[d]</sup> Reinhard Schomäcker,<sup>[b]</sup> and Arne Thomas\*<sup>[a]</sup>

**Abstract:** The direct partial oxidation of methane to methanol is a challenging scientific and economical objective to expand the application of this abundant fuel gas as a major resource for one-step production of value-added chemicals. Despite substantial efforts to commercialize this synthetic route, to date no heterogeneous catalyst can selectively oxidize methane to methanol by O<sub>2</sub> with an economically acceptable conversion. Cu-exchanged zeolites have been recently highlighted as one of the most promising bioinspired catalysts toward the direct production of methanol from methane under mild conditions. In this work, Cu-based cata-

lysts were prepared using mesoporous silica SBA-15 as an alternative support and their activity for this conversion was investigated. The results demonstrate that highly dispersed CuO species on SBA-15 are able to react with methane and subsequently produce methanol with high selectivity (>84%) through water-assisted extraction. Furthermore, it was confirmed that the main intermediate formed after interaction of the catalyst with methane is a methoxyl species, which can be further converted to methanol or dimethyl ether on extraction with water or methanol, respectively.

## Introduction

As supplies of crude oil are declining, methane, which is the major component of abundant resources such as natural gas, methane hydrates, and biogas, has emerged as a potential alternative feedstock for the chemical industry.<sup>[1]</sup> However, methane is not widely utilized on a commercial scale because of its high chemical inertness.<sup>[2]</sup> In the current energy-intensive route, methane is first converted to syngas, typically at 1000 °C and 30 bar, which can subsequently be transformed into methanol and hydrocarbons by hydrogenation and Fischer–Tropsch synthesis, respectively.<sup>[3]</sup> Developing an alternative process to produce value-added chemicals such as methanol from methane, preferably in one step, has therefore been a research field

of increasing interest in recent years. Unfortunately, direct oxidation strategies showed low yields and productivity due to the much higher reactivity of the oxygenated products compared to methane.<sup>[1a,3a,4]</sup> Efficient activation of methane under milder conditions and control of reaction selectivity toward the desired products are therefore the main challenges in heterogeneous catalysis.

Biological catalysts have motivated many researchers to tackle these challenges. Methane monooxygenase enzymes (MMOs) in methanotropic bacteria are able to consume methane as their sole source of both carbon and energy, selectively oxidizing methane to methanol under ambient conditions with atmospheric O<sub>2</sub>.<sup>[5]</sup> Two forms of MMOs are located at different cellular positions, namely, cytoplasmic MMOs (soluble form) and membrane-bound MMOs (particulate form). A bis(μ-oxo)-diiron core is known to be the active site in the soluble MMOs, while the particulate form contains di- and tricopper clusters that are proposed to efficiently activate the C–H bond of methane.<sup>[6]</sup> Inspired by these prototypical natural machines, in the last decade, Cu-, Co-, and Fe-exchanged zeolites have been used as heterogeneous catalysts for methane-to-methanol conversion due to their ability to activate methane at low temperatures and show high selectivities to methanol. This is typically achieved in a stepwise process in which the catalyst is first oxidized in O<sub>2</sub> or N<sub>2</sub>O at high temperature (>200 °C) and then reacts with methane at lower temperature (≤200 °C). The resulting intermediate, stabilized on the catalyst surface, is subsequently transformed into methanol by final treatment with water.<sup>[7]</sup>

As the most active catalysts so far, Cu/zeolites have been intensively studied to identify the possible structures of active Cu sites and the catalytic mechanisms to finally develop im-

[a] H. V. Le, Prof. Dr. A. Thomas  
Institute of Chemistry–Functional Materials, BA2  
Technische Universität Berlin  
Hardenbergstrasse 40, 10623 Berlin (Germany)  
E-mail: arne.thomas@tu-berlin.de

[b] S. Parishan, Prof. Dr. R. Schomäcker  
Institute of Chemistry–Technical Chemistry, TC8  
Technische Universität Berlin  
Strasse des 17. Juni 124, 10623 Berlin (Germany)

[c] A. Sagaltchik, Dr. H. Ahi  
BasCat-UniCat BASF Joint Lab  
Technische Universität Berlin, EW K 01  
Hardenbergstrasse 36, 10623 Berlin (Germany)

[d] Dr. H. Ahi, Dr. A. Trunschke  
Department of Inorganic Chemistry  
Fritz Haber Institute of the Max Planck Society  
Faradayweg 4–6, 14195 Berlin (Germany)

Supporting information and the ORCID identification number(s) for the author(s) of this article can be found under:  
<https://doi.org/10.1002/chem.201801135>.

proved procedures.<sup>[6a,7d,8]</sup> Interestingly, no steady-state activity was observed for large copper oxide nanoparticles supported on pure silica MFI (average size of 30 nm for copper oxides) or on pure silica BEA (average size of 40–60 nm for copper oxides) in a continuous isothermal process in which a predetermined mixture of methane, O<sub>2</sub>, and water was introduced into the catalyst bed at 200 °C,<sup>[8a]</sup> while a small amount of methanol was produced over amorphous silica impregnated with Cu(OAc)<sub>2</sub>·H<sub>2</sub>O in the original work of Grootaert et al., in which the above-described stepwise procedure was applied.<sup>[7a]</sup> To expand this promising material class, we report here the first demonstration of methane-to-methanol conversion over an SBA-15-supported Cu catalyst. Unlike Cu oxo complexes in zeolite matrix previously suggested to be the active sites for the hydroxylation of methane, the catalytic activity of CuO/SBA-15 is attributed to small/ultrasmall CuO nanoclusters that are highly dispersed throughout the SBA-15 framework. Our results are expected to accelerate the development of novel Cu-based catalysts on supports other than zeolites for this reaction.

## Results and Discussion

Cu species were supported on SBA-15 by wet impregnation. The catalyst synthesized from Cu<sup>II</sup> acetylacetonate [Cu(acac)<sub>2</sub>] was named Cu-AA/SBA, whereas that obtained by using Cu<sup>II</sup> acetate [Cu(OAc)<sub>2</sub>] was named Cu-OA/SBA. Similar Cu loadings (≈2.7 wt%) were obtained for both Cu-AA/SBA and Cu-OA/SBA.

The powder XRD pattern at small angles of unloaded SBA-15 showed three diffraction peaks indexed as (100), (110), and (200) planes corresponding to the well-ordered two-dimensional hexagonal structure of SBA-15 (Figure 1 a).<sup>[9]</sup> Observation of the (100) diffraction peak for both CuO/SBA-15 materials indicated that the porous structure of SBA-15 was maintained during impregnation. The decreased intensity of the peaks for Cu-containing materials can be attributed to the presence of Cu species in the SBA-15 channels.<sup>[10]</sup> Wide-angle XRD measurements on the CuO/SBA-15 materials gave results that depended on the Cu<sup>II</sup> precursor (Figure 1 b). No obvious peaks for any crystalline phase were observed for Cu-AA/SBA, indicating that the Cu species are well-dispersed on the support. In contrast, the diffractogram of Cu-OA/SBA showed two peaks at 2θ = 36 and 39°, indicative of the formation of CuO particles on the support.

The structure of the CuO/SBA-15 materials was further investigated by TEM. Regular hexagonal mesochannels were seen for all materials, before and after impregnation and calcination (Figure 2). No nanoparticles were detected in the TEM images of Cu-AA/SBA (Figure 2b), while nanoparticles with various sizes (10–50 nm) were clearly seen for Cu-OA/SBA (Figure 2c). Nitrogen sorption measurements showed a decrease in surface area and total pore volume after impregnation of SBA-15 with Cu species, which was found to be more significant for Cu-AA/SBA (Table 1). In addition, both mesopore and micropore volumes of Cu-AA/SBA are lower than those of Cu-OA/SBA. In combination with TEM and XRD results, it can be concluded

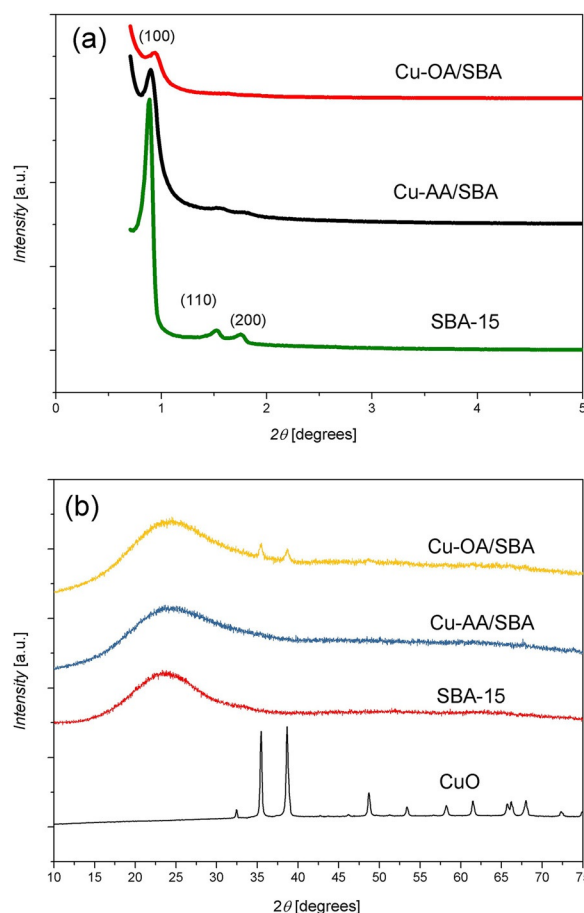


**Figure 1.** PXRD patterns of the materials at a) low angles and b) wide angles.

that Cu species are indeed mainly located within the pores of Cu-AA/SBA, while for Cu-OA/SBA larger CuO nanoparticles are also located on the outer surface of SBA-15.

The catalytic activity of the CuO/SBA-15 materials was investigated in the selective oxidation of methane to methanol according to the well-known stepwise procedure first reported by Grootaert et al.<sup>[7a]</sup> Typically, the catalyst was activated in oxygen at 550 °C and then allowed to interact with methane at 200 °C. The last step for extraction of methanol could be performed with liquid water (off-line extraction) or steam (on-line extraction). For comparison, Cu/mordenite with a Cu loading of about 2.6 wt%, prepared by a recently reported solid-state ion-exchange reaction between NH<sub>4</sub>-mordenite and Cu(acac)<sub>2</sub>, was used as a reference zeolite-based catalyst.<sup>[8b]</sup>

After extraction with water, methanol was detected in catalytic cycles over both CuO/SBA-15 catalysts, indicating that methane was indeed activated by Cu sites in SBA-15 at low temperature (200 °C) and then converted to methanol on the treatment with water (Table 2). Cu-AA/SBA yielded 30.2 μmol g<sub>cat</sub><sup>-1</sup> of methanol (Table 2, entry 1), whereas a smaller amount of methanol amount of 11.1 μmol g<sub>cat</sub><sup>-1</sup> was produced over Cu-OA/SBA (Table 2, entry 3), which is even comparable to the original result reported by Grootaert et al. using a Cu/mordenite catalyst.<sup>[7a]</sup> However, in the latter work, the catalyst

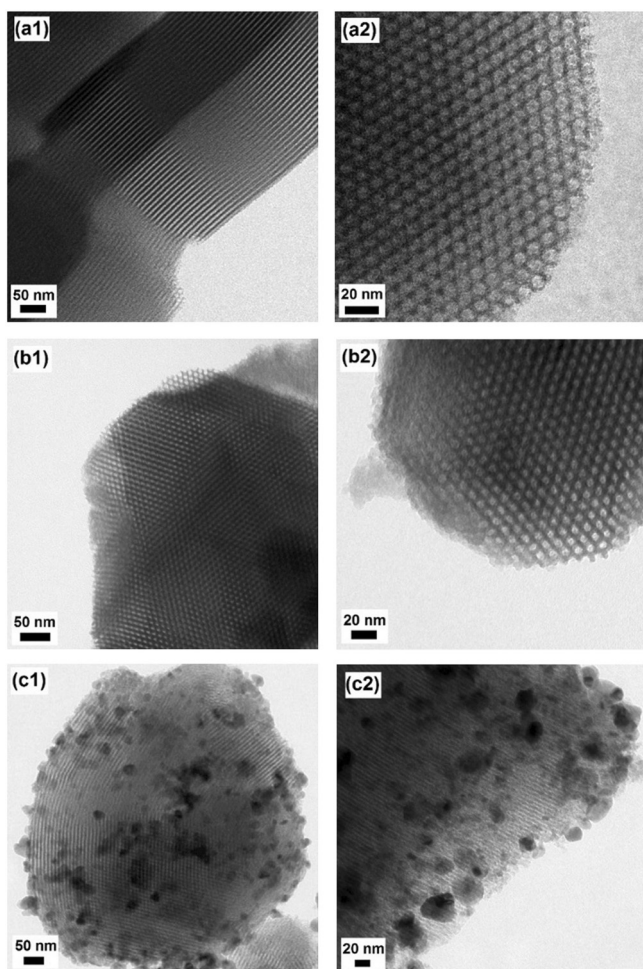


Figure 2. TEM images of a1), a2) pure SBA-15, b1), b2) calcined Cu-AA/SBA, and c1), c2) calcined Cu-OA/SBA.

Table 1. Textural properties of SBA-15-based materials.

Material	Cu loading [wt%]	SA <sup>[a]</sup> [m <sup>2</sup> g <sup>-1</sup> ]	V <sub>meso</sub> <sup>[b]</sup> [cm <sup>3</sup> g <sup>-1</sup> ]	V <sub>micro</sub> <sup>[b]</sup> [cm <sup>3</sup> g <sup>-1</sup> ]	V <sub>total</sub> <sup>[c]</sup> [cm <sup>3</sup> g <sup>-1</sup> ]
SBA-15	–	899.1	0.92	0.18	1.10
Cu-AA/SBA	2.71	508.8	0.45	0.10	0.55
Cu-OA/SBA	2.78	588.5	0.52	0.12	0.64

[a] SA = surface area calculated by the BET method. [b] V<sub>meso</sub> = mesopore volume, V<sub>micro</sub> = micropore volume calculated by the NLDFT method. [c] V<sub>total</sub> = total pore volume calculated at P/P<sub>0</sub> = 0.99.

Table 2. Catalytic performance of CuO/SBA-15 materials.

Entry	Catalyst	Cu loading [wt%]	Product yield [μmol g <sub>cat</sub> <sup>-1</sup> ]			Oxidized CH <sub>4</sub> <sup>[c]</sup> [μmol g <sub>cat</sub> <sup>-1</sup> ]	Selectivity to MeOH and DME <sup>[d]</sup> [%]
			MeOH <sup>[a]</sup>	DME <sup>[b]</sup>	CO <sub>2</sub> <sup>[b]</sup>		
1	Cu-AA/SBA	2.71	30.2	0	3.4	33.6	89.9
2	Cu-AA/SBA <sup>[e]</sup>	2.71	31.7	0	5.8	37.5	84.5
3	Cu-OA/SBA	2.78	11.1	0	1.0	12.1	91.7

[a] Methanol was analyzed by GC after off-line extraction with liquid water. [b] Gas-phase products were analyzed by MS during online extraction with steam. [c] Amount of oxidized methane = moles(MeOH) + 2 × moles(DME) + moles(CO<sub>2</sub>). [d] Selectivity to MeOH and DME = [moles(MeOH) + 2 × moles(DME)]/moles(reacted CH<sub>4</sub>). [e] Reused catalyst for the second cycle.

was activated in O<sub>2</sub> at 450 °C, and only 2 mL of water was used to extract methanol, whereas in the present study the activation step was performed at 550 °C, and 10 mL of water was added to the catalyst for collection of methanol. It was previously demonstrated that the methanol yield can be significantly improved by increasing the activation temperature and using more water.<sup>[8b,c,11]</sup> Similar to our previous report on Cu/mordenite,<sup>[8b]</sup> CO<sub>2</sub> was observed when the extraction was performed above 100 °C (Figure 3). Notably, the selectivity toward

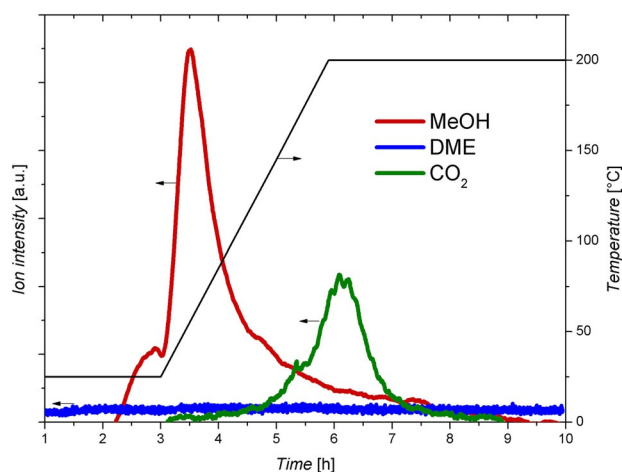


Figure 3. Mass-spectral signals of products after interaction of Cu-AA/SBA with methane at 200 °C, followed by online extraction in an He flow saturated with water.

methanol in the reaction with the CuO/SBA-15 catalysts (> 84%) is comparable to that obtained with Cu/mordenite. Besides Cu-oxo sites, small/ultrasmall copper oxide clusters have been proposed to be reactive to methane molecules under appropriate reaction conditions in recent studies on Cu-exchanged zeolite catalysts.<sup>[8a,c]</sup> The well-ordered porous structure of SBA-15 is advantageous in ensuring good dispersion of active copper oxide species, whereas large copper oxide nanoparticles (30–60 nm) supported on pure silica were previously shown to be inactive.<sup>[8a]</sup> The increased production of methanol over Cu-AA/SBA is attributed to the highly dispersed Cu species in the SBA-15 framework. It can be therefore concluded that the Cu source and the method of material preparation can significantly affect the size of the formed Cu clusters and consequently their catalytic performance.

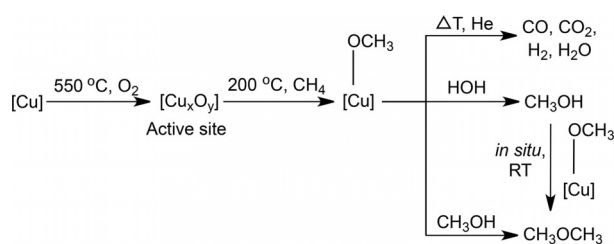
Dimethyl ether (DME) can be considered to be a side product due to acidic zeolite-catalyzed in situ dehydration of methanol, as the extraction with steam was performed at elevated temperature ( $\geq 135^\circ\text{C}$ ).<sup>[6a,7b]</sup> However, in our earlier study applying a Cu/mordenite catalyst, methanol and DME were detected at room temperature, and this suggests that different intermediates were generated on the catalyst surface and transformed into methanol and DME, respectively, by treatment of the catalyst with steam.<sup>[8b]</sup> In this study, no DME was produced over CuO/SBA-15 catalysts, whereas  $1.6\ \mu\text{mol g}_{\text{cat}}^{-1}$  of DME was obtained in the catalytic cycle with Cu/mordenite (Table S1 in the Supporting Information). To investigate the mechanism of formation of DME on the Cu-based catalysts, online extraction with a methanol-saturated He stream at room temperature was performed after their interaction with methane.

Notably,  $27.6\ \mu\text{mol g}_{\text{cat}}^{-1}$  of DME was obtained with Cu-AA/SBA after treatment with methanol vapor (Table 3). Also, the

Entry	Catalyst	DME produced <sup>[a]</sup> [ $\mu\text{mol g}_{\text{cat}}^{-1}$ ]	
		Online extraction with steam	Online extraction with methanol vapor
1	Cu-AA/SBA	0	27.6
2	Cu/mordenite	1.6	48.6

[a] Analyzed by MS.

production of DME on Cu/mordenite was remarkably increased to  $48.6\ \mu\text{mol g}_{\text{cat}}^{-1}$ . These DME yields are close to the amounts of methanol produced in the water-mediated extraction step, indicating that DME obtained in the experiment with a methanol-saturated inert flow is a product of the reaction of methanol used in the extraction protocol with the bound intermediate species. It can be thus concluded that the intermediate is indeed a methoxyl species bound on the catalyst surface after the reaction of active Cu species with methane (Scheme 1). The rate of such a reaction could be significantly enhanced by acidic sites, which are abundantly available in zeolite catalysts. Mass spectrometry detected signals of DME with approximately 30 times higher intensity for Cu/mordenite after its contact with the methanol-saturated He flow compared to the results



**Scheme 1.** Proposed formation of products on the Cu-based catalyst, based on former studies<sup>[8a,b,12]</sup> and mass spectrometric data.

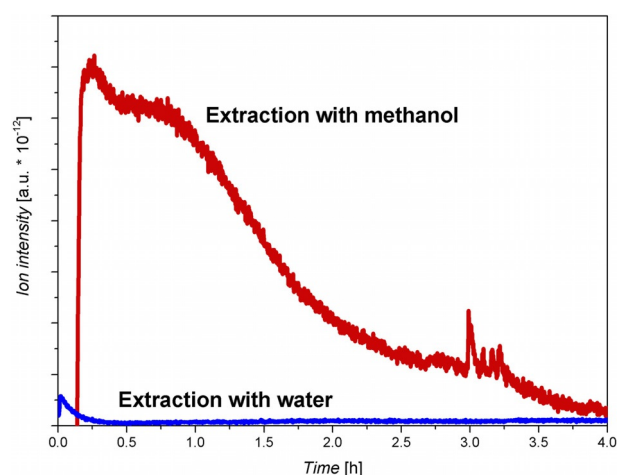


**Figure 4.** Comparison of mass-spectral signals of DME extracted from Cu-AA/SBA in the online stage at room temperature by using different solvents.

obtained with Cu-AA/SBA (Figure 4 and Figure S6 in the Supporting Information, red curves). Furthermore, DME can be also produced in an online extraction stage with water due to the attack of in situ produced methanol on unconverted intermediate species. Such as-formed methanol species will be retained for a longer time within the zeolite framework, which mainly has micropores as opposed to the mesopores of SBA-15. This can explain the small amount of DME generated along with methanol over Cu/mordenite in the steam-assisted extraction step at room temperature.

To gain more insight into the location of the Cu sites in SBA-15,  $\text{H}_2$  temperature-programmed reduction ( $\text{H}_2$ -TPR) measurements were performed for both CuO/SBA-15 materials in comparison with the  $\text{H}_2$ -TPR data of Cu oxide standards. The first reduction stage for CuO/SBA-15 materials is observed from 200 to  $300^\circ\text{C}$  and is attributed to CuO nanoparticles on the surface and at the readily accessible mesopores of SBA-15 (Figure 5). Most of the Cu species in Cu-OA/SBA-15 were reduced by  $\text{H}_2$  in this temperature range, consistent with the

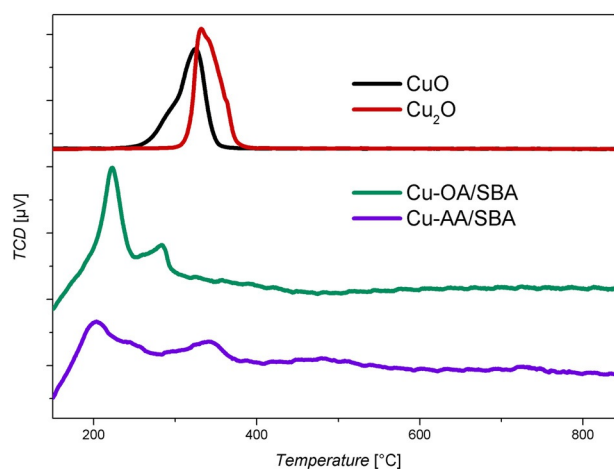


**Figure 5.**  $\text{H}_2$ -TPR profiles of Cu oxides, calcined Cu-OA/SBA, and calcined Cu-AA/SBA.

above characterization result that the Cu phase of this material consists of larger CuO nanoparticles. Besides, further H<sub>2</sub> reduction steps at 350 and 500 °C are found for Cu-AA/SBA, indicating that Cu species are also distributed at less accessible sites of SBA-15, namely, micropores in the main-channel wall, by using Cu(acac)<sub>2</sub> for the preparation of CuO/SBA-15. It is therefore suggested that the formation of smaller CuO clusters in Cu-AA/SBA led to the better catalytic performance of Cu-AA/SBA compared to Cu-OA/SBA. Calculation of H<sub>2</sub> consumption in the TPR measurements further indicated that, after activation in O<sub>2</sub>, the samples indeed contain Cu<sup>II</sup> species only as found in Cu/zeolites, which were responsible for activation of methane in earlier studies.<sup>[6a, 7d, 8b, 13]</sup>

Since the first report on the stepwise manner of the gas-phase direct production of methanol from methane over Cu-exchanged zeolites,<sup>[7a]</sup> only zeolites and zeotypes have been used as supports for preparation of Cu-based catalysts. In spite of many attempts over the last decade, the nature of the active species in the Cu/zeolite catalysts is still unknown.<sup>[8a]</sup> On the basis of both theoretical and spectroscopic analyses, several different structures of Cu sites that can be activated in O<sub>2</sub> and subsequently react with methane molecules have been suggested for a zeolitic model with a cation-exchangeable framework.<sup>[8e, 14]</sup> In situ UV/Vis spectroscopy is one of the essential characterization techniques to obtain more information on the activated Cu sites. In earlier studies, the UV/Vis spectra of O<sub>2</sub>-activated Cu/ZSM-5 and Cu/mordenite showed a band at about 22 500 cm<sup>-1</sup>, the intensity of which rapidly decreased when methane was added to the materials.<sup>[7a, 8d, 15]</sup> This band is assigned to a monooxo dicopper ( $\mu$ -Cu<sub>2</sub>O) active site.<sup>[16]</sup> However, several studies have recently reported the absence of this band for Cu/mordenite during the O<sub>2</sub>-activation step.<sup>[6a, 8a, c]</sup> Instead, Grundner et al. reported another broad band at about 31 000 cm<sup>-1</sup>, which was stable in O<sub>2</sub> and disappeared after 30 min of contact with methane.<sup>[6a]</sup> Also in this study, a [Cu<sub>3</sub>( $\mu$ -O)<sub>3</sub>]<sup>2+</sup> core was suggested to be responsible for the activation of methane. A similar result was reported recently by Kim et al.<sup>[17]</sup> In addition, several other Cu sites embedded in the zeolite channels have been proposed as potential sites for the activation of methane, namely, a simple monocopper site,<sup>[18]</sup> larger Cu oxo clusters such as [Cu<sub>4</sub>O<sub>4</sub>]<sup>2+</sup> and [Cu<sub>5</sub>O<sub>5</sub>]<sup>2+</sup>,<sup>[8e]</sup> and even small/ultrasmall CuO clusters.<sup>[8a, c]</sup>

SBA-15 is known as a porous silica material without ion-exchangeable positions. Therefore, the formation of isolated Cu oxo species, which are regarded as active sites for Cu/zeolites, in SBA-15 seems to be impossible. After O<sub>2</sub> activation up to 550 °C, indeed no band in the region of 20 000–25 000 cm<sup>-1</sup> was found in the in situ UV/Vis spectra, demonstrating the absence of a mono- $\mu$ -oxo dicopper site. The spectra of the samples activated in O<sub>2</sub> show an absorption band centered at about 13 000 cm<sup>-1</sup>, which is assignable to d–d transitions of Cu<sup>II</sup> ions.<sup>[19]</sup> Interestingly, similar to the results recently reported for Cu/mordenite,<sup>[6a, 17]</sup> considerable development of the broad band centered at about 32 000 cm<sup>-1</sup> was observed for both Cu-AA/SBA and Cu-OA/SBA during the activation step (Figure 6a and Figure S7a in the Supporting Information). The  $\approx$ 32 000 cm<sup>-1</sup> absorption commonly appears in UV/Vis spectra

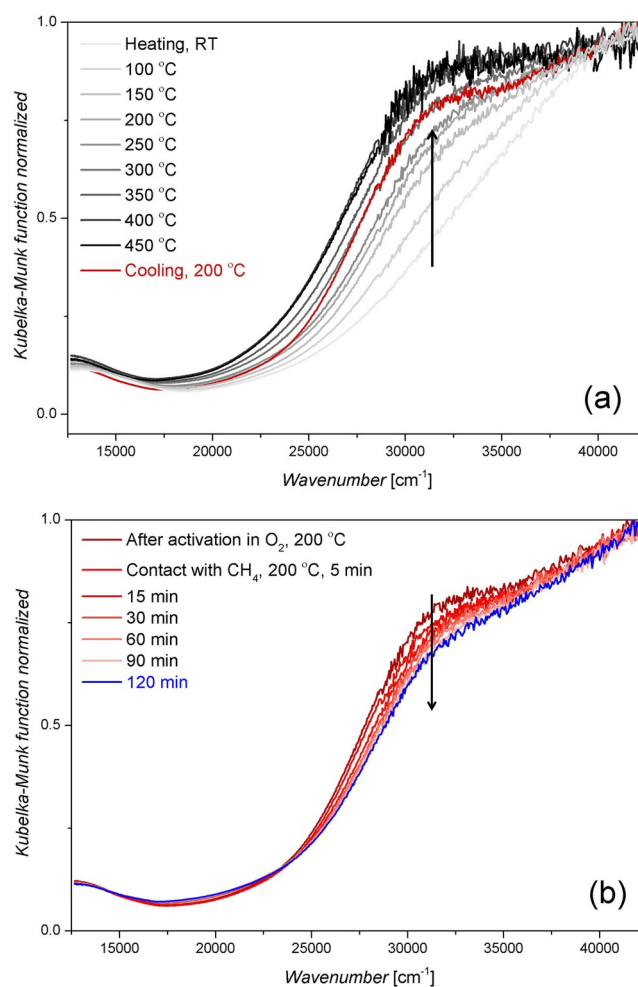


**Figure 6.** In situ UV/Vis spectra of Cu-AA/SBA after a) activation in O<sub>2</sub> and b) subsequent reaction with methane at 200 °C.

of Cu-based materials due to a charge transfer of O<sup>2-</sup>-Cu<sup>2+</sup> in CuO clusters.<sup>[19b, 20]</sup> This increasing feature observed in the UV/Vis spectra of CuO/SBA-15 materials is therefore assigned to activated CuO species deposited on SBA-15. As expected, in the next step of interaction with methane at 200 °C, the intensity of the 32 000 cm<sup>-1</sup> band started to decrease as methane was introduced to the sample (Figure 6b and Figure S7b in the Supporting Information), proving that the O<sub>2</sub>-activated CuO species are reactive towards methane. Importantly, MS analysis of the outlet stream during contact of the catalysts with methane revealed that water, which is typically generated on simple reduction of CuO in the presence of methane at higher temperatures (> 500 °C),<sup>[21]</sup> and methanol were not detected. Such a decrease in the 32 000 cm<sup>-1</sup> band intensity is therefore attributed to the activation of methane by CuO species at 200 °C, which yields the corresponding intermediate stabilized on the catalyst surface. However, the incomplete disappearance of the band after 2 h of interaction with methane, which is more significantly observed for Cu-OA/SBA, showed that the CuO species in the materials consist of both active and inactive sites. Together with the better production of methanol observed for Cu-AA/SBA, we therefore conclude that

well-dispersed small CuO nanoparticles located within the SBA-15 framework are more active for the methane-to-methanol conversion. Also, according to the in situ UV/Vis spectroscopic data of Cu/mordenite catalysts previously reported,<sup>[8b,c,17]</sup> it is suggested that Cu/zeolites may have different active sites including Cu oxo complexes stabilized by aluminum in the zeolite framework and small CuO nanoclusters.

In the second catalytic cycle, Cu-AA/SBA was able to produce a similar amount of methanol under identical conditions. Mass-spectrometric analysis during the on-line extraction of products with steam also showed similar results to those of the first run (Figure S4 in the Supporting Information). No considerable changes in structure and morphology of the used catalyst were found by TEM, XRD, and N<sub>2</sub>-sorption measurements. Therefore, it can be concluded that CuO species are stable in SBA-15 and can be reactivated after the first cycle.

## Conclusion

CuO/SBA-15 catalysts were prepared by wet impregnation and tested for the partial oxidation of methane to methanol in a three-step manner. This study showed that methanol is indeed produced on CuO/SBA-15. CuO species are able to activate methane to methoxyl species and stabilize them on the surface. Methanol or DME can be produced depending on the solvent used in the subsequent extraction step. The reactivity of CuO species on SBA-15 with methane was further demonstrated by in situ UV/Vis spectroscopic measurements, in which the intensity of the band centered at 32000 cm<sup>-1</sup> increased on O<sub>2</sub> activation and considerably decreased after contact with methane. The catalyst prepared from Cu(acac)<sub>2</sub> showed better catalytic performance than the Cu(OAc)<sub>2</sub>-based catalyst due to high dispersion of small/ultrasmall CuO species in the SBA-15 framework. However, further studies on supported CuO are needed to gain more insight into the size of the active clusters and subsequently to improve the performance. While the active sites for the hydroxylation of methane over Cu-exchanged zeolites is not fully defined, CuO/SBA-15 can be seen as a much simpler model catalyst. On the basis of this first demonstration, it might be worthwhile to test a variety of further porous silica or other materials as supports for Cu<sup>II</sup> for the challenging direct conversion of methane to methanol.

## Experimental Section

### Synthesis of materials

**Synthesis of SBA-15:** SBA-15 was prepared according to the procedure previously described.<sup>[9,22]</sup> Typically, P123 (EO<sub>20</sub>PO<sub>70</sub>EO<sub>20</sub>, M<sub>av</sub> = 5800, 2 g) was dissolved in a mixture of water (30 g) and 2 M hydrochloric acid (60 g) at 35 °C. After vigorous stirring for 1 h, tetraethoxysilane (4.2 g) was added. The resulting mixture was stirred at the same temperature for 24 h before aging in a Teflon-lined autoclave at 100 °C for another 24 h. The white solid was then collected by filtration, washed with water, dried at 105 °C for 12 h, and calcined under static air at 500 °C for 4 h.

**Synthesis of CuO/SBA-15:** Cu<sup>II</sup> acetylacetonate or Cu<sup>II</sup> acetate (0.45 mmol) was added to a mixture of SBA-15 (0.975 g) and abso-

lute ethanol (10 mL). After sonication for 10 min, slow evaporation of ethanol was conducted at 40 °C under vigorous stirring until a sludgelike phase was obtained. The product was dried at 80 °C for 12 h for complete removal of ethanol. The resulting powder was then pressed into pellets at 100 bar for 60 s, lightly ground, and sieved to a 200–400 μm diameter fraction. Calcination of the material was performed under static air at 550 °C for 4 h. The Cu content in the materials was determined by inductively coupled plasma optical emission spectrometry (ICP-OES).

**Synthesis of Cu/mordenite:** Cu/mordenite (2.58 wt.% of Cu) was prepared by intensively grinding Cu(acac)<sub>2</sub> (0.120 g) and NH<sub>4</sub>-form mordenite (Si/Al = 10, 0.975 g) in a mortar for 30 min.<sup>[8b,23]</sup> The resulting mixture was pressed and sieved to a 200–400 μm diameter fraction, after which Cu exchange was performed in situ during the activation step of the catalytic testing.

### Catalytic tests

A U-shaped quartz reactor (ID = 6 mm) was loaded with ≈ 0.6 g of the catalyst and placed in an oven. The catalyst bed was then treated at 550 °C (2 °C min<sup>-1</sup>) in a 50 mL<sub>STP</sub> min<sup>-1</sup> flow of O<sub>2</sub> for 8 h. After cooling to 60 °C (10 °C min<sup>-1</sup>), the excess of gas-phase O<sub>2</sub> was removed by a 50 mL<sub>STP</sub> min<sup>-1</sup> flow of N<sub>2</sub> for 5 min. A mixture of 5 mL<sub>STP</sub> min<sup>-1</sup> CH<sub>4</sub> and 30 mL<sub>STP</sub> min<sup>-1</sup> N<sub>2</sub> was then introduced to the reactor. The temperature was kept unchanged for 20 min, after which the catalyst was heated under the same flow to 200 °C at a rate of 5 °C min<sup>-1</sup>. After interaction of the catalyst with methane for 60 min, the methane-containing flow was switched off, and the catalyst bed was cooled to room temperature. For quantification of methanol, the resulting material was dispersed in 10 mL of water with vigorous stirring for 2 h. After centrifugation and filtration, the liquid phase was transferred to a volumetric flask, mixed with a predetermined volume of acetonitrile as internal standard, and analyzed with a gas chromatograph. Analysis of aqueous samples was performed with a Shimadzu GC 2010-Plus equipped with a flame ionization detector and a SUPELCOWAX 10 column (length = 30 m, ID = 0.53 mm, and film thickness = 1.00 μm). The oven was held at 60 °C for 8 min, and then heated at a rate of 30 °C min<sup>-1</sup> to 120 °C. Temperatures of inlet and detector were set constant at 180 °C.

In an experiment using the on-line extraction method, after interaction of the catalyst with methane for 60 min at 200 °C, the gas stream was switched off and the catalyst bed was cooled to room temperature. The outlet stream was connected to a quadrupole mass spectrometer (InProcess Instruments GAM 200). A 50 mL<sub>STP</sub> min<sup>-1</sup> flow of water-saturated He was introduced into the reactor at room temperature for 3 h, after which the reactor was heated at a rate of 1 °C min<sup>-1</sup> to 200 °C. This temperature was kept constant for another 3 h. The temperature of the gas-washing bottle was maintained at 25 °C during the whole experiment. The products were identified on the basis of the evolution of the signals at *m/z* = 31, 44, and 45 characteristic for methanol, CO<sub>2</sub>, and DME, respectively. The He signal (*m/z* = 4) was used as an internal standard to quantify DME and CO<sub>2</sub>.

### Characterization of materials

TEM and energy dispersive X-ray spectroscopy (EDX) analyses were performed with a TECNAI G<sup>2</sup>20 S-TWIN electron microscope operated at 200 kV, equipped with an EDAX EDX system [Si(Li) SUTW detector, energy resolution of 136 eV for Mn<sub>Kα</sub>]. For sample preparation, a drop of the material dispersed in ethanol was deposited on a carbon-coated nickel grid by evaporation.

N<sub>2</sub> sorption analysis was performed at 77 K by using a QUADRASORB SI instrument equipped with an automated surface area analyzer. Before analysis, samples were degassed at 150 °C for 12 h. Specific surface area was determined in the partial-pressure range of  $P/P_0 = 0.05\text{--}0.30$  by the BET method. Total pore volume was determined at  $P/P_0 = 0.99$ . Average pore width was calculated by the nonlocal DFT method.

Powder XRD was performed with a Bruker-AXS D8 Advanced diffractometer of DAVINCI equipped with a Lynx Eye detector design by using Cu<sub>Kα</sub> radiation ( $\lambda = 1.5418 \text{ \AA}$ ).

In situ UV/Vis diffuse-reflectance spectra were measured on a Cary 5000 spectrometer (Agilent) equipped with a Harrick Praying Mantis diffuse-reflectance attachment (DRP-P72) and a reaction chamber (HVC-VUV). The in situ cell was connected to a gas-delivery system for operation under flow conditions. Spectralon was used as a white standard. Spectra were taken in the 200–800 nm (50000–12500 cm<sup>-1</sup>) range with a step size of 1 nm every 3 min during the treatment of materials. Results were shown as the Kubelka–Munk function  $F(R)$ , which was calculated from the recorded reflectance data.

The in situ cell was heated to 550 °C at a rate of 10 °C min<sup>-1</sup> in a 50 mL<sub>STP</sub> min<sup>-1</sup> flow of O<sub>2</sub>. The sample was held at 550 °C for 60 min and then cooled to 200 °C at a rate of 10 °C min<sup>-1</sup> under the same flow. After O<sub>2</sub> removal by a 50 mL<sub>STP</sub> min<sup>-1</sup> flow of He for 5 min, a mixture of 15 mL<sub>STP</sub> min<sup>-1</sup> CH<sub>4</sub> and 15 mL<sub>STP</sub> min<sup>-1</sup> He was sent to the cell for 120 min at 200 °C.

H<sub>2</sub>-TPR experiments were conducted with a BELCAT II instrument (Version 0.4.5.13). Prior to measurements, Cu/mordenite materials were pretreated in a 40 mL<sub>STP</sub> min<sup>-1</sup> flow of O<sub>2</sub> at 550 °C for 3 h and then cooled to 40 °C. H<sub>2</sub>-TPR profiles of the samples were recorded in a 30 mL<sub>STP</sub> min<sup>-1</sup> flow of 5% H<sub>2</sub>/N<sub>2</sub> at a heating rate of 3 °C min<sup>-1</sup> up to 900 °C.

## Acknowledgements

This work is funded by the Cluster of Excellence Unifying Concepts in Catalysis (UniCat) and was conducted in the framework of the BasCat collaboration between BASF SE, FHI and TU Berlin. We acknowledge C. Eichenauer for N<sub>2</sub> sorption measurements, M. Unterweger for XRD measurements, and S. Selve and Dr. C. Göbel for TEM measurements. H.V.L. would like to thank Deutscher Akademischer Austauschdienst (DAAD) for funding his Ph.D. fellowship and M. König for a valuable discussion on UV/Vis analysis.

## Conflict of interest

The authors declare no conflict of interest.

**Keywords:** copper • heterogeneous catalysis • mesoporous materials • oxidation • supported catalysts

- [1] a) C. Hammond, S. Conrad, I. Hermans, *ChemSusChem* **2012**, *5*, 1668–1686; b) P. Schwach, X. Pan, X. Bao, *Chem. Rev.* **2017**, *117*, 8497–8520.
- [2] P. Tomkins, M. Ranocchiarì, J. A. van Bokhoven, *Acc. Chem. Res.* **2017**, *50*, 418–425.
- [3] a) A. I. Olivos-Suarez, À. Szécsényi, E. J. M. Hensen, J. Ruiz-Martínez, E. A. Pidko, J. Gascon, *ACS Catal.* **2016**, *6*, 2965–2981; b) B. Wang, S. Albarra-cín-Suazo, Y. Pagán-Torres, E. Nikolla, *Catal. Today* **2017**, *285*, 147–158; c) E. V. Kondratenko, T. Poppel, D. Seeburg, V. A. Kondratenko, N. Kalevaru, A. Martin, S. Wohlrab, *Catal. Sci. Technol.* **2017**, *7*, 366–381.
- [4] M. Ravi, M. Ranocchiarì, J. A. van Bokhoven, *Angew. Chem. Int. Ed.* **2017**, *56*, 16464–16483; *Angew. Chem.* **2017**, *129*, 16684–16704.
- [5] J. M. Bollinger Jr., *Nature* **2010**, *465*, 40–41.
- [6] a) S. Grundner, M. A. C. Markovits, G. Li, M. Tromp, E. A. Pidko, E. J. M. Hensen, A. Jentys, M. Sanchez-Sanchez, J. A. Lercher, *Nat. Commun.* **2015**, *6*, 7546; b) R. Banerjee, Y. Proshlyakov, J. D. Lipscomb, D. A. Proshlyakov, *Nature* **2015**, *518*, 431–434; c) R. Balasubramanian, S. M. Smith, S. Rawat, L. A. Yatsunyk, T. L. Stemmler, A. C. Rosenzweig, *Nature* **2010**, *465*, 115–119; d) S. I. Chan, S. S. F. Yu, *Acc. Chem. Res.* **2008**, *41*, 969–979.
- [7] a) M. H. Groothaert, P. J. Smeets, B. F. Sels, P. A. Jacobs, R. A. Schoonheydt, *J. Am. Chem. Soc.* **2005**, *127*, 1394–1395; b) E. V. Starokon, M. V. Parfenov, L. V. Pirutko, S. I. Abornev, G. I. Panov, *J. Phys. Chem. C* **2011**, *115*, 2155–2161; c) N. V. Beznis, A. N. C. van Laak, B. M. Weckhuysen, J. H. Bitter, *Microporous Mesoporous Mater.* **2011**, *138*, 176–183; d) V. L. Sushkevich, D. Palagin, M. Ranocchiarì, J. A. van Bokhoven, *Science* **2017**, *356*, 523–527.
- [8] a) K. Narsimhan, K. Iyoki, K. Dinh, Y. Román-Leshkov, *ACS Cent. Sci.* **2016**, *2*, 424–429; b) H. V. Le, S. Parishan, A. Sagaltchik, C. Göbel, C. Schlesiger, W. Malzer, A. Trunschke, R. Schomäcker, A. Thomas, *ACS Catal.* **2017**, *7*, 1403–1412; c) P. Tomkins, A. Mansouri, S. E. Bozbag, F. Krumeich, M. B. Park, E. M. C. Alayon, M. Ranocchiarì, J. A. van Bokhoven, *Angew. Chem. Int. Ed.* **2016**, *55*, 5467–5471; *Angew. Chem.* **2016**, *128*, 5557–5561; d) P. Vanelderden, B. E. R. Snyder, M.-L. Tsai, R. G. Hadt, J. Vancauwenbergh, O. Coussens, R. A. Schoonheydt, B. F. Sels, E. I. Solomon, *J. Am. Chem. Soc.* **2015**, *137*, 6383–6392; e) D. Palagin, A. J. Knorpp, A. B. Pinar, M. Ranocchiarì, J. A. van Bokhoven, *Nanoscale* **2017**, *9*, 1144–1153; f) G. Li, P. Vassilev, M. Sanchez-Sanchez, J. A. Lercher, E. J. M. Hensen, E. A. Pidko, *J. Catal.* **2016**, *338*, 305–312.
- [9] J. Zhu, K. Kailasam, X. Xie, R. Schomaecker, A. Thomas, *Chem. Mater.* **2011**, *23*, 2062–2067.
- [10] Q. Yang, F. Gu, Y. Tang, H. Zhang, Q. Liu, Z. Zhong, F. Su, *RSC Adv.* **2015**, *5*, 26815–26822.
- [11] D. K. Pappas, E. Borfecchia, M. Dyballa, I. A. Pankin, K. A. Lomachenko, A. Martini, M. Signorile, S. Teketel, B. Arstad, G. Berlier, C. Lamberti, S. Bordiga, U. Olsbye, K. P. Lillerud, S. Svelle, P. Beato, *J. Am. Chem. Soc.* **2017**, *139*, 14961–14975.
- [12] E. M. C. Alayon, M. Nachtegaal, A. Bodi, J. A. van Bokhoven, *ACS Catal.* **2014**, *4*, 16–22.
- [13] R. A. Himes, K. D. Karlin, *Proc. Natl. Acad. Sci. USA* **2009**, *106*, 18877–18878.
- [14] a) M. H. Mahyuddin, A. Staykov, Y. Shiota, M. Miyanishi, K. Yoshizawa, *ACS Catal.* **2017**, *7*, 3741–3751; b) P. J. Smeets, M. H. Groothaert, R. A. Schoonheydt, *Catal. Today* **2005**, *110*, 303–309; c) M. H. Mahyuddin, A. Staykov, Y. Shiota, K. Yoshizawa, *ACS Catal.* **2016**, *6*, 8321–8331.
- [15] P. Vanelderden, R. G. Hadt, P. J. Smeets, E. I. Solomon, R. A. Schoonheydt, B. F. Sels, *J. Catal.* **2011**, *284*, 157–164.
- [16] J. S. Woertink, P. J. Smeets, M. H. Groothaert, M. A. Vance, B. F. Sels, R. A. Schoonheydt, E. I. Solomon, *Proc. Natl. Acad. Sci. USA* **2009**, *106*, 18908–18913.
- [17] Y. Kim, T. Y. Kim, H. Lee, J. Yi, *Chem. Commun.* **2017**, *53*, 4116–4119.
- [18] A. R. Kulkarni, Z.-J. Zhao, S. Siahrostami, J. K. Nørskov, F. Studt, *ACS Catal.* **2016**, *6*, 6531–6536.
- [19] a) M. J. Wulfers, S. Teketel, B. Ipek, R. F. Lobo, *Chem. Commun.* **2015**, *51*, 4447–4450; b) C.-H. Liu, N.-C. Lai, J.-F. Lee, C.-S. Chen, C.-M. Yang, *J. Catal.* **2014**, *316*, 231–239; c) K. Narsimhan, V. K. Michaelis, G. Mathies, W. R. Gunther, R. G. Griffin, Y. Román-Leshkov, *J. Am. Chem. Soc.* **2015**, *137*, 1825–1832; d) P. Vanelderden, J. Vancauwenbergh, M. L. Tsai, R. G. Hadt, E. I. Solomon, R. A. Schoonheydt, B. F. Sels, *ChemPhysChem* **2014**, *15*, 91–99.
- [20] a) M. C. N. A. de Carvalho, F. B. Passos, M. Schmal, *Appl. Catal. A* **2000**, *193*, 265–276; b) Z. R. Ismagilov, S. A. Yashnik, V. F. Anufrienko, T. V. Larina, N. T. Vasenin, N. N. Bulgakov, S. V. Vosel, L. T. Tsykoza, *Appl. Surf. Sci.* **2004**, *226*, 88–93; c) S. L. Nauert, F. Schax, C. Limberg, J. M. Notestein, *J. Catal.* **2016**, *341*, 180–190.
- [21] a) E. R. Monazam, R. Siriwardane, R. W. Breault, H. Tian, L. J. Shadle, G. Richards, S. Carpenter, *Energy Fuels* **2012**, *26*, 2779–2785; b) J. Adánez, P. Gayán, J. Celaya, L. F. de Diego, F. García-Labiano, A. Abad, *Ind. Eng.*

- Chem. Res.* **2006**, *45*, 6075–6080; c) N. Guilhaume, M. Primet, *J. Chem. Soc. Faraday Trans.* **1994**, *90*, 1541–1545.
- [22] D. Zhao, J. Feng, Q. Huo, N. Melosh, G. H. Fredrickson, B. F. Chmelka, G. D. Stucky, *Science* **1998**, *279*, 548–552.
- [23] C. Hammond, M. M. Forde, M. H. Ab Rahim, A. Thetford, Q. He, R. L. Jenkins, N. Dimitratos, J. A. Lopez-Sanchez, N. F. Dummer, D. M. Murphy, A. F. Carley, S. H. Taylor, D. J. Willock, E. E. Stangland, J. Kang, H. Hagen,

C. J. Kiely, G. J. Hutchings, *Angew. Chem. Int. Ed.* **2012**, *51*, 5129–5133;  
*Angew. Chem.* **2012**, *124*, 5219–5223.

---

Manuscript received: March 6, 2018  
Revised manuscript received: May 21, 2018  
Accepted manuscript online: May 26, 2018  
Version of record online: July 23, 2018

# CHEMISTRY

## A **European** Journal

### Supporting Information

#### **Stepwise Methane-to-Methanol Conversion on CuO/SBA-15**

Ha V. Le,<sup>[a]</sup> Samira Parishan,<sup>[b]</sup> Anton Sagaltchik,<sup>[c]</sup> Hamideh Ahi,<sup>[c, d]</sup> Annette Trunschke,<sup>[d]</sup>  
Reinhard Schomäcker,<sup>[b]</sup> and Arne Thomas\*<sup>[a]</sup>

chem\_201801135\_sm\_miscellaneous\_information.pdf

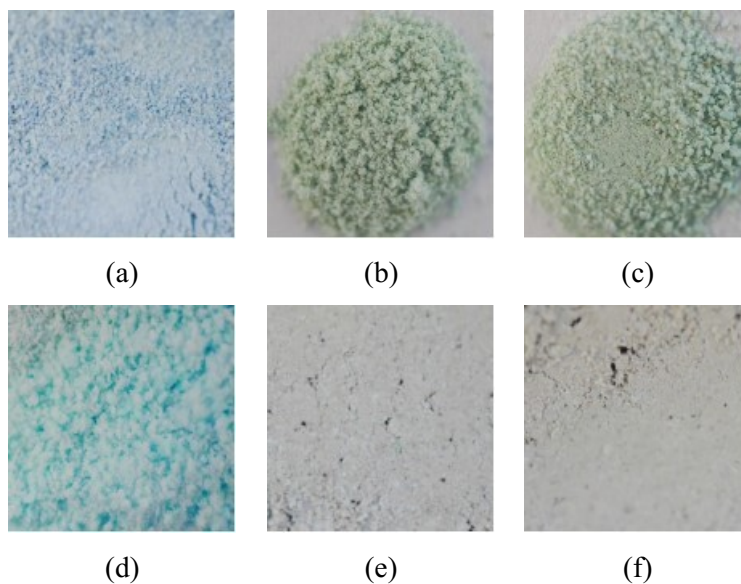


**Figure S1.** Photographs of Cu-loaded SBA-15 samples, Cu-AA/SBA (a) before calcination, (b) after calcination, and (c) after the first catalyst cycle; Cu-OA-SBA (d) before calcination, (e) after calcination, and (f) after the first catalyst cycle.

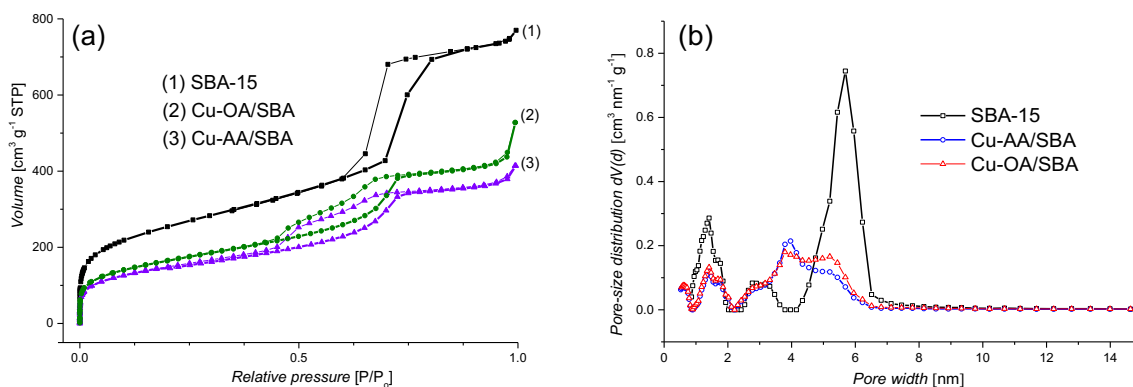


**Figure S2.** (a)  $N_2$ -sorption isotherms and (b) pore size distribution of as-synthesized SBA-15, calcined Cu-AA/SBA, and calcined Cu-AC/SBA.

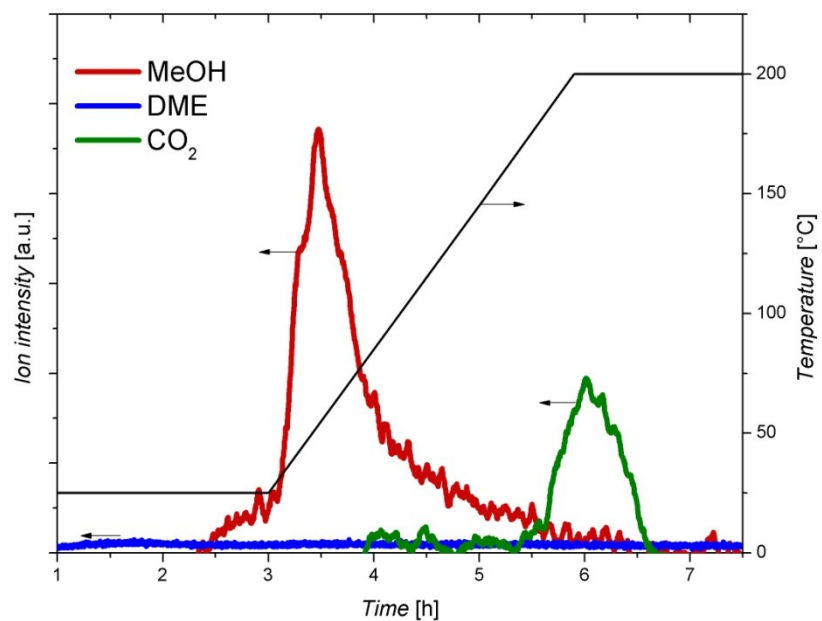


**Figure S3.** Mass-spectral signal of the products in the online extraction of Cu-OA/SBA with water.

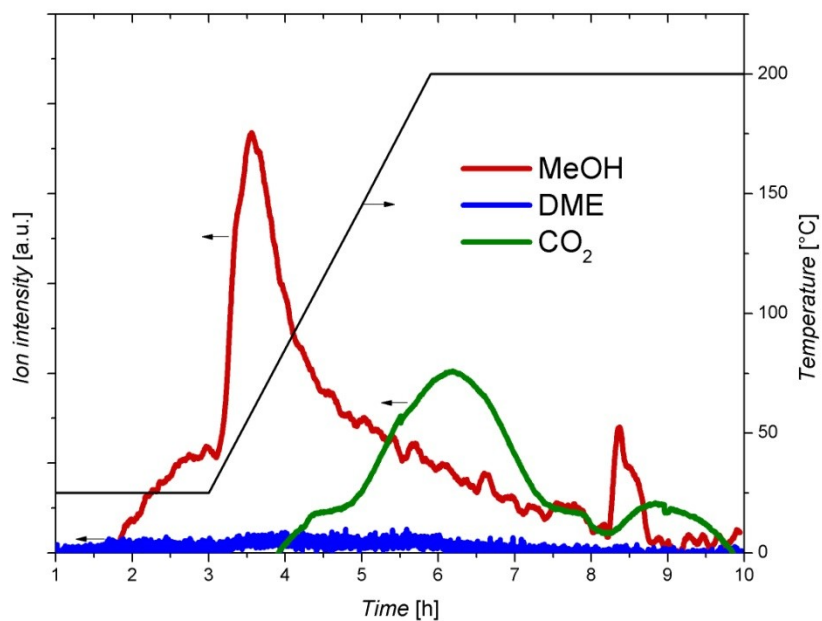


**Figure S4.** Mass spectral signal of the products extracted from Cu-AA/SBA by online extraction with water in the second catalytic cycle.

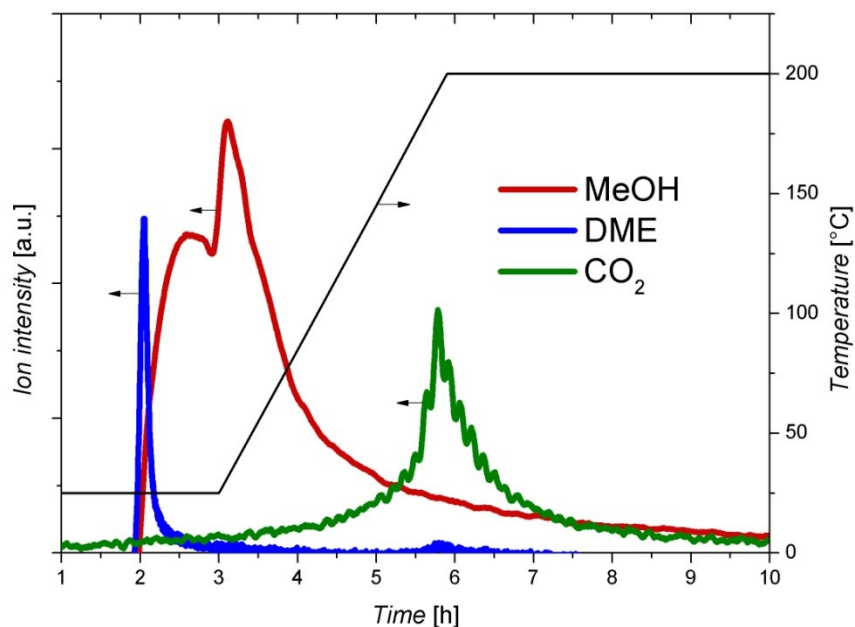


**Figure S5.** Mass-spectral signal of the products in the online extraction of Cu/mordenite with water.

**Table S1.** Catalytic performance of Cu/Mor.

Cu loading (wt.%)	Product yield ( $\mu\text{mol g}_{\text{cat}}^{-1}$ )			Oxidized methane <sup>c</sup> ( $\mu\text{mol g}_{\text{cat}}^{-1}$ )	Selectivity to MeOH & DME <sup>e</sup> (%)
	MeOH <sup>a</sup>	DME <sup>b</sup>	CO <sub>2</sub> <sup>b</sup>		
2.58	56.0	1.6	9.0	68.2	87.7

<sup>a</sup>Methanol was analyzed by GC after off-line extraction with liquid water.  
<sup>b</sup>Gas-phase products were analyzed by MS during online extraction with steam.  
<sup>c</sup>Amount of oxidized methane was = moles(MeOH) + 2\*moles(DME) + moles(CO<sub>2</sub>).  
<sup>d</sup>Turnover number (TON) = moles(oxidized methane)/moles(Cu).  
<sup>e</sup>Selectivity to MeOH and DME = [moles(MeOH) + 2\*moles(DME)]/ moles(reacted CH<sub>4</sub>).

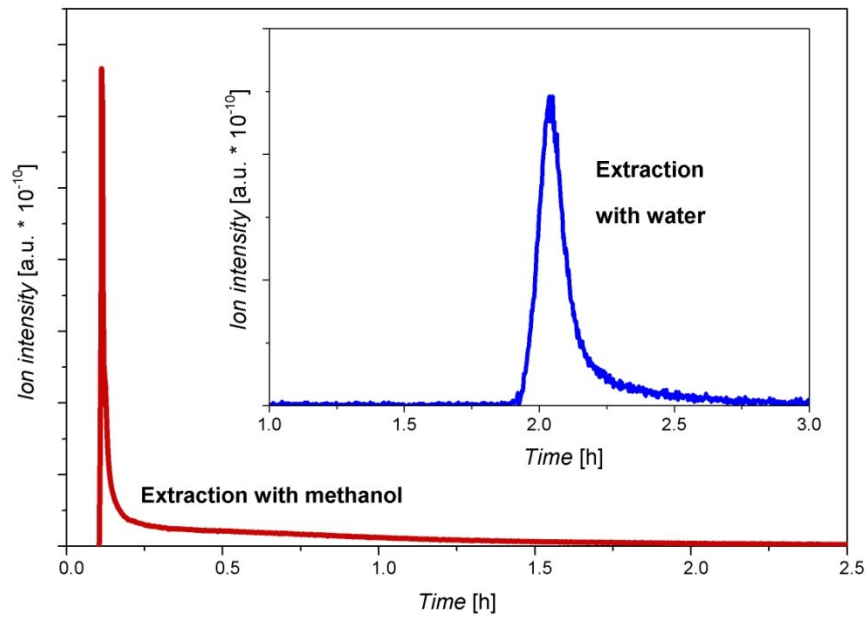


**Figure S6.** Comparison of mass-spectral signals of DME released from Cu/mordenite in the online extraction stage at room temperature using different solvents.

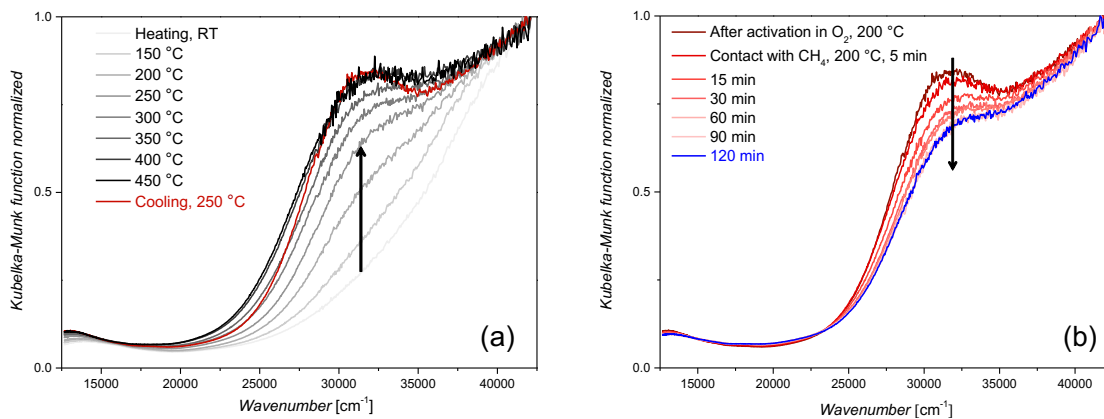


**Figure S7.** *In situ* UV-vis spectra of Cu-OA/SBA (a) after activation in  $O_2$  and (b) subsequent reaction with methane at  $200^\circ C$ .

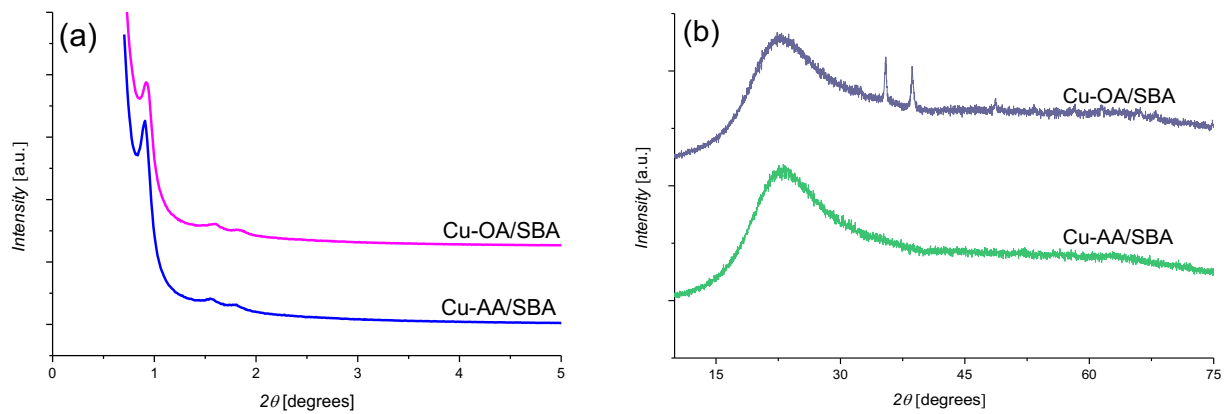


**Figure S8.** (a) Small-angle and (b) wide-angle XRD patterns of Cu-AA/SBA and Cu-OA/SBA after the first cycle.

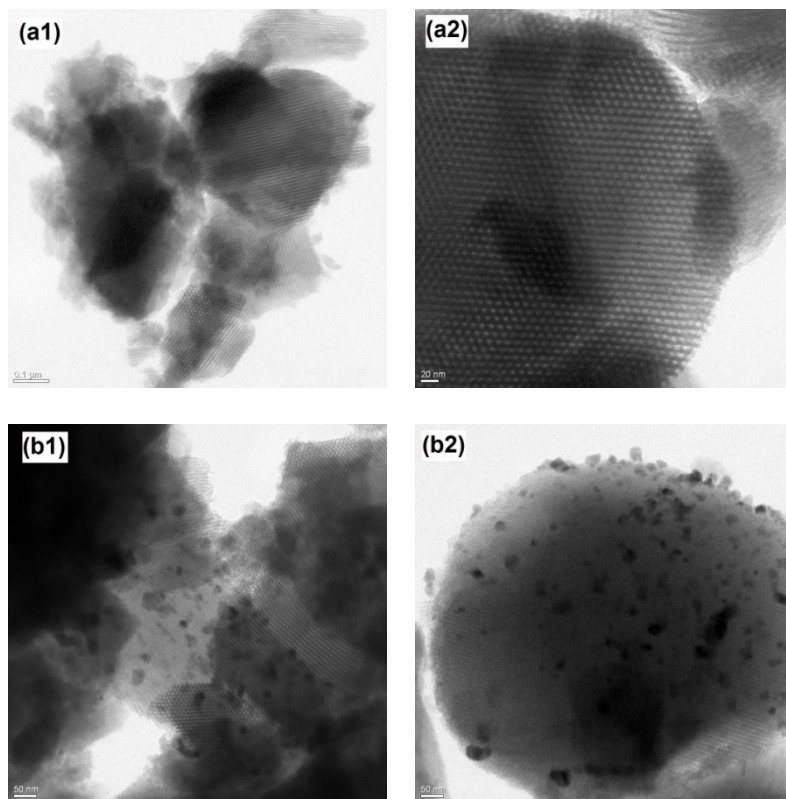


**Figure S9.** TEM images of (a1, a2) Cu-AA/SBA and (b1, b2) Cu-OA/SBA after the first catalytic cycle.

**Table S2.** Textural properties of CuO/SBA-15 catalysts after the first use.

Sample	SA <sup>a</sup> (m <sup>2</sup> g <sup>-1</sup> )	V <sub>meso</sub> <sup>b</sup> (cm <sup>3</sup> g <sup>-1</sup> )	V <sub>micro</sub> <sup>b</sup> (cm <sup>3</sup> g <sup>-1</sup> )	V <sub>total</sub> <sup>c</sup> (cm <sup>3</sup> g <sup>-1</sup> )
Cu-OA/SBA	647.8	0.58	0.12	0.88
Cu-AA/SBA	515.6	0.49	0.09	0.72

<sup>a</sup> SA = surface area calculated by the BET method.  
<sup>b</sup> V<sub>meso</sub> = mesoporous volume, and V<sub>micro</sub> = microporous volume calculated by the NLDFIT method.  
<sup>c</sup> V<sub>total</sub> = total pore volume calculated at p/p<sub>0</sub> = 0.99.

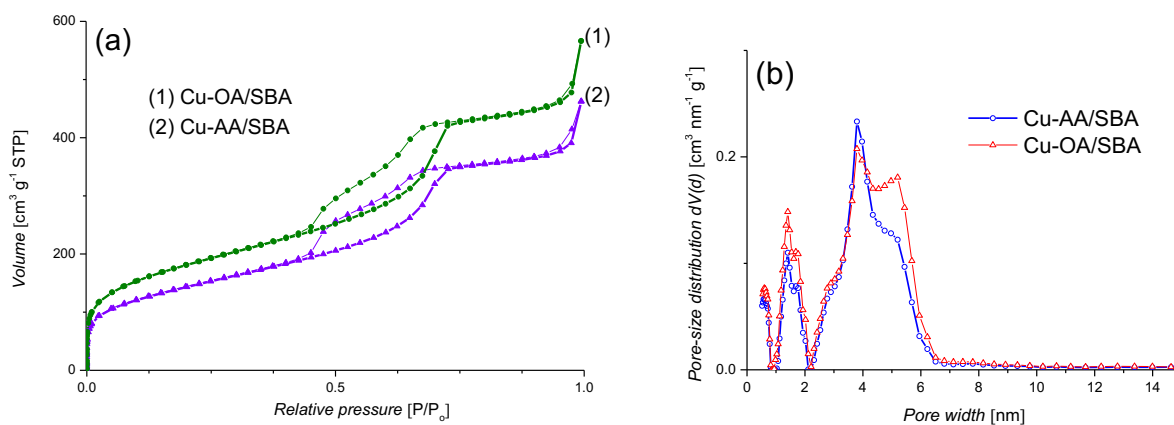


**Figure S10.** (a) N<sub>2</sub>-sorption isotherms and (b) pore size distribution of calcined Cu-AA/SBA and calcined Cu-OC/SBA after the first use.